11th International Conference on "Energy, Sustainability and Climate Crisis" ESCC 2024

Book of Proceedings

Corfu, Greece,
August 26 – 30, 2024

ESCC

ISSN 3057-4269

Book of Proceedings

ESCC 2024

ISBN: 978-618-5765-04-0
ISSN 3057-4269

11th International Conference on "Energy, Sustainability and Climate Crisis"
ESCC 2024

Edited by: Georgios K.D. Saharidis

Publication
Department of Mechanical Engineering, University of Thessaly

ISBN 978-618-5765-04-0

ISSN 3057-4269

Text editing
Georgios K.D. Saharidis

Layout & Book design
Eleousa Zygouri

Table of Contents

ISBN: 978-618-5765-04-0
ISSN 3057-4269

ISBN: 978-618-5765-04-0
ISSN 3057-4269

A Secure and Privacy Preservation Framework for Energy Data Collection and Sharing

Konstantinos Tsatsakis
Suite5 Data Intelligence Solutions LTD
Limassol, Cyprus
kostas@suite5.eu

***Abstract*— Electrical power and energy systems are undergoing an unprecedented transformation, demanding urgent upgrades to make them more reliable, resilient and secure. In order to develop holistic risk management systems for the energy systems, there is a need for improving collection and homogeneous representation of data coming from legacy equipment and modern communication devices, i.e. IoT and DERs. The scope of this paper is to establish a framework for data collection mechanisms that should be developed in the frame of an energy data platform towards establishing a secure and trustful data sharing framework for all energy data value chain stakeholders. The proposed framework is under demonstration and evaluation in 3 demo sites around Europe and the preliminary evaluation actions are reported in this paper.**

Keywords—data sharing, privacy, security, IoT/DER, SCADA, IEC 61850

INTRODUCTION

Conventional power systems primarily rely on a handful of centralized large power plants to supply the majority of electricity to consumers. However, this model, characterized by one-way power distribution from major generators to consumers, is evolving. The imperative to reduce carbon emissions and combat climate change has spurred the adoption of environmentally friendly methods for electricity generation (such as wind turbines, solar panels), transportation (electric vehicles), and space heating (heat pumps). The emergence of distributed generation, the introduction of new energy demands, and the rise of prosumers are not only reshaping the grid's framework but also altering how power adequacy and supply security are assessed and managed. As the power system incorporates a growing array of new devices, components, and stakeholders, it becomes more intricate and challenging to analyse.

Simultaneously, the significance of data within the power system is escalating. The installation of a greater number of sensors and smart meters is yielding a wealth of data. This environment necessitates leveraging data for asset management, as decisions increasingly require support from data-driven methodologies. In the transition towards "smart grids," data collection and management assume a pivotal role. Consequently, investigating how data collection and processing can be enhanced with security and privacy is crucial for maintaining satisfactory cost and supply security levels on the grid sector.

For legacy grid level systems, various open-source approaches exist for data aggregation over SCADA, Distributed Control System (DCS) and Integrated Control Systems (ICS), whereas for modern communication devices at decentralized grid level (DER/IoT devices) they are mostly based on solutions collecting data over IP networks. A key issue for data handling has to do with privacy/security-preserving data computation and privacy/security-preserving data aggregation. Among other approaches encryption over data, pseudonym technology secure data storage, especially considering the limited storage capabilities of IoT and edge devices, should be considered. In the following, in Section II the elicitation of the data collection methods from grid level systems is provided while in section III the analysis is performed for DER/IoT devices. Considering privacy/security aspects that have to be considered in the field of data collection and sharing, in Section IV the relevant data handling methods are reported while in Section V the same analysis is provided for DER/IoT assets. In section VI, the application of the proposed framework in real life is provided focusing on the demonstration characteristics and the preliminary evaluation results.

DATA COLLECTION FROM DSO LEVEL ASSETS

In this section a reference to the key standardization is provided with focus on data ingestion from substation systems. The analysis is covering data integration from SCADA and DCS (mainly PMU and IED devices) devices to ensure the prompt data collection from grid level assets.

With a history of proprietary system components from specialized vendors, the trend today is to rely increasingly on off-the-shelf products, both for hardware and for software, when developing and upgrading power system control and operation systems with focus on the use of standard communication interfaces to ensure interoperability between components from different vendors. Legacy protocols, such as Modbus and the proprietary protocols of equipment vendors, are slowly replaced by protocols standardized in the last decade for RTU/IED communication like DNP3[1], 60870-5 for data acquisition and control [3], or IEEE C37.118-2005 [4] for PMU data. Moreover, communication and automation technology have changed at a faster pace in the past decade, especially with the fast deployment of substation-oriented protocols, like IEC 61850 [2]. In the recent years, a major shift towards the IEC 61850 standard has been considered and the following key features have been adopted widely as part of the specifications of the model:

- IEC 61850 is a substation object-oriented protocol that standardizes the signals as per electrical terminologies and primary equipment into the software world. The IEC working group has incorporated the Generic Object Models for Substation and Feeder Equipment concept into its standard, which is used to present substation data into objects or blocks.
- IEC 61850 provides signal addressing in the form of intuitive names that are called logical nodes.
- IEC 61850 governs a unique methodology of peer-to-peer communication to send highspeed signals across the network, which is called Generic Object-Oriented Substation Event (GOOSE) messaging. Comparing hardwired electrical cabling between different devices, GOOSE messaging reduces cost and time to send high-speed signals for intertripping,

ISBN: 978-618-5765-04-0
ISSN 3057-4269

blocking, etc., over the Ethernet network and still maintains the same performance as required by the protection application.

- Part of the IEC 61850 standard also provides a secure and reliable method to transfer files from one device to another over the same Ethernet medium using MMS file transfer. IEDs, like protection relays, implement MMS file transfer to transfer data as files and to provide the hierarchal structure for those files to manage data. These files may include relay settings, Configured IED Description (CID) files and fault-event files to be collected from IEDs using MMS file transfer.

With all the digital information available through substation IEDs, operators in the control centre can use the IEC 61850 data received over GOOSE messages to analyse and troubleshoot the fault in the holistic power system view. It is evident, that the standardization efforts today focus mainly on power system models like the Common Information Model (CIM) with the goal to ease the exchange of engineering data between and within utilities in a large variety of applications.

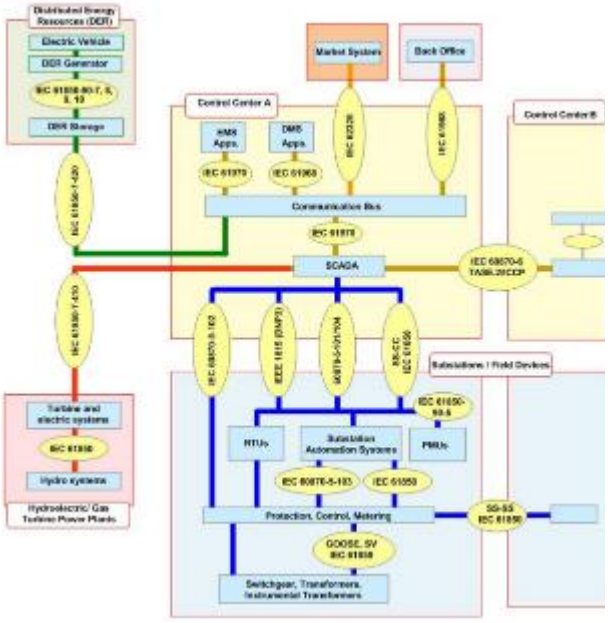

Figure 1: IEC standardization landscape

DATA COLLECTION FROM DER AND IOT DEVICES

In the last decade, it is evident a mass penetration of new DER components at low/medium voltage grid level. Local generation, EV charging points, smart home/building automation systems are massively installed and thus there is an increasing demand for data integration and further incorporation of new assets in new business schemas and use cases. The data collection process from these new types of DERs is an important task, and a series of standards and guidelines (both at communication and semantic level) have been defined in order to ensure the smooth data integration.

There is a series of relevant standards in the field addressing the integration of small-scale DER assets but the IEEE 1547 (Standard for Interconnecting Distributed Resources with Electric Power Systems) is the standard of the Institute of Electrical and Electronics Engineers meant to provide a set of criteria and requirements for the interconnection of distributed energy resources into the power grid. The standard is intended to be universally adoptable, technology-neutral, and cover distributed resources as large as 10 MVA. Based on the standard specifications, all DER—such as photovoltaic (PV) inverters, energy storage systems (ESSs), and synchronous generators—in those jurisdictions must include a standardized SunSpec Modbus [5], IEEE 2030.5 [6], or IEEE 1815 [7] (DNP3) communication interface. The SunSpec Modbus is the most common instantiation of the Modbus communication protocol and more specifically the instance as specified by SunSpec Alliance, named as the SunSpec protocol.

Apart from the inverter based DERs (addressing small generation/ battery systems), the EV charging points are also considered as a significant DER asset of the electricity grid. Towards this direction, the OCPP protocol [8] is (among other approaches) the industry standard for the integration of EV CP/ EVSE data to external systems. The details of OCPP are provided in brief. Essentially this protocol has been designed to enable the communication between an EVSE and a CPO. In addition to OCPP, IEC 63110[9] is rather new standard to provide communication links for the conductive charging station and electric vehicles. IEC 63110 is also known as the protocol for the Management of Electric Vehicles charging and discharging infrastructures. The IEC 63110 is responsible for a higher and swift level of interoperability in the front-end communication and signal distribution between smart grid infrastructures such as EVs and the conductive charging spots/stations. Apart from the communication protocol, there is a need for a unified semantic data model - a reference ontology (protocol-independent semantic layer by explicitly specifying recurring core concepts in the smart appliances' domain, the relationships between these concepts, and mappings to other concepts used by different assets/standards/models). Currently, the SAREF ontology [10] is a shared model of consensus aiming to facilitate the matching of existing assets (standards, protocols, etc.) in the smart appliances' era. It provides building blocks that allow separation/ recombination of different parts of the ontology to cover different needs. The SAREF model is currently being extended to add semantic models for data associated with multiple domains ranging from smart cities, industry and manufacturing, smart agriculture and the food chain, water, automotive, eHealth/ aging well and wearables.

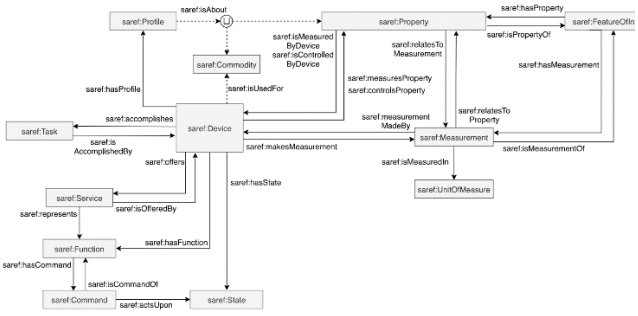

Figure 2: SAREF model overview

In particular, a multitude of different domains are currently on the roadmap turning SAREF into "Smart Anything REFerence ontology", which enables better integration of semantic data from various vertical domains in the IoT arena. On the other hand, there are also numerous market-based implementations available to support the end-to-end

ISBN: 978-618-5765-04-0
ISSN 3057-4269

integration of smart building assets. The main interest is about the different means of IoT devices communication with cloud platforms taking into account the type of devices, network conditions, and specific requirements of the IoT application [11]; data collection methods that are relevant in the field are MQTT, CoAP, AMQP, DDS, LwM2M etc.

PRIVACY AND SECURITY ON DSO ASSETS DATA SHARING

In relation to the standardization analysis for data collection at grid level as defined in Section II, a series of standards have been defined under IEC 62351 family [12] in order to cover the security related aspects specifically for the IEC 60870-5 series, the IEC 60870-6 series, the IEC 61850 series, the IEC 61970 series, and the IEC 61968 series. An overview of the different standards that are part of the62351 family is provided in Figure 3.

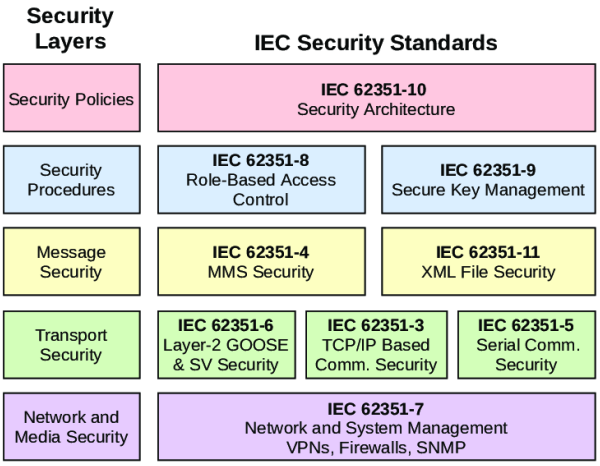

Figure 3: IEC 62351 security layers overview

The security measures specified in IEC 62351 address various aspects of security, including:

- Access Control: IEC 62351 defines access control mechanisms to restrict unauthorized access to components and data. This involves user authentication, authorization, and role-based access control (RBAC) and is related mainly to the privacy of data. More details presented below.
- Data Security: IEC 62351 defines data security measures to protect sensitive IACS data from unauthorized access, modification, or disclosure. This includes data encryption, data integrity protection, and data loss prevention (DLP).
- Cryptographic Key Management: IEC 62351 outlines secure key management practices to protect cryptographic keys used for encryption and digital signatures. This includes key generation, storage, distribution, usage, and revocation.
- Security Management: IEC 62351 provides a framework for implementing security management practices, including risk assessment, incident response, and continuous monitoring. It also emphasizes the importance of training and awareness programs for the relevant personnel.
- Network Security: IEC 62351 outlines network security measures to protect IACS networks from unauthorized access, data interception, and Denial-of-Service (DoS) attacks. This includes network segmentation, firewalls, intrusion detection systems (IDS), and intrusion prevention systems (IPS). Also, IEC 62351 recommends using secure communication protocols, such as Transport Layer Security (TLS) or IPsec, to encrypt and authenticate data transmitted over networks.
- Device Security: IEC 62351 addresses device security by specifying secure device configurations, secure firmware updates, and secure communication protocols. It also promotes device hardening techniques to minimize vulnerabilities.

Special remark in this analysis in 62351-4 [13] and 62351-6 [14] as the relevant with IEC 61850 related assets. The key details covered within both standards are about:

- Security Mechanisms: defining various security measures and mechanisms to ensure the integrity, authenticity, and confidentiality of communication between different devices and components within power systems.
- Message Integrity: Ensuring that data transmitted between devices remains unchanged and uncorrupted during transmission.
- Authentication Mechanisms: Specifying methods to authenticate the identity of devices and users participating in the communication process, preventing unauthorized access.
- Network and System Architecture Security: Recommendations for designing secure network and system architectures for power systems.
- Protection Against Cyber Threats: Addresses various cyber threats such as denial-of-service attacks, man-in-the-middle attacks, and other potential vulnerabilities.
- Encryption: Addressing encryption techniques to protect sensitive data from being accessed or intercepted by unauthorized entities.
- Digital Signatures: Describing how to use digital signatures to verify the authenticity and origin of transmitted data.

In relation to data encryption and signatures use, the cryptographic algorithms specified in IEC 62351 vary depending on the specific part of the standard, as the suite encompasses a range of security mechanisms for industrial automation and control systems. Namely for the standards elicitated above we have the following encryption algorithms:

- AES-CCM: Symmetric-key encryption algorithm for MMS messages. NIST SP 800-38, Recommendation for Block Cipher Modes of Operation: Advanced Encryption Standard (AES)
- ECDSA: Asymmetric-key signature algorithm for MMS messages: FIPS PUB 186-4, Digital Signature Standard (DSS)
- HMAC-SHA-256: Message authentication code (MAC) algorithm for MMS messages: FIPS PUB 198-A, The Keyed-Hash Message Authentication Code (HMAC)
- RSA: Asymmetric-key encryption and signature algorithm for MMS messages and IEC 62351-9 certificates. PKCS #1, RSA Cryptography Standard
- SHA-256: Hash function for generating message digests: FIPS PUB 180-4, Secure Hash Standard (SHS)

Apart from secure data communication, the secure data storage is a crucial aspect of cybersecurity, especially in

ISBN: 978-618-5765-04-0
ISSN 3057-4269

sensitive grid assets related information. IEC 62351 addresses secure data storage through various measures to protect the confidentiality, integrity, and availability of critical data.

- Use of secure hardware devices: IEC 62351 recommends using secure hardware devices, such as tamper-resistant modules (TRMs) [16] that provide a secure foundation for various security-related functions in computing devices. TPMs are typically integrated into the motherboard of a computer or added as a separate module in order to serve the different security functions such as: Secure Storage, Secure Boot, Attestation, Key Generation and Management. Secure Communication, Device Identity etc.. TPMs play a crucial role in enhancing the overall security of computing devices and are commonly used in enterprise environments, secure systems, and platforms where data protection and system integrity are paramount.
- Encrypt data at rest: IEC 62351 mandates encrypting sensitive data at rest, even if it is stored on secure hardware devices.
- Control access to storage devices: IEC 62351 emphasizes the importance of controlling access to storage devices through physical security measures, such as access control lists (ACLs) and multi-factor authentication (MFA).
- Data storage minimization: IEC 62351 recommends minimizing the amount of sensitive data stored on devices and systems.
- Implement data classification: IEC 62351 suggests classifying data based on its sensitivity level to determine appropriate storage and access controls.
- Regularly back up data: IEC 62351 mandates regularly backing up sensitive data to prevent data loss due to hardware failures, cyberattacks, or other incidents.

On the other hand, data access control [15] (as also mentioned above) is a critical cybersecurity measure: to restrict unauthorized access to sensitive information, minimize the risk of data breaches and leaks, Ensure data integrity and availability. IEC 62351 emphasizes the importance of data access control and outlines various techniques to implement it effectively in a dedicated 62351-8 [15] standard, namely:

- User authentication: Verify the identity of users attempting to access data using strong authentication mechanisms, such as passwords, multi-factor authentication (MFA), or digital certificates.
- Authorization: Grant users access to specific data based on their roles and responsibilities, ensuring that only authorized individuals can access the information they need.
- Access control lists (ACLs): Define access rules for specific users or groups, explicitly granting or denying access to particular data resources.
- Role-based access control (RBAC): Assign access permissions based on user roles, simplifying access management and ensuring that users have access to the data they need to perform their tasks.
- Attribute-based access control (ABAC): Grant access based on attributes of the user, the data, or the current context, providing more granular control over access decisions.

The aforementioned key principles as defined in the relevant regulation are also considered as best practices for enhancing data security and privacy at grid level.

PRIVACY AND SECURITY ON DER /IOT DATA SHARING

Similar to the review of the different security/privacy preservation mechanisms that are considered for network level assets, the same analysis applies for the data collection methods defined for IoT/ DER Level. Starting with the SunSpec/Modbus model, a series of specifications ([17][18][19]) have been defined to support security on data exchange and a brief overview of them is provided:

- TLS 1.2 encryption: This ensures that DER data is encrypted while in transit, protecting it from interception and eavesdropping.
- Message authentication code (MAC): This provides data integrity verification, ensuring that DER data has not been tampered with during transmission. The SunSpec Secure Modbus protocol uses the HMAC-SHA-256 algorithm to generate a MAC for enhancing the transfer of data.
- Data anonymization: DER data can be anonymized to remove personally identifiable information (PII).
- Client authentication: This verifies the identity of the client device requesting data from the DER device, preventing unauthorized access.

The SunSpec Secure RESTful Web Service provides a standardized interface for secure data exchange between DER devices and other applications. This interface supports HTTPS to ensure that DER data is encrypted while in transit using the HTTPS protocol and JSON Web Tokens (JWTs) used to authenticate clients and authorize access to DER data. In addition, Role-based access control (RBAC) is supported by SunSpec specifications to restrict access to DER data based on the role of the user or application.

A very important standard in the field as named above is OCPP for EV Charging points management. Special emphasis is delivered also on security related aspects as specified in OCPP reference documentation. Based on these considerations, OCPP security is based on TLS [20]. In the TLS with Basic Authentication profile, the communication channel is secured using Transport Layer Security (TLS). The CSMS authenticates itself using a TLS server certificate. The Charging Stations authenticate themselves using HTTP Basic Authentication. In the TLS with Client-Side Certificates profile, the communication channel is secured using Transport Layer Security (TLS). Both the Charging Station and CSMS authenticate themselves using certificates. In the field of users' authorization, OCPP protocol describes all the authorization-related functionalities at EV charging level; it contains different ways of authorizing a user, online and/or offline. In terms of data privacy, similar principles are considered in data handling with focus on purpose Specification, Data Minimization, Data Access Control, Data Integrity and Anonymization.

When it comes to building IoT devices integration, the same good practices as mentioned above are also considered for data handling from the smart home environment. Special remark for the security of MQTT based communication (as defined in MQTT Security Model):

- Use of TLS to encrypt the communication between MQTT clients and brokers. Configuration of the

ISBN: 978-618-5765-04-0
ISSN 3057-4269

MQTT broker to support secure connections, and ensure clients use TLS for encryption.

- Encryption of the payload of MQTT messages, especially if it contains sensitive information. MQTT payload encryption solves the problem of protecting application messages from malicious listeners or untrusted MQTT clients.
- Enforce strong authentication for MQTT clients to verify their identities. Use mechanisms like username/password combinations, client certificates, or other secure authentication methods.
- Implement access control lists (ACLs) to specify which clients are allowed to publish or subscribe to specific topics. Implement fine-grained access control to restrict clients' access to specific topics or actions.
- Careful management of MQTT sessions to control the state and duration of client connections. Configuration of appropriate session timeouts and consider using persistent sessions based on your application's needs.
- Set of appropriate keepalive and timeout values to manage the lifecycle of MQTT connections.

We presented above, the key security principles as defined in the relevant standardization. These specifications are further incorporated in the data collection and sharing framework to be established in the overall ICT solution and to be tested in three demo sites around Europe. The initial details of the demo set up as well as the early trials are presented in the following section.

DEMO SITES AND EARLY TRIALS

Apart from the framework definition and the elicitation of the different data gathering and collection methods (as well as the security/privacy mechanisms that needs to be considered for data management and exchange), the in-life demonstration at specific demo scenarios is required. For that reason, a demo set up has been considered in 3 European countries: Spain, Italy and Ukraine with the elicitation of the different physical assets (and the associated data gathering methods as well as data collection characteristics).

In Spain, the distribution network is located near the village of Escúzar, to set the demo-site to validate the demonstration at micro grid and end-user level. This area counts with 450 supply points and a peak load close to 0.55 MW, the LV distribution grid serves mostly residential consumers and near the village there are 2 PV plants of 4 MW and 1.8 MW each one connected to the MV grid. In the area there are also deployed 28 residential households with self-generation (3 kW each one), 1 household with a private EV charger (7,4 kW) and self-generation (3 kW), 5 households with control of the boiler and HVAC. Also, a public EV fast charger of 22 kW is available in the town and is projected the deployment for V2G chargers in some households.

At the DSO level, the Escúzar electrical substation, built in 2008, will be also used as a complementary demo-site to validate digital substation developments. It currently has two 30 MVA transformers operated at 66/20 kV. The 66 kV voltage has two 20 kV bars with a total of 14 output lines (7 per bar), which provide electricity to different municipalities and industrial estate of the region. In addition, one of the main elements of the local electric distribution network is the Substation Automation System (SAS) which is a mission-critical task that allows to control and monitor the electric infrastructure. Gateways, controllers, protections relays, RTUs, etc., enclose serial and ethernet communications by relying on industrial protocols, providing data logging capabilities, analogic and digital inputs/outputs, among other functions. These devices send real-time data in a reliable way to the SCADA so the operators would have an updated and accurate information on the status of the grids.

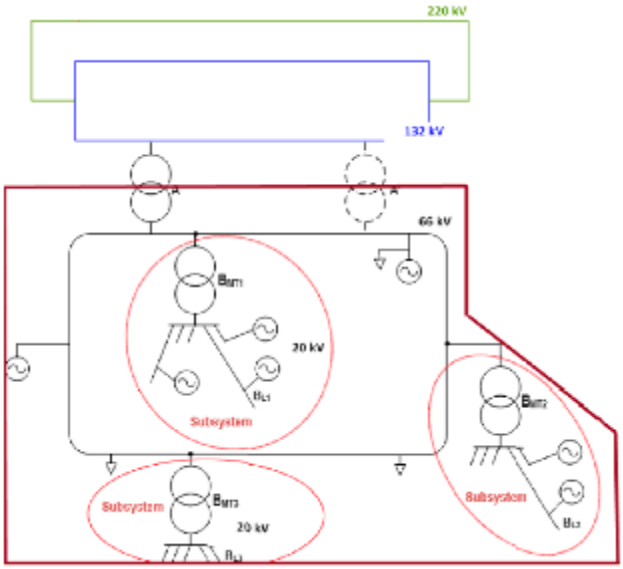

Figure 4: Indicative schema of Escúzar electrical substation

The Italian demo site is located in Sarentino Valley in the centre of South- Tyrol, north of Bolzano (Italy). In this region the local DSO is managing 8,608 km of network and supplying electric power to 230,000 customers. The pilot demonstration is going to be performed in the MV and LV grid supplied by the HV/MV substation and consists of:

- 2x 66/20 kV transformers 25 MVA. / 5 MV feeders.
- 10.4 MW of installed production in the MV and LV grid (3.6 MW hydroelectric, 2.7 MW PV and 4.1 MW thermal power generation).
- 2 local network installations connected to the MV grid, with other 10.6 MW of installed production (9.8 MW hydroelectric).
- 24.6 MW of total loads (3,000 LV and MV customers).

On the field side of the controlled smart grid, the bilateral flow of measurement and control signal for critical assets is established though a peripherical equipment which is a Smart Grid Controller. This component plays an essential role for observability of the DSO grid and for the coordination of the assets as it allows control functions. The tool interacts with SCADA system placed in the DSO control room.

The demo in Ukraine in the Ivano-Frankivsk region consists of the substation (110/35/10 kV) to guarantee the proper development and validation of the activities as defined above. The substation includes: switching equipment, relay protection and automation, telemechanic equipment (The substation is telemechanized by receiving status and position signals of all switching devices, and uses control commands for 110, 35 and 10 kV switches with discrete signals), collection of all information from microprocessor terminals (via Modbus-RTU protocol). The data transfer from the substation to the SCADA system is performed according to the protocols IEC60870-5-10. Between the branch and the

ISBN: 978-618-5765-04-0
ISSN 3057-4269

dispatch service, the communication is performed according to the DNP 3.0 protocol. Data transfer from the substation to the server of the control point is performed using fibre optics and GSM.

By taking into account the list of physical assets (with the associated communication protocols) as well as the data collection and handling framework specifications as presented in previous sections, we list the implementation details over the different physical assets to be examined at the different demo sites during a more than one year demonstration and validation period.

Table 1 Demo site details and security features

Demo Site	Protocol	Access Control	Anonymization	Encryption
ES - EV	OCPP	+	+	+
ES - PV	MODBUS	+		
ES - IoT	MQTT	+	+	+
ES- RTU	IEC/61850	+	+	
IT-SGC	IEC/61850	+	+	
UA-RTU	IEC/60870	+	+	
UA-SGC	DNP/3.0	+	+	

Considering the criticality of the data from the RTU/SCADA and smart controller, these are considered as private datasets with restricted access and thus bilateral licence agreements are required for data exchange. Access control policies with ABAC control methods should be supported in order to ensure classified access over the data based on the user roles. In addition, need for anonymization of the data coming from RTU/SCADA as data for substations normally includes the aggregation of plenty of end users. In addition, smart metering data needs to be anonymized at source level in order to ensure that any personal identifier has been removed. No specific requirements about additional encryption (apart from the default encryption that applies at communication exchange of the relevant protocol) over the data are defined at this stage, but the demo partners are interested to experiment with the data-level encryption mechanisms that are considered at grid level. On the other hand, encryption methods (SHA-256) are mandatory for the personal data made available from the DER/IoT environment with focus on smart home devices and EV charging points.

ACKNOWLEDGMENT

The work presented in this paper is co-funded by the EU HORIZON Europe Program (topic: " HORIZON-CL5-2021-D3-02-07 - Reliability and resilience of the grid: Measures for vulnerabilities, failures, risks and privacy" under grant agreement no. 101075665 project title: " eFORT-Establishment of a FramewORk for Transforming current EPES into a more resilient, reliable and secure system all over its value chain", https://efort-project.eu/).

REFERENCES

[1] DNP3 standard, https://www.ensotest.com/dnp3/introduction-to-the-ieee-1815-dnp3-standard/
[2] IEC 61850, https://iec61850.dvl.iec.ch/
[3] IEC 60870-5, https://webstore.iec.ch/preview/info_iec60870-5-104%7Bed2.0%7Den_d.pdf
[4] IEEE C37.118-2005, https://www.osti.gov/biblio/1504742
[5] SunSpec Modbus, https://sunspec.org/
[6] IEEE 2030.5, https://www.qualitylogic.com/wp-content/uploads/2020/06/QL-Intro-to-2030.5-Webinar.pdf
[7] IEEE 1815, https://standards.ieee.org/ieee/1815/5414/
[8] OCPP Protocol, https://openchargealliance.org/protocols/open-charge-point-protocol/
[9] IEC 63110, https://webstore.iec.ch/publication/60000
[10] SAREF model, https://saref.etsi.org/
[11] IoT-to-cloud communication protocols, https://iot.telenor.com/iot-insights/what-is-iot-communications-protocols/
[12] IEC 62351, https://iec61850.dvl.iec.ch/what-is-61850/technical-principles/61850-cybersecurity/
[13] IEC 62351-4- Application Layer Security for IEC 61850, https://ieeexplore.ieee.org/iel7/6287639/8948470/09115626.pdf
[14] IEC 62351-6- Security for IEC 61850 GOOSE and SV Messages, https://webstore.iec.ch/preview/info_iec62351-6%7Bed1.0%7Db.pdf
[15] IEC 62351-8: Role-Based Access Control for Power System Management, https://webstore.iec.ch/publication/61822
[16] Trusted Platform Module Overview, https://trustedcomputinggroup.org/resource/trusted-platform-module-tpm-summary/
[17] SunSpec Modbus Certification Procedures for Data and Communications Security of DER, https://sunspec.org/sunspec-cybersecurity-specifications/
[18] SunSpec Modbus Recommendations for Trust and Encryption in DER Interoperability Standards https://sunspec.org/wp-content/uploads/2020/01/Recommendations-for-Trust-and-Encryption-in-DER-Interoperability-Standards-SAND2019-1490.pdf
[19] SunSpec Modbus Roadmap for Photovoltaic Cyber Security https://sunspec.org/wp-content/uploads/2020/01/Roadmap-for-Photovoltaic-Cyber-Security-SAND2017-13262-4-10-2018.pdf
[20] OCPP Protocol Security, https://www.openchargealliance.org/news/enhanced-security-for-ocpp-16/

Industrial Heat Pumps Past Present Future

Renato Lazzarin
Dept. of Management and
Engineering*University of Padova*
Vicenza, Italy
renato.lazzarin@unipd.it

***Abstract*— Industry is responsible in Europe of 1/4 of final energy consumption. About 2/3 of industrial energy use can be attributed to process heating. Temperature required for process heating are in a wide range from the space heating with values lower than 60°C to the high values of the metallurgy sector that can be above 1500°C. Many industrial sectors require process heating at temperatures lower than 200°C as, for example, food and beverage, paper and textile sectors.**
In correspondence with process heating huge amounts of waste heat are produced. A fraction of this waste heat, estimated at about 42%, is low waste heat at temperatures lower than 100°C, frequently of no use for passive heat recovery. Heat pumps can exploit this heat, making it suitable to many heating processes. To this end high temperature heat pumps are welcome, thus designating heat pumps able to operate at temperatures well higher than 100°C. They are much different from conventional heat pumps, regarding not only the larger capacity and special refrigerants, but also the technologies. Open cycles mechanical vapour recompression systems (MVR) allow impressive reduction in energy demand in processes as concentration, distillation, drying and desalination. Heat transformers are able to upgrade a fraction of waste heat to useful temperature heat.
In the past an industrial heat pump was a device able to operate at temperatures just above 100°C with a suitable refrigerant. Nowadays an industrial heat pump is designed and developed on purpose for industrial use with equipment that can operate at temperatures as high as 200°C, making it possible to increase useful recovery of waste heat. Recent developments could increase the ratios of actual to ideal COP and the temperature lift from heat source and heat supply.
The aim of this paper is to illustrate the technology developments in the field from the first applications to the actual state of the art with the possible developments.

Keywords—Heat pump, Industry, HTHP

INTRODUCTION

About 20% of total world energy consumption is due to industrial heat production mainly obtained by fossil fuels combustion. Around 50% of industrial energy input turns into waste heat. Low temperature waste heat (< 220 °C) represents 60%. Steam generation is estimated to require about 30% of energy consumption in the manufacturing industry. The demand for process heating accounts for 66 % of the total final energy demand.

Energy consumption in the industrial sector in UE27 is about 3200 TWh (275 Mtoe) per year, representing about 26% of the total consumption in EU. (fig. 1).

High temperature heat pumps (HTHPs) can exploit waste heat increasing its temperature to useful values, for example producing steam. Industrial HTHPs could cover about 28 TWh/year (2.4 Mtoe) of thermal requirement in the range 100-200°C, which means about 1.5% of the total heat consumption. The heat pump "cold" source would be about 21 TWh/year (1.8 Mtoe, a COP of 4 is postulated), that is 7% of the total heat potential in EU industries [1]. A focus on the industry is needed as it is currently responsible for 25 % of final energy consumption (FEC) and 20 % of the GHG (*GreenHouse Gas*) emissions (not including indirect emissions attributed to external energy supply) in EU-28 countries. The majority (66 %) of industrial energy use is for process heating purposes [2].

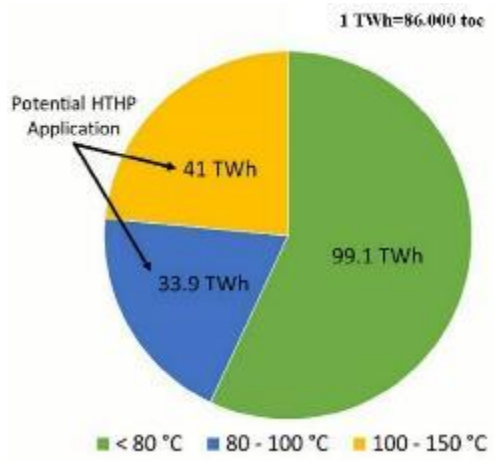

Figure 1 : Distribution of heat by temperature and potential quantity of heat demand that can be covered by HTHPs [3]

GENERALITIES

Whenever the waste heat temperature (source) is higher than the sink, it is better a heat exchange. Only when the two temperature levels are inverted a heat pump may be a useful solution. The statement may seem obvious, but this criterion is not always followed. Then a heat pump is often preceded by a heat exchanger.

A rough evaluation of a heat pump COP is allowed by the *Carnot* ratio. Nowadays heat pumps can reach about 60% of *Carnot* ratio:

$$COP = 0.6\frac{T_1}{T_1 - T_2}$$

where T_1 is the sink temperature and T_2 the source.

When the heat pump is driven by electricity, the acceptable *COP* depends on how electricity is produced. If the production is thermoelectrical by natural gas the COP should exceed 2.5 to reach primary energy parity. For a sink temperature of 150°C the temperature lift limit is 100°C but usually not more than 60-70 K to obtain a concrete superiority in terms of primary energy.

These considerations lose validity in the case of electricity produced by other means, from hydroelectric to photovoltaic to nuclear. A possible picture of the nowadays situation is represented in fig. 2.

ISBN: 978-618-5765-04-0
ISSN 3057-4269

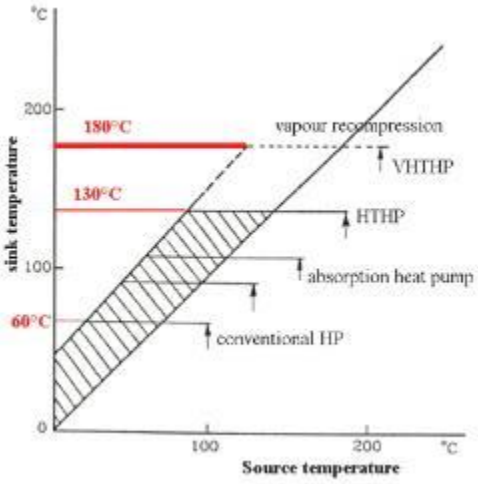

Figure 2 : Temperature limits of different industrial heat pumps

The currently prevalent techniques feature mechanical compression with approximately half of the large installations being open cycle (they perform the compression of water vapour). Very important are also sorption systems. An overview of the different technologies is represented in fig. 3:

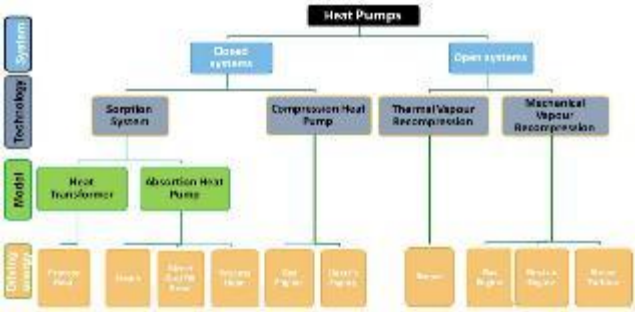

Figure 3 : An overview of different heat pump technologies

THE PAST: 1855-2000

The first heat pump in history was built in 1855 by the Austrian Peter Ritter von Rittinger who installed it in the salt mines of Ebensee. It was an open-cycle heat pump with mechanical vapor recompression driven by a waterfall (fig. 4). The compressor sucked the vapor produced in the concentrators of the aqueous salt solution at 117°C and at a pressure of 170 kPa, compressing it to 300 kPa, a pressure at which the condensation temperature is 138°C.

In this way, the condensation of the steam allowed the production of an equivalent quantity with a COP higher than 10.

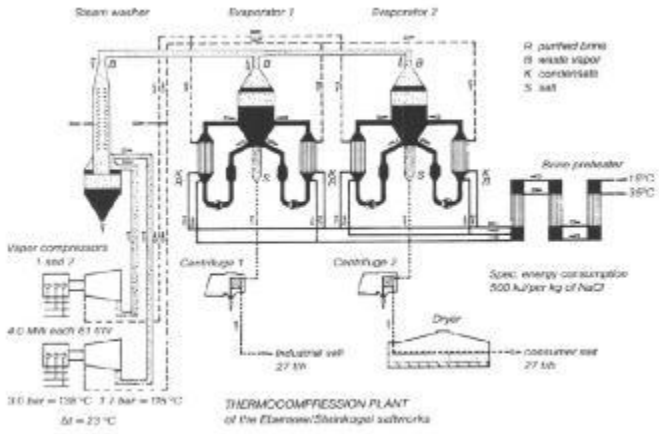

Figure 4 : Open cycle vapour recompression heat pump by Peter Ritter con Rittersdorf (1855)

First industrial compression heat pumps were similar in principle to the ones of the residential and commercial market, differing mainly in thermal levels, working fluids and capacities. The first problem that posed itself to the designers was that of the refrigerant. The relatively high thermal level prevented the utilisation of most widespread refrigerants then used such as CFC-12 and HCFC-22. CFC-114 was usually preferred to work above 100°C as it retained a good stability even at those temperatures.

The schematic is very similar to a conventional heat pump (fig. 5). In the upper left part the evaporator is powered by waste heat at 90°C. The refrigerant vapor produced at 80°C is compressed and can condense at 135°C, making useful heat available. A machine, called *Templifier*, could reach 100°C with a COP of 3.5 for a cold source at 60°C.

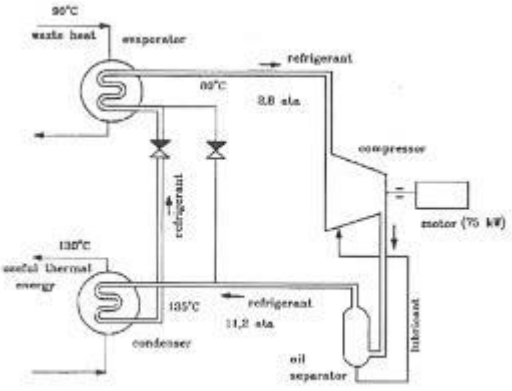

Figure 5 : Scheme of an industrial compression heat pump realized in the '70

A means devised to reduce the compression work and the highest temperature at the outlet of the compressor was the use of an economizer with refrigerant injection at an intermediate pressure (fig. 6).

The principle of absorption was applied on first absorption heat pumps, usually driven by steam (*Mitshubishi-York*). They were usually driven by steam at a temperature of about 165°C, heating up water from 50 to 90°C, using waste heat at 40°C as cold source. The COP was claimed at 1.7, which can be consider high as the input is thermal.

ISBN: 978-618-5765-04-0
ISSN 3057-4269

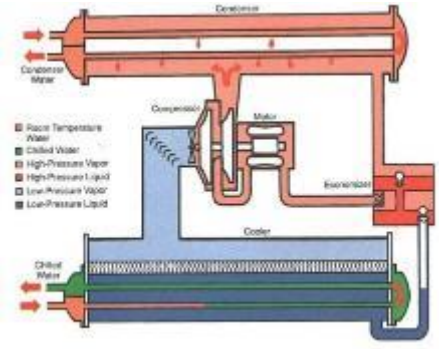

Figure 6 : Heat pump equipped with an economizer and a two stage centrifugal compressor

Fig. 7 reports the thermodynamic cycle on the pressure-temperature diagram of the mixture H_2O-LiBr.

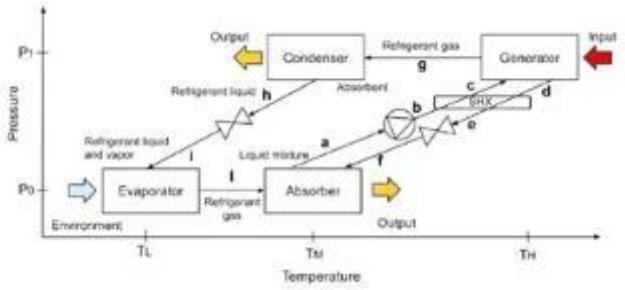

Figure 7 : Thermodynamic cycle of the absorption heat pump

Fig. 8 represents a block diagram of an absorption heat pump with the two cylinders of higher and lower pressure..

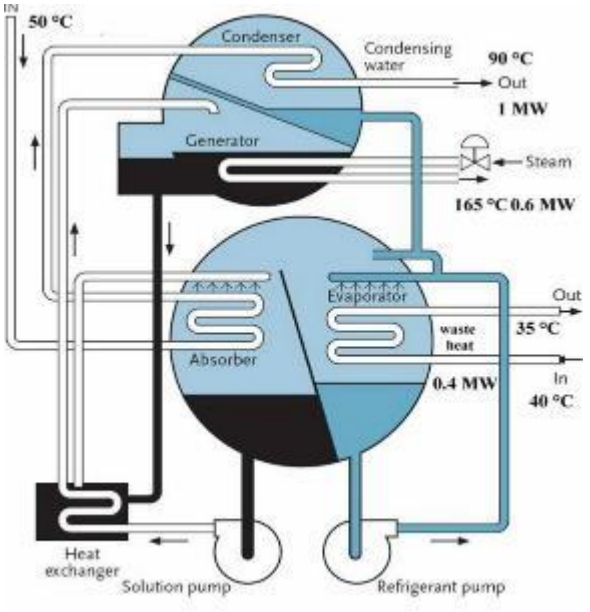

Figure 8 : Schematic of an absorption heat pump with the two cylinders of higher and lower pressure

Heat transformers are another significant application of the absorption principle. The heat transformer exploits thermal energy at a non-useful temperature level to enhance a part of it at a usable thermal level. Fig. 9 illustrates the energy supplied to the machine at an intermediate temperature, valorizing one part at a high temperature, dissipating the other at a lower temperature.

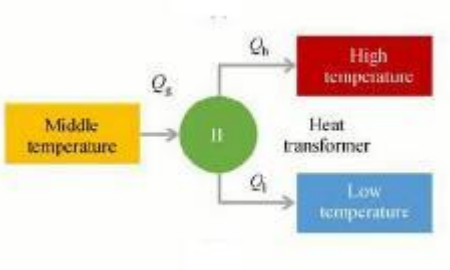

Figure 9 : Block diagram of a heat transformer with the energy fluxes

The thermodynamic cycle of a heat transformer is represented in fig. 10. Waste heat at 60-100°C can produce heat at a thermal level 40-50 K higher useful for many industrial processes (it might be steam at 5 bar). The COP can be around 0.4-0.5 so that almost a half of the waste thermal energy is available at a higher temperature.

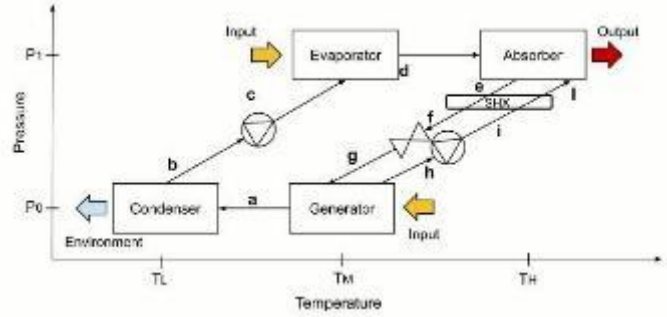

Figure 10 : Thermodynamic cycle of a heat transformer in a diagram pressure-temperature of H_2O-LiBr

THE PRESENT : 2000-2024

Since the beginning of this century, of the large family of organic refrigerants, only HFCs remained alive, completely free of the chlorine atom, such as, for example, R32 or R134a or R152, due to the requirement to respect the limit due to the ODP (*Ozone Depletion Potential*)

Among the possible replacements for traditional refrigerants, multicomponent mixtures were used, that is, the mixing of two or more pure refrigerants.

In few years another severe limitation regarded the refrigerants: the *Global Warming Potential (GWP).* The European *F*-gas directive has provided for the replacement of refrigerants in use with refrigerants that have a GWP<2500 and in the long term <150, practically nowadays. Only two HFCs appear to be able to meet this last requirement (R161 and R152a).

A group of refrigerants developed in recent years are able to comply with the constraints of the *F*-gas directive. These are unsaturated HFCs (HFO-*hydro-fluoro-olephine*) produced as an alternative to HFCs with high GWP, based on the propylene molecule.

Considering the unfortunate story of all the proposed synthetic refrigerants (the actual most popular (R-245fa) is about to be banned!) the best solution according to many researchers is to use natural refrigerants:

- propane HC-290 (C_3H_8); very flammable;
- butane HC-600 (C_4H_{10}); very flammable;
- ammonia R-717 (NH_3); toxic and flammable;

ISBN: 978-618-5765-04-0
ISSN 3057-4269

- carbon dioxide R-744 (CO_2); very low critical pressure and high pressure drop;
- water R-718 (H_2O); very low volumetric heating capacity.

An important innovation was the use of the R-744 even with the very high pressure drop and the requirement of a transcritical cycle. The useful effect is obtained by a gas cooler instead of the usual condenser. It happens that pressurized water is heated up by the continuous cooling of CO_2 gas. In this way the efficient *Lorenz* cycle can be approached (fig. 11). A major drawback of R-744 is the very high pressure between evaporator and compressor discharge pressure. A modern innovation is able to exploit this pressure drop using an ejector at the outlet of the gas cooler, reducing the compressor work (fig. 12) [5].

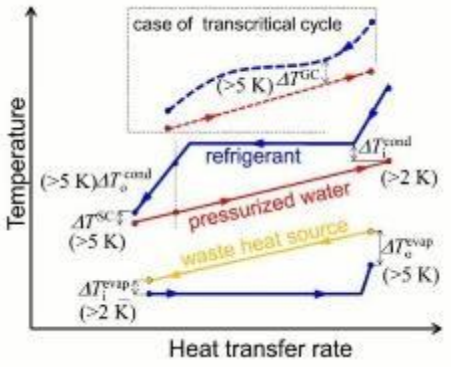

Figure 11 : Heating pressurized water by a gas cooler or by a traditional condenser in a heat pump. Temperature variation at the level of heat source is also represented.

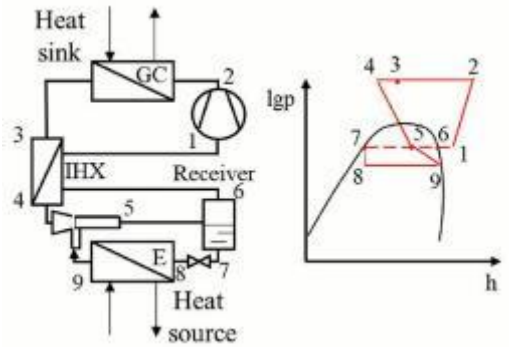

Figure 12 : R-744 heat pump cycle enhanced by an ejector

It is worth considering one scheme aimed at the production of technological steam with a two-stage heat pump in cascade The lower part of the scheme sees the classic cascade arrangement of two cycles with two different refrigerants.

The HT condenser that uses the 2'3' process produces the evaporation of water that is brought to the liquid separator in the saturation conditions 6 and then possibly further compressed up to the conditions 7 (steam) (Fig. 13).

One of the most wasteful energy process is the separation of two liquids (concentration), above all when one of the two is water. In fact this separation is often obtained by evaporating one of the liquids. This vaporization for water requires about 2500 $kJkg^{-1}$, (0.7 $kWhkg^{-1}$). The obtained vapour pressure and temperature are too low to make it useful inside the factory, then no significant heat recovery is possible. The involved industrial processes are far from marginal from macroeconomic point of view.

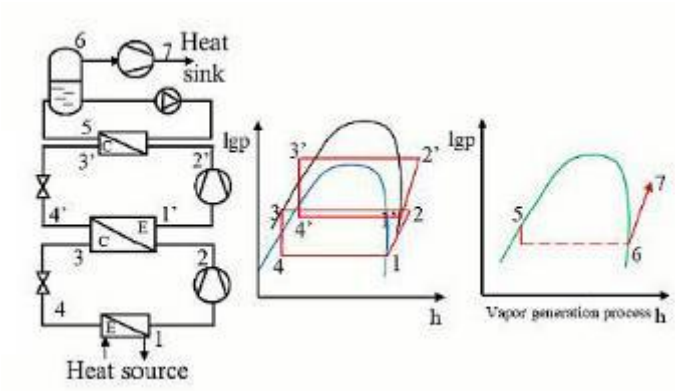

Figure 13 : Two stage cascade heat pump to produce high pressure water evaporation with a final steam production.

In Italian food industry 2 Mt of evaporated water are estimated in the dairy sector, 2.5 Mt in tomato and lemon processing, as much for starch production and 4.5 Mt for sugar (yearly values). The total amount of 11.5 Mt of water to be evaporated would require an overall energy cost higher than 700 ktoe, if obtained by single effect vaporization by heating (the value refers to the heat of vaporisation of water).

Desalination is another very energy intensive process as well as distillations and drying.

Mechanical vapour recompression (MVR) is a technology able to strongly reduce the energy cost in industrial processes such as concentration, distillation or drying and it is probably the most spread HTHP technology. A manufacturer claims about 2500 operating plants [4]. The process, is not so much different from the ancient Ritter's heat pump. The vapour formed in the process is mechanically compressed and this is enough to upgrade the vapour enthalpy so that it can be condensed at a temperature useful to supply energy to the process, developing further vapour. The small temperature difference between evaporation and condensation allows to reach very high COPs that can exceed even 10.

Fig. 14 represents a scheme for a concentration system by MVR. Steam is required by the process to be activated. Steam condensation releases vapour from the solution which is sucked and compressed at a suitable pressure so that condensation takes place at a temperature which allows to exchange heat with a reasonable heat exchanger area. Nowadays the usual temperature difference is of about 10 K, even if the difference sometimes arrives close to 5 K. As the compression ratio is small, blowers are used instead of the common positive displacement compressors. The name blower is used for compressors with low level of compression ratio, higher than fans, but lower than traditional compressors. Blowers are normally centrifugal devices with a single compression stage.

A MVR system with a compression isentropic efficiency 0.65[1] requires 25 kWh mechanical energy for evaporating 1000 kg of water. The energy required for the starting phase, obviously depending on the process management, can be

[1] The isentropic efficiency 0.65 is a reasonable value for common compressors in the considered field

ISBN: 978-618-5765-04-0
ISSN 3057-4269

considered conservatively, increasing of 5% the energy supplied. In any case the COP would be higher than 20.

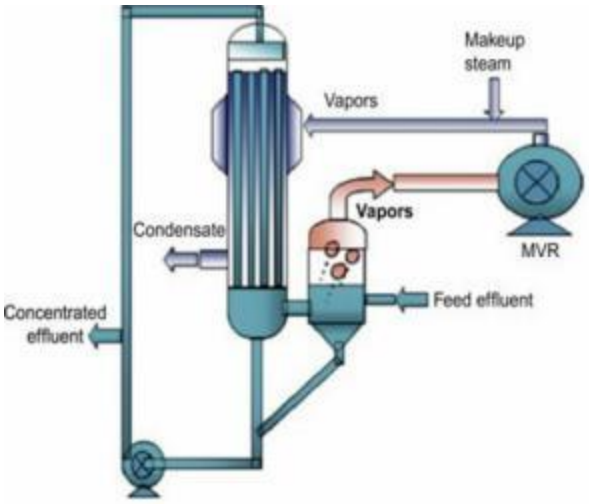

.

***Figure 14 : Concentration system MVR* (doc. Howden Co.).**

THE FUTURE : 2024-20??

In the future an important role of the principle of absorption can be predicted with the use of double effect systems or coupled with mechanical compression.

As with absorption refrigeration machines, double-effect systems can be developed to improve their performance. A possible scheme is represented in fig. 15. Energy is supplied to a generator at higher pressure (HPG) and temperature (typically in the order of 180°C). Condensation of the evaporated refrigerant occurs at a higher temperature in the high pressure condenser (HPC) which can then feed a second low pressure generator (LPG). The steam produced condenses in a low pressure condenser with a useful thermal effect. The condensate passes as always to an evaporator (E) from which it passes towards the absorber (A) with the second useful effect. Since the vapor separated from the solution in the LPG does not require external heat supply, the COP of the heat pump increases and in some prototypes reached 2.2 [4].

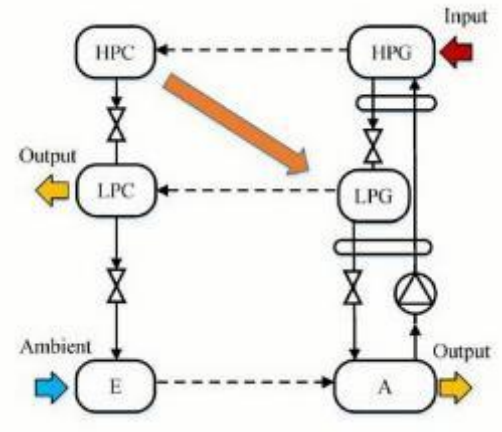

Figure 15 : Schematic of double effect absorption heat pump

A similar concept can be applied also to heat transformer. When plenty of waste heat is available there is the possibility of increasing the temperature difference obtainable through the double absorption heat transformer (the double-stage cycle is neglected here due to its great complexity). The block diagram of the machine is represented in fig. 16. The waste heat is sent to both the generator and the evaporator as in the single-stage heat transformer and similarly the absorption of the vapor produces a thermal effect. In this case the thermal effect is aimed at producing steam at a higher pressure in an evaporator where part of the liquid refrigerant is sent with a pump. Absorption at higher pressure allows for a useful thermal effect at higher temperatures. The higher pressure absorber interfaces directly with the generator for the arrival of the concentrated solution and with the lower pressure absorber for the return of the diluted solution (which will be further diluted in the lower pressure absorber). The block diagram represented on the pressure-temperature-concentration plane of the solutions (fig. 17) allows us to better follow the complex transformations involved. Application examples underline the interest of the presented scheme. A system built according to this scheme with a useful power of 200 kW made it possible to produce technological steam at 180°C, using waste heat at 88°C, system cooled at 25°C with a COP of 0.278 [4].

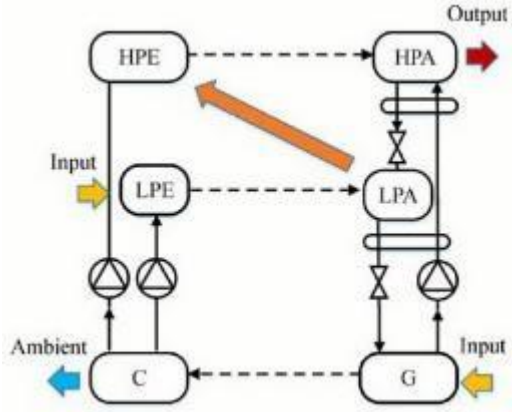

Figure 16 : Schematic of double absorption heat transformer

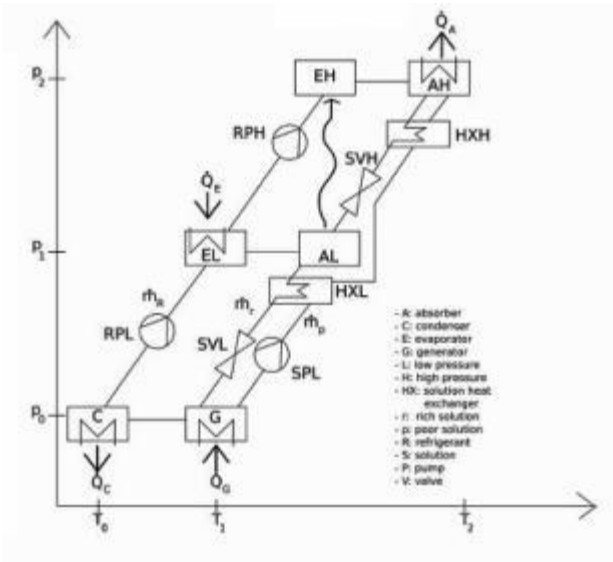

Figure 17 : Thermodynamic cycle of a double absorption heat transformer in a diagram pressure-temperature of H_2O-LiBr

The most promising technical development in the field of VHHTHP (*Very High High Temperature Heat Pumps*) is hybrid absorption compression.

As the temperature of the heat produced increases, compression heat pumps must operate at increasing pressures, particularly those that use ammonia. A solution to limit the pressure by reaching even high temperatures is the use of the hybrid absorption/compression cycle. A scheme is

ISBN: 978-618-5765-04-0
ISSN 3057-4269

represented in fig. 18 [6]. The starting point can be the so-called desorber (DES), a sort of partial generator which is heated by the cold source, but from which the solution comes out in saturated conditions with partial evaporation of ammonia. In the liquid-vapour separator (LVS) the ammonia vapor is separated and sucked by the compressor (COM). The solution now depleted in ammonia is brought by the solution pump (SP) to a higher pressure. From there, the liquid solution mixes with the vapor coming from the compressor and enters the absorber (ABS) where useful thermal development occurs. The solution, now diluted, after heat exchange with the solution coming from the liquid separator, passes to the lower pressure in the desorber.

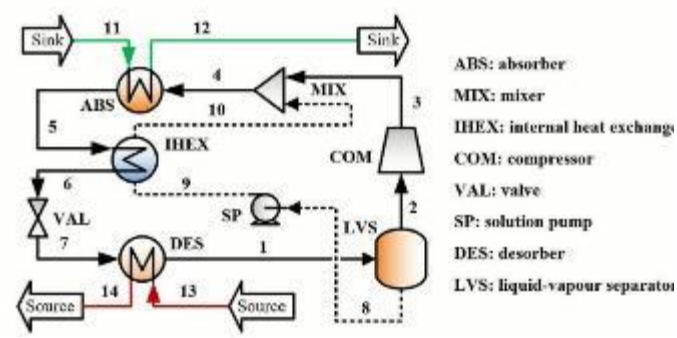

Figure 18 : Scheme of a hybrid absorption compression heat pump

It should also be noted that the progressive increase in the concentration of refrigerant in the absorption process involves a continuous temperature variation between the mixture entering the absorber and exiting it. This temperature trend is advantageous when a single-phase fluid is heated, since the temperature differences between the solution being absorbed and the heated fluid always remain very close to each other, approaching the *Lorenz* cycle scheme [7]. The same trend is found at the desorber level (fig. 20). In the upper part of the graph the progressive cooling that occurs in the absorber starting from the mixing between the pure refrigerant coming from the compressor and the strong solution arriving from the pump is represented. At the exit from the absorber is the inlet of the fluid to be heated whose temperature will increase up to the final value. A similar trend is encountered with reversed roles in the desorber where the temperature progressively increases for the solution at the expense of the cooling of the flow relative to the cold source (ΔT_{lift}). The COP of these machines must take into account the work necessary for the compressor and pump and the efficiency of their electric motors:

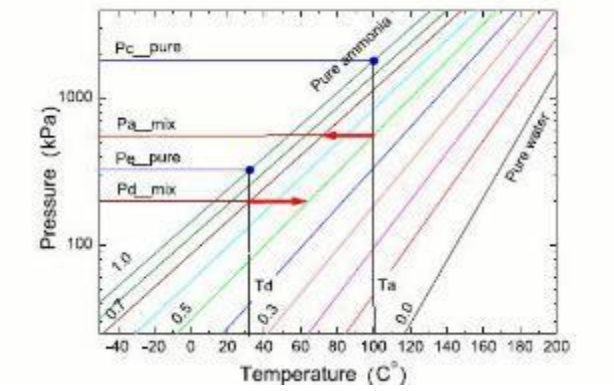

Figure 19 : Comparison of pressures at different temperatures of pure ammonia and water-ammonia mixtures

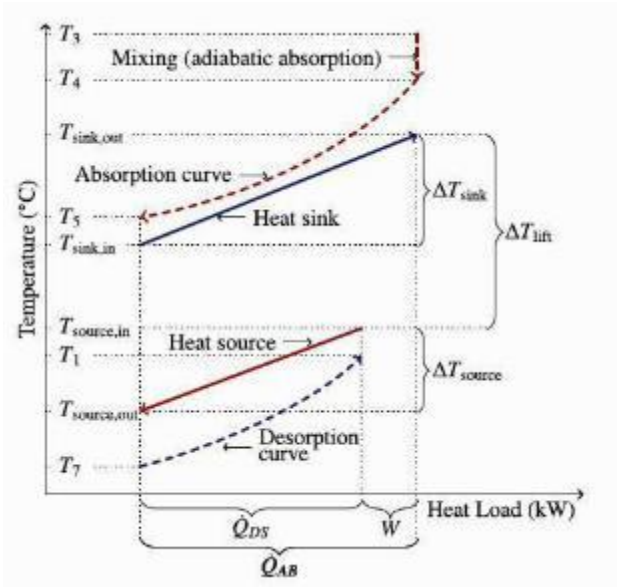

Figure 20 : Temperature trend in the absorption and regeneration phases compared with the temperature trend of the useful effect and the cold source

$$COP = \frac{Q_{ABS}}{W_{SP} + W_{COM}} \eta_{el}$$

Values above 3 are often obtained and, although the scheme is complex, there are commercial products based on it.

CONCLUSIONS

Although the diffusion of heat pump applications in industry is not yet widespread, there are various commercial proposals for machines ready for installation. The most mature technology regards MVR heat pumps with increasing applications in drying, concentration, distillation processes. In the near future hybrid absorption/compression heat pumps are expected to exceed 200°C sink temperature with important applications in other industrial fields.

REFERENCES

[1] G. Kosmadaki, "Estimating the potential of industrial (high-temperature) heat pumps for exploiting waste heat in EU industries". Appl Therm Eng;156: 287–98, 2019.

[2] White paper: Strengthening Industrial Heat Pump Innovation, HTHP Symposium, SINTEF, 2020.

[3] O. Bamigbetan et al., "Review of vapour compression heat pumps for high temperature heating using natural working fluids", Int. J. of Refrg., 80, 197-211, 2017.

[4] Howden Chart Industries, https://www.chartindustries.com/Products/Mechanical-Vapor-Recompression, visited August, 2024

[5] Z. Xu, R. Wang, "Absorption heat pump for waste heat reuse: current states and future development", Energy, 11(4): 414–436 , 2017 https://doi.org/10.1007/s11708-017-0507-1

[6] C.Liu et al., "A high-temperature hybrid absorption-compression heat pump for waste heat recovery", Energy Conv. and Mgmt., 172, 391-401, 2018.

[7] J. Kim et al., " Experimental study of operating characteristics of compression/absorption high-temperature hybrid heat pump using waste heat ", Renewable Energy 54. 13-19, 2013.

ISBN: 978-618-5765-04-0
ISSN 3057-4269

A New Approach to Solar Irradiance Forecasting: Using Complex-Valued Time Series

Cyril Voyant
SPE Laboratory Univ of Corsica (FR)
OIE Laboratory Mines-PSL
cyril.voyant@minesparis.psl.eu
https://orcid.org/0000-0003-0242-7377

Gilles Notton
SPE Laboratory Univ of Corsica (FR)
https://orcid.org/0000-0002-6267-9632

Jean-Laurent Duchaud
SPE Laboratory Univ of Corsica (FR)
https://orcid.org/0000-0001-7490-7260

Luis Garcia-Gutierrez
SPE Laboratory Univ of Corsica (FR)
https://orcid.org/0000-0002-3480-1784

Ghjuvan Antone Faggianelli
SPE Laboratory Univ of Corsica (FR)
https://orcid.org/0000-0002-9954-5910

***Abstract*— A novel method for short-term probabilistic forecasting of global solar irradiance using complex-valued time series is introduced. The real part represents the measurement, while the imaginary part captures volatility. A complex autoregressive model is applied to data from Corsica, France. Results show that the method, despite its simplicity and low data/resource requirements, aligns well with experimental data, with a root mean square error between 0.196 and 0.325. It outperforms traditional models like Gaussian processes, bootstrap, and quantile regression in some cases, and may have wide applications in physics.**

***Keywords*— Probabilistic; Forecasting; Univariate; Interval**

INTRODUCTION

To address the variability of solar energy and facilitate its integration, advancements in energy storage, smart grid management, and forecasting methods are essential [1]. This paper focuses on a new nowcasting method for photovoltaic (PV) power generation [2]. While many machine learning methods are assessed by accuracy, they often fail to capture rapid fluctuations. Advanced nonparametric models may overfit or be impractical due to data limitations. In line with the "No Free Lunch theorem," this paper introduces a simple, nonparametric probabilistic method that predicts both solar irradiance and its volatility, capturing trends and rapid fluctuations.

MATERIAL AND METHODS

Data

Accurate forecasting for time series with seasonal or cyclic behaviors, such as Global Horizontal Irradiance (GHI), requires careful analysis and modeling, particularly considering its yearly and diurnal cycles [3]. Since the 1960s, research on stationary processes and periodic correlation has shown the importance of addressing trends in such time series. Box and Jenkins formalized this in 1976, proposing a decomposition method, particularly useful when seasonality is easily identifiable [4]. In solar forecasting, a multiplicative approach is typically used, relying on the clear-sky index (κ), which normalizes GHI [5] by comparing it to clear-sky GHI (GHI_CS), as shown in $\kappa(t)=GHI_{CS}(t)/GHI(t)\in[0,1]$. Most solar forecasting models are built around κ rather than directly on GHI, as it is considered more stable. In this study, GHI measurements are taken from Ajaccio, Corsica (41.92N, 8.74E), which has a Mediterranean climate with an annual solar irradiation of 1642 kWh/m² [6]. The study focuses on daytime irradiance values, filtering out data where the solar zenith angle exceeds 85°, and GHI_CS is calculated using the Solis model, which accounts for atmospheric conditions using radiative transfer and the Lambert-Beer relation. This paper aims to predict GHI volatility and generate prediction intervals for time horizons ranging from 1 to 6 hours, using data from 2008–2017 for training and 2018 for testing [7]. Methods like autoregressive conditional heteroskedasticity (ARCH) models, well-established in econometrics, are applied here for the first time in GHI prediction for photovoltaic energy management. Though ARCH models have not been used before in this context due to their complexity and assumptions, they offer promising results. In line with Occam's razor, simpler forecasting models often yield the best accuracy, as noted by previous research.

Methodology

The method presented in this paper introduces a new formalism for:

- Predicting conditional volatility using parameters such as the *return* and its *standard deviation* (see the definition below).
- Generating GHI prediction intervals.

From the computed clear-sky index (κ) time series, another series reporting its intrinsic variability or volatility [8], denoted as $\sigma_\tau(t)$, is created, highlighting the concept of predictive risk. The standard deviation of the *return* of κ, $r(t)=\kappa(t)-\kappa(t-1)$, is computed over sliding windows of size τ as follows:

$$\sigma_\tau(t)=\sqrt{\frac{1}{\tau}\sum_{i=0}^{\tau-1}\left(r(t-i)-\frac{1}{\tau}\sum_{n=0}^{\tau-1}r(t-n)\right)^2}$$

This method, using a 30-hour window ($\tau=30\backslash tau = 30\tau=30$), offers the best performance. Although other definitions of volatility exist (e.g., using logarithmic or absolute-value norms), this approach is simpler and yields the best results. Instead of modeling κ and σ_τ separately, a complex-valued time series is constructed as $z=\{\kappa(t)+j\sigma_\tau(t)\}$, where $j^2=-1$, and modeled using an autoregressive process of order p. This approach simplifies the forecasting system by replacing separate equations for κ and σ_τ with a single regression.

ISBN: 978-618-5765-04-0
ISSN 3057-4269

RESULTS

The primary objective of this paper is to propose a novel probabilistic method for forecasting Global Horizontal Irradiance (GHI) using a complex-valued approach, denoted as the "Compl" method. However, to assess its performance, it is essential to compare it with classical forecasting tools such as a Gaussian parametric process (Gauss), a non-parametric bootstrapped process (Boot), and a Ridge quantile regression model (Quant). These comparisons are made using both deterministic and probabilistic error metrics. The deterministic comparison is based on normalized root mean square error (nRMSE), while the probabilistic evaluation uses metrics such as normalized mean interval length (MIL), percentage interval coverage probability (PICP), continuous rank probability score (CRPS), and mean scaled interval score (MSIS). These metrics are widely recognized in the literature for evaluating forecasting models' reliability and accuracy. The comparison between the proposed complex-valued method (Compl) and traditional methods is summarized in Table I [9], which highlights the results for a nominal coverage probability of 80% (α=0.2α=0.2). From the table, it is evident that the Compl method is highly competitive in terms of deterministic forecasting accuracy, with nRMSE values nearly identical to those of the other methods across all time horizons. However, the most striking advantage of the Compl method lies in its probabilistic performance. For instance, the MIL, which measures the width of the prediction intervals, is significantly reduced for the Compl method compared to the others. This reduction in MIL is crucial for grid operators seeking to minimize prediction intervals while maintaining a high level of coverage probability (PICP). Another notable result is that both the Quant and Compl methods achieve PICP values very close to the target nominal coverage of 80%, unlike the Gauss and Boot methods, which either overestimate or underestimate the coverage probability. For example, at the 1-hour horizon, the Compl method achieves a PICP of 80.01%, while Gauss slightly overpredicts at 83.81%, and Boot underperforms at 75.21%. This alignment between the nominal and actual coverage probabilities demonstrates the robustness of the Compl method in probabilistic forecasting.

Table 1 : Models comparison for a nominal coverage probability of 80% (α = 0.2)

Horizons	Metrics	Gauss	Boot	Quant	Compl
1h	*nRMSE*	0.197	0.203	0.201	0.196
	PICP(%)	83.81	75.21	79.65	80.01
	MIL(%)	51.24	40.36	42.24	41.24
2h	*nRMSE*	0.251	0.267	0.258	0.252
	PICP(%)	81.39	76.67	79.90	80.74
	MIL(%)	64.57	55.47	58.72	56.72
3h	*nRMSE*	0.282	0.304	0.289	0.282
	PICP(%)	80.68	73.27	80.07	80.06
	MIL(%)	70.97	58.22	67.32	63.09
4h	*nRMSE*	0.302	0.327	0.312	0.303
	PICP(%)	80.42	81.69	80.64	80.02
	MIL(%)	75.39	76.82	74.47	67.10
5h	*nRMSE*	0.316	0.362	0.328	0.317
	PICP(%)	80.99	74.44	80.81	79.49
	MIL(%)	78.73	64.45	79.08	69.32
6h	*nRMSE*	0.324	0.358	0.339	0.325
	PICP(%)	81.40	78.69	81.43	79.66
	MIL(%)	81.41	73.79	82.73	70.05

In the case of MIL, the Compl method consistently delivers narrower prediction intervals compared to Gauss and Quant, particularly at the 1-hour and 2-hour horizons. This reduced interval width is valuable for real-time grid management, as it provides more precise forecasts with lower uncertainty, making the Compl method more suitable for operational applications where decision-making depends on accurately predicting variability in solar energy generation.

The distribution of prediction intervals for the Compl method at a 1-hour horizon is illustrated. The prediction intervals adapt to the variability observed in the past data, reflecting the advantage of the complex-valued approach. This adaptability highlights the sensitivity of the Compl method to changing conditions and its ability to adjust forecast uncertainty accordingly [9].

To quantify the overall performance of the probabilistic forecasts, the CRPS score is used. The CRPS score evaluates both reliability and sharpness, making it a robust metric for comparing probabilistic and deterministic forecasts. Although the Quant method slightly outperforms the Compl method in terms of CRPS, the performance of the Compl method remains highly competitive and acceptable for practical purposes [9]. Furthermore, the MSIS score, which considers all forecast horizons within a single metric, shows that the Compl method achieves a lower and better score (0.95) compared to Gauss and Boot, and is comparable to Quant (0.89). In summary, the complex-valued method (Compl) proves to be a highly effective probabilistic forecasting tool for GHI. Its ability to reduce the prediction interval width while maintaining the desired coverage probability makes it highly valuable for operational energy management. The Compl method performs on par with traditional methods in deterministic forecasting (nRMSE) and shows superior results in probabilistic metrics such as MIL and MSIS. Given its adaptability and low computational requirements, the Compl method offers a promising approach for future solar forecasting applications in grid management.

CONCLUSION

The objective of this paper is to present a new method for predicting GHI that is able to take into account fast fluctuations. Often the literature boasts some sophisticated approaches, but when focusing on the existing installations, one remarks that the highly-developed models yield way to simpler methods. Although less effective, they are more robust and easier to use. From a practical point of view, a ``good" method concerns a tool that would be easily usable in a stand-alone application (problems of some toolboxes), and which doesn't involve a lot of different concepts or data. The procedures used for smart management shall be self-sufficient and consistent with continuous learning and with some eventual detectors failure. It is in this perspective we tested a new univariate methodology based on the complex-valued time series generated from GHI measurements. With only a few parameters (6 complex numbers in the studied case) and some basic mathematical operations, this approach makes it possible to predict GHI with accuracy compared with classical probabilistic and deterministic predictions. This method proposes the lowest MIL considering a fixed nominal coverage rate (80\%). Once the parameters have been estimated and provided that real-time GHI measurements are available, a simple spreadsheet can become a tool of choice in the management of PV installations.

The validation of this approach will require many more tests by varying time steps, horizons, and forecastability or predictability. However, this new forecast methodology is simple to implement and may facilitate the integration of

ISBN: 978-618-5765-04-0
ISSN 3057-4269

renewable energies and improve the management of installations using solar radiation as energy sources (smart grid, building, district, etc.). Interesting perspectives will be to apply it to other kinds of time series (not necessarily in connection with renewable energies), to construct the imaginary part concerning other variables than volatility (residuals, exogenous or ordinal data, etc.), and perhaps adapt the method to others predictors kinds (artificial neural network, support vector regression, etc.).

ACKNOWLEDGEMENTS

This work was partially supported by ANR grant SAPHIR project ANR-21-CE04-0014-03.

REFERENCES

[1] Lauret, Philippe; Voyant, Cyril; Soubdhan, Ted; David, Mathieu; Poggi, Philippe; ,A benchmarking of machine learning techniques for solar radiation forecasting in an insular context,Solar Energy,112, 446-457,2015, Pergamon

[2] Voyant, Cyril; Notton, Gilles; Kalogirou, Soteris; Nivet, Marie-Laure; Paoli, Christophe; Motte, Fabrice; Fouilloy, Alexis; ,Machine learning methods for solar radiation forecasting: A review,Renewable energy,105,,569-582,2017, Pergamon

[3] Notton, Gilles; Nivet, Maire-Laure; Voyant, Cyril; Darras, Christophe; Motte, Fabrice; Paoli, Christophe; ,"Intermittent and stochastic character of renewable energy sources: consequences, cost of intermittence and benefit of forecasting",Renewable & Sustainable Energy Reviews,87,96-105,2018

[4] Lauret, Philippe; Rodler, Auline; Muselli, Marc; David, Mathieu; Diagne, Hadja; Voyant, Cyril; ,A Bayesian Model Committee Approach to Forecasting Global Solar Radiation,"World Renewable Energy Forum 2012. Denver Colorado, USA",2012,

[5] Join, Cédric; Voyant, Cyril; Fliess, Michel; Muselli, Marc; Nivet, Marie Laure; Paoli, Christophe; Chaxel, Frédéric; ,Short-term solar irradiance and irradiation forecasts via different time series techniques: A preliminary study,3rd International Symposium on Environment-Friendly Energies and Applications (EFEA 2014) in Paris (France),2014,

[6] Duchaud, Jean-Laurent; Notton, Gilles; Fouilloy, Alexis; Voyant, Cyril; ,"Hybrid renewable power plant sizing–Graphical decision tool, sensitivity analysis and applications in Ajaccio and Tilos",Applied Energy,254,,113601,2019,Elsevier

[7] Duchaud, Jean-Laurent; Voyant, Cyril; Fouilloy, Alexis; Notton, Gilles; Nivet, Marie-Laure; ,Trade-off between precision and resolution of a solar power forecasting algorithm for micro-grid optimal control,Energies,13,14,3565,2020,MDPI

[8] Voyant, Cyril; Lauret, Philippe; Notton, Gilles; Duchaud, Jean-Laurent; Fouilloy, Alexis; David, Mathieu; Yaseen, Zaher Mundher; Soubdhan, Ted; ,A Monte Carlo based solar radiation forecastability estimation,Journal of Renewable and Sustainable Energy,13,2,,2021,AIP Publishing

[9] Voyant, Cyril; Lauret, Philippe; Notton, Gilles; Duchaud, Jean-Laurent; Garcia-Gutierrez, Luis; Faggianelli, Ghjuvan Antone; ,Complex-valued time series based solar irradiance forecast,Journal of Renewable and Sustainable Energy,14,6,,2022,AIP Publishing

ISBN: 978-618-5765-04-0
ISSN 3057-4269

Reevaluating Container Throughput Forecasting Models in Ningbo-Zhoushan Port during the COVID-19 Pandemic

Chuqiao Liu
Southampton Business School
University of Southampton
Southampton, The United Kingdom
cl2g20@southamptonalumni.ac.uk

Yue Wu
Southampton Business School
University of Southampton
Southampton, The United Kingdom
y.wu@soton.ac.uk

Abstract*—Since the outbreak of the COVID-19 pandemic, countries around the world have been affected in more or less different ways—economically, medically, and trade-related. Global trade production and transportation have been hampered by work stoppages and city lockdowns around the world, which greatly impact port container throughputs. In a period of such turbulence and complexity of change, it is important for ports to forecast container throughput to avoid unnecessary consumptions, such as labor, yard, machines, and vehicles, due to their very expensive cost, while effectively utilizing resources to safeguard the environment. This research evaluates various container throughput forecasting models for the Ningbo-Zhoushan Port in China during the COVID-19 pandemic, including the Holt-Winters exponential smoothing model, seasonal auto-regressive integrated moving average model, multiple linear regression models, and support vector regression model. Mean Square Error (MSE) and Akaike Information Criterion (AIC) are used as evaluation criteria to determine the optimal model. MSE represents the variance of the prediction error. It is one of the most used criteria to evaluate the performance of forecasting models. The smaller the MSE, the better the accuracy of the models. AIC is based on information theory, with the aim of selecting the model that best explains the data. The optimal model can be determined using AIC. The smaller the AIC, the better the model. With the data from the Ningbo-Zhoushan Port in China from January 2020 to December 2021 during the COVID-19 pandemic, the results show that the auto-regressive integrated moving average model has the best forecasting performance, followed by the support vector regression model. Moreover, this research considers the number of COVID-19 new infections as a variable in the multivariate forecasting model. The results also reveal that the number of COVID-19 new infections has a strong negative relationship with the container throughput in Ningbo-Zhoushan Port, and it is a significant factor in the prediction model. Additionally, a multivariate forecasting model is built up with the Ningbo Port Freight Index as an additional predictor. The results demonstrate that the Ningbo Port Freight Index has a weak positive correlation with Ningbo-Zhoushan Port container throughput and is an insignificant predictor in the forecasting model. This research demonstrates the importance of re-evaluating various forecast models for container throughput at ports during natural disasters like the COVID-19 pandemic. Such reevaluation enables more effective resource utilization at ports, thereby contributing to environmental protection efforts.

Keywords—COVID-19, container throughput, ARIMA, SVR, multiple linear regression model

INTRODUCTION

Ports are an important component of the global supply chain, as most cargoes are transported by sea through ports to complete the import/export trade process; thus, port construction is important and fundamental to international trade and world and national economic development [1]. The container throughput of a port reflects the position of the city in the international trade market and its economic development and influences port planning and development [2]. Therefore, container throughput forecasting is beneficial for port planning to avoid inefficient scheduling, cargo accumulation, and waste of time. In December 2019, COVID-19 appeared in the world for the first time and made a huge impact on almost all aspects of the world, including economy, healthcare, tourism, trade, and transport. In times of such turbulence and rapid change, effective port planning, such as forecasting container throughput at ports, is crucial to prevent the unnecessary use of resources. The container throughput forecasting models therefore need to be re-evaluated using the data from the COVID-19 pandemic and selecting the best container throughput forecasting model.

China was the most severely affected region when the COVID-19 outbreak first emerged and implemented the strictest measures in the world to prevent and control its spread. As a result, China suffered the most from the impact of COVID-19, which can be seen in the maritime industry. This research examines whether the best forecasting model of container throughput at Ningbo Zhoushan Port has changed during the COVID-19 period. To quantify the impact of COVID-19, we incorporate the number of newly infected COVID-19 cases and the Ningbo Port Tariff Index in predicting the container throughput at Ningbo Zhoushan Port. Two variables representing COVID-19 newly infected people and the Ningbo Port Tariff Index are introduced in a multiple linear regression model for container throughput. In order to select the best forecasting model for the COVID-19 period, this research analysis different time series forecasting methods, trains four container throughput forecasting models at Ningbo Zhoushan Port, and compares their performance using key evaluation metrics.

LITERATURE REVIEW

Container Throughput Forecasting Methods

Some scholars utilize multiple univariate benchmark models simultaneously to forecast container throughput, comparing their performance to identify the optimal model. Schulze and Prinz use Holt-Winters exponential smoothing and Seasonal Autoregressive Integrated Moving Average (SARIMA) models to forecast German container throughput for seasonal time series [3]. The two methods are found to be equivalent methods from a theoretical point of view, but the

ISBN: 978-618-5765-04-0
ISSN 3057-4269

SARIMA model provides better forecasts when analysing the results [3].

In contrast, some scholars select a range of relevant predictors and use multivariable models to make predictions. Tang et al. identify five factors as dependent variables, including total retail sales of consumer goods, local urban GDP, import and export trade, total output value of secondary industry, and total fixed asset investment. They then develop four multi-factor-based container throughput forecasting models—a grey model, a triple exponential smoothing model, a multiple linear regression model, and a back propagation neural network model—to forecast the container throughput of Lianyungang and Shanghai ports [4].

In addition to the various factors related to container throughput mentioned above, ACIK states that freight rate is a cost metric for shippers and affects the demand for sea transport at ports directly; therefore, there is a correlation between freight rate and the number of containers handled at ports [5]. To investigate the relationship between the container freight index and the number of containers handled in Turkish ports, ACIK uses the causality in variance approach to identify the relationship between the two [5]. The results indicate that the fluctuation in freight rates is responsible for the fluctuation in the volume of containers handled in Turkey. Therefore, in this study, the freight index, which was not used in previous studies, was also included as a predictor in the container throughput forecasting model for the first time.

The following studies use both single and multiple variable models for forecasting and comparison. Chan, Xu and Qi utilize six time series methods, MA, MARS, ARIMA, GM(1,1), SVR, and ANN, to forecast the container throughput of Ningbo port [2]. Their results show SVR is the best forecasting method, and the ARIMA method among the traditional regression methods performs better than the other three methods. Feng et al. develop an ARIMA model, a linear regression model, and a GM (1, 1) model to forecast container throughput for the Shanghai, Zhejiang, and Jiangsu of the Yangtze River Delta multi-port system [6]. After empirical analysis, they conclude that ARIMA has the best forecasting effect when the time series is nearly linear [6]. However, when the time series is non-linear, the predicted variables need to be divided into multiple components and then aggregated; this process is called indirect forecasting [6].

Forecasting Considering the Impact of COVID-19

Loske develops a linear regression model to examine the relationship between the increase in shipment volumes, defined as the difference between actual and expected shipments, and the impact of COVID-19 [7]. The results show a strong positive linear correlation between the growing volume of dry goods shipments and new COVID-19 infections per day in Germany and that the growing volume of dry goods shipments in retail logistics is determined by the number of new COVID-19 infections per day rather than the length of time COVID-19 lasted [7]. They quantify consumer behaviour during COVID-19 using the number of new confirmed COVID-19 cases as a variable and measure the overall impact of the pandemic [7]. Inspired by their work, this paper develops multiple variable prediction models using the number of COVID-19 new infections per day as a predictor. A linear regression model is also formulated to explore the impact of COVID-19 on container throughput.

Previous studies use the data before COVID-19 occurred to compare benchmark forecasting methods. In contrast, this paper analyses data covering the entire pandemic period, from January 2020 to December 2021, to develop several models aimed at selecting the optimal container throughput forecasting model for the COVID-19 period.

METHODOLOGY

Research Method

Holt-Winters Exponential Smoothing Model: The Holt-Winters Exponential Smoothing model is one of the exponential smoothing methods and is suitable for time series with trends and seasonal variations [8]. The Holt-Winters Exponential Smoothing method can also be divided into additive and multiplicative methods depending on the characteristics of the seasonal variation of the time series [8]. Time series with fixed seasonal variation use the additive method, while time series with incremental seasonal variation use the multiplicative method [8].

Seasonal Auto-regressive Integrated Moving Average Model: The ARIMA model is proposed by Box and Jenkins, also known as the Box-Jenkins model, and is formed by the combination of an autoregressive (AR) and moving average (MA) process with the same degree of integration [9]. ARIMA models can be divided into non-seasonal general ARIMA models and seasonal SARIMA models [9]. The SARIMA model is used for time series with trend, seasonality, and short-time correlation [10]. The time series in this paper meets their conditions, and therefore the SARIMA model is used.

Multiple Linear Regression Model: Multiple linear regression models are often used to explain the relationship between several independent explanatory variables and a dependent variable and can also be applied to predict the dependent variable [11]. This paper uses the Multiple Linear Regression Model to examine the relationship between COVID-19 and the freight rate index with the container throughput and their impact on the container throughput forecasting model, while taking the COVID-19 factor into account in the container throughput forecasting model simultaneously.

Support Vector Regression Model: Support vector regression (SVR) is a machine learning model that uses observed data to estimate functions and is commonly used to solve regression problems for time series forecasting [12], specifically by mapping the input data x into a high-dimensional feature space F through a non-linear mapping and generating and solving linear regression problems in this feature space [13]. As SVR has better predictive performance compared to other methods [14], it is also selected for comparative study in this paper.

Data collection

The time period for data collection in this paper spans from January 2020 to December 2021. Cross-sectionally, 24 monthly data sets are used in this study. Vertically, this study collects data on five variables: the monthly container throughput of Ningbo Zhoushan Port (CT), the container freight index of Ningbo Zhoushan Port (NCFI), the number of new COVID-19 infections per month in China (CN), the total retail sales of consumer goods (TRSCG), and the import and export trade (IETV).

ISBN: 978-618-5765-04-0
ISSN 3057-4269

Criteria for Evaluating Forecasting Models

To evaluate the forecasting model and select a better model, the following evaluation criteria are used: Mean square error (MSE) and Akaike information criterion (AIC). Mean square error is the variance of the prediction error, which is one of the commonly used criteria to evaluate the forecasting performance of a model. The smaller the MSE, the smaller the prediction error, and the better the accuracy of the model. The AIC can be used for model selection, and the optimal model can be determined based on the criterion that the smaller the AIC, the better [15].

RESULTS AND ANALYSIS

Holt-Winters Exponential Smoothing Method

After analyzing the time series plot of container throughput data from Ningbo Zhoushan Port, it is found that the time series show an upward trending and variability constant seasonality, so it was decided to use the additive seasonal method. Then, the data is pre-processed, power transformed, and logarithmically transformed to produce six sets of data with different processes. Furthermore, the model is trained using the holt-winter additive seasonality method for the six data sets. However, as the time period of the selected data was not long enough to potentially affect the judgment of the time series characteristics, the holt-winter multiplicative method is used for comparison. The results yield better forecasts using holt-winter additive method, with smaller MSE values for all additive models. The results of the model using the additive method are shown in Table 1.

Table 1: The Mean Squared Error Values for Each Model of the Holt-winters Exponential Smoothing Method

Models	Mean Squared Error
Model 1 (power-transformation)	127.02
Model 2 (original)	108.01
Model 3 (logarithmic transformation)	152.93
Model 4 (power-transformation and calendar adjustment)	265.17
Model 5 (original data with calendar adjustment)	151.95
Model 6 (logarithmic transformation and calendar adjustment)	1204.95

We conclude that the use of the original data, i.e., data not subject to transformation and calendar adjustment, produced the best forecasting model with a minimum MSE value of 108.00752.

Seasonal Auto-regressive Integrated Moving Average Model

Because the time series has seasonality and a period of 12 months, the parameter s=12. As well as the fact that a seasonal differencing and a first-order differencing are done before obtaining a stationary time series and the MA (1) model is selected, so the parameters of the SARIMA model chosen are: p=0, d=1, q=1, P=0, D=1 and Q=1. In summary, the model chosen was SARIMA (0, 1, 1) x (0, 1, 1) x 12.

The fitted and predicted results of the SARIMA (0, 1, 1) x (0, 1, 1) x 12 model show an AIC of 105.031 and an MSE of 119.98. The model also passed the Ljung-Box test, as the p-value for the Q-statistic is 0.28, which is greater than 0.05. Moreover, the distribution of the residuals of the model is normal, and the DW test value is 1.97, very close to 2, indicating that the residuals are not correlated, and the model has good predictive performance.

Other models with different parameter combinations of p, d, q, P, D, and Q values are tested to find a better model, and the model with the lowest AIC is selected. We also discover that the SARIMA (1, 1, 1) x (0, 1, 0) x12 model has the smallest AIC of 100.76, which is smaller than the AIC of the initially selected model. At the same time, the MSE of the model was 71.68, which was also much smaller than 119.98. The p-value of the Q-statistic of the model is 0.98 greater than 0.05, which passed the Ljung-Box test. Furthermore, the residual distribution of the model is a normal distribution, and the DW test value is 1.95, which is very close to 2, illustrating that the residuals are not correlated. From the above demonstration, it follows that SARIMA (1, 1, 1) (0, 1, 0)12 is also a valid forecasting model. In summary, SARIMA (1, 1, 1) (0, 1, 0)12 is the optimal ARIMA model.

Multiple Linear Regression Model

A preliminary analysis of the data is conducted to observe the correlations between the variables and the results are shown in Table 2. The variable of the number of new COVID-19 infections has the strongest correlation with container throughput. The correlations between the remaining three explanatory variables and the dependent variable are all weak, with TRSCG having the weakest correlation.

Table 2: Correlation Coefficients between CT and NCFI, CN, IETV and TRSCG

	CT	NCFI	CN	IETV	TRSCG
CT	1.000000	0.236082	-0.648831	0.455789	0.203945
NCFI	0.236082	1.000000	-0.220210	0.842593	0.285776
CN	-0.648831	-0.220210	1.000000	-0.424063	-0.620035
IETV	0.455789	0.842593	-0.424063	1.000000	0.471721
TRSCG	0.203945	0.285776	-0.620035	0.471721	1.000000

From the results of the forecasting using exponential smoothing in A, the best forecasts are obtained using the original data, and thus a linear regression model is fitted using the original time series.

Table 3: The Mean Square Error of Three Multiple Linear Regression Forecasting Models

Models	Mean Squared Error
Model 1	557.20
Model 2 (11 additional monthly indicator variables)	818.45
Model 3 (11 additional monthly indicator variables + time-related Variables)	5781.33

A multiple linear regression model fitted with the initial four independent variables provides the best predictions, which is better than the models fitted with 11 additional monthly indicator variables and time-dependent explanatory variables.

ISBN: 978-618-5765-04-0
ISSN 3057-4269

Support Vector Regression Model

We select four kernel functions: linear, radial basis function, poly, and sigmoid, and manually enter different parameters to fit the SVR model. In addition, a grid search method and k-fold cross-validation are used, with cv set to 8, to automatically select out the parameter combinations for the model with the smallest MSE. However, using the linear kernel function, and a C setting of 1000, the MSE is the lowest, at 93.19, and the optimal SVR model is obtained.

We also want to test whether the additional two variables, the number of new COVID-19 infections and the Ningbo port freight index, can improve the prediction accuracy of the SVR model. Training the prediction model with the same combination of kernel functions and parameters and a dataset without the two additional predictors yields an MSE of 254.45. Then, adding the two variables, namely the number of COVID-19 new infections and the Ningbo port freight index, respectively, to train the prediction model, the MSEs obtained were 192.51 and 121.55, respectively.

The results show that the use of two variables, the number of COVID-19 new infections and the Ningbo Port Freight Index model, are both effective in improving the accuracy of the prediction for the SVR prediction model.

DISCUSSION

The Optimal Forecasting Model

Table 4: The Mean Square Error of Four Forecasting Models

Model	Mean Squared Error
Holt-Winters Exponential Smoothing Method	108.01
Seasonal Auto-regressive Integrated Moving Average Model	71.68
Multiple Linear Regression Model	557.20
Support Vector Regression Model	93.19

The SARIMA model has the smallest MSE and RMSE and therefore has the best forecasting performance, followed by the SVR model. The Holt-Winters model ranks third in terms of forecasting performance, while the multiple linear regression model has the worst prediction performance.

This study finds that the SARIMA model has a higher prediction accuracy than the SVR model for the period in which Covid-19 occurred, in contrast to the findings in [2] which indicate that the SVR model had the best predictive performance and better predictive performance than the ARIMA model. In this study, the data is selected for a short period of time, a total of 24 months of monthly data, with a small total sample size, and the SARIMA model is better at forecasting with a small sample size. On the other hand, the use of machine learning models needs to consider the quantity of the study sample and cannot be used arbitrarily [2]. The SVR model performs better and may outperform the ARIMA model when the data of the study sample has to be large enough [16]. Also, the time series of container throughput in this study has seasonal fluctuations, and the SARIMA model is better at predicting seasonal time series.

The reason why the SVR model does not perform as well as the ARIMA model may be that the optimal hyperparameters are not well tuned, i.e., the combination of parameters that gives the best predictive performance is not used, which is a common problem with other machine learning models [16]. This is because the model cannot try all combinations of parameters and only tests the best-performing combination out of the potential possible combinations of parameters provided. Although this study uses manual input adjustment, grid search cross-validation methods, and random search methods and provides as wide a range of available choices for each type of parameter as possible, it is still possible to miss the best combination of parameters.

The Significance of the Number of New Covid-19 Infections on Container Throughput

The number of new COVID-19 infections has the strongest correlation with container throughput and a strong negative impact on container throughput. Moreover, the number of new COVID-19 infections can can significantly improve the forecasting accuracy of the SVR forecasting model. It indicates that this variable has a significant impact on the container throughput forecasting model, which is beneficial for training the container throughput forecasting model and improving the forecasting accuracy, rather than being an irrelevant variable.

The Significance of the Freight Rate Index for Container Throughput

This study finds that the Ningbo Port Freight Index is weakly correlated with the container throughput of Ningbo Zhoushan Port. In the multiple linear regression model, the Ningbo Port Freight Index has essentially no effect on the container throughput of Ningbo Zhoushan Port. However, the Ningbo Port Tariff Index can significantly reduce the MSE of the SVR model and effectively improve the forecasting accuracy of the SVR forecasting model. In summary, port container freight rates affect container traffic, and there is a relationship between the freight rate index and container throughput [5]. However, the freight index may not always be significant in the container throughput forecasting model, and the impact on container throughput may not be as great as expected.

The Significance of the Remaining Predictors for Container Throughput

The findings from the research by Tang, Xu and Gao regarding an optimal model based on multi-factor container throughput forecasting differ from the conclusions mentioned above [4]. The predictors the total retail sales and the import and export trade in their work are highly correlated with both the Shanghai port and the Lianyungang port, while our study finds that the correlation between these two predictors and the Ningbo Zhoushan port is weak, which is not beneficial for training a multiple linear regression forecasting model and improving the accuracy of the forecasts.

CONCLUSION

Main Finding

1) The best forecasting model for container throughput at Ningbo Zhoushan Port during the COVID-19 pandemic is influenced by COVID-19. It is changed from the SVR model derived from previous literature studies to the SARIMA model in this paper.
2) It is feasible to quantify the influencing factor of covid-19 as the number of new covid-19 infections, and the number of new covid-19 infections is meaningful for the study of container throughput at Ningbo Zhoushan Port. In the forecasting model, the number of new

ISBN: 978-618-5765-04-0
ISSN 3057-4269

COVID-19 infections has a significant negative impact on container throughput in Ningbo Zhoushan Port.

3) Ningbo Port Tariff Index as an explanatory variable added to the container throughput forecasting model of Ningbo Zhoushan Port is insignificant. This indicates that the Ningbo Port Tariff Index basically has a very weak and arguably no effect on container throughput.

Limitation of Research

1) *Data inadequacy:* The data set collected in this study is only for the last two years with a total of 24 months of data, which is not a long time, and the sample size is not large enough.
2) This paper uses only some of the commonly used and well predicted benchmark methods for time series forecasting, without further specific adjustments to each model or hybrid model. Adjustments or hybridization of the models may improve the forecasting accuracy of the models.
3) Insufficient number of comparison models.
4) Predictors are not comprehensive enough.
5) The lack of comparison with other forecasting models for container throughput in the COVID-19 period.
6) Other predictors were not significant enough.

Recommendation for Future Research

1) When there is a global or widespread pandemic of an infectious disease, and the impact of the disaster needs to be investigated, an attempt can be made to quantify the impact of the disaster by using the number of new infections as an impact variable.
2) The container throughput forecasting model used in this paper can be optimized and adjusted.
3) Future research can consider excluding the freight index as a predictor and adding more variables related to the container throughput of Ningbo Zhoushan Port but belonging to different aspects as predictors in the forecasting model in order to improve the forecasting accuracy.

REFERENCES

[1] T. Notteboom, "The adaptive capacity of container ports in an era of mega vessels: The case of upstream seaports Antwerp and Hamburg," Journal *of Transport Geography*, vol. 54, pp. 295-309, 2016.

[2] H. Chan, S. Xu, and X. Qi, "A comparison of time series methods for forecasting container throughput," *International Journal of Logistics Research and Applications*, vol. 22, pp. 1-10, 2018.

[3] P. M. Schulze and A. Prinz, "Forecasting container transshipment in Germany," *Applied Economics*, vol. 41, no. 22, pp. 2809-2815, 2009.

[4] S. Tang, S. Xu, and J. Gao, "An Optimal Model based on Multifactors for Container Throughput Forecasting," *KSCE Journal of Civil Engineering*, vol. 23, no. 9, pp. 4124-4131, 2019.

[5] A. Açık, "Volatility Spillover from Global Container Freight Indices to Port Throughputs in Turkey," *International Journal of Economics and Innovation*, vol. 5, pp. 101-113, 2019.

[6] H. Feng, M. Grifoll, P. Zheng, A. Martin-Mallofre, F. Murphy, and S. Li, "Evolution and container traffic prediction of Yangtze River Delta multi-port system (2001-2017)," *International Journal of Shipping and Transport Logistics*, vol. 13, pp. 44-69, 2021.

[7] D. Loske, "The impact of COVID-19 on transport volume and freight capacity dynamics: An empirical analysis in German food retail logistics," *Transportation Research Interdisciplinary Perspectives*, vol. 6, p. 100-165, 2020.

[8] B. L. Bowerman and R. T. O'Connell, Forecasting and Time Series: An Applied Approach (Duxbury advanced series in statistics and decision sciences). Duxbury Press, 1993.

[9] K. Koyuncu, L. Tavacioğlu, N. Gökmen, and U. Ç. Arican, "Forecasting COVID-19 impact on RWI/ISL container throughput index by using SARIMA models," *Maritime Policy & Management*, vol. 48, no. 8, pp. 1096-1108, 2021.

[10] J. Mladenović, V. Lepojevic, and V. jankovic-milic, "Modelling and Prognosis of the Export of the Republic of Serbia by Using Seasonal Holt-Winters and Arima Method," *Economic Themes*, vol. 54, 2016.

[11] J. Adamowski, H. Fung Chan, S. O. Prasher, B. Ozga-Zielinski, and A. Sliusarieva, "Comparison of multiple linear and nonlinear regression, autoregressive integrated moving average, artificial neural network, and wavelet artificial neural network methods for urban water demand forecasting in Montreal, Canada," *Water Resources Research*, vol. 48, no. 1, 2012.

[12] N. I. Sapankevych and R. Sankar, "Time Series Prediction Using Support Vector Machines: A Survey," *IEEE Computational Intelligence Magazine*, vol. 4, no. 2, pp. 24-38, 2009.

[13] K.-Y. Chen and C.-H. Wang, "Support vector regression with genetic algorithms in forecasting tourism demand," *Tourism Management*, vol. 28, no. 1, pp. 215-226, 2007.

[14] C. Ingle, D. Bakliwal, J. Jain, P. Singh, P. Kale, and V. Chhajed, "Demand Forecasting: Literature Review on Various Methodologies," in *2021 12th International Conference on Computing Communication and Networking Technologies (ICCCNT)*, pp. 1-7, 2021.

[15] A. Huang, K. K. Lai, H. Qiao, S. Wang, and Z. Zhang, "An Interval Knowledge Based Forecasting Paradigm for Container Throughput Prediction," *Procedia Computer Science*, vol. 55, pp. 1381-1389, 2015.

[16] M. Zafeiraki, "A Comparison of ARIMA and SVR in Short-Term Ship Motion Prediction," Master thesis, Utrecht Univ. 2022.

ISBN: 978-618-5765-04-0
ISSN 3057-4269

Biodiesel Production from Spent Coffee Grounds with Supercritical Ethanol: Economic Analysis and Life Cycle Assessment

Wirasinee supang
Program in Biotechnology,
Faculty of Science
Chulalongkorn University
Bangkok, Thailand
ORCID: 0009-0005-2817-1084

Prathana Nimmanterdwong
Department of Chemical Engineering,
Faculty of Engineering,
Mahidol University,
Nakhon Pathom, Thailand
ORCID: 0000-0002-1630-9489

Ruengwit Sawangkeaw
Institute of Biotechnology and
Genetic Engineering
Chulalongkorn University,
Bangkok, Thailand
ORCID: 0000-0003-3479-0672

Winatta Sakdasri
Program in Food Process Engineering,
School of Food Industry
King Mongkut's Institute of Technology
Ladkrabang
Bangkok 10520, Thailand
ORCID: 0000-0003-2624-6677

Panusorn Hunsub
Faculty of Food Technology,
Rangsit University
Pathum Thani, Thailand
ORCID: 0009-0009-8896-2768

Somkiat Ngamprasertsith
Fuels Research Center,
Department of Chemical Technology,
Faculty of Science
Chulalongkorn University
Bangkok, Thailand
ORCID: 0000-0003-0549-5412

***Abstract*— Biodiesel is an alternative fuel that could be produced from food waste. Spent coffee grounds (SCGs), solid food waste generated from the coffee industry, are promising feedstock for biodiesel production because they have high lipid content. Applying ethanol as an extracting solvent and a reactant creates an environmentally friendly route for biodiesel production from SCGs since it reduces the chemical consumption in the process. Furthermore, biodiesel production in a supercritical state simplified the process by not involving any chemicals except ethanol. However, the study on the economic feasibility of biodiesel production from SCGs with ethanolic extraction and supercritical ethanol transesterification, called EE-SET hereafter, is still deficient. This research focused on techno-economic analysis (TEA) and life cycle assessment (LCA) of biodiesel production from SCGs by EE-SET process. The computer simulation was used to design the production line and calculated the data for evaluating the viability of the process. LCA was applied to understand the impact on the environment generated by the EE-SET process. The TEA results showed that using the EE-SET process reduced the production cost. Since the obtained coffee oil-ethanol mixture from the extraction unit was straight-fed into the reacting unit, the evaporating unit was eliminated. LCA results showed that the distillation unit generated the highest environmental impact because of the CO_2 emission, while the drying unit had the lowest environmental impact. This study indicated that using TEA and LCA as evaluation tools could help develop biodiesel production from SCGs through the EE-SET process, making it more economically viable and environmentally responsible.**

Keywords—biodiesel, ethanolic extraction, spent coffee grounds, supercritical ethanol, economic analysis

INTRODUCTION

For three reasons, SCGs have been demonstrated as a promising feedstock for biodiesel production. First, the number of SCGs increases worldwide yearly due to the high growth of the coffee industry. Second, SCGs have a high lipid content of approximately 20% on a dried basis. Third, the fatty acid profile of SCGs is similar to plant oils such as palm and rapeseed oils. The utilization of SCGs as biodiesel feedstock can simultaneously reduce the amounts of waste and generate renewable energy for coffee processing plants.

In our previous work, ethanol was used to extract solvent and reactant to produce biodiesel from SCGs under supercritical conditions [1]. This EE-SET process significantly consumes less energy because the solvent removal step is eliminated. After ethanolic extraction, coffee oil-ethanol can directly feed into the supercritical reactor. This work aims to estimate the EE-SET process's economic feasibility and environmental impact using TEA and LCA, respectively.

METHODOLOGY

Process Description

The process flow diagram is shown in Figure 1. Fresh SCGs, with moisture content at 58.69 wt% as observed in our previous experiments [1], were fed to the dryer to remove the excess water from the SCGs and to obtain dried SCGs (DSCGs). To extract coffee oil from dried SCGs, ethanol was fed to the extractor along with dried SCGs. Ethanolic extracted coffee oil (MIX) contained 20 wt% of coffee oil. Defatted SCGs were considered solid waste. Then, the ethanol-coffee oil mixture was fed to a high-pressure pump to increase the mixture pressure to 15 MPa. The high-pressure mixture (HP-MIX) was transferred through a heat exchanger, and the mix was preheated before entering the reaction unit. A supercritical reactor was employed, and the reaction conditions were set at 350 ºC and 15 MPa without any catalyst. Before the ethanol-coffee oil mixture was fed into the reactor, the molar ratio was set to 30:1. The product line (HP-HT-PROD) consisting of biodiesel, glycerol, and excess ethanol was sent to the heat exchanger as a heating source for pre-heating the ethanol-coffee oil mixture (HP-MIX) of the next batch and cooling down product line (HP-LT-PROD). The throttling valve relieved the product line pressure to atmospheric pressure (LP-LT-PROD) before feeding the product to the distillation unit to remove the excess ethanol. The excess ethanol was recycled to the extraction unit. The final product was separated into biodiesel and glycerol in the separation unit.

ISBN: 978-618-5765-04-0
ISSN 3057-4269

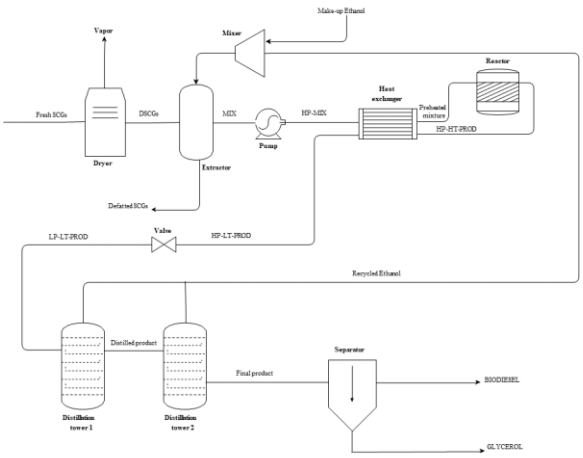

Figure* 1*: Process Flow Diagram of EE-SET Process

Process simulation

Aspen Plus® V12 simulated the biodiesel production process from SCGs by EE-SET process. Proximate and ultimate analysis of SCGs were defined [2] and SCGs was set as the non-conventional component. HCOALGEN and DCOALIGT were used as the enthalpy and density models of the feedstock. Extracted coffee oil was assumed to be triolein ($C_{57}H_{98}O_6$), the primary fatty acid in coffee oil extracted from SCGs [3]. The biodiesel production capacity was set at 1,000 tons per year as the main product. The thermodynamic model was UNIQUAC, which is suitable for transesterification reactions involving two liquid phases. The process simulation used ethyl linoleate ($C_{20}H_{36}O_2$) to represent a biodiesel product. The reaction temperature and pressure were based on conditions from our previous work (Supang, Ngamprasertsith, Sakdasri, & Sawangkeaw, 2024). The equipment size, utility usage, and material balance in the production were used to validate the economic feasibility of the process.

Techno-economic analysis (TEA)

Economic analysis was conducted to assess the feasibility of biodiesel production by the EE-SET process from SCGs. The project life plan was assumed to be 20 years. The production plant is located in Chumphon province, Thailand's largest coffee production province. The cost of equipment in process was estimated by the MS-Excel add-in program CAPCOST. The chemical engineering plant cost index (CEPCI) was applied to adjust the estimated cost for inflation and time variation, making the cost estimates more realistic and current. This adjustment was made using Equation (1), where $C_{Current}$ and C_{Base} represent the estimated equipment costs at the present time and at the reference time, respectively. $CEPCI_{Current}$ and $CEPCI_{Base}$ are the cost index for present and reference time, respectively. The CAPCOST add-in program was used to estimate the equipment cost based on price in 2017, of which *CEPCI* was 567.5. As of February 2024, the *CEPCI* present time was 800.9, which was used to update the cost estimates.

$$C_{Current} = C_{Base}\left(\frac{CEPCI_{Current}}{CEPCI_{Base}}\right) \quad (1)$$

The total cost of production (TPC) was calculated using methods described by Turton et al. [4]. TPC was the summation of direct manufacturing cost, the production fixed cost, and the general manufacturing expenses. The project's cash flow was used to calculate the net present value (NPV), which determined the project's profitability as represented in Equation (2), where *t* was the operating year of the project. R_t was the summation of inflows and outflows during each year of the project, while *i* was the discount rate, and *N* was the number of project life plans.

$$\text{NPV} = \sum_{t=0}^{N} \frac{R_t}{(1+i)^t} \quad (2)$$

Internal rate of return (IRR) was used to estimate the project's discount rate, which made NPV equal to zero. Equation (3) shows the calculation of IRR, where T is the total project life plan, t is the number of periods, Ct represents the net cash flow during the period t, and C0 represents the total initial investment costs.

$$\text{NPV} = 0 = \sum_{t=1}^{T} \frac{C_t}{(1+IRR)^t} - C_0 \quad (3)$$

Life cycle assessment (LCA)

LCA aims to assess and compare the environmental impact of utilizing SCGs as feedstock for biodiesel production. The system boundaries excluded the construction of the plant, equipment, infrastructure, transportation activities, and coffee brewing, as SCGs were considered non-hazardous waste. This study assessed a cradle-to-cradle life cycle. The functional unit (FU) used for evaluation was the production of 1 ton of biodiesel.

For the life cycle inventory (LCI) in Table 2 and life cycle impact assessment (LCA), materials, chemicals, water supply, electricity, resources, and emissions were collected from scientific literature and received from the Ecoinvent 3.4 database (Ecoinvent, Zurich, Switzerland). The standard LCA approach was carried out using the IMPACT 2002+ method and then analyzed by the Simapro version 8.0.5 software (PRé Consultants B.V. Netherlands). Mid-point and end-point categories were employed for interpretation.

RESULT AND DISCUSSION

Techno-economic analysis

According to Figure 1, the process simulation of EE-SET showed that the process reduced the complexity of the production plant when compared to the conventional biodiesel production plant. Applying supercritical ethanol can eliminate catalyst usage and reduce production costs. Additionally, a purification unit is not required in the EE-SET process, as the only contaminant in the product stream is ethanol. This allows the product to be sent directly to the distillation unit for ethanol recovery.

ISBN: 978-618-5765-04-0
ISSN 3057-4269

Figure 2 shows the total direct manufacturing cost for each category. The results revealed that total labor cost was the most influential factor in manufacturing costs. However, the total labor cost is difficult to adjust because laws and regulations, minimum wages, process safety, and plant location influence it. On the other hand, the second contributor was the waste treatment cost, around 0.17 million dollars per year, or 23% of the total cost. Defatted SCGs were the only waste generated in the process. It was treated as non-hazardous waste and cost 36 dollars per ton, according to Turton et al. [4]. Although the treatment cost of non-hazardous waste is cheap, the amount of solid waste generated from EE-SET was significant compared to the amount of the biodiesel product. The results also show that the high cost required in waste treatment and the labor cost affect the gross profit of the project. As illustrated in Table 1, the NPV and IRR of the project show a negative result at 0.75 million dollars and 12%, respectively. The result indicated that the project could profit from the plant within the project life plan.

Table 1: Fixed capital cost, total raw material cost

Item	$USD
Fixed capital cost	477,576
Direct manufacturing cost	
Raw material	
- SCG	1,170
- Ethanol	78,729
Total raw material	*79,899*
Waste treatment	174,425
Utility cost	71,609
Operating labor	263,774
Chemical labor	47,479
Maintenance and repair	28,655
Operating supplies	4,298
Laboratory change	39,566
Patents and royalties	36,293
Total direct manufacturing costs	*745,999*
Fixed cost	
- Plant overhead	203,945
- Taxes & insurance	15,282
Total fix cost	*219,227*
General Manufacturing expense	
- Administration costs	50,986
- Distribution and selling cost	133,075
- Research and development	60,489
Total general Manufacturing expenses costs	*244,550*
Total production cost (COM)	1,209,776
Revenue from Biodisel	1,199,681
Net annual profit	**(10,095)**
Net Present Value in 20 Years	**(746,925)**
Internal return rate (IRR)	**- 12%**

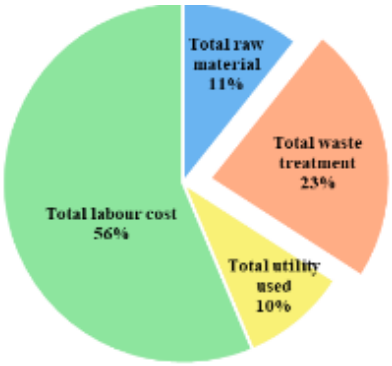

Figure 2: Distribution of Total Manufacturing Cost

Life-cycle assessment

Table 2 shows materials and energy balance in biodiesel production via the EE-SET process. Those values were normalized to calculate the life-cycle inventory (LCI) based on 1 ton of biodiesel production before estimating the environmental impacts, as shown in Figure 3.

Table 2: Inventory data for biodiesel production by using the EE-SET process based on a production capacity of 2.94 tons/day

Phase	Value	Unit/day
Input		
1. Drying		
SCGs (58.69 wt%)	33.80	ton
Electricity of dryer	610.64	kWh
2. Ethanolic extraction		
Ethanol [a]	0.45	ton
3. Heat exchanger		
Electricity of high-pressure pump	2.82	kWh
4. Supercritical extraction		
Electricity of reactor	5.84	kWh
5. Distillation		
Electricity of condenser	97.35	kWh
Electricity of reboiler	109.02	kWh
6. Separator		
Electricity of separator	2.27	kWh
Output		
1. Product		
Biodiesel	2.94	ton
2. By-product		
Glycerol	0.29	ton
3. Waste treatment		
DFSCGs	14.00	ton

[a] Calculated based on ethanol make-up and initial in the system

The estimated environmental performance in all impact categories of the EE-SET process at mid-point analysis is shown in Figures 3A and 3B. The sanitary landfill of DFSCGs had the most impact in most mid-point categories, especially in aquatic ecotoxicity at the value of 1.2 × 105 kg of triethylene glycol into water-eq. Moreover, the results indicated that the number of DFSCGs caused a higher impact than the electricity usage from all unit operations, including the dryer, pump, and reactor in the mid-point impact category. The comparison of the mid-point environmental performance between EE-SET and the conventional biodiesel production process is presented in Figures 3A and 3B. For traditional biodiesel production, the computer simulation used palm oil and methanol as feedstock to represent Thailand's commercialized biodiesel production plant. EE-SET impacted the environment less than conventional biodiesel production in almost all categories except aquatic ecotoxicity.

ISBN: 978-618-5765-04-0
ISSN 3057-4269

Similar to the mid-point analysis of EE-SET, the large amount of defatted SCGs greatly impacted the environment. Although DFSCGs were defined as non-hazardous waste, the amount of generated DFSCGs in EE-SET was significantly higher than solid wastes generated from the conventional biodiesel production from palm oil. Furthermore, direct landfill SCGs emit greenhouse gases, mainly methane, contributing around 95% of the total impact compared to the other greenhouse gases [5]. Nonetheless, using SCGs as feedstock for biodiesel production is a valuable route for reducing the environmental impact than direct landfill [5], but at the end-point analysis of EE-SET (Figure 3C) indicated that DFSCGs still had the most effect on climate change because the amount of greenhouse gas released from DFSCGs landfilled. Therefore, to reduce the impact of the EE-SET process on environmental performance, the utilization of DFSCGs is necessary. For example, DFSCGs could be sold as solid fuel or used as feedstock for thermo-conversion processes such as combustion and gasification to generate surplus energy [6].

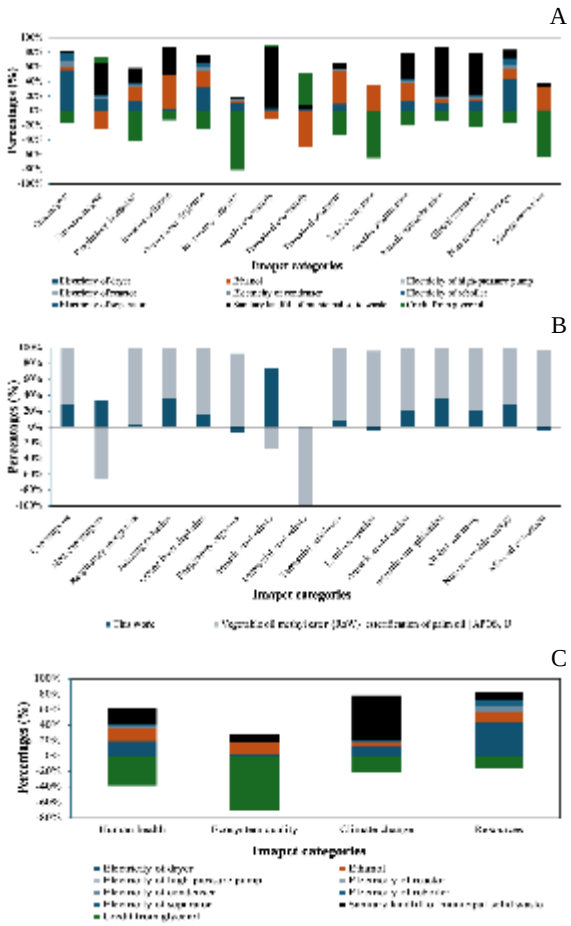

Figure 3: Environmental Impacts of 1 Ton of Biodiesel (A and B: midpoint categories, and C: endpoint categories)

CONCLUSION

This study successfully applied computer simulation using Aspen Plus V12, along with techno-economic analysis (TEA) and life cycle assessment (LCA), to evaluate biodiesel production from SCGs via the EE-SET process. Material and energy balances generated from the simulation were incorporated into the TEA and LCA to assess the profitability and sustainability of the proposed process. The TEA results indicated that the EE-SET process for biodiesel production from SCGs is currently unprofitable, as waste management costs account for over 23% of total manufacturing expenses. Furthermore, the LCA revealed significant environmental impacts, primarily due to the disposal of defatted SCGs (DSFSCGs) in sanitary landfills, which emits large amounts of greenhouse gases, particularly methane. A promising solution to reduce waste management costs is to sell defatted SCGs as solid fuel by adding a pelletizing machine or using defatted SCGs as a heating source in a boiler integrated into the EE-SET process. Both LCA and TEA will need to be recalculated in future studies once these additional unit operations are incorporated.

ACKNOWLEDGMENT

This research is funded by Thailand Science research and Innovation Fund Chulalongkorn University.

REFERENCES

[1] W. Supang, S. Ngamprasertsith, W. Sakdasri and R. Sawangkeaw, "Biodiesel Production from Spent Coffee Grounds by Using Ethanolic Extraction and Supercritical Transesterification," *BioEnergy Research*, 2024.

[2] L. Bartolucci, S. Cordiner, P. Mele and V. Mulone, "Defatted spent coffee grounds fast pyrolysis polygeneration system: Lipid extraction effect on energy yield and products characteristics," *Biomass and Bioenergy* , vol. 179, p. 106974, 2023.

[3] K. Somnuk, P. Eawlex and G. Prateepchaikul, "Optimization of coffee oil extraction from spent coffee grounds using four solvents and prototype-scale extraction using circulation process," *Agriculture and Natural Resources*, vol. 51, no. 3, pp. 181-189, 2017.

[4] R. Turton, R. C. Bailie, W. B. Whiting and J. A. Shaeiwitz, Analysis, synthesis and design of chemical processes, London, United Kingdom: Pearson Education, 2008.

[5] A. Forcina, A. Petrillo, M. Travaglioni, S. di Chiara and F. De Felice, "A comparative life cycle assessment of different spent coffee ground reuse strategies and a sensitivity analysis for verifying the environmental convenience based on the location of sites," *Journal of Cleaner Production*, vol. 385, p. 135727, 2023.

[6] S. B. Kang, H. Y. Oh, J. J. Kim and K. S. Choi, "Characteristics of spent coffee ground as a fuel and combustion test in a small boiler (6.5 kW)," *Renewable Energy*, vol. 113, pp. 1208-1214, 2017.

Design and Investigation of a Membrane Gas Separation Process for the Post-combustion CO_2 Capture from Flue Gas

Chrysovalantou Koutsiantzi
Dept. of Chemical Engineering
Aristotle University
Thessaloniki, Greece
ckoutsian@cheng.auth.gr

Alexandros Chatzis
Dept. of Chemistry
Aristotle University
Thessaloniki, Greece
adchatzis@chem.auth.gr

Ioannis Kellartzis
Dept. of Chemical Engineering
Aristotle University
Thessaloniki, Greece
ikellar@chem.auth.gr

Elissavet Lamprinidou
Dept. of Chemistry
Aristotle University
Thessaloniki, Greece
elamprini@chem.auth.gr

Effrosyni Peleka
Dept. of Chemistry
Aristotle University
Thessaloniki, Greece
peleka@chem.auth.gr

E. Kikkinides
Dept. of Chemical Engineering
Aristotle University
Thessaloniki, Greece
kikki@cheng.auth.gr

Anastasios I. Zouboulis
Dept. of Chemistry
Aristotle University
Thessaloniki, Greece
zoubouli@chem.auth.gr

***Abstract*— The urgent need to reduce greenhouse gas emissions holds significant social and scientific importance. Today, one of the main contributors to climate change is the energy sector, with the fossil fuels combustion accounting for approximately 65% of the total anthropogenic GHGs globally. The present study discusses the fabrication of a membrane gas separation system as an innovative technology for post-combustion CO_2 capture from flue gases, in order to both control the CO_2 emissions of the exhaust gases and simultaneously reuse the captured CO_2 for energy production via methanation, able to be installed and distributed to the natural gas grid or fabricated and distributed to remote areas. Membrane gas separation is an innovative technology for capturing CO_2 from flue gases in electricity production units like PPC and commercially available polymeric membranes can enhance CO_2 capture of such production capacities. This separation method involves the use of specialized membranes that selectively allow CO_2 to pass through while retaining other gases, such as nitrogen and oxygen, from the flue gas stream. Membrane-based CO_2 capture offers several advantages, including a smaller footprint, lower energy consumption, easy scalability, and integration with existing facilities. The separation process operates by pressurizing the flue gases and directing them into the membrane, where the CO_2 permeates through the fibers, leaving behind a concentrated N_2 stream. The permeate stream can then be captured and utilized or stored, contributing to the reduction of greenhouse gas emissions. The target is to obtain high concentrations of CO_2 reaching up to 95%. For this purpose, the process conditions of the flue gas stream separation are first simulated in lab scale for the N_2 and CO_2 synthetic mixture in 1- and multiple stage configuration, and their validation of the system conditions will follow during its fully operation at the premises of the Agios Dimitrios V, PPC Power Plant, which is located at Ptolemaida Mines, for a sufficient period of time in order to optimize the processes.**

Keywords*— *post-combustion CO_2 Capture; Greenhouse Gases (GHG); Polyimide membrane; Flue Gas; Membrane Gas Separation.

Abbreviations and Acronyms

CCU – Carbon Capture and Utilization

GHG – Greenhouse Gas

HF – Hollow Fiber

PI – Polyimide

PLC – Programmable Logic Controller

PPC – Public Power Cooperation

INTRODUCTION

In the recent years, there is an urgent need to reduce Greenhouse Gas emissions (GHG). Today, one of the main contributors to climate change is the energy sector, with fossil fuels combustion accounting for approximately 65% of the total anthropogenic GHGs globally. Carbon Capture and Utilization (CCU) represents the total of technologies able to capture carbon at point sources of directly from air and use it to produce essential products, leading to emissions' reduction, and eliminating the need of using virgin fossil feedstock [1]. CO_2 captured from processes as a by-product, can be valorized into various products important for the Oil and Gas industry. Modern facilities that produce biomethane include and take advantage of carbon capture and reuse. CO_2 derived from biogas upgrading is one of the most sustainable sources of biogenic CO_2. Likely, post-combustion CO_2 separation of energy production units is vital, in terms of sustainable management. Polyimide (PI) membranes have been employed for CO_2 separation as an effective and low-cost method with a high potential of larger-scale applications [2]. This study includes the evaluation of a PI module, regarding the

ISBN: 978-618-5765-04-0
ISSN 3057-4269

successful CO_2 / N_2 separation of flue gas mixtures, for future utilization biogenic CO_2 feed in biological methanation.

In biomethanation, biogenic CO_2 reacts with hydrogen for CH_4 production, according to the equation:

$$4H_2 + CO_2 \rightarrow CH_4 + 2H_2O \quad (1)$$

EXPERIMENTAL

Preliminary evaluation of the 1 – stage membrane separation application.

Before the startup and the initial operation of the membrane separation apparatus, preliminary experimental tests were carried out in a one-stage configuration membrane unit, employing a 1-stage membrane module UBE CO-0302SES. The binary gas separation experiments have been performed in a laboratory-scale unit, specially designed for this application. The experimental membrane separation unit involves the study of a single stage separation system, which is comprised of: the polymeric membrane module, a mass flow and separation pressure control system using the Genie Runtime Software©, a back pressure regulator (Brooks) to maintain the separation pressure, mass flow meters (Aalborg) connected at every gas stream of the process and a gas analyzer for the efficient output streams' analysis in terms of % CO_2 purity.

The hollow fiber (HF) polyimide module which is used for the CO_2 separation was fabricated by UBE, CO-0302SES and is the smallest-area UBE CO_2 Separator with 1inch diameter (body part) and 380mm length, suitable for lab scale testing (Fig. 1).

Figure 1 UBE CO-0302SES membrane module for CO_2 separation.

The certain membrane module can handle up to 10L/min of inlet gas for efficient separation, meeting comprehensive requests for lab scale tests. More information on the PI membrane characteristics and operating condition is available at Table 1 below.

Table 1: Separation Conditions of the PI Membrane Module

Separation Conditions	
Max. Pressure	10 barG
Max. Temperature	60 ºC
Feed Gas Temperature	5 - 60 ºC
Feed gas oil content	≤ 0.01 mgf/Nm^3(0.008 ppm w/w)
Feed gas relative humidity	≤ 80 %
Feed gas particle size	≤ 0.01 μm

The feed gas is delivered by 2 gas cylinders of 99.99% purity (Allertec, Air Liquide). The initial gas feed is simulating the % volumetric flue gas composition (equal to 10 – 15% CO_2 and 85 – 90% N_2), according to information provided by PPC S.A. and existing bibliography, regarding coal-fired Power Plants. Furthermore, separation test have been also conducted for the separation of lower – N_2 compositions (e.g. 60% N_2 – 40% CO_2)

In particular, during the separation tests, pressure and mass flow measurements were conducted, while the % CO_2 purity and recovery were evaluated in the product gas (permeate stream).

Operation of the pilot scale 2- stage membrane separation system

The pilot-scale system fabrication is based on the findings of the single stage results: the connection of more membrane modules can lead to higher CO_2 purities, by re-entering the permeate stream at a 2nd stage after necessary compression to the desired separation pressure [3]. The addition of compressors and more stages may increase the total energy consumption of the system, and different multistage configurations have been tested and evaluated lately to achieve lower energy consumptions for high membrane – gas contact area [4].

The CO_2 – capture setup that was evaluated during operation, consists of 4 identical membrane modules, CO-0302SES fabricated by UBE (as described at the single stage configuration) arranged in 2 stages: The first stage includes 3 membrane modules and the 2nd stage 1 membrane module. The preliminary study, which includes the results presented in this paper, was performed at the Chemical Engineering A' Laboratory of Aristotle University of Thessaloniki, where the separation of CO_2 / N_2 binary gas mixtures was investigated in the pilot-scale membrane separation setup. % CO_2 purity and recovery were studied in different conditions and compared to already existing results, in order to optimize the CO_2 separation system operation.

The 2-stage membrane configuration, employing 4 polyimide hollow fiber (HF) membrane modules (3 at the 1st stage and 1 at the 2nd stage) with recirculation of the 2nd retentate stream is presented in Fig. 2. In total, the separation apparatus (as shown in Fig. 2) has dimensions of 1.80 x 3.0 (m).

ISBN: 978-618-5765-04-0
ISSN 3057-4269

Figure 2 Membrane separation setup for CO_2 / N_2 separation

In this multistage application, the control of the process was performed through a Programmable Logic Controller (PLC). The total system consists of different instruments for control and measurement of the separation characteristics and conditions. Fig. 3 and Fig. 4 below, present the flowsheets of the 1- and 2- stage separation systems, accordingly, along with the necessary equipment employed for the operation of the 2 different systems.

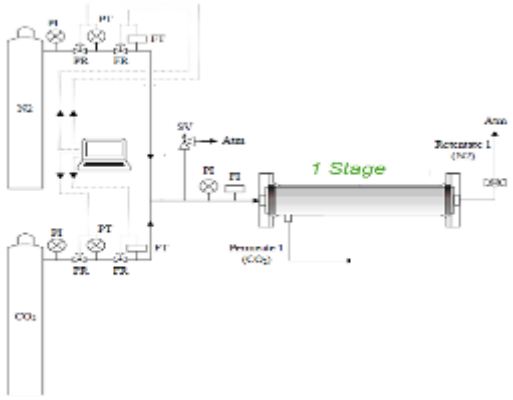

Figure 3 Flowsheet of the 1-stage membrane separation system

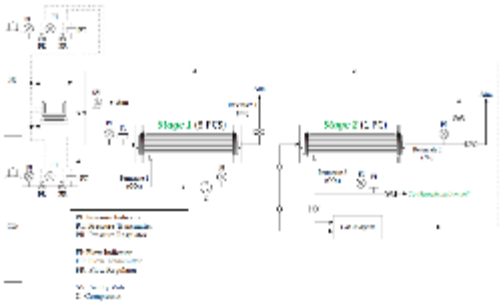

Figure 4 Flowsheet of 2-stage membrane separation system

The initial supply of the separation system (mL/min) is controlled by 2 Automatic Mass Flow Controllers with real-time Mass Flow Indicators (MFCI), fabricated by Silver Automation Instruments Ltd, China. The initial pressure of the gases is indicated too for safety reasons, and it is stable under 2 barG. The initial gas mixture, after combining the 2 initial streams, is then pressurized using an oil-less compressor, 80RAD Double Head Type Model (C-1, G&M Tech Inc., Korea). The initial gas stream is pressurized up to 7 bars, according to the incoming feed supply to the compressor. After reaching the desired separation pressure, the gas mixture enters the 1st stage which comprises of 3 CO-0302SES membrane modules connected in serial configuration. A Back Pressure Regulator (BPR, Alicat Scientific B.V.) is connected to the retentate stream in the exit of the 3rd membrane module in order to maintain the desired upstream pressure during separation stable in the membranes. The pressure before and after the 1st stage of separation are constantly checked through Pressure Indicators (PI, WIKA). The 2 outlets of the 1st stage are: a) The retentate stream, consisting mainly of N_2, which is directly exhausted to the outdoor air safely through a vent-gas system, and b) The permeate stream, consisting of high CO_2 purity levels and exits in ambient temperature and pressure the 1st stage. The latter stream is then directly subjected to further separation in the 2nd separation stage to enhance % CO_2 purity of the final product.

The permeate of the 1st stage is checked by a Mass Flow Indicator, calibrated for CO_2 measurement (FI, Aalborg Instruments & Controls, INC.) and directly inserts the 2nd compressor C2 (G&M Tech Inc.) for feed compression to the desired separation pressure. Then, the pressurized stream enters the 4th membrane module (2nd stage) which is connected to a 2nd Back Pressure Regulator (Alicat Scientific B.V.) and separates again the feed stream to 2 product streams: a) The retentate stream, consisting of CO_2 and N_2 which is directly recirculated to the C1 input to enhance separation efficiency, and b) The permeate stream consisting of a high- purity CO_2 stream, reaching up to 90% CO_2, which is the final product of the membrane separation process. The product stream is monitored by a Mass Flow Indicator (MFI, Kytola Instruments) and a Pressure Indicator (PI, WIKA) in order to adjust to the desired input variables of the methanation unit. The % vol. CO_2 purity of the gas streams in every step of the separation is monitored by a suitable Gas Analyzer (Gas Data GFM406).

The full-scale application and operation of the CO_2 – capture system will be performed at the premises of the Agios Dimitrios V, PPC Power Plant, located at Ptolemaida, to optimize the processes and utilize the CO_2 product for energy – production applications. During operation in the PPC, the captured CO_2 product stream can be directed to a biomethanation unit for hybrid energy production. In this process, the CO_2 is combined with hydrogen, derived from an electrolyzer, to produce CH_4. This biomethanation approach not only contributes to sustainable energy production but also enables the efficient utilization of captured CO_2, aligning with efforts to enhance the overall environmental impact of the electricity production unit.

RESULTS

Separation results – 1 stage configuration

Initially, the lab scale separation experiments in single - stage configuration were carried out with a CO_2 / N_2 gas mixture in ratios of 40/60, respectively. The total flow rate of the gas feed stream was adjusted to 2100 mL/min by varying the separation pressure from 1 to 8 bar. The stage cut fraction (stage cut, θ) and CO_2 recovery (% CO_2 Recovery) were calculated to evaluate the level of separation. The Equations used for such calculations, are presented below:

$$\text{Stage cut}, \theta = \frac{Q_{permeate}}{Q_{feed}} \qquad (2)$$

ISBN: 978-618-5765-04-0
ISSN 3057-4269

Where Q is the volumetric flow of the permeate ($Q_{permeate}$) and the feed (Q_{feed}).

$$\%\ CO_2\ \text{Recovery} = \frac{Q_{permeate} \times y_p}{Q_{feed} \times y_{p,0}} \quad (3)$$

Where y is the CO_2 concentration at the permeate stream (y_p) and at the feed stream ($y_{p,0}$).

The % CO_2 purity and recovery levels achieved in the single stage configuration are presented below at Fig. 5. In a range of pressure values between 4.5 – 6.5 bar, CO_2 purity is decreasing between 39% and 33%, while CO_2 recovery is increasing, reaching up to 100%. This happens due to the increased flow of the gas in the permeate stream in higher ΔP values in the membrane.

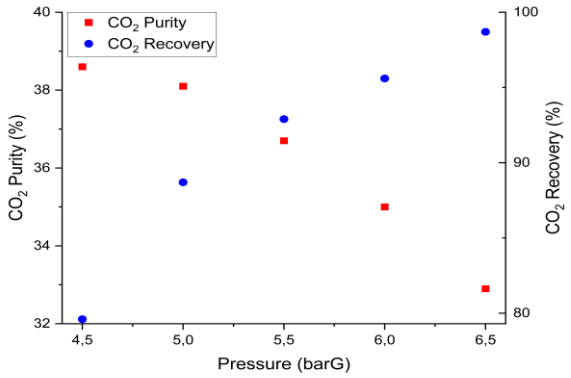

Figure 5 %CO_2 Purity and Recovery change at the permeate stream according to ΔP during separation

In the case of the separation pressure of 4 barG, which is presented in the Table 2, and initial composition of 15% CO_2, the permeate stream after membrane separation contains 53.1% CO_2, achieving 38.1% purity enrichment, with a recovery of 44.5%

Table 2 1 stage application: (Feed stream flow rate: 1500 mL/min, Feed stream composition: 85 N_2/15 CO_2 and ΔP = 4 bar)

CO_2 Purity @Permeate	53.1 %
CO_2 Recovery	44.5 %

Separation results in 2 stage configuration – comparison

In the 2-stage pilot scale application, the initial gas flow rate was controlled at 10 L/min with 15% CO_2 initial purity while keeping the ΔP value stable at 4 bars. The final CO_2 product stream, meaning the permeate stream of the 2nd stage, reached up to 82.9% purity with a CO_2 recovery of 17.1%, as presented in Table 3. It is therefore clear, that the contribution of the 2nd stage is quite important for the membrane process.

Table 3 2 - stage application: Feed stream flow rate: 10 L/min Feed stream composition: 85 N_2/15 CO_2 and ΔP = 4 bar)

CO_2 Purity @Permeate$_2$	82.9 %
CO_2 Recovery	17.1 %

However, lower %recovery values lead to greater CO_2 losses during the separation process. For that reason, further investigation was done on the parameters influencing the CO_2 recovery. The addition of the recirculation stream is a change that can lead to increase of the product stream flow, and thus to the total recovery of the process. Further investigation on the CO_2 purity and recovery rates is performed in Fig. 6, where separation tests for the initial compositions of 90 N_2/10 CO_2 (% vol) and b) 75 N_2/25 CO_2 respectfully were performed. By evaluating the diagram behavior, an optimal combination of CO_2 recovery and purity should be considered, in order to provide the preferable CO_2 purity, without further feed losses in the environment.

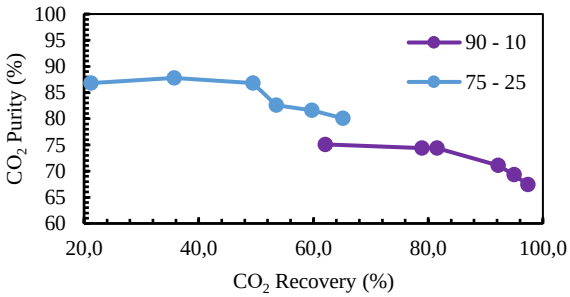

Figure 6 CO_2 purity and recovery (%) changes for 2 different feed mixture compositions equal to a) 90 N_2/10 CO_2 (% vol) and b) 75 N_2/25 CO_2 (% vol) at the flow rate of 10 L/min, 25 ºC.

From the diagram above, the 90 – 10 feed gas concentration reaches 75% CO_2 purity and 60% recovery at the same time, for the experimental conditions of 3 barG. Consequently,lower Pressure values are recommended for more efficient CO_2 separation in the permeate stream.

CONCLUSIONS

The addition of the 2nd stage at the permeate stream enhances the produced CO_2 purity for effective CO_2 capture and reuse, as the 2nd stage configuration leads to a 56.12% purity increase. However, the increase of streams and the removal of the 1st stage's retentate stream led to a decrease in the CO_2 recovery by 61.6%. Thus, the optimization of the system and the successful operation of the CO_2 capture with a multistage system, should take into consideration those parameters, and achieve the best product CO_2 purity and recovery combination.

After the successful installment and operation of the CO_2 separation unit at the PPC plant in continuous flow, the captured CO_2 stream can be directed to a biomethanation plant for hybrid energy production. In this process, the CO_2

ISBN: 978-618-5765-04-0
ISSN 3057-4269

is combined with hydrogen, sustainably generated from an electrolyzer, to produce CH_4. By this process, high – purity biomethane production will take place in the plant, leading to renewable energy production. This application will achieve further utilization of the CO_2, contributing to sustainable energy production and improving the overall environmental impact of the plant. The end goal of the produced biomethane is to be installed and meet the energy needs of remote energy systems that generally have lower required capacity, such as remote areas and islands that are not interconnected to the central natural gas distribution system.

ACKNOWLEDGMENTS

The "Demonstration of a mobile unit for hybrid energy storage based on CO2 capture and renewable energy sources (LIFE CO2toCH4)" project has received funding from LIFE Programme of the European Union, Grant agreement LIFE 20CCM/GR/001642.

REFERENCES

[1] CO2 Value Europe, “The contribution of carbon capture & utilization towards climate neutrality in Europe: A scenario development and model exercise,” Brussels, 2024. [Online]. Available: https://shorturl.at/cCM16

[2] P. Gkotsis, E. Peleka, and A. Zouboulis, “Membrane-Based Technologies for Post-Combustion CO2 Capture from Flue Gases: Recent Progress in Commonly Employed Membrane Materials,” *Membranes (Basel)*, vol. 13, no. 12, 2023, doi: 10.3390/membranes13120898.

[3] M. Scholz, T. Melin, and M. Wessling, “Transforming biogas into biomethane using membrane technology,” *Renewable and Sustainable Energy Reviews*, vol. 17, pp. 199–212, 2013, doi: 10.1016/j.rser.2012.08.009.

[4] J. Xu, H. Wu, Z. Wang, Z. Qiao, S. Zhao, and J. Wang, “Recent advances on the membrane processes for CO2 separation,” *Chin J Chem Eng*, vol. 26, no. 11, pp. 2280–2291, 2018, doi: https://doi.org/10.1016/j.cjche.2018.08.020.

EV Charging Demand Prediction

Vasileios-Martin Nikiforidis
Research Division
Public Power Corporation
Athens, Greece
v.nikiforidis@ppcgroup.com

Stamatina Karakitsiou
Research Division
Public Power Corporation
Athens, Greece
m.karakitsiou@ppcgroup.com

Anestis Anastasiadis
Research Division
Public Power Corporation
Athens, Greece
an.anastasiadis@ppcgroup.com

Kostas Hrissagis-Chrysagis
Research Division
Public Power Corporation
Athens, Greece
k.chrysagis@ppcgroup.com

George Papadakis
Research Division
Public Power Corporation
Athens, Greece
g_a.papadakis@ppcgroup.com

Abstract*— Electric vehicles (EVs) are crucial for reducing greenhouse gas emissions and improving energy efficiency, but their integration into the electrical grid presents challenges. A core task in this process is the prediction of charging demand in a network of EV chargers, which allows for optimizing grid management and making the most of renewable energy sources (green charging). This study explores predictive modeling techniques to forecast EV charging demand using data from the largest network of charging stations in Greece, which includes charging sessions from ~1,200 chargers from June 2022 to January 2024. We employed both univariate and multivariate models: the former focus solely on historical energy consumption, while the latter incorporate additional, contextual data, such as daily temperature, to enhance prediction accuracy. Our approach involved extensive data preprocessing, including cleaning and normalization, to remove noise. We evaluate various machine learning models, such as Linear Regression, Ridge Regression, and Lasso Regression, alongside deep learning models like Long Short-Term Memory (LSTM) networks and Convolutional Neural Networks (CNNs). The results indicate that while LSTM models excel in univariate settings, due to their ability to capture temporal dependencies, traditional regression models are more effective in multivariate contexts, where additional features are available. These findings highlight the importance of selecting appropriate learning models based on data characteristics and prediction objectives, providing valuable insights for optimizing EV charging infrastructure and enhancing grid reliability.

Keywords— ***Electric Vehicles (EVs); EV Chargers; Grid stability.***

INTRODUCTION

Electric vehicles (EVs) are becoming an essential and indispensable component in the efforts of reducing greenhouse gas emissions and achieving a net-zero future [1]. Their ability to operate without producing tailpipe emissions and their higher energy efficiency compared to internal combustion engines make them a favorable choice in the transition towards sustainable transportation. However, the widespread adoption of EVs introduces new challenges for managing the electrical grid, particularly in predicting and accommodating fluctuating charging demands [2]. Accurate prediction of EV charging demand is critical not only for optimizing grid operations but also for demand response scenarios, which aim to maximize the consumption of renewable energy sources, such as solar and wind. Effective demand forecasting can help balance loads, reduce peak demand stress on the grid, and improve overall energy management.

In this study, we aim to develop robust predictive models for EV charging demand by leveraging both traditional machine learning (ML) techniques [3] and advanced deep learning (DL) algorithms [4]. We use a comprehensive dataset comprising all charging sessions from approximately 1,200 EV charging stations across Greece, covering the period from June 2022 to January 2024. Our modeling approach includes both *univariate models*, which rely solely on historical charging data, and *multivariate models*, which incorporate additional contextual information, such as the daily temperature, humidity and global radiation corresponding to weather stations all over Greece. The data underwent careful preprocessing, including cleaning and normalization, to ensure accurate comparisons and low levels of noise.

More specifically, our study evaluates five models: Linear Regression [5], Ridge Regression [6], Lasso Regression [7], Long Short-Term Memory (LSTM) networks [8], and Convolutional Neural Networks (CNNs) [9]. By comparing the performance of these models across different settings, we seek to identify the most effective strategies for predicting EV charging demand. Our findings contribute to a better understanding of how different modeling approaches can be applied to optimize the stability of the electrical grid, enhance energy efficiency, and support the integration of renewable energy sources.

DATA COLLECTION AND PREPROCESSING

The dataset utilized in this study comprises daily measurements of energy consumption, charging duration etc. from PPC's network of EV chargers. The charging stations are located throughout Greece, while the recorded data span from June 2022 to January 2024.

Initially, the dataset included data from 1,116 EV chargers. However, to ensure the robustness and reliability of our analysis, we conducted a thorough data cleaning process. Chargers that were operational for only a single day were excluded from the dataset to prevent skewed results caused by outliers or incomplete data. This filtering reduced the dataset to 1,063 chargers, providing a more stable and representative sample for the study. Detailed statistics are provided in Table 1, where the left and right columns report the original and the clean data characteristics, respectively. Data cleaning had a minor impact on the data used in our analysis: the number of chargers was reduced by just 4.7% and the overall duration by 6.6%, while the number of

ISBN: 978-618-5765-04-0
ISSN 3057-4269

charging sessions and the overall consumed load were reduced by less than 0.3%.

Table 1: Dataset utilized in this study

	Original Data	After cleaning
Time period	May 31, 2022 – January 31, 2024	
Number of chargers	1,116	1,063
Number of municipalities	234	198
Number of charging sessions	131,535	131,186
Overall load consumed	2.021 GWh	2.015 GWh
Overall Duration	268,060 hrs	250,388 hrs

Following data cleaning, we normalized the energy consumption and duration data to account for varying operational periods of the chargers. Normalization was performed by dividing the total energy consumption and duration of each charger by the number of active days from the first recorded usage to the end of the measurement period, January 2024. This approach allowed us to compare usage patterns across chargers that were installed at different times and had different lengths of operational data, ensuring fair and accurate comparisons.

Additionally, we aggregated the data by area to explore usage patterns at the municipality level. This involved grouping the chargers by their geographical locations and calculating total energy consumption and usage duration for each area. We noticed, though, that there were many duplicates in the municipality information associated with the chargers (e.g., “Kalithea” also appeared as “Kallithea”). The original 234 municipalities were reduced to 198, after the deduplication process.

The cleaned data provide a comprehensive view of EV charger utilization across diverse regions, as explained below in more detail.

EXPLORATORY DATA ANALYSIS

The exploratory data analysis of the EV charging data is essential to understanding usage patterns and guiding the modeling approach. First, we examine two aspects per charger and per municipality:

i) usage frequency, and
ii) the distribution of energy consumption.

Our analysis in Figures 1-6 indicates that both aspects follow a *power law distribution*, where a small number of chargers or municipalities accounts for a large proportion of the total usage. More specifically, the power law distribution is a type of statistical distribution characterized by the fact that a few events are extremely common, whereas the majority are rather rare. In the context of EV charging stations, the power law distribution suggests that most charging sessions are concentrated in a few high-demand locations, while most chargers are used rather infrequently and to a much lower extent. This has significant implications for managing the EV charging network; for example, targeted interventions at high-demand sites could have a disproportionate impact on the overall grid management and load balancing, whereas the identification of less popular chargers allows the charging point operator (i.e., PPC) to exploit the unused capacity through dynamic contracts with the distribution system operator.

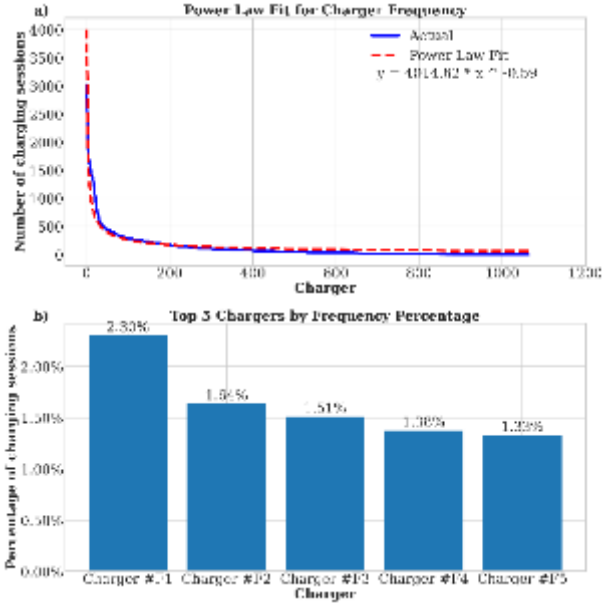

Figure 1: a) Frequency of charging sessions per charger, and b) Top 5 chargers with most charging sessions.

Frequency of Usage

Figure 1a) represents the usage frequency (i.e., the number of charging sessions) per charger, while Figure 2a) shows the aggregated usage frequency of chargers per municipality. We observe that a handful of chargers and municipalities are extremely popular, while the majority experience much lower demand. This pattern is crucial for understanding the uneven distribution of demand across the network and for highlighting the importance of focusing on key locations for optimization strategies.

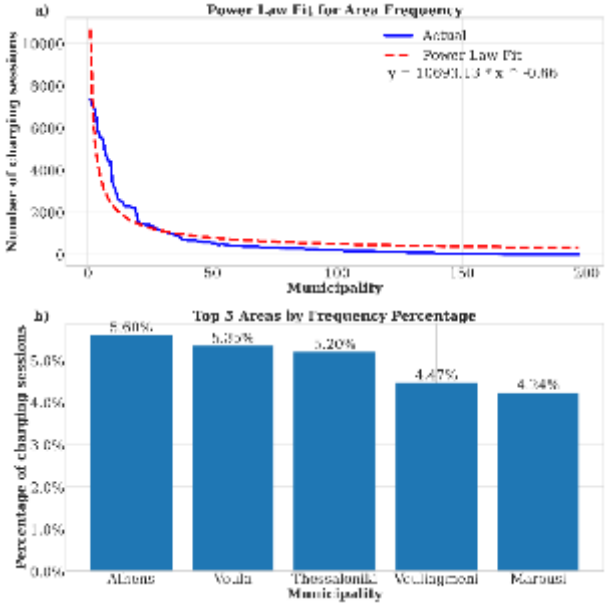

Figure 2: a) Frequency of charging sessions per municipality, and b) Top 5 municipalities with mots charging sessions.

Figures 1b) and 2b) isolate the top 5 chargers and municipalities, respectively, based on their percentage

ISBN: 978-618-5765-04-0
ISSN 3057-4269

contribution to the overall frequency. The former account for almost 10% of the overall charging sessions, while the latter for almost 25%. Moreover, the top 20% of chargers are responsible for approximately 72% of the total charging frequency, while the top 20% of municipalities account for 77% of the total sessions. These patterns illustrate the Pareto principle [10], also known as the 80/20 rule, which states that a small proportion of the input accounts for the majority of the output. This finding emphasizes the concentrated nature of demand.

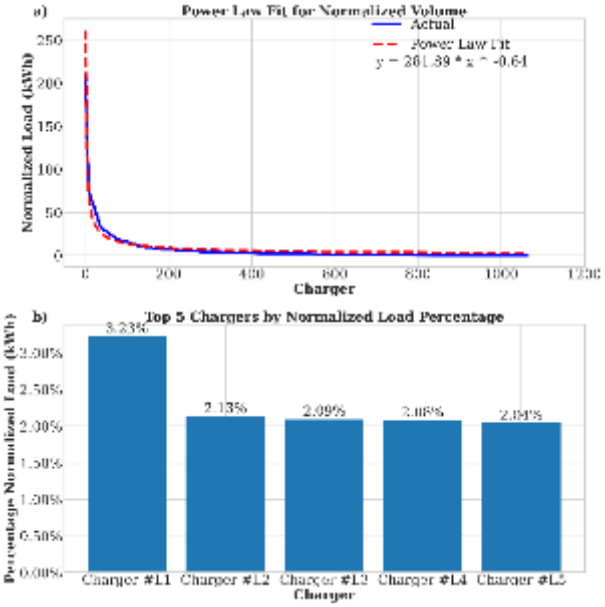

Figure 3: a) Normalized energy load per charger, and b) Top 5 chargers in terms of energy load.

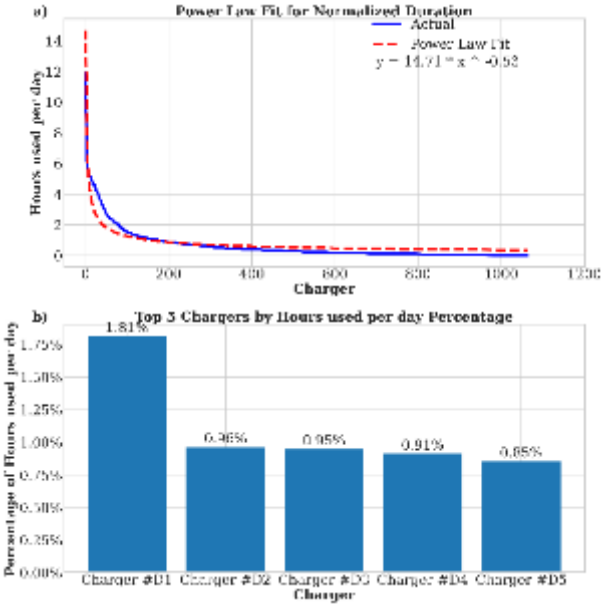

Figure 4: a) Normalized charging duration per charger, and b) Top 5 chargers in terms of longest duration.

Normalized Energy Load and Duration

Next, we explore the energy consumption and duration of charging sessions across the network, which we normalized to account for the varying installation times of chargers. To ensure fair comparisons, we divided each charger's (or municipality's) total energy consumption or duration by the number of active days—defined as the period from the first recorded usage to the end of January 2024. For municipalities with multiple chargers, the first recorded use of any charger within that municipality was used to calculate the active days.

Figures 3a) and 4a) depict the normalized energy consumption (in kWhs per day) and charging duration (in hours per day) of each charger, respectively. The power law fit again reveals that very few chargers dominate both measures. Figures 3b) and 4b) further highlight the contribution of the top 5 chargers, which amounts to almost 10% of all normalized energy consumption and almost 6.5% of the overall duration. Notably, 77% of total energy consumption and 70% of the overall duration stem from the top 20% chargers, demonstrating the presence of the Pareto principle in this context as well.

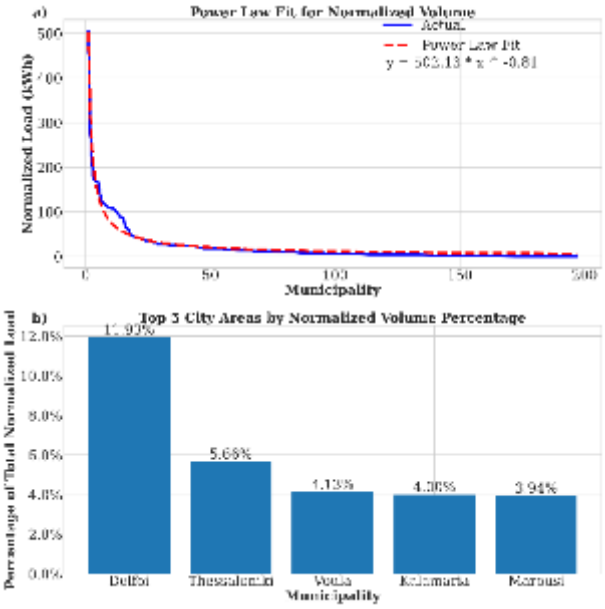

Figure 5: a) Normalized energy load per municipality, and b) Top 5 municipalities with respect to energy load.

ISBN: 978-618-5765-04-0
ISSN 3057-4269

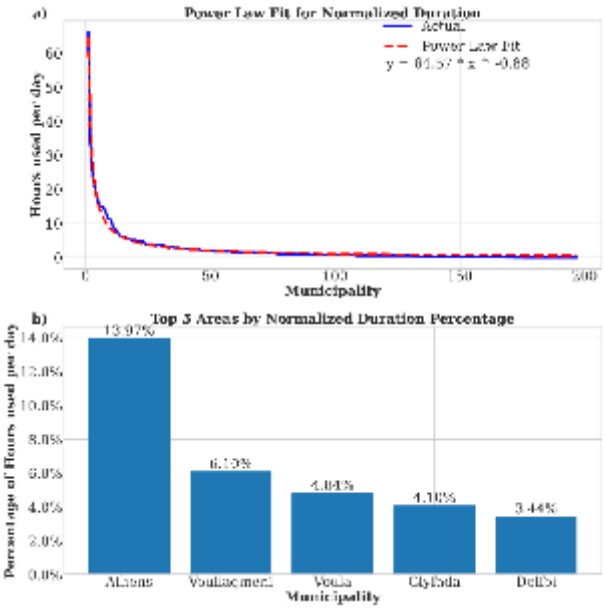

Figure 6: a) Normalized charging duration per municipality, and b) Top 5 municipalities with respect to longest duration.

Normalized Energy Load and Duration per Municipality

The above patterns remain consistent when we shift our focus to municipalities. Figures 5a) and 6a) present the normalized energy consumption and charging duration per municipality, respectively. Similar to individual chargers, a few municipalities account for the bulk of the network's energy usage and session duration. Figures 5b) and 6b) isolate the top 5 municipalities by their contribution to normalized energy consumption and duration, respectively. They account for almost 25% and 30% of the overall energy usage and session duration, respectively. Moreover, 75% of the total energy consumption occurs within the top 20% of the municipalities, while 74% of the total duration can be attributed to the same top 20% municipalities. These patterns verify the validity of the Pareto principle in this context, too.

Overall, these findings are significant as they highlight not only the uneven distribution of charging activity across the network but also the importance of focusing on key chargers and municipalities to maximize operational efficiency and optimize resource allocation.

MODEL DEVELOPMENT AND PREDICTION

To predict EV charging demand, we employed both machine learning (ML) and deep learning (DL) models, each providing unique advantages for modeling time-series data and capturing complex patterns.

Machine Learning (ML) leverages statistical techniques to train prediction models that combine high effectiveness (i.e., accuracy) with high time efficiency (i.e., low run-times) for both training and testing. ML models such as Linear, Ridge and Lasso Regression are particularly suited for problems where relationships between input features and outputs are linear or can be approximated linearly. These models are straightforward to interpret and computationally efficient, thus providing a good starting point for predictive modeling:

- *Linear Regression* assumes a direct, linear relationship between the input variables and the target variable. On the downside, it may not capture complex, non-linear patterns in the data [5].
- *Ridge Regression* enhances Linear Regression by adding an L2 regularization term to the loss function to penalize large coefficients, preventing overfitting, especially in the presence of multicollinearity among input features [6].
- *Lasso Regression* is similar to Ridge Regression but uses a different form of regularization, the L1 one. This way, it can shrink some coefficients to zero, effectively performing feature selection and simplifying the model [7].

Deep Learning (DL) yields more advanced prediction models that use neural networks with multiple layers to learn from large datasets [11]. These models excel in capturing intricate patterns and dependencies in high-dimensional data such as time-series. For this study, we chose the following two models due to their effectiveness in modeling sequential data:

- *Long Short-Term Memory* (LSTM) Networks are a type of recurrent neural network (RNN) designed to learn from sequences of data [8]. LSTMs can capture long-term dependencies, which are essential for time-series forecasting tasks such as predicting EV charging demand over time. They are particularly useful for data with temporal dependencies, as they can remember and forget information over extended sequences.
- *Convolutional Neural Networks* (CNNs), while traditionally used for image processing, can be adapted for time-series data, capturing local temporal patterns [9]. By applying convolutional filters, CNNs can identify significant short-term dependencies in sequential data, making them effective for capturing temporal variations.

To evaluate the performance of these models, we used two primary metrics:

- *NRMSE* (Normalized Root Mean Square Error) [12] is a normalized version of RMSE, which measures the standard deviation of the prediction errors (residuals). NRMSE provides a relative measure of the accuracy of predictions, normalized by the range or mean of the observed data, making it useful for comparing errors across different scales or datasets. It is particularly valuable for assessing model performance in scenarios where the scale of the output varies significantly.
- *R-squared* (R^2) [5], or the coefficient of determination, measures the proportion of variance in the dependent variable that is predictable from the independent variables. An R^2 value closer to 1 indicates that the model explains a significant portion of the variance, while a value closer to 0 indicates a poor fit. This metric was chosen because it provides an intuitive measure of how well the model captures the underlying data patterns.

RESULTS AND ANALYSIS

We now present the results of our predictive modeling efforts, comparing the performance of the aforementioned ML and DL models in forecasting the overall EV charging demand (i.e., across all PPC charging stations) per day across univariate and multivariate settings.

More specifically, the problem we tackle can be defined as follows:

ISBN: 978-618-5765-04-0
ISSN 3057-4269

[Univariate Charger Load Prediction] *Given the load demand of a particular charging station for a specific time period, predict the load demand for the next day so as to minimize the difference between the prediction and the actual value.*

Note that this definition considers solely the historical charging sessions data. To achieve higher accuracy, we can combine this data with contextual information, e.g., the environmental conditions. These settings are called **Multivariate Charger Load Prediction** (for brevity, we omit a formal definition for this problem). Below, we examine each problem in a separate subsection. In both cases, we defined as training data all historical data up to the end of Decembe 2023, while the testing data comprise all days in January 202

Univariate Model Performance

Figures 7-9 show the best-performing DL and ML models for each algorithm based on their respective NRMSE and R^2 scores across the different timesteps. The LSTM model wi a single layer and a timestep of one day emerged as the most effective predictor in the univariate setting, achieving the lowest NRMSE and highest R^2 values (see Figure 7). This result indicates that LSTMs are particularly well-suited to capturing the temporal dependencies inherent in time-series data, such as EV charging demand. The CNN model, configured with two convolutional layers and using a one-day timestep, also performed competitively, demonstrating its capability to identify local temporal patterns effectively.

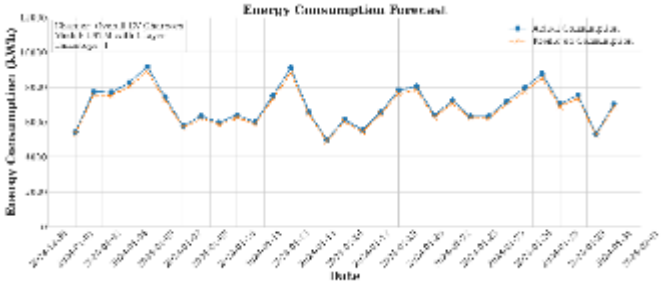

Figure 7: Univariate model performance of the LSTM model.

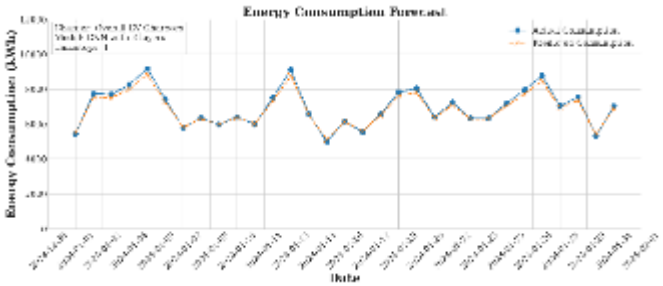

Figure 8: Univariate model performance of the CNN model.

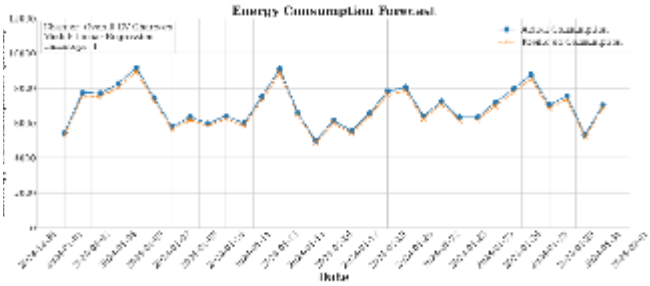

Figure 9: Univariate model performance of Linear Regression.

Table 2:NRMSE values for the Univariate prediction models.

Time step	Linear Regression	Ridge Model	Lasso Model	LSTM 1 layer	LSTM 2 layers	CNN 1 layer	CNN 2 layers
1	**0.0250**	0.0258	0.0319	**0.0237**	0.0592	0.0509	**0.0238**
3	0.0663	0.0806	0.0712	0.2256	0.0888	0.0833	0.0701
7	0.1583	0.1517	0.1508	0.1869	0.1664	0.1531	0.1933
15	0.1671	0.1597	0.1729	0.1548	0.1598	0.1550	0.1546

In more detail, Table 2 presents the NRMSE values for the univariate models across different timesteps (1, 3, 7, and 15 days). The results show that LSTM with one layer achieves the lowest NRMSE at a one-day timestep (0.0237), closely followed by CNN with two layers (0.0238). These values indicate almost perfect predictions, as shown in Figures 7 and 8. Even Linear Regression (in Figure 9) exhibits high performance for timestep 1, with its NRMSE being just 5% higher. However, as the timestep increases, the performance of all models deteriorates, with traditional ML models such as Linear and Lasso Regression becoming more competitive, with the latter exhibiting the best performance at a seven-day timestep.

Although DL models excel at capturing short-term dependencies, they are more prone to overfitting in this univariate setting, where fewer features are available to guide predictions. This can explain why their performance deteriorates at longer timesteps. Conversely, ML models maintain a more consistent performance as the timestep increases. For example, Linear Regression performs well across multiple timesteps, with an NRMSE of 0.0663 at a three-day timestep and 0.1583 at a seven-day timestep.

The reason for this is twofold. First, DL models are highly complex and often require large amounts of data to train effectively. In the context of this study, the dataset may not be large enough to fully exploit the power of DL models. As noted in various studies, including [13], DL models frequently underperform on tabular datasets, where the relationships between features are often simpler and more linear than in unstructured data like images or text. Second, ML models such as Linear and Lasso Regression are more robust to smaller datasets and can generalize well without the need for large amounts of data or complex feature interactions.

Multivariate Model Performance

The multivariate models incorporate additional environmental features—temperature, humidity, and global radiation—to enhance the accuracy of EV charging demand predictions. These features were chosen to capture external factors that could influence charging behavior, such as

ISBN: 978-618-5765-04-0
ISSN 3057-4269

weather conditions affecting driving patterns and chargi needs.

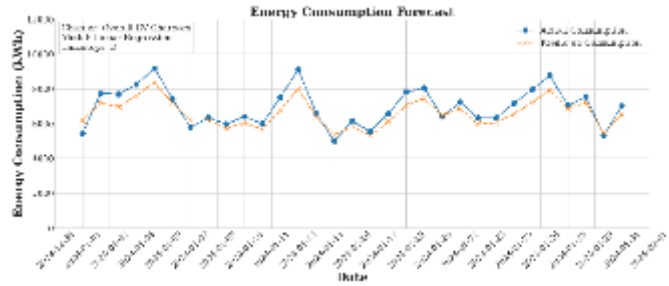

Figure 10: Multivariate model performance of Linear Regression.

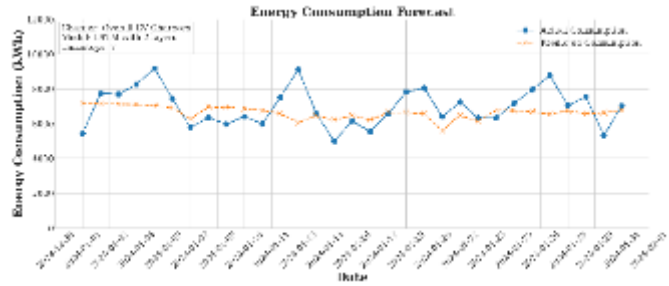

Figure 11: Multivariate model performance of the LSTM model.

Figures 10-12 illustrate the performance of the best multivariate ML and DL models for each algorithm, while Table 3 shows the NRMSE values for the multivariate models. Here, the results are mixed, with Linear Regression continuing to perform strongly at shorter timesteps (NRMSE of 0.0753 at a three-day timestep). However, unlike the univariate case, DL models such as LSTM with two layers and CNN with one layer show competitive performance at longer timesteps. Specifically, LSTM with two layers achieves the lowest NRMSE at a seven-day timestep (0.1614), and CNN with one layer also performs well at a fifteen-day timestep (0.1637).

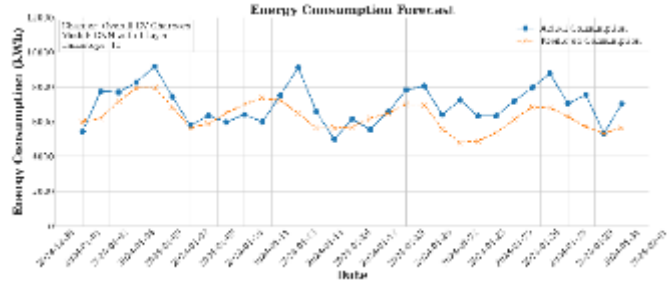

Figure 12: Multivariate model performance of the CNN model.

This shift in performance should be attributed to the additional contextual features used in the multivariate setting. DL models are better suited to capturing complex patterns in multivariate data, where interactions between features (e.g., temperature, humidity, and energy consumption) can influence the predictions. These models benefit from having more features to learn from, which allows them to model the non-linear relationships between the input features and the target variable more effectively.

Table 3:NRMSE values for the Multivariate model performance

Time step	Linear Regression	Ridge Model	Lasso Model	LSTM 1 layer	LSTM 2 layers	CNN 1 layer	CNN 2 layers
1	0.0960	0.0972	0.0838	0.2079	0.1761	0.2293	0.1749
3	**0.0753**	0.0844	0.0956	0.3307	0.2982	0.3585	0.3152
	0.1573	0.1692	0.1457	0.1770	**0.1614**	0.2590	0.2465
	0.1672	0.1778	0.1770	0.2068	0.2581	**0.1637**	0.1884

However, the fact that Linear and Ridge Regression still perform well, especially at shorter timesteps, suggests that the added complexity of DL models is not always necessary when the relationships between features remain relatively simple and the size of the training set is limited. This finding aligns with previous benchmarks that have shown that traditional ML models can often outperform DL models on structured, tabular datasets [13].

Comparative Analysis and Insights

In both univariate and multivariate settings, the choice of model depends on the nature of the data and the prediction horizon. DL models, particularly LSTM, excel when there are complex temporal or feature interactions, as seen in the multivariate setting with longer timesteps. In these cases, the more training data are available, the higher is the prediction accuracy of LSTM. On the other hand, ML models such as Linear and Lasso Regression consistently perform well across various timesteps and are more reliable in settings with fewer features or shorter prediction horizons.

The results of this study suggest that while DL models have the potential to provide highly accurate predictions, their performance is sensitive to the size and complexity of the dataset. ML models, being simpler and less prone to overfitting, offer more stable and interpretable solutions, especially in smaller datasets or when the relationships between features are less complex. Therefore, the choice between ML and DL should be guided by the specific characteristics of the data and the prediction task at hand.

These results provide a comprehensive overview of the effectiveness of various predictive models in different settings, offering valuable insights for optimizing EV charging infrastructure and improving grid management

CONCLUSION

This study offers a comparative analysis of machine learning (ML) and deep learning (DL) models for predicting EV charging demand, using data from 1,063 charging stations in Greece. In the univariate case, DL models like LSTM and CNN performed well, particularly at shorter timesteps, while ML models provided competitive results. However, in the multivariate case, where additional features such as temperature and humidity were included, ML models like Linear and Lasso Regression outperformed DL models, highlighting that the complexity of DL models did not always lead to better predictions.

These findings underscore that model performance is context-dependent, influenced by the nature of the data and the prediction task. By exploring both ML and DL approaches, we identified key differences that provide valuable insights for selecting models to optimize grid management, enhance energy efficiency, and support the integration of renewable energy in EV charging infrastructure.

ACKNOWLEDGMENTS

ISBN: 978-618-5765-04-0
ISSN 3057-4269

This research was partially funded by the EU Horizon Europe GA No 101056765 (EV4EU).

REFERENCES

[1] C. Li *et al.*, "Hidden Benefits of Electric Vehicles for Addressing Climate Change," *Sci. Rep.*, vol. 5, no. 1, p. 9213, 2015.
[2] M. T. Hussain, D. N. Bin Sulaiman, M. S. Hussain, and M. Jabir, "Optimal Management strategies to solve issues of grid having Electric Vehicles (EV): A review," *J. Energy Storage*, vol. 33, p. 102114, 2021.
[3] I. H. Sarker, "Machine Learning: Algorithms, Real-World Applications and Research Directions," *SN Comput. Sci.*, vol. 2, no. 3, p. 160, 2021.
[4] Y. LeCun, Y. Bengio, and G. Hinton, "Deep learning," *Nature*, vol. 521, no. 7553, pp. 436–444, 2015.
[5] N. R. Draper and H. Smith, "Checking the Straight Line Fit," in *Applied Regression Analysis*, 1998, pp. 47–77.
[6] A. E. Hoerl and R. W. Kennard, "Ridge Regression: Biased Estimation for Nonorthogonal Problems," *Technometrics*, vol. 12, no. 1, pp. 55–67, Sep. 1970.
[7] R. Tibshirani, "Regression Shrinkage and Selection via the Lasso," *J. R. Stat. Soc. Ser. B*, vol. 58, no. 1, pp. 267–288, Sep. 1996.
[8] S. Hochreiter and J. Schmidhuber, "Long Short-Term Memory," *Neural Comput.*, vol. 9, no. 8, pp. 1735–1780, Nov. 1997.
[9] Y. Lecun, L. Bottou, Y. Bengio, and P. Haffner, "Gradient-based learning applied to document recognition," *Proc. IEEE*, vol. 86, no. 11, pp. 2278–2324, 1998.
[10] H. L. Moore, "Cours d'Économie Politique. By VILFREDO PARETO, Professeur à l'Université de Lausanne. Vol. I. Pp. 430. I896. Vol. II. Pp. 426. I897. Lausanne: F. Rouge," *Ann. Am. Acad. Pol. Soc. Sci.*, vol. 9, no. 3, pp. 128–131, 1897.
[11] Y. Bengio, I. Goodfellow, and A. Courville, *Deep learning*, vol. 1. MIT press Cambridge, MA, USA, 2017.
[12] C. J. Willmott and K. Matsuura, "Advantages of the mean absolute error (MAE) over the root mean square error (RMSE) in assessing average model performance," *Clim. Res.*, vol. 30, no. 1, pp. 79–82, Sep. 2005.
[13] R. Shwartz-Ziv and A. Armon, "Tabular data: Deep learning is not all you need," *Inf. Fusion*, vol. 81, pp. 84–90, 2022.

ISBN: 978-618-5765-04-0
ISSN 3057-4269

Evaluating Biological Methanation within Trickle Bed Reactors

Alexandros Chatzis
Department of Chemistry, Aristotle University of Thessaloniki
Soil and Water Resources Institute, Hellenic Agricultural Organisation DIMITRA,
Thessaloniki, Greece
Alexandroschatzis01@gmail.com

Maria Gaspari
Soil and Water Resources Institute, Hellenic Agricultural Organisation DIMITRA,
Thessaloniki, Greece
mgaspariswri@gmail.com

Konstantinos Kontogiannopoulos
Soil and Water Resources Institute, Hellenic Agricultural Organisation DIMITRA,
Thessaloniki, Greece
k.kontogiannopoulos@elgo.gr

Laura Treu
Department of Biology, University of Padova
Padua, Italy
laura.treu@unipd.it

Stefano Campanaro
Department of Biology, University of Padova
Padua, Italy
stefano.campanaro@unipd.it

Anastasios Zouboulis
Department of Chemistry, Aristotle University of Thessaloniki
Thessaloniki, Greece
zoubouli@chem.auth.gr

Panagiotis Kougias
Soil and Water Resources Institute, Hellenic Agricultural Organisation DIMITRA,
Thessaloniki, Greece
p.kougias@swri.gr

Abstract*— This study is part of the CO2toCH4 LIFE project, aligned with the circular economy initiative. The project aims to develop and demonstrate an innovative hybrid energy storage system powered by renewable energy sources (RES). It involves capturing, storing, and utilizing carbon dioxide from conventional power plant flue gases, converting it into biomethane. The project's pilot mobile unit will consist of three key components: (1) an electrolyzer for hydrogen production, (2) a flue gas purification system that separates CO_2 from the gases, producing a concentrated CO_2 stream, and (3) an ex-situ biomethanation unit that converts CO_2 into CH_4. Biological methanation is a promising process that makes use of hydrogenotrophic methanogenesis to transform captured CO_2. This technology has been explored using various reactor setups, with Trickle Bed Reactors (TBR) proving the most effective, as they address the primary limitation of the process—H_2 gas-liquid mass transfer. TBRs consist of reactor columns packed with materials that allow microorganisms to immobilize and form biofilms. This design holds great potential for improving biomethanation efficiency. The study evaluated three different packing materials—focused on carbon dioxide conversion, pH stability, and volatile fatty acid (VFA) levels. Additionally, it explored the microorganisms during the biomethanation process. The results indicated that the reactor filled with Raschig rings was the most efficient, achieving over 95% CO_2 conversion. Microbial analysis revealed that the dominant methanogens were from the Methanobacter genus.

Keywords— Carbon Utilization, Biological Methanation, Trickle Bed Reactors, Packing Materials

Abbreviations and Acronyms

GRT – Gas Retention Time

PtG – Power to Gas

RES – Renewable Energy Sources

TBR - Trickle Bed Reactor

VFA – Volatile Fatty Acids

INTRODUCTION

Fossil fuels remain dominant in the energy sector due to their easy storage, low cost, and high energy density, but they are unsustainable and harmful to the environment and health. In contrast, renewable energy sources like wind and biomass are eco-friendly, inexhaustible, and emit zero CO_2, making them increasingly popular alternatives. These sources support the shift to a green, circular economy aimed at reducing the use of finite resources. However, their intermittent nature requires effective management and long-term energy storage to maintain grid stability [1]. Power-to-Gas (PtG) technology offers a solution to energy storage challenges while reducing CO_2 emissions. It supports the circular economy by using renewable energy to power an electrolyzer that splits water into hydrogen (H_2) and oxygen. The H_2 is then combined with CO_2 to produce methane (CH_4), which can be injected into the natural gas grid, storing excess renewable electricity. Compared to other technologies like redox flow batteries, PtG provides higher energy density, and greater storage capacity, and utilizes existing gas infrastructure [2].

Within an engineered system, biological methanation (or biomethanation), a process for valorizing (waste) CO_2 as feedstock (with renewable H_2), is highly influenced by the

ISBN: 978-618-5765-04-0
ISSN 3057-4269

applied reactor type. Trickle-Bed Reactors (TBRs), which allow the immobilization of microorganisms on appropriate packing materials, show great promise in improving biomethanation efficiency [3]. This study evaluated and compared different packing materials in terms of methane output, pH stability and volatile fatty acid (VFA) concentration levels. Specific additional aim was to test the applicability of biochar as a packing material. Moreover, the dynamics of developed (distinct) microbial communities, participating in the biomethanation process, were examined.

MATERIALS AND METHODS

Three custom-made stainless steel TBRs were utilized, denoted as R1 (Raschig rings), R2 (activated carbon) and R3 (biochar), respectively. These reactors operated under thermophilic conditions (i.e., 55 ± 1° C) and ambient pressure. Enriched hydrogenotrophic inoculum was used as the initial inoculum for the TBRs operation. A gas mixture (1:4, CO_2 /H_2) was inserted into the top of TBR units through a peristaltic pump. The liquid (nutrient) medium was provided from a vessel to the TBRs by another peristaltic pump. The experimental procedure examined for different subsequently applied and gradually decreased Gas Retention Times (GRT) for the case of R1, R2 and R3 bioreactors.

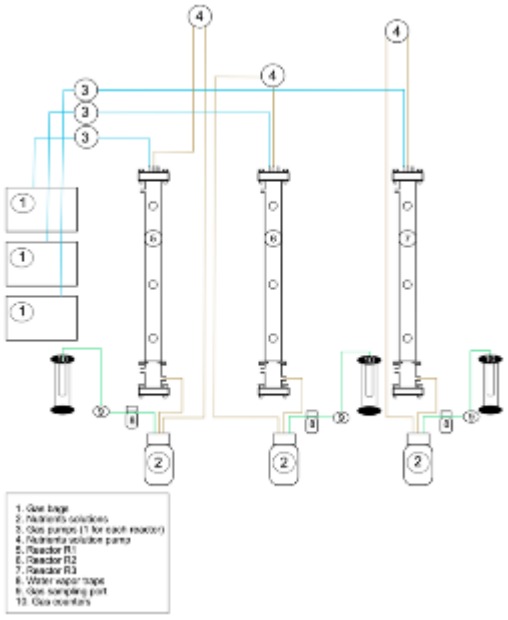

Figure 1. The experimental process diagram for reactors R1, R2 and R3.

RESULTS AND DISCUSSION

According to the results (Fig.2), R1 achieved 96 % CH_4 content in the output gas at the lowest GRT, approaching the highest rate in the bibliography [4]. The R2 achieved its highest CH_4 content (99 %) during the 2 h GRT but experienced a significant drop to 28%within the next GRTs. The R3 surpassed activated carbon in 1 h GRT with over 95% CH_4 concentration yet struggled to maintain sufficient efficiency in 45 min GRT.

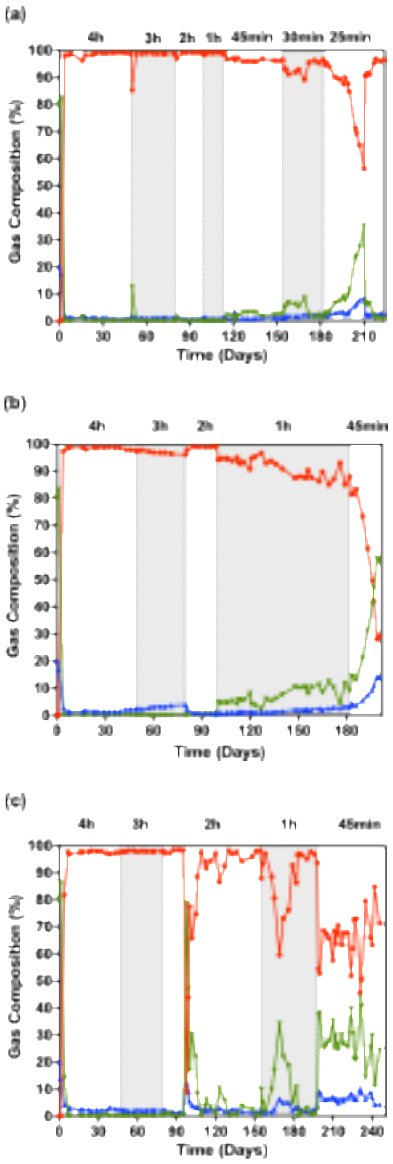

Figure 2. Output gas composition (%) of CH_4, CO_2, and H_2 of the three TBRs during the different GRTs of the experiment, for the assessment of three different packing materials.

In all TBRs, the VFA concentrations remained low except R1, which experienced a significant increase in the VFA levels at the lowest GRT, though this spike subsided within a week. Furthermore, the pH values in all TBRs maintained relatively stable, even though slightly above the optimal range for the biomethanation process (6.0-8.5) [5]. Microbial analysis revealed that the Methanobacter genus ultimately dominated the microbial communities in all three reactors during all GRTs.

ISBN: 978-618-5765-04-0
ISSN 3057-4269

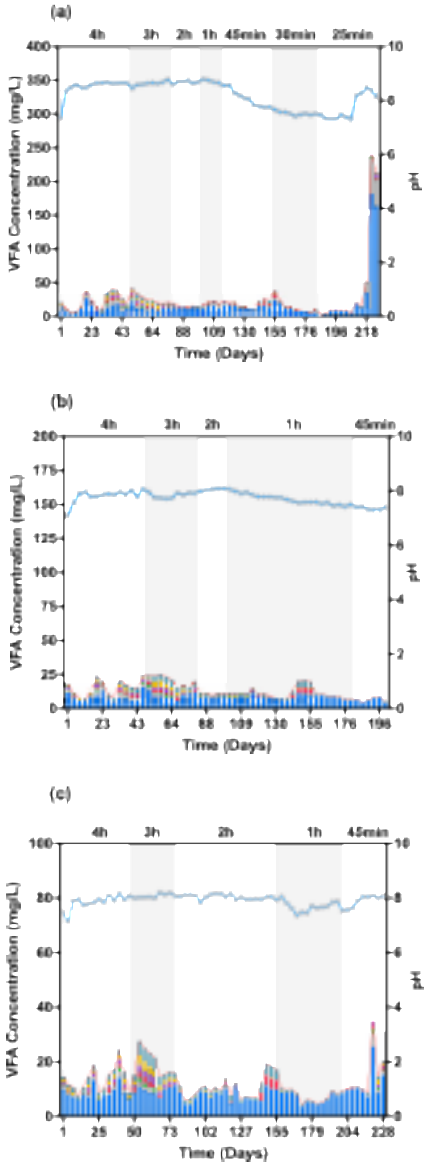

Figure 3. Volatile Fatty Acids concentrations (mg/L) of the bioreactors.

CONCLUSIONS

Raschig rings have proven to be a superior packing material compared to activated carbon and biochar. In research studies, Raschig rings facilitated the highest methane production rate. This high performance was accompanied by stable and satisfactory pH levels, though slightly above the optimal range, while volatile fatty acid (VFA) concentrations remained low, below 0.25 g/L. Although biochar did not match the efficiency of Raschig rings, it presents a promising alternative packing material worth further investigation, particularly due to its potential to enhance the biomethanation process.

ACKNOWLEDGMENT

The project has received funding from the LIFE Programme of the European Union, Grant agreement LIFE 20CCM/GR/001642.

REFERENCES

[1] Götz M, Lefebvre J, Mörs F, McDaniel Koch A, Graf F, Bajohr S, et al. Renewable Power-to-Gas: A technological and economic review. Renew Energ 2016;85:1371–90. https://doi.org/10.1016/j.renene.2015.07.066.

[2] Buchholz OS, van der Ham AGJ, Veneman R, Brilman DWF, Kersten SRA. Power-to-Gas: Storing Surplus Electrical Energy. A Design Study. Energy Procedia 2014;63:7993–8009. https://doi.org/10.1016/j.egypro.2014.11.836.

[3] Feickert Fenske C, Strübing D, Koch K. Biological methanation in trickle bed reactors - a critical review. Bioresource Technology 2023;385:129383. https://doi.org/10.1016/j.biortech.2023.129383.

[4] Strübing D, Huber B, Lebuhn M, Drewes JE, Koch K. High performance biological methanation in a thermophilic anaerobic trickle bed reactor. Bioresour Technol 2017;245:1176–83. https://doi.org/10.1016/j.biortech.2017.08.088.

[5] Kougias PG, Angelidaki I. Biogas and its opportunities—A review. Front Environ Sci Eng 2018;12:14. https://doi.org/10.1007/s11783-018-1037-8.

[6] Götz M, Lefebvre J, Mörs F, McDaniel Koch A, Graf F, Bajohr S, et al. Renewable Power-to-Gas: A technological and economic review. Renew Energ 2016;85:1371–90. https://doi.org/10.1016/j.renene.2015.07.066.

ISBN: 978-618-5765-04-0
ISSN 3057-4269

Decarbonization in Wineries: a Case Study of Mallorca Winery

Andreu Moià-Pol
GREEN reseach group, Engineering
and Construction Department,
Universitat de les Illes Balears
Palma, Spain
andreu.moia@uib.eu

***Abstract*—Mallorca has experienced growth in wine production in the last 30 years, it has gone from 25 to 100 wineries with 1,600 hectares of vineyards, although in the 19th century with Phylloxera in Europe it reached 30,000 hectares. Wineries have gone from passive and manual systems to having high energy consumption to have quality wines, especially for the cooling and heating processes. With an optimal design, biomass systems with solar energy can be installed to have zero emissions and reduce their impact. Most wineries, being small in size, can implement simple compression systems combined with solar energy. This work analyzes 4 wineries in Mallorca with renewable energy and how they can reduce the impact of climate change to zero emissions. It is about increasing energy efficiency in winemaking processes and finding the right renewable energy system.**

Keywords— Winery, Solar thermal, Photovoltaic energy, Refrigeration

INTRODUCTION

Since the 1st century BC, Pliny spoke of Balearic wines comparing them with the best wines of Italy, also Jules Verne admires the wine of Binissalem in the book Clovis Dardentor. There are dozens of vineyards scattered around Mallorca. In just 30 years, it has gone from 25 wineries to more than 100 wineries in 2022 [3], spread over the other five areas of Mallorca, and some more are under construction. Most of them very small, less than 100,000 bottles, and four bigger, with a production over 1,000,000 of bottles. The total surface actually is around 1.781 ha of vineyards. Different than the mainland's where the wineries are between 10 to 50 times bigger with high quality and lower production costs. Some wineries in Spain produce the same wine as all of Mallorca. The last years the climate change it's reducing the production and in a few years could be disaster for the industry, worse than was the Phylloxera in the past. The only future is descarbonizate all the sectors including the wineries.

Figure *1*: : Distribution production areas and Winery in Mallorca. Source; Balearic Government

There are two Protected Designations of Origin of Wine (D.O.Ps): D.O. Binissalem and D.O. Pla i Levante that have been around for more than 40 years. There are also Two Protected Geographical Indications of Wine (PGIs), which are Wines of the Land (V.T.): V.T. Majorca; V.T. Serra de Tramuntana-Costa Nord [11].

Table 1: Surface of wine yards and wine production different areas in Mallorca at 2023 [11]

Wine area	Surface (ha)	Wine (hl)	Nº Winery
DO Binissalem	257,3	8.747	12
DO Pla i Llevant	369,1	13.742	13
Vi de la terra Serra de Tramuntana	2,4	107	5
Vi de la terra Mallorca	1151,9	37.684	72
TOTAL Mallorca	1.781	60.280	102

ENERGY CONSUMPTION

Wine energy consumption studied occurs in two major phases: agricultural, the growth of grapes in a vineyard, and industrial, their transformation to wine in stores though a winery [1]. When measured as a percentage of GDP, industrial wine expenditures account for 1.3% of the European economy [2]. Vineyards also cover 3.48% of Europe available cropland, making it a major contribution to the agricultural sector which is itself estimated to contribute 14% of greenhouse gas emissions. Many studies have separately looked at ways to improve energy efficiency for wine in both the manufacturing and agricultural sectors, but a comparison across the two may be useful to focus energy saving innovation in a particular sector for maximum effectiveness. In this paper will be use metric is the amount of energy it takes to make a liter of wine, and we will focus in the manufacturing. Assuming that winery additives like yeast give negligible volume change, combining the vineyard and winery energy contributions gives an overall energy density of 2,96 MJ/L, between the 80-95% of the energy is due to vineyard processes, meaning the agricultural portion of production usually uses from 6 to 9 times more energy than the industrial portion [1]. In Spain scaling factors that are associated with the operation of different size vineyards and wineries have different energy consumption variability between growing regions, especially in Mallorca where the industrial energy consumption could arrive the same amount of the vineyard, due to smaller size of the winery and vineyard. To decrease the energy in Mallorca use of wine production most effectively, interested parties should focus on grape agriculture and wine manufacturing. In the manufacturing phase, when grapes from a vineyard arrive at

ISBN: 978-618-5765-04-0
ISSN 3057-4269

winery, electric motors remove undesired plant matter, leaving the grape pulp and juice, called the must. This must be then pumped, again using electric pumps, to fermentation tanks, where yeast turns the sugar content of the grapes into alcohol. In this point is where there is more consumption, with a big amount of cooling energy for control the fermentation. When the wine is ready, in order to have quality wines the solids are removed using cooling systems (usually electric compression system), pumps and motors, and the liquid is bottled and stored using electric filling, corking, and labeling machines. Since machines are used for all the major steps, the energy consumption can be monitored well though analysis of the winery's energy bill. The storage of the wines usually was made underground to avoid energy consumption to keep cold, if they are built on the surface the energy consumption will be bigger. Most of the cases are cold areas with millions of bottles production (France, North of Spain, Italy, Portugal ..) from 7.000 to 400.000 kL, in the opposite Mallorca, with hottest weather and smaller wineries, from 50 kL to 1.000 kL, the most usual production is about 100 kL. The energy indicators in Spain could be from 0,2 MJ/L in the biggest wineries to 15,6 MJ/L in the smallest, in Mallorca it's difficult to reduce this lower to 0,8 MJ/L, in Spain could be 0,4 MJ/L [7]. The difference is due to weather conditions, the size of the facilities and the use of some spaces. The average price of Majorcan wines is higher than that of the peninsula due to the scale factor mentioned above, because they have a higher energy consumption and because most of them are organic.

Table 2: Surface of wine yards and wine production different European countries compare with Mallorca [11][12]

	Surface (ha)	**Wine (hm^3)**	**HL/ ha**	**Energy (MWh)**	**kWh/HL**	**Biomass Potential MWh**
Spain	1.032.000	3.57	35	520.408	14,6	15.877.485
France	807.000	4.56	57	459.372	10,1	12.415.824
Italy	786.000	4,98	63	479.076	9,6	12.092.736
Portugal	240.000	0.68	28	86.076	12,7	3.692.438
Greece	64.000	0,17	27	44.200	26,0	984.650
Mallorca	1.781	0,06	34	3496	58	27.396

RENEWABLE ENERGY SYSTEMS IN MALLORCA WINERY

This energy could be supply by Solar Energy (Thermal and PV) and Biomass, all them could be produced at the same vineyard, analyzing 4 wineries in Mallorca we have studied the optimal design of the energy process and the best renewable energies systems. The big facilities of the center of Spain could be installed systems with Biomass and a high solar heating and cooling systems, but in Mallorca they are small facilities and they need simple and mature design, with PV and Solar Thermal systems and with a low biomass fraction.

Solar thermal

Hot water is needed in the winery for different uses: from hygienic and sanitary water till preheating water since boilers or steam production for washing and sterilization. Several systems can be used for heating water like Heat Recovery and Solar Thermal, between the 5 to 10% of the energy consumption is the Hot Water. The solar radiation is high in the Balearic Islands, with more than 2600 hours of sun with a potential of 1800 kWh/m^2 year. Low-temperature (80-150°C) solar collectors guarantee a very high efficiency (up to 60%) in the conversion of solar radiation into useful thermal energy according [6] they can provide more than 600 kWh/m^2 year, that's mean in Mallorca a normal winery could have installed between 8 to 24 m^2, with a peak power from 8 to 24 kW, with storage tank from 2 to 4 m^3.

Figure 2: Winery with a ST system in the roof.

The solar cooling system can be integrated by solar thermal energy, contributing to prevent overheating, especially during the summer, avoiding electrical loads peak. Large thermal systems with vacuum tube collectors are needed (more than 200 m^2) with absorption chiller with cooling capacity between 300 kW to 600 kW coupled with a cooling tower. Such system is able to produce hot water at the average temperature of about 93°C, but in Mallorca most of the wineries are small for install these technologies and with only two months of peak consumption, when the radiation is lower, that made difficult to be economical feasible, it's better for lager wineries like in the Castilla La Mancha or la Rioja, with a properly mix of technologies could be interesting system. Three of the four wineries analyzed in Mallorca they need a fraction of the cooling with negative temperatures, where it's necessary compression systems with electricity and make impossible use absorption systems.

Photovoltaic Energy

PV systems are very present in the Balearic Islands it's increasing the installed power 150% every year [11]. This technology could provide in this latitude between 1300 to 1600 kWh/kWp, in the 4 Mallorca wineries analyzed we have found installing 50 to 200 kWp that provide around 30% to the 100% of the energy, the majority with panels integrated into the roof. It is necessary to have neetmeetering, because the peak of consumption is concentrated in three months, from August to October. We could reach 100% of electrical production, increasing efficiency and installing more power in these warehouses, about 50 Wp/HL, for the size of the wineries is between 50 to 200 kWp,. In the analyzed wineries the electrical consumption it's about the 90% of the total energy consumption, but from these, the 50% is for cooling systems, with positive and negative temperatures.

ISBN: 978-618-5765-04-0
ISSN 3057-4269

Figure 3: Winery with a PV system in the roof

Biomass

The vineyards they produce a big amount of biomass, in order to increase the production and quality every year they need to cut the branches of the vine strain, as well all the skins and seeds are wasted for the wine, but they need a previous treatment (crush and dry) before use in the boiler. Bigger wineries in the mainland they are used to obtain alcoholic spirit distilled but in Mallorca they use like a fertilizer. All this biomass could be used to produce thermal energy and in bigger facilities even electricity, but usually the biomass boiler they need maintenance and high investment that usually is difficult to adapt in these facilities, other sectors with high thermal consumption they are using this technology, in Mallorca some Olive Oil Producers use the biomass, but they have larger thermal consumption and the biomass fraction has more energy power and less treatment. Combining these with solar thermal could be interesting for large wineries with absorption chillers, in the case of Mallorca, only 3 or 4 have enough size to install and absorption machine that could be combined with solar thermal for the systems cooling working at positive temperatures.

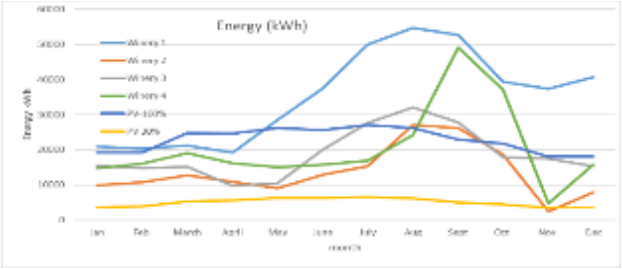

Figure 4: Monthly Energy consumption of 4 Mallorca winery with PV fraction from 30 to 100%.

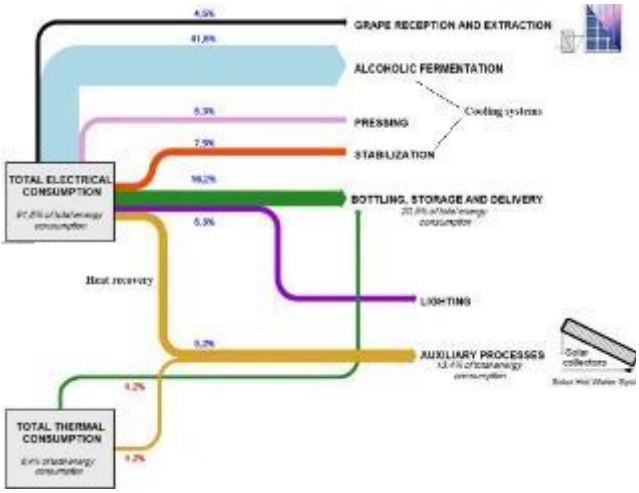

Figure 5: Shankey diagram of a Mallorca Winery with Solar Energy [10]

CONCLUSIONS

Mallorcan producers are expected to increase the fraction of renewable energy used in the future and will increasingly look for a more efficient energy route, to reduce the impact of climate change. This implies that increases in process and machine energy efficiency in both vineyard and winery practices will have a greater effect on the overall price of wine production than similar advances in energy efficiency in the winery processes together with a greater implementation of renewable energies that achieve a balance of zero emissions. Fortunately, in Mallorca most producers are organic and the price of the wine already includes part of these practices, so taking advantage of solar radiation and Biomass production can be relatively easy and cheap. As seen in the island's wineries, 100% of all energy demand can be met with zero emissions, with only solar energy.

ACKNOWLEDGMENT

The author would like to thank the Mallorca wineries for their collaboration.

REFERENCES

[1] S. Marras et al., "Carbon Footprint Assessment on a Mature Vineyard," Agric. For. Meteorol. 214-215, 350 (2015).

[2] K. Anderson, V. Pinella, and S. Nelgen, Global Wine Markets, 1860 to 2016 (Saint Philip Street Press, 2020).

[3] Jancis Robinson. The wine revolution I stumbled upon in Mallorca. Finacial Times SEPTEMBER 3 2022.

[4] M. Malvoni, P. M. Ongedo, and D. Laforgia, "Analysis of Energy Consumption: A Case Study of an Italian Winery," Energy Procedia 126, 227 (2017).

[5] Dylan Drescher. Energy Consumption of Wine Production. December 5, 2022. Coursework for PH240, Stanford University, Fall 2022.

[6] Mervyn Smyth , Alistair Nesbitt . Energy and English wine production: A review of energy use and benchmarking. Energy for Sustainable Development. Vol 23, Dec. 2014, Pag 85-91.

[7] Joaquín Fuentes-Pila and José Luis García . Efficient Wineries IEE/12/758/SI2.644752. UPM, Technical University of Madrid. February 2014.

[8] Bartali R. et Alt. Decarbonization of industrial processes: technologies, applications and perspectives of low-temperature solar heat (80-150°C) EuroSun 2020 Proceedings

[9] F. ARREDONDO-RUIZ et Alt. Designs for energy-efficient wine cellars (ageing rooms): a review. Australian Journal of Grape and Wine Research 26, 9–28, 2020.

[10] European project Teslaproject.org

[11] Balearic Island's Government www.caib.es

[12] Wine production worldwide in 2023 Statista.com

Management of Container Port Terminals: The Effect of Cold Ironing to the Terminals Cooperation

Vasileios Sitokonstantinou
Department of Management Science and Technology
Athens University of Economics and Business
Athens, Greece
vsito@aueb.gr

Mihalis Golias
Department of Shipping
Cyprus University of Technology
Limassol, Cyprus
michail.gkolias@cut.ac.cy

Dimitris Zissis
Department of Management Science and Technology
Athens University of Economics and Business
Athens, Greece
dzisis@aueb.gr

George Ioannou
Department of Management Science and Technology
Athens University of Economics and Business
Athens, Greece
ioannou@aueb.gr

***Abstract*— Capacity management of terminal operators at a port is crucial for seamless operations and the avoidance of vessel delays. Increasing vessel port times can have serious operational and financial consequences for terminal operators, particularly given the just-in-time requirements of logistics. Effective management of existing port capacity is essential for the reliability and productivity of marine terminals. Cooperation in maritime transport has attracted growing attention from both scholars and industry experts. Port and marine terminal cooperation is an important topic in public and business circles, and bibliometric studies on port-related academic research show that cooperation and integration among ports and terminal operators at a port is an emerging theme. This study shifts the focus to the tactical and operational level, where vessel selection becomes a practical decision for cooperation. Building upon prior research by** [1], **this paper investigates the impact of using both vessel selection and Twenty Foot Equivalent Units (TEUs) handled as decision variables for intra-port cooperation among terminals, particularly in scenarios where Cold Ironing (CI) is available at select terminals. CI refers to the practice of supplying electrical power to a ship at berth, while its main and auxiliary engines are turned off. This reduces the need for ships to run their onboard generators to produce electricity, while in port, thereby decreasing emissions and fuel consumption. The benefits of CI can vary depending on several factors and include fuel savings, emission and noise reductions, efficiency improvements, and potential port incentives. By analyzing the cost savings before and after cooperation, this study quantitatively evaluates and compares various cooperation scenarios, concession fee policies, and emissions reduction strategies, while gauging the willingness of terminals to cooperate under each model.**

Keywords—Maritime, Port Management, Cold Ironing, Container Terminals Operations, Energy Efficiency, Emissions

INTRODUCTION

Literature Review

Cold Ironing (CI), also known as “Alternative Maritime Power” (AMP), “Shore-to-Ship Power” (SSP), “Shore side electricity” (SSE) and “Onshore Power Supply” (OPS), has emerged as an effective solution for mitigating environmental pollution in ports [2]. Ships traditionally keep their auxiliary engines running while docked, to maintain essential functions, such as lighting, refrigeration, and communications, which results in significant emissions of sulfur oxides (SO_x), nitrogen oxides (NO_x), carbon dioxide (CO_2), and particulate matter. CI offers an alternative by allowing ships to connect to an onshore electrical grid, enabling them to power these functions with electricity. This power comes (or will come in the future) from cleaner energy sources. As regulations on maritime emissions tighten—particularly with initiatives from the International Maritime Organization (IMO) to reduce global shipping’s carbon footprint—CI has become an increasingly discussed strategy in both policy and academic literature [3]. For more details we refer to [2], where the authors review and analyze 33 published papers of game theory in seaport cooperation and competition, focusing on policy and operational improvements for container terminals.

Pujats et al. [1] examines cooperation between container terminals within ports. It focuses on how terminals can share resources and transfer vessel calls as mechanisms for improving operational efficiency and profitability. The authors develop mathematical models to analyze these strategies. The goal is to reduce congestion, enhance service efficiency, and manage capacity better. The study highlights the need for cooperation in ports with fluctuating container volumes and varying vessel sizes.

The models seek to balance economic and operational factors by exploring different levels of cooperation, such as handling containers together or transferring vessels between terminals. The findings show that cooperation improves port performance and reduces costs without the need for additional capital investment in infrastructure or port expansions. This approach can be particularly beneficial for ports facing capacity constraints or competitive pressures. The study provides a framework for more efficient and sustainable terminal operations, providing a quantitative framework for understanding both the benefits and challenges of terminal cooperation. These insights are valuable insights for both industry practitioners and policymakers.

ISBN: 978-618-5765-04-0
ISSN 3057-4269

Research Question – Motivation

Pujats et al. [1] explores the potential benefits of cooperation between container terminals, particularly regarding the sharing of capacity, and examines whether this cooperation can enhance profits without necessitating significant capital investment. Their research questions aim to understand whether cooperative strategies, such as vessel or volume sharing, can help terminals optimize existing resources and increase operational efficiency. In an increasingly competitive and capital-intensive environment, terminal operators are looking for ways to maximize their return on assets without constantly investing in new infrastructure. By sharing capacity, terminals may avoid the high costs associated with expanding physical infrastructure, while improving utilization rates, reducing congestion, and potentially improving profits through more efficient use of space and resources.

A key aspect of Pujats et al. [1] research is identifying which cooperation policies are most beneficial. Various models of terminal cooperation, including joint service agreements, alliances, and Vessel Sharing Agreements (VSAs), can play a critical role in determining the success of such strategies. The authors seek to explore whether it is more effective to cooperate based on vessel sharing, where shipping lines collaborate across terminals, or based on volume sharing, where the focus is on jointly managing container throughput. Their research questions suggest a focus on operational and tactical-level planning, where such cooperation can directly impact service quality, turnaround times, and overall terminal capacity management. Identifying the most advantageous policies could help terminal operators balance workloads, reduce handling costs, and enhance service reliability.

Our research question builds on these themes by adding a layer of complexity: the integration of CI technology and associated subsidies. The introduction of CI, while environmentally beneficial, introduces new variables into the cooperation framework between terminals. Understanding how CI infrastructure and government subsidies affect both terminal cooperation and profit margins is critical. CI facilities may require shared investments or operational adjustments among terminals, particularly where subsidies are offered for ports handling vessels utilizing shore power. Therefore, examining how this environmental technology interacts with existing cooperation models could provide valuable insights into both economic and environmental outcomes. This investigation would help reveal whether CI, coupled with cooperation, can lead to increased profitability while supporting regulatory compliance and environmental sustainability.

Significance of the Research

The significance of studying maritime pollution is underscored by the sheer scale and environmental impact of global seaborne trade. Maritime transport is responsible for over 80% of the volume of global trade, with container shipping alone comprising approximately 17% of that total [4]. As global trade continues to expand, so do the emissions associated with shipping. Over the past decade, greenhouse gas emissions from the maritime sector have surged by 20%, presenting a critical challenge to achieving global emission reduction targets and sustainable development goals [4]. This increase in emissions is particularly concerning given the urgent need for the shipping industry to decarbonize fully by 2050 to meet international climate agreements. Without substantial investment in green technologies and operational efficiency, including cold ironing and other emission-reducing solutions, the maritime sector will struggle to align with these global sustainability objectives. Therefore, research on the factors contributing to increased maritime pollution, and strategies for mitigation, is essential for guiding policy and industry efforts toward a sustainable future.

MODEL DESCRIPTION

The model presented in [1] assumes that container terminals can negotiate and share both seaside and landside resources. This cooperation leads to reduced handling costs while maintaining the same revenue. Shipping lines, through existing VSAs, can also utilize each other's capacity, further enhancing operational efficiency. This setup emphasizes the importance of collaboration between terminals to optimize the use of available resources.

In this work, we introduce CI capabilities for subsets of the cooperating terminals and subset of the vessels. Some terminals and vessels are equipped for cold ironing, although no terminal has full cold ironing capacity (i.e., not all berths have CI capabilities). Vessels can be served at any terminal, regardless of cold ironing capability. The model also includes subsidies for terminals that handle vessels utilizing cold ironing, providing financial incentives for environmentally friendly operations. These assumptions frame a cooperative environment that balances cost efficiency and sustainability.

To study the new model in practice, we have created a specific scenario. This assumes three different terminals, labeled T1, T2, and T3. We assume that each terminal has identical capacity, but varying productivity based on their volume-to-capacity (V/C) ratios. Terminal T1 reaches peak productivity when its V/C ratio is 90%, while T2 and T3 achieve maximum efficiency at 70% and 60%, respectively. In the research presented herein, only T1 is equipped with CI capabilities, while none of the vessels it serves (before cooperation) have CI capabilities. This setup emphasizes the role of terminal specialization and capacity in optimizing port operations, particularly in the context of energy efficiency measures like cold ironing.

The model further explores three pre-coordination terminal volume scenarios: ascending, descending, and random. In the ascending scenario, and pre-cooperation, T1 handles the smallest volume, and T3 the largest. Conversely, the descending scenario assigns the highest volume to T1 and the lowest to T3. The random volume assignment scenario distributes container volumes to terminals, without a specific pattern. These varying scenarios aim to investigate the effects of volume distribution on overall port performance, providing insights into how terminals with different characteristics respond to different operational loads.

The decision-making process is governed by two distinct policies. Policy 1 maximizes the sum of the profits (i.e., total welfare) while Policy 2 maximizes the minimum profit (i.e., equity). Additionally, the model integrates 13 different subsidy scenarios, where subsidies are calculated as a percentage of initial concession fees. This setup encourages terminals to report accurate profit margins. Higher reported profits could lead to increased taxation but also higher subsidies, whereas underreporting profits may result in lower subsidies. This system aims to balance financial incentives with regulatory compliance, providing a realistic framework for assessing terminal profitability and subsidy efficiency.

ISBN: 978-618-5765-04-0
ISSN 3057-4269

Finally, the model examines three different concession fee policies: maximum zero volume handling cost, minimum zero volume handling cost, and average zero volume handling cost. These policies affect the financial obligations of terminal operators, influencing their profitability under different volume conditions. In total, we considered 11,700 different problem instances, providing a comprehensive analysis of terminal cooperation, volume handling, and financial incentives under varying operational and economic conditions.

RESULTS

The results were very encouraging and are captured in the following six figures. It should be noted at this point that the x-axis represents the subsidy percentages across 13 cases (with 0% indicating no subsidy), while the y-axis represents the percentage increase in profit.

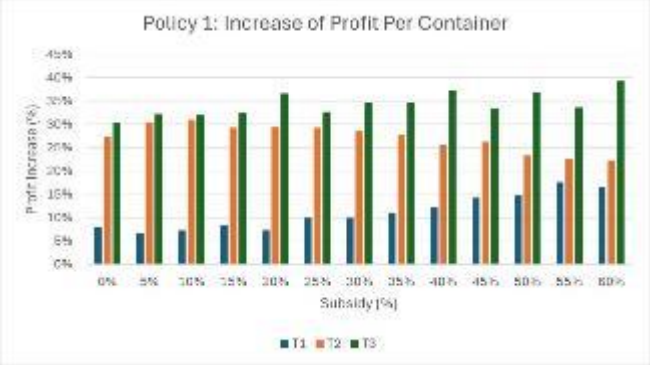

Figure 1: Ascending Volumes

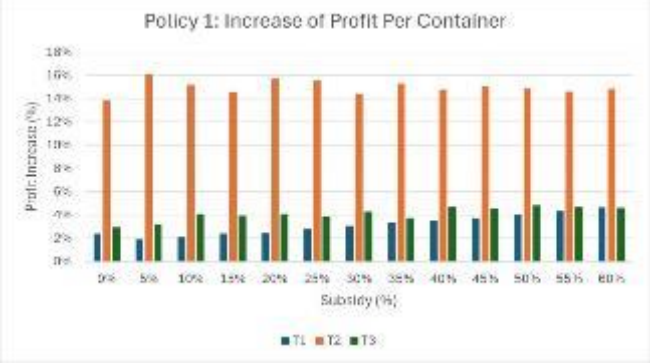

Figure 2: Descending Volumes

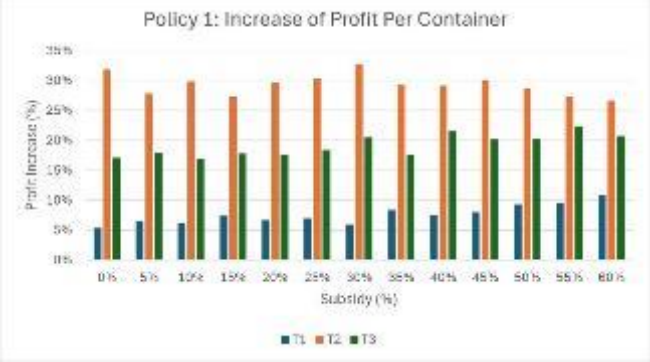

Figure 3: Random Volumes

The results for policy 1 are shown in Figure 1, Figure 2 and Figure 3, for ascending, descending and random volumes respectively. An intriguing finding from the analysis is that when volumes are directed to the most productive terminal, the T1, in the descending volume scenario, overall profits tend to decrease, contrary to expectations. Interestingly, the terminal with average productivity (i.e., T2), emerges as the overall winner, in terms of profit maximization, highlighting that optimal productivity does not necessarily align with the highest profit increase under a cooperative environment. Consistent with this, terminal T1, despite being the most efficient terminal, experiences the lowest percentage increase in profits. Additionally, as subsidies increase, T1's profits rise, which is expected given its operational advantage and financial incentives tied to the concession fees. This suggests that profitability is not solely tied to productivity but is also influenced by subsidy policies and volume allocation strategies.

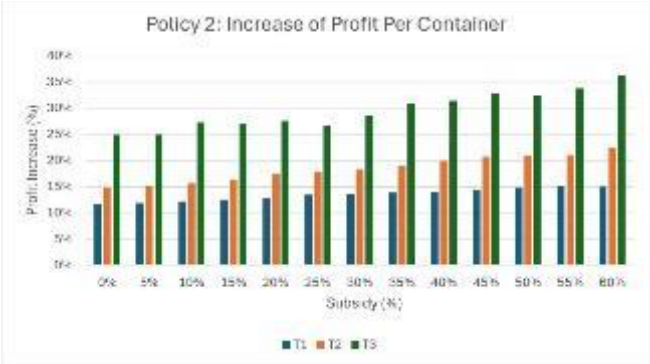

Figure 4: Ascending Volumes

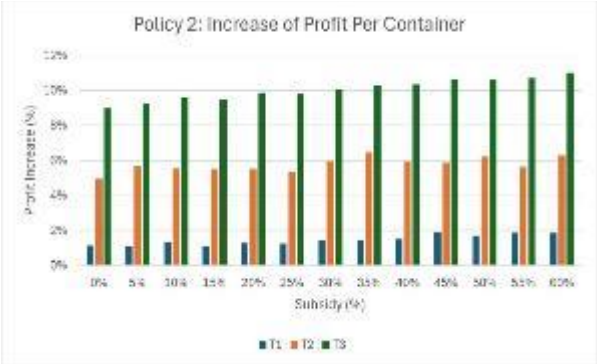

Figure 5: Descending Volumes

Figure 6: Random Volumes

ISBN: 978-618-5765-04-0
ISSN 3057-4269

The results for policy 2 are shown in Figure 4, Figure 5 and Figure 6, for ascending, descending and random volumes respectively. An interesting outcome of the analysis is that, the least productive terminal T3, emerges as the biggest beneficiary from the cooperation in terms of percentage profit increase. Despite having the lowest V/C ratio and overall efficiency, T3's performance improves the most under the various scenarios. On the other hand, terminal T1, the most productive terminal, sees the smallest percentage-wise increase in profit, which suggests that its higher initial efficiency leaves less room for significant improvement. Notably, under both decision policies, the model's rescheduling consistently results in profit increases across all terminals, demonstrating the effectiveness of the rescheduling mechanism in enhancing financial performance regardless of the terminal's baseline productivity. Overall remark, the results are dependent on the initial volumes and the terminal productivity.

DISCUSSION

The results show significant room for improvement through simple, easily implementable actions, without the need for major structural or infrastructural changes that would require substantial time and financial resources. This makes the study highly valuable. Importantly, all participants benefit, creating a win-win situation for everyone involved, either directly or indirectly. In comparison to the initial allocation of vessels across the terminals, the implementation of our model generates profits in all scenarios.

Future Research

For future research, several promising avenues can be explored to further enhance the robustness and applicability of the current model. First, increasing the number of terminals and vessels would allow for more granular insights into the dynamics of terminal operations, especially in more complex port systems. Additionally, varying the subset of terminals equipped with CI capabilities could provide a better understanding of how CI distribution affects overall productivity and profitability. Incorporating a CI capacity constraint would add another layer of realism, as not all terminals or vessels can process CI at the same rate, and this limitation could significantly impact scheduling and profitability.

Another interesting direction for future research is to differentiate between customers based on their specific requirements or preferences, which could lead to more tailored and efficient terminal assignments. Finally, incorporating second-order stability, specifically the stability of coalitions between terminals, can be examined either as a constraint or an objective. This would allow for the analysis of cooperative behavior and how long-term stability can be maintained within terminal networks, especially when competitive pressures and varying financial incentives are present. These extensions would deepen the model's relevance and expand its potential for real-world application.

Conclusion

This study examined how vessel allocation and TEU handling can be leveraged to improve cooperation between terminals equipped with CI capabilities. CI reduces emissions by supplying electrical power to ships while berthed, offering benefits such as lower fuel consumption, decreased emissions, and reduced noise and vibration in port areas. Through an analysis of cost savings derived from cooperation, the research evaluates different cooperation frameworks, subsidy policies, and emission reduction strategies. The findings offer valuable insights into how terminal collaboration, particularly when integrating environmental technologies like CI, can enhance profitability while promoting sustainable operational practices.

REFERENCES

[1] K. Pujats, D. Konur, and M. Golias, "Models for intra-port container terminal cooperation based on volume and vessel transfer," *Maritime Policy and Management*, 2024, doi: 10.1080/03088839.2021.2003458.
[2] K. Pujats, M. Golias, and D. Konur, "A review of game theory applications for seaport cooperation and competition," *J Mar Sci Eng*, vol. 8, no. 2, p. 100, 2020.
[3] IMO, "Ship-Port Interface and Energy Efficiency," Nov. 2015.
[4] UNCTAD, "Towards a green and just transition," Geneva, 2023.

ISBN: 978-618-5765-04-0
ISSN 3057-4269

Balancing Output Power and Efficiency in a Stirling Engine

Yoshihiko Haramura
Dept. of Mechanical Engineering
Kanagawa Univeristy
Yokohama, Japan
haramy01@kanagawa-u.ac.jp

***Abstract*—Stirling engines could potentially produce power from renewable fuels or waste heat. This requires engines to be developed for medium heat source temperatures. However, most optimization studies are on engines for high heat source temperatures. Output power and efficiency are often used as evaluation factors in the optimization, but there is a tradeoff between them. Lower speed increases the efficiency but reduces power. The same behavior is observed for most of the design parameters. We devised a method to balance power and efficiency by maximizing the efficiency among the combinations of design parameters for which output power is kept constant. We chose the major design parameters as the compression ratio and heat conductance ratios of the three heat exchangers, the heater, the regenerator, and the cooler. The sum of the heat conductances of the heat exchangers, swept volume, and phase-averaged pressure were kept constant. The relationships between efficiency and power output at which maximum efficiency is obtained were derived. The optimum design parameter values were calculated.**

Keywords—Stirling engine, Engine design, Optimization, Efficiency maximization for the same power

INTRODUCTION

Stirling engines could harness small-scale waste heat or biomass energy. High-performance engines have been developed [1][2] but they have been designed for high heat source temperatures. Optimization procedures have been proposed, for instance, by Organ [3], but they are also for high temperatures. It is reasonable to expect that the optimum compression ratio depends on the ratio of the heat source and sink temperatures since low-temperature difference engines have low compression ratios [4]. The effect of temperature ratio has only been reported by Nakajima et al. [5]. They correlated compression ratio as

$$(T_K/T_H)(V_{max}/V_{min}) \approx 1 \qquad (1)$$

where T_H and T_K are the heat source and sink temperatures, respectively, and V_{max} and V_{min} are the maximum and minimum volumes, respectively.

Stirling engines perform isothermal compression, isochoric heating, isothermal expansion, and isochoric cooling. The isochoric process is called the transfer process hereafter. Cycle work reflects heat transfer in compression/expansion processes. To achieve high efficiency, during the transfer processes it is important to store and release heat in and from the heat storage material, which we call the matrix, in the regenerator, a temporary heat storage device. The power output of engines is generally the product of cycle work and cycle frequency. Thus, a high-speed engine is preferable for high power. Since the amount of heat transferred in a cycle decreases with speed, the output power and engine efficiency have opposite relationships with engine speed. Therefore, balancing power and efficiency is important in designing Stirling engines.

Here, we propose a method to balance power and efficiency. First, we find the combinations of design parameters for which output power is constant, forming a surface in a multi-dimensional design parameter space. Then, we seek the maximum efficiency point on the surface. This gives the relationship between output power and efficiency. The designer selects a point in the relationship considering the balance of power output and efficiency. Once the power level is determined, the optimum design parameter values can be determined. A pressure drop due to flow resistance decreases output power, but this is neglected because it adds more dimensionless parameters and makes the system too complicated to analyze.

GOVERNING EQUATION AND ITS DIMENSIONLESS FORM

Asummptions and Governing Equations

The following is assumed for simplicity.

(1) The volumes of the heater (H), regenerator (R), and cooler (K) are neglected.
(2) Heat conductances of the heat exchangers take finite values of K_H, K_R, and K_K despite assumption (1), where the conductance is the product of heat transfer area and heat transfer coefficient.
(3) The working gas in the expansion (high-temperature) and compression (low-temperature) spaces changes its state adiabatically and immediately becomes uniform on mixing. Volumes V_E and V_C in high- and low-temperature spaces change linearly with phase and with zero minimum volumes (Fig. 1).

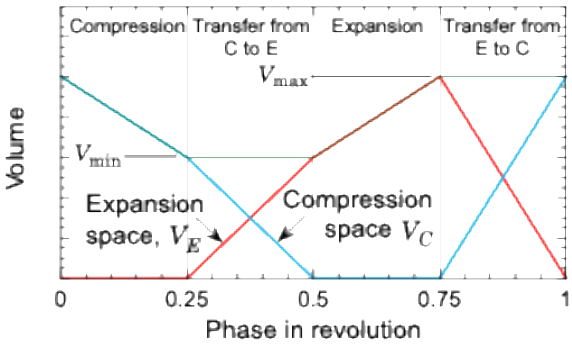

Figure 1: Volume change with phase

(4) Flow resistance is negligible, which yields uniform pressure at every instance.
(5) The matrix in the regenerator has sufficiently large heat capacity. Its temperature profile is interpolated with a

ISBN: 978-618-5765-04-0
ISSN 3057-4269

cubic spline [6] against the cumulative heat conductance from one end.

(6) The working fluid is an ideal gas with constant gas constant R and specific heat c_p at constant pressure.

The governing equations are the conservations of mass and energy for the working gas. The mass conservation of the gas in the expansion cylinder is expressed by

$$\frac{d}{dt}\left(\frac{PV_E}{RT_E}\right) = -\dot{m}_{EC}\,. \tag{2}$$

Here, P is pressure, V_E is volume, T_E is temperature, t is time, and $\dot{m}_{EC}$ is mass flow rate in the direction from the expansion space to the compression space. A similar equation is constructed for the compression space. The gas flows at the same rate throughout the heat exchangers at every instance. The conservation of energy for the gas in the expansion space is expressed by

$$\frac{c_v}{R}\frac{d}{dt}\left(PV_E\right) = -\dot{m}_{EC}\,c_p\,T_{EH} - P\frac{dV_E}{dt} \tag{3}$$

where c_v (= $c_p - R$) is specific heat at constant volume of the gas and T_{EH} is gas temperature at the boundary between the space and the heater. T_{EH} is T_E when the gas flows out, and it is determined from Eq. (8) when the gas flows in from the heater. The equation for the compression space is the same except that subscript E is replaced with C and $-\dot{m}_{EC}$ is replaced with $\dot{m}_{EC}$. The conservation of gas energy in the heat exchangers must be considered, which is expressed as

$$\frac{c_v}{R}\frac{dP}{dt}dV = -d\left(\dot{m}_{EC}\,c_p\,T\right) - dA_w\,h\left(T - T_w\right) \tag{4}$$

for infinitesimal volume dV with heat transfer area dA_w. Here, h is the heat transfer coefficient and T_w is the temperature of the heat exchanger wall, which takes constant heat source and sink temperatures T_H and T_K in the heater and the cooler, respectively, and a distributed steady value in the regenerator. Neglecting the transient term, and introducing dimensionless position x defined as

$$A_w = \xi\,A_{wj}\,, \tag{5}$$

Eq. (4) is rewritten

$$\frac{d}{d\xi}\left(\dot{m}\,c_p\,T\right) = -K_j\left(T - T_w\right). \tag{6}$$

Here, $\dot{m}$ is the absolute of $\dot{m}_{EC}$, A_w is the cumulative area from the heat exchanger inlet, and A_{wj} is the heat transfer area in heat exchanger j (= H, R, or K), and the product of h and A_{wj} is replaced with heat conductance K_j. When wall temperature T_w is expressed with a cubic function of x as

$$T_w = a_0 + a_1\xi + a_2\xi^2 + a_3\xi^3\,, \tag{7}$$

the gas temperature is

$$T = T_0\,e^{-\xi/\xi_1} + (a_0 - a_1\xi_1 + 2a_2\xi_1^2 - 6a_3\xi_1^3)\left(1 - e^{-\xi/\xi_1}\right) + (a_1 - 2a_2\xi_1 + 6a_3\xi_1^2)\xi + (a_2 - 3a_3\xi_1)\xi^2 + a_3\xi^3 \tag{8}$$

where

$$\xi_1 = \dot{m}\,c_p/K_j\,. \tag{9}$$

A constant of integration is determined from the initial condition that gas temperature is T_0 at the inlet (x = 0). Heat transferred from the wall is the integral of the R.H.S. of Eq. (6) with respect to x, and then the heat transferred to the gas in heat exchanger j is evaluated from inlet and outlet temperatures $T_{j,in}$ and $T_{j,out}$ from

$$\dot{Q}_j = \int_0^{A_{wj}} h\left(T_w - T\right)dA_w = \dot{m}\,c_p\left(T_{j,out} - T_{j,in}\right). \tag{10}$$

Dimensionless Design Parameters

Taking reference values of swept volume V_{SW} (= $V_{max} - V_{min}$), phase-averaged pressure P_0, heat sink temperature T_K, and engine speed f in hertz, Eqs. (2), (3), and (6) are rewritten as

$$\frac{d}{dt^+}\left(\frac{P^+V_E^+}{T_E^+}\right) = -\dot{m}_{EC}^+ \tag{11}$$

$$\frac{c_v}{c_p}V_E^+\frac{dP^+}{dt^+} + P^+\frac{dV_E^+}{dt} = -\dot{m}_{EC}^+T_{EH}^+ \tag{12}$$

and

$$dT^+/d\xi = -K_j^+\left(T^+ - T_w^+\right) \tag{13}$$

with parameters c_p/c_v, specific heat ratio, and dimensionless heat conductances,

$$K_j^+ = (R/c_p)(K_j T_K)/(P_0 V_{SW} f)\,. \tag{14}$$

Here, superscript + denotes a dimensionless parameter. The reference value of mass flow rate is $P_0V_{SW}f/(RT_K)$. To find optimum design parameters, we include constraints that P_0V_{SW} and the sum SK_j of K_j are constant. Then, the design parameters are reduced to relative heat conductances K_R/SK_j and K_K/K_H, and compression ratio V_{max}/V_{min} for the given conditions of temperature ratio T_H/T_K and a single gas property, c_p/c_v. Since the sum of SK_j has a fixed value, $(R/c_p)T_K$ S$K_j/(P_0V_{SW})$ is constant in the speed dimension, and solely depends on the specific heat ratio through R/c_p. When it is denoted with f_0, dimensionless speed is written as

$$f/f_0 = f/\left[(R/c_p)T_K\sum K_j/(P_0V_{SW})\right] = 1/\sum K_j^+ \tag{15}$$

and dimensionless power becomes

$$\dot{W}^+ = \dot{W}/(P_0V_{SW}f_0) = (c_p/R)\,\dot{W}/\left(T_K\sum K_j\right). \tag{16}$$

PROCEDURE

Finding the Tempearture Distribution and Pressure

The Stirling cycle consists of four processes (Section I). Since the compression and expansion spaces are assumed to be adiabatic and the processes occur only in a single, uniform space, these processes happen isentropically, and temperature and work are calculated analytically.

The following procedure is used to solve Eqs. (2) and (3) in the transfer processes. When the temperatures in both spaces, T_E and T_C, the pressure and temperature distribution of the matrix are given at an arbitrary phase, we can determine

ISBN: 978-618-5765-04-0
ISSN 3057-4269

flow rate $\dot{m}_{EC}$ and pressure–time derivatives *dP/dt* from Eq. (3) and dT_E/dt and dT_C/dt from Eq. (2). We employ the Runge–Kutta method [7] to find *P*, T_E, and T_C at the next time step. We also determine the gas temperature distribution from T_E, T_C, and $\dot{m}_{EC}$ using Eq. (8). We repeat one cycle calculation to converge in the following scenarios: when temperatures and pressure at phase zero take the same values as those in a phase exactly one cycle before; when the sum of the heat added to the matrix is zero in a single cycle in each interval bounded by two adjacent nodes; and when the phase-averaged pressure becomes a designated value. Heat added from the wall is calculated from Eq. (10). Work output is also calculated from the integration of *P* with respect to *V*. The efficiency is calculated as the ratio of the work output to the heat added to the heater in a single cycle. To improve the accuracy of the heat and work calculation, the three-point Legendre–Gauss quadrature formula [6] is used with values evaluated at phases at the center of 40 uniformly divided phase intervals and at phase locations shifted by $\pm\sqrt{3/20}$ of this interval. The difference between the net work out and net heat added to the whole portion of the engine is within 0.03%, and the calculation is performed within this relative error.

Special treatment at the beginning of the transfer process

The volume of a space into which the gas flows starts from zero. However, because this causes infinite *dT/dt*, a special treatment is used. A detailed description can be found in Haramura [9].

Additional condition to determine cubic spline for the matrix temperature

We approximate the matrix temperature with a cubic spline, which has one end node at each end. Since the energy equation is given for each interval and the number of nodes is one more than that of their intervals, an additional condition is necessary. We choose the condition

$$\sum_{i=1}^{n-1}\left(\frac{T_{w,j+1}-T_{w,j}}{\xi_{i+1}-\xi_i}-\frac{T_{w,j}-T_{w,j-1}}{\xi_i-\xi_{i-1}}\right)^2\rightarrow\text{minimum} \qquad (17)$$

where *i* denotes the node number. The sum becomes zero when the temperature is linearly distributed. Differentiating this with respect to temperature at the first (i = 0) node $T_{w,0}$ yields

$$\sum_{i=0}^{n-1}\left[\frac{1}{\xi_{i+1}-\xi_i}\left(\frac{\partial T_{w,j+1}}{\partial T_{w,0}}-\frac{\partial T_{w,j}}{\partial T_{w,0}}\right)-\frac{1}{\xi_i-\xi_{i-1}}\left(\frac{\partial T_{w,j}}{\partial T_{w,0}}-\frac{\partial T_{w,j-1}}{\partial T_{w,0}}\right)\right]$$

$$\times\left(\frac{T_{w,j+1}-T_{w,j}}{\xi_{i+1}-\xi_i}-\frac{T_{w,j}-T_{w,j-1}}{\xi_i-\xi_{i-1}}\right)=0\,. \qquad (18)$$

Since the heat flow between the gas and the matrix determined from the temperature difference between them and heat flow at each interval is mainly determined from the average temperature of the matrix in the interval, the condition

$$T_{w,j+1}+T_{w,j}=\text{const}\,. \qquad (19)$$

is also applied. This gives

$$\partial T_{w,j}/\partial T_{w,0}=(-1)^i\,, \qquad (20)$$

and then Eq. (18) is reduced to

$$\sum_{i=1}^{n-1}(-1)^i\left\{(w_{i,j}+w_{i,j-1})T_{w,j+1}-(w_{i,j}+2w_{i,j-1}+w_{i-1,j-1})T_{w,j}+(w_{i,j-1}+w_{i-1,j-1})T_{w,j-1}\right\}=0 \qquad (21)$$

where

$$w_{i,j}=\frac{1}{\xi_{i+1}-\xi_i}\cdot\frac{1}{\xi_{j+1}-\xi_j}\,. \qquad (22)$$

RESULTS

General Tendencies of Output Power and Efficiency

Figures 3 to 5 show the effect of speed on output power and efficiency. Since heat transfer is the most important factor for performing a Stirling cycle, the cycle work increases at lower speeds, approaching that of the ideal cycle. Output power is a product of cycle work and speed; thus, power tends to increase with speed, as far as cycle work does not decrease as much. Power however levels off and then decreases at high speed because the cycle work is reduced by the lower heat transfer.

Output power behaves as described above for all conditions in Figs. 2 to 4. Figures 2(b) to 4(b) show the maximum power ($\dot{W}_M$; solid circles) against speed and the speed (open circles) at which maximum power occurs.

Figure 2 shows the effect of compression ratio, V_{max}/V_{min}. Output power is small for a low compression ratio, increases as the ratio increases, then decreases, especially at low speeds. The maximum power against speed varies greatly, reaching a maximum at a certain compression ratio. The speed at which the power reaches its maximum increases monotonically with ratio. Efficiency decreases with speed. The dependency of compression ratio is small, except for at extreme values.

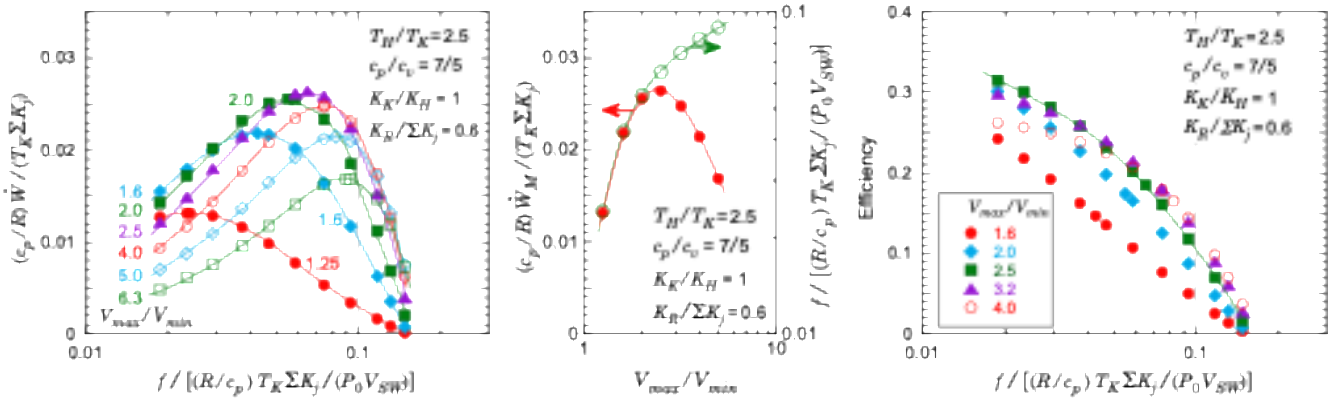

(a) Output power (b) Maximum power against speed (c) Efficiency

ISBN: 978-618-5765-04-0
ISSN 3057-4269

Figure 2: Effect of speed and compression ratio

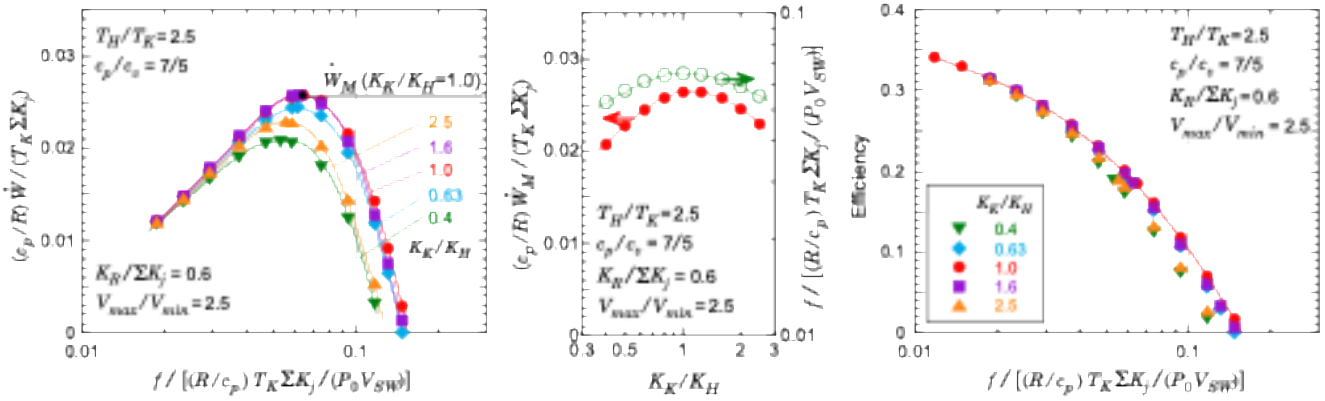

(a) Output power (b) Maximum power against speed (c) Efficiency

Figure 3: Effect of speed and heat conductance ratio of the cooler to the heater

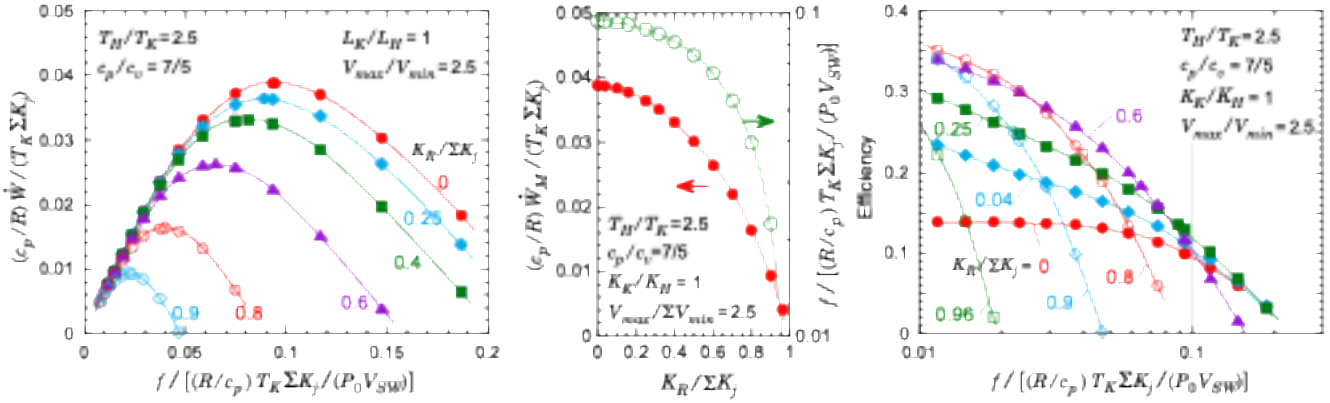

(a) Output power (b) Maximum power against speed (c) Efficiency

Figure 4: Effect of speed and heat conductance in the regenerator

Figure 3 shows the effect of heat conductance ratio K_K/K_H of the cooler to the heater. The power is not affected strongly by the conductance ratio. The speed at which the output power reaches its maximum changes little. The relation between efficiency and speed is almost identical, independent of the conductance ratio.

Figure 4 shows the effect of the heat conductance of the regenerator, K_R. Output power is higher for smaller conductance, and any additional regenerator heat conductance reduces power. The behavior of the efficiency is complex. K_R = 0 gives a low efficiency. The efficiency is increased with only a small conductance of $K_R/\mathrm{S}K_j$ = 0.04. Efficiency is high for dimensionless conductance of 0.4 to 0.7. However, the efficiency at high speed decreases rapidly when the conductance of the regenerator is too large, meaning that the heat conductances of the heater and the cooler are too small.

Contour surface with constant output power

We conclude from the results in Section IV *A* that the heat conductance of the regenerator increases efficiency but decreases output power. The best engines are those with high power and high efficiency, and there is no simple optimization rule to balance these two measures. Therefore, we construct a contour surface on which output power is constant for various combinations of the design parameters. The combination of the parameters at the highest efficiency points on the surface are candidate parameters.

Figure 5 is an example of such contour for T_H/T_K = 2.5 and c_p/c_v = 1.4. Figure 5(a) and 5(b) show $\dot{W}/\dot{W}_{\mathrm{max,max}}$ = 0.7 and 0.5, respectively. The axes for heat conductance ratio K_K/K_H of the cooler to the heater and compression ratio V_{max}/V_{min} are logarithmic, and the axis for the conductance proportion of the regenerator $K_R/\mathrm{S}K_j$ is linear. The surface indicates that the combination of K_K/K_H, V_{max}/V_{min}, and $K_R/\mathrm{S}K_j$ on which output power has a certain fraction of the absolute maximum power, which is obtained at K_R = 0. The combinations of the rest of the parameters are listed in Table 1. Color indicates efficiency with a scale on the right.

The efficiency increases with increasing regenerator conductance and the efficiency changes greatly with the location on the surface where output power is constant. A curve on the surface where efficiency takes the same value spreads wide in the K_K/K_H direction but less in the V_{max}/V_{min} direction. This is reflected by the behavior shown in Section IV *A*. The maximum efficiencies on the contour surface are 0.182 and 0.212 for $\dot{W}/\dot{W}_{\mathrm{max,max}}$ = 0.7 and 0.5, respectively. This condition is obtained under the condition that the partial derivatives of power $\dot{W}_M$, the maximum power on speed, with respect to K_K/K_H and V_{max}/V_{min} are both zero. Derivatives are approximated with a finite difference for ±10% and ±2% shifts of the variables.

Optimum design parameters

Assuming that the optimum condition is the combination of design parameters at which efficiency reaches its maximum on the contour surface, we can find the relation between relative maximum power $\dot{W}/\dot{W}_{\mathrm{max,max}}$ and efficiency. This is

ISBN: 978-618-5765-04-0
ISSN 3057-4269

shown in Fig. 6 for eight combinations of c_p/c_v and T_H/T_K (Table 1).

When output power is near the absolute maximum, efficiency is low, but as output power decreases, the efficiency rapidly increases and then increases at a constant rate from

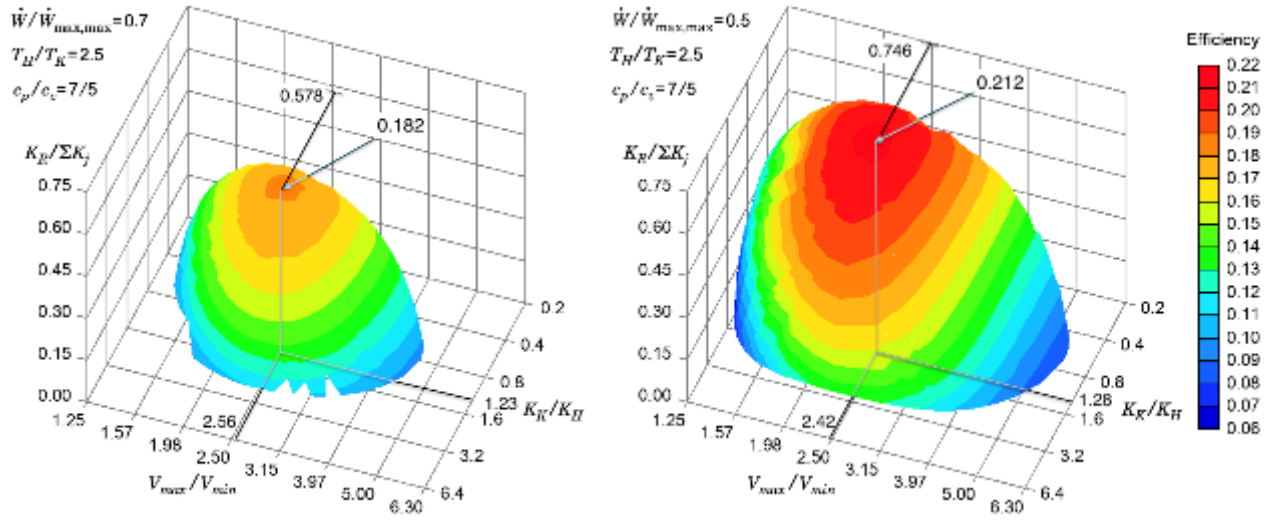

(a) $\dot{W}/\dot{W}_{\mathrm{max,max}}$ = 0.7 (b) $\dot{W}/\dot{W}_{\mathrm{max,max}}$ = 0.5

Figure 5: Contour surface of output power for various combinations of design parameters and efficiency

Table 1: Absolute maximum power obtained for zero regenerator conductance

c_p/c_v	T_H/T_K	V_{max}/V_{min}	K_K/K_H	$\frac{c_p}{R}\frac{\dot{W}_{max,max}}{T_K \Sigma K_j}$
7/5	2.5	2.583	1.129	0.0390
	2.0	2.047	1.099	0.0202
	1.6	1.759	1.099	0.00841
	1.25	1.258	1.033	0.00169
5/3	2.5	1.764	1.109	0.0268
	2.0	1.536	1.084	0.0139
	1.6	1.393	1.094	0.00575
	1.25	1.148	1.028	0.00115

90% to 20% of the absolute maximum. The increase is greater as the power approaches zero. Three horizontal lines on the left side of the graph show $1-\sqrt{T_K/T_H}$ for T_H/T_K <= 2, which is proposed by Curzon and Ahlborn [5] as the maximum efficiency of a Carnot engine for which output power is maximized. Our results approach 70%–80% of this efficiency. This reduced efficiency may come from the irreversibility of the mixing of gas stays in and flows into a space with different temperatures. The efficiency may exceed the Curzon–Ahlborn efficiency for a lower speed.

The optimum values of design parameters are plotted in Figs. 7 to 9. Figure 7 shows the optimum compression ratio, which does not change much as the target power is reduced but increases greatly as the temperature ratio increases. This quantitative dependency is shown in Fig. 7(b) using the optimum compression ratio for the condition where the target power is 60% of the absolute maximum. The optimum compression ratio is correlated as

$$V_{max}/V_{min} = T_H/T_K \quad \text{for} \quad \frac{c_p}{c_v} = \frac{7}{5} \tag{23a}$$

$$V_{max}/V_{min} = 1 + 0.51\left(T_H/T_K - 1\right)^{0.9} \quad \text{for} \quad \frac{c_p}{c_v} = \frac{5}{3}. \tag{23b}$$

Correlation (1) of Nakajima et al. [5] based on air engines is identical to the present results in Eq. (23a).

Figure 8 shows the optimum heat conductance ratio of the cooler to the heater. The ratio falls in a narrow range of 1.05–1.3, although it is larger for higher heat source temperature and for lower specific heat ratio.

Figure 9 shows the optimum heat conductance of the regenerator, which is a unique function of $\dot{W}/\dot{W}_{\mathrm{max,max}}$ independent of any combination of prescribed parameters and is expressed by

$$\left(K_R/\sum K_j\right)_{opt} = 1.05\left(1-\dot{W}/\dot{W}_{max,max}\right)^{0.52}. \tag{24}$$

Comparison with existing emgines

Table 2 shows the comparison with existing engines. The constant Nusselt number is assumed to obtain the heat conductance ratio, although this is not true for a wire netting matrix. Missing data († or ‡) are completed as shown. Most engines were designed for a high temperature ratio of around 3.

The compression ratios are near the present optimum values for three out of four helium engines. Values of K_K/K_H vary widely among existing engines. Since the heater is usually constructed with a tube bundle heated with a combustion frame, thin tubes are avoided because of burn-out or ash clogging. This may make K_H smaller, and thus increase K_K/K_H. Many existing engines have large $K_R/\Sigma K_j$ near unity and do not match the present results. Emphasizing high efficiency resulted in this large conductance, but it seems overdoing because power would decrease so much.

CONCLUSION

We proposed a new way to balance the two major evaluation factors, output power and efficiency, in a Stirling engine design in which efficiency is maximized for the same power. The contour surface of Fig. 5 verifies the suitability of our method.

ISBN: 978-618-5765-04-0
ISSN 3057-4269

A designer should select the optimum point from Fig. 6, depending on their priority for power or efficiency. The three optimum design parameters are shown in Figs. 7 to 9. The optimum value formulae are given as Eqs. (23a), (23b), and (24) for compression ratio and regenerator heat conductance.

Further studies using multi-component analysis should be performed using our optimization method.

‡: 1 mm high clearance + theoretical minimum dead volume of $(V_{SW}/2)[1-\cos(\varepsilon/2)]$ for a two-cylinder engine. e is the phase shift of the volume change.
Beale number (N-Beale) = $\dot{W}/(P_0 V_{SW} f)$, NA: not available.

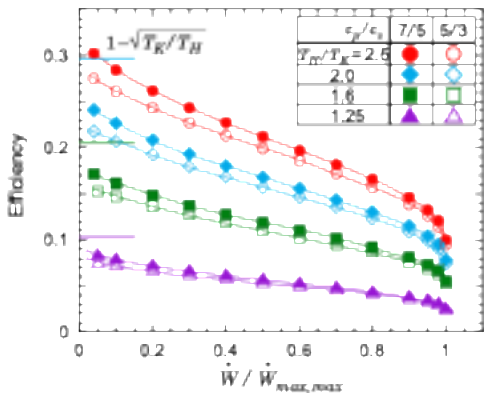

Figure 6: Efficiency change with maximum power

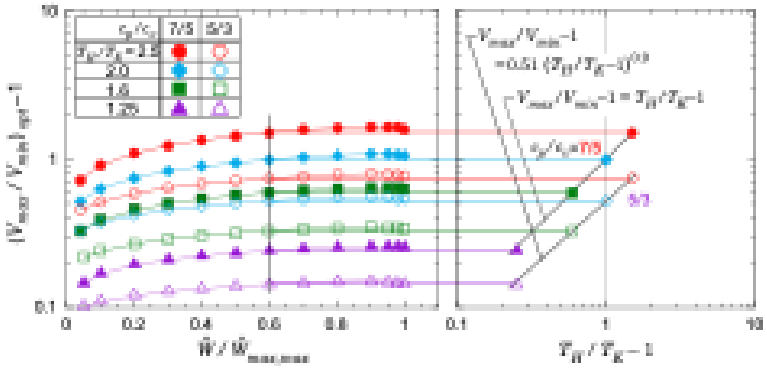

(a) Compression ratio vs. power (b) Change with temperature ratio

Figure 7: Optimum compression ratio

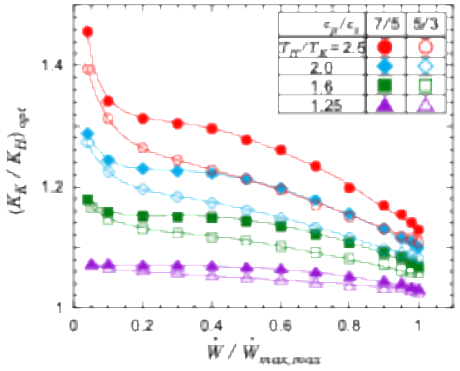

Figure 8: Optimum heat conductance ratio of cooler to heater

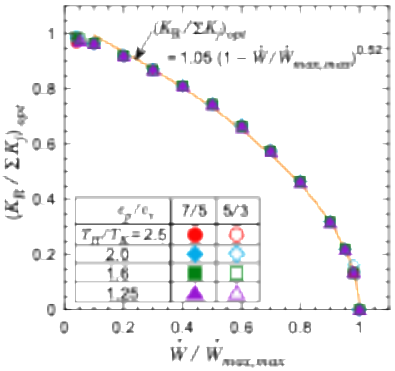

Figure 9: Optimum regenerator heat conductance

Table 2 Design parameters of existing engines

	Gas	T_H/T_K	V_{dE}/V_{SW}	V_{dH}/V_{SW}	V_{dR}/V_{SW}	V_{dK}/V_{SW}	V_{dC}/V_{SW}	V_{max}/V_{min} actual	V_{max}/V_{min} optimum (Eq. (23))	K_K/K_H	K_R/S K_j	N-Beale
PHILIPS 400 HP/CYL [10]	He	3.09	0.0057†	0.241	0.298	0.0956	0.0057†	2.548	1.99	4.409	0.375	0.151
ALLOSPM PD46 [10]	He	2.67	0.0352†	0.3388	0.7332	0.1033	0.0352†	1.803	1.81	1.005	0.998	0.076
CLAPHAM 5.0CC [10]	He	3.07	0.0635†	0.4118	0.354	0.162	0.0635†	1.948	1.98	0.400	0.718	0.058
MELSE II [11]	He	3.04	0.115‡	0.272	0.432	0.092	0.115‡	1.974	1.97	2.403	0.996	0.106
GPU 3 [10]	H_2	3.28	0.1016	0.595	0.461	0.1117	0.1795	1.690	3.28	1.443	0.995	0.182
USS P-40/4-95 [10]	H_2	3.07	0.1714‡	0.2463	1.298	0.209	0.1714‡	1.477	3.07	7.705	0.998	0.336
PHILIPS MP1002CA [10]	Air	2.92	0.1266	0.0918	0.316	0.0918	0.1495	2.289	2.92	1.000	0.969	0.117
Tomcat10 [12]	Air	2.93	0.409‡	0.227	0.874	0.227	0.409‡	1.466	2.93	1.000	0.659	0.184
AP1R-1/250 [13][14]	N_2	1.93	NA	NA	NA	NA	NA	1.34	1.93	NA	NA	0.078

†: Assumed 1 mm clearance of the piston for a coaxial displacer engine.

ISBN: 978-618-5765-04-0
ISSN 3057-4269

REFERENCES

[1] SAAB, Global, “The secret to the world´s most silent submarine,” https://www.saab.com/newsroom/stories/2015/march/the-secret-to-the-worlds-most-silent-submarine, accessed on 17, Sep. 2024.

[2] Qnergy, “Free Piston Stirling Engines,” https://qnergy.com/tech/, accessed on 17, Sep. 2024.

[3] A. J. Organ, "The Regenerator and the Stirling Engine," Mechhanical Engineerign Publications, 1997, pp. 365-479.

[4] J. R. Senft, “Miniature Ringbom Engines,” Moriya Press, 2000, pp. 40-69.

[5] K. Nakajima, F. Toda, T. Isono, K. Ikeda and K. Funabashi, “Influence of Temperature ratio and Compression ratio on Output,” Procs. of 12th Stirling Cycle Symposium, 2009, pp. 9-12.

[6] D. Zwillinger, "Handbook of Integration," Jones and Bartlett Publishers International, 1992, pp. 285-291.

[7] W. H. Press, S. A. Teukolsky, W. T. Vetterling and B. P. Flannery, "Numerical Recipes in Fortran 77," Second Edition, Cambridge University Press, 1997, pp. 107-110.

[8] Y. Haramura, “The optimization of Stirling engine with heat exchangers with zero-volume and finite heat conductance and flow resistance,” Procs. of 23rd Stirling Cycle Symposium, 2021, A2.

[9] F. Curzon and B. Ahlborn, "Efficiency of a Carnot engine at maximum power output," American. Journal of Physics. 43, 22, 1975, pp. 22-24.

[10] A. J. Organ, "The Regenerator and the Stirling Engine," Mechanical Engineering Publications, 1997, pp. 553-589.

[11] I. Yamasita et al., “Fundamental Studies of Stirling Engine and Its Principal Components,” Report of Mechanical Engineering Laboratory, No.145, (1988).

[12] Y. Kato, "Effect of heat storage material shape on the performance of
the Stirling engine," Master's thesis, Kanagawa University, 2015, pp. 60-91.

[13] M. Takeuchi, S. Suzuki, Y. Abe and A. Kitahara, Procs. of 13th International Stirling Engine Conference, 2007, pp. 38-41.

[14] M. Takeuchi, S. Suzuki, Y. Abe and A. Kitahara, Procs. of 13th Stirling Cycle Symposium, 2010, pp. 15-18.

ISBN: 978-618-5765-04-0
ISSN 3057-4269

Optimizing Electric Vehicles Charging Through Smart Energy Allocation and Cost-Saving

Luca Ambrosino
Dipartimento di Elettronica e Telecomunicazioni (DET)
Politecnico di Torino
Torino, Italy
luca.ambrosino@polito.it

Giuseppe Calafiore
Dipartimento di Elettronica e Telecomunicazioni (DET) / College of Engineering and Computer Science (CECS)
Politecnico di Torino / Vin University
Torino, Italy / Hanoi, Vietnam
giuseppe.calafiore@polito.it

Khai Manh Nguyen
College of Engineering and Computer Science (CECS)
Vin University
Hanoi, Vietnam
21khai.nm@vinuni.edu.vn

Riadh Zorgati
R&D Department
Électricité de France (EDF)
Paris, France
riadh.zorgati@edf.fr

Doanh Nguyen-Ngoc
College of Engineering and Computer Science (CECS) and College of Enviromental Intelligence (CEI)
Vin University
Hanoi, Vietnam
doanh.nn@vinuni.edu.vn

Laurent El Ghaoui
College of Engineering and Computer Science (CECS) and College of Enviromental Intelligence (CEI)
Vin University
Hanoi, Vietnam
laurent.eg@vinuni.edu.vn

***Abstract*— As the global focus on combating environmental pollution intensifies, the transition to sustainable energy sources, particularly in the form of electric vehicles (EVs), has become paramount. This paper addresses the pressing need for Smart Charging for EVs by developing a comprehensive mathematical model aimed at optimizing charging station management. The model aims to efficiently allocate the power from charging sockets to EVs, prioritizing cost minimization and avoiding energy waste. Computational simulations demonstrate the efficacy of the mathematical optimization model, which can unleash its full potential when the number of EVs at the charging station is high.**

Keywords—Smart Charging, EVs, Optimization Model, Sustainability, Transportation, Energy, Electricity.

INTRODUCTION

In light of the intensifying environmental crisis, the imperative to transition towards sustainable energy solutions has become more pressing than ever. Central to this transition is the widespread adoption of electric vehicles (EVs) [1], [2], which offer a promising avenue for curbing pollution and mitigating climate change. However, the effective integration of EVs into our daily lives necessitates innovative approaches to address the challenges posed by their charging infrastructure.

Until now, most of the literature concerning electrical vehicles have focused on issues related to electricity and power grid [3]. Data-driven models to reduce EVs impact on the grid itself have been investigated [4], helping to mitigate the risk of overloading the electrical infrastructure finding ways to shift the charging to off-peak hours [5], ensuring a stable and reliable supply of electricity. Furthermore, considering the limited driving range of EVs, they may need to be recharged frequently, especially across long journeys. Consequently, the convenience of charging becomes a primary concern for EV owners and some studies on charging stations location problem have been conducted trying to help this crucial research field [6], [7], even by applying reinforcement learning techniques [8].

On the other hand, our approach deviates from this dominant trend, instead focusing on the optimization of a single charging station when facing the EVs requirements. To predict the charging duration and energy demand of EVs, a hybrid kernel density estimator that uses both Gaussian- and Diffusion-based approach has been developed [9]. Moreover, while there are two types of interaction between vehicles and the charging sockets of charging stations, namely grid-to-vehicle (G2V) and vehicle-to-grid (V2G) [10], our model focuses on grid-to-vehicle interaction. The V2G interaction, on the other hand, allows for the development of more intricate and complex models, for example involving the use of Particle Swarm Optimization (PSO) [11], but has the serious drawback of damaging the integrity and longevity of EV batteries in the long run [12], making this technology less sustainable. This underscores the need for Smart Charging optimization methods to efficiently manage and charge electric vehicles (EVs).

Unlike traditional charging methods, Smart Charging leverages advanced technologies and data-driven algorithms to optimize the utilization of charging stations. By intelligently allocating resources and dynamically adjusting charging schedules, Smart Charging aims to enhance operational efficiency, reduce costs, and alleviate strain on the electrical grid. In essence, Smart Charging transcends the mere act of replenishing the energy reserves of EVs; it represents a holistic approach towards reimagining the entire charging ecosystem. From minimizing peak load demand and optimizing energy distribution to promoting renewable energy integration and accommodating varying user needs, Smart Charging embodies the convergence of sustainability, efficiency, and innovation [13].

Optimization frameworks on smart charging for EVs have seen a growing interest starting from the past decade. In [14] an heuristic method considering the State of Charge (SoC) has been proposed to minimize the charging costs. A real-time management system for the EV charging process is proposed in [15], which identifies the optimal charging periods for each EV with the aim of reducing peak load. Home charging is also worth studying due to the growing number of private EV owners, and an empirical study in [16] lead to an optimal schedule model for home charging at minimum cost. In [17], they propose an optimization model that maximizes the profit

This paper is based upon work supported by Vin University under Grant No. VUNI.2223.FT08. Furthermore, Luca Ambrosino is supported by the he FAIR - Future Artificial Intelligence Research and received funding from the European Union Next-Generation EU (PIANO NAZIONALE DI RIPRESA E RESILIENZA (PNRR) – MISSIONE 4 COMPONENTE 2, INVESTIMENTO 1.3 – D.D. 1555 11/10/2022, PE00000013). This manuscript reflects only the authors' views and opinions, neither the European Union nor the European Commission can be considered responsible for them.

of an EV aggregator in charging stations which is formulated as a mixed-integer linear programming problem.

Our research distinguishes itself by emphasizing the optimization of decision-making processes within the charging station, building a mathematical optimization model introduced in Section 0, formulated as a Linear Programming problem (LP) and therefore can be solved efficiently using polynomial-time algorithms. Our objective in this paper is to assume the perspective of a charging station owner, optimizing the EVs charging process from a business point of view. We tackle the complexities of internal station management, deciding which vehicles to charge and for how long, as well as how much power to allocate to that EV, in order to help maximizing operational efficiency and reduce overall operational costs due to EVs charging process. Additionally, in Section 0 a Robust Optimization approach is provided for dealing with real-world uncertainties in input data such as variations in electricity prices and energy demand by EVs, encompassing the broader goal of system resilience and reliability. The main results of the cost-saving effects brought by the introduced optimization model are highlighted in Section 0, showing a huge potential of this model especially when the number of EVs grows. This innovative approach aims to make a significant contribution to the development of the field of Smart Charging both in the present and future of transportation.

NOMINAL OPTIMIZATION MODEL

Some simple strategies have already been taken into account when dealing with EV's recharge, like the "First Come, First Served" (FCFS) principle [18] which ensures fairness by serving vehicles in the order they arrive. However, it doesn't consider factors like changing energy prices or demand patterns, which can lead to higher costs for charging stations. Furthermore, the risk of overloading the electricity grid must be considered. By using more flexible strategies, like adjusting prices based on demand or prioritizing urgent charging needs, stations can save money while still being fair to all users and can mitigate electricity demand peak. This helps make electric transportation more sustainable and affordable for everyone.

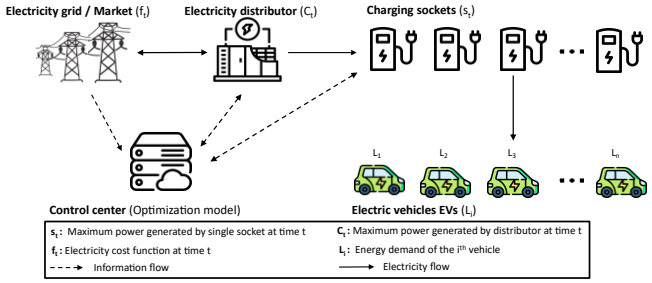

Figure 1: *Charging station structure related to our model.*

As already mentioned, this paper aims to look at the business opportunity provided by the smart charging optimization problem from the charging station's owner point of view. ***Figure 1*** represents the scheme of the charging station as we think of it. The electricity is bought from the market and stored in the electricity distributor inside the charging station. Every charging socket in the charging station has its own power but they all share a common total power from the electricity distributor. The optimization model proposed in Eq. (1) aims to minimize the management costs of an EV charging station. These costs are associated with energy consumption, which the charging station must purchase from external suppliers following electricity market prices, assuming it does not have its own energy production, such as from solar or photovoltaic panels. Additionally, we consider that the sale of electricity from the charging station to EV customers always occurs at the same price, so that maximizing the charging station's profits is equivalent to minimizing costs.

Our optimization model deals with the power allocation to N electrical vehicles over a discrete time horizon of T steps of duration Δ, considering the variable Y such that Y_{ti} is the power allocated to vehicle i at time t:

$$\begin{aligned} p^* = \min_Y & \sum_{t=1}^{T} f_t\left((1 + y_t^0) \cdot \sum_{i:t \in [a_i, d_i]} Y_{ti}\right) \\ s.t. \quad & \sum_{t=a_i}^{d_i} Y_{ti} \geq L_i, \quad i = 1, \dots, N \\ & \sum_{i=1}^{N} Y_{ti} \leq C_t, \quad t = 1, \dots, T \\ & 0 \leq Y_{ti} \leq s_t, \quad t = 1, \dots, T, i = 1, \dots, N. \end{aligned} \tag{1}$$

Where:

- $f_t: \mathbb{R} \to \mathbb{R}, t = 1, \dots, T$, are convex increasing functions that encode the cost of energy at time t. In particular, if we assume that $f_t(z_t), z_t \in \mathbb{R}$ is linear $\forall t$, e.g. $f_t(z_t) = \pi_t \cdot z_t$ then the above Eq. (1) is a linear problem (LP).
- y^0 is a given T-dimensional-vector that corresponds to a systematic waste of energy during the charging process, for example as heat generation. We have a waste of energy if and only if the charging port is active at time t. The more energy we allocate, the more energy is waste. Theoretically, y_t^0 is depending on time, but for this paper we suppose it to be fixed as a small percentage as 1%.
- $L \in \mathbb{R}^N$ is the load vector, that is L_i is the required energy demand E_i for the i-th vehicle, divided by the time step length Δ.
- (a_i, d_i) are arrival and departure times for vehicle i. Of course the difference between d_i and a_i corresponds to the total parking time of vehicle i. Intuitively, we have $1 \leq a_i, d_i \leq T$. Address uncertainty to the EVs' arrival process rather than a scenario-based one, can be tricky and goes beyond the scope of this work.
- C_t is the maximum power generated by the station at time t. C_t may include a time-varying term that takes into account the self-production, coming, e.g., from solar panels. Although in general C_t can be time-varying, we consider a fixed $C_t = C, t = 1, \dots, T$ when dealing with simulations, because we address the focus of the optimization on the on the time-varying electricity prices and load vectors issues.
- While C_t is considered as the global charging station budget, s_t instead is the maximum power generated by a single charging socket and of course is an upper bound for the variable Y_{ti}. For the same reason as C_t, we also consider a fixed $s_t = s, t = 1, \dots, T$.

The costs consist of a fixed component y_0, for example, due to the activation of the plug for charging or setup costs, and a variable component that naturally increases with the

ISBN: 978-618-5765-04-0
ISSN 3057-4269

amount of electricity used. We assume that every charging plug has the same power, so that the cost generated by them is considered regardless to which plug is used to charge. The first constraint $\sum_{t=a_i}^{d_i} Y_{ti} \geq L_i, \quad i = 1, \dots, N$, is a kind of demand satisfaction, explaining that the total energy delivered to each vehicle i must be greater or equal than its total energy request L_i. The second constraint $\sum_{i=0}^{N} Y_{ti} \leq C_t, \quad t = 1, \dots, T$, is instead a budget constraint, assuring that at each time instant t the total power delivered by the station is never greater than the station's power capacity C_t. If we had wanted to emphasize the cost-saving objective more in the optimization model, we would have avoided imposing a direct budget constraint, opting instead to incorporate a penalty into the objective function for exceeding the budget. In our context, it's important to highlight that the goal of the model is also to promote energy sustainability by preventing grid overload, despite the potential for greater cost savings from overloading. This balance is crucial to ensure the long-term stability and efficiency of the energy system, thereby contributing to the overall sustainability of the energy infrastructure. Finally, $0 \leq Y_{ti} \leq s_t, \quad t = 1, \dots, T, i = 1, \dots, N$, states that each variable Y_{ti} must obviously be non-negative, since it represents power directionally allocated to vehicle i at time t, and has s_t as upper bound.

In order to simplify the representation and the simulations code, we use a binary matrix A of size $T \times N$ to encode arrival and departure times (a_i, d_i). Each element A_{ti} equals 1 if t falls into the interval $[a_i, d_i]$ for vehicle i, 0 otherwise. This matrix allows us to condense the information regarding the arrival and departure times of each vehicle into a more compact format. With this matrix representation, we can reformulate the optimization problem stated above in a more concise matrix form useful for Matlab simulations:

$$\begin{aligned} \min_{Y}\colon\ & F\big(diag(AY^T) + y^0 \cdot diag(AY^T)\big) \\ s.t.\colon\ & diag(A^T Y) \geq L, \\ & diag(AY^T) \leq C, \\ & Y \geq 0, \\ & Y \leq s. \end{aligned} \tag{2}$$

Where:

- $F\colon \mathbb{R}^T \to \mathbb{R}$ aggregates all the cost functions f_t, that is $F(z) := \sum_{t=1}^{T} f_t(z_t), \quad z \in \mathbb{R}^T$.
- The diagonal elements of the N×N-dimensional matrix $A^T Y$, say $(A^T Y)_{ii}$, are the total power absorbed by the vehicle i during its whole charging.
- The diagonal elements of the T×T-dimensional matrix AY^T, say $(AY^T)_{tt}$, are the total power available at time t.
- L and C are respectively the vectors related to the power requirement and the capacity (i.e. energy available). Finally, s is the vector related to the single socket maximum power generated.

ROBUST OPTIMIZATION OVERVIEW

The sources of uncertainty considered in this optimization model are related to electricity prices π_t and to load vectors L_i, i.e. energy required by EVs. The electricity price fluctuates not only periodically with time (during a day of operation there are peak-price periods and low-price periods, e.g., at night) but also in response to unforeseeable network and real-time electricity market conditions, which can be difficult to forecast. Concerning the energy demand from EVs, we do not know exactly in advance how much energy each vehicle would need to be charged. Several factors affect this uncertainty and a huge problem may arise during peak hours if there are many EVs in the charging station needing a great amount of charge. These uncertainties can be characterized by the fact that the objective function and constraints of the problem are dependent on additional parameters $u \in \mathcal{U} \subset \mathbb{R}^d$, which represent the uncertainties. The functions $f_i(x, u)$, which can be either objective function or constraint, represent the uncertain components of the problem. Depending on the approach chosen to define and manage uncertainty, various methods for optimization under uncertainty are available.

In this paper, the two robust optimization methods used to deal with uncertainties in electricity prices and in load vector are respectively the norm-bounded uncertainty in dimension 2 and the interval uncertainty [19]. In formula, a norm-bounded uncertainty set (a.k.a. norm ball) is a set of the form:

$$\mathcal{U}\colon \{u\colon \|u - \hat{u}\|_p \leq \mathrm{r}\} = \{r = \hat{u} + rz\colon \|z\|_p\} \leq 1 \tag{3}$$

Where $\hat{u}$ is the center of the ball, r is its radius, and p denotes the type of norm, typically $p = 1, 2, \infty$. In particular, in the common case when $p = 2$ the norm ball is a hypershpere and the problem is a second order cone programming (SOCP) problem. For our specific smart charging problem in Eq. (2), we assume that π, i.e. the time-varying vector encoding electricity prices, is only known up to a sphere: $\|\pi - \hat{\pi}\|_2 \leq r$, where the "nominal" cost $\hat{\pi} \in \mathbb{R}^T$ and the uncertainty level $r \geq 0$ are both known. The robust counterpart to the model in Eq. (2) with linear prices π is the SOCP:

$$\begin{aligned} \min_{Y}\colon\ & \pi \cdot \big(y^0 + diag(AY^T)\big) + \mathrm{r} \cdot \|y^0 + diag(AY^T)\|_2 \\ s.t.\colon\ & diag(A^T Y) \geq L, \\ & diag(AY^T) \leq C, \\ & Y \geq 0, \\ & Y \leq s. \end{aligned} \tag{4}$$

We observe that when $r = 0$, we recover the nominal problem with fixed costs, because the uncertainty ball has radius 0, while for r large, the solution drives toward the problem with quadratic costs instead of linear.

In practice, due to uncertainty on the initial charge of vehicles, also the load vector L is uncertain. Assume for example that the load vector L is only known to satisfy $L \in [\underline{L}, \overline{L}]$, where the lower and upper bounds $\underline{L}$ and $\overline{L}$ are known somehow. The robust counterpart has a trivial expression, in the same form as Eq. (4), but with values of L replaced with their worst-case (largest) values $\overline{L}$, which means:

$$\begin{aligned} \min_{Y}\colon\ & \pi \cdot \big(diag(AY^T) + y^0 \cdot diag(AY^T)\big) + \\ & + \mathrm{r} \cdot \|diag(AY^T) + y^0 \cdot diag(AY^T)\|_2 \\ s.t.\colon\ & diag(A^T Y) \geq \overline{L}, \\ & diag(AY^T) \leq C, \\ & Y \geq 0, \\ & Y \leq s. \end{aligned} \tag{5}$$

In some practice applications, if the infrastructure of the charging station allows to measure, at charging time, the actual desired load from EVs, then an affine recourse strategy may improve the performance of robust optimization.

SIMULATIONS AND RESULTS

After the optimization model theoretical introduction, we want to show the benefits that this smart charging approach can give to one charging station's finances. With this aim, we perform numerical simulations comparing our model in Eq.

ISBN: 978-618-5765-04-0
ISSN 3057-4269

(1) to a more trivial charging decision algorithm like the First Come First Served (FCFS) process. This standard algorithm states that, whenever an EV enters the charging station, it is put into charge if the total amount of energy deliverable by the charging station allows it. In formula, the power allocated to vehicle i at time t, say X_{ti}, is:

$$X_{ti} = min([s_t, L_i^{res}, C_t^{res}]) \quad (7)$$

If the charging station is full when an EV arrives, it must wait until another EV completes its recharge. In fact, when the total power deliverable by the charging station C_t is already in use for other Evs, we will have $C_t^{res} = 0$ in Eq. (7) forcing into $X_{ti} = 0$. L_i^{res} is instead the residual energy required by vehicle i considering the charging already done in the previous time steps, so that if an EV needs a small amount of energy, the algorithm gives it only the amount needed in order to avoid waste of energy and useless costs. The decision process in Eq. (7) is a standard procedure currently adopted by many charging stations which do not use smart charging methods. It is a basic method which already takes care about the energy waste, therefore is better than other simpler algorithms. The weakness of this method is that it does not consider the changing electricity prices during the different time instants t, instead it aims to charge the EVs as soon as possible. This can be a reasonable decision, but if we know that an EV stays parked in the station for a long time, a smart charging method that considers time-varying electricity prices can improve the performances and optimize the cost-saving.

The operational cost minimization is obviously related also to a lower use of electricity and leads to a greener economy. To show the benefit of our approach, we run MATLAB simulations comparing the optimization model in Eq. (2) with the more trivial algorithm just introduced in Eq. (7). The input data considered are taken from the Caltech university charging station in California (USA) [20], which provides a common and open-source dataset useful to conduct analysis on EVs. The specific dataset that we used to generate in our simulations both the load vector L and the EVs arrival scenarios A contains records for 861 days, starting from *25-Apr-2018*. The final day recorded in our Caltech.csv dataset is *12-Apr-2021*. The dates within the dataset are not always consecutive, as there are 223 missing dates. Most of the missing dates are after *19-Mar-2020*, which marks the beginning of the lockdown in California due to the COVID-19 pandemic [21]. Other missing days may be attributed to days when no electric vehicles visited the charging station, especially on Sundays. Despite the gaps, we can consider each recorded day as a separate scenario, each providing its own set of input data for the model. This means that each day, regardless of continuity, offers a unique dataset that can be independently analyzed and modeled.

The dataset contains records of EVs' arrival and departure time, charging duration and total energy absorbed in kWh. From this data, we can easily compute the input matrix A and the load vector L of energy required by EVs for each day in kWh, considering a fixed time horizon $T = 24$ hours, i.e. 24 optimization time steps. The other parameters of the model have been fixed: y_t^0 even if theoretically can vary in time, has been set to a reasonable small value; C_t and s_t can also depend on time, but we chose to refer to the exact values of Caltech charging station [22]. It is not easy to extract electricity prices data from California, since we need hour-by-hour prices information. The input vector π used comes from the open source European electricity prices [23], specifically from Italy, considering the same day as matrix A and vector L refer to, in order to have coherent scenarios. Be aware that, even if the electricity prices do not correspond to the same geographical area of the EVs data, our model is consistent and general enough to be applied to different electricity prices. In fact, different electricity prices schemes only affect the percentage of cost-saving, and do not undermine the model efficiency. All input data are summarized in ***Table 1:*** *Input values for simulations*.

Table 1: *Input values for simulations*

Input data	Value
A, L	Estimated from Caltech data
y_t^0	$0.01, \forall t$
C_t	$300\ kW, \forall t$
s_t	$7\ kW, \forall t$
π	Italian electricity prices in €

Already analyzing the simulation performed on the first day of the dataset, i.e. *25-Apr-2018*, it is clear that the time-aware approach with respect to electricity prices benefits a lot, compared to the trivial algorithm decision process in Eq. (7). In fact, the huge cost-saving on this specific day is 28.98%.

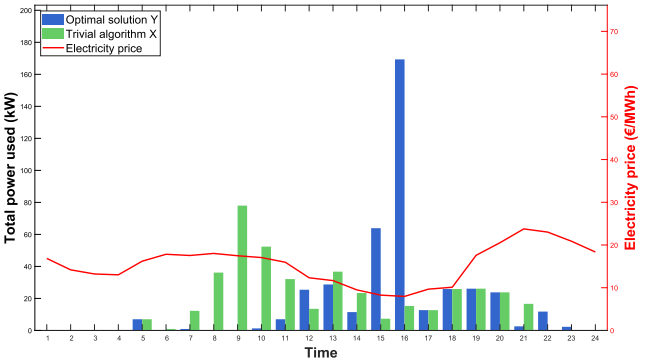

Figure 2: *Total power allocated to EVs during one single day (25-Apr-2018), divided by hours.*

Figure 2: *Total power allocated to EVs during one single day (25-Apr-2018), divided by hours.* shows the total power allocated by the two methods over the whole charging station, for each time step. We can notice that while the trivial algorithm allocate power to charge EVs as soon as they enter the charging station, our optimization model aims to charge as much as possible when the electricity price is lower during the day.

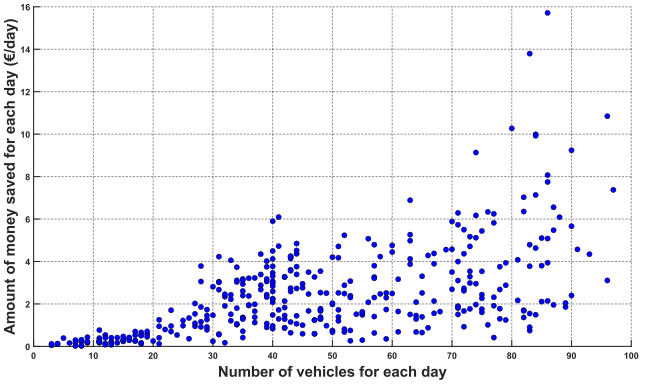

Figure 3: Total money saved for each day, over 365 scenarios simulations, starting from 25-Apr-2018.

It is easy to understand that applying this reasoning to a bigger number of EVs, manages to achieve an higher cost-saving. The scatter plot in ***Figure 3*** shows the positive correlation between the number of EVs entering the charging

ISBN: 978-618-5765-04-0
ISSN 3057-4269

station during the whole day and the amount of money saved on that day, due to our model's smart allocation of the recharging power. Each blue dot in ***Figure 3*** represents one of the 365 days over the simulation horizon. The cost-saving percentage obtained by applying our optimization model every day for 365 days scenarios is 8.78% on average, with a maximum cost-saving of 55.25% and a minimum of 0.66%, obtained on 31-Dec-2018 when only 7 EVs visited the charging station due to New Year's Eve.

The scatter plot in ***Figure 3*****Σφάλμα! Το αρχείο προέλευσης της αναφοράς δεν βρέθηκε.** implicitly suggests a huge potential of smart charging for the future, when the number of Electric Vehicles will increase in order to obtain a greener economy for a long-term sustainable world. This smart charging optimization model fits well the long-term needs because we can save always more money when we apply this power allocation decision process over a longer time period, as shown in the area plot in ***Figure 4***. A 2-year long simulation period, i.e. 730 different scenarios, shows the potential of our smart charging mathematical model when it is continuously applied to reduce the operational costs of a charging station. The optimized cost are always lower than the cost obtained by applying the trivial decision algorithm for EVs charging, and this gap is growing in time also due to the higher number of EVs on the market. The average cost-saving percentage over 730 scenarios is 8.95%.

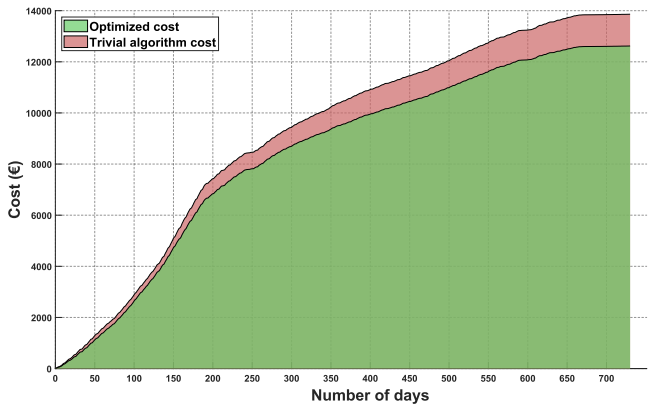

Figure 4: *Total operational cost in time, over a 730 scenarios period starting from 25-Apr-2018.*

In ***Figure 4*** we can notice that the cost is increasing quite fast in the first half of the simulation time period, while it becomes more flat in the second half. This is surely an effect of fewer EVs coming to the charging station after the outbreak of COVID-19 pandemic. In fact, not only after the *19-Mar-2020* there are a lot of missing days in the dataset, but there are reasonably also many days with very few EVs. More in details, the average number of EVs among the 861 scenarios is 30.1. Another computational simulation has been performed considering only the 455 scenarios with number of EVs $N \geq 30$, obtaining an average cost-saving percentage of 9.88%. A summary of the simulation results is exposed in ***Table 2***, comparing the different costs obtained applying either the trivial decision algorithm or the smart charging optimization model, with same input parameters as in ***Table 1*** but different settings related to number of scenarios T and to filtered condition on the number N of EVs in each scenario. Here the *Trivial Cost* and the *Optimized Cost* are computed by summing up all the daily operational costs over the number of scenarios T. The numbers in ***Table 2*** indicate once again that the smart charging optimization model has a huge potential in cost-saving during the days with a lot of EVs in the charging station. In fact, in the dataset there are 574 scenarios out of 861 where the number of electric vehicles (EVs) is at least 10, accounting for exactly two-thirds of the dataset. However, these 574 scenarios generate almost 97% of the total operational costs either we consider the trivial algorithm or the mathematical optimization model.

Table 2: *Simulations results summary.*

T	EVs Number	Trivial Cost	Optimized Cost	Average Cost-Saving
100	N>0	2890.03€	2642.52€	8.56%
365	N>0	10454.64€	9554.42€	8.61%
861	N>0	14033.47€	12780.11€	8.93%
574	N≥10	13599.24€	12370.08€	9.04%
455	N≥30	12579.39€	11430.53€	9.13%

CONCLUSIONS AND FUTURE WORKS

Smart Charging is a research field that has recently attracted the attention of the world and is developing day by day. The EVs market is still at the beginning of its expansion, but it is only a matter of time that it is going to exponentially grow, since the climate crisis is striking more and more, and many governments have already adopted some preventive measures that will lead to an always higher number of EVs in the streets. Of course, charging stations already adopt decision algorithms to determine a strategy to follow when many EVs approach the station. Anyway, not always the decision made turns out to be optimal. In fact, we have shown that following a Smart Charging optimization model significantly reduces the charging station operational cost, while keeping the same service level and customer satisfaction.

The mathematical optimization model presented in this paper utilizes a time-aware strategy to efficiently allocate the energy needed for each EV to recharge, intelligently selecting the time interval and vehicle to charge in order to minimize the operational costs associated with purchasing electricity from the power grid by the charging station. This smart charging model indeed ensures an average 9% cost saving compared to a standard algorithm when tested across 730 days, i.e. 730 different scenarios related to vehicle arrivals, EVs energy requirement, and electricity costs. Moreover, this model, allows for good flexibility to be used within the realm of robust optimization, aiming to find an optimal smart charging policy even when the input parameters are uncertain.

Although our model reach interesting results in optimization, there are some aspects that deserve to be taken into account as potential improvements. The objective function of the proposed optimization model focuses on the cost-saving without considering the profitability of the charging station. If the electricity is sold to the customer at a fixed price, then this approach can be considered optimal. However, challenges arise when the prices of electricity vary over time or if discounts are offered for extended charging periods. In that case the potential of our smart charging optimization model would significantly grow, but it could be convenient to re-formulate the optimization problem under a profit maximization point of view for the objective function. This idea can easily fit a company needs in the real-world, but these non-linearities are going to significantly complicate the model and its computational resolution.

Another consideration about the proposed optimization model is the assumption that all charging sockets have uniform power output. However, it's worth noting that many

ISBN: 978-618-5765-04-0
ISSN 3057-4269

charging stations currently offer various types of sockets with different charging capabilities, such as slow, standard, or fast charging. These distinctions not only affect the charging speed but can also influence pricing, introducing additional complexity to the optimization process. Our model already incorporates factors like electricity cost fluctuations over time and manages to efficiently schedule EV recharges based on their parking durations, as outlined in matrix A. Should the charging station feature different socket types, exploring the interplay between EV energy requirements and parking durations could potentially yield even more optimal charging schedules. As already mentioned, the EV market is likely to grow in the next few years, and when this happens it could be useful to consider adding an upper bound constraint on the cardinality of the optimization problem solution. Some constraint relaxation techniques may help keeping the computational problem at an acceptable difficulty despite a non-linear cardinality constraint.

Considering what we have observed and the few assumptions made to deeply analyze the performances of this mathematical model, it is important to emphasize that this smart charging model aspires to be a benchmark for other optimization strategies related to Smart Charging for EVs. Certainly, developing more complex models based on this one's idea will be a central goal for this research field's future, which aims to reconcile humanity's daily practical transportation needs with the global shared objective of shifting the world economy towards long-term energy sustainability to safeguard the health of our planet.

REFERENCES

[1] P. IEA (2024), "Global EV Outlook 2024." Accessed: Jun. 06, 2024. [Online]. Available: https://www.iea.org/reports/global-ev-outlook-2024

[2] Hannah Ritchie, "Tracking global data on electric vehicles," *OurWorldInData.org*, *https://ourworldindata.org/electric-car-sales*, 2024.

[3] J. Rivera, C. Goebel, and H.-A. Jacobsen, "Distributed Convex Optimization for Electric Vehicle Aggregators," *IEEE Trans Smart Grid*, vol. 8, no. 4, pp. 1852–1863, Jul. 2017, doi: 10.1109/TSG.2015.2509030.

[4] S. Powell, G. V. Cezar, L. Min, I. M. L. Azevedo, and R. Rajagopal, "Charging infrastructure access and operation to reduce the grid impacts of deep electric vehicle adoption," *Nat Energy*, vol. 7, no. 10, pp. 932–945, Sep. 2022, doi: 10.1038/s41560-022-01105-7.

[5] J. de Hoog, T. Alpcan, M. Brazil, D. A. Thomas, and I. Mareels, "Optimal Charging of Electric Vehicles Taking Distribution Network Constraints Into Account," *IEEE Transactions on Power Systems*, vol. 30, no. 1, pp. 365–375, Jan. 2015, doi: 10.1109/TPWRS.2014.2318293.

[6] S. H. Chung and C. Kwon, "Multi-period planning for electric car charging station locations: A case of Korean Expressways," *Eur J Oper Res*, vol. 242, no. 2, pp. 677–687, Apr. 2015, doi: 10.1016/j.ejor.2014.10.029.

[7] Z.-H. Zhu, Z.-Y. Gao, J.-F. Zheng, and H.-M. Du, "Charging station location problem of plug-in electric vehicles," *J Transp Geogr*, vol. 52, pp. 11–22, Apr. 2016, doi: 10.1016/j.jtrangeo.2016.02.002.

[8] Z. Zhao, C. K. M. Lee, J. Ren, and Y. P. Tsang, "Optimal EV Fast Charging Station Deployment Based on a Reinforcement Learning Framework," *IEEE Transactions on Intelligent Transportation Systems*, vol. 24, no. 8, pp. 8053–8065, Aug. 2023, doi: 10.1109/TITS.2023.3265517.

[9] Y.-W. Chung, B. Khaki, C. Chu, and R. Gadh, "Electric Vehicle User Behavior Prediction Using Hybrid Kernel Density Estimator," in *2018 IEEE International Conference on Probabilistic Methods Applied to Power Systems (PMAPS)*, IEEE, Jun. 2018, pp. 1–6. doi: 10.1109/PMAPS.2018.8440360.

[10] S. Mittal, A. Singh, and P. Chittora, "EV Control in G2V and V2G modes using SOGI Controller," in *2022 IEEE 3rd Global Conference for Advancement in Technology (GCAT)*, IEEE, Oct. 2022, pp. 1–6. doi: 10.1109/GCAT55367.2022.9972182.

[11] D. A. Hussien, W. A. Omran, and R. M. Sharkawy, "Smart Charging of Electric Vehicles in Charging Stations," in *2023 5th International Youth Conference on Radio Electronics, Electrical and Power Engineering (REEPE)*, IEEE, Mar. 2023, pp. 1–5. doi: 10.1109/REEPE57272.2023.10086885.

[12] J. D. K. Bishop, C. J. Axon, D. Bonilla, M. Tran, D. Banister, and M. D. McCulloch, "Evaluating the impact of V2G services on the degradation of batteries in PHEV and EV," *Appl Energy*, vol. 111, pp. 206–218, Nov. 2013, doi: 10.1016/j.apenergy.2013.04.094.

[13] Energy Saving Trust, "Smart charging for electric vehicles, https://energysavingtrust.org.uk/advice/smart-charging-electric-vehicles/."

[14] Y. Cao *et al.*, "An Optimized EV Charging Model Considering TOU Price and SOC Curve," *IEEE Trans Smart Grid*, vol. 3, no. 1, pp. 388–393, Mar. 2012, doi: 10.1109/TSG.2011.2159630.

[15] G. Benetti, M. Delfanti, T. Facchinetti, D. Falabretti, and M. Merlo, "Real-Time Modeling and Control of Electric Vehicles Charging Processes," *IEEE Trans Smart Grid*, vol. 6, no. 3, pp. 1375–1385, May 2015, doi: 10.1109/TSG.2014.2376573.

[16] E. Bjørndal, M. Bjørndal, E. Kjerstad Bøe, J. Dalton, and M. Guajardo, "Smart home charging of electric vehicles using a digital platform," *Smart Energy*, vol. 12, p. 100118, Nov. 2023, doi: 10.1016/j.segy.2023.100118.

[17] S. de la Torre, J. A. Aguado, and E. Sauma, "Optimal scheduling of ancillary services provided by an electric vehicle aggregator," *Energy*, vol. 265, p. 126147, Feb. 2023, doi: 10.1016/j.energy.2022.126147.

[18] D. Wang and F. Liao, "Analysis of first-come-first-served mechanisms in one-way car-sharing services," *Transportation Research Part B: Methodological*, vol. 147, pp. 22–41, May 2021, doi: 10.1016/j.trb.2021.03.006.

[19] A. Ben-Tal, L. El Ghaoui, and A. Nemirovski, "Robust Optimization," in *ROBook*, 2021, pp. 159–167.

[20] Z. J. Lee, T. Li, and S. H. Low, "ACN-Data," in *Proceedings of the Tenth ACM International Conference on Future Energy Systems*, New York, NY, USA: ACM, Jun. 2019, pp. 139–149. doi: 10.1145/3307772.3328313.

[21] Jason Kandel, "Timeline: A Look at Key Coronavirus Pandemic Events and Milestones in California," *NBC Los Angeles*, Mar. 23, 2020.

[22] "California Institute of Technology, Caltech." Accessed: Jun. 07, 2024. [Online]. Available: http://ev.caltech.edu/

[23] EMBER, "European wholesale electricity price data." Accessed: Jun. 07, 2024. [Online]. Available: https://ember-climate.org/data-catalogue/european-wholesale-electricity-price-data/

ISBN: 978-618-5765-04-0
ISSN 3057-4269

Start-Up Phase of Pilot Plant Denitrifying Bioreactor Used for Simultaneous Removal of Pesticides

Jitka Malá
Brno University of Technology, Faculty of Civil Engineering,
Brno, Czech Republic
ORCID 0000-0002-1399-0694

Karel Hrich
Brno University of Technology, Faculty of Civil Engineering,
Brno, Czech Republic
ORCID 0000-0002-4017-0739

Petr Karásek
Research Institute for Soil and Water Conservation
Prague, Czech Republic
ORCID 0000-0002-0991-076X

Martina Siglová
EPS Biotechnology
Kunovice, Czech Republic
martina.siglova@epsbiotechnology.cz

Zuzana Bílková
ALS Czech Republic
Prague, Czech Republic
ORCID 0000-0002-3911-860X

***Abstract*— Denitrifying woodchip bioreactors (DWB) are natural treatment systems that have been developed for the reduction of nitrates in agricultural runoffs without requiring any energy. A pilot plant DWB with a volume of 4.2 m^3 filled with poplar chips was installed in October 2023 in an agricultural area near Brno, Czech Republic, with the intention of testing its ability to reduce concentrations of pesticide compounds in addition to nitrates. After minimum water discharge until January 2024, the DWB was operated from February to mid-May with an average hydraulic retention time of 11 h. The average influent NO_3-N concentration was 10.4 mg/L. Maximum NO_3-N removal of 84% was achieved. The water temperature did not exceed 11.6 °C, resulting in low concentrations of organic matter leached from the filling – chemical oxygen demand was typically below 50 mg/L. Microbiological analyses indicate that the predominance of microbial biomass is bound to the surface of the wood chips. Its abundance is 1 to 3 orders of magnitude higher than the amount of microorganisms in the liquid phase. Most of the denitrifying bacteria belong to the genera *Pseudomonas* and *Flavobacterium*. A wide range of pesticides (about 360 including both parent substances and their metabolites) were investigated in the DWB inlet/outlet water samples. The sampling campaigns ran from October to November 2023 and from February to May 2024. The majority of the pesticides analysed did not exceed the limit of quantification, with the exception of six pesticides (DNOC, fluazifop, glyphosate, chlorotoluron, isoproturon, and propamocarb) and eight metabolites (1,2,4-triazole, AMPA, dimethachlor ESA, metazachlor ESA, metolachlor ESA, metolachlor NOA 413173, metolachlor OA, and pethoxamid ESA). The sum of the concentrations of the identified substances in the inlet water was in the range of 0.7 to 3.1 µg/L. Metolachlor ESA, pethoxamid ESA, and AMPA accounted for the majority of these. Approximately 70% of the total amount of pesticides and their metabolites (Except for AMPA) were removed from water in the DWB. The concentrations of AMPA (a metabolite of glyphosate) was increased. One possible explanation for this phenomenon is the use of glyphosate as a weed herbicide in poplar cultivation.**

***Keywords*— zero-energy, sustainable agriculture, pesticides**

INTRODUCTION

Denitrifying woodchip bioreactors (DWBs) are natural treatment systems that have been developed for the reduction of nitrates in agricultural runoffs without requiring any energy input. They are typically constructed in the form of beds or containers filled with organic material, such as woodchips. The fill medium releases organic carbon, thereby fostering heterotrophic denitrification, which converts nitrates to nitrogen gases released to the atmosphere [1] [2].

Agricultural runoffs are known to contain a variety of pollutants, including pesticides and veterinary pharmaceuticals. The results of previous studies suggest that these substances could be removed from the incoming water by biodegradation and/or adsorption to the DWB filling [3] [4] [5] [6] [7]. However, their biotransformation can result in metabolites that are even more toxic than the original compound [8] [9].

The objectives of this study were (1) to evaluate the start-up phase of a DWB pilot plant and (2) to determine the extent to which it can contribute to pesticide compounds removal during this phase of operation.

MATERIALS AND METHODS

Denitrifying bioreactor and its operation

In October 2023, we installed a pilot plant DWB with a volume of 4.2 m^3 filled with poplar chips in an agricultural area near the city of Brno, Czech Republic. It is a circular reactor with two baffles (see details in ***Figure 1***). The baffles serve as service shafts for the inlet and outlet pipes and for servicing the dissolved oxygen (DO) on-line probes (FIEDLER AMS, s.r.o.). The reactor is also equipped with an ultrasonic level sensor. It was fed by a nearby stream whose only source of water was drainage and surface runoff from fields in its catchment area. The water flow through the DWB is directed from the bottom the top, therefore the baffle at the outlet is perforated at the top and the outlet pipe is behind the baffle.

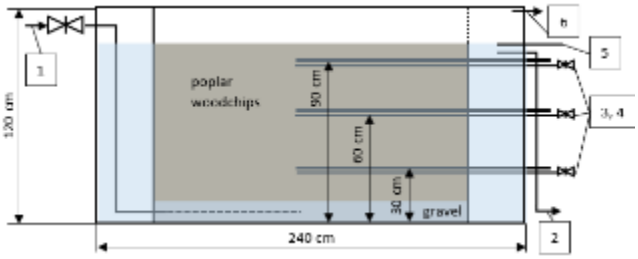

Funding: Technology Agency of the Czech Republic, project SS06020006 "Comprehensive Assessment of Soil Contamination by Pesticides and In-Situ Remediation Measures to Prevent Their Entry into Groundwater."

ISBN: 978-618-5765-04-0
ISSN 3057-4269

Figure 1: Schematic diagram of the DWB pilot plant; 1) Inlet, 2) Outlet, 3) Sampling point from different heights, 4) On-line ORP probes, 5) Sampling of outlet water, 6) Safety overflow.

The flow of water through the reactor was controlled manually using a valve, in front of which a regular water meter (BMETERS – GMDM-I, DN32) was placed. The flow of water was read once a week and the average flow (m^3/h) was calculated. Hydraulic Retention Time (HRT) was calculated as the ratio of the empty DWB volume to the water flow rate.

This article presents the results of the start-up phase from 18 October 2023 to 15 May 2024, interrupted by the winter period.

Chemical analyses

We inspected the facility once a week and sampled the DWB inlet and outlet for chemical analyses. The following analytical methods were used to determine the parameters of interest: pH – Hach HQ40d multi-parameter meter (Loveland, Colorado, USA); NO_3-N – UV absorption method with a Hach optical Nitratax plus sc Sensor (Loveland, Colorado, USA); the chemical oxygen demand (COD) – semi-micro method with potassium dichromate in acidic medium and photometric evaluation (445 nm); NH_4^+-N – photometric determination (425 nm) with Nessler agent. The analysis of pesticides was performed on a Waters system composed of Acquity UPLC I-Class System, equipped with an Acquity UPLC BEH C18 2.1 x 100 mm 1.7 µm column, and a XEVO TQ/TQ-XS mass spectrometer.

Microbiological analyses and calculations

Microbiological analyses were performed once a month to determine the total number of heterotrophic aerobic and anaerobic microorganisms and the amount of denitrifiers in both the liquid phase and the biofilm on the wood chip surface. Liquid samples were taken from the influent, the interior of the DWB at 3 different levels, and the effluent. In the case of wood chips, samples were collected from a special sampler at three different fill heights. In addition, the influent zone (aerobic) and the reduced oxygen zone (depending on the actual DWB conditions) were sampled.

Results and Discussion

Operating conditions

During the period studied, the temperature of the incoming stream water varied between 0.2 and 11.6 °C (***Figure 2***). The low temperature was favorable for reducing the release of high concentrations of organic matter from the DWB filling, which is a threat during the start-up phase [10]. COD at the DWB outlet was typically less than 50 mg/L. On one occasion, an increase in COD of 111 mg/L was detected after passing through the DWB, but the increase was typically around 20 mg/L. At the end of the study period, COD decreased after passing through the reactor to <20 mg/L.

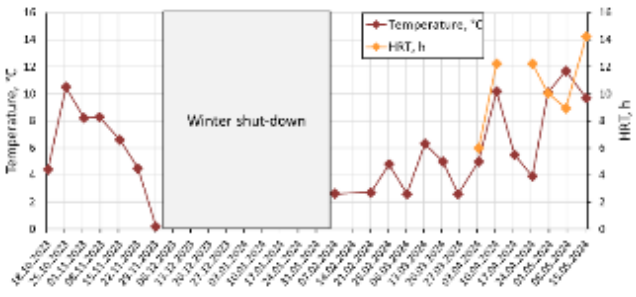

Figure 2: Operating conditions: temperature and hydraulic retention time

Water flow through the DWB depends on water flow in the stream from which the DWB inlet is taken and can be only partially controlled. Flow measurements began in the spring. Between April 3 and May 15, HRT varied from 6.0 to 14.2 hours with an average of 10.6 hours (***Figure 2***).

Dissolved oxygen concentrations in the stream increased to about 11 mg/L in the fall and remained at that level through the spring. They began to decline in mid-April and reached 7.5 mg/L by the end of the study period. DO concentrations at the DWB outlet increased in autumn as temperature decreased and biochemical processes, particularly oxidation of organic matter released from the DWB filling, were inhibited. In the spring period, they gradually decreased to almost zero values from the beginning of April, creating favorable conditions for denitrification [11].

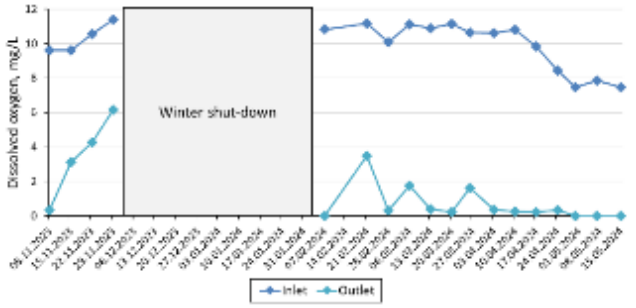

Figure 3: Operatin conditions: dissolved oxygen

Microbiological colonization of DWB filling

The results so far show that the majority of the microbial biomass is bound to the surface of the wood chips and that its colonization is 1 to 3 orders of magnitude higher than the amount of microorganisms in the liquid phase. Most of the denitrifying bacteria belong to the genera *Pseudomonas* and *Flavobacterium*.

Removal of nitrates

Input NO_3-N concentrations fluctuated during the study period, with higher values in the fall and early spring and decreasing values from early April on. Overall, NO_3-N concentrations were rather low with an average of 10.4 mg/L.

NO_3-N removal efficiency followed a similar pattern to temperature (***Figure 2***) and was strongly influenced by the DO concentration, with persistently favorable anoxic conditions being established only in the spring period (***Figure 3***). In the fall, after about one month of operation, an efficiency of more than 80% was achieved, but then it dropped to 10% with decreasing feed water temperature and increasing DO concentration. This is in line with expectations, as

ISBN: 978-618-5765-04-0
ISSN 3057-4269

heterotrophic denitrification is strongly affected by low temperatures [11] states that under natural conditions denitrification is inhibited at temperatures below 5 °C. Spring temperatures in 2024 showed considerable fluctuations. This was matched by fluctuations in NO_3-N removal efficiency, which gradually increased and reached its maximum value of 84% (***Figure 4***).

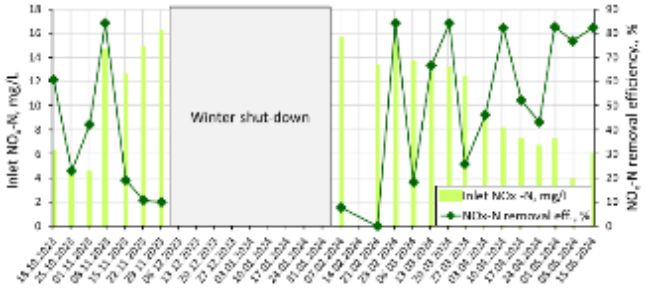

Figure 4: Removal efficiency of nitrate nitrogen

Removal of pesticides

We monitored around 360 pesticide substances, including both parent compounds and metabolites. The majority of them were found to be present in the feed water below the limit of quantification. ***Figure 5*** shows the top 10 pesticide compounds with the highest concentrations at reactor inlet: chlorotoluron and glyphosate (parent compounds) and 1,2,4-triazole, AMPA, dimethachlor ESA, metazachlor ESA, metolachlor ESA, NOA 413173, and OA, and pethoxamid ESA (metabolites). Total pesticide concentrations in influent water ranged from 0.7 to 3.1 µg/L, with metolachlor ESA (metabolite of metolachlor) being the most abundant pesticide compounds in most samples. All of these compounds are commonly used in the Czech Republic and are found in arable land and surface waters [12].

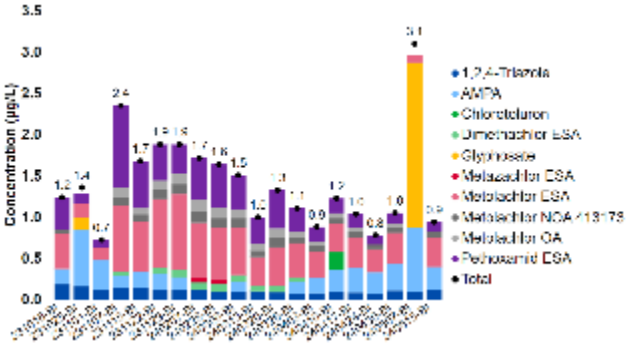

Figure 5: TOP 10 pesticides – DWB inlet

Figure 6 then shows how the concentrations of these compounds changed after passing through the DWB. Total pesticide concentrations decreased and ranged from 0.6 to 1.8 µg/L. However, the relative abundance of individual substances changed. It is evident that pesticides are removed with different efficiencies in the DWB. AMPA behaved differently from the other compounds detected, with concentrations increasing after passing through the DWB. AMPA is a metabolite of glyphosate, but glyphosate was mostly absent in the reactor influent. However, we found that glyphosate is used as a weed herbicide in poplar cultivation [13]. It is possible that AMPA accumulates in poplar wood and is released from wood chips in the DWB. This needs to be further investigated in future research.

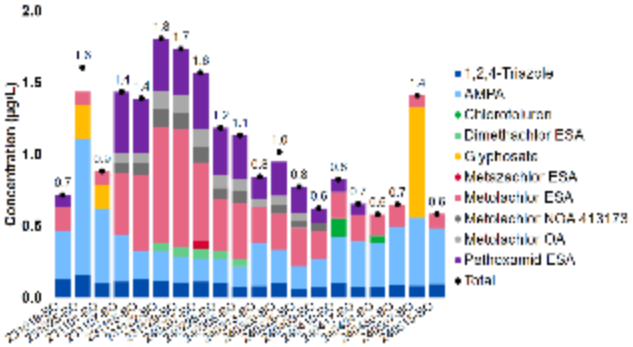

Figure 6: TOP 10 pesticides – DWB outlet

For this reason, we excluded AMPA from the pesticide removal efficiency evaluation. The trend of pesticide removal efficiency is shown in ***Figure 7***. It fluctuated during the fall period. In the spring period, it gradually increased from 18% in early February to 70% in mid-May. The main mechanism of pesticide removal, especially in the beginning, was probably adsorption. However, the retention of the substances in the reactor filling significantly prolongs their residence time in the DWB, creating favorable conditions for their following biochemical degradation. The mechanism of removal of pesticide substances in the DWB will be the subject of further research.

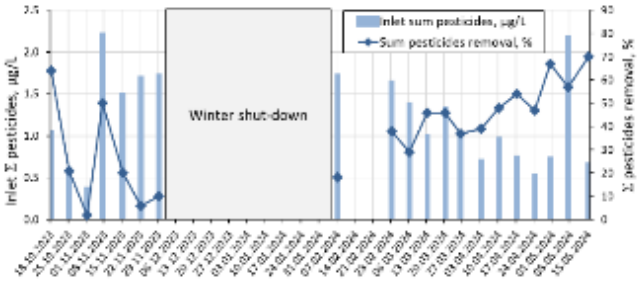

Figure 7: Σpesticides removal efficiency

CONCLUSION

Results from the pilot DWB indicate that concentrations of commonly occurring pesticide substances decrease as agricultural runoff passes through the DWB, even very soon after its start-up. The onset of this process follows a similar course to the onset of denitrification efficiency. The main mechanism, especially in the beginning, appears to be adsorption on the wood chips. This increases the residence time of the pesticide compounds in the DWB and creates the conditions for their further potential biochemical degradation.

REFERENCES

[1] L. A. Schipper, W. D. Robertson, A. J. Gold, D. B. Jaynes and S. C. Cameron, "Denitrifying bioreactors – an approach for reducing nitrate loads to receiving waters," *Ecological Engineering*, vol. 36, pp. 1532-1543, 2010.

[2] L. Christianson and L. Schipper, "Moving denitrifying bioreactors beyond proof of concept: Introduction to the special section," *Journal of Environmental Quality*, vol. 45, no. 3, pp. 757-761, 2016.

[3] S. Aslan, "Combined Removal of pesticides and nitrates in drinking waters using biodenitrification and sand filter system," *Process Biochemistry*, vol. 40, pp. 417-424, 2005.

[4] A. Cesar and M. Ros, "Long-term study of nitrate, nitrite and pesticide removal from groundwater: A two-stage biological process,"

ISBN: 978-618-5765-04-0
ISSN 3057-4269

International Biodeterioration and Biodegradation, vol. 82, pp. 117-123, 2013.

[5] B. Krause Camilo, A. Matzinger, N. Litz, L. P. Tedesco and G. Wessolek, "Concurrent nitrate and atrazine retention in bioreactors of straw and bark mulch at short hydraulic residence times," *Ecological Engineering*, vol. 55, pp. 101-113, 2013.

[6] O. Wrightwood, M. Hattaway, T. Young and H. Bischel, "Assessment of woodchip bioreactor characteristics and their influences on joint nitrate and pesticide removal," *ACS Environmental Science and Technology Water*, vol. 2, no. 1, pp. 106-116, 2022.

[7] M. Escolá Casas, M. Guivernau, M. Vinas, B. Fernández, R. Cáceres and e. al., "Use of wood and cork in biofilters for the simultaneous removal of nitrates and pesticides from groundwater," *Chemosphere*, vol. 313, p. 137502, 2023.

[8] R. Gothwal and T. Shashidhar, "Antibiotic Pollution in the Environment: A Review," *CLEAN Soil, Air, Water*, vol. 43, pp. 479-489, 2015.

[9] R. M. de Souza, D. Seibert, H. B. Quesada, F. de Jesus Basetti, M. R. Fagundes-Klen and R. Bergamasco, "Occurrence, impacts and general aspects of pesticides in surface water: A Review," Process Safety and Environmental Protection, vol. 135, pp. 22-37, 2020.

[10] M. Healy, T. Ibrahim, G. Lanigan, A. Serrenho and O. Fenton, "Nitrate removal rate, efficiency and pollution swapping potential of different organic carbon media in laboratory denitrification bioreactors," *Ecological Engineering*, vol. 40, pp. 198-209, 2012.

[11] M. Gerardi, Nitrification and Denitrification in the Activated Sludge Process, New York: Wiley, 2002.

[12] M. Hvězdová, P. Kosubová, M. Košíková, K. Scherr, Z. Šimek and et al., "Currently and recently used pesticides in Central European arable soils," *Science of the Total Environment*, Vols. 613-614, pp. 361-370, 2018.

[13] K. Ault, V. Viswanath, J. Jayawickrama, C. Ma, J. Eaton and et al., "Improved growth and weed control of glyphosate-tolerant poplars," *New Forests*, vol. 47, pp. 653-667, 2016.

ISBN: 978-618-5765-04-0
ISSN 3057-4269

Autotrophic Denitrification with Granulated Sulfur and Limestone During Intermittent Operation

Karel Hrich
Dept. of Chemistry, Faculty of Civil Engineering
Brno University of Technology
Brno, Czech Republic
Karel.Hrich@vut.cz; 0000-0002-4017-0739

Jitka Malá
Dept. of Chemistry, Faculty of Civil Engineering
Brno University of Technology
Brno, Czech Republic
Jitka.Mala@vut.cz; 0000-0002-1399-0694

***Abstract*— The sulfur-driven autotrophic denitrification (SDAD) process is based on the reduction of sulfur compounds, which act as electron donors for nitrate reduction. This process is therefore suitable for treatment of wastewater with a low C/N ratio. The SDAD process can be employed as a tertiary treatment of tailwater in small, domestic or wetland treatment plants. Granulated zero-valent sulfur is typically used to fill SDAD columns due to its good availability and low cost. During the SDAD, hydrogen ions are released, which causes a decrease in pH and thus a reduction in the functionality of denitrifiers. The addition of limestone as a buffer solves this problem. Limestone also serves as a carrier and carbon source for the microorganisms. Due to the often-uneven inflow of water to small treatment plants, this study focused on the impact of intermittent operation on denitrification. Laboratory experiments were conducted using columns fed with nitrate-enriched river water. Two of the most commonly used filling ratios (S:$CaCO_3$ = 1:2 and 1:4) were tested in two different modes. Firstly, the NO_3-N load was increased at a stable daily dosing time of 12 hours (mode 1). Secondly, the NO_3-N load was fixed and the dosing time was gradually shortened (mode 2). In addition, one column (1:2) was operated without interruption as a control (mode C). The temperature, pH, nitrate-nitrogen (NO_3-N), nitrite-nitrogen (NO_2-N) and bicarbonate (HCO_3^-) concentrations were measured. If a hydrogen sulfide odor was identified in the effluent, the sulfides were also analyzed. The specific daily nitrate-nitrogen load (B_N – inlet mass flow of NO_3-N related to mass of S^0 (mg/(g·d)) and the daily denitrification rate (r_D – kg/(m³·d) – mass of denitrified NO_3-N related to filling volume) were calculated. The best results were achieved when the columns were operated in mode 1, with r_D achieving 0.25 kg/(m³·d) – mode 1-1:2 and 0.16 kg/(m³·d) – mode 1-1:4, respectively, when B_N was 0.61 mg/(g·d). The nitrate removal efficacy was >90% in both cases. At the same B_N, a similar denitrification rate of 0.28 kg/(m³·d) was achieved in mode C. In mode 2, the gradual shortening of the dosing time resulted in a reduction in the denitrification rate to 0.22 kg/(m³·d) for mode 2-1:2 and 0.15 kg/(m³·d) for mode 2-1:4. This was accompanied by a decline in nitrate removal efficacy to approximately 70%. Furthermore, intermittent operation also resulted in the formation of sulfides in column 1:2, which must be avoided. The SDAD is an applicable method for small treatment plants with highly fluctuating flow, if the formation of sulfides can be limited by maintaining a concentration of NO_3-N in the treated water at approximately 5 mg/L.**

Keywords*— denitrification, sustainable wastewater treatment, granulated sulfur

INTRODUCTION

The removal of nitrates and nitrites is one of the main processes in wastewater treatment. Nitrate pollution leads to eutrophication and ecological disturbance of groundwater and surface water. In addition, higher levels of NO_3^- and NO_2^- can lead to human health disorders and diseases such as methemoglobinemia, non-Hodgkin's lymphoma (blood cancer), and gastrointestinal cancer [1].

Commonly used processes aimed at removing nitrates and nitrites from water are heterotrophic denitrification, or denitritation based on the activity of heterotrophic bacteria in an anoxic environment in the presence of organic substances that act as a carbon source and electron donor [2] [3]. In the last decade, autotrophic processes such as sulfur-driven autotrophic denitrification (SDAD) have received extensive attention. The SDAD process does not require organic substances because the reduced sulfur compounds (zero-valent sulfur, sulfide, and thiosulfate) serve as electron donors for nitrate reduction. Zero-valent sulfur (S^0) is the most widely used compound in SDAD columns due to its good availability and low cost. The use of an inorganic electron donor makes the method suitable for treating wastewater that is poor in organic matter and reduces the risk associated with the presence of organic residues in treated water. The slow growth rate of autotrophic bacteria leads to lower sludge production, which substantially reduces plant operating costs. Another advantage of autotrophic denitrification is that it usually produces less N_2O [4] [3] [5] [6]. During the SDAD process, H^+ ions are released, as seen from equation (1). The decrease in pH impairs the function of microorganisms. Thus, maintaining the pH near a neutral value (7-8) is crucial for optimal denitrification efficiency [7]. At a pH lower than 5.5, denitrification is severely inhibited [8].

$$1.06\ NO_3^- + 1.11\ S^0 + 0.3\ CO_2 + 0.785\ H_2O \rightarrow 0.06\ C_5H_7O_2N + 0.5\ N_2 + 1.11\ SO_4^{2-} + 1.16\ H^+ \quad (1)$$

$$CaCO_3 + H^+ \rightarrow Ca^{2+} + HCO_3^- \quad (2)$$

Limestone has been found to be a suitable “solid buffer” (see equation (2)), as it also provides inorganic carbon for the growth of microorganisms [8] [9]. Its solubility is very limited, being inversely proportional to pH, and approaches zero at a pH of approximately 7.1. Previous studies determined that the optimal mass ratio of S^0 to limestone ($CaCO_3$) was 1:1, which led to a nitrogen removal rate of 500 g N/(m³·d) [8] [10].

The oxidation of S^0 generates sulfates (SO_4^{2-}) [10]. Their presence in denitrified water does not represent a threat to the environment, but they can be reduced to hydrogen sulfide in

This work was supported by a Ministry of Industry and Trade Applied Research program [MPO 321282/21/61200/417, QK21010159].

ISBN: 978-618-5765-04-0

the presence of sulfate-reducing bacteria (SRB). However, the production of sulfides requires relatively high concentrations of organic matter expressed as chemical oxygen demand (COD; minimum COD/SO_4^{2-} ratio of 0.67) [11]. These conditions are unlikely to occur in SDAD effluent following secondary treatment [12].

Despite the progress of autotrophic denitrification techniques in recent years, driven by their cost-effectiveness and practical feasibility, there are still bottlenecks hindering their widespread use [13].

Many research campaigns have been carried out using methods such as batch tests [14] [15] [1], laboratory column tests [16] [17] [10], and semi- or fully operated tests [10] [9] [18]. Except for the batch tests, all of the above experiments concerned continuous operation, and none have yet dealt with intermittent operation.

The main goal of this paper was to discover how intermittent operation affected S^0-driven autotrophic denitrification. The reason was the potential use of this process as a tertiary wastewater treatment method in small, domestic and possibly wetland treatment plants, where there is a low C/N ratio. The operating conditions of the columns, such as pH, temperature, HRT, nitrogen removal efficacy (NRE), specific nitrate-nitrogen load (B_N), denitrification rate (r_D), and pumping interruption, were investigated.

MATERIALS AND METHODS

The experiments ran in 2021 from January to October under laboratory conditions in columns that differed in packing (S:$CaCO_3$ mass ratio) and mode of operation (for more details, see ***Table 1***). To achieve a low C/N ratio, river water from a local stream (sampling point on the Svratka River – GPS: 49°12'33.7"N 16°33'28.4"E) was enriched with KNO_3 (PENTA, Czech Republic, purity 99%) to a resulting concentration of NO_3-N of approximately 50 mg/L and with KH_2PO_4 (PENTA, Czech Republic, purity 99%) to a resulting concentration of PO_4-P of approximately 1 mg/L. Cylindrical PVC columns with a diameter of 100 mm and a height of 330 mm (at the beginning of continuous operation) and a diameter of 50 mm and a height of 500 mm (at the end of continuous operation and through the whole period of intermittent operation) were used. The reduction in column dimensions mainly occurred because the river water consumption was too high at short HRTs, and the frequency of water delivery was unrealizable. The columns were packed with a mixture of granulated sulfur (OQEMA, Czech Republic, purity >99%) with a grain size of >4.75 mm and natural crushed limestone (AQUA EXCELENT, Czech Republic) with a grain size of 2-4 mm in ratios of 1:2 and 1:4. A 25 mm-high foam filter was placed under and above the packing. The flow through the columns was vertical. First, it was from top to bottom (continuous operation), while later, it was changed to bottom to top (intermittent operation). The water was dosed by PCD 1031 peristaltic pumps (KOUŘIL, Czech Republic).

Table 1: Operational conditions in modes

	Mode C		**Mode 1**		**Mode 2**	
S:CaCO₃	***1:2***		***1:2***	***1:4***	***1:2***	***1:4***
Sulfur, g	500	172	140	80	140	80
Limestone, g	1000	342	280	320	280	320
Volume, ml	1072	368	325	280	325	280
Porosity, %	40.0	40.0	42.5	38.6	42.5	38.6

	Mode C		**Mode 1**		**Mode 2**	
S:CaCO₃	***1:2***		***1:2***	***1:4***	***1:2***	***1:4***
Flow area, cm^2	78.5	78.5	19.6	19.6	19.6	19.6
Inlet pH	7.39-7.98	7.59-9.06	7.48-7.98	7.57-8.03	7.45-8.10	7.58-8.09
Outlet T, °C	13.8-18.6	21.6-22.8	19.1-21.0	19.8-21.1	17.3-20.3	17.3-20.1
Outlet $c(SO_4^{2-})$, mg/L	201-439	343-406	373-461	312-402	479	323

Start-up of the columns lasted 7 weeks. The experiments began when the outlet NO_x-N concentration fell below 1 mg/L.

One column (namely, the column with packing S:$CaCO_3$ = 1:2; diameter 100 mm and height 330 mm) was operated continuously. The specific nitrate-nitrogen load B_N (mg/(g·d) or mg/(g·h); inlet mass flow of NO_3-N related to mass of S^0) was gradually increased up to 0.85 mg/(g·d). After reaching this B_N, a part of the original packing was transferred to a smaller column (diameter 50 mm and height 500 mm), and continuous operation was maintained by raising the B_N to 0.98 mg/(g·d). Because the concentration of NO_3-N in the inlet water was constant, the increase in B_N was accompanied by a decrease in HRT from 8.6 h to 2.6 h. This column is further referred to as mode C.

Two columns were operated in intermittent mode. First, the increase in the NO_3-N load during intermittent operation with a 12 h daily dosing time was tested in such a way that the B_N of the columns started at 0.3 mg/(g·d) (column 1:2) and 0.6 mg/(g·d) (column 1:4) and was gradually raised to 0.8 mg/(g·d) (column 1:2) and 1.3 mg/(g·d) (column 1:4). Similarly, as in the case of continuous operation, the HRT decreased with increasing B_N from 4.0 h to 1.7 h (column 1:2) and from 3.3 h to 1.7 h (column 1:4). The intermittent operation modes of both columns slightly differed: column 1:2 - 4 h ON - 6 h OFF - 8 h ON - 6 h OFF and column 1:4 - 6 h ON - 6 h OFF - 6 h ON - 6 h OFF. These modes are further referred to as mode 1-1:2 and mode 1-1:4.

Second, intermittent operation with gradual shortening of dosing time at the same B_N was tested with the same columns (1:2 and 1:4) that were operated at a fixed daily load of approximately 0.7 mg/(g·d). The dosing time was gradually shortened, with 2 equally long dosing periods per day (10 h + 10 h, 9 h+ 9 h, 8 h + 8 h, 7 h + 7 h, 6 h + 6 h). The HRT gradually decreased from 3.4 h to 1.9 h (column 1:2) and from 6.0 h to 3.0 h (column 1:4). These modes are further referred to as mode 2-1:2 and mode 2-1:4.

The experiments were performed at temperatures ranging from 13.8 to 22.8 °C. Inlet and outlet water samples were always taken on Mondays, Wednesdays and Fridays. The pH, NO_x-N (which, due to the absence of NO_2-N, corresponded to the concentration of NO_3-N) and PO_4-P were measured in the inlet water. Temperature, pH, NO_x-N, NO_2-N and HCO_3^-, and sometimes also sulfates, were measured in the outlet water. If a hydrogen sulfide odor was identified in the effluent, the sulfides were also analyzed. The water flow was verified and/or readjusted.

Temperature and pH were measured via a HACH HQ440d multimeter (Loveland, USA). The concentration of HCO_3^- was measured by potentiometric titration as the acid neutralizing capacity ($ANC_{4,5}$) [19] using the same device. NO_x-N was measured by the UV absorption method [20] with a Hach optical Nitratax plus sc Sensor (Loveland, Colorado,

ISBN: 978-618-5765-04-0
ISSN 3057-4269

USA). A HACH DR3900 VIS spectrophotometer (Hach-Lange, Germany) was used for analyses of 1) PO_4–P as a molybdophosphate complex [19]; 2) NO_2-N with the Griess reagent method [21]; 3) S_2^- using the Hach Methylene Blue Method 8131; and 4) COD (ISO 8192:2007). The gravimetric method with barium chloride was used for the determination of SO_4^{2-} concentration [19]. NO_3-N was calculated as the difference between NO_x-N and NO_2-N.

The daily denitrification rate r_D (kg/(m^3·d)) was calculated as follows:

$$r_D = \frac{\Delta c(NO_3 - N) \times Q}{V_{fill} \times 1000} \quad (3)$$

where Δc(NO_3-N) is the difference between the NO_3-N concentrations in the inlet and outlet water (mg/L), Q is the flow rate through the column (ml/d), and V_{fill} is the packing volume (ml). From equation (3), the hourly r_D (kg/(m^3·h)) was related to dosing time.

Results and Discussion

Increasing of nitate nitrogen load at dosing 12 hours per day

In the column in continuous mode (mode C), r_D increased with daily B_N. It achieved its maximum of 0.37 kg/(m^3·d) at B_N = 0.82 mg/(g·d) and HRT = 3.1 h. Similar results have been reported previously [22] – r_D = 0.38 kg/(m^3·d) at an HRT of 2.8 h and [16] – r_D = 0.36 kg/(m^3·d) at an HRT of 2-3 h. Up to this load, the column was operated with NRE >90%. With a further increase in B_N and a decrease in HRT, the process started to collapse, and the r_D and NRE dropped (Figure 1). The pH in the column was between 7.2 and 7.7 throughout the operation. This is near the neutral value, which was reported as the optimum for sulfur denitrification [23] [7]. However, reducing the HRT led to the lowering of the concentration of HCO_3^- in the system (Figure 2) below 3.0 mmol/L, which is the level considered necessary for the successful course of the process [23]. The process started to collapse at an HRT of 3.1 h and an HCO_3^- concentration of 2.3 mmol/L. Another effect of the decrease in HRT was a shortening in the time available for the dissolution of sulfur, the solubility of which is limited [3].

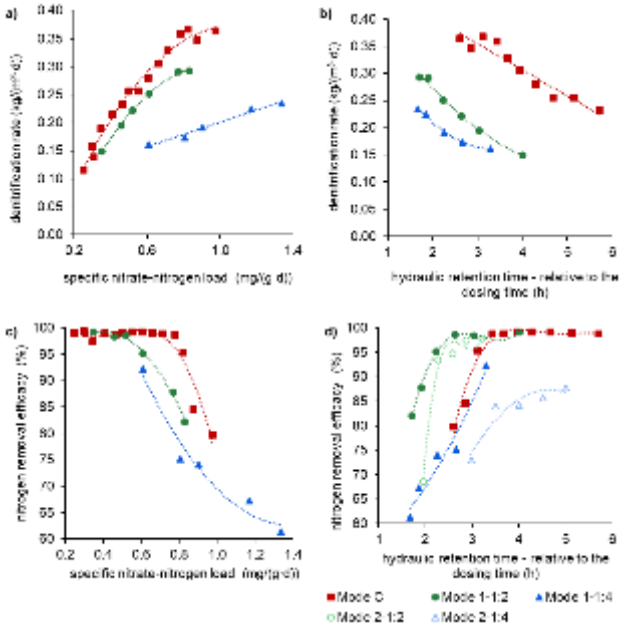

Figure 1: Relationship between: a) denitrification rate and specific nitrate-nitrogen load; b) denitrification rate and hydraulic retention time; c) nitrogen removal efficacy and specific nitrate-nitrogen load; d) nitrogen removal efficacy and hydraulic retention time

The behavior of the columns in mode 1 was similar, but they achieved lower daily r_D. Both achieved NRE >90% at a maximum daily B_N of 0.61 mg/(g·d). In mode 1-1:2, it was at HRT = 2.2 h and r_D = 0.25 kg/(m^3·d), in mode 1-1:4 at HRT = 3.3 h and r_D = 0.16 kg/(m^3·d) (Figure 1). With the subsequent increase in B_N and decrease in HRT, r_D grew to 0.29 kg/(m^3·d) (mode 1-1:2) and 0.23 kg/(m^3·d) (mode 1-1:4), but NRE dropped. The lower daily r_D was caused by dosing interruptions and thus shorter daily reaction time, and in the case of mode 1-1:4 also by a lower content of sulfur in the bed. The columns in mode 1 showed a similar decrease in HCO_3^- concentration with the decrease in HRT as in mode C, but the HCO_3^- concentrations achieved at the same HRTs were higher (Figure 2).

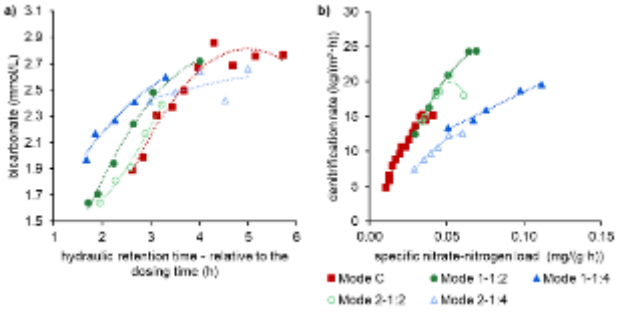

Figure 2: Relationship between: a) hydrogencarbonate and hydraulic retention time ; b) denitrification rate and specific nitrate-nitrogen load

The comparison of hourly B_N and r_D provided a different picture. The hourly r_Ds achieved during intermittent operation were much higher than those during continuous dosing (Figure 2). Between B_N 0.4 and 0.8 mg/(g·d), the difference was 69-71%. This could have been caused by the presence of better conditions for denitrification in the intermittent mode. The stagnation of water in the columns during dosing interruptions acted to prolong HRTs. Longer HRTs enable the dissolution of more sulfur, allowing a higher pH to be reached, thus resulting in the dissolution of limestone and the achievement of higher concentrations of HCO_3^- [8]. Mode 1-1:4 was operated at favorable pH values between 7.3 and 8.1, with pH increasing with increasing HRT. Mode 1-1:2 showed the same dependence of pH on HRT, but due to the lower content of limestone in the bed, the pH dropped below 7 at an HRT of 1.91 h (Figure 3). This value is considered to inhibit the process of sulfur denitrification [23]. Higher HCO_3^- concentrations at the same HRTs were reached in the intermittent mode than in the continuous mode, and the difference was greater at lower HRTs (Figure 2).

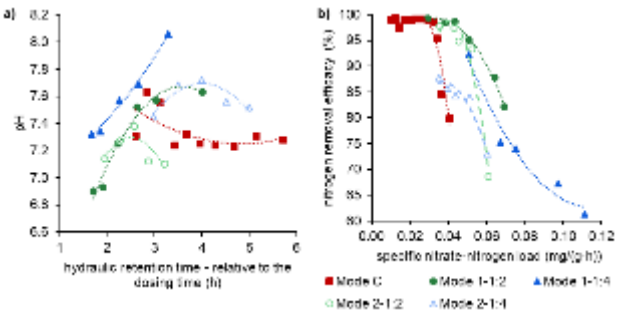

ISBN: 978-618-5765-04-0
ISSN 3057-4269

Figure 3: Relationship between: a) pH and hydraulic retention time; b) nitrogen removal efficacy and specific nitrate-nitrogen load

A particular problem that appeared during mode 1-1:2 was the production of sulfides. This manifested in the emanation of an odor of hydrogen sulfide from the effluent after the interruption of dosing. The sulfide concentration in the effluent gradually increased with increasing load. The experiment was terminated when the first portion of the column effluent intensively smelled hydrogen sulfide after the resumption of dosing, and the sulfide concentration reached 9.86 mg/L. This occurred at a B_N of 0.83 mg/(g·d) and an HRT of 1.71 h. The column was overloaded; its NRE decreased to 82 %, and therefore, 9.1 mg/L NO_3-N appeared in the effluent. The production of sulfides at such a high concentration of NO_3-N is not common. An NO_3-N concentration above 3 mg/L is considered the limit above which sulfide formation is inhibited [24]. Mode 1-1:4 showed different behaviors. No odor was detected during its operation, and the sulfide concentration ranged from 0 to 22 µg/L.

Gradual shortening of dosing time at the same daily specific nitrate-nitrogen load

The inclusion in the tests of the gradual shortening of dosing time while maintaining the same daily B_N had several effects on the operation of the columns. The HRT related to dosing time decreased (see Materials and Methods), and the hourly B_N increased (from 0.036 to 0.061 mg/(g·h) – mode 2-1:2 and from 0.035 to 0.060 mg/(g·h) – mode 2-1:4). This worsened the conditions for denitrification, which resulted in a decrease in NRE (mode 2-1:2 – from 97.8 to 68.6%; mode 2-1:4 – from 87.8 to 73.0%; see Figure 3.

HRT and dosing time go hand in hand. To shorten the dosage period while maintaining the same daily B_N, it was necessary to shorten the HRT. The shortening in HRT caused the calcium-carbonate balance to not be achieved, and therefore, the outlet HCO_3^- concentration decreased (Figure 2). The low solubility of calcium carbonate, which depends on pH and the presence of dissolved CO_2, played a large role [8] [25]. In our experiments, carbon dioxide was partly consumed during denitrification, as shown in equation (1). The decrease in HCO_3^- concentration caused further deterioration of the denitrification conditions [8] [24], e.g., in mode 2-1:2. The HCO_3^- concentration was 2.39 mmol/L at 97.8% NRE, while at 68.6% NRE, it was 1.64 mmol/L HCO_3^-.

The outlet pH in both columns rose slightly with increasing HRT, but after reaching HRT 2.6 h (mode 2-1:2) and 4.0 h (mode 2-1:4), the pH dropped to its original level (7.1 and 7.5, respectively), which was a similar behavior to that of the mode 1-1:2. Mode 2-1:4 achieved a higher pH (max 7.7) than mode 2-1:2, where the highest pH was 7.4. All operational modes, except for mode 2-1:2, achieved a higher pH than in mode C. The lower pH in the mode 2-1:2 was caused by the lower content of limestone in the bed and by the shorter HRT (Figure 3).

In both modes 2 the inlet pH ranged from 7.6 to 8.1 and from 7.5 to 8.1, respectively, which is close to optimum (pH approximately 7.5) for the SRB activity that is responsible for the formation of sulfides [26] [27]. As is written in the literature, the presence of a minimum SO_4^{2-} concentration (270 mg/L) was also one of the fundamental pillars for the formation of sulfides [12], so the SO_4^{2-} concentration in our water, as shown in ***Table 1***, is sufficient. Finally, an important condition for the formation of sulfides by SRB is the presence of organic matter. Ref. [12] and [28] determined that the minimum necessary COD is 100 mg/L. Ref. [29] also observed the formation of sulfides and sulfate reduction in a UASB reactor by treating domestic water with a COD of approximately 235 mg/L and a low COD/SO_4^{2-} ratio (from 1.1 to 1.85). In our case, the inlet river water contained COD amounting to approximately 23 mg/L, as well as a low COD/SO_4^{2-} ratio (approximately 0.5), yet this concentration was enough for the formation of sulfides. The concentrations of sulfides measured in outlet water (mainly mode 2-1:2) were compared with theoretical values calculated according to equation (4) from [30]. It was derived for the formation of sulfides in sewage and does not consider intermittent operation.

$$\Delta S = 0.0265 \times COD^{0.5} \times 1.07^{(T-20)} \times \left(t_h \times \frac{A}{V}\right) \times 10 \quad (4)$$

where ΔS is the increase in S^{2-} (µg/L), COD is the chemical oxygen demand (mg/L), T is the temperature (°C), A is the inside area of the column (m^2), V is the total column volume (m^3) and t_h is the HRT (h).

The columns with different packings behaved quite differently. Mode 2-1:2 showed a relatively low NO_3-N outlet concentration (approximately 4 mg/L) until a dosing time of 14 h/d and then gradually increased to 16.1 mg/L NO_3-N. In contrast, the NO_3-N outlet concentration of mode 2-1:4 sharply rose above 8 mg/L after the dosing time was shortened from 20 h/d to 18 h/d. The concentration then stayed at approximately 8 mg/L until the dosing time reached 12 h/d, whereupon the NO_3-N outlet concentration increased again up to 13.8 mg/L (Figure 4). The nitrites in the outlet did not exceed 1 mg/L in mode 2-1:2 until the end (12 h/d dosing time), when the NO_2-N concentration reached 1.67 mg/L. That was in contrast with mode 2-1:4, where during a dosing time of 18 h/d and under load B_N = 0.04 mg/(g·h), the NO_2-N rose to 1.22 mg/L, which signaled that the SRB could not achieve complete NO_3-N reduction due to the sudden increase in B_N [31].

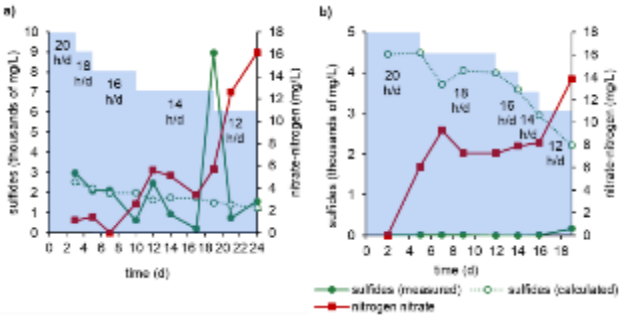

Figure 4: Relationship between sulfide and nitrate nitrogen outlet concentrations and different dosing times. a) mode 2-1:2, b) mode 2-1:4 (the height of the columns represents dosing time in hours per day).

Mode 2-1:2 worked with a higher NO_3-N removal efficiency at the same B_N = 0.7 mg/(g·d) than mode 2-1:4, but there was a problem with the sulfides in the effluent, which always appeared after the interruption and subsequent resumption of dosing. At the beginning of the experiment, the sulfide concentration decreased from 2980 µg/L (dosing time 20 h/d) to 618 µg/L (dosing time 16 h/d). This could have been caused by slow regeneration of the column between periods of operation (12-h intermittent). Only twice did the sulfide concentration rise sharply, first up to 2480 µg/L and

ISBN: 978-618-5765-04-0
ISSN 3057-4269

then up to 8960 μg/L (both at a dosing time of 14 h/d). The real concentrations of sulfides were mostly similar to or lower than the calculated ones. At the end of the experiment, at a dosing time of 12 h/d, B_N = 0.06 mg/(g·h), and HRT = 1.9 h, sulfides in the effluent had stabilized at 1560 μg/L. At that point, the experiment was terminated because the concentrations of NO_3-N and NO_2-N had increased (16.1 mg/L and 1.67 mg/L, respectively). In mode 2-1:4 The sulfide concentration did not exceed 22 μg/L almost throughout the duration of the test. At the end, at a 12 h/d dosing time, sulfides in the outlet had risen up to 168 μg/l, and at the same time, the concentrations of NO_3-N and NO_2-N had also increased (13.8 mg/L and 2.56 mg/L). The formation of sulfides was probably low because the outlet NO_3-N concentration did not drop below 5 mg/L. This is in line with the findings of [30], who determined that the reduction of sulfates to sulfides does not take place if more thermodynamically favored electron acceptors, such as nitrates, are present in the water. Similar findings were obtained by [24], who observed significant sulfide formation at NO_3-N concentrations below 3 mg/L. It is more advantageous to leave the operational setting on the same intermittent time (e.g., 12 h/d) and gradually increase the B_N than to gradually shorten the dosing time while maintaining the same B_N (e.g., 0.7 mg/(g·d)).

CONCLUSIONS

Autotrophic denitrification columns were able to achieve higher hourly B_N and r_D under intermittent dosing (mode1) of raw water than under continuous operation (mode C). In this sense, mode 1-1:2 showed better results than mode 1-1:4; however, the production of sulfides, demonstrated by the odor of hydrogen sulfide, was observed with this mode. The occurrence of toxic sulfides could be a serious problem, so the operating conditions that foster it (particularly column packing composition and length of pumping breaks) need to be studied further.

REFERENCES

[1] H. Barnes and A. R. Folkard, "The determination of nitrites," *Analyst*, vol. 76, pp. 599-603, 1951.

[2] H. Furumai, H. Tagui and K. Fujita, "Effects of pH and alkalinity on sulfur-denitrification in a biological granular filter," *Water Science and Technology*, vol. 34, pp. 355-362, 1996.

[3] C. T. Driscoll and J. S. Bisogni, "The Use of Sulfur and Sulfide in Packed Bed Reactors for Autotrophic Denitrification," *Journal of the Water Pollution Control Federation*, vol. 50, pp. 569-577, 1978.

[4] W. Fresenius, . K. E. Quentin and W. Schneider, Water Analysis, vol. 22, Berlin: Springer Verlag, 1988, pp. 2033-2062.

[5] Y.-X. Cui and et al., "Biological nitrogen removal from wastewater using sulphur-driven autotrophic denitrification," *Applied Microbiology and Biotechnology*, vol. 103, pp. 6023-6039, 2019.

[6] F. Chen, X. Li, C. Gu, Y. Huang and Y. Yuan, "Selectivity control of nitrite and nitrate with the reaction of S0 and achieved nitrite accumulation in the sulfur autotrophic denitrification process," *Bioresource Technology*, vol. 266, pp. 211-219, 2018.

[7] M. H. Gerardi, Nitrification and Denitrification in the Activated Sludge Process, New Jersey: John Wiley & Sons, Inc., 2002.

[8] L. Ghorbel, L. Coudert, Y. Gilbert, G. Mercier and J. F. Blais, "Sulfide Generation and Clogging during Infiltration of Denitrified Domestic Wastewater through Two Artificially Created Soils," *Journal of Environmental Engineering*, vol. 143, no. 12, 2017.

[9] H. Greben, L. Baloyi and S. N. Venter, "Grass cellulose as cost-effective energy source for biological sulphate removal," *Water SA*, vol. 30, no. 5, pp. 729-734, 2007.

[10] A. Harlina, M. Omar and A. K. Norli, "Empirical prediction on sulphide generation in Malaysian sewage," in *International Conference on Environment Science and Engineering*, Singapore, 2011.

[11] P. Harris, "Trace Nox Measurements by UV Spectroscopy: Recent Advances," in *Proceedings of the Annual ISA Analysis Division Symposium*, USA, 2003.

[12] K. Hasegawa, K. Shimizu and K. Hanaki, "Nitrate removal with low N2O emission by application of sulfur denitrification in actual agricultural field," *Water Science & Technology*, vol. 50, no. 8, pp. 145-151, 2004.

[13] N. H. Huan, N. X. Hai and N. N. Yem, "Factors effect to the sulfide generation rate in the To Lich River, Vietnam," *ARPN journal of engineering and applied sciences*, vol. 8, no. 3, pp. 190-199, 2013.

[14] A. Koenig and L. H. Liu, "Use of limestone for pH control in autotrophic denitrification: continuous flow experiments in pilot-scale packed bed reactors," *Journal of Biotechnology*, vol. 99, no. 2, pp. 161-171, 2002.

[15] A. Kostrysia and et al., "Elemental sulfur-based autotrophic denitrification and denitritation: microbially catalyzed sulfur hydrolysis and nitrogen conversions," *Journal of Environmental Management*, vol. 211, pp. 313-322, 2018.

[16] L. Kuai and W. Verstraete, "Autotrophic Denitrification with Elemental Sulphur in Small-Scale Wastewater Treatment Facilities," *Environmental Technology*, vol. 20, no. 2, pp. 201-209, 1999.

[17] Z. Liu, A. M. Maszenam, Y. Liu and W. J. Ng, "A brief review on possible approaches towards controlling sulfate-reducing bacteria (SRB) in wastewater treatment systems," *Desalination and Water Treatment*, vol. 53, no. 10, pp. 2799-2807, 2014.

[18] Y. Li, Y. Wang, D. Wan, B. Li, P. Zhang and H. Wang, "Pilot-scale application of sulfur-limestone autotrophic denitrification biofilter for municipal tailwater treatment: Performance and microbial community structure," *Bioresource Technology*, vol. 300, 2020.

[19] J. Malá, K. Hrich, K. Schrimpelová and Z. Bílková, "Production of sulphides in denitrifying woodchip bioreactors," *Environmental Science and Pollution Research*, vol. 27, pp. 40769-40776, 2020.

[20] H. S. Moon, K.-H. Anh, S. Lee, K. Nam and J. Y. Kim, "Use of autotrophic sulfur-oxidizers to remove nitrate from bank filtrate in a permeable reactive barrier system," *Environmental Pollution*, vol. 129, no. 3, pp. 499-507, 2004.

[21] S. E. Oh, Y. B. Yoo, J. C. Young and I. S. Kim, "Effect of organics on sulfur-utilizing autotrophic denitrification under mixotrophic conditions," *Journal of Biotechnology*, vol. 92, no. 1, pp. 1-8, 2001.

[22] J. Y. Park and Y. J. Yoo, "Biological nitrate removal in industrial wastewater treatment: which electron donor we can choose," *Applied Microbiology and Biotechnology*, vol. 82, pp. 415-429, 2009.

[23] E. Sahinkaya, A. Kilic and B. Duygulu, "Pilot and full scale applications of sulfur-based autotrophic denitrification process for nitrate removal from activated sludge process effluent," *Water Research*, vol. 60, pp. 210-2017, 2014.

[24] R. Sierra-Alvarez, R. Beristain-Cardoso, M. Salazar, J. Gómez, E. Razo-Flores and J. A. Field, "Chemolithotrophic denitrification with elemental sulfur for groundwater treatment," *Water Research*, vol. 41, no. 6, pp. 1253-1262, 2007.

[25] E. L. Subtil, S. T. Cassini and R. F. Goncalve, "Sulfate and dissolved sulfide variation under low COD/Sulfate ratio in Up-flow Anaerobic Sludge Blanket (UASB) treating domestic wastewater," *An Interdisciplinary Journal of Applied Science*, vol. 7, no. 1, pp. 130-139, 2012.

[26] J. J. Wang, B. C. Huang, J. Li and R. C. Jin, "Advances and challenges of sulfur-driven autotrophic denitrification (SDAD) for nitrogen removal," *Chinese Chemical Letters*, vol. 31, no. 10, pp. 2567-2574, 2020.

[27] E. Yeh, *Raw Sludge as Substrate for Sulphate Reducing Bacteria*, Toronto: University of Toronto, 2000.

[28] L. Zhang, Y. Y. Qiu, Y. Zhou, G. H. Chen, M. C. van Loosdrecht and F. Jiang, "Elemental sulfur as electron donor and/or acceptor: Mechanisms, applications and perspectives for biological water and wastewater treatment," *Water Research*, vol. 202, 2021.

[29] Q. Zhang, X. Xu, X. Zhou and C. Chen, "Recent Advances in Autotrophic Biological Nitrogen Removal for Low Carbon Wastewater: A Review," *Water* , vol. 14, no. 7, 2022.

[30] J. Zhou, Q. He, C. L. Hemme, A. Mukhopadhyay, K. Hillesland and A. Zhou, "How sulphate-reducing microorganisms cope with stress:

ISBN: 978-618-5765-04-0
ISSN 3057-4269

lessons from systems biology," *Nature Reviews Microbiology*, vol. 9, pp. 452-466, 2011.

[31] T. Zhu, H. Cheng, L. Yang, S. Su, H. Wang and S. Wang, "Coupled Sulfur and Iron(II) Carbonate-Driven Autotrophic Denitrification for Significantly Enhanced Nitrate Removal," *Environmental Science & Technology*, vol. 53, no. 3, pp. 1545-1554, 2018.

ISBN: 978-618-5765-04-0
ISSN 3057-4269

Preventive Fault Finding for Bus Air Compressor Units using Infrared Thermography

Alkiviadis Tromaras
Hellenic Institute of Transport
Centre for Research and Technology Hellas
Thessaloniki, Greece
atromaras@certh.gr, ORCID: 0000-0002-1887-7949

Vassilios Kappatos
Hellenic Institute of Transport
Centre for Research and Technology Hellas
Thessaloniki, Greece
vkappatos@certh.gr , ORCID: 0000-0002-5314-2622

Evangelos Spyrou
Hellenic Institute of Transport
Centre for Research and Technology Hellas
Thessaloniki, Greece
espyrou@certh.gr , ORCID: 0000-0002-2941-5301

Maria Kilikidou
Hellenic Institute of Transport
Centre for Research and Technology Hellas
Thessaloniki, Greece
mkilikidou@certh.gr, ORCID: 0000-0003-1821-3883

***Abstract*— The following paper presents the application of Non-destructive Testing methods such as thermography for fault finding in internal components of buses and specifically the air compressor unit. Such units consist of a small internal combustion engine that provides air to the vehicle's breaks, suspension and passenger door operations. Hoses transferring compressed air from the compressor to the rest of the system can get clogged, leading the air compressor to potential failure and even fire of the unit. Thermal imaging was applied in a number of Mercedes Citaro LE and Volvo B9 buses provided by a bus fleet operator, to evaluate whether such clogging can be detected at an early stage, during routine maintenance of the bus. A number of acquisitions, using a thermal camera were taken, with the air compressor under different loads and under heating or cooling phase of the unit. The paper presents that thermography can be used to detect such failures either by observing specific hoses of the unit as well as the overall thermal behaviour of the air compressor.**

Keywords—infrared thermography, thermal imaging, bus fleet inspections, bus fleet maintenance, condition monitoring

INTRODUCTION

Buses play a vital role in mass transportation, moving people between destinations and connecting the different parts of a transportation network with each other. Buses are the most available and common type of public transport, attributing to 7.1 % passenger kilometres across the EU while cars remain the dominant mode of transport with 79.7% of passenger-kilometres [1]. Bus operators are required to maintain their networks and fleets frequently and often stress their assets to their limit, to keep up with demand, while having to cope with aging fleets. More than half of European countries have buses with an average age of 10 years, while Romania and Greece have bus fleets with 20 and 19 year of average ages respectively [2]. Bus companies use maintenance planning and scheduling to decrease the downtime of their fleet, while taking into account budget restrictions [3].

Unexpected failures of buses on mechanical, electrical or structural components, may be in many cases simple. However, catastrophic failures may also lead to loss of an asset or even injuries. Predictive maintenance of bus fleets can lead to increased productivity, better utilisation of resources, reduced maintenance costs or even potential environmental impact of the vehicles [4].

Crucial to predictive maintenance of bus fleets is the ability of recording periodic data either through inspection or continuous monitoring. In this case the aim is to substitute or supplement the inspections carried out on buses under regular intervals at bus depots by using sensors for inspecting critical parts of the vehicle. Such inspection aims to identify parts that are running beyond normal operating conditions that may have been defined by the vehicle manufacturer or the fleet operator.

The current paper proposes the application of infrared thermography (IRT) as an early detection method for faults on bus fleets as part of predictive and preventive maintenance. Results from the application of IRT on buses and specifically air compressor units are presented in this paper.

INFRARED THERMOGRAPHY

Introduction to infrared thermography

IRT is a well-known non-destructive testing technique (NDT) with numerous applications of materials such as metals, composites, wood, ceramics, construction materials as well as others. IRT is a technique that is capable of measuring the electromagnetic energy radiated by an object. Through the use of a thermographic camera the radiometric values are translated into temperature values [5]. When a heat flux Φ falls on the surface of a body, part of it is absorbed Φ_A, reflected Φ_R and transmitted Φ_R [6]. This absorbed heat flux causes the internal thermal energy of the body and consequently its temperature. Thermography studies the distribution of surface temperature and radiation of the energy from a structure, over time, to identify potential surface of subsurface defects.

IRT can be categorised into passive and active. In passive thermography, an object is inspected in its natural environment without the use of any external thermal excitation sources. Thermal variations in the object under inspection, can be higher or lower than the background temperature indicating potential anomalies. Applications of passive IRT can be health monitoring of roadways [7], building inspections [8], road vehicles monitoring and inspections of components [9], [10], monitoring of composite

Identify applicable funding agency here. If none, delete this text box.

helicopter blades from ground level [11]. The research carried out within this paper deals with passive IRT

In contrast, active thermography uses an excitation source to induce a temperature change on the object under inspection. With the use of the thermal camera the object is studied during the heating, cooling or both phases in order to identify potential subsurface defects, where defective and non-defectives areas will create thermal contours in the produced thermal images [12]. Active thermography methods are categorised according to the excitation source which can be optical (i.e. photographic flashes, halogen lamps), electromagnetic (eddy currents), mechanical (mechanical oscillators, ultrasonic and sonic transducers) [12].

DESCRIPTION OF SYSTEM FOR INSPECTION

Buses carry an air compressor unit which consists of a small internal combustion engine. This unit provides compressed air to vehicle systems such as suspension, breaks and operates the passenger doors. Occasionally, specific parts of the air compressor unit such as the air line coming out of the cylinder head where the compressed air comes out hot and is then cooled, may get restricted due to lack of maintenance. A restricted/ clogged line could mean that temperatures may elevate drastically leading to the air compressor catching fire and potentially the bus itself. Hence, the application of thermography is suggested when simple maintenance is carried out on buses at the depot. Without any intrusiveness, a thermal camera can be setup in front of the air compressor unit while the bus runs stationary at different RPM. The suggested experimental procedures are explained in chapter IV. The thermography acquisitions were performed in two types of buses, a Volvo B9 and Mercedes Citaro LE shown in ***Figure 1***and ***Figure 2***. In the Volvo bus, the air compressor is located at the outside and back left side of the vehicle, where it is easily accessible by lifting an engine cover. In contrast, in the Mercedes type bus, the air compressor is located inside the bus's floor at the back side of the vehicle where it can be accessed by also removing a cover.

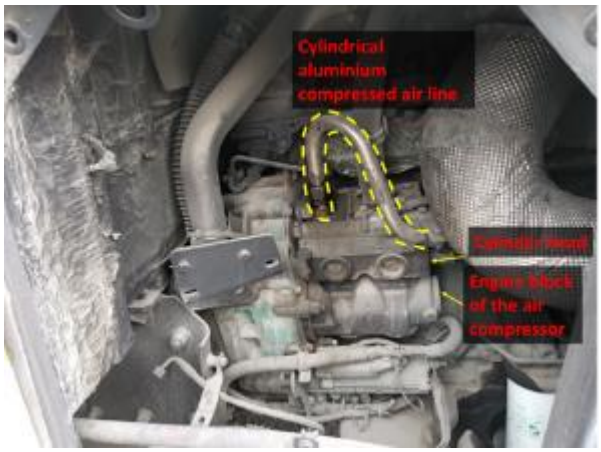

Figure 1. Air compressor from Volvo B9 bus

EXPERIMENTAL SETUP AND PROCEDURES

The IRT setup consisted of a FLIR A655sc uncooled microbolometer, with a 45° lens, placed on a tripod in front of the air compressor at a distance between 0. 6- 1.50 m while the camera angle was between 0-70° depending on the bus type. 70° was used in the Mercedes vehicles due to the fact that the tripod had to be place in front and above the air compressor which is situated at the floor. In addition, FLIR's ResearchIR software was used both for capturing the acquisitions as well as part of the analysis that was carried out. The acquisition frame rate was set up at 50Hz to accommodate for fast changes in object temperature rise.

Figure 2. Air compressor from Mercedes Citaro LE

The aim of the experimentation was to take acquisitions from a number of buses from a bus operator in order to potentially identify restricted air lines in the air compressor unit.

For each acquisition, regions of interest (ROI) were drawn using 3x3 pixel areas (total of 9 pixels) where the FLIR software would measure the mean/max/min temperature along the different areas of the air compressor. This is referred as a cursor ROI in the FLIR ResearchIR software. These points of measurement were along the air line, cylinder head and engine block where potential clog in the line would produce significant temperature difference between restricted and unrestricted areas or potentially the block and cylinder head areas would also overheat. ***Table 1*** presents the number of acquisitions and their description. All acquisitions were carried out inside the maintenance depot to minimise reflections from foreign objects or the sun.

Table 1. Description of acquisitions

Acquisition #	Vehicle name	Description	Duration (min)	Vehicle manufacturer
1	A	Engine startup with high RPM. Test acquisition	10	Mercedes
2	B	Engine startup with high RPM. Test acquisition	10	Volvo
3	C	Cold engine start with engine on idle followed by high engine RPM after 3:20 min	10	Volvo
4	C	After acquisition #3 on low RPM	5	Volvo
5	D	Engine startup, on idle for 4:20 min. Engine was turned off at 10:38 min	11	Mercedes
6	D	After acquisition #5	5	Mercedes

ISBN: 978-618-5765-04-0
ISSN 3057-4269

		with engine turned off		

During the acquisitions certain issues were encountered. Specifically, thermal imaging of the Volvo air compressors was more difficult due to the air line being made of aluminium which is a material with low emissivity causing in some cases false readings due to heat reflections from surrounding hot objects since the main engine compartment in very close in this model. In contrast, the air line in the Mercedes vehicle, because is it is made of rubber, which naturally has higher emissivity, it was easier to do so. In such cases, the overall behaviour of the air line was studied and the adjacent areas i.e. where the line meets the cylinder head. In addition, in some acquisitions post processing of the images was difficult due to the changes of RPM in the engine which meant that the image moved from its initial position.

The acquisitions were also processed using the IR View software by Visiooimage, Canada, that is capable of using various denoising and image processing techniques. Specifically, principal component thermography (PCT) [13], amplitude (FTA) and phase (FTP) signal of the Fourier Transform. These are standard thermography image processing techniques that would potentially allow the detection of further defects in the acquisitions.

Furthermore, during the acquisitions in some cases the target object would move due to starting up/switching off the engine or revving up to increase the load. This meant that the areas where the cursor ROIs targeted would move, making the temperature readings more difficult, and the ΔT diagrams less reliable. Also, in such cases the results from the image processing would be affected. Thus, the images where the target would move, would have to be cut out to avoid blurred and offset images.

INSPECTION RESULTS

Acquisitions #1 and #2 were mostly used for calibration purposes and to establish the analysis method for the rest of the acquisitions. Points C1-C4 (where C is short for cursor) indicate the measurement points of interest placed on the image to acquire all relevant information. Due to limited space only selected acquisitions are presented in the results section.

Results from acquisition #3 are presented at Figure 4 and Figure 5, showing the air compressor unit at different time instances i.e. t_1= 2.3m where the engine is idling and at t2= 8.1m high load conditions. Figure 5 presents the temperature rise (ΔT) over time including the two time instances where the images where taken. The periodic peaks and dips in the temperatures recorded over time in the ΔT diagram shown in Figure 5, are attributed to the system's pressure release valve that prevents the system from excessive pressure building up. Both images from acquisition 3 show that the aluminium air line of the Volvo bus, does not seem to be restricted. The different contours are attributed to the emissivity of the material where parts of it seem to be colder while other hotter especially towards the right side of the image where the heat shield of the vehicle's exhaust is situated (see ***Figure 1***). Dirt and lubricant oil on the air line's surface, as well as the aforementioned heat reflections, can cause these temperature contours. Regardless, of this fact the engine block and cylinder head temperatures are even as well as the temperatures recorded between ROIs C1 and C3. The image processing from PCT and FTAs (Figure 6) show the same consistent results where no significant hotspots are detected in any of the areas of interest. Potential cracks on the cylinder head or engine block can also potentially be detected through the image processing since the acquisition contained the time sequence, beginning with the compressor unit being cold and then heating up. Such subsurface defects would cause the material to behave in a different manner creating colder spots due to the difference in heat dissipation between defective and non-defective areas.

Results from acquisition #5 are presented at Figure 7 to Figure 9. This acquisition is taken from the Mercedes bus where the rubber air line is easier to read. The raw image presented in Figure 7 shows that the air compressor unit works as intended. Compressed air circulates in the air line on the right side and when it reaches the cylindrical canister (middle of image), it expands and cools down on the air line exiting the canister to the left. The rubber material of the air line makes the acquisition easier and temperature readings easier due to the higher emissivity. However, dirt and lubricant oil that these units have, can provide false impressions of colder or hotter spots. Thus, no restriction in the air line is identified at least with the use of thermography.

DISCUSSIONS AND CONCLUSIONS

The current paper presented the application of passive IRT as an NDT method that could be used to detect potential defects in buses and specifically their air compressor unit. The application of IRT can help bus fleet operators predict or diagnose early defects in such units and mores specifically restrictions in the air line where the compressed air comes out. The results that we presented were taken from stationary buses from a fleet operator while they were located at the bus depot. Detection of such fault could be crucial for the operators since it can lead to potential fires. Thus, what is suggested in this paper is a non-invasive inspection that can be carried out while the bus is located at the terminal depot before or after a scheduled route. This inspection can take place at scheduled intervals to ensure that no faults have been detected. An estimated 10 min check similar to the duration of the acquisitions that were performed in this research, can provide adequate results. Benchmark, sample acquisitions can be taken when the buses have been maintained and at regular intervals in order for the operator to have comparable results.

The results from the acquisitions presented in the paper did not detect any fault in the compressor units of the buses that were inspected. However, the task of performing IRT requires certain considerations such as performing the inspections under the shade or in sheltered areas. In addition, the emissivity of the materials can be an issue as demonstrated in the previous section. A simple solution, especially for hoses that are made of aluminium is to paint them black with a simple water-based paint or coating (high emissivity paints are also commercially available at a cost). All the acquisitions that were performed in this research were done while the bus has not been operating for a long period of time. The difference is that these systems could behave in a different manner while loaded with passengers, under heat and under load while moving.

Furthermore, IRT is not limited to the application presented in the paper. Other passive IRT applications could be: testing the vehicle's main powerplant in order to identify potential faults, or other parts of the vehicle such as the tyres as the vehicles come into the depot where thermal imaging can provide information about the wear and tear of the tyres.

ISBN: 978-618-5765-04-0
ISSN 3057-4269

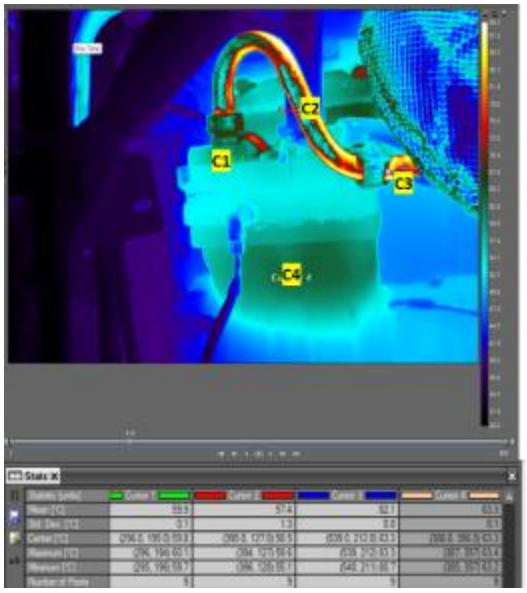

Figure 3. Acquisition #3 for vehicle C at t_1=2.3m with the engine on idle

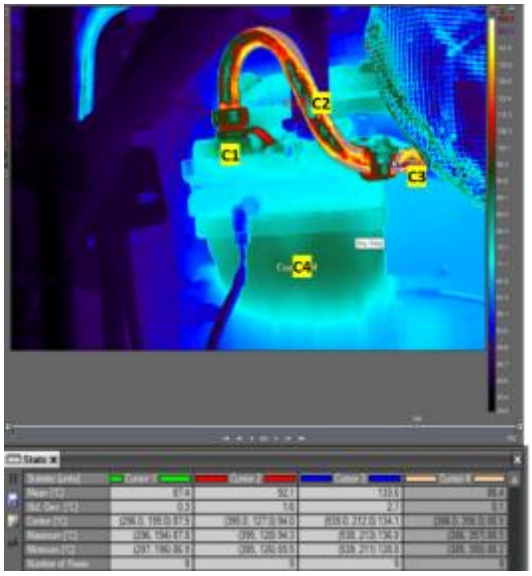

Figure 4. Acquisition #3 for vehicle C at t_2=8.1m with the engine on high load

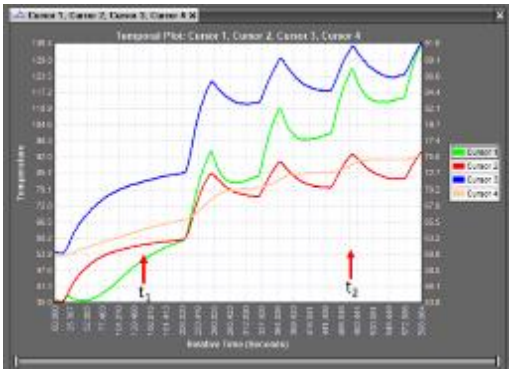

Figure 5. ΔT diagram for acquisition #3

Figure 6. PCT (left) and FT amplitude (right) processed images from acquisition #3

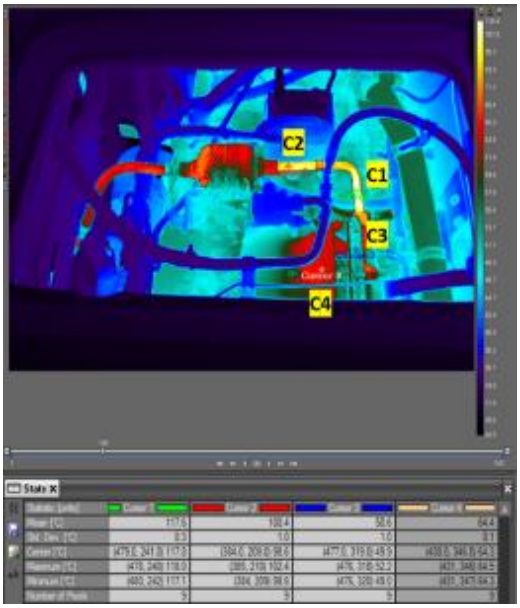

Figure 7. Acquisition #5 for vehicle D at t_1= 1.98 min with the engine idling

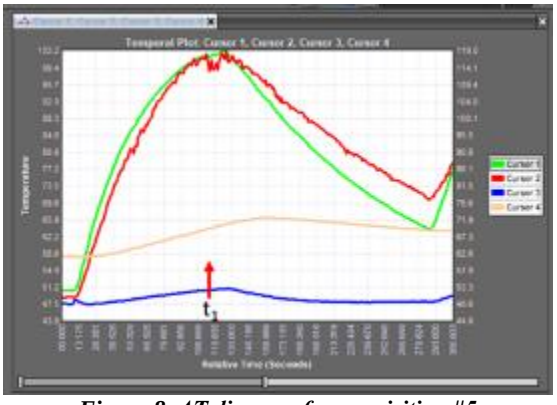

Figure 8. ΔT diagram for acquisition #5

Figure 9. PCT (left) and FT amplitude (right) processed images from acquisition #5

ISBN: 978-618-5765-04-0
ISSN 3057-4269

REFERENCES

[1] Eurostat, 2023. [Online]. Available: https://ec.europa.eu/eurostat/web/products-eurostat-news/w/edn-20230918-1. [Accessed 22 07 2024].

[2] Statista, "Average age of registered buses in European countries in 2021," 2023. [Online]. Available: https://www.statista.com/statistics/1199847/buses-in-use-average-age-europe/. [Accessed 22 07 2024].

[3] R. Martins, F. Fernandes, V. Infante and A. R. Andrale, "Simultaneous scheduling of maintenance crew and maintenance tasks in bus operating companies: a case study," *Journal of Quality in Maintenance Engineering,* vol. 28, no. 2, pp. 506-532, 2022.

[4] A. Toni, M. V. Corazza and D. Vasari, "Improving the environmental performance of bus fleets in Europe," *Transportation Research Procedia,* vol. 69, pp. 147-154, 2023.

[5] X. Maldague, "Introduction to NDT by Active Infrared Thermography," *Materials Evaluation,* vol. 60, no. 9, p. 1060–1073, 2002.

[6] W. Minkina, "Theoretical basics of radiant heat transfer–Practical examples of calculation for the infrared (IR) used in infrared," *Quantitative Infrared Thermography Journal,* vol. 18, no. 2, pp. 269-282, 2021.

[7] N. N. Kulkarni, K. Raisi, N. A. Valente, J. Benoit, T. Yu and A. Sabato, "Deep learning augmented infrared thermography for unmanned aerial vehicles structural health monitoring of roadways," *Automation in Construction,* vol. 148, no. April, 2023.

[8] S. Pozzer, Z. Omidi, A. E. Refai, F. López, C. Ibarra-Castanedo and X. Maldague, "Passive infrared thermography for subsurface delamination detection in concrete infrastructure: Capabilities," *Construction and Building Materials,* vol. 419, 2024.

[9] FLIR, "FLIR Thermal Imaging Enables Autonomous Inspections of Mining and Trucking Vehicles in Australia," 16 July 2020. [Online]. Available: https://www.flir.com/discover/industrial/flir-thermal-imaging-enables-autonomous-inspections-of-mining-and-trucking-vehicles-in-australia/. [Accessed 29 07 2024].

[10] T. Tichý, D. Švorc, M. Růžička and Z. Bělinová, "Thermal Feature Detection of Vehicle Categories in the Urban Area.," *Sustainability,* vol. 13, 2021.

[11] Y. R. and H. Y., "Optically and non-optically excited thermography for composites: A Review," *Infrared Physics & Technology,* vol. 75, pp. 26-50, 2016.

[12] C. Ibarra-Castanedo, J.-M. Piau, S. Guilbert, N. Avdelidis, M. Genest, A. Bendada and X. Maldague, "Comparative Study of Active Thermography Techniques for the Nondestructive Evaluation of Honeycomb Structures," *Research in Nondestructive Evaluation,* vol. 20, no. 1, pp. 1-31, 2009.

[13] N. Rajic, "Principal component thermography for flaw contrast enhancement and flaw depth characterisation in composite structures," *Composite Structures,* vol. 58, pp. 521-528, 2002.

ISBN: 978-618-5765-04-0
ISSN 3057-4269

Artificial Intelligence Techniques for Optimal Sizing of Battery Energy Storage Systems with Renewable Resources

Behzad Pirouz
Department of Mechanical, Energy and Management Engineering, University of Calabria
Rende, Italy
behzad.pirouz@unical.it

Francesca Guerriero
Department of Mechanical, Energy and Management Engineering, University of Calabria
Rende, Italy
francesca.guerriero@unical.it

***Abstract*—Despite the significant economic and environmental benefits of renewable energy sources, such as wind turbines and photovoltaic generators, the intermittent nature and uncertainty in their sources, such as wind speed and solar radiation, make efficient use of these sources challenging. These uncertainties have dramatically increased the need for battery energy storage systems (BESS). Accurately predicting energy production from renewable sources and fluctuations in energy consumption demand is effective in the optimal management of BESS. Artificial intelligence (AI) techniques can significantly improve the accuracy of predictions by training on relevant data. AI techniques enable BESS operators to comprehensively understand and control various influencing factors, from the output status of renewable energy sources to making decisions about charging and discharging schedules. This study aims to provide an optimal energy management strategy by presenting a new multi-objective optimization model based on AI to determine the optimal size of BESS.**

Keywords—energy management, artificial intelligence techniques, battery energy storage systems, renewable energy, multi-objective optimization.

INTRODUCTION

The intermittent nature of renewable energy sources (RES) is a major challenge for their efficient use. On the other hand, the demand for electrical energy is also intermittent. Battery energy storage systems (BESS) have been proposed as an effective solution to reduce fluctuations and compensation for uncertainties in electricity generation from RES and electricity demand [1]. BESS stores the energy generated during the period of availability of generating units and dispatches this energy in case of a power outage or during off-peak periods. In addition, BESS can help manage peak load, regulate voltage and frequency, improve power quality, and further RES penetration. In this way, using BESS increases the reliability and security of the power grid [2].

However, BESSs are expensive components with a relatively short lifespan, and finding the optimal size according to the features and requirements is an important factor in the financial success of the project [1]. However, determining the optimal size of BESSs takes time and effort. If they are oversized, their cost can be unjustified; if they are undersized, they may not fulfill the system requirement [1].

Various indicators and criteria can be considered according to the objectives and basic requirements of the system to determine the optimal size of BESS. These criteria are generally classified into four categories: financial, technical, environmental, and hybrid criteria [3]. In the literature, the optimal size of BESSs has been determined using various techniques. These optimization techniques are probabilistic, analytical, directed search-based, artificial intelligence (AI) based, and hybrid methods [3].

In addition to BESS, which is added to the system to maintain reliability and stability, hybrid renewable energy systems can consist of various other components, including renewable and non-renewable energy generators. The literature generally divides renewable energy systems into four categories: distributed renewable energy systems, microgrids, standalone hybrid renewable energy systems, and power plant systems [3]. Determining the optimal size of BESS requires a set of sizing criteria. These four categories lead to different BESS sizing criteria.

In distributed renewable energy systems, solar PV is integrated directly into the distribution grid for end-user or regional distribution grid applications, usually to reduce the electricity costs of consumers [3]. Microgrid energy systems are usually created with two operation modes: grid-connected and islanded. In grid-connected mode, system performance and BSSS are similar to distributed renewable energy systems. However, In the islanded mode, the microgrid works as an independent system, and the BESS is used as a voltage source or a microgrid performance enhancer. Standalone hybrid renewable energy systems include non-renewable energy sources, such as diesel generators, and renewables, such as solar PV. The main purpose of using BESS in these systems is generally to match the imbalance between renewable energy production and electricity demand to ensure the continuity of electricity supply. Power plant renewable energy systems are classified into "market" or "non-market". Their scale is usually much larger than that of other systems, and therefore, the size of BESS is determined based on more parameters. BESS is generally used in these systems to obtain better performance, smooth output power, load management, minimize operating costs, and compensate for the mismatch between predicted and actual production [3].

In [1], a multi-objective mixed-integer quadratic model is proposed to determine the optimal capacity and power of BESS in a Grid-Connected microgrid (MG), taking into account the economic and technical criteria and the uncertainty of dispatchable generators (DG) and RESs. [4] has proposed a techno-economic model by introducing the energy-to-power ratio as a factor to enable a quick assessment of the feasibility of a BESS. For the optimal size of BESS in solar energy electric vehicles (SEEV) in [5], combinatorial optimization using a genetic algorithm and neural network is

ISBN: 978-618-5765-04-0
ISSN 3057-4269

used. The main goal of their model was to minimize the total capital cost of the BESS.

In [6], an artificial bee colony optimization algorithm is used to optimize the size of BESS to minimize the total cost of MG integrated with RES. A genetic algorithm-based method for sizing microgrid energy storage systems is proposed in [7]. The main goal of their proposed method is to find the energy and power capacities of the storage system that minimizes the operating cost of the microgrid. In [8], a BESS capacity planning model is proposed for the problem of peak and load shaving. They considered two different optimization objectives: one is to reduce the difference between the peak load and the valley load, and the other is to minimize the daily load variance. An optimal BESS sizing method is developed in [9] for a smart microgrid with PV systems and air conditioning resources. The proposed model is solved by differential evolutionary algorithms and iterative algorithms. In [10], a multi-year operational planning model is proposed to optimally determine the BESS optimal power rating, energy capacity, and the year of installation, considering its coordinated performance in isolated microgrids.

This paper investigates a multi-objective optimization approach to obtain the optimal capacity and power rating of BESS in a grid-connected MG, taking into account the uncertainties and intermittency of renewable energies.

The main contributions of this paper can be stated as follows:

(1) This paper presents a novel multi-objective optimization model to optimize the size of BESS, in which total costs are minimized and renewable energy consumption is maximized.

(2) An AI controller is developed to assist energy management in the proposed model.

(3) According to the proposed multi-objective optimization model, instead of an optimal solution, a set of Pareto optimal solutions will be available. In this case, the decision maker can choose one of them as the optimal solution according to other management criteria.

The rest of the paper is structured as follows: Section II contains our general model and scenario. Section III presents the proposed multi-objective optimization model. Section IV provides computational experiments, and Section V is devoted to conclusions.

General Model and Scenario

This study aims to develop a multi-objective optimization model to obtain the optimal capacity and power of BESS considering the intermittency of renewable energies. Also, an optimal energy management strategy is presented to increase the reliability of the power grid with renewable energies and BESS devices by evaluating its performance based on AI prediction of energy consumption and solar production. An AI controller moves everything towards desired goals. The tasks of this AI controller are:

- Prediction load consumption
- Prediction of the energy generation from PV panels.
- Peak shavings and Load shifting.
- Optimize BESS operation by:
  - ✓ Predicting charging and discharging periods.
  - ✓ Predicting stored energy levels to optimize the battery lifetime.

We have considered the energy consumption demand in an apartment that supplies its energy needs from three main sources: the grid, PV panels, and BESS. Our model is actually a microgrid energy system connected to the grid. Figure 1 shows an overview of our model.

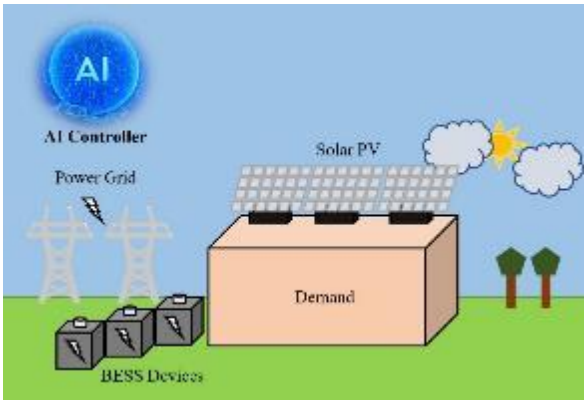

Figure 1: Overview of our general model.

Proposed Multi-Objective Optimization Model

This section presents the proposed multi-objective optimization model. Due to the stochastic nature of energy consumed, energy injected through renewable energy sources (caused by variable weather conditions), and other related factors, an energy management program as a multi-objective stochastic optimization model that considers all possible scenarios to reduce the effects of fluctuations is appropriate. However, in this short article, we have considered the proposed model in its deterministic state (assuming the occurrence of only one of the possible scenarios).

Objective functions

The first objective function is used to minimize the total costs and calculated using the following formula:

$$f_1 = Cost_{Total\_DEP} + Cost_{Cap\_BESS} + Cost_{Total\_OM} + Cost_{Total\_ENS} + Cost_{Total\_DEC} + Cost_{Total\_Load} \quad (1)$$

where $Cost_{DEP\_Total}$, $Cost_{Cap\_BESS}$, $Cost_{Total\_OM}$, $Cost_{Total\_ENS}$ and $Cost_{DTEC}$, $Cost_{Total\_Load}$ are the total depreciation cost, the total capital cost of $BESS$, the total operation and maintenance cost, the total costs of the energy not supplied, the total daily energy cost, and the load curtailment cost, respectively. The calculation of each of them is shown below:

$$Cost_{Total\_DEP} = Cost_{DEP\_PG} + Cost_{DEP\_BESS} + Cost_{DEP\_PV} \quad (2)$$

where $Cost_{DEP\_PG}$, $Cost_{DEP\_BESS}$ and $Cost_{DEP\_PV}$ are the total depreciation costs of the power grid, BESS, and PV panels, respectively.

$$Cost_{Cap\_BESS} = Cost_{BESS\_kwh} * EC_{BESS}^{max} + Cost_{BESS\_kw} * PC_{BESS}^{max} \quad (3)$$

where $Cost_{BESS\_kwh}$, EC_{BESS}^{max}, $Cost_{BESS_kw}$and PC_{BESS}^{max} are BESS capacity rating cost per kWh, maximum energy capacity of BESS, BESS power rating cost per kW, and maximum power capacity of BESS, respectively.

ISBN: 978-618-5765-04-0
ISSN 3057-4269

$$Cost_{Total\_OM} = Cost_{Sup\_OM} + Cost_{PV\_OM} + Cost_{BESS\_OM} \quad (4)$$

where $Cost_{Sup\_OM}$, $Cost_{PV\_OM}$ and $Cost_{BESS\_OM}$ are the energy supplier (power grid) related, PV-related, and BESS-related costs (including operation and maintenance costs) and calculated as follows:

$$Cost_{Sup\_OM} = \sum_{t} Cost_{Sup_{OM}\,t} \quad (5)$$

$$Cost_{PV\_OM} = \sum_{i}\sum_{t} Cost_{PV\_OM_{i\,t}} \quad (6)$$

$$Cost_{BESS\_OM} = \sum_{k}\sum_{t} Cost_{BESS\_OM_{k\,t}} \quad (7)$$

where t is the time unit, i is the index of PV panels ($i = 1, \dots, N_{PV}$), k is the index of BESS ($k = 1, \dots, N_{BESS}$), N_{PV} is the number of PV panels and N_{BESS} is the number of BESS.

$$Cost_{Total\_ENS} = \sum_{t} Cost_{ENS\,t} \quad (8)$$

$$Cost_{Total\_DEC} = \sum_{t} \Big(PC_{\mathrm{APP_{sh}}t} + PC_{\mathrm{APP_{ns}}\,t} - (PG_{PV\,t} + PS_{BESS\,t}) \Big) \times UC_{Sup\,t} \quad (9)$$

where $PC_{\mathrm{APP_{sh}}t}$ and $PC_{\mathrm{APP_{ns}}\,t}$ are hourly power consumption against shiftable and non-shiftable appliances per kWh at time t. $PG_{PV\,t}$ is hourly total active power generation per kWh from PV panels at time t:

$$PG_{PV\,t} = \sum_{i} PG_{PV_i\,t} \quad (10)$$

$PS_{BESS\,t}$ is hourly total power storage per kWh in BESS at time t:

$$PS_{BESS\,t} = \sum_{k} PS_{BESS_k\,t} \quad (11)$$

$UC_{Sup\,t}$ is the unit cost of purchasing power from an energy supplier (power grid) per €/kWh at time t.

The second objective function is designed to increase the ratio of renewable energy consumption to total energy consumption. The second objective function is described as follows:

$$f_2 = \frac{\sum_t (PG_{PV\,t} + PS_{BESS\,t})}{\sum_t \left(PC_{\mathrm{APP_{sh}}t} + PC_{\mathrm{APP_{ns}}\,t}\right)} \quad (12)$$

Model Constraints

In this section, the constraints of the model are introduced.

Equation 13 shows the total daily supply-demand balance constraint.

$$TPD_{EPG\,t} = \left(PC_{\mathrm{APP_{sh}}t} + PC_{\mathrm{APP_{ns}}\,t} + PC_{BESS\,t} + PD_{BESS\,t}\right) - (PG_{PV\,t} + PS_{BESS\,t} + P_{ENS\,t}) \quad (13)$$

where $TPD_{EPG\,t}$ is the total power demand (load demand) per kWh, which is supplied from the external power grid at time t.$PC_{BESS\,t}$ and $PD_{BESS\,t}$ are the needed charging and discharging power of BESS device per kWh during the period t. $P_{ENS\,t}$ is the total hourly power per kWh that is not supplied in the system at the time t.

As shown in equation 14, the total capital cost of the BESS cannot exceed the budget limits:

$$Cost_{Cap\_BESS} \le Budget_{BESS} \quad (14)$$

where $Budget_{BESS}$ is the budget limit for BESS.

Considering that the capacity of the transmission line is limited, inequality (15) is defined for the grid power:

$$GP^{min} \le GP_t \le GP^{max} \quad (15)$$

where GP_t is the grid power per kWh at time t. GP^{min} and GP^{max} are minimum and maximum power capacity of the line transmission.

Grid power is obtained from the following equation:

$$GP_t = PC_{\mathrm{APP_{sh}}t} + PC_{\mathrm{APP_{ns}}\,t} \quad (16)$$

The energy supplier (power grid) related cost is calculated as follows:

$$Cost_{Sup_{OM}t} = UC_{Sup\,t} * GP_t * \Delta t \quad (17)$$

The charge and discharge model of the BESS is shown as follows:

$$PS_{BESS_k\,t} = PS_{BESS_k\,t-1}\left(1 - PLR_{BESS_k\,t}\right) + \xi\,\eta C_{BESS_k} CP_{BESS_k\,t} - (1-\xi)\frac{DP_{BESS_k\,t}}{\eta D_{BESS_k}} \quad (18)$$

$PS_{BESS_k\,t}$ and $PS_{BESS_k\,t-1}$ are hourly total power storage per kWh in k^{th} BESS device before and after charging and discharging at the time t and $t-1$, respectively. $PLR_{BESS_k\,t}$ is the power loss rate of k^{th} BESS device at the time t.ηC_{BESS_k} and ηD_{BESS_k} are the charging efficiency and discharging efficiency of k^{th} BESS device per kW at the time t, respectively. $CP_{BESS_k\,t}$ is charge power of k^{th} BESS device at the time t. $DP_{BESS_k\,t}$ is discharge power of k^{th} BESS device at the time t. ξ is status variable to judge whether the system is charging at time t, 0 for discharging, and 1 for charging:

$$\xi = \begin{cases} 1 & if\ charging\ mode \\ 0 & if\ discharging\ mode \end{cases} \quad (19)$$

The hourly total power storage in the kth BESS device applies in the following constraint:

$$PS^{min}_{BESS_k} \le PS_{BESS_k\,t} \le PS^{max}_{BESS_k} \quad (20)$$

where $PS^{min}_{BESS_k}$ and $PS^{max}_{BESS_k}$ are the minimum and maximum energy capacity of kth BESS device.

COMPUTATIONAL EXPERIMENT

The understudy system includes several PV modules with a total maximum capacity of 100 kW as renewable energy production units. The amount of energy generated by PV panels is variable and depends on various factors, including weather conditions. The energy consumption is also variable and depends on various factors. Figure 2 shows the energy consumption and the total energy production from PV panels on a specific day.

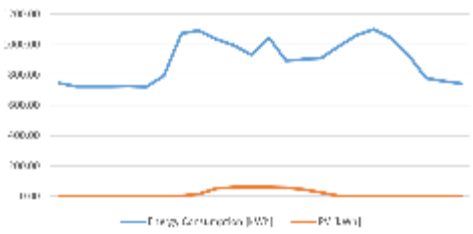

ISBN: 978-618-5765-04-0
ISSN 3057-4269

Figure 2: Energy consumption and total energy production from PV panels in one day.

We have used AI techniques to predict the amount of energy consumption and energy production from PV panels as accurately as possible in the days ahead. However, we have not presented the prediction results to avoid making them too long.

Among the various technologies available in the market, the BESS based on lithium-ion (Li-ion) will be used in our system due to its advantages. The lifetime and lifecycle against the depth of discharge (DOD) variations of the Li-ion battery are considered according to [11].

Other technical parameters of BESS are round trip efficiency: 95%, min depth of discharge: 10%, power rating cost: 250 $/kW, capacity rating cost: 600 $/kWh. The power grid costs include energy cost (peak period): 10.68 $/kWh, energy cost (off-peak period): 5.8 $/kWh [1].

To solve the multi-objective optimization problems, we used the "Global Solve" of the global optimization package in MAPLE version 18.01.

Figure 3 shows the results of the Pareto frontier of multi-objective optimization model. The horizontal axis represents the first objective function (the total cost), and the vertical axis represents the second objective function (the ratio of renewable energy consumption).

Figure 3 clearly shows an indirect linear relationship between the total cost and the ratio of renewable energy consumption to total energy consumption in this system.

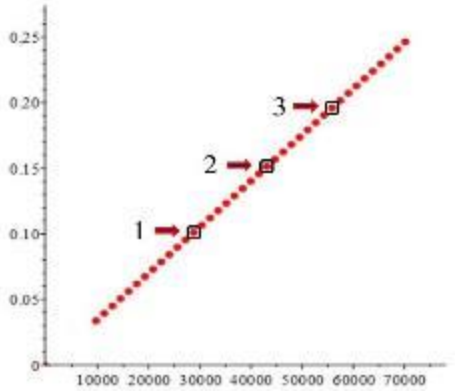

Figure 3: The results of the multi-objective optimization model (Pareto frontier) and selected Pareto solutions.

We have selected three Pareto optimal solutions for further investigation, specified in Figure 3. The results are displayed in Table 1.

Table 1: The results of three Pareto optimal solutions of the multi-objective optimization model

Pareto solution	*BESS Capacity (kWh)*	*BESS Power (kW)*	*Total cost ($)*	*Ratio of renewable energy (%)*
1	570.25	91.14	30413	11%
2	710.97	108.63	43139	16%
3	899.67	130.75	55865	20%

According to the results of Table 1, by increasing the capacity and power of BESS, the ratio of renewable energy consumption to total energy consumption gradually increases while the total cost increases.

CONCLUSIONS

In this paper, a multi-objective optimization approach was proposed to obtain the optimal capacity and power of BESS, in which total costs are minimized and renewable energy consumption is maximized simultaneously. Also, the benefits of using an AI controller for energy management are explained. In the proposed multi-objective optimization model, a set of Pareto optimal solutions is provided to decision-makers instead of an optimal solution.

Due to the random nature of consumed and injected energy through renewable energy sources, a multi-objective stochastic optimization model of fluctuations is more appropriate. However, in this short article, the proposed model was considered in the deterministic state. In future research, a multi-objective stochastic optimization model will be developed to obtain the optimal capacity and power of BESS. Also, developing a comprehensive method based on AI techniques to select an optimal solution from among the Pareto solutions for determining the final optimal capacity and power of BESS will be discussed.

ACKNOWLEDGMENT

We acknowledge financial support from PNRR MUR project PE0000013-FAIR.

REFERENCES

[1] R. Garmabdari, M. Moghimi, F. Yang, E. Gray and J. Lu, "Multi-objective energy storage capacity optimisation considering Microgrid generation uncertainties," *International Journal of Electrical Power & Energy Systems*, vol. 119, p. 105908, 2020.

[2] H. Alharbi, K. Bhattacharya, "Optimal sizing of battery energy storage systems for microgrids," *In2014 IEEE Electrical Power and Energy Conference*. IEEE, 2014, pp. 275-280.

[3] Y. Yang, S. Bremner, C. Menictas, M. Kay, "Battery energy storage system size determination in renewable energy systems: A review," *Renewable and Sustainable Energy Reviews*. 2018, pp. 109-25.

[4] A. Ashabi, M.M. Peiravi, P. Nikpendar, S. Salehi Nasab, and F. Jaryani, "Optimal sizing of battery energy storage system in commercial buildings utilizing techno-economic analysis," *International Journal of Engineering, Transactions B: Applications*, 35(8), pp.1662-1673. 2022.

[5] S. Zhou, L. Kang, M. Cheng, and B. Cao, "Optimal Sizing of Energy Storage System in Solar Energy Electric Vehicle Using Genetic Algorithm and Neural Network," *In Advanced Intelligent Computing Theories and Applications. With Aspects of Artificial Intelligence: Third International Conference on Intelligent Computing*, ICIC 2007, Qingdao, China, August 21-24, 2007. Proceedings 3. pp. 720-729.

[6] M. Gholami, S.M. Muyeen, and S.A. Mousavi, "Optimal sizing of battery energy storage systems and reliability analysis under diverse regulatory frameworks in microgrids," *Energy Strategy Reviews*, 51, p.101255. 2024.

[7] J.P. Fossati, A. Galarza, A. Martín-Villate, and L. Fontan, "A method for optimal sizing energy storage systems for microgrids," *Renewable Energy*, 77, pp.539-549. 2015.

[8] C. Lu, H. Xu, X. Pan, and J. Song, "Optimal sizing and control of battery energy storage system for peak load shaving," *Energies*, 7(12), pp.8396-8410. 2014.

[9] C. Xie, D. Wang, C.S. Lai, R. Wu, J. Huang, and L.L. Lai, "September. Optimal sizing of battery energy storage system in smart microgrid with air-conditioning resources," In 2020 IEEE International Smart Cities Conference (ISC2) pp. 1-8. 2020.

[10] H. Alharbi, and K. Bhattacharya, "November. Optimal sizing of battery energy storage systems for microgrids". In 2014 IEEE Electrical Power and Energy Conference, pp. 275-280. IEEE. 2014.

[11] A. Ahsan, Q. Zhao, A.M. Khambadkone, and M.H.Chia, "Dynamic battery operational cost modeling for energy dispatch," In 2016 IEEE Energy Conversion Congress and Exposition (ECCE), 2016, pp. 1-5.

ISBN: 978-618-5765-04-0
ISSN 3057-4269

Determination of Environmental Impacts of a Processed Meat Product by Life Cycle Analysis (LCA)

Nur Seda Sahin
Istanbul University-Cerrahpaşa, Faculty of Engineering, Department of Environmental Engineering, Avcilar Campus, Avcilar, 34320, Istanbul, Turkey
Istanbul Topkapi University, Department of Architecture and Urban Planning, Kazlicesme Campus, Zeytinburnu, 34087, Istanbul, Turkey
nursedasahin@topkapi.edu.tr

Ilda Vergili
Istanbul University-Cerrahpaşa, Faculty of Engineering, Department of Environmental Engineering, Avcilar Campus, Avcilar, 34320, Istanbul, Turkey
ilda@iuc.edu.tr

Yasemin Kaya
Istanbul University-Cerrahpaşa, Faculty of Engineering, Department of Environmental Engineering, Avcilar Campus, Avcilar, 34320, Istanbul, Turkey
y_kaya@iuc.edu.tr

Abstract*— Red meat products of animal origin, such as sausage, beef bacon, and salami, are among the most produced and consumed animal foods in Turkey. Increasing meat production is remarkable in terms of the environmental impacts occurring in meat integrated plants and red meat production processes. The Life Cycle Analysis (LCA) is an impact assessment method that has been frequently used recently to measure sustainability and reveal its quantitative impacts. The aim of this study is to determine the environmental impacts of fermented sausage produced in a meat integrated plant using LCA. The system boundary of the study starts with the transfer of live animals from the livestock producer using diesel-fueled vehicles, and includes the transportation of carcass meat to the meat integrated plant, sausage production stages, packaging and distribution to market. One-year data for 2020 was taken from a meat integrated plant in Turkey, Afyonkarahisar. The SimaPro 9 software package and the CML-IA impact assessment method were used in the study. The functional unit (FU) for LCA was 1 pieces of sausage (0.5 kg) produced. Three environmental impact categories were evaluated: global warming potential (GWP), acidification potential (AP), and eutrophication potential (EP). The FU caused an impact on GWP of 1.56E+01 kg CO_2 eq. The results for the other studied environmental impact categories are as follows: 6.01E-02 kg SO_2 eq for AP and 6.56E-02 kg PO_4 eq for EP. For all the three environmental impact categories (GWP, AP and EP), the impact of FU is mainly due to the raw material stage. So, 91.21% of GWP, 88.17% of AP and 93.43% of EP consist of livestock (red meat from cattle). While the cooling process was determined to be the second process that made a significant contribution (6.64%, 9.57% and 5.70%), the contribution of other processes was found to be below 1%.

Keywords*— Environmental impact, processed meat, life cycle analysis

INTRODUCTION

Meat and meat products are among the most consumed food products in the world due to their high protein content. Considering that meat production and consumption are expected to increase further in the near future, the implementation of sustainable agriculture within the livestock supply chain is of great importance [1].

The production and consumption of meat and meat products is increasing in our country as well as in all developing countries. Continuously increasing meat production also draws attention to the environmental impacts that occur in integrated meat plants and red meat production processes. Various environmental impacts occur starting from animal husbandry, especially farm, agriculture and fertilizer stages, land use, water use, electricity and natural gas use. As a result of current production in these plants, it is important to evaluate all environmental emissions and natural resource consumption in the supply chain, from animal feeding, slaughtering, production, distribution, consumption, and waste disposal, together in order to fully reveal the environmental impact of the product/process. The results of the practices to be implemented to reduce the environmental impacts and ensure sustainability should also be presented and improvement should be measurable. Life Cycle Analysis (LCA) is one of the methods developed to measure and quantify sustainability. The LCA consists of four stages: goal and scope definition; inventory analysis and data collection; impact assessment; and interpretation [2]. In this study environmental impacts of processed meat product were determined by LCA.

MATERIALS AND METHODS

This LCA study was conducted using data from a meat integrated plant located in Afyonkarahisar province of Turkey. The 2020 data of the meat integrated plant located in Afyonkarahisar Province Organized Industrial Zone and engaged in fermented sausage production are primary data obtained through personal communication with the plant.

The functional unit (FU) for LCA was 1 pieces of sausage (0.5 kg) produced. The SimaPro 9 software package version 9.1.1.7 and the CML-IA impact assessment method were used in the study [3].

Inputs for sausage production as raw materials, transfer distances, flows of energy, water and similar (etc.) were collected and inventory information was created with 1-year data (2020) and modeled using the “Ecoinvent 3” and “Agri-footprint 5” databases in the SimaPro software. In the impact analysis phase, the effects of possible environmental

ISBN: 978-618-5765-04-0
ISSN 3057-4269

emissions identified by the inventory analysis on human health and environmental values as well as natural resource consumption were characterized according to the CML-IA calculation method. The three most common impact categories originating from the livestock sector were investigated: global warming potential (GWP), acidification potential (AP) and eutrophication potential (EU).

In this study, the LCA system boundary starts with the transfer of live animals from the livestock producer with diesel-fueled vehicles and includes the transportation of carcass meat to the meat integrated plant, sausage production stages, packaging and distribution to the market.

The system boundaries of the LCA study for the selected processed meat product (sausage production) are given in Figure 1.

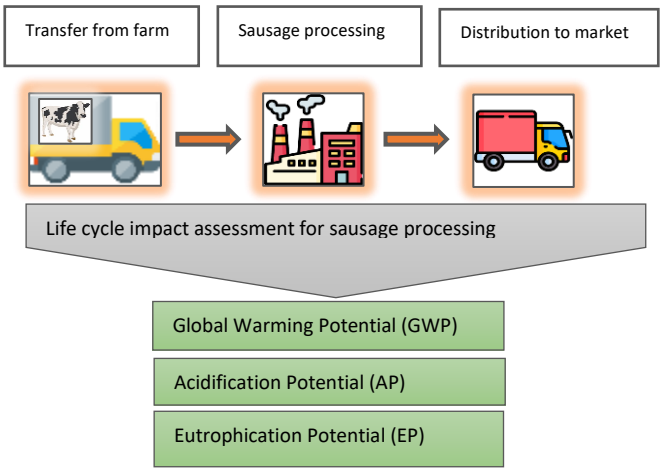

Figure 1: System boundary and life cycle impact assessment for sausage processing.

RESULTS

Environmental impact assessment results per FU (processed meat product = 1 sausage) for all production stages are given in Table 1. The total environmental impacts are as follows: 6.01E-02 kg SO_2 eq for AP, 6.56E-02 kg PO_4 eq for EP and 1.56E+01 kg CO_2 eq for GWP. For all the three environmental impact categories (GWP, AP and EP), the impact of FU is mainly due to the raw material stage. The percentage contributions to environmental impacts of the processed meat product are shown in Figure 2. The 91.21% of GWP, 88.17% of AP and 93.43% of EP consist of livestock (red meat from cattle). While the cooling process was determined to be the second process that made a significant contribution (6.64%, 9.57% and 5.70%), the contribution of other processes was found to be below 1%.

Table 1: Environmental impact assessment results of the processed meat product.

Impact category	**GWP**	**AP**	**EP**
Unit	**kg CO_2 eq**	**kg SO_2 eq**	**kg PO_4 eq**
Raw materials	1,42E+01	5,30E-02	6,13E-02
Raw material transfer	9,41E-02	3,10E-04	6,19E-05
Slaughter	5,18E-02	2,89E-04	1,86E-04
Cooling	1,03E+00	5,75E-03	3,74E-03
Mince	7,11E-03	3,96E-05	2,57E-05
Mixer	3,25E-03	1,81E-05	1,18E-05
Sausage filling	2,16E-02	1,20E-04	7,79E-05
Baking	3,47E-02	1,93E-04	1,25E-04
Shower	1,18E-04	5,05E-07	2,21E-07
Market Distribution	1,23E-01	3,85E-04	8,44E-05
Total	1.56E+01	6.01E-02	6.56E-02

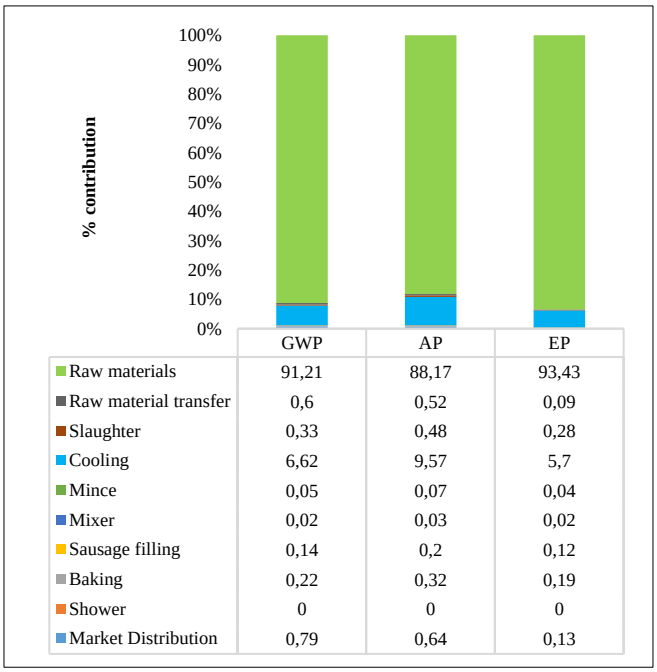

Figure 2: Percentage contributions to environmental impacts of the processed meat product.

GWP refers to the warming of the atmosphere due to climate change. Burning of fossil resources such as oil, coal and natural gas is one of the major human activities causing global warming. The main pollutants included in GWP are methane, carbon dioxide and nitrous oxide [4]. The total environmental impact was found as 1.56E+01kg CO_2 eq Almost all of the contribution (1.42E+01 kg CO_2 eq; 91.21%).) was originated from raw materials. Cooling also has a noticeable contribution of 6.62%. Higher values were obtained for GWP (2.66E+01–4.93E+01) in studies that included agriculture and farm stages in the system boundary [5], [6], [7]. In the studies conducted by [7] and [8], where the environmental impacts of meat production from different animals were evaluated, the highest environmental impact for GWP was found for beef.

AP is the impact category that expresses the pollution impact of acidifying regimes on soil, water, surface

ISBN: 978-618-5765-04-0
ISSN 3057-4269

water, organisms, ecosystems and processes. The most important anthropogenic acidification potential sources are combustion processes and transfer in electricity and heating production, but emissions of ammonia (NH_3) related to meat production are also important [9]. The total environmental impact value in the AP impact category was found as 6.01E-02 kg SO_2 eq. The raw material stage accounts with 5.30E-02 kg CO_2 eq (88.17%), while cooling has also a noticeable contribution of 9.57%. Although the same impact assessment method was used, a higher value (1.22E-01 kg CO_2 eq) was obtained in another study for the AP impact category [10]. Also, in an another study where the same impact assessment method was used for 1 kg of beef patties, a processed meat product, a higher value (4.06E-01 kg CO_2 eq) was calculated for AP [11].

EP is one of the impact categories expressing the effects caused by the increase in macronutrients due to excessive release of nutrients to air, water and soil. The total environmental impact value in the EP impact category was 6.56E-02 kg PO_4 eq and the raw material stage accounts with 6.13E-02 kg PO_4 eq (93.43%). Although the same impact assessment method was used, higher values were reported (1.06E-01–1.54E-01 kg PO_4 eq) in some studies [10, 12]. In an another study [11], where the CML-IA method was used for 1 kg of beef patties, which is a processed meat product, a higher EP effect (2.54E-01 kg PO_4 eq) was calculated.

This study helped to identify the three most significant environmental burdens of mass production of sausage meat with a LCA for the meat sector.

ACKNOWLEDGMENT

This study was supported by Istanbul University-Cerrahpaşa Scientific Research Projects Coordination Unit with the Project Number 35203.

REFERENCES

[1] McAuliffe, G.A., Chapman, D.V., Sage, C.L., "A thematic review of life cycle assessment (LCA) applied to pig production", *Environmental Impact Assessment Review*, vol. 56, pp. 12–22, 2016.

[2] Abyar, H., Younesi, H., Nowrouzi, M., "Life cycle assessment of A_2O bioreactor for meat processing wastewater treatment: An endeavor toward the achievement of environmental sustainable development", *Journal of Cleaner Production*, vol. 257, pp. 120575, 2020.

[3] SimaPro Database Manual-Methods Library, PRé Sustainability, various authors, 2020.

[4] Angerer, V., Sabia E., Von Bortel U.K., Gauly M., "Environmental and biodiversity effects of different beef production systems", *Journal of Environmental Management*, vol. 289, pp. 112523, 2021.

[5] Asem-Hiablie, S., Battagliese, T., Stackhouse-Lawson, K.R., Rotz, C.,E., "A life cycle assessment of the environmental impacts of a beef system in the USA", *The International Journal of Life Cycle Assessment*, vol. 24, pp. 441–455, 2019.

[6] Saerens, W., Smetana, S., Campenhout, L.V., Lammers, V., Heinz, V., "Life cycle assessment of burger patties produced with extruded meat substitutes", *Journal of Cleaner Production*, vol. 306, pp. 127177, 2021.

[7] Ferronato, G., Corrado, S., De Laurentiis, V., Sala, S., "The Italian meat production and consumption system assessed combining material flow analysis and life cycle assessment", *Journal of Cleaner Production*, vol. 321, pp. 128705, 2021.

[8] Arrigoni, A., Marveggio, D., Allievi, F., Dotelli, G., Scaccabarozzi, G., "Environmental and health-related external costs of meat consumption in Italy: estimations and recommendations through life cycle assessment", *Science of the Total Environment*, vol. 869, pp. 161773, 2023.

[9] Mogensen, L., Nguyen, T.L.T., Madsen, N.T., Pontoppidan, O., Preda, T., Hermansen, J.E., "Environmental impact of beef sourced from different production systems - focus on the slaughtering stage: input and output", *Journal of Cleaner Production*, vol. 133, pp. 284-293, 2016.

[10] Chen, W., Jafarzadeh, S., Thakur, M., Ólafsdóttir, G., Mehta, S., Bogasan, S., Holden, N.M., "Environmental impacts of animal-based food supply chains with market characteristics", *Science of the Total Environment*, vol. 783, pp. 147077, 2021.

[11] Ahmad, S., Wong, K.Y., Rashid, A.F.A., Khan, M., "Environmental impacts and improvement implications for industrial meatballs manufacturing: scenario in a developing country", *The International Journal of Life Cycle Assessment*, vol. 29, pp. 1510-1522, 2023.

[12] Presumido, P.H., Sousa, F., Gonçalves, A., Dal Bosco, T.C., Feliciano, M., "Environmental impacts of the beef production chain in the northeast of Portugal using life cycle assessment", *Agriculture*, vol. 8, pp. 165, 2018.

Allocation of Airport Flight Slots using a Vickrey-Clarke-Groves Auction

Evangelos D. Spyrou
Hellenic Institute of Transport
Centre for Research and Technology Hellas
Thessaloniki, Greece
espyrou@certh.gr

Vassilios Kappatos
Hellenic Institute of Transport
Centre for Research and Technology Hellas
Thessaloniki, Greece
vkappatos@certh.gr

***Abstract*—Airport slot allocation is a significant procedure with a number of benefits that emerge for the airport itself but for the airlines as well. Market-based approaches have gained interest to address slot allocation since the airlines are essentially bidders that compete for the slots. Market based approaches have significant benefits over other methods including efficiency. In this paper, the slot allocation of airports is addressed using the Vickrey-Clark-Groves (VCG) auction model. The auction is implemented to impose a constraint to the allocation process by allowing acquisition of one slot per airline. Moreover, the seminal model has been implemented to allow more slots obtained by a single airline. Results show the best possible slot allocation and further research is essential to describe the multiple slots acquisition and whether this takes place due to unwanted behavior of the airline in its bidding process**

Keywords—auction, slot, allocation, payment, VCG, welfare, market.

INTRODUCTION

Air traffic has surged significantly over recent decades and is projected to continue growing. This ongoing increase in traffic has made airport capacity a highly limited resource at major airports. Expanding airport capacity, such as building new runways, faces significant challenges due to cost, land constraints, and political barriers. As a result, the efficient use of existing airport resources has become crucial.

An airport slot is defined as "a permission granted by a coordinator for a planned operation to use all necessary airport infrastructure to arrive or depart from a Level 3 airport at a specific date and time". Airlines must competitively secure a limited number of coordinated slot pairs for both the origin and destination airports to operate their desired flight schedules. As a result, the efficient allocation of these slots among airlines is a crucial issue in the aviation industry Currently, airport slots are allocated semi-annually through a central system. Airlines submit their preferred flight schedules to a slot coordinator, and the slots are distributed in accordance with the Worldwide Slot Guidelines established by the International Air Transport Association (IATA). Airlines that utilized at least 80% of their allocated slots during the previous season are entitled to "grandfather rights," allowing them to retain those slots in the next season. After honoring these rights, the remaining non-grandfathered slots are distributed [1].

However, the existence of grandfather rights introduces inefficiencies in slot allocation. Airlines may continue to operate flights even when demand is insufficient to cover costs, solely to retain their slots for future use. Also, they perform the ghost flights to keep their slots. This practice undermines the optimal utilization of airport capacity and creates challenges in achieving a more efficient allocation of slots.

The field of slot allocation has garnered significant attention. Broadly, there are three key areas of focus in airport capacity scheduling: the first involves capacity management through allocation rules, the second explores market-based approaches, and the third combines elements of both in a hybrid model. Capacity management strategies focus on developing mathematical models to create departure and arrival schedules based on airport capacity and safety constraints. In contrast, market-based strategies address congestion by using economic tools like secondary trading and slot auctions during peak periods [2]. For a thorough review of strategic slot allocation models, provide an extensive analysis [3].

In this paper we take on board the airport slot allocation using a market-based approach. In particular, we employ the VCG algorithm to allocate slots to airline companies. The algorithm has been modified to ensure that each airline can acquire only one slot. We provide results on the behavior of the algorithm and also give the seminal algorithm results whereby an airline can acquire more slots.

RELATED WORK

Some studies have approached congestion management from an economic standpoint, exploring ways to address the demand-capacity mismatch through financial incentives and strategic allocation. Several market-based instruments, such as slot trading [4], slot auctions [5], and congestion pricing [6], have been discussed as tools for balancing airport traffic and managing peak demand periods. These mechanisms aim to optimize the allocation of scarce airport resources by assigning monetary values to slots, which in turn encourages airlines to make more efficient use of their schedules.

For instance, [7] developed an econometric model to assess how airlines internalize congestion. Their work delves into strategies such as slot hoarding and concentration, particularly following mergers and acquisitions, revealing how airlines manipulate slot allocations to maintain competitive advantages. By focusing on slot allocation behavior, their study provides insights into the strategic dynamics of congestion management in the aviation sector.

In a different approach, [8] introduced a bilevel integer optimization model designed to create market mechanisms that maximize social welfare while adhering to core and

ISBN: 978-618-5765-04-0
ISSN 3057-4269

budget constraints. This method ensures that the market functions efficiently by incorporating fairness and economic viability into the slot allocation process, providing a mathematically grounded solution to congestion management.

In [9], the authors proposed a voting mechanism for slot allocation that integrates stakeholder preferences, offering a democratic alternative to market-based mechanisms. This voting-based approach ensures that the interests of all parties—airlines, regulators, and airport authorities—are taken into account when deciding on slot allocations at congested airports.

These economic methods share the common goal of incentivizing airlines to schedule fewer flights during peak hours by imposing costs on slots, thereby mitigating congestion and reducing delays. However, despite their theoretical appeal, market-based approaches often encounter practical challenges. The introduction of monetary transfers and implicit barriers, such as regulatory and legal restrictions, can make these strategies difficult to implement in real-world settings. For instance, the political and economic implications of redistributing airport slots, especially in highly regulated aviation markets, often complicate the adoption of these market-driven solutions.

In addition to market-based approaches, technological innovations are increasingly being used to tackle congestion. The authors in [10] applied machine learning techniques to forecast and manage flight delays and cancellations. By leveraging large datasets and predictive models, machine learning has the potential to improve traffic flow management and reduce congestion by providing real-time insights into flight disruptions. These advancements highlight the growing role of artificial intelligence in optimizing airport operations and complementing traditional economic strategies for congestion management.

Overall, while economic models offer theoretical frameworks for congestion mitigation, the integration of machine learning and other technological innovations may provide more immediate and practical solutions to the complex problem of airport congestion, potentially bridging the gap between economic theory and operational reality.

OUR PROPOSAL: VCG AUCTION

A VCG auction [11-13] is a type of sealed-bid auction for multiple items where bidders submit bids representing their valuations without knowledge of other bidders' offers. The system then allocates the items in a socially optimal way, charging each bidder based on the negative impact their presence has on others. This structure incentivizes bidders to submit their true valuations, as doing so is the optimal strategy.

However, the auction can be vulnerable to bidder collusion, and in some cases, a single bidder can manipulate the process by submitting multiple bids under different identities. The VCG auction is an extension of the Vickrey auction designed for multiple items. We can see an airline slot allocation example in Figure 1.

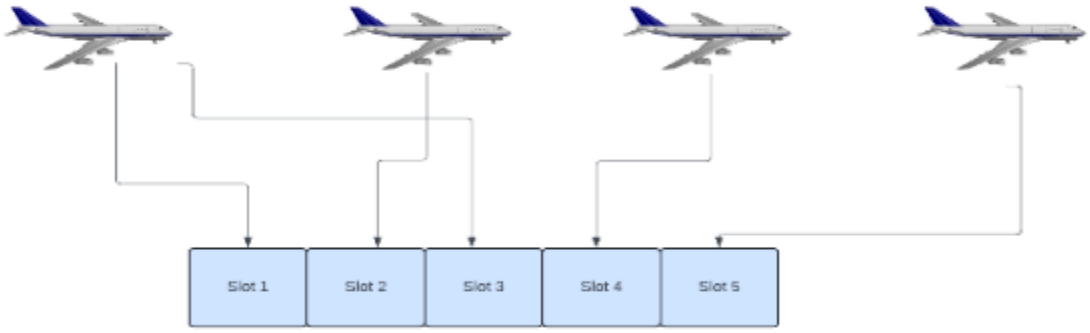

Figure 1: Slot Allocation Example

The VCG auction is a specific application of the broader VCG mechanism, which aims to select the socially optimal outcome from a set of possibilities. When the risk of collusion is present, the VCG auction tends to outperform the generalized second-price auction in terms of both seller revenue and allocative efficiency. The steps of the VCG auction in our case study are the following.

- **Bid Collection:** In this step, bids are gathered from all airlines, covering all possible subsets of airport slots. Each airline submits their valuation for the different slot combinations they are interested in, forming the foundation for the subsequent allocation process.
- **Welfare Maximization and Payment Calculation:** Next, the allocation that maximizes social welfare is determined. This involves finding the allocation where the total benefit to all airlines is highest. Afterward, payments for each airline are calculated. The payment is based on the difference between the total welfare achieved without the airline's participation and the welfare achieved with their inclusion in the allocation process.
- **Output the Results:** Finally, the optimal allocation of slots, along with the calculated payments for each airline, is provided as the output. This ensures that each airline receives its slots based on the welfare-maximizing strategy and pays an appropriate amount corresponding to its impact on the overall system.

The advantages of using VCG to airport slot allocation are that it fosters fairness and genuine preferences among bidders,

ISBN: 978-618-5765-04-0
ISSN 3057-4269

it ensures transparency and equity in slot allocation and it can be modified to allow an airline to win multiple slots based on congestion levels or airline costs.

More formally the VCG algorithm is as follows:

Each airline i submits bids $b_i(S)$ for airport slots and especially every possible subset S of slots. The assumption is that each bid equals the airline's true valuation $u_i(S)$.

The optimal allocation A is then computed by determining in when it maximizes the total declared valuation or social welfare. Here A_i' is the allocation of slots to airline i an an alternative allocation.

$$A = \arg\max_{A'} \sum_{i=1}^{n} u_i(A_i') \quad (1)$$

Thereafter the payments for each airline are calculated. The airline i is then removed from the auction and the optimal allocation is computed, A_{-i}.

$$A_{-i} = \arg\max_{A_{-i}'} \sum_{j \neq i} u_j(A_j') \quad (2)$$

Then the welfare without airline i is calculated (the other airlines under this optimal allocation)

$$h_i = \sum_{j \neq i} u_j(A'_{-ij}) \quad (3)$$

Thereafter the payment p_i of airline i which reflects the externality that the airline imposes on others when it is participating in the auction

$$p_i = h_i(A_{-i}) - \sum_{j \neq i} u_j(A_j) \quad (4)$$

RESULTS

The main slot allocation simulated experiment involves 6 slots and 6 airlines, where the bids and slots are generated randomly. The VCG algorithm allocates more slots to an airline based on the principle of maximizing social welfare, which is the total sum of all participants' valuations for the items they receive. In this work, we modified the algorithm to ensure that each airline is allocated one slot. Additionally, we implemented the vanilla algorithm, where multiple slots may be assigned to a single airline.

The outputs of the experiment include payments and the best allocation mechanism. The payments ensure that each agent's payment reflects the externality they impose on other agents by participating in the auction. We present the payments made for each slot. Additionally, the best feasible slot allocation determines the slot allocation that maximizes the total declared valuation, or social welfare, ensuring an optimal distribution of slots among airlines.

In Table 1, the reader can see the allocations when the one slot per airline constraint is imposed. The payments of each airline per slot are given in Figure 2. In these results a randomly generated 6x6 matrix is created that represents how much each airline bids on each item. Also, a randomly generated list of values for the items is provided as well..

The difference in the payments occurs because airlines pay based on the effect they have on the overall auction's outcome. If an airline's presence in the auction reduces the overall social surplus, they need to pay more. Conversely, if their bid does not reduce the social surplus much, they pay less.

Table 1: Slot Allocation (I slot per airline)

Airline	*Slot*
1	6
2	3
3	5
4	1
5	2
6	4

Thereafter, the seminal auction model has been used whereby multiple slots may be acquired by a single airline. This case has been investigated since, there might be airlines that utilize their time allocation just to keep them and not perform any flights. However this requires further research. In Table 2 the reader can see the results of the auction model execution.

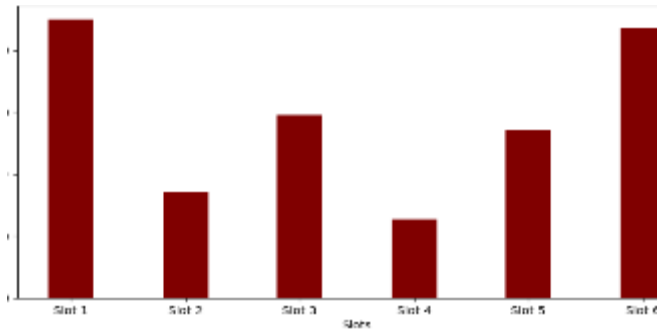

Figure 2: Payments per slot

Table 2: Slot Allocation (more than 1 slot per airline)

Airline	*Slot*
4	1
1	2
1	3
2	4
3	5
4	6

The results show that airlines 1 and 4 obtain two slots each. This requires further research in order to attribute this behavior to a real scenario where airlines are excluded from the slot auction.

CONCLUSIONS

In this paper we addressed the airport slot allocation using the VCG algorithm. We changed the algorithm with the constraint of one slot per airline and provided the allocation when this constraint is not present as well.

The market-based slot allocation Approach ensures the optimal use of airport slots, maximizing capacity utilization while minimizing delays. By reducing operational costs for

ISBN: 978-618-5765-04-0
ISSN 3057-4269

airlines and driving profitability, it helps airlines avoid unnecessary expenses. This approach also eliminates ghost flights, which significantly reduces carbon emissions and supports sustainability goals, aligning the aviation industry with environmental objectives. The VCG auction model guarantees fair and honest slot allocation by compelling airlines to submit truthful bids. It can be adapted to allow airlines to win single or multiple slots based on their needs, encouraging them to optimize schedules and operations. This fosters a more responsive aviation industry.

Together, market-based slot allocation and the VCG auction model represent forward-thinking strategies that ensure a sustainable, efficient, and economically viable future for the aviation industry, benefiting all stakeholders: airlines, passengers, airports, and the environment.

ACKNOWLEDGMENT

This research was done as part of the HAIKU project. This project has received funding from the European Union's Horizon Europe research and innovation programme HORIZON-CL5-2021-D6-01-13 under Grant Agreement no 101075332 but this document does not necessarily reflect the views of the European Commission.

REFERENCES

[1] H. Lee, J. Jung and D.J. Lee, "An auction-based airport slot reallocation scheme considering the grandfather rights of airlines," *Journal of Air Transport Management*, 118, 102612, 2024.

[2] W. Liu, Q. Zhao, and Delahaye, D, "Research on slot allocation for airport network in the presence of uncertainty,". *Journal of Air Transport Management*, 104, 102269, 2022.

[3] K. G. Zografos, M. A. Madas and K. N. Androutsopoulos, "Increasing airport capacity utilisation through optimum slot scheduling: review of current developments and identification of future needs," *Journal of Scheduling*, 20, 3-24, 2017.

[4] P. Pellegrini, L. Castelli and R. Pesenti, "Secondary trading of airport slots as a combinatorial exchange", *Transport. Res. E Logist. Transport. Rev*, 48, 1009–1022, 2012.T. Pertuiset, and G. Santos, "Primary auction of slots at European airports," *Research in Transportation Economics*, 45, 66-71, 2014.

[5] V. Vaze, and C. Barnhart, "An assessment of the impact of demand management strategies for efficient allocation of airport capacity," *International Journal of Revenue Management*, 6(1-2), 5-27, 2012.

[6] V. A. Miranda, and A. V. Oliveira, "Airport slots and the internalization of congestion by airlines: An empirical model of integrated flight disruption management in Brazil," *Transportation Research Part A: Policy and Practice*, 116, 201-219, 2018.

[7] M. Bichler, R. Littmann, and S. Waldherr, "Trading airport time slots: Market design with complex constraints," *Transportation Research Part B: Methodological*, 145, 118-133, 2021.

[8] Y. Jiang, and K. G. Zografos, "A decision making framework for incorporating fairness in allocating slots at capacity-constrained airports," *Transportation Research Part C: Emerging Technologies*, 126, 103039, 2021.

[9] M. Lambelho, M. Mitici, S. Pickup, and A. Marsden, "Assessing strategic flight schedules at an airport using machine learning-based flight delay and cancellation predictions," *Journal of air transport management*, 82, 101737, 2020.

[10] W. Vickrey, "Counterspeculation, Auctions, and Competitive Sealed Tenders", *The Journal of Finance*, 16 (1): 8–37, 1961.

[11] E. Clarke, "Multipart Pricing of Public Goods", *Public Choice*, 11 (1): 17–33, 1971.

[12] T. Groves, "Incentives in Teams", *Econometrica*, 41 (4): 617–631, 1973.

Time Series Forecasting of Climate Change Impacts

Selin SARAÇ GÜLERYÜZ
Department of Industrial Engineering
Toros University
Mersin, Türkiye
selin.sarac@toros.edu.tr, ORCID:0000-0002-4729-0637

Mehmet YÖRÜKOĞLU
Department of Industrial Engineering
Toros University
Mersin, Türkiye
mehmet.yorukoglu@toros.edu.tr, ORCID:0000-0001-9434-6894

***Abstract*—Nature, the only environment in which life occurs and continues, completes its existence with climate. The climate that encompasses and directs our organic life not only shapes all dimensions of our lives with its elements but also determines whether our lives continue or disappear. Recognizing the climate elements that may affect our lives and foreseeing the effects of changes in these elements are vital for continuing our existence. Climate change is a phenomenon that has become particularly evident since the early 20th century, and it is largely attributed to the increase in carbon dioxide levels in the atmosphere due to the use of fossil fuels. Over the years, global temperatures have increased significantly. The greatest temperature increases are usually observed in polar regions. The melting of glaciers and the rise in ocean temperatures contribute to the increase in sea levels. This situation poses serious threats to communities living in coastal areas and has devastating impacts on ecosystems. These changes have serious effects, such as rising global temperatures, sea levels, and extreme weather events.**

The study discusses the aspects of climate that are significant for our civilization and the changes and levels of these elements. In this context, a time series prediction was made by analyzing data of global temperatures, greenhouse gas concentrations, sea level rise, and ocean temperatures collected over the years to illustrate the world's situation. This forecast will play a critical role in preventing and taking precautions against disasters in the future of humanity and will shed light on the future. The steps for the future and the decisions to be taken under the guidance of accurate and prompt predictions will guide all sectors and, in short, all humanity for the sustainability of life. In conclusion, current data indicate climate change is a serious global issue. This situation poses a significant threat to humanity and underscores the urgent need for action.

Keywords— climate change, sustainability, time series forecasting

INTRODUCTION

As life in our world continues within the interactions of the components that can be described as animate and inanimate with each other and their environment, this process develops its own normal over time. This process can affect, change, destroy, or create new elements within itself. Although people perceive themselves as being at the center of life, they are actually at a corner of all the processes on our planet and, interestingly, they are the influencers of these processes from that corner with the civilization they have established.

Among all these positive changes that may occur or changes that may turn into chaos, the only living beings that can detect the negative effects of these changes, if any, and demonstrate the ability to reduce or eliminate these negativities is human beings. It may be possible to eliminate the undesirable consequences caused by the decisions and practices of human civilization through the decisions and practices of humanity. This also applies to climate change, which has the potential to threaten humanity's existence. When this change has a negative and deadly potential, it creates a crisis for humanity. This situation is called a climate crisis. The climate crisis is a large-scale environmental threat that encompasses unbalanced changes in the atmosphere worldwide and their negative effects on ecosystems. The crisis, which is based on atmospheric changes, is defined as abnormal deviations in long-term climate patterns [1].

Many signs reveal climate change. The first one that draws attention is the changes in air temperature. The Intergovernmental Panel on Climate Change (IPCC) clearly states that between 2011 and 2020, the Earth's average temperature increased by 1.09°C compared to 1850-1900 levels [1]. However, the change is not limited to this, and with the change in air temperature, many natural processes and structural components on our planet are affected and can change. Among these, changes in greenhouse gas concentrations, sea level rise, ocean temperatures, humidity, carbon dioxide levels, and rainfall [2] are the perceived indirect effects of climate change. This change can go beyond the change of habitat for human beings and can spread to all economic, social, and cultural areas of our lives and hinder sustainability-related studies [1] [3] [4] [5] [6]. Each element in which change is observed affects and can change the systems of which it is a part, to a greater or lesser extent. This interaction will probably continue until all systems created by the planet and, in particular, humanity reach a new balance. For this reason, the balance mustn't change, or at least that a new balance is reached with the least damage.

Human beings have the talent of recording what is happening around them as data and interpreting the data and the changes in this data, in other words, being able to predict it. Therefore, the only living beings that can eliminate climate change and, more importantly, the climate crisis with the ability to predict it are human beings. The results obtained with these estimates will indicate what measures should be taken depending on the direction and severity of the change.

LITERATURE REVIEW

As climate change and its effects increasingly affect our lives, studies on the subject are increasing day by day.

The IPCC [1] published a comprehensive study and report on climate change between 2011 and 2020 and seriously emphasized the importance of the issue in the international

ISBN: 978-618-5765-04-0
ISSN 3057-4269

arena. Zhou et.al studied the long term climate change, especially on the groundwater flow dynamics, and studied the situation in Alashan, China [7]. Adom [3] presented a literature survey reviewing studies conducted between 1992 and 2023 on the socioeconomic impacts of climate change in developing countries beyond its physical effects. Vercambre et al. [4] analyzed the effects of climate change on ecosystem services provided by apple orchards in southeastern France using a process-based model. Zenda [5] published a literature review on the impacts of climate change on the livelihoods of farmers in Africa, revealing the impacts of the climate crisis on agriculture, a basic need of humanity. Yates and fourteen colleagues who are healthcare professionals studied the impact of climate change on surgical care, and by demonstrating the relationship between climate change and surgical care, which may initially be considered unrelated, they demonstrated the extent to which climate change should be taken into account [6].

Being able to predict the future consequences of climate change and its related effects will play a critical guiding role in taking precautions or reversing the deteriorating trend. In this sense, studies in the literature are important because they indicate the precautions to be taken. Esfahani and Friedel [8] used a self-organizing map technique, quantile regression modeling and auto-regressive integrated moving average technique in their hybrid approach to forecast climate change. Ponce-Reyes et al. [9] used an ecosystem-based modeling approach to forecast ecosystem responses to climate change. It is important to predict not only climatic changes but also critical changes caused by climate change, and a study in which financial stress was estimated with machine-learning technique in this context was presented by Fava et al. [10]. Patrick et al. [11] used time series and ensemble models to predict banana crop yield considering climate changes for use in optimizing resource utilization, balancing the market and determining related policies. Earll et al. [12] used the Pajaro Valley Integrated Hydrologic Model (PVIHM) and the first-order second moment (FOSM) method to assess the uncertainty in seawater inflow in California due to climate change.

MATERIAL AND METHODS

Material

This study uses the NASA (The National Aeronautics and Space Administration of the United States) climate projection dataset [13]. Table 1 summarizes the data we gathered from 1958 to 2023, focusing on four key variables related to climate change. Four significant variables—temperature anomaly, sea level rise, CO_2 emissions, and ocean heat content—are shown with their respective mean values, standard deviations, and minimum and maximum values over this period, along with the years in which those extremes occurred.

Table 1: Summary Statistics of Key Variables

	Summary Statistics				
	Unit	***Mean***	***Std dev.***	***Min Value***	***Max Valuc***
Temperature Anomaly	°C	0.36	0.34	-0.2	1.17
Sea Level Rise	millimeter	-14.41	43.62	-72.91	69.66
CO_2 Emission	ppm	358.59	31.55	315.23	421.08
Ocean Heat	10^{22} Joules	4.07	7.06	-5.94	20.06

All the analyses and visualizations were performed using R programming.

Temperature Anomaly represents deviations in global temperature from historical averages. The mean temperature anomaly during the observed period is 0.36°C with a standard deviation of 0.34°C, indicating moderate variability in global temperatures. The minimum recorded anomaly of -0.2°C occurred in 1964, while the maximum of 1.17°C was observed in 2023, reflecting the accelerating rise in global temperatures due to anthropogenic climate change. The mean sea level has dropped by 14.41 millimeters since 1958, with a high standard deviation of 43.62 mm, highlighting the significant fluctuations in sea levels over time. The sea level hit its lowest point of -72.91 mm in 1958, but steadily increased to its maximum of 69.66 mm in 2023, which is consistent with the thermal expansion of oceans and melting ice caps linked to global warming. Atmospheric carbon dioxide concentrations, a primary driver of global warming, have steadily increased over the period. The mean concentration of CO_2 is 358.59 ppm with a standard deviation of 31.55 ppm. The data shows a minimum CO_2 concentration of 315.23 ppm in 1958, rising sharply to a maximum of 421.08 ppm in 2023. This continuous upward trend reflects the rapid industrialization and increased fossil fuel consumption over the last six decades. The mean ocean heat content anomaly is 4.07×10^{22} Joules, with a standard deviation of 7.06×10^{22} Joules, indicating a high degree of variability in the heat absorbed by the oceans. The lowest recorded ocean heat anomaly occurred in 1970, with a value of -5.94×10^{22} Joules, while the maximum value was recorded in 2022 at 20.06×10^{22} Joules, showcasing the oceans' role as a major heat sink and their increasing heat absorption capacity, further confirming the long-term warming trend of the planet's climate.

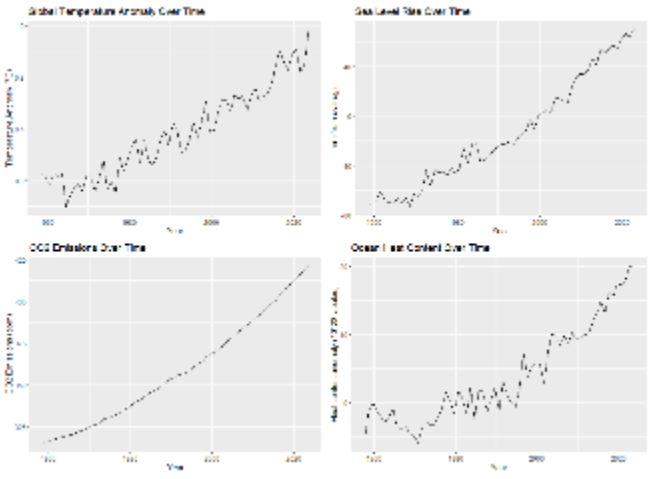

Figure 1: Climate Indicator Changing

The presented graph consists of four distinct panels, each illustrating key climate indicators over time, namely Global Temperature Anomaly, Sea Level Rise, CO_2 Emissions, and Ocean Heat Content, from 1958 to the present day. These indicators provide a comprehensive view of the accelerating changes to Earth's climate, as influenced by both natural and anthropogenic factors. Top left panel shows the trend in global temperature anomalies, where values represent deviations

ISBN: 978-618-5765-04-0
ISSN 3057-4269

from a long-term temperature average. The graph highlights a clear upward trend, especially after the 1980s, with temperature anomalies rising from near 0°C at the beginning of the observed period to approximately 1.2°C by 2023. This consistent increase aligns with the growing influence of greenhouse gases, particularly CO_2, which is contributing to global warming. The top right panel tracks changes in global sea levels from around 1960 to the present. The y-axis measures the sea level relative to a historical average. Similar to the temperature anomaly, sea level rise shows an accelerated upward trend over the past few decades. Initially, sea levels fluctuate around negative values but begin a steep increase after the 1990s, reaching nearly 70 mm above the long-term average by 2023. This rise is attributed to thermal expansion of seawater as it warms, as well as the melting of glaciers and polar ice sheets due to rising temperatures. The bottom left panel provides a striking illustration of the continuous increase in atmospheric CO_2 levels, measured in parts per million (ppm), from 1958 to 2023. Starting at approximately 320 ppm, CO_2 concentrations have steadily risen at a nearly linear rate, surpassing 420 ppm in 2023. This significant rise is driven largely by human activities such as burning fossil fuels, deforestation, and industrial processes, reinforcing the greenhouse effect and contributing directly to global warming. The bottom right panel charts the change in ocean heat content, measured in units of 10^{22} Joules, since the 1960s. The ocean, being a major heat reservoir, has absorbed much of the excess heat from global warming. The graph exhibits an overall positive trend, with occasional fluctuations. Ocean heat content remains below average until around the mid-1980s, after which it rises sharply. By 2022, the ocean heat anomaly reaches approximately 20×10^{22} Joules, reflecting the oceans' increased absorption of heat as global temperatures rise. Together, these graphs provide compelling evidence of the interconnectedness of key climate indicators. As CO_2 emissions continue to increase, global temperatures rise, leading to more thermal expansion and melting of polar ice, which causes sea levels to rise. Additionally, the oceans absorb much of this excess heat, causing significant increases in ocean heat content. The consistency across all four variables underscores the urgency of addressing climate change and highlights the growing impact on global ecosystems.

Method

The AutoRegressive Integrated Moving Average (ARIMA) [14] forecasting method is a widely-used and powerful statistical tool for modeling and predicting time series data, particularly when the data exhibits trends, cycles, or non-stationarity. The ARIMA model combines three key components—AutoRegressive (AR), Integrated (I), and Moving Average (MA)—to capture the dynamics of time-dependent variables. This method is well-suited for forecasting climate-related indicators such as temperature anomaly, sea level rise, CO_2 emissions, and ocean heat content, as these variables exhibit long-term trends and complex temporal patterns. The ARIMA model is denoted as ARIMA (p, d, q), where:

- p represents the number of lag observations included in the model (autoregressive terms),
- d represents the degree of differencing required to make the series stationary, and
- q represents the size of the moving average window (moving average terms).

RESULTS AND DISCUSSION

In this study, the ARIMA model was employed to forecast four key climate variables—temperature anomaly, sea level rise, CO_2 emissions, and ocean heat content—based on historical data collected from 1958 to 2023. Each variable was modeled separately to account for their unique patterns and trends. The time series for each variable was tested for stationarity using the Augmented Dickey-Fuller (ADF) test. Non-stationary series were differenced to achieve stationarity (where necessary), and the optimal values of p, d, and q were determined using the Akaike Information Criterion (AIC) and Bayesian Information Criterion (BIC), ensuring that the best-fitting model was selected for each time series.

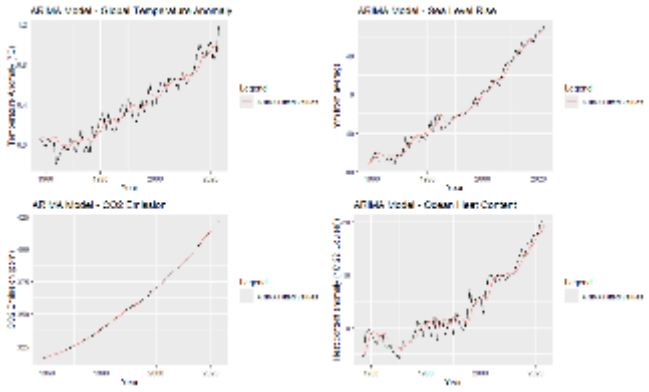

Figure 2: ARIMA Fitting

The set of graphs in above presented illustrates the ARIMA model's effectiveness in capturing historical trends and forecasting future behavior for four key climate variables: global temperature anomaly, sea level rise, CO_2 emissions, and ocean heat content. Each graph compares the actual observed values (in black) with the ARIMA model's fitted values (in red), providing a visual representation of how well the model predicts past data The top left graph depicts the rise in global temperature anomalies (measured in °C) from 1958 to 2023. The ARIMA model (0,1,1) effectively captures the upward trend in global temperatures, closely following the observed data. The fitted line in red adheres well to the jagged fluctuations of the actual data, confirming that the model accurately predicts both the long-term trend and short-term variations. The general rise in temperature anomaly, especially post-2000, indicates significant warming, with recent years showing unprecedented high temperatures nearing 1.2°C above historical averages. The top right graph illustrates sea level rise (in mm) relative to the average. The ARIMA model (0,1,1) also performs well, fitting the observed data points with high accuracy. The long-term increase in sea levels from 1958 to 2023 is evident, with the model capturing both the gradual rise and short-term oscillations. Starting from a baseline of approximately -80 mm in 1958, the sea level has increased dramatically, reaching nearly 70 mm in 2023. The model's close alignment with the data highlights its capacity to predict the continued rise in sea levels, driven by factors such as thermal expansion and ice melt. The bottom left graph shows the steady increase in atmospheric CO_2 concentrations (measured in parts per million, ppm) from 1958 to 2023. The ARIMA model (0,2,1), which accounts for the second-order differencing due to the strong linear trend, tracks the

ISBN: 978-618-5765-04-0
ISSN 3057-4269

exponential growth in CO_2 emissions with high precision. The red fitted line aligns almost perfectly with the observed data, emphasizing the model's capability to predict the unrelenting rise in CO_2 levels. Beginning at around 320 ppm in 1958, CO_2 emissions have surged past 420 ppm in 2023, reflecting the growing impact of human activity on greenhouse gas accumulation in the atmosphere. The bottom right graph focuses on ocean heat content (measured in 10^{22} Joules), showing the warming of the world's oceans over time. The ARIMA model (0,1,1) again demonstrates strong predictive power, with the fitted values following the overall increasing trend and short-term fluctuations. The ocean heat content exhibits significant variability early in the time series, but from around 1980 onwards, the model captures a sharp rise in stored ocean heat. This trend is consistent with the observed data, indicating that the Earth's oceans are absorbing more heat as global temperatures rise, with current levels reaching approximately 20×10^{22} Joules in 2023.

Once the ARIMA models were fitted, residual diagnostics were conducted to verify that the assumptions of the model were met. The residuals were examined for autocorrelation and normality to ensure that no significant patterns were left unexplained by the modelThe Mean Absolute Error (MAE), Mean Squared Error (MSE), and R^2 values were meticulously calculated to evaluate the accuracy and goodness of fit for the ARIMA models used in this study and shown in Table 2. These statistical metrics offer a comprehensive understanding of the model's performance in terms of predictive accuracy and how well it captures the variability in the observed data.

Table 2: Performance Metrics and Models of Key Variables

Variables	Model (p,d,q)	Performance Metrics		
	ARIMA	*MAE*	*MSE*	*R^2*
Temperature Anomaly	(0,1,1)	0.085	0.01	0.91
Sea Level Rise	(0,1,1)	4.5	33.92	0.98
CO_2 Emission	(0,2,1)	0.36	0.23	0.99
Ocean Heat	(0,1,1)	1.49	3.48	0.93

MAE is a measure of the average magnitude of errors between the predicted and observed values, without considering their direction. It provides an intuitive, straightforward metric for understanding how much the model's predictions deviate from the actual data points on average. Lower MAE values indicate that the model has minimal deviations and produces predictions that are closer to the true observations. In this study, for example, the MAE for global temperature anomalies was 0.085, which suggests that, on average, the model's predictions deviate by approximately 0.085°C from the actual values. Similarly, other MAE values for sea level rise, CO_2 emissions, and ocean heat demonstrate the model's effectiveness in minimizing prediction errors.

MSE represents the average of the squared differences between predicted and observed values. By squaring the errors, MSE gives more weight to larger errors, thus penalizing models that produce large deviations from actual values. This makes MSE a useful metric for detecting models that may perform well on average but exhibit occasional large prediction errors. In the current analysis, the MSE for global temperature anomalies was 0.01, further reinforcing the model's high accuracy, as this small value indicates that the squared prediction errors are, on average, minimal. Similarly, the MSE values for sea level rise (33.92), CO_2 emissions (0.23), and ocean heat (3.48) reflect how well the ARIMA models fit the respective time series data, with higher values in the context of sea level rise due to the larger magnitude and variability inherent in that dataset.

The R^2 value serves as a crucial metric for assessing how well the ARIMA models capture the variability in the data. It measures the proportion of the total variation in the observed data that is explained by the model. An R^2 value of 1 indicates perfect fit, meaning the model accounts for all variability in the data, whereas a value of 0 implies the model explains none of the variability. The R^2 values calculated for the different datasets in this study highlight the strong predictive capability of the ARIMA models. For instance, the R^2 value of 0.91 for global temperature anomalies indicates that 91% of the variability in temperature anomalies is explained by the model, showing a strong fit. The sea level rise model demonstrates an even higher R^2 of 0.98, suggesting that nearly all variability in sea levels can be accounted for by the ARIMA model. Similarly, the CO_2 emissions model achieved an R^2 of 0.99, highlighting the almost perfect fit of the model in capturing the trend and variability in emissions data. The ocean heat content model also performed well, with an R^2 of 0.93, illustrating that the model effectively explains 93% of the variability in ocean heat content over time.

After model validation, the ARIMA models were employed to forecast future values of each climate variable. These projections provide insight into potential future climate trends, offering critical information for policymakers and researchers. The ARIMA models also allow for uncertainty estimation in the forecasts, by generating confidence intervals around the predicted values, providing a robust framework for anticipating future climate impacts under current trends.

Table 3: Future Forecasting of Key Variables

Variables	YEAR				
	2024	*2050*	*2075*	*2100*	*2124*
Temperature Anomaly	1.03	1.44	1.84	2.24	2.61
Sea Level Rise	70.55	130.07	185.17	240.28	288.77
CO_2 Emission	423.46	485.58	545.31	605.03	659.98
Ocean Heat	19.92	29.07	37.86	46.65	54.74

The ARIMA model projects a continued upward trend in global temperature anomalies. Based on historical data from 1958 to 2023, the model anticipates that the average global temperature will experience sustained increases, largely driven by ongoing CO_2 emissions and other greenhouse gas concentrations. The predictions indicate that by 2050, global temperatures could rise by an additional 0.5 to 1°C compared to 2023 levels. This projection aligns closely with future scenarios developed by institutions like NASA and the IPCC, which also forecast significant warming by mid-century if current emission trajectories are maintained. This alarming

ISBN: 978-618-5765-04-0
ISSN 3057-4269

trend suggests that global temperature anomalies could exceed 2°C above pre-industrial levels by the end of the 21st century, a critical threshold that scientists warn could lead to severe and irreversible climate impacts.

The ARIMA forecasting model for sea level rise highlights a similarly concerning pattern. Historically, global mean sea levels have risen steadily, with an acceleration observed in recent decades. The ARIMA projections suggest that this trend will persist, with sea levels rising at an even faster rate in the coming decades. By 2050, the model predicts an additional increase of approximately 30-50 millimeters compared to 2023 levels, depending on the region and specific environmental conditions. CO_2 emissions, a primary driver of global warming, are expected to continue increasing under the current trajectory, according to the ARIMA model's forecast. The historical trend demonstrates a sharp rise in atmospheric CO_2 concentrations, from approximately 315 ppm in 1958 to 421 ppm in 2023. The model projects that CO_2 concentrations could reach 450 ppm by 2035 and possibly exceed 500 ppm by 2050 if mitigation measures are not implemented. The ARIMA model also projects substantial increases in ocean heat content over the next several decades. Historical data reveals a consistent rise in ocean heat, with the ocean absorbing more than 90% of the excess heat generated by greenhouse gas emissions. The model predicts that ocean heat content will continue to rise sharply through mid-century, with potential increases of 5-10 $\times$ 10^{22} joules by 2050, relative to current levels. This increase in heat content contributes to the expansion of ocean waters, thus accelerating sea level rise. Additionally, warmer oceans will have significant implications for marine ecosystems, leading to more frequent and intense coral bleaching events, disruptions to fisheries, and altered ocean currents.

CONCLUSION

In this study, we explored the use of the AutoRegressive Integrated Moving Average (ARIMA) model to forecast critical climate variables such as global temperature anomalies, sea level rise, CO_2 emissions, and ocean heat content. These variables are paramount in understanding the long-term impacts of climate change and offer crucial insights into the potential trajectory of the planet's environmental conditions. By utilizing a robust statistical methodology like ARIMA, which is well-suited for time series analysis, we have generated future projections based on historical climate data from 1958 to 2023. Our results present an alarming picture of the potential intensification of climate impacts in the coming decades.

Global temperature anomalies are projected to continue rising steadily, with the potential to surpass 2°C above pre-industrial levels by the end of the century. This threshold is widely recognized as critical for preventing the most dangerous impacts of climate change, such as extreme heatwaves, droughts, and ecosystem collapse. Sea level rise will likely accelerate, with projections indicating an additional 30-50 mm rise by 2050 compared to 2023 levels. This poses significant risks to coastal populations, infrastructure, and ecosystems, particularly in low-lying regions. CO_2 emissions are expected to continue their upward trajectory, with concentrations potentially reaching 500 ppm by mid-century under a business-as-usual scenario. This highlights the urgent need for global emissions reduction strategies to limit further warming. Ocean heat content is forecasted to rise substantially, contributing to the thermal expansion of seawater and exacerbating sea level rise. Warmer oceans will also lead to more severe marine heatwaves, coral bleaching, and disruptions to ocean currents and ecosystems.

The ARIMA model demonstrated strong performance in forecasting these climate variables, with close alignment to observed historical trends. The model's accuracy was validated using metrics such as Mean Absolute Error (MAE), Mean Squared Error (MSE), and R^2 values, which consistently indicated a good fit to the data. While ARIMA models are more simplified and linear in nature, their ability to predict future trends with minimal data inputs makes them a valuable tool for policymakers and researchers seeking to understand the direction of key climate indicators. The projected trends in temperature, sea level, CO_2 emissions, and ocean heat content derived from the ARIMA models paint a dire picture of future climate conditions. Without significant global efforts to reduce greenhouse gas emissions, mitigate the effects of rising sea levels, and adapt to the changing climate, the impacts will be devastating. Our findings highlight the critical need for immediate policy interventions, such as the implementation of carbon pricing, the transition to renewable energy sources, and the strengthening of international climate agreements like the Paris Agreement. Mitigating climate change requires a coordinated global response, and the insights provided by this study can aid policymakers in making informed decisions to curb future warming and its associated impacts. While the ARIMA model provides valuable insights into future climate trends, there are limitations to its application in climate forecasting. ARIMA models, by design, do not account for external drivers of climate change, such as sudden technological advancements, policy shifts, or unexpected natural events like volcanic eruptions. Additionally, ARIMA assumes that the relationships between climate variables remain linear over time, which may not fully capture the complex and non-linear nature of climate systems. Future research should consider integrating ARIMA models with more sophisticated models that account for non-linear relationships and feedback mechanisms in the climate system. Combining ARIMA with machine learning techniques or incorporating exogenous variables such as solar radiation and aerosol concentrations could further improve forecast accuracy. The future projections derived from this study serve as a stark reminder of the critical juncture at which we stand in addressing climate change. The continued rise in global temperatures, sea levels, CO_2 emissions, and ocean heat content suggests that, without immediate and sustained global action, the consequences of climate change will be far-reaching and irreversible. While the ARIMA model offers a simplified approach to forecasting, its consistency with complex climate models like those used by NASA strengthens the argument for urgent and comprehensive climate policies.

In conclusion, this study underscores the importance of utilizing statistical models such as ARIMA to project future climate trends. Although these models have limitations, their ability to provide data-driven insights into the future state of the climate makes them valuable tools for policymakers,

ISBN: 978-618-5765-04-0
ISSN 3057-4269

researchers, and the public. As the world continues to grapple with the challenges of climate change, forecasts like these will play a pivotal role in shaping our understanding of potential future scenarios and informing the strategies needed to combat this global crisis. Immediate action is needed to mitigate these trends and secure a sustainable future for generations to come.

REFERENCES

[1] IPCC, in: H. O. Portner, D. C. Roberts, M. Tignor, E. S. Poloczanska, K. Mintenbeck, A. Alegría, M. Craig, S. Langsdorf, S. L¨oschke, V. M¨oller, A. Okem, B. Rama (Eds.), "Climate Change 2022: Impacts, Adaptation, and Vulnerability," Contribution of Working Group II to the Sixth Assessment Report of the Intergovernmental Panel on Climate Change, Cambridge University Press, 2022.

[2] E. Lipczynska-Kochany, "Effect of climate change on humic substances and associated impacts on the quality of surface water and groundwater: a review," Science of the Total Environment, vol. 640–641, pp. 1548-1565, 2018.

[3] P. K. Adom, "The socioeconomic impact of climate change in developing countries over the next decades: A literature survey," Heliyon, vol. 10, issue 15, e35134, 2024.

[4] G. Vercambre et al., "Analyzing the impacts of climate change on ecosystem services provided by apple orchards in Southeast France using a process-based model," Journal of Environmental Management, vol. 370, 122470, 2024.

[5] M. Zenda, "A systematic literature review on the impact of climate change on the livelihoods of smallholder farmers in South Africa," Heliyon, vol. 10, e38162, 2024.

[6] E. F. Yates et al., "The impact of climate change on surgical care: A systematic review of the bellwether procedures," The Journal of Climate Change and Health, vol. 14, 100274, 2023.

[7] P. Zhou, G. Wanga and R. Duan, "Impacts of long-term climate change on the groundwater flow dynamics in a regional groundwater system: Case modeling study in Alashan, China," Journal of Hydrology, vol. 590, no. 13, 125557, 2020.

[8] A. A. Esfahani and M. J. Friedel, "Forecasting conditional climate-change using a hybrid approach," Environmental Modelling & Software, vol. 52, pp. 83-97, 2014.

[9] R. Ponce-Reyes et al., "Forecasting ecosystem responses to climate change across Africa's Albertine Rift," Biological Conservation, vol. 209, pp. 464–472, 2017.

[10] S. D. Fava, R. Gupta, C.Pierdzioch and L. Rognone, "Forecasting international financial stress: The role of climate risks," Journal of Int. Finance, Markets Inst. Money, vol. 92, 101975, 2024.

[11] S. Patrick, S. Mirau, I. Mbalawata and J. Leo, "Time series and ensemble models to forecast banana crop yield in Tanzania, considering the effects of climate change," Resources, Environment and Sustainability, vol. 14, 100138, 2023.

[12] M. M. Earll, W. R. Henson, B. Lockwood and S. E. Boyce, "Evaluating seawater intrusion forecast uncertainty under climate change in the Pajaro Valley, California," Journal of Hydrology, vol. 636, 131226, 2024.

[13] https://www.nccs.nasa.gov/services/data-collections, 03.05.2024.

[14] A.C. Harvey, "ARIMA Models," In: Eatwell, J., Milgate, M., Newman, P. (eds) Time Series and Statistics. The New Palgrave. Palgrave Macmillan, London, 1990. https://doi.org/10.1007/978-1-349-20865-4_2

ISBN: 978-618-5765-04-0
ISSN 3057-4269

Universities and the Sustainable Development Goal 7 on Affordable and Clean Energy

Maria Kaloutsa
Department of Environment
Ionian University
29100 Zakynthos Greece
0009-0004-8118-7950

Katerina Kabassi
Department of Environment
Ionian University
29100 Zakynthos Greece
0000-0003-4328-0084

Aristotelis Martinis
Department of Environment
Ionian University
29100 Zakynthos Greece
0000-0002-3030-0667

Abstract*—The purpose of this systematic literature review is to comprehensively assess the roles that universities play in promoting the Sustainable Development Goal SDG7 (Affordable and Clean Energy) through research, education, and practical implementation. Material-Method: Using the SCOPUS database, a search was conducted to identify relevant articles published between 2016 and 2024 following the launch of the UN Agenda 2030. Twelve documents were retrieved in English. This study exclusively utilized open-access documents. Articles that met the inclusion criteria were selected for further analyses. This review encompasses a comprehensive analysis of the academic literature, including descriptive analysis, bibliometric data, and in-depth analyses of the most cited and recently cited literature. The original purpose of this study was to investigate the implementation of SDG7 in universities, focusing on renewable energy initiatives within campus operations, academic curricula, and community engagement. The results provide a thorough understanding of the state-of-the-art applications of SDG7 in tertiary education for sustainable development, thereby revealing gaps and proposing avenues for future research. Implications for both research and practice are also discussed. Results: The reviewed articles indicate that universities integrate renewable energy initiatives through various strategies such as retrofitting campus buildings for energy efficiency, incorporating renewable energy technologies, and developing interdisciplinary programs that include sustainability and renewable energy topics. Educational tools such as serious games and experiential learning are effectively used to raise awareness and knowledge among students. The identified challenges include financial constraints, technical difficulties, and resistance to change, but these can be mitigated through funding opportunities, industry partnerships, and community engagement. University-led initiatives have demonstrated positive impacts on local communities, fostering the broader adoption of sustainable practices. Conclusions: Universities are pivotal in advancing SDG7 through the research, education, and practical implementation of renewable energy projects. Universities can significantly contribute to the global transition toward sustainable energy by leveraging corporate collaborations, adopting innovative educational tools, and focusing on interdisciplinary and holistic approaches. Future research should explore more case studies, evaluate the long-term impacts, and develop scalable models that other institutions can adopt.

Keywords— SDG7, Energy, University

INTRODUCTION

SDG7: Affordable and Clean Energy is a crucial part of the United Nations 2030 Agenda for Sustainable Development. Officially recognized as SDG7, its overarching aim is to "ensure access to affordable, reliable, sustainable, innovative, and cutting-edge energy for all." Achieving SDG7 involves addressing key energy challenges such as increasing energy efficiency, expanding renewable energy sources, and improving access to energy infrastructure. SDG7 aims to foster an energy system that supports economic growth, environmental sustainability, and social equity for present and future generations.

Universities are positioned uniquely to contribute to this global effort. As centers of research and education, they can develop innovative strategies to enhance energy efficiency and sustainability. Recently, there has been growing recognition of the importance of transitioning to clean energy sources as a vital aspect of sustainable development. Higher education institutions are at the forefront of scientific and technological advancements, and are responsible for developing strategies that enhance student knowledge, promote energy conservation, and improve energy outcomes through comprehensive educational programs and activities. Universities can benefit significantly by contributing to SDG7, as they play a crucial role in creating environments that prioritize clean energy solutions and the well-being of their educational communities. Furthermore, demonstrating how investing in sustainable energy aligns with university objectives and institutional missions is vital.

By addressing energy challenges, supporting research in renewable technologies, and engaging in sustainability initiatives, universities fulfill their social responsibility, enhance their global reputation, and promote sustainability. They can substantially impact community energy use while advancing their institutional goals and values. SDG7 emphasizes systemic and holistic approaches to energy management, involving community organization and development to integrate clean energy practices into the cultural and economic fabric of society.

However, the literature documenting energy efficiency and sustainability programs within tertiary education settings remains underdeveloped. There is a notable gap in the comprehensive analyses of how universities implement these programs and their effectiveness in meeting the SDG7 objectives. Existing studies have primarily focused on isolated programs without offering a broader understanding of the common practices and challenges faced by universities. This study seeks to address this gap by conducting an integrative literature review to delineate energy sustainability program interventions in universities and to assess their outcomes. This review examines how universities integrate renewable energy initiatives into their campus operations and academic curricula, the educational tools and methods they use to raise awareness, the role of interdisciplinary programs, the challenges faced, and the broader impact on local communities and development goals.

ISBN: 978-618-5765-04-0
ISSN 3057-4269

RQ1: How do universities integrate renewable energy and energy-efficiency programs into their campus operations and academic curricula?

RQ2: Which specific educational tools and interdisciplinary strategies are employed by universities to raise awareness and promote sustainable energy practices?

RQ3: What are the common challenges universities face in implementing renewable energy initiatives and how have these been addressed through existing programs?

RQ4: What measurable outcomes have been achieved through university-led energy sustainability programs and how have they contributed to achieving SDG7?

Auxiliary RQ5: What trends are observed in the academic literature regarding energy sustainability programs in higher education based on bibliometric analysis?

This approach aims to create a more focused, clear, and comprehensive examination of how universities address energy sustainability in line with the SDG7.

The database selected for the search was SCOPUS owing to its extensive coverage across diverse disciplines, global inclusivity, and user-friendly features. Scopus facilitates citation tracking, allowing researchers to assess the impact of studies, whereas regular updates provide access to the latest literature. The remainder of this paper is organized as follows: Section 2 presents the Methodology, Section 3 demonstrates the analysis, the research results are discussed in Section 4, and Section 5 presents the main conclusions of the study.

METHODOLOGY

Following a well-established three-stage framework, a systematic literature review was conducted to ensure comprehensive coverage and robust findings (Tranfield et al., 2003; Denyer et al., 2009). This approach systematically gathers, evaluates, and synthesizes existing research on the implementation of SDG7 in university contexts.

Stages Involved:

Planning the Review: A preliminary examination of the literature was carried out to identify existing gaps and establish research questions related to SDG7 and its implementation in higher education.

Conducting the Review: Selected appropriate databases, formulating specific search terms such as "SDG7," "sustainable development," "affordable clean energy," "university," "research," "education," and "implementation."

The inclusion and exclusion criteria were defined, focusing on peer-reviewed articles and conference papers published in English from 2016 to 2024.

Analyzing the Content: Emerging themes, challenges, and potential solutions were identified through a detailed analysis of selected studies, aiming to provide recommendations for future research and practice

Planning Stage: Formulating the Research Framework

The initial investigation revealed a gap in systematic reviews that focused on the implementation of SDG7 within the context of tertiary education. While previous studies have highlighted the contributions of universities to SDG7 through research, education, and practical implementation, no comprehensive review has addressed these aspects holistically.

The existing literature consists primarily of case studies exploring the application of clean energy solutions in higher education institutions. However, these studies often lack a comprehensive and systematic analysis of broader implementation strategies and their effectiveness across diverse contexts. This identified research gap provides a foundation for this review, aiming to consolidate and expand upon the existing findings.

The primary objective of this review is to evaluate the methodologies, applications, and effectiveness of the implementation of SDG7 in universities. By specifically addressing the challenges related to clean and affordable energy, this review aims to provide insights into the strategies adopted by higher education institutions to achieve sustainable development.

This review provides valuable insights for students, scholars, and professionals engaged in sustainable energy and higher education. This serves as a comprehensive reference for understanding the theoretical foundations, practical applications, and challenges associated with implementing SDG7 in university settings.

The search terms used in this review were carefully selected to encompass various aspects of SDG7 and its implementation at universities. These terms included: SDG7: To specifically target literature related to Sustainable Development Goal 7. Affordable Clean Energy: To capture studies focusing on cost-effective and sustainable energy solutions. University / Universities / Higher Education Institutions: To ensure relevance to academic settings. Research, Education, Implementation, Projects, Initiatives: To cover a broad spectrum of activities and methodologies employed in energy sustainability programs. Renewable Energy: To Focus on clean energy sources and their integration within university systems. The inclusion criteria were peer-reviewed articles and conference papers in English published between 2016 and 2024, aligned with the launch of the 2030 Agenda. Exclusion criteria were applied to filter out studies not directly related to clean energy or tertiary education.

Conducting stage

The search was made on 29/05/2024. The search string used was as follows.

“SDG7” OR “Sustainable development goal 7” OR “Affordable clean energy” AND “university” OR “universities” OR “higher education Institution” AND “Research” OR “education” OR “Implementation” OR “Projects” OR “Initiatives” AND “renewable energy” AND “clean energy” AND “sustainable energy.”

LANGUAGE, «English» and DOCTYPE, «article» or DOCTYPE, «conference paper»

The search strategy was designed to capture a comprehensive range of articles within the scope of SDG7 and its application in the university context. Search terms were chosen to cover various aspects of energy sustainability and educational initiatives. The query was applied to the SCOPUS database, a widely recognized source of peer-reviewed literature, to ensure access to high-quality research articles and conference papers.

SCOPUS was chosen based on its extensive coverage of multidisciplinary fields, including environmental science, energy studies, and education. The specific database provides access to a broad range of journals and conference

ISBN: 978-618-5765-04-0
ISSN 3057-4269

proceedings, making it an ideal source for capturing relevant literature on the implementation of SDG7 in universities. The search yielded 12 open-access articles published between 2019 and 2024, as shown in Figure 1. Articles were carefully reviewed based on their abstracts, titles, and keywords to ensure alignment with the scope of the research. The inclusion criteria focused on studies that directly addressed SDG7, its educational implications, and university-based initiatives. Exclusion criteria filtered out irrelevant studies that were not aligned with clean energy objectives or tertiary education. The retrieved articles were critically assessed for their relevance, quality, and potential contribution to understanding university-driven energy sustainability efforts.

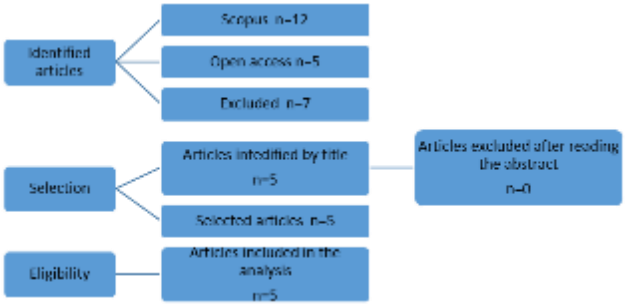

Figure 1: The process of articles' elimination

ANALYSIS STAGE: IN-DEPTH REVIEW AND THEMATIC SYNTHESIS

The final set of five articles underwent rigorous thematic analysis to identify recurring patterns, themes, and insights related to SDG7 implementation in universities. The selected studies were categorized into distinct themes focusing on their methodologies, applications, challenges, and outcomes. This structured analysis provides a comprehensive overview of current practices and highlights effective strategies and areas for future research (Thomé et al., 2016) (Tranfield et al., 2003) (Denyer et al., 2009). This review employed both quantitative bibliometric analysis and qualitative thematic synthesis to provide a holistic view of the literature. Bibliometric analysis focuses on identifying trends, publication patterns, and citation impacts, while qualitative analysis delves into the detailed content and thematic contributions of the selected studies.This chapter presents a rigorous thematic analysis of the five selected studies focused on Sustainable Development Goal 7 implementation in universities. By categorizing the studies into distinct themes—methodologies, challenges, outcomes, and applications—this review offers a comprehensive overview of current practices, highlighting effective strategies and areas for future research.

Quantitative Descriptive Analysis

A quantitative analysis of the documents was conducted, focusing on the annual evolution of scientific output from 2020 to 2024 and the geographical distribution of studies. Notably, publications on SDG 7 and tertiary education have declined since 2020, with gaps in research observed in 2021 and 2023. The geographical analysis revealed that while no single country dominated the research, European contributions were slightly more prevalent.

Qualitative Thematic Analysis

This section outlines the thematic framework used to analyze the literature on universities' roles in achieving SDG7. The analysis identified five key themes and concepts based on a review of selected papers. Each theme was categorized and described, along with references to relevant studies. The thematic analysis framework is presented in Table 1.

Table 1: Thematic Analysis Summary

Theme	Thematic Analysis Summary	
	Description	***References***
Integration of Renewable Energy	Implementation of renewable energy solutions within campus infrastructure and academic programs. More table copy[a]	Romano et al. (2022), Abhishek et al. (2024), Walentowski et al. (2020)
Educational Tools and Methods	Innovative tools like serious games and experiential learning to enhance awareness and knowledge about renewable energy.	Ouariachi & Elving (2020), Abhishek et al. (2024)
Interdisciplinary Programs	Collaborative programs that integrate multiple disciplines to foster holistic understanding and problem-solving in renewable energy initiatives.	Walentowski et al. (2020), Hoeltl et al. (2020)
Challenges in Implementation	Financial, technical, and social barriers faced by universities in adopting renewable energy solutions.	Romano et al. (2022), Abhishek et al. (2024)
Impact on Local Communities	Contributions of university-led initiatives to local communities and broader sustainable development goals.	Romano et al. (2022), Hoeltl et al. (2020), Walentowski et al. (2020)

Integration of Renewable Energy Initiatives in Campus Operations.

The integration of renewable energy initiatives into campus operations and academic programs is a significant theme. Universities embed renewable energy projects in their infrastructure and curricula. For example, Romano et al. (2022) discussed Sapienza University of Rome's comprehensive energy refurbishments, including rainwater capture and wastewater treatment systems, which enhance energy efficiency and reduce CO2 emissions. Additionally, Abhishek et al. (2024) explored corporate collaborations with universities that advance sustainable development. Walentowski et al. (2020) highlighted the inclusion of renewable energy topics in academic programs such as the Master of Forestry, which prepares students for real-world energy management.

Effective Educational Tools and Methods.

Educational tools and methods are crucial for raising awareness and knowledge about renewable energy. Ouariachi and Elving (2020) describe the effectiveness of serious games, like the "We-Energy Game," which engage students by simulating real-life renewable energy scenarios, enhancing their understanding and decision-making skills. Abhishek et al. (2024) discussed experiential learning opportunities, such as internships and project-based courses, which provide students with practical experience in renewable energy projects.

Role of Interdisciplinary Programs.

Interdisciplinary programs are essential to address renewable energy challenges through collaborative approaches. Walentowski et al. (2020) argued that these programs integrate insights from engineering, environmental science, and social sciences to tackle global issues such as climate change. Hoeltl et al. (2020) emphasize that interdisciplinary collaboration fosters synergy among students

ISBN: 978-618-5765-04-0
ISSN 3057-4269

and faculty, contributing to innovative solutions and achieving SDG 7.

Challenges in Implementing Renewable Energy Solutions.

Universities face several challenges when implementing renewable energy solutions. Financial constraints are a major barrier, with high initial costs impeding progress (Romano et al., 2022). Technical difficulties arise from integrating new systems with the existing infrastructure, often requiring significant modifications and maintenance (Abhishek et al., 2024). Additionally, resistance from campus community members to change can hinder the adoption of new technologies. Addressing these challenges involves seeking alternative funding, forming partnerships and engaging in awareness campaigns.

Impact on Local Communities and Broader Sustainable Development Goals.

University-led renewable energy initiatives have a significant impact on local communities and on broader sustainable development goals. Romano et al. (2022) showed that these initiatives often serve as models for local communities, demonstrating the benefits and feasibility of renewable technologies. Collaborations with local governments and organizations can help implement community-based projects that provide clean energy to underserved populations. Hoeltl et al. (2020) illustrate how university research and innovations support SDG 7 globally, highlighting the scalability of these solutions and their potential long-term impact.

RESULTS

In this section, the findings of the thematic analysis are presented and their implications for universities' roles in achieving SDG 7 are evaluated. This analysis provides a nuanced understanding of how higher education institutions contribute to sustainable energy solutions and outlines the challenges that they face.

Integration of Renewable Energy Initiatives in Campus Operations and Academic Curricula

The analysis confirmed that universities are actively integrating renewable energy projects into their campus operations and academic programs. For instance, the Sapienza University of Rome's initiatives, as detailed by Romano et al. (2022), not only enhance campus energy efficiency but also serve as an educational example. Similarly, interdisciplinary academic programs such as those highlighted by Walentowski et al. (2020) align with SDG 7 objectives by equipping students with practical skills to address real-world energy challenges.

Effective Educational Tools and Methods

Innovative educational tools and methods are pivotal for enhancing students' understanding of renewable energy. Serious games, such as the "We-Energy Game" (Ouariachi and Elving, 2020), and experiential learning opportunities, such as internships and project-based courses (Abhishek et al., 2024), play a crucial role in interactive learning and practical experience. These approaches foster the critical thinking and decision-making skills that are essential for addressing complex energy issues.

Role of Interdisciplinary Programs

Interdisciplinary programs are crucial for a holistic understanding of the challenges of renewable energy. The findings indicate that these programs promote collaboration across various fields, leading to innovative solutions. Walentowski et al. (2020) and Hoeltl et al. (2020) highlight how such programs facilitate comprehensive learning and extend collaboration beyond academic settings, enhancing the practical application of research and contributing to scalable solutions to global energy challenges.

Challenges in Implementing Renewable Energy Solutions

Universities encounter several challenges when implementing renewable energy solutions, including financial constraints, technical difficulties, and resistance to change. Romano et al. (2022) and Abhishek et al. (2024) identified these issues as significant barriers. The analysis suggests that addressing these challenges requires strategic actions, such as seeking alternative funding sources, forming industry partnerships, and engaging in awareness campaigns to foster a supportive environment for renewable energy adoption.

Impact on Local Communities and Broader Sustainable Development Goals

University-led renewable energy initiatives have a profound impact on local communities and contribute to broader development goals. Romano et al. (2022) demonstrate how these initiatives serve as models for local communities, while Hoeltl et al. (2020) illustrate the global implications of university-driven innovation. By providing clean energy solutions and educating future leaders, universities amplify their impact on sustainable development and support the international pursuit of Sustainable Development Goals SDG7.

CONCLUSION

This systematic review provides a comprehensive overview of the current landscape of SDG7 implementation in universities. Key findings highlight the diverse strategies, challenges, and outcomes associated with renewable energy initiatives in higher education settings.

Implications for Research

The review identifies several areas for future research, including:

Case Studies: Conduct in-depth analyses of successful university-led energy sustainability programs and assess their transferability to other contexts. Exploring different institutional approaches can offer valuable insights into the best practices and innovative solutions.

Longitudinal Studies: Evaluate the long-term impact of energy initiatives on university operations and community engagement. This research will help to understand how sustained efforts in renewable energy can influence institutional policies, behaviors, and community relationships over time.

Scalable Models: Develop scalable models and frameworks that other institutions can adopt to drive sustainable energy practices. By creating adaptable and replicable solutions, universities can play a crucial role in their widespread implementation across various regions and contexts.

Implications for Practice

The findings offer practical insights for universities seeking to enhance their energy sustainability efforts:

Strategic Partnerships: Collaborate with industry partners, government agencies, and community organizations to

ISBN: 978-618-5765-04-0
ISSN 3057-4269

leverage resources and expertise. These partnerships can foster innovation, provide technical support, and facilitate funding opportunities for renewable energy projects.

Innovative Funding Mechanisms: Explore alternative financing models such as green bonds and public-private partnerships to support renewable energy projects. Creative funding approaches can alleviate financial constraints and enable the realization of ambitious sustainability goals.

Holistic Approaches: Integrate energy sustainability into all aspects of university operations, from infrastructure development to curricula and community engagement. A comprehensive approach ensures that sustainability is an inherent part of the university's mission and activities.

By adopting these strategies, universities can play a pivotal role in advancing SDG 7 and contribute to a sustainable future. As institutions that foster innovation, research, and education, universities have the unique opportunity to lead by creating a ripple effect that extends beyond their campuses and impacts global energy sustainability efforts.

REFERENCES

[1] United Nations. (2015). Transforming our world: The 2030 agenda for sustainable development. UN General Assembly. https://sustainabledevelopment.un.org/post2015/transformingourworld

[2] Abhishek, N., Rahiman, H. U., Suraj, N., Kulal, A., Ashoka, M. L., Divyashree, M. S., & Raghupathi, S. (2024). Renewable energy initiatives by corporates and sustainable development: A mediation analysis. Journal of Cleaner Production, 276, Article 123137. https://doi.org/10.1016/j.jclepro.2020.123137

[3] Romano, G., Martellucci, G., Mancini, F., & Battisti, A. (2022, December). Energy and environmental refurbishment of the hygiene institute within the Sapienza University of Rome campus. Journal of Physics: Conference Series, 2385(1), Article 012011. IOP Publishing. https://doi.org/10.1088/1742-6596/2385/1/012011

[4] Ouariachi, T., & Elving, W. (2020). Accelerating the energy transition through serious gaming: Testing effects on awareness, knowledge, and efficacy beliefs. Electronic Journal of e-Learning, 18(5), 410-420. https://doi.org/10.34190/EJEL.20.18.5.004

[5] Walentowski, H., Kietz, B., Horsch, J., Linkugel, T., & Viöl, W. (2020). Development of an interdisciplinary master of forestry program focused on forest management in a changing climate. Forests, 11(6), Article 632. https://doi.org/10.3390/f11060632

[6] Hoeltl, A., Brandtweiner, R., Bates, R., & Berger, T. (2020). The interactions of sustainable development goals: The case of urban informal settlements in Ethiopia. International Journal of Sustainable Development and Planning, 15(3), 287-294. https://doi.org/10.18280/ijsdp.150304

[7] Thomé, A. M. T., Scavarda, L. F., & Scavarda, A. J. (2016). Conducting systematic literature review in operations management. Production Planning & Control, 27(5), 408–420. https://doi.org/10.1080/09537287.2015.1129464

[8] Tranfield, D., Denyer, D., & Smart, P. (2003). Towards a methodology for developing evidence-informed management knowledge by means of systematic review. British Journal of Management, 14(3), 207–222. https://doi.org/10.1111/1467-8551.00375

[9] Denyer, D., & Tranfield, D. (2009). Producing a systematic review. In D. A. Buchanan & A. Bryman (Eds.), The SAGE handbook for organizational research methods (pp. 671-689). SAGE Publications. https://doi.org/10.4135/9781446268261.n29

[10] Snyder, H. (2019). Literature review as a research methodology: An overview and guidelines. Journal of Business Research, 104, 333-339. https://doi.org/10.1016/j.jbusres.2019.07.039

ISBN: 978-618-5765-04-0
ISSN 3057-4269

Eco-Friendly Ride-Sharing for Sustainable Transportation

Konstantinos Psaraftis
Dept. of Business Administration
University of West Attica
Egaleo, GREECE
kostaspsaraftis@hotmail.com

Klimis Ntalianis
Dept. of Business Administration
University of West Attica
Egaleo, GREECE
kntal@uniwa.gr

Dimitrios Stranis
Dept. of Business Administration
University of West Attica
Egaleo, GREECE
dstrani@uniwa.gr

Sofia Ioannidou
Dept. of Business Administration
University of West Attica
Egaleo, GREECE
sioannidou@uniwa.gr

***Abstract*— Carpooling and ride-sharing initiatives seek to make better use of empty seats in private cars, tackling the financial, environmental, and social challenges caused by single-occupancy vehicle use. These approaches offer economic advantages and help alleviate traffic congestion and pollution by reducing the number of cars on the road. Fuel consumption may be reduced, limiting gas emissions. However, the various existing carpooling recommendation systems struggle to effectively balance the conflicting goals of drivers and passengers. To address this issue, this paper proposes, an innovative scheme which focuses on quality of experience and eco-friendliness. Several factors are considered for passengers and drivers such as time delay tolerance, preferred vehicle capacity, importance of fare reduction, tolerance for driving distance overhead, driver safety and eco-friendliness preferences, and past ratings of both drivers and passengers. The eco-effectiveness of the proposed scheme is evaluated on a real-world dataset, which contains GPS trajectories from a fleet of more than 10,000 taxis in China. Results show that the proposed scheme outperforms state-of-art systems.**

Keywords*— *Intelligent Transportation System, Carpooling, Eco-friendly, Sustainability

INTRODUCTION

Collaborative commuting strategies aim to maximize the use of empty seats in personal vehicles, tackling financial, environmental, and social concerns linked to single-driver commutes. These methods offer not only economic advantages but also contribute to traffic reduction and pollution mitigation by lowering the number of cars on the road [1], [2]. On-demand ridesharing takes this concept a step further. Unlike traditional carpooling, it functions in real-time, allowing passengers to instantly request rides through digital platforms, with drivers having the option to accept or reject. This system connects drivers and passengers based on their travel routes and schedules, aiming to lessen traffic congestion, enhance mobility, and provide a cost-effective transportation alternative. The rise of transportation network companies (TNCs) like UberPool [3], Lyft [4], and Grab [5] has further propelled on-demand ridesharing's popularity. By leveraging real-time data and sophisticated algorithms, these companies have transformed traditional transportation services, ushering in a new era of dynamic mobility solutions. Research on on-demand ridesharing has attracted considerable interest from transportation planners, policymakers, and researchers, with a focus on addressing challenges like matching algorithms, pricing models, user behavior, and social acceptance within ridesharing systems.

This study proposes a recommendation system that incorporates diverse user preferences from both drivers and passengers to generate optimal carpooling matches. Within this system, 11 parameters are quantified that influence the ridesharing experience. Then, a matching procedure aggregates and analyzes these values, ultimately generating a recommendation that strives to strike a balance between the requirements and incentives of all stakeholders involved in the carpooling service. The selection of these parameters was meticulously chosen based on a comprehensive analysis of user needs in carpooling scenarios. The core principle behind selecting these 11 parameters is to ensure a thorough assessment of the factors that most significantly influence the carpooling experience for both drivers and passengers. For passengers, parameters such as flexibility tolerance, preferred vehicle size, cost reduction importance, detour tolerance, driver safety rating, driver eco-friendliness, and weight placed on past passenger and driver ratings were incorporated to address crucial aspects like scheduling flexibility, group travel, economic incentives, potential detours, safety concerns, environmental consciousness, and maintaining a high-quality service. For drivers, parameters like preferred vehicle capacity, compensation interest, and weight on passenger past ratings facilitate efficient management of vehicle occupancy, ensure adequate compensation, and maintain service quality by considering passenger behavior and reliability. By focusing on this well-balanced set of parameters encompassing economic considerations, convenience, safety, and environmental factors, our framework aims to address the most critical needs and preferences of all participants. Additionally, the inclusion of parameters like past ratings ensures that the system leverages historical data to enhance recommendation accuracy and user satisfaction.

To ensure a fair distribution of fares among both new and existing passengers, a policy is implemented that reduces the fare for each passenger proportionally to their travel distance. The additional cost incurred for picking up a new passenger is incorporated into the fare for the new passenger to compensate drivers. By maintaining a balance among the incentives of all parties involved in carpooling, the recommendation framework enhances the effectiveness of dynamic carpooling.

Publication fees were fully covered by the M.Sc "Public Administration – Public Management" of the University of West Attica

ISBN: 978-618-5765-04-0
ISSN 3057-4269

Real-world data from T-Drive [6] is used to evaluate the framework's effectiveness. Results demonstrate the superiority of the proposed system compared to traditional vacant taxicab services.

The subsequent sections of this paper are structured as follows. Section II, provides an overview of the state-of-art. Section III outlines the proposed vehicle recommendation scheme. Experimental results are illustrated in Section IV, while Section V concludes this paper.

STATE-OF-ART

The field of ride-hailing recommendations has emerged as a prominent area of research in recent years. These recommendation systems serve a vital role in facilitating efficient connections between passengers seeking rides and drivers with available vehicle capacity.

Prior research has explored methods to optimize taxi routes. For instance, Yuan et al. [6] leveraged GPS data to identify the fastest routes for taxis, considering traffic conditions at different times of day. Similarly, Zhang et al. [7] developed a system that recommends efficient routes for taxi drivers to reach passengers, aiming to minimize unnecessary travel distances. However, these approaches were designed for single-occupancy taxis, often resulting in underutilized vehicle capacity. Furthermore, their focus was primarily on driver needs, whereas our approach prioritizes a balance between driver and passenger preferences.

The rise of dynamic carpooling and ridesharing has spurred the development of innovative urban mobility solutions, including Public Vehicle (PV) systems designed for smart cities. Building on the foundational work of [8] who introduced a framework for PV systems demonstrating significant reductions in traffic congestion, parking needs, and environmental impact, researchers have continued to refine these systems. [9] explored path planning strategies within PV systems, leveraging advanced scheduling techniques to reduce computational complexity while improving operational efficiency. Real-world simulations confirmed these improvements.

In the realm of dynamic ridesharing, several key advancements have been made. [10] formally defined the problem and proposed a scalable taxi ridesharing framework. Their approach demonstrated efficiency, effectiveness, and scalability, highlighting its potential to transform urban transportation.

Matching algorithms and optimizing rider-driver experiences have been a focus of further research. Agatz et al. [11] aimed to minimize travel distances and user costs through their carpooling system. Zhang et al. [12], [13] introduced the concept of "detour ratio" to measure passenger detours and proposed pricing strategies to incentivize both riders and drivers. However, these approaches did not fully account for potential passenger delays.

Other researchers have focused on dynamic taxi-sharing and ridesharing algorithms. Orey et al. [14] and Setzke et al. [15] developed methods for managing customer requests and matching them with suitable drivers, considering factors like routes and time constraints. Cao et al. [16] presented a scalable ridesharing service where riders set their preferences for fare and wait times. Their system uses a cost model to find drivers who meet these requirements.

Moving beyond cost minimization, [17] explored maximizing overall rider satisfaction. They introduced the "utility-aware ridesharing problem" (URR) which aims to create optimal rider schedules for vehicles, maximizing overall satisfaction while considering various constraints. The study proposes efficient algorithms for assigning new riders with minimal disruption and establishes the NP-hard nature of the URR problem.

A prior study, which is the most relevant to the proposed scheme, introduced a recommendation framework for ride-sharing carpooling [18]. This framework uses a scoring system to balance the needs of both drivers and passengers, considering factors such as vehicle capacity, travel time, fare reduction, and driver profit. However, our scheme offers several key improvements. First, it utilizes a more comprehensive set of parameters for user profiles. Nine parameters are incorporated instead of five used in the previous study. These additional parameters allow for a more personalized user experience and take environmental considerations into account. This results in a more accurate representation of user preferences and their impact on the environment. Second, our recommendation scheme considers additional constraints. When identifying suitable vehicles, our system factors in both maximum acceptable travel time and detour distance. This approach, in contrast to the previous study, which selects any vehicle with available space, enhances overall efficiency and user experience. Additionally, our framework allows for group ride requests, whereas the prior study only considered individual users. Third, our framework utilizes a more nuanced scoring system for vehicle selection. The system not only considers the total value of each parameter but also its relative weight compared to other parameters. This allows for a more precise comparison between vehicles, compared to the prior study's simple summation of all parameters. Finally, the proposed fare calculation reflects a more realistic pricing structure. We consider both travel distance and time, aligning with the pricing models used by most ride-sharing companies. The previous study only factored in distance. These advancements contribute to a more comprehensive and user-friendly framework for ride-sharing and carpooling services, with a positive impact on both user experience and environmental sustainability.

Building upon our prior research in social computing, recommender systems, and crowdsourcing [19], [20], [21], [22], we introduce the novel proposed scheme, the details of which are described in Section III.

THE PROPOSED SCHEME

The introduced ride-sharing platform is eco-friendly and proposes a sustainable pricing model, which is fair to both riders and drivers. Initially, the pricing model is introduced and then several parameters are discussed, which are related to environmental and other factors.

In particular the total cost for travelers is calculated as:

$$t_i.fare(D,T) = BaseFare + DR * D + TR * T \quad (1)$$

Where:

BaseFare is charged at the start of every ride.

DR is the rate per kilometer.

D is the total driving distance.

ISBN: 978-618-5765-04-0
ISSN 3057-4269

TR is the rate per minute.

T is the total time (from initial to drop-off location).

In case of carpooling, the driver's total income can be modeled as:

$$P_{cp.income}(D,T) = u_{cp.income}(D,T) - u_{income}(D,T) \quad (2)$$

Where:

$$u_{cp.income}(D,T) = \sum_{j \in u_l.c_r} r_j.ef \quad (3)$$

$u_l.c_r$ are the requests that the taxi is currently serving and $r_j.ef$ indicates the estimated fare that each traveler is projected to pay by sharing the taxi.

Then, the total savings $u_l.t_s$ is shared among all travelers and the taxi driver:

$$u_l.t_s = \sum_{i \in u_l.c_l} (t_i.fare(D_{total}, T_{total}) - t_i.fare(D_{actual}, T_{actual})) \quad (4)$$

Where, D_{total} and T_{total} are the distance and time that the taxi would be forced to travel if each traveler's request was accepted without carpooling. The regular fare for the existing traveler is estimated by:

$$r_j.nf = t_i.fare(d_{exist}, t_{exist}) \quad (5)$$

$r_j.nf$ indicates the regular fare that the traveler would pay if they used the taxi exclusively, while d_{exist} and t_{exist} are the distance and time from the current location to the drop-off location of the traveler. Then, in case of carpooling, the estimated fare of each passenger ($r_j.ef$) for taxi u_j is calculated by:

$$r_j.ef = r_j.nf - \mu * u_l.ts * \left(\frac{\Delta d_j}{\sum_{j \in u_l.cr} \Delta d_j} + \frac{\Delta t_j}{\sum_{j \in u_l.cr} \Delta t_j}\right) \quad (6)$$

Where μ is a constant that determines the percentage of savings that will be distributed among the travelers and Δd_j / Δt_j is the additional distance / time that the traveler will be asked to cover /endure. Additionally, the overall time delay score can be calculated by:

$$td_{selected}.score = \frac{\sum_{w=1}^{W}(r_w.sdt - r_w.edt)}{W * t_w.p_1} \quad (7)$$

Where $r_j.sdt$ indicates the actual scheduled drop-time at the requested location, $r_j.edt$ indicates the earliest feasible drop-time at the requested location and $t_w.p_1$ denotes traveler's *w* time delay tolerance. Then, the normalized time delay score for a selected taxi can be calculated by:

$$ntd_{selected}.score = \frac{td_{Min}.score}{td_{selected}.score} \quad (8)$$

Where $td_{Min}.score$ is the minimum delay among all eligible taxis.

On the other hand, the preferred taxi capacity score (indication of how desirable it is to travel with fewer people) can be calculated by:

$$tc_{selected}.score = \frac{\sum_{w=1}^{W} u_{selected}.mc * t_w.p_2}{W+1} + \frac{u_{selected}.mc * d_{selected}.p_1}{W+1} \quad (9)$$

Where $u_{selected}.mc$ is the taxi's maximum capacity, $t_w.p_2$ denotes traveler's *w* preferred vehicle capacity and $d_{selected}.p_1$ denotes the selected driver's preferred vehicle capacity. Then, the normalized capacity score can be calculated by:

$$ntc_{selected}.score = \frac{tc_{selected}.score}{tc_{Max}.score} \quad (10)$$

Where, $tc_{Max}.score$ is the highest score among all eligible taxis.

Additionally, the fare reduction score for the selected taxi can be calculated by:

$$t_i.fr_{score} = \left(\frac{\Delta d_j}{\sum_{j \in u_l.cr} \Delta d_j} + \frac{\Delta t_j}{\sum_{j \in u_l.cr} \Delta t_j}\right) * t_i.p_3 \quad (11)$$

Where, $t_i.p_3$ denotes t_i traveler's importance of fare reduction. Therefore, the total fare reduction score for all travelers (*u.ct*) of the selected taxi $u_{selected}$ can be calculated by:

$$tfr_{selected}score = \sum_{i \in u.ct} t_i.fr_{score} \quad (12)$$

And the normalized fare reduction score is given by:

$$ntfr_{selected}score = \frac{tfr_{selected}score}{tfr_{Max}score} \quad (13)$$

Where $tfr_{Max}score$ is the maximum score for the set of eligible taxis.

On the other hand, the total profit for a taxi driver (if the new request is assigned to her taxi) can be calculated by:

$$v_{selected}.ts = \sum_{j \in u_l.c_r} (r_j.nf - r_j.ef) \quad (14)$$

By taking into consideration the selected taxi driver's preference ($d_{selected}.p_2$) regarding her interest in profit increment, the profit increment score for the selected taxi can be calculated as:

$$pi_{selected}.score = v_{selected}.ts * d_{selected}.p_2 \quad (15)$$

And the normalized value can be calculated as:

$$npi_{selected}.score = \frac{pi_{selected}.score}{pi_{Max}.score} \quad (16)$$

Where $pi_{Max}.score$ is the maximum score among eligible taxis.

The average driving distance overhead score is an indication of how much more distance a traveler has to endure in order to arrive at destination. For an occupied taxi, this score can be calculated as:

$$dd_{selected}.score = \frac{\sum_{w=1}^{W} distance(r_w.BR \rightarrow r_w.p)}{W * t_j.p_4} \quad (17)$$

Where $r_w.p$ is the pick-up location, *BR* is a list that stores the proposed sequence of waypoints for all taxi passengers and $t_j.p_4$ is the tolerance to driving distance overhead of passenger t_j (passenger's preference). Then, the normalized score can be calculated as:

ISBN: 978-618-5765-04-0
ISSN 3057-4269

$$ndd_{selected}.score = \frac{dd_{Min}.score}{dd_{selected}.score} \quad (18)$$

Where $dd_{Min}.score$ is the minimum score among all eligible taxis.

Additionally, the driver's safety score can be calculated by:

$$ds_{selected}.score = \frac{\sum_{w=1}^{W}(ds_{selected}.value * t_w.p_5)}{W} \quad (19)$$

Where $ds_{selected}.value$ is the driver's safety score and $t_w.p_5$ is the passenger's preference regarding driver safety score. Then, the normalized score is calculated by:

$$nds_{selected}.score = \frac{ds_{selected}.score}{ds_{Max}.score} \quad (20)$$

where $ds_{Max}.score$ is the maximum score among eligible taxis.

Another very important factor is the driver's eco-friendliness score, which expresses how friendly is to the environment, a driver's driving way. This score can be calculated by:

$$de_{selected}.score = \frac{\sum_{w=1}^{W}(de_{selected}.value * t_w.p_6)}{W} \quad (21)$$

where $de_{selected}.value$ is the driver's eco score and $t_w.p_6$ is the passenger's preference regarding driver's eco-friendliness. In this case the normalized score is given by:

$$nde_{selected}.score = \frac{de_{selected}.score}{de_{Max}.score} \quad (22)$$

Where $de_{Max}.score$ is the maximum score among eligible taxis.

Furthermore, the driver's past ratings score can be calculated by:

$$dpr_{selected}.score = \frac{\sum_{w=1}^{W}(d_{selected}.pr * t_w.p_7)}{W} \quad (23)$$

Where $d_{selected}.pr$ is the past rating of the selected driver and $t_w.p_7$ is the passenger's preference regarding driver's past rating. And the normalized score is:

$$ndpr_{selected}.score = \frac{dpr_{selected}.score}{dpr_{Max}.score} \quad (24)$$

Where $dpr_{Max}.score$ is the maximum score among eligible taxis.

Moreover, each traveler's past ratings score for a selected taxi is calculated by:

$$tpr_{selected}.score = t_{new}.pr * d_{selected}.p_8 + \sum_{w=1}^{W-1} t_{new}.pr * t_w.p_8 + \sum_{W-1}^{w=1} t_w.pr * t_{new}.p_8 \quad (25)$$

And the normalized score is given by:

$$ntpr_{selected}.score = \frac{tpr_{selected}.score}{tpr_{Max}.score} \quad (26)$$

Where $tpr_{Max}.score$ is the maximum score among eligible taxis.

Finally, the proposed ridesharing recommender system aggregates all normalized scores and the taxi with the best score is recommended to the new passenger:

$$u_{selected}.fscore = (8) + (10) + (13) + (16) + (18) + (20) + (22) + (24) + (26) \quad (27)$$

EXPERIMENTAL RESULTS

The proposed eco-friendly ride-sharing scheme has been developed using C# and two key libraries: 1) Bing Maps Routing API [23] and 2) Damoov [24]. The experimental analysis utilized the T-Drive trajectory data sample [6], which encapsulates GPS trajectory data from a fleet of 10,357 taxis in Beijing over the period spanning February 2 to February 8, 2008. A representative sample of GPS data from 250 taxis was extracted from the dataset and used, leading to an input of 135,874 real-world traces. The number of travelers is determined through a random allocation process that varies between 0 and the taxi's maximum capacity.

Simulations and Comparison to Existing Schemes

In this study a comparative analysis is performed among the proposed scheme and three prevalent methods: Highest Aggregated Score Vehicle Recommendation (HASVR) [18], Nearest Vehicle Recommendation (NVR), and No-Carpooling. HASVR's approach offers a vehicle recommendation based on an aggregated scoring system. On the other hand, the NVR model employs a heuristic algorithm designed to minimize passenger wait times. It accomplishes this by preferentially recommending the vehicle closest to the passenger, with a bias toward occupied vehicles. This strategy ensures efficient resource utilization by reducing idle times. In contrast, the No-Carpooling system operates without providing carpooling services. In this model, each passenger request is met with a recommendation for a vacant vehicle within a specified search radius. If a vacant vehicle is unavailable at the requested time, the system may reject the request, prompting the passenger to resubmit their request. Experimental parameters are presented in Table 1.

Table 1: Average Passengers' Preference Weights

Parameter	Average Score
Time Delay Tolerance	4.2
Preferred Vehicle Capacity	4.0
Importance of Fare Reduction	4.5
Tolerance to Driving Distance Overhead	3.8
Preference for Driver Safety	4.3
Preference for Driver Eco-friendliness	3.9
Weight on Driver Past Ratings	4.1
Weight on Co-traveler Past Ratings	3.7

Before providing the results and since this paper focuses on eco-friendly ride-sharing and sustainable transportation, the following two metrics are introduced:

Average Eco-Score of Recommended Taxis (AVES): it expresses the mean eco-score of all taxis recommended by the proposed scheme and it is calculated by:

$$AVES = \frac{\sum_{i=1}^{n} de_{value_i}}{n} \quad (28)$$

where n is the total number of recommended taxis and de_{value_i} is the eco-score of the i-th taxi.

ISBN: 978-618-5765-04-0
ISSN 3057-4269

Percentage of reduced total mileage (PRTM): it determines the mile reduction. Let M_{vac} denote the total mileage to deliver all passengers separately and M_{BR} denote the total mileage used to deliver all passengers using the taxis recommended by the proposed scheme (either vacant or occupied taxis). Thus, PRTM is calculated by:

$$PRTM = \left(1 - \frac{M_{BR}}{M_{vac}}\right) * 100 \quad (29)$$

Then, the impact of travelers' eco-preference $t_w.p_6$ on the average eco score of recommended taxis is presented in Figure 1. In the simulation, three categories of traveler eco-awareness have been used: Low, Moderate, and High. Results are contrasted with the general mean eco-score of 0.70.

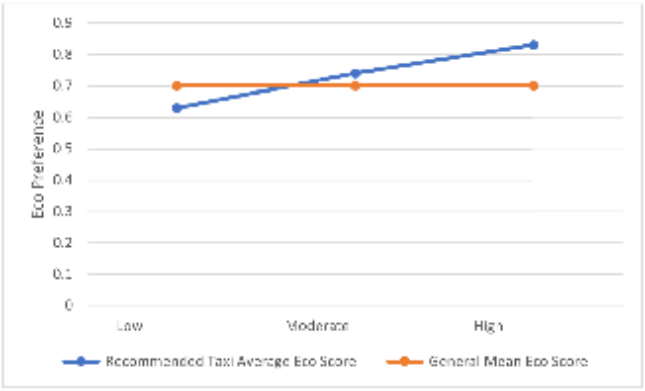

Figure 1: Average eco-score of recommended taxis

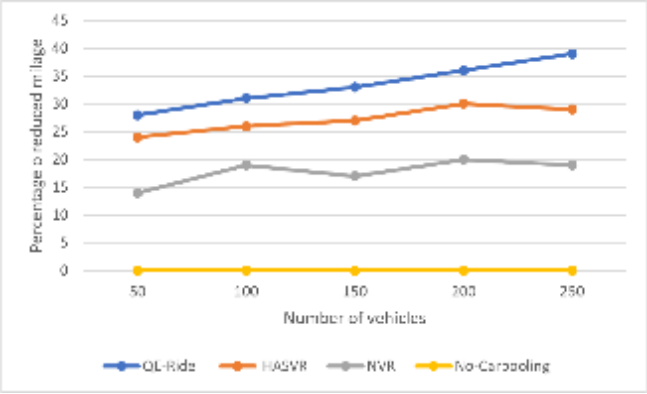

Figure 2: PRTM vs Number of Taxis

Regarding the three categories of traveler eco-awareness: (a) Travelers belonging to the "Low" category prompted the system to recommend taxis averaging an eco-score of 0.63, slightly below the overall mean, (b) Travelers belonging to the "Moderate" category led the system to recommend taxis with an eco-score of 0.74, providing slightly more eco-friendly rides and (c) Travelers belonging to the "High" category guided the scheme to pick taxis with a high eco-score of 0.83 on average, emphasizing the system's ability to prioritize eco-friendliness substantially when detected as a chief traveler's preference.

Regarding PRTM versus the number of taxis, Figure 2 illustrates results. In particular, performance of all carpooling schemes improves with the number of vehicles. This finding is expected, since the more the vehicles, the greater the probability to find an optimal taxi in terms of PRTM. Here it should be mentioned that the No-Carpooling scheme remains at 0%, due to its nature. Additionally, the proposed scheme outperforms HASVR and NVR for any number of vehicles, since eco-friendliness is a parameter specifically taken into account. In particular, for 250 taxis, the proposed scheme provides a 39% PRTM, HASVR is second with 29% and NVR achieves 19%. Interestingly, while the proposed scheme and HASVR provide an increase in performance with the number of vehicles, NVR does not follow this pattern in the interval between 100 and 200 vehicles. NVR primarily considers waiting times and it does not focus to find the optimal taxi in terms of reduced mileage. Thus, its performance may vary, depending on the dataset.

Regarding PRTM versus searching radius (SD_0), Figure 3 illustrates the results. The proposed scheme and HASVR provide improved performance as SD_0 increases. Again, NVR does not follow this pattern, providing the same performance for any SD_0, while the No-Carpooling scheme remains at 0%. Overall, the proposed scheme surpasses HASVR and NVR across all examined SD_0. For instance, for SD_0=6km, the proposed scheme provides a PRTM equal to 46%, while HASVR reaches 36% and NVR 23%.

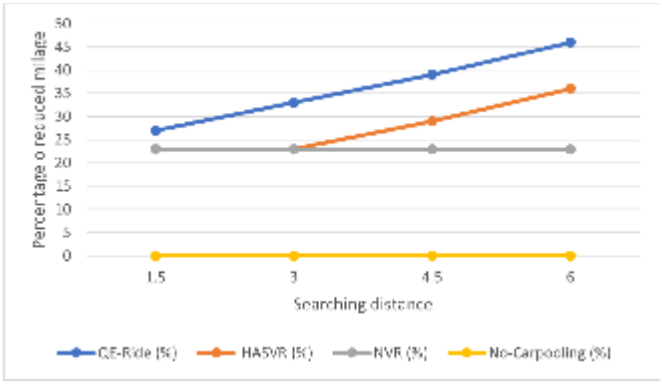

Figure 3: PRTM vs Searching Radius

Regarding PRTM by considering different hours of the day (Poisson distribution), Figure 4 illustrates results. As it can be observed, performance of the proposed scheme, HASVR and NVR varies throughout the day. The proposed scheme provides and initial PRTM of 17% at 04:00 a.m., which rises to a maximum of 27% by 16:00 p.m. and falls to 23% by 20:00 p.m. Results show that the proposed scheme performs better during afternoons, since rides (and thus ridesharing opportunities) increase. On the other hand, HASVR reaches a maximum performance of 19% at 16:00 p.m., while NVR provides it peak of 12% at noon. However, the performance of both schemes falls in the evening, reaching a 13% for HASVR and 7% for NVR by 20:00 p.m.. The No-Carpooling scheme remains static at 0%, since there is not any mileage reduction.

ISBN: 978-618-5765-04-0
ISSN 3057-4269

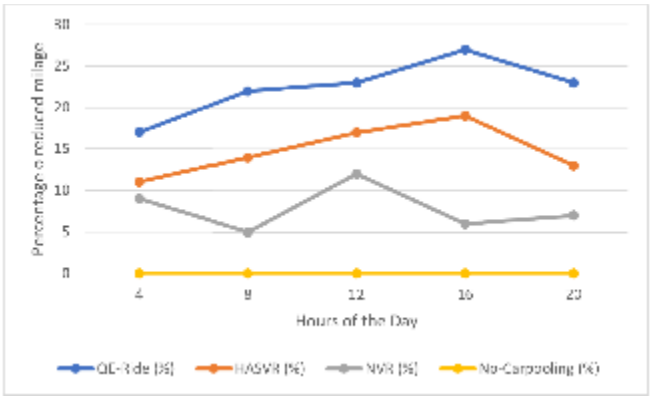

Figure 4: PRTM vs Day Hours

Finally, regarding satisfied ride requests for different SD_0, Figure 5 illustrates the results. As SD_0 increases, all schemes improve their percentages of satisfied ride requests. This is expected, as a larger SD_0 considers more taxis for each request, increasing the chances of a suitable ride. The No-Carpooling scheme provides the worst performance, as it does not take advantage of the benefits of carpooling. However, it should be stated that even without carpooling, the scheme is still able to satisfy a substantial percentage of ride requests. The proposed scheme provides a worse performance compared to HASVR, due to its stricter time and distance constraints, which give priority to certain aspects of user satisfaction over a simple request satisfaction. While these constraints reduce the percentage of satisfied requests compared to HASVR, they ensure that satisfied requests follow specific quality criteria, offering a more personalized and quality-oriented user experience.

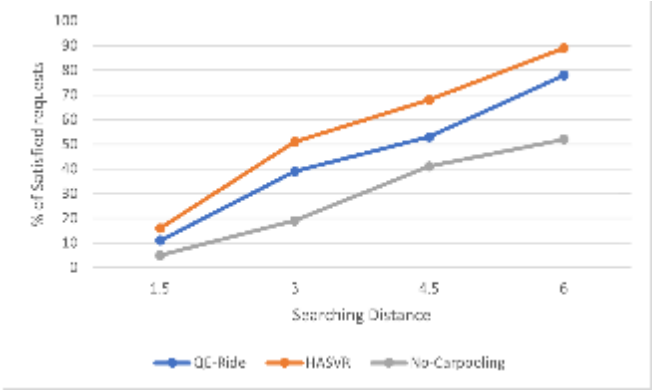

Figure 5: Satisfied Ride Requests (%)

ACKNOWLEDGMENT

Special thanks to the Master's students Mr. Louka Dalakli, Mr. Antonio Spintio, Ms. Anna Maratsola, Ms. Ioustini Pietri, Ms. Theodora Xeniou and Mr. Pavlo Paschali for their support and fruitful comments especially in completing the experiments.

REFERENCES

[1] Hua Cai et al. "Environmental benefits of taxi ride sharing in Beijing". In: Energy 174 (2019), pp. 503–508.
[2] Filippo Bistaffa et al. "A computational approach to quantify the benefits of ridesharing for policy makers and travellers". In: IEEE Transactions on Intelligent Transportation Systems 22.1 (2019), pp. 119–130.
[3] Uber Pool. Accessed: July 22, 2024.
[4] Lyft. Accessed: July 22, 2024.
[5] Grab. Accessed: July 22, 2024.
[6] Jing Yuan et al. "T-drive: driving directions based on taxi trajectories". In: Proceedings of the 18th SIGSPATIAL International conference on advances in geographic information systems. 2010, pp. 99–108.
[7] Desheng Zhang et al. "Online cruising mile reduction in large-scale taxicab networks". In: IEEE Transactions on Parallel and Distributed Systems 26.11 (2014), pp. 3122–3135.
[8] Ming Zhu et al. "Public vehicles for future urban transportation". In: IEEE transactions on intelligent transportation systems 17.12 (2016), pp. 3344–3353.
[9] Ming Zhu, Xiao-Yang Liu, and Xiaodong Wang. "An online ride-sharing path-planning strategy for public vehicle systems". In: IEEE Transactions on Intelligent Transportation Systems 20.2 (2018), pp. 616–627.
[10] Shuo Ma, Yu Zheng, and Ouri Wolfson. "T-share: A large-scale dynamic taxi ridesharing service". In: 2013 IEEE 29th International Conference on Data Engineering (ICDE). IEEE. 2013, pp. 410–421.
[11] Niels Agatz et al. "Dynamic ride-sharing: A simulation study in metro Atlanta". In: Procedia-Social and Behavioral Sciences 17 (2011), pp. 532–550.
[12] Desheng Zhang et al. "CallCab: A unified recommendation system for carpooling and regular taxicab services". In: 2013 IEEE International Conference on Big Data. IEEE. 2013, pp. 439–447.
[13] Desheng Zhang et al. "A carpooling recommendation system for taxicab services". In: IEEE Transactions on Emerging Topics in Computing 2.3 (2014), pp. 254–266.
[14] Pedro M d'Orey, Ricardo Fernandes, and Michel Ferreira. "Empirical evaluation of a dynamic and distributed taxi-sharing system". In: 2012 15th International IEEE Conference on Intelligent Transportation Systems. IEEE. 2012, pp. 140–146.
[15] David Soto Setzke et al. "Matching drivers and transportation requests in crowdsourced delivery systems". In: (2017).
[16] Bin Cao et al. "Sharek: A scalable dynamic ride sharing system". In: 2015 16th IEEE International Conference on Mobile Data Management. Vol. 1. IEEE. 2015, pp. 4–13.
[17] Peng Cheng, Hao Xin, and Lei Chen. "Utilityaware ridesharing on road networks". In: Proceedings of the 2017 ACM International Conference on Management of Data. 2017, pp. 1197–1210.
[18] Hajra Qadir et al. "An optimal ride sharing recommendation framework for carpooling services". In: IEEE Access 6 (2018), pp. 62296–62313.
[19] Klimis Ntalianis et al. "Automatic annotation of image databases based on implicit crowdsourcing, visual concept modeling and evolution". In: Multimedia Tools and Applications 69 (2014), pp. 397–421.
[20] Konstantinos Psaraftis, Theodoros Anagnostopoulos, and Klimis Ntalianis. "An innovative quality lane change evaluation scheme based on reliable crowd-ratings". In: Computer Science and Information Systems 19.3 (2022), pp. 1093–1114.
[21] Klimis Ntalianis et al. "Social relevance feedback based on multimedia content power". In: IEEE Transactions on Computational Social Systems 5.1 (2017), pp. 109–117.
[22] Klimis S Ntalianis, Andreas Kener, and Jahna Otterbacher. "Feelings' Rating and Detection of Similar Locations, Based on Volunteered Crowdsensing and Crowdsourcing". In: IEEE Access 7 (2019), pp. 90215–90229.
[23] Microsoft. Bing Maps Routing API. 2024. URL: https://www.microsoft.com/en-us/maps/routing/.
[24] Damoov. 2024. URL: https://www.damoov.com/.

ISBN: 978-618-5765-04-0
ISSN 3057-4269

Nanofluids for Automotive Radiators: Enhancing Cooling Performance and Efficiency

Mert Gülüm
Mechanical Engineering Department
Karadeniz Technical University
Trabzon, Turkey
gulum@ktu.edu.tr

***Abstract*—Heat transfer in internal combustion engines is one of the most important topics since it affects engine performance, exhaust emissions, and thermal damage. Conventional coolants (water, ethylene glycol, propylene glycol, and engine oil) are widely utilized. However, these coolants have limitations in thermal conductivity. Nanofluids have become more attractive recently because of their advanced thermophysical properties (higher thermal conductivity), compared to conventional coolants. This study provides a comprehensive review of recent literature on using nanofluids as alternative coolants in engines. The findings highlight the promising role of nanofluids in addressing the thermal management challenges of engines.**

Keywords—internal combustion engines, heat transfer, nanofluids, nanoparticles, automobile cooling systems

INTRODUCTION

Temperatures within the combustion chamber of an engine can reach around 2700 K and higher [1]. Engine materials cannot withstand high temperatures and quickly fail without proper heat transfer. Therefore, removing heat is important to prevent thermal damage to the engine [1]. Conversely, it is beneficial to operate an engine at the highest possible temperature to maximize thermal efficiency [1]. Engine oil serves as both a lubricant and a coolant in engines [2]. Friction between moving parts decreases efficiency by converting kinetic energy into heat [2]. The primary role of the engine oil is to reduce this friction [2]. Additionally, it helps prevent corrosion, enhances sealing, and cleans the engine [2]. Engine oil also cools the engine by removing heat away from the moving parts [2]. Similar to engine oil, there are water-cooled and air-cooled methods to cool the combustion chambers of engines. In the air-cooled method, a finned exterior surface on the engine block over which air is directed is used [1]. In the water-cooled method, the engine block is surrounded by a water jacket. This jacket contains a coolant fluid circulated through the engine to decrease temperatures [1]. Although water is widely used as a heat transfer fluid, it has also some disadvantages (corrosion risk, high freezing point (0^{o}C at 101 kPa), and low boiling temperature (100^{o}C at 101 kPa)) [1]. To overcome these disadvantages of water, in most engines, the water-ethylene glycol (EG) blends or the water-propylene glycol (PG) blends are used [1]. EG has a lower freezing point (-11^{o}C at 101 kPa) and higher boiling point (197^{o}C at 101 kPa), compared to water. However, EG has relatively lower thermal conductivity (0.30 W/mK), compared to diesel fuel (0.69 W/mK) [1]. PG is used as the base ingredient in some commercial engine coolants. PG has a freezing point of -14^{o}C at 101 kPa, a boiling temperature of 188^{o}C at 101 kPa), and a thermal conductivity (0.15 W/mK) [3].

Researchers have investigated new methods to improve heat transfer rates in engines. One of these methods is the use of nanofluids. Due to the advancements in nanotechnology, nanofluids have taken significant attention as encouraging alternatives to conventional coolants due to their improved thermal conductivity. Nanofluids are composed of nanoparticles (metals, oxides, carbon nanotubes, etc.). These nanoparticles have sizes from 1 to 100 nm, and are dispersed in base fluids such as water, EG, PG, or engine oil [3]. According to Maxwell's theory [4], solids generally have a higher thermal conductivity than liquids. That is why nanofluids exhibit superior thermal conductivity compared to their base fluids. This improvement in thermal conductivity represents a breakthrough in energy efficiency for automotive cooling systems. It also enables radiators to achieve better cooling performance without increasing their size, weight, cost, or heat exchange area [3, 5, 6]. Moreover, enhanced thermal conductivity can lead to better engine performance and decrease some exhaust emissions.

Considering the important role of heat transfer in engine performance and the potential benefits of using nanofluids to increase thermal conductivity, there has been extensive research over recent decades focusing on the thermophysical properties and heat transfer performance of nanofluids based on water, EG, PG, and engine oil. This study presents a comprehensive review of the latest literature, analyzing the thermophysical properties and heat transfer efficiency of nanofluids used in automotive radiator systems.

LITERATURE REVIEW

Afrand et al. [2] explored the impacts of temperature and nanoparticle concentration on the dynamic viscosity values of SiO_2 (silica)-MWCNTs (multi-walled carbon nanotubes)-engine oil (SAE40) hybrid nanofluids. The experiments covered a solid volume fraction of 0.0625%, 0.125%, 0.25%, 0.5%, 0.75% and 1.0%. A correlation was developed to estimate the dynamic viscosity values of SiO_2-MWCNTs-engine oil (SAE40) hybrid nanofluids. These nanofluids were prepared using a two-step method. To obtain stable nanofluid samples, the suspensions were magnetically stirred for 2.5 hours. Then, these samples were mixed with an ultrasonic processor for 6-7 hours. After 15 days, visual inspection showed that the nanofluid samples had remained stable, with no significant sedimentation. The viscosity measurements were done at different shear rate ranges (667-6667 1/s). The viscosity of nanofluid was measured at a solid volume fraction of 1% under various shear rates (1/s) and temperatures (from 30^{o}C to 60^{o}C). Since the shear stress (dyne/cm^2) changed linearly with the shear rate at each temperature, the hybrid nanofluids were determined to behave as a Newtonian fluid. The dynamic viscosity of nanofluids was measured at various

ISBN: 978-618-5765-04-0
ISSN 3057-4269

temperatures (25ºC- 60ºC). It was observed that, at each temperature, the viscosity of the hybrid nanofluids increased with higher solid volume fractions. The viscosity of nanofluids decreased with increasing the temperature. The relative dynamic viscosity increased with the solid volume fraction (0%-1%). The relative dynamic viscosity also slightly increased with temperature (25ºC-60 ºC), but it became more pronounced at higher solid volume fractions. Additionally, the maximum deviations in relative viscosity between 25ºC and 60ºC were found to be 1.4%, 2.9%, and 2.5% at the solid volume fractions (0.0625%, 0.125%, and 0.25%, respectively). This showed that the relative viscosity remained nearly constant under different temperatures at these lower solid volume fractions. However, at higher solid volume fractions (0.5%, 0.75%, and 1%), the maximum deviations in relative viscosity were found to be 8.3%, 7.4%, and 10.0%, respectively. Additionally, the viscosities of SiO_2-SAE40 and MWCNTs-SAE40 mono nanofluids were measured and compared with that of the SiO_2-MWCNTs-SAE40 hybrid nanofluid at 25ºC and 50ºC. The relative viscosity of the hybrid nanofluid was observed to be between those of the mono nanofluids at these temperatures. The relative viscosity of MWCNTs-SAE40 was considerably higher than that of both SiO_2-MWCNTs-SAE40 and SiO_2-SAE40 nanofluids. The cylindrical shape and extended length of MWCNTs reduced their ability to move between the oil layers. Consequently, the viscosity of the MWCNTs-SAE40 mono nanofluid increased significantly. The relative viscosity of SiO_2-MWCNTs-SAE40 hybrid nanofluids was estimated using theoretical models (Einstein and Wang models) based on solid volume fraction at 40ºC. However, these models could not accurately predict the viscosity. Therefore, a 4th-degree polynomial correlation was proposed to estimate the relative dynamic viscosity of these nanofluids at different temperatures (25ºC-60ºC). The correlation was a function of the solid volume fraction and the dynamic viscosity of the base fluid. The maximum deviation between the measured data and computed values was found to be 0.75%.

Li et al. [3] investigated the heat transfer performance and thermophysical properties of hybrid nanofluids (mixtures of EG, silicon carbide, and multi-walled carbon nanotubes). These hybrid nanoparticles were prepared using hexane, magnetic agitator, and ultrasonic vibrator. The hybrid nanoparticle was added to EG at different volume fractions (0.04%, 0.1%, 0.2%, and 0.4%) by using a vertical closed sand mill. The thermal conductivity values of hybrid nanofluids linearly increased with increasing hybrid nanoparticles. At all fractions, the thermal conductivity of hybrid nanofluids was found to be higher than that of nanofluids including only silicon carbide and EG. This was due to the higher thermal conductivity of carbon nanotubes than silicon carbide. The maximum enhancement in the thermal conductivity was found to be 32.01% with the use of the hybrid nanofluids including 0.4 vol.%. At every volume fraction, the thermal conductivity of hybrid nanofluids and pure EG increased with increasing temperature. The increase in thermal conductivity was found to be small for EG. Thermal conductivity was more sensitive to the change of temperature at higher fractions. For example, the hybrid nanofluid including 0.4 vol.% showed a 9.8% increase in thermal conductivity at 50ºC, compared to 20ºC, whereas the EG demonstrated a 2.7% increase over the same temperature range. At room temperature, the viscosity of hybrid nanofluids and pure EG was measured at different shear rates (10 to 500 s-1). The viscosities of pure EG and hybrid nanofluids showed only minor changes with increasing shear rate. That is why the hybrid nanofluids could be classified as Newtonian fluids. The adding hybrid nanoparticles did not change the fluid behavior of the base fluid (EG). This was advantageous for fluid pumping and transportation. However, higher particle volume fractions led to a significant increase in the viscosity of hybrid nanofluids. The addition of solid particles (hybrid nanofluids) increased the viscosity of the base fluid (EG). The viscosity of hybrid nanofluids was measured between 25ºC and 60ºC. The viscosity of hybrid nanofluids and pure EG decreased with increasing temperature. The Reynolds number, Prandtl number, Nusselt number, and convective heat transfer coefficient of the hybrid nanofluids were investigated under different temperatures (30ºC, 40ºC, and 50ºC) and volume fractions (0%-0.4%). At 50ºC, the maximum convective heat transfer coefficient of the hybrid nanofluid including 0.4% vol. of hybrid nanoparticle was found to be 26% higher than pure EG. This result showed the hybrid nanofluids were expected to significantly enhance the heat dissipation performance of automobile engines. Finally, the hybrid nanofluids showed considerable improvement in thermal conductivity. However, this enhancement coincides with an increase in viscosity for all volume fractions, which impacts pumping energy consumption and time.

Oliveira et al. [5] investigated the thermal performance of multi-walled carbon nanotubes/water nanofluids in an automotive radiator. The mass flow rate was changed from 30 to 70 g/s. The inlet temperature was changed from 50ºC to 80ºC. The concentration was changed from 0 to 0.16 wt%. The nanofluids' properties (thermal conductivity and viscosity) were determined using a transient hot bridge sensor and a viscometer. The nanofluids were created using a two-step method. The nanofluid had a significantly higher dynamic viscosity than water. At a temperature of 30ºC, the viscosity increased by 8.5%, 20.6%, and 54% for concentrations of 0.05 wt%, 0.08 wt%, and 0.16 wt%, respectively. For all samples, the viscosity decreased as the temperature increased from 30ºC to 90ºC. Thermal conductivity (W/mK) was measured at 25ºC and 50ºC. A slight increase in thermal conductivity of nanofluids was observed compared to water at each temperature. At 50ºC, the thermal conductivity enhancement was found to be approximately 5% for concentrations of 0.08 wt% and 0.16 wt%. At 25ºC, the enhancement was lower, with a 1.6% increase for the 0.16 wt% concentration. The variation in heat transfer rate (W) was investigated at different inlet temperatures (50ºC, 60ºC, 70ºC, and 80ºC) and mass flow rates of the liquid (30 g/s, 40 g/s, 50 g/s, 60 g/s, and 70 g/s) for nanofluids and pure water. The heat transfer rate for nanofluids was slightly lower compared to pure water. The heat transfer rate increased with a higher liquid mass flow rate for all nanofluids. However, the heat transfer rate decreased with higher nanoparticle concentrations. For the 0.05 wt% concentration, the heat transfer rate was almost the same as that of pure water. For the 0.08 wt% concentration, the heat transfer rate was 3% lower (at an inlet temperature of 80ºC and mass flow rate of 70 g/s) and 8.8% lower (at an inlet temperature of 50ºC and mass flow rate of 30 g/s) than pure water. Finally, for the highest concentration of 0.16 wt%, the reduction in heat transfer rate was more significant, varying from 7.3% (at 80ºC and 70 g/s) to 17% (at 80ºC and 30 g/s).

Hajiakbari et al. [7] numerically investigated the effects of different nanoparticles (TiO_2 (titanium dioxide), SiO_2, and Al_2O_3 (alumina)) on convective heat transfer coefficient, Nusselt number, and entropy values to improve radiator cooling processes. These nanoparticles were used in different vol. concentrations (0.2%-0.8%). The most efficient nanofluid

ISBN: 978-618-5765-04-0
ISSN 3057-4269

composition was determined as 80% water, 20% EG, and 1% SiO_2. The numerical values were compared to the measured data given in the four-stroke Mercedes-Benz OM502 V8 2023 diesel engine catalog. Adding 1% SiO_2 to the water-EG blend (volumetrically 20% water-80% EG) significantly improved the convective heat transfer coefficient. The average improvement of convective heat transfer coefficient was determined as 74.7% at the coolant inlet temperature of 85°C and 127.1% at the coolant inlet temperature of 95°C. The average increase in Nusselt number for coolants based on SiO_2, TiO_2, and Al_2O_3 was determined as 200.9%, 70.4%, and 23.1% at 85°C coolant inlet temperature, and 291.2%, 97.4%, and 72.7% at 95°C coolant inlet temperature, respectively. The numerical results demonstrated a 75.1% and 128.1% improvement in heat transfer rate as well as a decrease in coolant outlet temperature by 23.8°C and 21.4°C when the inlet coolant temperature was 85°C and 95°C. Moreover, economic analyses showed that using the optimal coolant composition could result in annual cost savings of about $2700.

Esfe et al. [8] measured the dynamic viscosity of alumina (Al_2O_3)-engine oil (10 W-40) nanofluids depending on solid volume fraction and temperature. Al_2O_3 nanoparticles with an average diameter size of 20 nm were dispersed into the engine oil at the solid volume fractions of 0.25%, 0.5%, 0.75%, 1%, 1.5%, and 2%. Dynamic viscosity was measured under the temperatures of 5ºC, 15ºC, 25ºC, 35ºC, 45ºC, 55ºC, and 65ºC using by a viscometer. The nanofluids were prepared by a two-step method. To make the most stable and homogenous samples, after magnetic stirring for 2.5 h, the samples were exposed to an ultrasonic processor for 7 h. The change of dynamic viscosity of nanofluids depending on shear rate (2000-12000 1/s) was investigated at different solid volume fractions (0%-2%) and temperatures (5ºC-65ºC). The viscosity of the samples did not change for different shear rates. Therefore, all samples exhibited Newtonian behavior. The viscosity of the nanofluid increased with increasing the solid volume fraction. The increase in dynamic viscosity with solid volume fraction was found to be more significant at lower temperatures, compared to higher temperatures. The increase in viscosity with solid volume fraction was due to the larger nanoclusters resulting from Wan Der Waals forces between the nanoparticles and the engine oil. These nanoclusters stopped the movement of base fluid on each other. Additionally, as the temperature was increased, the viscosity of the nanofluids decreased because of the depreciation of the intermolecular interactions between the molecules. Finally, the regression correlations (third-degree) were suggested depending on the solid fraction for each temperature. Experimental data and correlation values showed a minor deviation, suggesting that the proposed correlations demonstrated acceptable accuracy at each temperature.

Sundar et al. [9] investigated the rheological properties of Fe_3O_4 (iron oxide) nanoparticles dispersed in EG and water blends at different temperatures. The magnetic nanoparticles (Fe_3O_4) were created using the chemical coprecipitation method in which the aqueous solution of ferrous chloride/ferric chloride and sodium hydroxide was used. The EG and water blends (base nanofluid) were prepared in a mass ratio of 60:40, 40:60, and 20:80, respectively. Fe_3O_4 nanoparticle was added to the EG and water blends at different volume concentrations (from 0.0% to 1.0%). The viscosity values of blends were measured between 0ºC and 50ºC. The viscosity values of blends increased with increasing volume concentration of Fe_3O_4 nanoparticle and decreased with increasing temperatures. They suggested an equation similar form the Einstein model, to estimate the viscosity values of nanofluids based on the base fluid viscosity and the particle (Fe_3O_4) volume concentration. The equation had an average deviation of 6.1% and a standard deviation of 8.2%. However, the Einstein model consistently underestimated the experimental viscosity data for all blends including Fe_3O_4 nanoparticle. At the temperature of 50ºC, the viscosity values of EG and water blends (with mass ratios of 60:40, 40:60, and 20:80) increased by 2.94 times, 1.61 times, and 1.42 times, respectively, with the addition of a 1% volume concentration of Fe_3O_4. At the temperature of 0ºC, the viscosity values of EG and water blends (with mass ratios of 60:40, 40:60, and 20:80) increased by 2.13 times, 1.92 times, and 1.4 times, respectively, with the addition of a 1% volume concentration of Fe_3O_4. They suggested the magnetic nanofluids as heat transfer fluids. They stated that their unique advantage lies in their magnetic response, even when the nanoparticles are fully dispersed in the base fluid.

Sokhal et al. [10] investigated the thermal and flow characteristics of water-based alumina nanofluids in a radiator. The experiments were performed under different nanofluid inlet temperatures, Reynolds numbers (12000-30000), particle concentrations, and air velocities (0.25 m/s-0.55 m/s). Nanofluids were created using the two-step method in which double-distilled water (base fluid) and alumina nanoparticles were used at various concentrations (0.2-1% by volume). The thermal conductivity (W/mK) values of Al_2O_3/water nanofluids increased with increasing temperature (30ºC-70ºC) and nanoparticle concentration (0.2%-1% vol.). The thermal conductivity of nanofluids was found to be more sensitive to the change in temperature compared to the base fluid (water). At higher temperatures, nanofluids exhibited higher thermal conductivity than the base fluid (water). For example, the thermal conductivity of a 1.0% (v/v) nanofluid at 30ºC (0.673 W/mK) was 8% higher than that of the base fluid (0.619 W/mK). Moreover, at 70ºC, it (0.796 W/mK) was 20% higher than the base fluid (0.660 W/mK). The improvement in the thermal conductivity of nanofluids was due to the presence of a liquid nanolayer as well as the Brownian motion of the nanoparticles. The viscosity values of nanofluids increased with increasing particle volume concentrations (0.2%-1% vol.). The viscosity values also decreased with increasing temperature (30ºC-90ºC). The density values of nanofluids increased with increasing particle volume concentrations (0.2%-1% vol.). The density values decreased with rising temperature (30ºC-80ºC). The specific heat of nanofluids (kJ/kgK) was found to be more sensitive to the concentration of Al_2O_3 than to temperature. The specific heat of the base fluid (water) increased by only 0.7% when the temperature was increased from 40ºC to 90ºC. The heat capacity of nanofluids increased with increasing temperature but decreased with increasing particle volume concentrations due to the lower specific heat of Al_2O_3 than water. The variation of the heat transfer coefficient (W/m^2K) for both the base fluid and nanofluids in a vertical tube as a function of Reynolds number was investigated for a fluid inlet temperature of 40ºC. The concentration of nanoparticles (0.25%-1% vol.) played a crucial role in enhancing the heat transfer coefficient. Nanoparticles in the base fluid increased the heat transfer coefficient. The heat transfer rate (W) enhancement was 5% and 7% for a nanoparticle concentration of 0.25% (v/v) at Reynolds numbers of 12000 and 30000, respectively. It was investigated that the effects of the fluid inlet temperature (40ºC, 50ºC, 60ºC, 70ºC, 80ºC, and 90ºC) on heat transfer coefficient (W/m^2K). With increasing the

ISBN: 978-618-5765-04-0
ISSN 3057-4269

fluid inlet temperature, the heat transfer coefficient increased due to the enhancement in thermal conductivity and the reduction in density and viscosity of the nanofluids. For instance, increasing the inlet temperature from 40ºC to 60ºC resulted in a 16% improvement in the heat transfer coefficient.

CONCLUSION

This review study has investigated nanofluids' potential as alternative coolants for automotive radiators. The use of nanoparticles significantly improves the thermophysical properties of the base fluids, which improves heat transfer rate and energy efficiency. Furthermore, nanofluids can offer a promising way to design more efficient and compact radiator systems. However, alongside these benefits, the higher viscosity of nanofluids leads to challenges, such as increased pumping power and flow resistance. Moreover, long-term stability, cost-effectiveness, and material compatibility must be carefully considered before nanofluids can be widely adopted in automotive radiators. Optimizing nanoparticle concentrations and formulating stable nanofluids can be studied for future studies.

REFERENCES

[1] W. W. Pulkrabek, "Engineering Fundamentals of the Internal Combustion Engine," Prentice Hall, New Jersey 07458, 1997.

[2] M. Afrand, K. N. Najafabadi and M. Akbari, "Effects of temperature and solid volume fraction on viscosity of SiO2-MWCNTs/SAE40 hybrid nanofluid as a coolant and lubricant in heat engines," Applied Thermal Engineering, vol. 102, pp. 45-54, 2016.

[3] X. Li, H. Wang and B. Luo, "The thermophysical properties and enhanced heat transfer performance of SiC-MWCNTs hybrid nanofluids for car radiator system," Colloids and Surfaces A: Physicochemical and Engineering Aspects, vol. 612, pp. 125968, 2021.

[4] J. C. Maxwell, "A treatise on electricity and magnetism," Clarendon Press Google Schola, vol. 2, pp. 3408-3425, 1873.

[5] G. A. Oliveira, E. M. C. Contreras and E. P. B. Filho, "Experimental study on the heat transfer of MWCNT/water nanofluid flowing in a car radiator," Applied Thermal Engineering, vol. 111, pp. 1450-1456, 2017.

[6] M. Kh. Abdolbaqi, N. A. C. Sidik, M. F. A. Rahim, R. Mamat, W. H. Azmi, M. N. A. W. M. Yazid and G. Najafi, "Experimental investigation and development of new correlation for thermal conductivity and viscosity of BioGlycol/water based SiO2 nanofluids," International Communications in Heat and Mass Transfer, vol. 77, pp. 54-63, 2016.

[7] M. Hajiakbari, A. M. Nejad and E. Houshfar, "Enhancing diesel engine cooling efficiency: A comprehensive numerical study on nanofluid coolants with exergy and economic analysis," *Case Studies in Thermal Engineering*, vol. 56, pp. 104217, 2024.

[8] M. H. Esfe, M. Afrand, S. Gharehkhani, H. Rostamian, D. Toghraie and M. Dahari, "An experimental study on viscosity of alumina-engine oil: Effects of temperature and nanoparticles concentration," *International Communications in Heat and Mass Transfer*, vol. 76, pp. 202-208, 2016.

[9] L. S. Sundar, E. V. Ramana, M. K. Singh, A. C. M. De Sousa, "Viscosity of low volume concentrations of magnetic Fe_3O_4 nanoparticles dispersed in ethylene glycol and water mixture," *Chemical Physics Letters*, vol. 554, pp. 236-242, 2012.

[10] G. S. Sokhal, D. Gangacharyulu and V. K. Bulasara, "Heat transfer and pressure drop performance of alumina-water nanofluid in a flat vertical tube of a radiator," *Chemical Engineering Communications*, vol. 205, pp. 257-268, 2018.

ISBN: 978-618-5765-04-0
ISSN 3057-4269

Optimal Product Line Re-Design for Reducing Food Wasted due to Marketing Standards

Stelios Tsafarakis
School of Production Engineering and Management, Technical University of Crete
Chania, Greece
tsafarakis@tuc.gr

Konstantinos Zervoudakis
School of Production Engineering and Management, Technical University of Crete
Chania, Greece
kzervoudakis@tuc.gr

***Abstract*— The aim of this study is to apply a multi-objective product line optimization approach for reducing food waste while balancing profit and buyer's welfare. The proposed approach is based on a Non-dominated Sorting Genetic Algorithm II (NSGA-II) and it is used for addressing the NP-hard problem of product line redesign, by optimizing both economic and social objectives. The results reveal that NSGA-II performs great in detecting non-dominated solutions, ensuring a better distribution among those solutions, while converging faster to optimal product configurations at the same time. By using buyer's welfare into the optimization process, the model offers an important tool for reducing food waste by promoting suboptimal products, thereby enhancing sustainability.**

Keywords*— *Product Line Re-design, Food Waste Reduction, NSGA-II, Buyer's Welfare, Multi-objective Optimization

INTRODUCTION

Waste of food is a well-known global issue, with large amounts of edible food being wasted every day. One of the reasons behind this waste is the marketing standards used for food products, which help ensure that food looks good and meets certain quality expectations, even though they can also lead to food being wasted unnecessarily. For example, food that doesn't meet cosmetic standards, is often discarded even though it may be considered to be safe to eat [1].

The problem with these marketing standards is that they focus too much on appearance, which can lead consumers to avoid buying food that is in good condition. As a result, a large amount of food waste comes from packages that do not meet those standards. This creates an important challenge for food firms to satisfy consumers who want to reduce waste [2].

The aim of this paper is to apply a methodology that balances two important factors, the profit of firms and the welfare of buyers, while creating a product line. By using this approach product lines can be redesigned to improve the marketability of food products, instead of just focusing on increasing profit. In doing so, firms can still achieve good profits while reducing food waste and better meeting consumer needs better [3].

LITERATURE REVIEW

Marketing standards play an important role in the food industry, since they affect food waste. They are designed for ensuring that products meet certain quality and appearance criteria, such as size and shape. However, research shows that appearance often leads to the rejection and disposal of food that is actually in good condition and is considered safe to consume. For example, food that is not in a specific package as expected or it is slightly damaged, it is discarded, even though it is considered safe to buy and consume. This problem has been highlighted by previous studies, which mention that even though marketing standards are important, they can also result in food waste [2], [4], [5], [6], [7].

The Product Line Design (PLD) problem is a complex NP-hard class optimization problem, and it is a key research area in marketing that focuses on determining the optimal features of the products offered by a firm, often formulated in the context of Conjoint Analysis [8]. PLD aims at optimizing an objective set by the firms, like maximizing profits or market share [9], [10], [11]. However, focusing solely on economic objectives can lead on food waste [12].

In recent years, growing awareness of the need to incorporate sustainability into marketing practices is noticed [13]. Companies are starting to recognize that sustainability goes beyond profitability and includes social and environmental considerations. As a result, product managers have to find ways to reduce waste and meet consumer welfare expectations for sustainable products. Studies have shown that consumers are more likely to buy products that are considered to be environmentally friendly, which has altered the way companies design their products [14]. By incorporating sustainability into the PLD process, firms not only reduce waste but also improve their reputation as eco-friendly brands.

METHODOLOGY

The aim of this paper is to address PLD balancing the two objectives of maximizing profit for firms and improving the welfare of buyers, in order to avoid food waste [9]. This challenge stems from the need to determine the optimal configuration of the product line, a decision that involves selecting which products to offer, how they should be packaged, how they should be prized and how they can appeal to consumers who might otherwise avoid purchasing suboptimal ones. This approach allows companies to retain profitability while reducing waste.

Multi-objective optimization

To optimize the conflicting objectives of maximizing profit and buyers' welfare, using BTL as a choice model [15], this paper uses a multi-objective optimization approach based on the Non-dominated Sorting Genetic Algorithm II (NSGA-II) [16], a method that allows the optimization of both objectives. NSGA-II generates a range of solutions that lie on a Pareto front, where no single solution is better according to all criteria without compromising another. In this case, the trade-offs between profit and buyer's welfare are explored, with a specific focus on reducing food waste. By optimizing both objectives, firms can identify product line configurations that help them maintain profitability while ensuring that their products are still attractive to consumers. This method is expected to lead to less food being wasted, as more products are selected by consumers even when they do not meet strict

ISBN: 978-618-5765-04-0
ISSN 3057-4269

appearance standards. The performance of NSGA-II is compared to that of a Multi-Objective Particle Swarm Optimization combined with Crowding Distance (MOPSO-CD) [17] according to popular comparison metrics [16], [18].

Regarding the parameter selection of each algorithm, the parameters of NSGA-II were chosen according to previous research on applying a genetic algorithm on PLD [19], and the parameters of MOPSO-CD were also chosen according to previous research on applying PSO on PLD [20].

Dataset

The dataset used in this study is based on a market survey conducted on olive oil products using Choice-Based Conjoint Analysis (CBCA) [21]. The dataset includes the partworths of 417 consumers regarding five attributes of olive oil products, including olive oil type, package type, package size, brand, and price per liter. These attributes have multiple levels, with each level having specific partworths for each consumer, which represent the consumer's perceived value of that feature. Additionally, the dataset includes information on marginal costs associated with each feature, which are essential for the accurate calculation of profit.

The dataset also includes details about the olive oil consumption of consumers, with statistics such as their olive oil usage per month, as well as prohibitions for certain combinations of product features (e.g., glass packaging with large packages like 5 liters), which add further complexity to the problem. This dataset allows the application of multi-objective optimization, to balance firm profitability with buyer's welfare to reduce food waste.

RESULTS

In this section, the results from both multi-objective optimizers are presented in detail. Both algorithms run 50 times, until 50,000 functions evaluations are reached.

In Figure 1, a comparison between the Pareto fronts of NSGA-II and MOPSO-CD is presented. This figure clearly demonstrates that NSGA-II is able to detect non-dominated solutions faster.

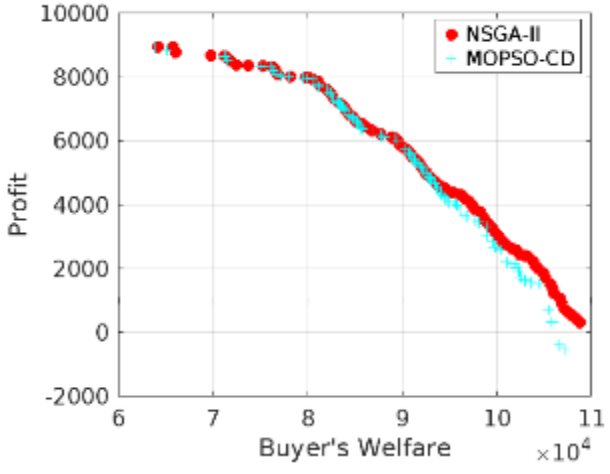

Figure 1: Pareto comparison

This finding is verified by the results of the *C* metric which are presented in Table1. Table 1 presents the average *C* metric values of both mutli-objective optimizers from all 50 runs. From those results, it is clear that the non-dominated solutions retrieved from NSGA-II dominate that of MOPSO-CD in most cases.

Table 1: Table Type Styles

Method	NSGA-II	MOPSO-CD
NSGA-II	1	0.64
MOPSO-CD	0.28	1

Figure 2 demonstrates the average convergence behavior of the two optimizers towards the profit-optimum solution, across all 50 runs. From this figure, it is clear that both algorithms, even though having differences in their convergence behavior, they manage to converge towards the profit-optimum solution within 50,000 function evaluations.

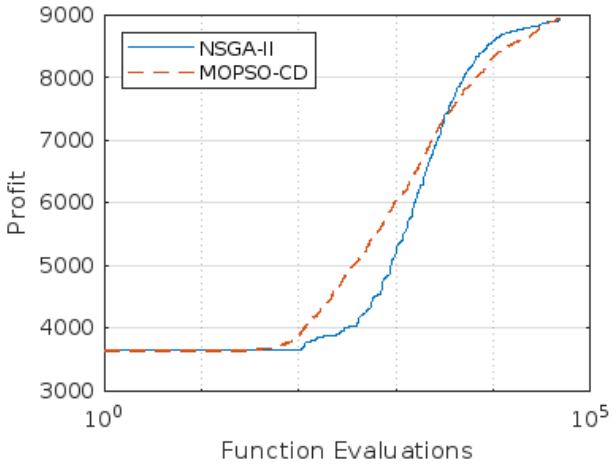

Figure 2: Convergence behavior towards profit-optimum line

Figure 3 demonstrates the average convergence behavior of the two optimizers towards the buyer's welfare-optimum solution. From this figure, it is clear that NSGA-II manages to converge faster towards the buyer's welfare-optimum solution within 50,000 function evaluations.

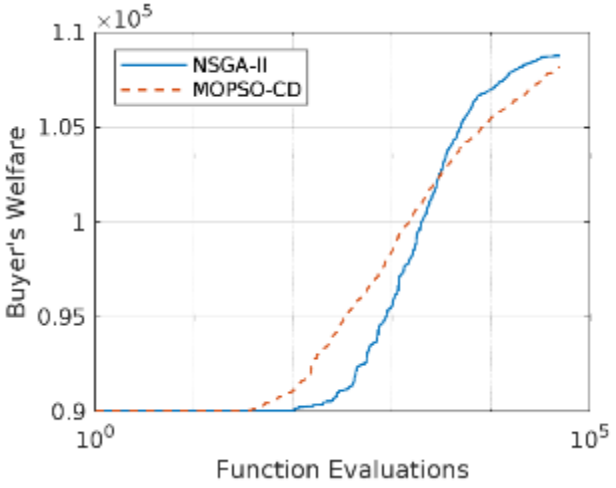

Figure 3: Convergence behavior towards buyer's welfare-optimum line

The above findings are confirmed by Figure 4 which demonstrates the M1 metric values from each of the 50 runs. In those violin plots, each dot corresponds to a value from the 50 runs, while the black square corresponds to the median values and the white circles corresponds to the mean values. Since the M1 metric reveals the distance from the optimal Pareto front, it is clear that NSGA-II's non-dominated solution

ISBN: 978-618-5765-04-0
ISSN 3057-4269

set is closer to the optimal Pareto front than that of MOPSO-CD.

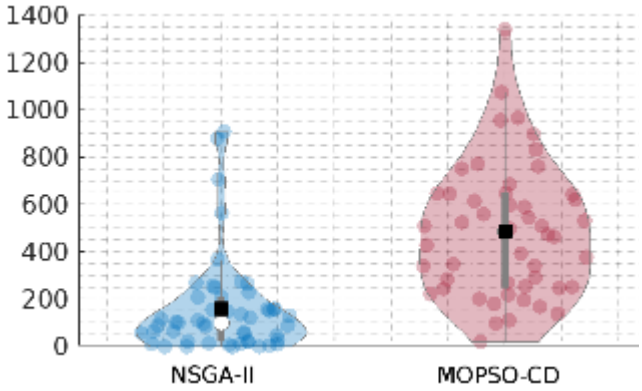

Figure 4: Results of M1 metric

Figure 5 demonstrates the results of the Δ metric, which evaluates the distribution among the solutions. Low values of the Δ metric indicate better distribution among the non-dominated solutions. As a result, NSGA-II has a better distribution among the solutions, according to this metric.

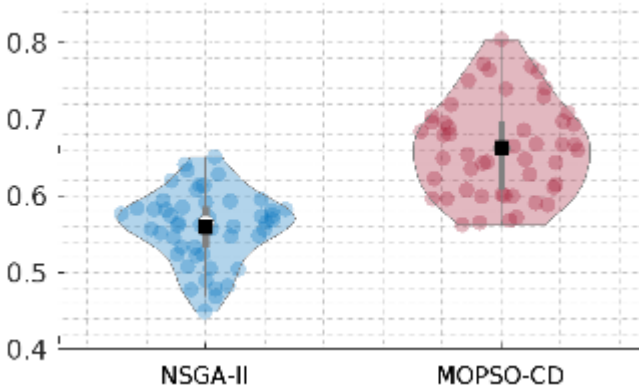

Figure 5: Results of Δ metric

Finally, *M3* metric demonstrates the percentage of the maximum extent ever found of each front of non-dominated solutions. While MOPSO-CD is able to detect a greater percentage, it appears to get trapped in local optima points (especially when optimizing buyer's welfare according to Figure 3). As a result, NSGA-II has better average and median values of the *M3* metric, which means that NSGA-II is able to identify a better extent of the non-dominated solutions most of the times.

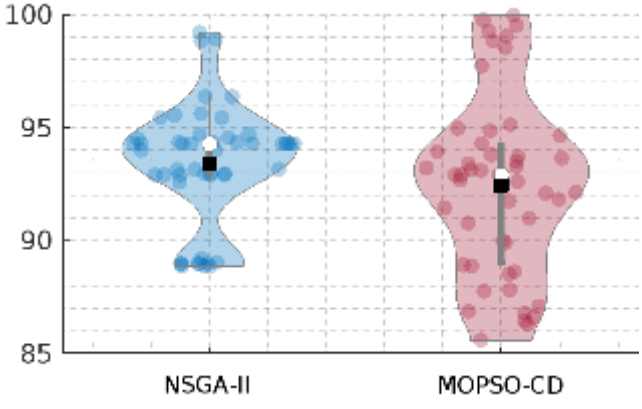

Figure 6: Results of M3 metric

The results presented above demonstrate that NSGA-II outperforms MOPSO-CD in several key areas, including faster convergence to non-dominated solutions, better distribution of solutions, better extent of the front and a more consistent ability to find optimal solutions. These findings have important implications for real-world applications, especially in the PLD optimization used for reducing food waste.

Particularly, the superior performance of NSGA-II means that firms can redesign their product lines more effectively, by balancing the conflicting objectives of maximizing profit and buyer's welfare. For example, NSGA-II's ability to quickly converge on solutions that optimize both profit and buyer's welfare allows companies to make decisions in time, about which products to offer, how to price them, and how to create suboptimal products that might be discarded otherwise, due to packaging.

Additionally, NSGA-II's better distribution and extent of non-dominated solutions ensures that companies have a broader range of options to choose when making decisions about the configuration of their product lines. This is crucial in the food industry, where firms must explore complex trade-offs between consumer preferences, cost efficiency, and sustainability goals [22]. By adopting NSGA-II, firms can produce food products that may not meet strict appearance standards but are still perfectly safe to consume, resulting in reduced food waste and contributing to sustainability. The use of NSGA-II in product line redesign offers a promising approach for firms trying to achieve both profitability and sustainability. By optimizing product lines according to buyer's welfare, businesses can address the important issue of food waste while still maintaining a competitive advantage in the market.

CONCLUSIONS

This study aimed to address the issue of food waste by developing and applying a multi-objective product line optimization approach that not only focuses on maximizing profit but also integrates buyer's welfare. By employing a NSGA-II firms are able to address the NP-hard problem of PLD, by balancing conflicting objectives, and thus, redesign their product lines in a way that supports marketability, consumer satisfaction, and reduces food waste.

The results of this study demonstrated that NSGA-II outperforms MOPSO-CD, when it comes to identifying non-dominated solutions faster and achieving better distribution across the Pareto front. Various performance metrics like the *C* metric, the *M1* metric, the *M3* metric, and the Δ metric, confirmed the robustness and efficiency of NSGA-II, showing it to be more effective in exploring the trade-offs between profitability and buyer's welfare.

This study revealed that the proposed model is able to assist in the creation of a broader range of product configurations, which might have been overlooked due to cosmetic standards or other marketing criteria. By redesigning product lines to include products that would otherwise be rejected, firms can maximize profit and reduce unnecessary waste, at the same time. This is crucial nowadays where sustainability is becoming more and more important, both for consumers and firms [23].

NSGA-II also appeared to have a superior convergence behavior, consistently reaching optimal solutions in fewer

ISBN: 978-618-5765-04-0
ISSN 3057-4269

function evaluations. These findings suggest that the optimizer is not only effective but also computationally efficient, making it a very useful tool for firms looking to make their product lines more sustainable.

Moreover, the practical implications of this study are important for firms in the food industry. For instance, products that are cosmetically flawed can be positioned within the market as sustainable choices for eco-conscious consumers. As a result, products that would have been wasted, turn into an opportunity for revenue for the firms.

Additionally, the model's ability to balance buyer's welfare with profit offers a new path to marketing standards. By optimizing buyer's welfare, firms can offer products that align with the high consumer demand for environmentally friendly practices. This shift can improve brand loyalty, enhance a firm's reputation, and create new market opportunities [24].

While this study provides great insights for the optimization of product lines in the food industry with the use of the two objectives of buyer's welfare and maximizing profit, future research could further enhance the model and its applications. For example, our model can be extended to other product categories beyond food. Many industries, including fashion, electronics, and cosmetics, face similar issues of waste due to strict marketing standards or consumer expectations [25]. Applying the optimization model in these sectors could offer valuable insights about how firms in other industries can also reduce waste while earning profits.

Finally, while NSGA-II was found to be highly effective, there are other advanced recently developed optimization algorithms that could be explored in future research [26], [27], [28], [29]. Those techniques may offer even greater efficiency and accuracy in solving complex product line redesign problems.

REFERENCES

[1] M. Rao, N. Bernaz, and A. de Boer, "Holding Retail Corporations Accountable for Food Waste: A Due Diligence Framework Informed by Business and Human Rights Principles," *Journal of Business Ethics*, vol. 193, no. 3, pp. 679–689, Sep. 2024, doi: 10.1007/S10551-023-05572-0/FIGURES/2.

[2] K. Nes and P. Ciaian, "EU marketing standards and sustainability," *Appl Econ Perspect Policy*, vol. 44, no. 4, pp. 1844–1863, Dec. 2022, doi: 10.1002/AEPP.13265.

[3] S. Ahmadi Kaliji, S. M. Mojaverian, H. Amirnejad, and M. Canavari, "Simultaneous consideration of consumer preferences and seller revenue as a smart retail sales and management strategy," *European Journal of Management and Business Economics*, 2024, doi: 10.1108/EJMBE-04-2022-0105/FULL/PDF.

[4] C. Casonato, L. García-Herrero, C. Caldeira, and S. Sala, "What a waste! Evidence of consumer food waste prevention and its effectiveness," *Sustain Prod Consum*, vol. 41, pp. 305–319, Oct. 2023, doi: 10.1016/J.SPC.2023.08.002.

[5] I. do C. Stangherlin, J. L. Duarte Ribeiro, and M. Barcellos, "Consumer behaviour towards suboptimal food products: a strategy for food waste reduction," *British Food Journal*, vol. 121, no. 10, pp. 2396–2412, Sep. 2019, doi: 10.1108/BFJ-12-2018-0817/FULL/XML.

[6] E. Varese, M. C. Cesarani, and M. Wojnarowska, "Consumers' perception of suboptimal food: strategies to reduce food waste," *British Food Journal*, vol. 125, no. 1, pp. 361–378, Jan. 2023, doi: 10.1108/BFJ-07-2021-0809/FULL/XML.

[7] M. Rao, N. Bernaz, and A. de Boer, "Holding Retail Corporations Accountable for Food Waste: A Due Diligence Framework Informed by Business and Human Rights Principles," *Journal of Business Ethics*, vol. 193, no. 3, pp. 679–689, Sep. 2024, doi: 10.1007/S10551-023-05572-0/FIGURES/2.

[8] S. Tsafarakis, K. Zervoudakis, A. Andronikidis, and E. Altsitsiadis, "Fuzzy self-tuning differential evolution for optimal product line design," *Eur J Oper Res*, vol. 287, no. 3, pp. 1161–1169, Dec. 2020, doi: 10.1016/j.ejor.2020.05.018.

[9] M. Pantourakis, S. Tsafarakis, K. Zervoudakis, E. Altsitsiadis, A. Andronikidis, and V. Ntamadaki, "Clonal Selection Algorithms for Optimal Product Line Design: A Comparative Study," *Eur J Oper Res*, vol. 298, no. 2, pp. 585–595, Jul. 2022, doi: 10.1016/J.EJOR.2021.07.006.

[10] K. Zervoudakis, S. Tsafarakis, and S. Paraskevi-Panagiota, "A New Hybrid Firefly – Genetic Algorithm for the Optimal Product Line Design Problem," in *Learning and Intelligent Optimization. LION 2019. Lecture Notes in Computer Science*, N. Matsatsinis, Y. Marinakis, and P. Pardalos, Eds., Springer, Cham, 2020, pp. 284–297. doi: 10.1007/978-3-030-38629-0_23.

[11] S. Tsafarakis, "Redesigning product lines in a period of economic crisis: a hybrid simulated annealing algorithm with crossover," *Ann Oper Res*, vol. 247, no. 2, pp. 617–633, 2016, doi: 10.1007/s10479-015-2032-0.

[12] W. C. Tsai, X. Chen, and C. Yang, "Consumer Food Waste Behavior among Emerging Adults: Evidence from China," *Foods*, vol. 9, no. 7, p. 961, Jul. 2020, doi: 10.3390/FOODS9070961.

[13] R. Garg, R. Chhikara, G. Agrawal, R. Rathi, and Y. Arya, "Sustainable marketing mix and supply chain integration: A systematic review and research agenda," *Sustainable Futures*, vol. 8, p. 100269, Dec. 2024, doi: 10.1016/J.SFTR.2024.100269.

[14] P. Duarte, S. C. Silva, A. S. Roza, and J. C. Dias, "Enhancing consumer purchase intentions for sustainable packaging products: An in-depth analysis of key determinants and strategic insights," *Sustainable Futures*, vol. 7, p. 100193, Jun. 2024, doi: 10.1016/J.SFTR.2024.100193.

[15] R. A. Bradley and M. E. Terry, "Rank Analysis of Incomplete Block Designs: I. The Method of Paired Comparisons," *Biometrika*, vol. 39, no. 3/4, p. 345, Dec. 1952, doi: 10.2307/2334029.

[16] K. Deb, A. Pratap, S. Agarwal, and T. Meyarivan, "A fast and elitist multiobjective genetic algorithm: NSGA-II," *IEEE Transactions on Evolutionary Computation*, vol. 6, no. 2, pp. 182–197, Apr. 2002, doi: 10.1109/4235.996017.

[17] C. R. Raquel and P. C. Naval, "An effective use of crowding distance in multiobjective particle swarm optimization," in *Proceedings of the 2005 conference on Genetic and evolutionary computation - GECCO '05*, New York, New York, USA: ACM Press, 2005, p. 257. doi: 10.1145/1068009.1068047.

[18] E. Zitzler, K. Deb, and L. Thiele, "Comparison of Multiobjective Evolutionary Algorithms: Empirical Results," *Evol Comput*, vol. 8, no. 2, pp. 173–195, Jun. 2000, doi: 10.1162/106365600568202.

[19] A. Belloni, R. Freund, M. Selove, and D. Simester, "Optimizing Product Line Designs: Efficient Methods and Comparisons," *Manage Sci*, vol. 54, no. 9, p. 1544−1552, 2008, doi: 10.1287/mnsc.1080.0864.

[20] S. Tsafarakis, Y. Marinakis, and N. Matsatsinis, "Particle swarm optimization for optimal product line design," *International Journal of Research in Marketing*, vol. 28, no. 1, pp. 13–22, 2011, doi: 10.1016/j.ijresmar.2010.05.002.

[21] J. Mansuy, S. Verlinde, and C. Macharis, "Understanding preferences for EEE collection services: A choice-based conjoint analysis," *Resour Conserv Recycl*, vol. 161, p. 104899, Oct. 2020, doi: 10.1016/J.RESCONREC.2020.104899.

[22] J. Broeze, X. Guo, and H. Axmann, "Trade-Off Analyses of Food Loss and Waste Reduction and Greenhouse Gas Emissions in Food Supply Chains," *Sustainability*, vol. 15, no. 11, p. 8531, Jun. 2023, doi: 10.3390/SU15118531/S1.

[23] A. Siraj, S. Taneja, Y. Zhu, H. Jiang, S. Luthra, and A. Kumar, "Hey, did you see that label? It's sustainable!: Understanding the role of sustainable labelling in shaping sustainable purchase behaviour for sustainable development," *Bus Strategy Environ*, vol. 31, no. 7, pp. 2820–2838, Nov. 2022, doi: 10.1002/BSE.3049.

[24] D. González-Viralta, I. Veas-González, F. Egaña-Bruna, C. Vidal-Silva, C. Delgado-Bello, and C. Pezoa-Fuentes, "Positive effects of green practices on the consumers' satisfaction, loyalty, word-of-mouth, and willingness to pay," *Heliyon*, vol. 9, no. 10, pp. 2405–8440, Oct. 2023, doi: 10.1016/J.HELIYON.2023.E20353/ASSET/73E88200-1144-4E25-94FB-C11ABC62D5BE/MAIN.ASSETS/GR002.JPG.

[25] V. Schiaroli, | Rosa, M. Dangelico, | Luca Fraccascia, A. Ruberti, and L. Fraccascia, "Mapping sustainable options in the fashion industry: A systematic literature review and a future research agenda," *Sustainable Development*, 2024, doi: 10.1002/SD.3129.

[26] K. Zervoudakis and S. Tsafarakis, "A mayfly optimization algorithm," *Comput Ind Eng*, vol. 145, p. 106559, May 2020, doi: 10.1016/j.cie.2020.106559.

[27] K. Zervoudakis and S. Tsafarakis, "A global optimizer inspired from the survival strategies of flying foxes," *Eng Comput*, vol. 39, pp. 1583–1616, Jan. 2023, doi: 10.1007/S00366-021-01554-w.

[28] D. Połap and M. Woźniak, “Red fox optimization algorithm,” *Expert Syst Appl*, vol. 166, p. 114107, Mar. 2021, doi: 10.1016/J.ESWA.2020.114107.

[29] L. Deng and S. Liu, “Snow ablation optimizer: A novel metaheuristic technique for numerical optimization and engineering design,” *Expert Syst Appl*, vol. 225, p. 120069, Sep. 2023, doi: 10.1016/J.ESWA.2023.120069.

ISBN: 978-618-5765-04-0
ISSN 3057-4269

Correlation Analysis of Wind and Wave Power in the Eastern Mediterranean Sea

Tahsin Görmüş
Department of Civil Engineering
Gebze Technical University
Kocaeli, Turkey
tgormus@gtu.edu.tr

Burak Aydoğan
Department of Civil Engineering
Gebze Technical University
Kocaeli, Turkey
baydogan@gtu.edu.tr

Berna Ayat
Department of Civil Engineering
Yildiz Technical University
İstanbul, Turkey
bayat@yildiz.edu.tr

***Abstract*— This study aims to quantify the correlation levels of wind and wave power for specified nearshore locations in the Eastern Mediterranean Sea. Correlation level between two energy sources is an important indicator of their ability as a hybrid working couple. ERA5 hourly dataset from the European Centre for Medium-Range Weather Forecasts (ECMWF) between the years 1959 and 2021 is used as the data source with the variables of 100 m altitude wind speed components and significant wave heights and periods of the surface waves. Three analysis locations are selected to investigate wind and wave power computed from the raw variables. Selected analysis locations included Northern Aegean Sea (P1), Southern Aegean Sea (P2), and the Levantine Basin (P3). Yearly and seasonal averages of wind and wave power are investigated. Statistical properties of time-series are investigated with average and 95% values, and bivariate histograms considering different magnitude classes for the two sources. The correlation analysis is carried out with both Pearson correlation coefficient (CC) and Kendall's Tau CC with an aim of also comparing the two estimation methods. Among the selected locations, P2 has the highest potential of wind power with 416.3 W/m^2 mean value and 1268.6 W/m^2 95% value. The highest wave power potential is also obtained in P2 with nearly 5 kW/m average and 17.6 kW/m 95% value. Pearson CC values are computed as 0.89, 0.84, and 0.76 for the analysis locations P1, P2, and P3, respectively. Kendall's Tau CC values are computed as 0.68, 0.65, and 0.45 for the analysis locations P1, P2, and P3, respectively. This shows the highest correlation in the Northern Aegean Sea, with lower correlation values in the South. The differences between the two CCs are also revealed. Kendall's Tau is always lower for the considered analysis locations between 23% and 41% difference comparing to the Pearson CC. These findings highlighted the differences between the regions in the Eastern Mediterranean in terms of wind and wave power and their correlation.**

Keywords*— correlation, offshore energy, wind and wave hybrids

INTRODUCTION

The total energy consumption of the world was 24700 TWh in 2021, representing a 6% over the previous year. This increase likely to be continued, which necessitates advancement on renewable sources, also considering their mitigating effects on the climate change [1]. The marine resources reported to be greater than that of land, with no limitation on development. The visual and acoustic impacts are lower, and there are possibilities to take advantage of the other marine resources in hybrid facilities. Offshore winds have greater potential because of the higher altitudes with greater wind speeds and less fluctuations. These advantages are promising for offshore energy to be an important candidate as an energy solution [2].

Integrating different renewable energy sources such as wind, wave, and solar could prove valuable for the world growing necessity for energy consumption. The combination of wave and wind is a promising solution, increasing accessibility for operation and maintenance tasks over 13% [3], protecting the floating system and its structures against the extreme events [4]. Hybrid energy platforms introduce benefits by the co-working ability of different renewable energy sources, but also necessitates the investigation of patterns about their behavior in a simultaneous manner.

To that end, the assessment of complementarity between these sources is crucial for efficient energy generation. Assessing the correlation and complementarity between energy sources can help reduce variability and optimize energy output. This study evaluates the correlation levels between wind and wave energy in three selected locations in the Eastern Mediterranean Sea using one wind turbine and eight selected wave energy converter (WEC) couples. Additional analysis has been carried out about their potential and capacity factors (CFs) as well as the directionality of wind and wave energy potential. By quantifying the statistical characteristics and the correlation levels of the two sources, it is aimed to understand how well the wind and wave energy devices work with each other and how suitable are the selected locations for a hybrid configuration.

METHODS

Power Density

The wind power (P_{wind}) per rotor area (W/m^2) is calculated using the expression [5]:

$$P_{wind} = 0.5\rho_{air}WS^3 \quad (1)$$

where ρ_{air} is air density and WS is the wind speed. A wind turbine with following working condition is used in this study: cut-in wind speed of $WS_{cut\text{-}in}$=3.5 m/s, cut-out wind speed of $WS_{cut\text{-}off}$=25 m/s, rated wind speed of WS_{rated}=12 m/s, and a rotor diameter of 120 m.

The offshore wave power (P_{wave}) is defined as the potential energy density per wave front (kW/m), and computed by the expression [6]:

$$P_{wave} = 0.5H_s^2T_e \quad (2)$$

where H_s and T_e show the significant height and the energy period of the ocean waves, respectively.

The WECs selected in this study is given in Table 1 with their classification, structure, and rated power values. Necessary information is gathered from the study of [7] and [8]. Rated power values are used to normalize the average power values which will result in CF of the devices.

ISBN: 978-618-5765-04-0
ISSN 3057-4269

Table 1: The main features of the selected WECs

No	WEC Device	Device Properties		
		Classification/Energy Mode	***Structure***	***Rated Power (kW)***
1	Pelamis	Attenuator/Heave and sway	Four-body floating	750
2	OE_buoy	Oscillating water column/ Surge	Single body floating	2880
3	AquaBuoy	Point absorber/Heave	Two-body floating	250
4	AWS	Point absorber/Heave	Two-body submerged	2470
5	SeaPower	Attenuator/Pitch	Two-body platform	3587
6	Wavebob	Point absorber/Heave	Two-body floating	1000
7	Pontoon	Multiple point absorber/Heave	Multibody floating	3619
8	Langlee	Oscillating wave surge converter/Surge	Semi-submergible	1665

Correlation Coefficient (CC)

Pearson CC is the division of the covariance between the two variables to the multiplication of standard deviations of each. The Pearson CC is defined by the following formulation:

$$R_{x,y} = \frac{\frac{1}{N}\sum_{k=1}^{N}(x_k - \bar{x})\,(y_k - \bar{y})}{s_x s_y} \quad (3)$$

where σ denotes the standard deviation. Kendall Tau's CC is calculated using the formulation:

$$\tau = \frac{2}{n(n-1)}(N_C - N_D) \quad (4)$$

where N_C and N_D show the number of concordant and discordant pairs, respectively [8]. Correlation coefficients are presented for both raw time series, and the device time series where the actual energy production values are considered using the device working conditions of both wind turbine and WECs.

Data Source

The significant wave height of combined wind waves and swell, the mean wave period, and the 100-m hourly wind speed data are used from the ERA5 reanalysis dataset [9] between the years of 1959 and 2021. The length of the data ensures the time characteristics of the energy sources are well presented.

STUDY AREA

The analysis locations have been selected for the study (Fig. 1). Two of the locations situated nearshore in Northern Aegean Sea (P1) and Southern Aegean Sea (P2), where and one location is situated in the offshore area of Levantine Basin (P3).

RESULTS ANS DISCUSSION

Results are presented based on the power densities of both sources, dominant directions, capacity factors, and correlation coefficients using two methods.

Power Density

Power density values for both sources are investigated for analysis locations. Values in Fig. 2 represent raw values computed from the data source without considering the device properties.

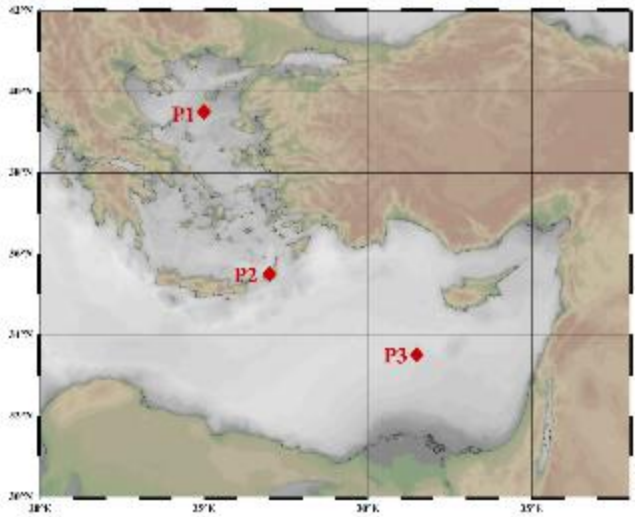

Figure 1: Study area, Aegean and the Eastern Mediterranean Sea

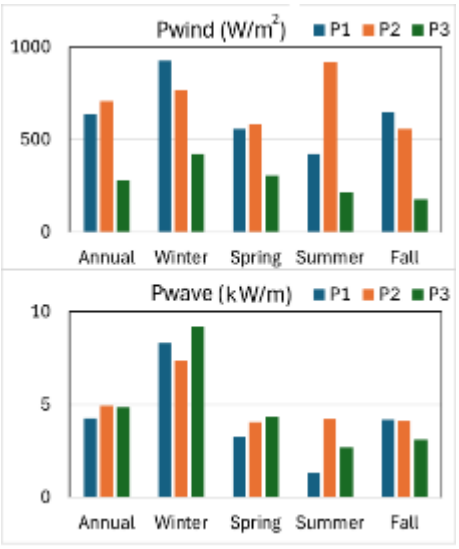

Figure 2: Wind and wave power density values for analysis locations.

The annual P_{wind} is calculated as 637 W/m^2, 708 W/m^2, and 281 W/m^2 for P1, P2, and P3, respectively. This shows that the analysis locations in the Aegean Sea have greater potential with the highest value in P2. The seasonal analysis in those locations showed that the average values are higher in winter, and lower in summer comparing to the annual values. The difference between the averages are higher in the winter comparing P1 and P2 with P3 which has lower P_{wind}. It is seen that the contribution of winter is greater in P1 to the annual average, where for P2, the contribution of spring and summer is higher.

P_{wave} has relatively closer values comparing the analysis locations, ranging between 4.3 kW/m (P1) and 4.9 kW/m (P3). For wave climate, a different scheme is evident between the analysis points, since when the wind waves could find long distances to travel without breaking such as P3 located in an far offshore location comparing the others, they would produce higher waves. This can be seen from the winter season, where the highest P_{wave} is computed for P3 with 9.2

ISBN: 978-618-5765-04-0
ISSN 3057-4269

kW/m. It is also true for the waves that the average values are higher than the annual averages.

The 2D histogram in Fig. 3 shows the most probable locations in the axial configuration where x axis shows P_{wind} and y axis shows P_{wave}. The analysis gives the opportunity of investigating the co-working capabilities of wind and wave power, and what are the magnitude pairs of wind and wave energy densities with corresponding probability values.

In general, the occurrences below 3 kW/m for wave power density and below 300 W/m^2 for wind power density have higher share in the two variable probability scenarios. For P1 and P2, lower extreme values are observed in the wave side, where the maximum value reaches to 200 kW/m. On the other hand, the maximum P_{wave} reaches over 400 kW/m. For wind power, the occurrences near the maximum value 12*10^3 W/m^2 have higher share in the time-series.

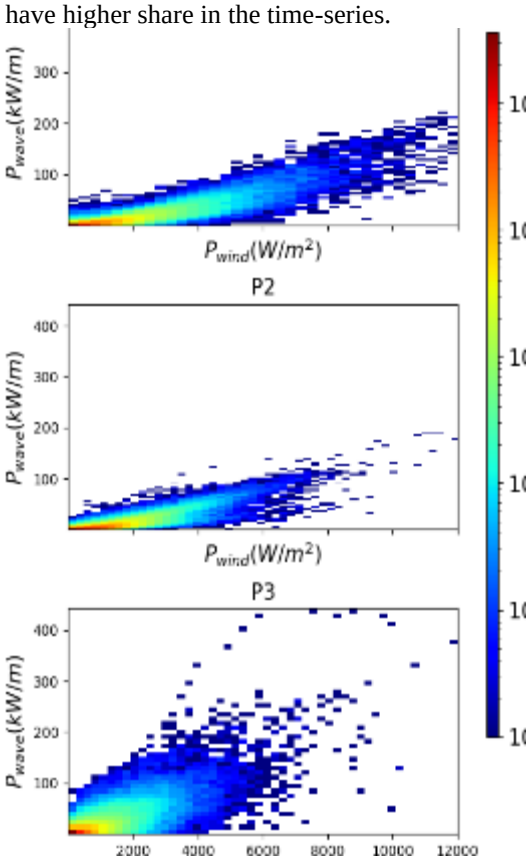

Figure 3: 2D histogram of wind and wave power density values in the analysis locations.

Capacity factors (CFs)

CF analysis for the wind turbine and eight different WECs are given in Fig. 4.

CF of the devices showed that the wind turbine has more capacity to benefit from the available source. The highest CF is calculated for P2, reflecting that the turbine has the greatest performance at the location. For the annual time-series, CF is 0.4, 0.5, and 0.23 for P1, P2, and P3, respectively. The highest CF is calculated for P2 with 0.68 in the summer where the lowest value is calculated for P3 with 0.15 in the fall.

The main results from the CF analysis for the WECs is that the devices have lower metric comparing to the wind turbine. Maximum value in the annual case is 0.07 achieved by Pelamis in P2 and P3. The WEC CF increases up to 0.13 in the winter season for Pelamis in P3. In general, the lowest CF is computed for OE buoy and AWS WECs.

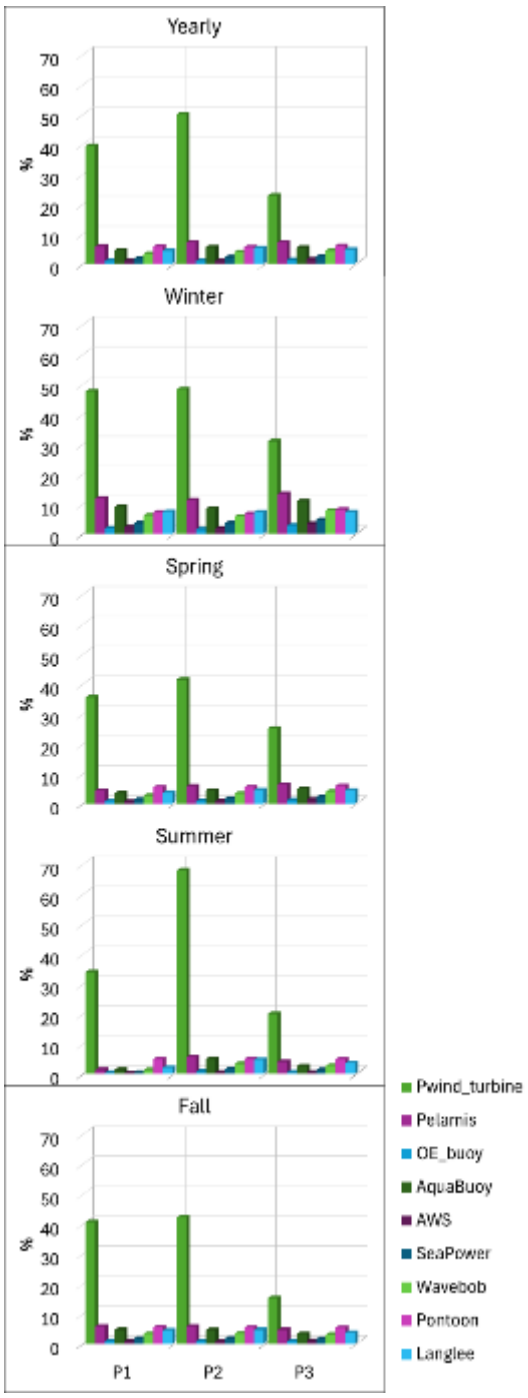

Figure 4: Yearly and seasonal averages of CFs for the devices.

Dominant wind and wave directions

Wind and wave roses showing the dominant direction of the wind and wave climate is given in Fig. 5 for P1, in Fig. 6 for P2, and in Fig. 7 for P3.

The dominant direction with the highest probability is the same for wind and waves in the analysis locations. The dominant direction is Northeast for P1, Northwest for P2, and West-Northwest for P3. The maximum occurrence percentages for directions reach 24%, 34%, and 28% for winds, and 31%, and 30%, and 49% for waves, respectively for analysis locations P1, P2, and P3. This shows that the waves are less dispersed into directions in the offshore area P3.

ISBN: 978-618-5765-04-0
ISSN 3057-4269

The big majority of the time-series has wind speed values smaller than 30 m/s, and wave height values smaller than 8 m.

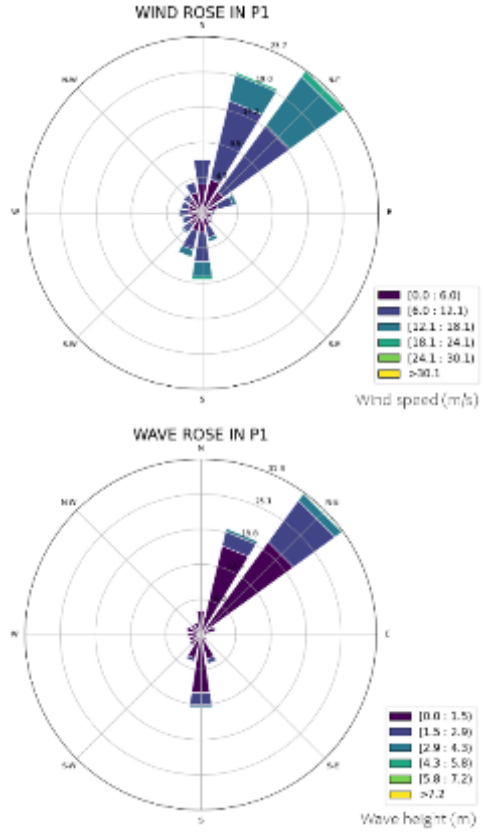

Figure 5: Wind and wave roses for analysis location P1.

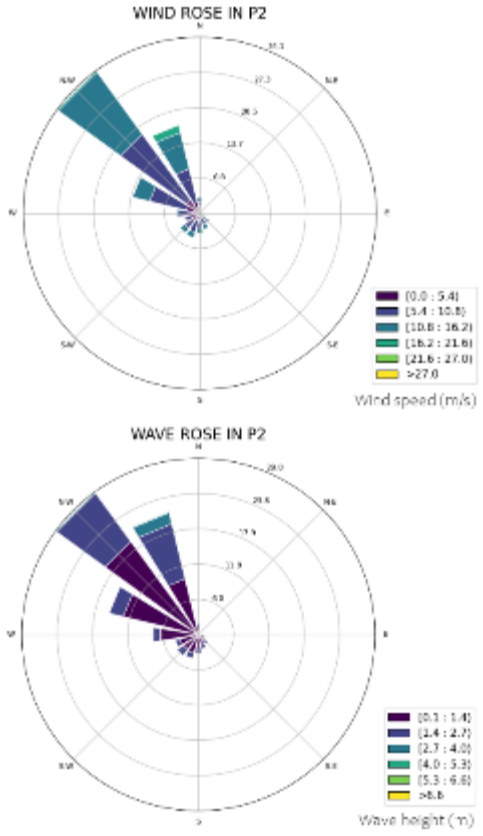

Figure 6: Wind and wave roses for analysis location P2.

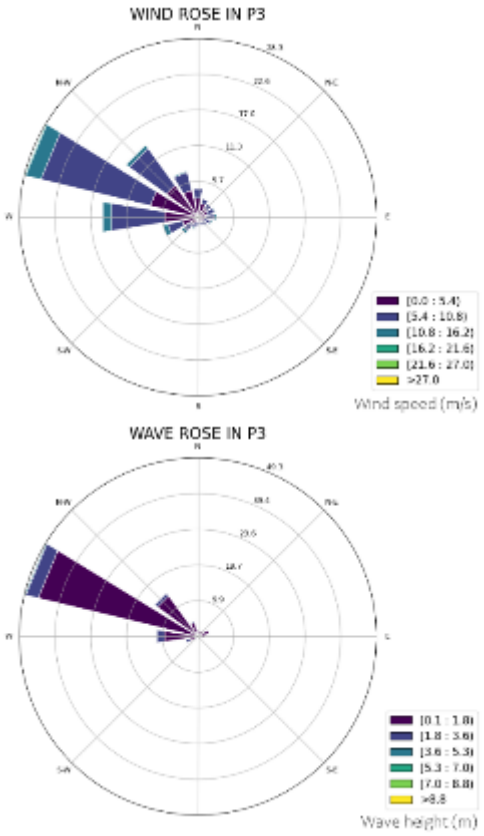

Figure 7: Wind and wave roses for analysis location P3.

Correlation

CC between the wind and wave power is computed using two methods of Pearson and Kendall's Tau. The results are presented in Table 2 for analysis locations. In the table, raw data means the CC is calculated from the original ERA5 time series. Additionally, WECs are compared with the wind turbine considering the working conditions for both side. This analysis shows which WEC has the higher or lower correlation with the wind turbine.

The most prominent result is that the raw data from the wind and waves exhibit higher correlation values. This is due to the fact that the waves considered here are wind waves and swell. However, possibilities occur about the co-working capability of the wind and waves, where the values are lower in the analysis of WECs. In the annual case, the Pearson CC is computed as 0.89, 0.84, and 0.76 for P1, P2, and P3 respectively for the raw data. For the WECs, the higher correlation is computed for Langlee with 0.65 in P1, and the lower correlation is computed for Pontoon with 0.21 in P2.

Between the two methods, Kendall's Tau generally computed higher CCs for the WECs, and lower CCs for the raw data. In the annual case, the Kendall's Tau CC is computed as 0.68, 0.65, and 0.45 for P1, P2, and P3 respectively for the raw data. For the WECs, the higher correlation is computed for OE buoy and AquaBuoy with 0.63 in P2, and the lower correlation is computed for Pontoon with 0.22 in P1. The results reflect that Pontoon has the lowest CC in the analysis locations showing possibility of complementarity when one of the energy sources can still provide power while the counterpart is not active.

ISBN: 978-618-5765-04-0
ISSN 3057-4269

Weaker seasonality is observed in the correlation analysis comparing to the power density and directionality analysis, and the values are relatively closer to their annual counterparts (Table 2).

Table 2: Yearly and seasonal correlation coefficients for the devices based on two methods

		Pearson			Kendall's Tau		
		P1	P2	P3	P1	P2	P3
Annual	Raw data	0.89	0.84	0.76	0.68	0.65	0.45
	Pelamis	0.59	0.57	0.66	0.62	0.59	0.34
	OE_buoy	0.34	0.38	0.46	0.63	0.66	0.43
	AquaBuoy	0.58	0.58	0.62	0.63	0.66	0.44
	AWS	0.36	0.34	0.45	0.61	0.52	0.25
	SeaPower	0.48	0.48	0.59	0.19	0.34	0.26
	Wavebob	0.53	0.54	0.58	0.58	0.55	0.32
	Pontoon	0.22	0.21	0.54	0.22	0.35	0.31
	Langlee	0.65	0.62	0.48	0.58	0.55	0.33
Winter	Raw data	0.91	0.89	0.79	0.75	0.67	0.53
	Pelamis	0.65	0.66	0.72	0.70	0.61	0.46
	OE_buoy	0.38	0.46	0.50	0.72	0.68	0.49
	AquaBuoy	0.61	0.62	0.65	0.73	0.69	0.52
	AWS	0.42	0.43	0.51	0.67	0.50	0.32
	SeaPower	0.53	0.57	0.64	0.37	0.44	0.41
	Wavebob	0.56	0.61	0.61	0.68	0.59	0.45
	Pontoon	0.32	0.36	0.61	0.26	0.36	0.42
	Langlee	0.72	0.71	0.76	0.68	0.59	0.48
Spring	Raw data	0.87	0.85	0.70	0.64	0.59	0.43
	Pelamis	0.57	0.59	0.60	0.58	0.53	0.35
	OE_buoy	0.34	0.42	0.42	0.59	0.61	0.44
	AquaBuoy	0.58	0.61	0.57	0.60	0.62	0.45
	AWS	0.35	0.38	0.40	0.57	0.48	0.27
	SeaPower	0.47	0.50	0.54	0.13	0.25	0.22
	Wavebob	0.53	0.57	0.54	0.54	0.47	0.31
	Pontoon	0.18	0.24	0.48	0.20	0.33	0.32
	Langlee	0.63	0.64	0.64	0.54	0.47	0.31
Summer	Raw data	0.85	0.86	0.63	0.68	0.70	0.36
	Pelamis	0.60	0.58	0.49	0.51	0.65	0.22
	OE_buoy	0.58	0.47	0.41	0.52	0.70	0.35
	AquaBuoy	0.70	0.70	0.57	0.52	0.70	0.37
	AWS	0.37	0.36	0.26	0.51	0.63	0.14
	SeaPower	0.40	0.44	0.46	-0.10	0.41	0.15
	Wavebob	0.60	0.58	0.48	0.50	0.64	0.22
	Pontoon	-0.15	0.01	0.43	0.20	0.36	0.27
	Langlee	0.62	0.61	0.53	0.50	0.64	0.22
Fall	Raw data	0.91	0.90	0.76	0.73	0.71	0.42
	Pelamis	0.63	0.66	0.65	0.66	0.64	0.28
	OE_buoy	0.42	0.44	0.45	0.68	0.70	0.38
	AquaBuoy	0.63	0.69	0.62	0.68	0.70	0.39
	AWS	0.40	0.41	0.43	0.66	0.59	0.20
	SeaPower	0.51	0.56	0.59	0.23	0.33	0.19
	Wavebob	0.61	0.63	0.58	0.64	0.59	0.25
	Pontoon	0.16	0.21	0.52	0.21	0.35	0.23
	Langlee	0.69	0.70	0.69	0.64	0.59	0.26

CONCLUSION

In this study, several aspects of wind and wave energy potential in the Eastern Mediterranean Sea is investigated in three analysis locations. The purpose of the study was to investigate the renewable sources in terms of energy potential and CFs and investigate the directional statistics of the two sources. The main and highlighted part of the study is the analysis of correlation between the wind and wave power using two methods of Pearson and Kendall's Tau.

Up to 930 W/m^2 wind power potential and 7.3 kW/m wave power potential can be achieved according to the seasonal analysis in the analysis locations. The results showed that wind turbine has higher CFs up to 0.5 in the annual case. On the other hand, WECs have lower values where the maximum CF is computed as 0.13 in the winter season for Pelamis in P3. The dominant directions of the wind and wave showed similarity. The prevailing direction from the statistical analysis resulted that Northeast is dominant for P1, Northwest is dominant for P2, and West-Northwest is dominant for P3. Correlation levels between the wind and wave power have found to be higher between the time series of wind and wave power up to 0.89. The device limitations are considered in the correlation analysis to highlight which device couple could be more operationally viable in a hybrid configuration. The comparison of wind turbine with eight different WECs showed that the higher correlation is computed for Langlee with 0.65 in P1, and the lower correlation is computed for Pontoon with 0.21 in P2. It is evaluated that lower CC values might reflect possibility of complementarity when one of the energy sources can still provide power while the counterpart is not active.

ACKNOWLEDGMENT

This research is a part of a project supported by The Scientific and Technological Research Council of Turkey (TÜBİTAK) under grant number 122M279. Tahsin Görmüş is supported by TÜBİTAK 2211 PhD scholarship programme.

REFERENCES

[1] F. A. Canales, P. Sapiega, E. Kasiulis, E. Jonasson, I. Temiz and J. Jurasz, "Temporal dynamics and extreme events in solar, wind, and wave energy complementarity: Insights from the Polish Exclusive Economic Zone," *Energy*, p. 132268, 2024.

[2] A. Colmenar-Santos, J. Perera-Perez, D. Borge-Diez and C. dePalacio-Rodriguez, "Offshore wind energy: A review of the current status, challenges and future development in Spain," *Renewable and Sustainable Energy Reviews*, pp. 1-18, 2016.

[3] S. Astariz, A. Vazquez, M. Sanchez, R. Carballo and G. Iglesias, "Co-located wave-wind farms for improved O&M efficiency," *Ocean & Coastal Management*, vol. 163, pp. 66-71, 2018.

[4] A. Ulazia, J. Sáenz, A. Saenz-Aguirre, G. Ibarra-Berastegui and S. Carreno-Madinabeitia, "Paradigmatic case of long-term colocated wind–wave energy index trend in Canary Islands," *Energy Conversion and Management*, vol. 283, p. 116890, 2023.

[5] S. A. Gil Ruiz, J. E. C. Barriga and J. A. Martínez, "Assessment and validation of wind power potential at convection-permitting resolution for the Caribbean region of Colombia," *Energy*, vol. 244, p. 123127, 2022.

[6] B. Aydoğan, T. Görmüş, B. Ayat and T. Çarpar, "Analysis of potential changes in the Black Sea wave power for the 21st," *Renewable Energy*, vol. 169, pp. 512-526, 2021.

[7] S. Bozzi, G. Besio and G. Passoni, "Wave power technologies for the Mediterranean offshore: Scaling and performance analysis," *Coastal Engineering*, pp. 130-146, 2018.

[8] T. Görmüş, B. Aydoğan and B. Ayat, "Analysis of hybrid exploitation of wind and wave power in the Mediterranean and the Black Sea," *Energy Conversion and Management*, p. 117820, 2024.

[9] Copernicus Climate Data Store, "ERA5 hourly data on single levels," ECMWF, 2024.

Gross Value Added and Electricity Consumption by Sector of Activity in Portugal – An Analysis of Technical Efficiency

Olinda Sequeira
Smart Cities Research Center
Instituto Politécnico de Tomar Tomar,Portugal
olinda.sequeira@ipt.pt

Fernando Teixeira
Smart Cities Research Center
Instituto Politécnico de Beja Beja,Portugal
fernando.teixeira@ipbeja.pt

Abstract*— This article analyzes technical efficiency, by sector of activity in Portugal, over the last two decades, taking as reference the value of electricity consumption and the gross value added by sector of activity. Applying the concept of the Production Possibilities Frontier, the non-parametric Data Envelopment Analysis method, an approach to mathematical programming, is used to calculate the technical efficiency of each sector under analysis for the years 2002, 2012 and 2022. The analysis interspersed with these 3 years allows us to have an evolutionary view by sector from the point of view of technical efficiency over the last 20 years. Seven sectors of activity are analyzed: Agriculture, animal production, hunting, forestry and fishing; Extractive industries; Manufacturing industries; Construction; Wholesale and retail trade; Transport and storage; Accommodation, catering and similar. The study demonstrates that there are large variations in technical efficiency between sectors, with only one being considered efficient in the periods analyzed. It is also concluded that there are variations in technical efficiency for the 3 periods analyzed by sector and for the average technical efficiency. Surprisingly, the values indicate a decrease in average values from 2002 to 2012 and to 2022, which in turn determines that these sectors should be analyzed and try to understand what is happening, especially in relation to productivity values. For the amounts of electrical energy consumption, the wealth created by sector should be greater or for the values of wealth creation presented, the sectors should consume less electrical energy. This means that an increase in energy consumption cannot always lead to an increase in economic growth, despite the existence of a causal relationship between economic growth and energy consumption being recognized. In this study, it is not intention to obtain the definition of strategies through the DEA method and, therefore, it mainly constitutes a diagnosis, from which benchmarking practices could be developed, placing sectoral innovation at the center of the issue because the variation of technical efficiency is closely associated with the introduction of innovation.

Keywords— Electricity Consumption; Technical Efficiency Energy Sustainability and Industrry Productivity

INTRODUCTION

This article analyzes technical efficiency (TE), by sector of activity in Portugal. TE calculation has been widely applied in several studies, constituting a useful measure to improve performance [1,2]. In this study TE is calculated for 3 periods, the years of 2002,2012 and 2022. A relationship is assumed between electrical energy consumption and value added by sector of activity. The analysis allows us to have an evolutionary view by sector from the point of view of technical efficiency over the last 20 years. Seven sectors of activity are analyzed: Agriculture, animal production, hunting, forestry and fishing; Extractive industries; Manufacturing industries; Construction; Wholesale and retail trade; Transport and storage; Accommodation, catering and similar. Efficiency can be defined as the maximum result obtained according to the factors employed, or the ability of a production unit to use the inputs in an optimal ratio while minimizing costs [3,4]. These two definitions coexist and form the so-called economic efficiency [5]. In other words, it is more efficient who can produce more for less[6]. And TE can influence the level of productivity. But without a frontier function we are unable to measure efficiency [7]. In this work we are going to apply the Data envelopment analysis (DEA). Data envelopment analysis evaluates the performance of a set of peer entities called decision-making units (DMU) which convert multiple inputs into multiple outputs [8]. Through DEA it is possible to generate a single performance indicator for each DMU, from the ratio between the weighted inputs and outputs. The remainder of this paper is organized as follows. Section II presents the contextual setting. Section III details the methodology. Section IV presents results and conclusions.

ENERGY SUSTAINABILITY AND INDUSTRRY PRODUCTIVITY

[9] assert that the impact of climate change underscores the necessity for sustainable development. To meet the needs of future generations, resources must be managed within a circular economy rather than the traditional linear approach. Integrating energy, water, and environmental systems is crucial to curb resource overexploitation. [10] believe that public investment in transformative energy solutions has grown gradually, but energy policy is increasingly adopting an urgent approach. Trends such as decentralization, digitalization, and heightened concern about the climate crisis are driving more ambitious programs for energy system transformation. [11] highlight the positive relationship between renewable energy consumption and economic growth, suggesting that energy policies promoting renewable energy will benefit both the economy and environmental quality. [12] argue that the transition from natural to renewable and sustainable resources must be carefully phased and strategically implemented to avoid market disruption. The future of the energy industry depends on policy reform, prioritizing the halt of new site exploration and the shift towards renewable energy. [13] assert that logistics decisions significantly affect carbon emissions, contributing to global warming. The findings reveal that reducing emissions from

ISBN: 978-618-5765-04-0
ISSN 3057-4269

the cost-optimal solution is often expensive compared to current carbon market prices. However, emissions can be reduced most cost-effectively in scenarios where emissions are high relative to costs, which are typically considered sunk due to past investments. [14] state that most control centers worldwide do not perform dynamic contingency analysis in real-time due to high computational requirements. The proposed cache energy saving approach can lower energy dissipation, leading to increased supply efficiency. [15] propose a centralized DEA approach to determine efficient operating points for multiple plants within an organization, based on aggregate production targets. The study shows that emissions reductions achieved through centralized production planning are greater than those possible when individual plants set their own production plans. [16] argues that a just transition can drive economic growth, social transformation, and sustainable land use if public institutions engage investors responsibly. An ex-ante impact assessment is needed to ensure long-term profitability, secure jobs, and green innovation. [17] stated that the energy system is not isolated but is always interconnected with social, economic, and ecological systems. The shift towards renewable energy sources necessitates a profound transformation of the entire energy system, with significant social, economic, and ecological consequences that extend far beyond the energy sector.

[18] argues that access to energy is one of the most binding constraints on firms' business operations and growth. Some firm-specific characteristics, such as the sector of activity, export status, and location of operations, appear to be consistently associated with firms' energy constraints. Others, such as firms' age, size, and legal status, tend to be less consistent in their direction of influence. Moreover, foreign and government ownership of firms appears to be a broadly consistent predictor of energy constraints in most models analyzed. Overall, the results imply that developing a policy to improve firms' access to energy in developing countries requires considering both firm-specific and country-level factors. Finally, policy considerations will need to be made in accordance with the level of development in each country. [19] stated that, in general, all companies can reduce electricity consumption and improve energy efficiency (e.g., by installing solar panels on company buildings); enhance water efficiency (e.g., through green roofs, efficient devices and products, and hot water circulation and return); implement proper recycling practices and encourage all employees to participate diligently; and minimize material waste. [20] found that when companies view energy efficiency as strategic, they tend to implement stronger energy management. Additionally, the more a project is considered strategic, the less restrictive financial selection criteria become. This highlights the dominant role of strategic considerations over financial logic in investment decision-making. [21] found that firms receiving support for reducing energy consumption also tended to become more productive. Upon closer examination, this positive impact was mediated by spatial processes. Firms that were connected to competitors through selective long-distance cooperation networks, were closer to competitors' industrial specialization, and were located in areas with similar social capital, tended to experience a higher positive impact. [22], using firm-level panel data from the World Bank Enterprise Survey and controlling for firm, industry, and country heterogeneity, investigated the relationship between energy efficiency and firm-level productivity in a comparative study worldwide. Their findings revealed a positive relationship between alternative measures of energy efficiency and firm-level productivity. This result proved to be robust to different specifications and sensitivity analyses, although they identified some heterogeneity by firm size, industry, and geographical regions.

METHODOLOGY

The objective of the DEA method is to analyse the relative efficiency of homogeneous DMU's. The DEA method covers several models, and their classification is primarily based on the type of returns to scale and orientation used [3,15]. When the objective is to reduce inputs to improve efficiency, the DEA model assumes an input orientation. In this case the objective is to calculate the proportion to which the inputs can be reduced by maintaining the same production [24]. One component of efficiency is TE, wich reflects the ability of a firm to obtain maximal output from a set of inputs [23]. An input orientation assumes that managers have more control over production factors. In this study we are going to apply a DEA - input-oriented model. The aim of this technique is to define a frontier envelopment surface for all sample observations, which is determined by those units that lie on it, in this case the efficient sectors, and the sectors that do not lie on that surface are considered inefficient [3,24]. Through DEA it is possible to generate a single performance indicator for each sector, from the ratio between the weighted inputs and outputs. It is also possible to compare the resources used with the results obtained by each of the sectors, identifying those with the best performance and which are a reference for the other units [24]. This allows DEA to be defined as a benchmarking technique and a way for the inefficient units to improve their performance [4]. An intuitive way to introduce the model is to present it in fractional form [3]. Given a homogeneous set of N DMU´s, observations for M inputs and S outputs, the information for the jth firm is represented by the column vectors xj and yj. The input matrix MxN, X, and the output matrix SxN, Y, represent the total observations for all N DMU's. For each DMU the objective is to obtain a measure of the fraction of all outputs over all inputs:

$$Max_{w_r z_i} H_0 = \frac{\sum_r^s w_r y_{ro}}{\sum_i^m z_i x_{io}} \quad (1)$$

Subject to:

$$\frac{\sum_r^s w_r y_{rj}}{\sum_i^m z_i x_{ij}} \leq 1 \quad j = 1, \dots, N \quad (2)$$

$$w_r, z_i > 0 \;\; r = 1, \dots, S \;\; i = 1, \dots, m \quad (3)$$

Considering:

y = outputs.

x = inputs.

and w, z = weightings.

For the data we utilize one output and one input for the seven analyzed sectors. The analysis carried out was for 3 periods: 2002, 2012 and 2022. The output used is: Gross value added of companies by sector of activity. The input used is:Electricity consumption by sector of activity.

ISBN: 978-618-5765-04-0
ISSN 3057-4269

Table 1 presents the output and input values for the different sectors.

Table 1: Output and input values

Year	2002		2012		2022	
Sector	**Output Euro – Million**	**Input (kWh -kilowatt-hours**	**Output Euro - Million**	**Input (kWh-kilowatt-hours**	**Output Euro - Million**	**Input (kWh-kilowatt-hours**
Agriculture, animal production, hunting, forestry and fishing	795,1	847348874	1119	1004293990	2624	998563917
Extractive industries	526,4	441206034	474,4	573197097	593,7	687552552
Manufacturing industries	18264,7	15147870423	16316,9	15042822650	27494,2	16850301900
Construction	7162,4	820945516	5656,9	461811166	5948,3	381775737
Wholesale and retail trade	13882,1	3681063526	13905,9	4177125539	24421,9	3611620162
Transport and storage	7597,4	465860715	5768,6	535107835	8678,7	500723713
Accommodation, catering and similar	2378,7	2040791837	3138	1736534489	8306	2017554042

Source: PorData

The next section presents the results.

RESULTS AND CONCLUSIONS

The study demonstrates that there are large variations in technical efficiency between sectors, with only one being considered efficient in the periods analyzed.

It is also concluded that there are variations in technical efficiency for the 3 periods analyzed by sector and for the average technical efficiency.

Surprisingly, the values indicate a decrease in average values from 2002 to 2012 and to 2022, as observed in table 2, which in turn determines that these sectors should be analyzed and try to understand what is happening, especially in relation to productivity values.

Table 2: Technical Efficiency

Sector	***2002***	***2012***	***2022***
Agriculture, animal production, hunting, forestry and fishing	0.331	0.212	0.113
Extractive industries	1.000	1.000	1.000
Manufacturing industries	0.043	0.044	0.032
Construction	0.147	0.168	0.199
Wholesale and retail trade	0.095	0.085	0.061
Transport and storage	0.208	0.247	0.205
Accommodation, catering and similar	0.774	0.529	0.250
Mean	0,371	0,326	0,266

Source:Authors

For the Gross value added presented, the sectors should consume less electrical energy.

This means that an increase in energy consumption cannot always lead to an increase in economic growth, despite the existence of a causal relationship between economic growth and energy consumption being recognized.

In this study, it is not intention to obtain the definition of strategies through the DEA method and, therefore, it mainly constitutes a diagnosis, from which benchmarking practices could be developed, placing sectoral innovation at the center of the issue because the variation of technical efficiency is closely associated with the introduction of innovation.

In the future, this study could be more in-depth and include a more detailed analysis by sector of activity, but as mentioned, it is only a diagnosis.

REFERENCES

[1] F.Teixeira and O.Sequeira, "Poliempreende-an Analysis of the Efficiency Measures in 13 Portuguese Higher Education Institutions", *Journal of Global Business and Technology*, 20(2) (pp. 63-73), 2024.

[2] O. Sequeira and F.Teixeira, "A Meta-analysis Regression on Efficient and Productivity Energy Research" In: Silva, F., Ferreira, L., Sá, J., Pereira, M., Pinto, C. (Eds), *Flexible Automation and Intelligent Manufacturing: Establishing Bridges for More Sustainable Manufacturing Systems*. FAIM 2023. *Lecture Notes in Mechanical Engineering* (pp. 1113-1120). Switzerland: Springer Nature Switzerland, 2024. https://doi.org/10.1007/978-3-031-38165-2_127.

[3] O. Sequeira, F. Teixeira, J. Samartinho, "Methodological Approaches in Innovative Pedagogical HEIs: Case Studies/Best Practices – LINK ME UP PROJECT: A Case Study", In book: *The Impact of HEIs on Regional Development: Facts and Practices of Collaborative Work With SMEs* (pp. 227-243), IGI Global, 2023. DOI: 10.4018/978-1-6684-6701-5.ch013.

[4] C. Barros and O.Sequeira, "Productivity change in the oil blocks of Angola", *Energy Sources, Part B: Economics, Planning and Policy*, 9:4, 413-424, 2014. https://doi.org/10.1080/15567249.2010.497794.

[5] J. Coelli, D. Rao, J. O'Donnell, E. Battese, "An Introduction to Efficiency and Productivity Analysis", *(Second, Ed.) New York: Springer*, 2005.

[6] A. Werner, A.van Riel, L.Gijsberts, M. Visser, "Sustainability Through Efficiency" In: *Financial, Staffing and Societal Sustainability of Dutch Health Care*, Research for Policy. Springer, Cham., 2024. https://doi.org/10.1007/978-3-031-58564-7_5

[7] C. Barros and O. Sequeira, "Performance assessment of Portuguese wind farms: Ownership and managerial efficiency", *Energy Policy*, 39(6), 3055-3063, 2011.

[8] A. Charnes, W.Cooper, B. Golany, L. Seiford, J. Stutz, "Foundations of Data Envelopment Analysis for Pareto-Koopmans Efficient Empirical Production Functions", *Journal of Econometrics*, 30, 91-107,1985.

[9] H. Mikulčić, J. Baleta, X. Wang, N. Duić and R. Dewil, "Sustainable development in period of climate crisis," *Journal of environmental management*, vol. 303, pp. 1-20, 114271, 2022. https://doi.org/10.1016/j.jenvman.2021.114271.

[10] S. Hampton, T. Fawcett, J. Rosenow, C. Michaelis and R. Mayne, "Evaluation in an emergency: assessing transformative energy policy amidst the climate crisis," *Joule*, vol. 5, no. 2, pp. 285-289, 2021. https://doi.org/10.1016/j.joule.2020.12.019.

[11] S. Tiba, A. Omri and M. Frikha, "The four-way linkages between renewable energy, environmental quality, trade and economic growth: a comparative analysis between high and middle-income countries." *Energy Systems*, vol. 7, no. 1, pp. 103-144, 2016. https://doi.org/10.1007/s12667-015-0171-7.

[12] E. Dadd, V. Kirou, J.Velasquez, K. Kalhori, D.Galatro, "Sustainability and future of the oil and gas industry: a mini-review", *Dyna*, 90(226), 130-138, 2023. https://doi.org/10.15446/dyna.v90n226.105963.

[13] M. Turkensteen and W. van den Heuvel,"The trade-off between costs and carbon emissions from economic lot-sizing decisions," *INFOR: Information Systems and Operational Research*, vol. 61, no. 2, pp. 169-198, 2023. https://doi.org/10.1080/03155986.2023.2169493.

[14] S. Khaitan and J. McCalley, "Optimizing cache energy efficiency in multicore power system simulations," *Energy Systems*, vol. 5, pp. 163-177, 2014. https://doi.org/10.1007/s12667-013-0090-4.

[15] S. Lozano and I. Contreras, "Centralized production planning using reference operating points: application to fossil fuel power plants," *INFOR: Information Systems and Operational Research*, vol. 61, no. 3, pp. 368-398, 2023. https://doi.org/10.1080/03155986.2023.2209451.

[16] S. Pugliese, "Rethinking Just Transition in Investment Law Perspective: Incentives against Climate Crisis between Sustainability, Economic Security, and Strategic Industrial Planning," *Laws*, vol. 13, no. 3, 37, pp. 1-21, 2024. https://doi.org/10.3390/laws13030037.

[17] Y. Yang, S. Xia, P. Huang and J. Qian, "Energy transition: Connotations, mechanisms and effects," *Energy Strategy Reviews*,

vol. 52, pp. 1-13, 101320, 2024. https://doi.org/10.1016/j.esr.2024.101320.

[18] C. Mertzanis, "Institutions, development and energy constraints," *Energy*, vol. 142, pp. 962-982, 2018. https://doi.org/10.1016/j.energy.2017.10.073.

[19] S. Gomes, J. Lopes, M. Travassos, M. Paiva, I. Cardoso, B. Peixoto and C. Duarte, "Strategic organizational sustainability in the age of sustainable development goals," *Sustainability*, vol. 15, no. 13, pp. 1-19, 10053, 2023. https://doi.org/10.3390/su151310053.

[20] C. Cooremans and A. Schönenberger, "Energy management: A key driver of energy-efficiency investment?," *Journal of Cleaner Production*, vol. 230, pp. 264-275. 2019. https://doi.org/10.1016/j.jclepro.2019.04.333.

[21] A. Caragliu, "Energy efficiency-enhancing policies and firm performance: Evidence from the paper and glass industries in Italy," *Energy Policy*, vol. 156, pp. 1-14, 112415, 2021. https://doi.org/10.1016/j.enpol.2021.112415.

[22] P. Montalbano, S. Nenci and D. Vurchio, "Energy efficiency and productivity: A worldwide firm-level analysis," *The Energy Journal*, vol. 43, nno. 5, pp. 93-116, 2022. https://doi.org/10.5547/01956574.43.5.pmon.

[23] B. Golany and Y. Roll, "An application procedure for DEA", *Omega*, 17(3), 237-250, 1989.

[24] S. Camanho, G. D'Inverno, "Data Envelopment Analysis: A Review and Synthesis". In: Macedo, P., Moutinho, V., Madaleno, M. (eds) *Advanced Mathematical Methods for Economic Efficiency Analysis. Lecture Notes in Economics and Mathematical Systems*, vol 692. Springer, Cham., 2023. https://doi.org/10.1007/978-3-031-29583-6_3.

ISBN: 978-618-5765-04-0
ISSN 3057-4269

Economic Comparison of New Built Internal Combustion Gas Engine Power Plant in Uzbekistan and Europe Based on Levelized Cost of Electricity (LCOE) Method

Serkan Toplak
Energy Institue,
Energy Management &Technology
Istanbul Technical University
Istanbul, Türkiye
serkan.toplak@hotmail.com

***Abstract*— The study examines the economic analysis of a new gas-fired power plant in Uzbekistan, comparing it with similar projects in Europe using data from the Danish Energy Agency. It aims to aid decision-making for entrepreneurs by analyzing different scenarios, including the choice between new and second-hand machinery, using the Levelized Cost of Electricity (LCOE) as a key metric. The study highlights the stability of Uzbekistan's natural gas market, making it an attractive investment option, while Europe is shifting towards a mix of renewable energy and gas plants for grid balancing. It suggests that Uzbekistan can continue to leverage its natural gas reserves for stable energy production but should consider diversifying into renewables to align with global energy trends and enhance energy security.**

Keywords—energy transition, Europe, LCOE, natural gas, power plant

INTRODUCTION

Electricity generation remains a key area for large-scale investment, driven by the rising global demand for energy. In rapidly developing economies, investments in energy projects are especially appealing due to their significant growth in energy needs, whereas developed countries have shifted their focus toward renewable sources like wind, solar, and hydro, along with natural gas for electricity generation [1]. However, constraints in natural gas supply have recently forced these countries to explore alternative energy solutions [2]. Despite the advantages of renewable energy—such as zero emissions and independence from fossil fuels—challenges like geographical dependency, seasonality, and the need for substantial land and storage solutions persist [3], [4]. Consequently, the transition away from fossil fuels has been gradual, with natural gas often serving as a bridge in this energy transition [5].

In developing economies, natural gas remains crucial for electricity generation due to its cost-effectiveness and flexibility, particularly in small-scale systems using gas engines [6]. Domestic natural gas resources help these countries mitigate risks associated with fuel imports, while Power Purchase Agreements (PPAs) with foreign investors assist in managing operational challenges [7]. For companies entering such agreements, thorough feasibility studies that include detailed financial analyses are essential for ensuring profitability [8]. Utilizing second-hand gas engine equipment can lower initial capital expenditures under PPAs, but this requires rigorous technical and economic assessments to ensure long-term viability [9]. Furthermore, maintaining system reliability is vital for meeting PPA requirements, as it directly impacts the stability of electricity generation [10].

The use of second-hand machinery in industrial settings has been studied extensively, showing that it can improve technical efficiency in emerging economies [10]. For instance, Laborda Castillo et al. (2012) found that second-hand equipment's efficiency is influenced by wage levels [10]. Other studies have highlighted the importance of technical and economic evaluations when considering surplus equipment [11], [12]. While second-hand machinery can be beneficial in reducing capital costs, new machinery often provides better reliability and lower failure rates, especially in the initial years, adding a layer of security for investors [9]. Thus, assessing the technical suitability, cost-effectiveness, and energy efficiency of second-hand equipment is critical for decision-making in industrial projects, particularly in regions with evolving energy landscapes [13].

LITERATURE

Maintaining the Integrity of the Specifications (Heading 2)

Uzbekistan's energy sector is heavily dependent on natural gas, which accounts for over 85% of its total energy supply and electricity generation [14]. The country, which produced approximately 65,000 GWh of electricity from natural gas by 2019, remains one of the world's largest natural gas producers [15]. Despite facing a decline in reserves due to the global economic crisis and a reduction in production, Uzbekistan has since increased its natural gas output through infrastructure modernization and new projects [16]. The government aims to halt natural gas exports by 2025 to focus on domestic consumption and petrochemical production, aligning with plans to diversify the energy mix and improve energy security [17].

Uzbekistan's renewable energy potential is significant, particularly in solar and wind power, which are central to its strategy for reducing dependence on fossil fuels [18]. The country has set ambitious targets for expanding renewable energy capacity, which could reshape its energy landscape in

ISBN: 978-618-5765-04-0
ISSN 3057-4269

the coming decades. Estimates suggest that the technical potential of solar energy alone could exceed the current energy demand by a factor of four, making it a viable option for the country's energy transition [19]. However, challenges such as the need for backup power systems during periods of low solar activity and the country's increasing energy demand remain critical considerations [20].

In contrast, Europe is a leader in the global energy transition, with a well-developed framework for reducing carbon emissions and promoting renewable energy. The European Union's Green Deal aims to make Europe the first climate-neutral continent by 2050, driving significant investments in renewable energy, energy efficiency, and low-carbon technologies such as hydrogen and carbon capture and storage (CCS) [21]. Europe's energy transition policies are backed by stringent regulations, making it a model for decarbonization efforts worldwide [22]. Additionally, technological advancements have allowed European countries to integrate large-scale renewable energy projects into their energy grids, further decreasing dependence on fossil fuel-based power generation [23]. The adoption of CCS technologies in Europe, for example, has enabled coal-fired power plants to compete with natural gas plants in terms of LCOE, even when emission reductions are considered [24].

This comparative analysis aims to highlight the differences in cost-effectiveness, advantages, and challenges faced by each region. While Europe benefits from advanced technology and supportive policies for renewable energy, Uzbekistan's abundant natural gas reserves provide a competitive advantage in fossil fuel-based power generation [25]. The study also considers future energy transition scenarios for Uzbekistan, exploring how changes in policy, technological advancements, and economic factors might shape the role of natural gas and internal combustion gas engine power plants [26]. The findings are expected to offer valuable insights for policymakers, industry stakeholders, and researchers, informing energy infrastructure investments and strategies that balance economic growth with environmental sustainability [27].

METHODOLOGY

The Levelized Cost of Electricity (LCOE) is a commonly used metric to evaluate the cost-effectiveness of power generation technologies over their lifespans. According to the International Energy Agency (IEA) in their *Projected Costs of Generating Electricity* report, the LCOE formula is generally expressed as follows [28]:

$$LCOE = P_{MWh} = \frac{\sum(Capital_t + O\&M_t + Fuel_t + Carbon_T + D_t) * (1+r)^{-t}}{\sum MWh(1+r)^{-t}} \quad (1)$$

Where;

P_{MWh} = The constant lifetime remuneration to the supplier for electricity;

MWh = The amount of electricity produced annually in in MWh;

$(1+r)^{-t}$ = The real discount rate corresponding to the cost of capital;

$Capital_t$ = Total capital construction costs in year *t*;

$O\&M_t$ = Operation and maintenance costs in year *t*;

$Fuel_t$ = Fuel costs in year *t*;

$Carbon_t$ = Carbon costs in year *t*;

D_t = Decommissioning and waste management costs in year *t*.

Parameters

a. Lifetime

The expected lifetime of a power generation asset varies significantly across different technologies. Each technology type has its own physical constraints, maintenance requirements, and economic considerations that affect the feasible operational lifespan.

The lifetime parameter (*n*) appears in both the numerator (costs) and the denominator (electricity generated). Therefore, extending the lifetime of a plant allows the total costs, especially capital expenditures, to be amortized over a longer period, lowering the overall LCOE. Conversely, a shorter lifetime increases the LCOE because the same amount of capital must be recovered over fewer years of electricity production [29].

b. Discount rate

The discount rate is a fundamental factor in the economic evaluation of natural gas plants, as it accounts for the time value of money, reflecting how future cash flows are valued in present terms. It incorporates several key components, including the cost of capital, inflation, and the risk factors specific to the project. The selection of an appropriate discount rate is critical for accurately discounting future operational costs and revenues, ensuring that the Net Present Value (NPV) of the plant's economic performance is properly assessed.

The discount rate (*r*) is used to determine the present value of both costs and revenues over the plant's operational lifespan. A higher discount rate typically results in a lower present value for future cash flows, reflecting higher project risk or opportunity cost, while a lower discount rate implies more conservative assumptions regarding risk and cost of capital.

c. Capacity

Capacity modeling is critical for assessing the maximum electricity output that a power plant can achieve. This encompasses both installed capacity, which represents the theoretical maximum output, and actual operational capacity, which accounts for factors such as downtime for maintenance and other inefficiencies. The capacity factor, defined as the ratio of actual output to installed capacity expressed as a percentage, offers valuable insights into the plant's performance over time.

In this analysis, the power plant's capacity is assumed to be 240 MW, with a capacity factor of 85%, as referenced in the 2020 Projected Costs of Generating Electricity Report by the International Energy Agency (IEA) [28]. This capacity factor reflects the operational realities of the plant, excluding internal electricity consumption.

d. Total capital construction cost

The capital construction cost covers all expenses related to building the plant. This includes the costs of purchasing and

ISBN: 978-618-5765-04-0
ISSN 3057-4269

installing equipment, civil engineering works, labour, and any required permits or licenses. These costs are typically incurred upfront and can represent a significant portion of the total investment in the plant. Accurate modelling of these costs is essential for financial planning and securing funding.

In this input a general investment cost has considered according to Danish Energy Agency Technology Data catalogue [30]. Normally for more sensitive cases this input should be divided many sub inputs. It will be more beneficial if investment costs include direct construction costs plus pre-construction costs. Pre-construction costs can be express in terms of licensing, environmental testing, administrative costs etc. Total capital construction costs have taken as 1M€/MW. This cost calculated as investment cost, and it is assumed that all other specific costs included.

e. Operation and maintenance cost

Operation and maintenance (O&M) costs encompass the ongoing expenses necessary to keep the plant operational. These include routine maintenance, repairs, staff salaries, and administrative expenses. Proper modelling of O&M costs ensures that the plant operates efficiently and helps in budgeting for long-term operations.

O&M costs include yearly planned maintenance and resting operational costs. In this study variable O&M costs taken into fixed O&M costs since variable O&M costs does not affect too much to the results. The total O&M costs taken as 10 (USD/MWh) [31].

f. Fuel cost

Fuel costs are a major component of the total operating expenses for a natural gas plant. The cost of natural gas can be highly variable, influenced by market dynamics, geopolitical factors, and supply-demand balances. This section includes price forecasts for natural gas, incorporating historical data, current market trends, and future projections. Accurate fuel cost modelling is crucial for estimating the plant's operating expenses and overall economic performance.

g. Decommissioning and waste management cost

At the end of a power plant's operational lifetime, it becomes necessary to dismantle the plant, a process known as decommissioning. This involves a comprehensive set of activities aimed at safely deconstructing the plant's infrastructure and ensuring that the site is restored to a condition that meets environmental and regulatory standards. If deemed viable and economically beneficial, parts of the plant or the entire facility may also be relocated to a different location for further use.

The cost of decommissioning encompasses the total expenses associated with the dismantling process. This includes the physical deconstruction of plant structures, the removal and disposal of hazardous materials, site remediation, and administrative costs. Additionally, the decommissioning cost calculation accounts for any salvage value or residual value of the plant components, which can be offset against the total expenses. Residual value refers to the remaining value of plant equipment and materials that can be sold or reused after decommissioning.

RESULTS

The study analyzes three scenarios for Europe, each reflecting different levels of commitment to carbon reduction and sustainability. It explores how varying policies, technological advances, and socio-economic factors impact energy use and emissions. The results highlight the effectiveness of carbon pricing, renewable energy integration, and energy efficiency measures, showing how countries can use these tools to meet carbon reduction goals.

In contrast, Uzbekistan lacks clear carbon reduction targets, so the analysis is based on existing policies. This reveals the challenges of countries without firm climate commitments and underscores the need for a strategic framework to adopt more ambitious climate actions.

Overall, the study stresses the importance of comprehensive policy frameworks, international collaboration, and adaptable strategies to achieve meaningful carbon reduction. It aims to guide policymakers and stakeholders in navigating the complexities of carbon reduction on regional and global scales.

Results based on STEPS for Europe

In the first scenario, an insignificant increase in LCOE values is observed between the years 2030 and 2050 across all three discount rates. This trend can be attributed to the relatively stable projections for both carbon and fuel prices over this period. The stability of these input costs implies that the primary drivers of LCOE remain consistent, resulting in minimal fluctuations in the calculated values.

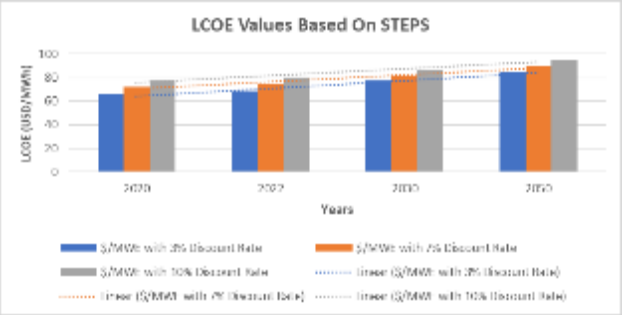

Figure 1. LCOE values based on STEPS

By applying these discount rates, the analysis provides a comprehensive view of how changes in economic conditions could impact the LCOE. However, due to the stable nature of fuel and carbon prices in this scenario, the variations in LCOE across different discount rates are relatively minor.

The findings from this analysis highlight the importance of fuel and carbon price stability in maintaining predictable and manageable electricity generation costs. The minor increase in LCOE between 2030 and 2050 suggests that, under the assumptions of STEPS, natural gas-fired power plants will continue to offer a relatively stable cost structure, even as the energy landscape evolves.

Results based on APS for Europe

In this scenario, carbon prices have been sourced from the DNV Energy Transition Report 2022, which forecasts carbon prices to reach approximately 130 USD/tonne by 2050. This significant rise in carbon prices is a critical factor in the economic evaluation of electricity generation costs. For fuel prices, data has been taken from the IEA World Energy Outlook 2022 report, ensuring that the most recent and relevant market conditions are incorporated into the analysis.

ISBN: 978-618-5765-04-0
ISSN 3057-4269

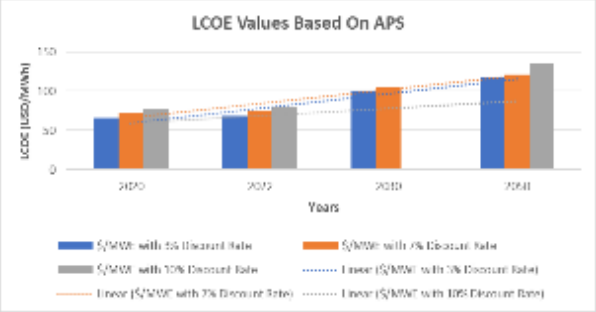

Figure 2. LCOE values based on APS

The results of this scenario highlight the critical importance of accelerating the transition to renewable energy sources, such as wind, solar, and hydropower, which are not only environmentally sustainable but also increasingly cost-effective. Furthermore, the integration of advanced carbon mitigation technologies, such as carbon capture, utilization, and storage (CCUS), will be essential in maintaining the economic feasibility of gas-fired power plants in the face of rising carbon costs. Without such measures, the financial burden imposed by escalating carbon prices may render traditional gas-fired generation less competitive in the future energy market.

In light of these challenges, a well-balanced and forward-thinking energy strategy must prioritize investment in renewable energy infrastructure, alongside the development of cutting-edge carbon mitigation solutions. This dual approach will be essential to ensuring a reliable and affordable supply of electricity while meeting the pressing need to mitigate climate change and reduce carbon emissions. As the energy landscape evolves, the ability to adapt to changing economic and environmental conditions will be key to securing a sustainable and economically viable energy future.

Results based on NZES for Europe

In this scenario, carbon prices emerge as a critical factor influencing the economic feasibility of energy technologies. The scenario assumes a significant phasing out of fossil fuels, which is expected to drive down the prices of these fuels due to reduced demand. However, this transition away from fossil fuels is accompanied by a substantial increase in carbon prices, as highlighted in the International Energy Agency's (IEA) World Energy Outlook 2022 report.

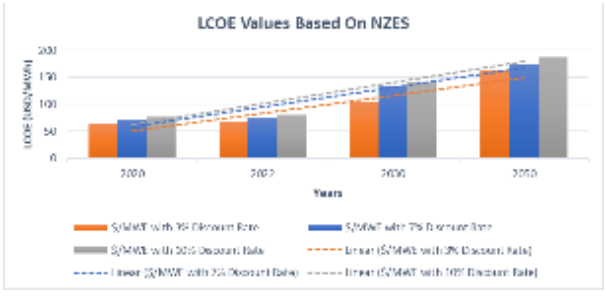

Figure 3. LCOE values based on NZES

This passage discusses the economic impact of carbon pricing on fossil fuel-based power generation, focusing on its effect on the Levelized Cost of Electricity (LCOE). As carbon prices rise, the LCOE for gas-fired and other fossil fuel power plants increases, making them less competitive compared to renewable energy sources. This trend is particularly evident in advanced economies with stringent carbon regulations, where the elevated costs are expected to drive a shift towards cleaner energy alternatives.

Although declining demand for fossil fuels may initially lower fuel prices, the overall increase in carbon costs keeps the LCOE of fossil fuel technologies high, challenging their long-term economic viability. This transition emphasizes the importance of investing in renewable energy infrastructure, both to ensure economic sustainability and to align with global climate goals. It also creates opportunities for innovation and job creation in green industries.

Overall, the analysis highlights the critical role of carbon pricing and market dynamics in shifting the energy sector towards renewables, signifying a broader transformation in energy production and consumption. This change is essential for achieving a sustainable energy future in the face of evolving regulatory frameworks and climate imperatives.

Results based on NZES for Europe

This section analyzes the Levelized Cost of Electricity (LCOE) for gas-fired power plants in Uzbekistan, highlighting the country's competitive advantage in power generation. Construction costs for new power plants in Uzbekistan are lower compared to Europe, driven by unique local factors.

Key among these is the absence of strict emissions targets or net-zero commitments, reducing the need for costly investments in emission reduction technologies. This regulatory environment helps maintain stable operational costs for power plants through 2050, making the transition to cleaner energy less urgent and financially demanding.

Additionally, Uzbekistan's substantial natural gas reserves play a pivotal role. These reserves support low fuel costs for electricity generation, allowing the country to leverage its resources to maintain a competitive LCOE. The reliance on domestic natural gas reduces vulnerability to global fuel price fluctuations, further bolstering the economic feasibility of gas-fired power generation.

Overall, Uzbekistan's low LCOE for gas-fired plants is driven by minimal regulatory burdens, stable operational costs, and abundant natural gas. These factors create a conducive environment for investment in gas-fired energy, making Uzbekistan an attractive market for power generation projects.

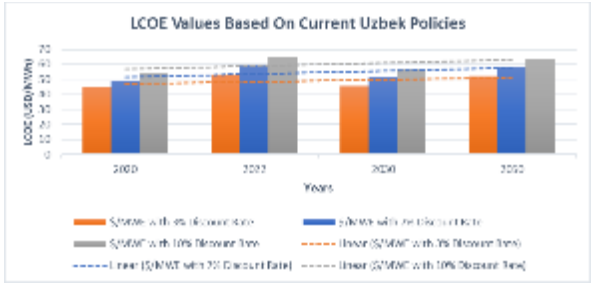

Figure 4. LCOE values based on Current Uzbek Policies

Overall, the findings underscore the substantial cost benefits associated with new gas-fired power plants in Uzbekistan when compared to their European counterparts.

ISBN: 978-618-5765-04-0
ISSN 3057-4269

They emphasize the crucial role that local resource availability, regulatory frameworks, and government policies play in shaping the economic performance of energy infrastructure projects.

This analysis highlights not only the attractiveness of investing in Uzbekistan's gas-fired power sector but also the broader implications for regional energy dynamics. As countries strive for energy security and affordability, Uzbekistan's advantageous position may serve as a model for other nations seeking to optimize their energy production capabilities while navigating the complexities of global energy markets. Moreover, the continued development of gas-fired power plants can contribute to a balanced energy portfolio that supports both economic growth and sustainability objectives in the region.

CONCLUSION

In Europe, a gradual phase-out of fossil fuels is anticipated, with a growing emphasis on renewable energy investment as stricter carbon pricing and environmental regulations drive up the costs of natural gas. By 2050, gas-fired power plants are expected to serve primarily as backup sources to stabilize grids as renewable energy sources, such as wind and solar, become the primary generators. To ensure grid reliability amidst this transition, Europe must invest in advanced energy storage technologies like batteries and pumped hydro storage, which can manage the intermittent nature of renewables. This shift to renewables also aims to reduce Europe's exposure to geopolitical risks and stabilize energy prices.

The successful transition in Europe will require cohesive policy efforts, industry collaboration, and consumer support. Governments need to promote renewable energy deployment and enhance grid infrastructure to support the increasing share of renewables. A balanced energy mix, with significant renewable capacity and gas-fired plants for backup, will help Europe achieve its sustainability and economic stability goals while maintaining energy security.

In contrast, Uzbekistan's energy landscape is shaped by its strategic location in Central Asia and abundant natural gas reserves. Its relatively stable fuel prices and predictable investment environment make it an appealing market for energy projects, especially in the natural gas sector. Uzbekistan's reliance on its domestic gas reserves allows it to maintain an affordable and reliable energy supply, making it less vulnerable to global price fluctuations.

However, to align with global energy transition trends, Uzbekistan should gradually diversify its energy mix by investing in renewable energy sources like solar, wind, and hydropower. This shift would help reduce its carbon footprint, stimulate economic growth, and reduce dependency on fossil fuels. Such diversification would also position Uzbekistan favorably in the international energy market and enhance its energy security.

In conclusion, while Europe focuses on expanding renewable energy capacity and integrating storage solutions to phase out fossil fuels, Uzbekistan leverages its natural gas reserves to maintain energy reliability. Yet, both regions share a common goal of moving toward a sustainable and resilient energy future. This alignment opens opportunities for cooperation, knowledge exchange, and investments, ultimately contributing to a more stable global energy landscape.

REFERENCES

[1] International Energy Agency, World Energy Outlook 2021, 2021.
[2] BP, Statistical Review of World Energy 2022, 2022.
[3] C. Denholm and R. M. Margolis, "Evaluating the limits of solar photovoltaics (PV) in traditional electric power systems," Energy Policy, vol. 36, no. 9, pp. 3531-3543, 2008.
[4] V. Smil, Energy and Civilization: A History, MIT Press, 2017.
[5] B. K. Sovacool, A. Hook, M. Martiskainen, and A. Brock, "The decarbonisation divide: Contextualizing landscapes of low-carbon exploitation and toxicity in Africa, Asia, and the Americas," Energy Research & Social Science, vol. 69, 2020.
[6] Guidehouse Insights, Global Distributed Natural Gas Generation Market, 2022.
[7] D. Olawuyi, "Energy Investments and Power Purchase Agreements in Emerging Markets," Journal of Energy & Natural Resources Law, vol. 39, no. 2, pp. 167-183, 2021.
[8] C. Stanitsas and K. Kirytopoulos, "Risk management in energy investments: A review," International Journal of Energy Research, 2023.
[9] S. Audu and E. Duclos, "Economic evaluation of second-hand industrial gas engines for energy projects," Journal of Applied Energy, 2024.
[10] L. Laborda Castillo et al., "Second-hand machinery and technical efficiency in emerging economies," Journal of Industrial Economics, vol. 60, no. 2, pp. 245-264, 2012.
[11] Hucul and T. Searle, "Technical assessment of surplus industrial equipment," Energy Economics, vol. 23, pp. 315-324, 2001.
[12] G. Schwartz, "Investment decisions in developing countries: New versus used machinery," World Development, vol. 1, pp. 47-59, 1973.
[13] L. Lovo et al., "Capital goods investments and energy efficiency: New vs. second-hand equipment," Energy Policy, vol. 72, pp. 174-185, 2014.
[14] Asian Development Bank, Energy Sector Analysis of Uzbekistan, Asian Development Bank, 2022.
[15] Asian Development Bank, Uzbekistan: Energy Sector Assessment, Strategy, and Road Map, Asian Development Bank, 2022.
[16] BP, Energy Outlook 2022 Edition, BP, 2022.
[17] European Commission, The European Green Deal, European Commission, 2019.
[18] European Commission, Advancing Renewable Energy Integration in the EU, European Commission, 2020.
[19] J. Fan, Y. Wang, Y. M. Wei, and L. C. Liu, "Comparative Analysis of LCOE in Coal Power Plants with CCS and Natural Gas Plants," Applied Energy, vol. 229, pp. 426-436, 2018.
[20] International Energy Agency (IEA), Uzbekistan Energy Profile, IEA, 2022.
[21] International Energy Agency (IEA), Uzbekistan: Electricity Generation and Consumption Data, IEA, 2021.
[22] International Energy Agency (IEA), Uzbekistan's Renewable Energy Potential, IEA, 2022.
[23] International Renewable Energy Agency (IRENA), Renewable Energy Roadmap for Uzbekistan, IRENA, 2021.
[24] M. Nuraliyev, et al., "Solar Energy in Uzbekistan: Challenges and Opportunities," Renewable Energy, vol. 159, pp. 432-442, 2023.
[25] S. Santecchia, et al., "Europe's Energy Transition: Challenges and Opportunities," Energy Reports, vol. 9, pp. 129-145, 2023.
[26] [26] World Bank, Energy Strategy for Uzbekistan, World Bank, 2020.
[27] MDPI, Natural Gas and Renewable Energy in Central Asia: A Comparative Analysis, MDPI, 2021.
[28] International Energy Agency, Projected Costs of Generating Electricity 2020. Paris, France: IEA, 2020.
[29] Danish Energy Agency, Technology Data for Energy Plants. Danish Energy Agency, 2022.
[30] Danish Energy Agency, "Technology Data for Energy Plants," 2022. [Online]. Available: https://ens.dk/en/our-services/technology-data/technology-data-energy-plants. [Accessed: 15-Oct-2024].
[31] Energinet, "System for Calculation of the Levelized Cost of Electricity," 2012. [Online]. Available: https://www.energinet.dk/. [Accessed: 15-Oct-2024].

ISBN: 978-618-5765-04-0
ISSN 3057-4269

Integrated Design Strategies for Sustainable Building Development: Optimizing Energy Efficiency from Micro to Macro Scales

Zeynep Karataş
Department of Sustainability, Istanbul Technical University, İstanbul, Türkiye
Montasır Doğmuş
Department of Sustainability, Istanbul Technical University, Istanbul, Türkiye

Sevim Beçet
Institute of Energy,
Istanbul Technical University, İstanbul, Türkiye

Hatice Sözer
Institute of Energy,
Istanbul Technical University, İstanbul, Türkiye
sozerh@itu.edu.tr

***Abstract*— This study explores building design strategies, covering urban planning to detailed building considerations, within a comprehensive framework that utilizes technological applications to identify buildings within their districts.**
The integrated approach considers different design tools across three scales: Urban, for identifying buildings within their environmental and man-made contexts; Building, for specifying physical and technical characteristics; and building integrated technology, for detailed assessment of energy efficiency or production.
For this purpose, Geographic Information Systems (GIS), Building Information Modeling (BIM), eQUEST (energy modeling software), and PV Syst (photovoltaic system modeling software) were employed. To ensure smooth integration and interoperability among these design tools, various strategies were developed. One crucial facilitator for interoperability was the use of Industry Foundation Classes (IFC), which serve to standardize data exchange between different software platforms. IFC enables seamless communication and exchange of information between GIS, BIM, eQUEST, and PV Syst, allowing for comprehensive analysis and optimization of energy usage. Specifically, IFC enhances the integration of the physical environment's impact on building-level energy usage with urban-scale GIS data. This integration enables detailed energy optimization analysis by considering factors such as building orientation, surrounding structures, and environmental conditions. Through the standardized data exchange facilitated by IFC, information such as building geometry, material properties, energy consumption data, and renewable energy potential can be seamlessly shared between different software tools. This ensures consistency and accuracy in the analysis and improves the efficiency of the design process.
Therefore, the integrated approach ensures a comprehensive thorough understanding of energy consumption patterns, renewable energy potential, and building performance. Interoperability among GIS, BIM, and energy modeling tools enhances the incorporation of environmental impacts on building-level energy usage. Furthermore, the evaluation of specific renewable energy system modeling and simulations serves as a basis for identifying areas for improvement. These models interact, facilitating discussions among their input and output data, as detailed within the developed model presented in this paper. This study underscores the significance of interdisciplinary collaboration and advanced technological tools in achieving energy-efficient and environmentally friendly urban developments.

Keywords: Energy; Sustainability; BIM; GIS; eQuest; IFC; Integrated Design; Interoperability; Renewable Energy

INTRODUCTION

Sustainable development necessitates a multidisciplinary and interdisciplinary approach, integrated into a holistic design framework from micro to macro scales. This study explores building design strategies, covering urban planning to detailed building considerations, within a comprehensive framework that utilizes technological applications to identify buildings within their districts.
For this purpose, this paper utilized Geographic Information Systems (GIS), Building Information Modeling (BIM), energy modeling software (eQUEST), and photovoltaic system modeling software (PV*Sol Premium). Various strategies were developed to ensure smooth integration and interoperability among these design tools.
This study aims to maximize energy efficiency in an area by working across all scales and integrating them.

GIS UTILIZATION IN URBAN SCALE STUDIES FOR ENERGY AND SUBSCALE INTEGRATIONS

In order to make interdisciplinary and multidisciplinary work sustainable, studies on an urban scale should be carried out as the first step of the holistic perspective. Evaluating the entire work area and the environment together with all its elements is one of the key points to make the study successful.

Although buildings have a very high importance when talking about all the concepts affecting energy performance and sustainability in a region, it would not be appropriate to conduct a discussion and study only on buildings. At this point, location, buildings, roads and transportation, technical infrastructure, social infrastructure, population and social structure are very important layers to find problems in the energy structure of the region and produce solutions.

ISBN: 978-618-5765-04-0
ISSN 3057-4269

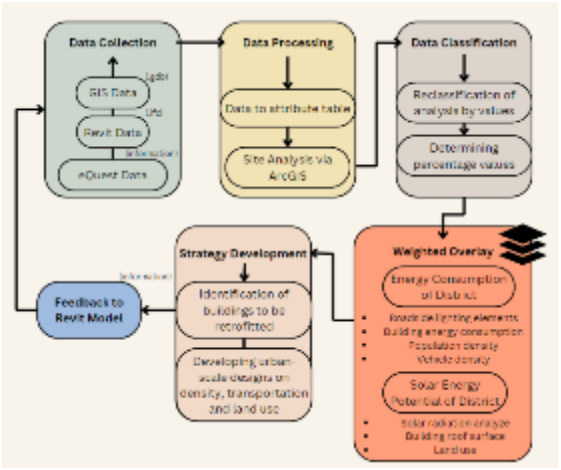

Figure 1: Process worklow of GIS and scale integration

In order to carry out a large-scale study, in the first stage, data is collected with a database where all scales support each other. At this point, data is collected at 3 different scales: district, building and building-integrated technology. The important data that is at the smallest scale and provides direct input to the upper scale is the eQuest data, which calculates the energy consumption of different types of buildings in the region. This data is evaluated at this scale, not in eQuest's own format, but on the basis of the information it outputs. The middle scale data in data collection for the upper scale is the building scale data and this data is provided from Revit models. At this point, the data is taken from the Revit base in .ifc format, the reason for this is that the IFC format can be integrated much more easily in the GIS base. GIS data, which is the last and highest scale data, is provided in (.gdb) format. (.gdb) format is one of the basic data formats for the GIS-based ArcGIS application used in this study. ArcGIS information provided by municipalities and other sources is required to be received in the common use format (.gdb) so that the study can be seamlessly integrated. Data in this format are generally essential data for carrying out district-scale energy efficiency studies such as topography lines, buildings, roads and transportation, technical infrastructure, and land use.

In the second stage, after data collection stage, the processing process of the collected data begins. In the first stage, the information obtained from eQuest and Revit is processed into the attribute table of the building layer in the ArcGIS application. Here, in order to obtain a map of building-based energy consumption, energy consumption information for pre-2000 buildings and post-2000 buildings taken from the subscale is integrated into the data with the calculation tool, after creating new columns in the building layer in ArcGIS, building total surface areas and energy consumption according to building ages. In addition, with the observation made in the study area, missing data such as road lighting elements and building ground usage types are added to the building and road layers.

After processing the data into attribute tables, study area boundary is determined and site analyses are initiated to complete the fieldwork. The analyses consider the following aspects:

- **Roads and Transportation**: Road grading, number of road lighting elements, traffic density.
- **Building**: Building age, building height, building roof surface area, total energy consumption of the building.
- **Infrastructure**: Electrical power lines, natural gas lines and waste water lines.
- **Land Use**: Building functions, land use types.
- **Population**: Density
- **Topography**: Slope, elevation, orientation, solar radiation.

These analyzes form the intermediate layers for the weighted overlay that will reveal the energy performance in the field.

The raw versions of the analyzes are not sufficient for weighted overlay, so the data classification stage must be performed. The reclassification tool reclassifies cell values according to importance, interest or similarity at specified intervals or serves to convert them into alternative values [1]. At this stage, the analyzes are first rendered raster so that the area can be evaluated as specific units in cells. Then, the desired number and type of classification for layer classes is performed again with the reclassification tool. In this way, when the layers are overlapped in the weighted overlay stage, a result that meets the purpose of the study is obtained. Before performing the overlay, the final step is to determine the importance percentages of the layers to be overlaid. Based on these importance percentages, the impact of each layer on the overlay can be adjusted by the individuals conducting the work. Thus, the overlay weights are determined according to the varying importance of the layers and their effects on the result, depending on the subject of the study. Besides the weighting of each macro/micro-scale input is based on factors such as local, regional, and national contexts, legal and regulatory frameworks, as well as technical and technological considerations [1]

In this part of the study, where energy efficiency in the area is tried to be achieved in an interscalar and interoperable way, it comes the stage of determining the amount of energy consumption in the entire area on a higher scale with a weighted overlay. The weighted overlay, which will be obtained by overlapping many layers, including data from subscales such as Revit and eQuest.

Layers in energy consumption study:

- Roadside lighting elements
- Building energy consumption
- Population density
- Vehicle density

Layers in solar energy potential study:

- Solar radiation analyzes
- Solar energy generation potential of building roof (according to size)
- Land use

In order to base the decision on choosing the impact levels of these layers on a reasonable basis, a literature review was conducted and the standards were examined. According to the standards, it was calculated how much energy consumption each layer had on an annual basis, and percentage values were decided by looking at its possible impact on the total energy consumption in the area. After the weight values were processed on the overlay tool, the overlay was run and an overlap was created in which these layers consisting of cells had an effect according to the weight values. What is obtained in the final product is that the amount of energy consumption of each cell containing a unit

ISBN: 978-618-5765-04-0
ISSN 3057-4269

area has certain degrees from less to more. Thus, points that consume more, less or average energy in the area have emerged, so areas with high potential for emerge intervention can be defined. Areas with high scores in the energy consumption overlay are the areas where energy consumption is highest and in need of retrofitting and some strategies. In the solar energy potential overlay, the areas with the highest scores emerge as the places with the highest potential for solar energy production. Thus, it is understood at which points technology integration should be prioritized. These overlays are which will form a very basic and spatial basis for strategy studies to be developed to increase energy efficiency at the urban scale and even at sub-scales.

After all these stages, the phase of creating a strategy that will have an impact on all scales is started for the areas that need improvement in energy consumption in the region. For urban scale, on road and transportation basis: strategies such as reducing vehicle use in axes where energy consumption is high and integrating pedestrian and sustainable modes into the area, using new lighting types with low electricity consumption and ensuring energy production by integrating solar panels into these lighting elements; On the basis of land use: increasing the use of green areas, creating a compact area that will help reduce energy consumption, strategies for integrating higher amounts of renewable energy sources for energy production in places where commercial use is available; On the basis of density: creating tools to raise awareness of the population in energy consumption, strategies to reduce the population density in the area must be created in future city planning. At the building scale, it is necessary to identify buildings with higher energy consumption due to reasons such as function, population density, building age and total surface area of the building, and develop retrofitting strategies on these buildings.

Finally, the strategy is determined, the information of the buildings where retrofitting strategies need to be applied is transferred to the Revit models. Thus, a holistic study can be carried out to create a sustainable and energy efficient space with the integration of lower scale and upper scale.

BIM INTEGRATION WITHIN BUILDING SCALE INTEROPERABILITY USING REVIT AND IFC STANDARDS

Building Information Modeling, specifically Autodesk's Revit software have transformed the construction industry by allowing more precise, efficient and collaborative design and management processes. BIM can provide us with a broad and detailed digital representation of the parametric and functional characteristics of the building in which can be meaninglessly shared and used by various parties during the building's lifetime [2]. Revit plays an important role in integrating BIM on a building scale. It's modeling capabilities allow for detailed and precise modifications allowing those changes to be automatically reflected throughout the whole model leading to consistency. It also supports the main designs; architectural, structural, and mechanical, creating a thorough documentation that is essential for building. The ability of Revit to integrate with various energy performance, sustainability studies, and structural analysis tools allows for a more thorough design process that contributes to achieving efficiency and performance objectives. According to the Industry Foundation Classes (IFC) principles, a key feature of Revit is interoperability, which facilitates data exchange with a variety of BIM tools and software platforms. By ensuring accurate and consistent information transfer throughout the project's phases, this enhances communication between numerous stakeholders, including architects, engineers, urban planners, and project managers [3].

BIM Modelling Process Using Revit:

1. **Starting the project:** Specifying the parametric data, such as levels, orientation, and location.
2. **Building Elements:** Creating elaborate building components (walls, floors, doors, and windows) and assigning U/R values while ensuring that material attributes match the original plan.
3. **System Integration:** Use Revit's ability to plan and analyze energy efficiency by assigning MEP systems depending on how the building is utilized and how its occupants behave.
4. **Energy Analysis:** Simulating energy performance results using built in tools on Revit or external software and comparing them with our e-Quest data accuracy.

Figure 1 depicts the process flow of Revit modeling for energy analysis, which incorporates numerous software tools to improve building performance and efficiency. The procedure starts with project setup in Revit, when important characteristics like location, orientation, and building levels are defined. This first phase involves creating geometry with IfcBuildingElements, IfcRelSpaceBoundaries, and IfcSpace, which serve as the building model's backbone

Following the setup, detailed building elements such as walls, slabs, members, columns, and beams are generated using IfcBuildingElements. These components are painstakingly specified to ensure correctness in the next analytical steps. Next, using the IfcSystem and IfcZone entities in the IFC hierarchy, MEP (Mechanical, Electrical, and Plumbing) systems must be included into the model. This integration is crucial for collecting the building's internal loads and behaviors having in mind changes in the seasons and the varied usage of the zones.

Integrating Revit's Green Building Studio (GBS) is an effective technique to create an interoperable energy

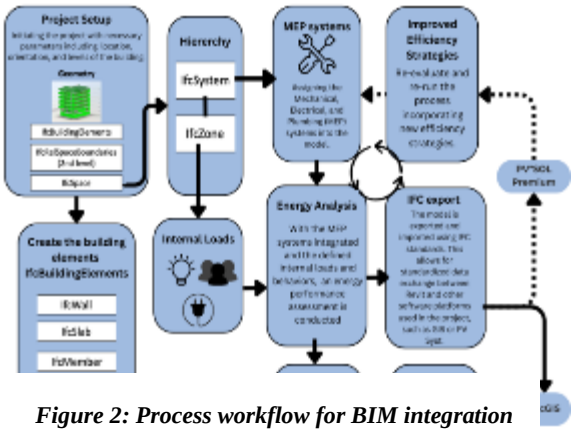

Figure 2: Process workflow for BIM integration

ISBN: 978-618-5765-04-0
ISSN 3057-4269

modeling strategy. Users may use GBS to develop an energy model directly from their existing BIM model, eliminating the need for repetitive labor. One of GBS's most notable features is its ability to export models in formats compatible with other energy analysis applications, such as eQuest. Detailed energy data, such as building geometry, material properties, and HVAC systems, may be smoothly converted into eQuest without having to start from scratch with a new model. Interoperability not only saves time and labor but also ensures that consistent data is maintained across several platforms, improving the accuracy of the energy model. Green Building Studio (GBS) increases process efficiency and lowers error risk by automating the BIM data translation, eliminating the need for human entry of design and performance parameters into eQuest. When GBS is utilized, teams may work together more cohesively since it is easy to study, change, and revise data thanks to the unified model, which results in a more reliable and accurate assessment of the building's energy performance.

With the HVAC systems in place, an energy performance evaluation is undertaken. This entails assessing the building's energy use habits and finding potential changes. The model is then exported and imported using IFC standards, allowing uniform data communication between Revit and other software platforms such as GIS or PV*SOL. This compatibility is important for future improvements and retrofits. Improved efficiency tactics are put into the model, re-evaluating and re-running the process to integrate new results and improvements. In order to improve the study and provide full understanding into the building's energy efficiency and possibilities for renewable energy cooperation, tools such as PV*SOL Premium and e-Quest are utilized. This cycle assures that building performance is continually enhanced and maximized, utilizing the capabilities of different software tools for an integrated approach to sustainable building design.

IFC Standards and Interoperability

The Industry Foundation Classes (IFC) standard improves cooperation in the construction industry by offering a uniform framework for data transmission, guaranteeing that all stakeholders may share and analyze data similarly, independent of the software used. This standardization decreases the likelihood of data misunderstanding and mistakes, ensuring that data is correct and dependable throughout the project's lifespan [3]. IFC supports interoperability across diverse software platforms, providing for smooth integration and communication among project tools. This flexibility allows stakeholders to utilize the software solutions that best meet their requirements while still collaborating successfully, minimizing the need for data re-entry or conversion and saving time and money [4]. By providing a common data environment, IFC helps interdisciplinary teams—including those working as architects, engineers, contractors, and facility managers—cooperate. It improves coordination of tasks and activities, fosters better communication and understanding among team members from different disciplines, and supports well-informed decision-making by providing all stakeholders with a comprehensive view of project data [5].IFC also makes it possible to create a complex, hierarchical data structure that records a variety of building data, from specific component information to high-level project data. This degree of information is crucial for specialist studies such as energy performance, structural integrity, and material characteristics, and it assures that all data changes and updates are traceable, resulting in a full record of project progress. IFC's integration with Building Information Modeling (BIM) processes improves its collaborative capabilities by enabling the creation, management, and sharing of digital representations of a building's physical and functional features. This leads to greater efficiency in design, construction, and operation by using shared data and collaborative procedures [3].

Benefits of IFC Integration:

1. Standardized Data Exchange: By enabling uniform building information exchange across a range of software systems, IFC reduces the risk of data loss or misunderstanding. For efficient interdisciplinary cooperation and the integration of many design tools, this standardization is essential.
2. Interdisciplinary Collaboration: Revit models may be exported from IFC and shared with stakeholders via other software programs, such eQUEST for energy modeling or GIS for urban planning. This interoperability facilitates thorough investigation and well-informed choices.
3. Enhanced Accuracy: Energy simulations and performance analyses are more accurate because to IFC's standardized data interchange. It guarantees accurate information transmission across software tools, including system specs, material qualities, and architectural geometry.
4. Enhanced Efficiency: By lowering the time and effort required to re-enter or convert data across tools, IFC integration optimizes operations. This effectiveness is especially useful for intricate tasks combining several different academic fields.

ENERGY SYSTEM INTEROPERABILITY WITHIN BIM – SOLAR ENERGY

Building Information Modelling, known as BIM, includes energy simulations of the building via calculating the buildings' current energy status by its own software. However, integration of renewable energy sources and systems to models is more complex and difficult task due to hardships in interoperability between energy simulation programs and tools, platforms that support BIM such as IFC and gbXML. In this part of the article there is a specific type of renewable energy source was chosen to be applied to buildings, which is solar energy, and focused on its integration. The way to produce and distribute solar energy is investigated by simulating Building Integrated PV (BIPV) with energy software and algorithm tools. The concept is explained in three parts, namely Solar Energy Software and BIM Interoperability, RES Modelling, and Challenges and Future Work.

Solar Energy Software and BIM Interoperability

To integrate solar energy systems into BIM, it is necessary to first define the system. There are many solar energy system programs available on the market. Some of these are programs

ISBN: 978-618-5765-04-0
ISSN 3057-4269

such as Homer, PVSyst, PV*Sol, PV*Sol Premium. Although these applications are useful for visual modeling and system modeling, there are problems in integrating them into BIM applications, more specifically the BIM format this project used to provide interoperability, IFC (Industry Foundation Classes).

The interoperability between applications can be facilitated by automating every part of the analysis process (structural or energy) that can be automated. This calls for a review of standardization efforts in data exchange and the existing approaches that have begun to establish interoperability between BIM and RES/energy analysis applications. [7]

RES Modelling

In this section, which aims to ensure the integration of Renewable Energy, three-dimensional models of the buildings and basic information of the location where the building is located are determined. The main aim is to read the output obtained from one program smoothly when transferred to the next program, because of this reason the buildings were designed in CAD applications in IFC format, a BIM-supported tool, and in 3D with Revit. Architectural and structural details are modelled in Revit.

Before starting RES modelling and system simulation, it is important to determine the current energy state of the buildings or sites, to calculate current energy consumption, which is needed to build a RES system. When integrating renewable energy systems into buildings, it is necessary to know the current energy status and energy costs of the building so that it can be decided whether the energy produced will be sufficient for the building and whether it needs to be stored. The consumption value calculation was made with the eQUEST program. eQUEST allows users to create simulations that incorporate building location, orientation, wall/roof construction, window properties, as well as HVAC systems, day-lighting and various control strategies. Energy consumption model of the building is created with eQUEST and achieved realistic results. The data obtained with eQUEST was used as consumption data in the simulation program for the solar energy system. eQUEST is an IFC compliant tool, hovewer it is not possible to export a 3D model of the buildings that interoperable with energy simulation sofware tools.

Once the consumption data was obtained, it was necessary to choose a simulation application for the solar energy system. It is possible to simulate BIPV with applications such as PV*Sol, PV*Sol Premium, Homer, PVSyst available on the market, but the fact that most of the applications work with two-dimensional visuals turned out to be a negative situation in terms of interoperability. These tools can model various types of renewable energy technologies, yet they are neither easy to use in conceptual design nor is interoperable with BIM model or platform. [6]

In order to ensure renewable energy integration in BIM applications, it is first necessary to perform energy simulation. Preliminary work is done with two solar energy system simulation applications named PVSyst and PVSol Premium. After building a two-dimensional modeling with PVSyst, three-dimensional model is obtained with PVSol Premium, using existing Revit building models, with Google Earth view and location information, and support for reading 2D, 3D and CAD files.

PVSyst model included two different types of solar power production and storage systems; namely grid-connected and stand-alone solar systems. It is possible to have realistic results with addressing the real location via Google Maps, and assigning accurate inverters, converters, specific PV panels and providing a cable plan. The data obtained from PVSyst can be used as a calibrator, since the results are not IFC compliant. PV*Sol Premium is a solar energy simulation software that makes it possible to create 3D models within, and import specific CAD formats such as 3D Max. To ensure working on real buildings it is possible with PV*Sol Premium to import 3D model into program and work on it with real location, which specified via Google Maps and climate data extracted from Meteonorm, a widely used and accepted solar radiation data source in the solar energy industry.

The process flow of RES integration to BIM model is shown in the Figure 3. The outputs from the REVIT model were received in IFC format and transferred to the next program as IFC. Afterwards, 3D Max was used to import Revit model into PV*Sol Premium. Although the primary purpose of IFC is to ensure communication between

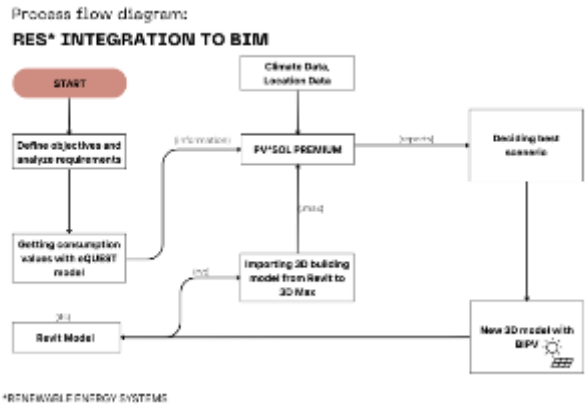

Figure 3: RES Integration to BIM

programs, 3D Max is used as an intermediate program since there is no solar energy simulation program with the infrastructure to adapt to it.

In PV*Sol Premium, different scenarios were created with panel layout and energy system details. After choosing the best scenario, the placement of PV panels was decided. Then solar panels modeled in PV*Sol Premium are manually added to the Revit model. Changes made in the Revit model will be reflected in the 3D Max file as it is possible to link them, and thus the three-dimensional drawing file will always be up to date when it is transferred back to PV*Sol Premium.

CHALLENGES AND FUTURE WORK

IFC offers a lot of advantages, but achieving smooth interoperability with them presents significant challenges. The variations in how different software systems interpret IFC data are a key issue that can lead to data loss and inconsistencies. Furthermore, when models from many sources must align coherently, discrepancies in level of detail

ISBN: 978-618-5765-04-0
ISSN 3057-4269

(LOD) across IFC files might generate integration challenges. Another challenge is that the IFC standard must be updated on a regular basis to keep up with changing business practices and technology improvements. To solve these challenges, future research should focus on providing comprehensive guidelines for standardized data transfer, improving IFC implementations across software platforms, and encouraging broader use of IFC in the construction sector. Focusing on these areas allows the industry to increase the reliability and efficiency of data interoperability, resulting in improved project outcomes.

The challenge is to adapt energy simulation programs to BIM platform via IFC, Industry Foundation Classes, a non-proprietary file format used for exchanging building information models. It is not possible yet to provide interoperability regarding renewable energy systems. The next step will be to remove the manual data entries and simplify the complex nature of renewable energy integration and make it compatible with IFC.

DISCUSSION

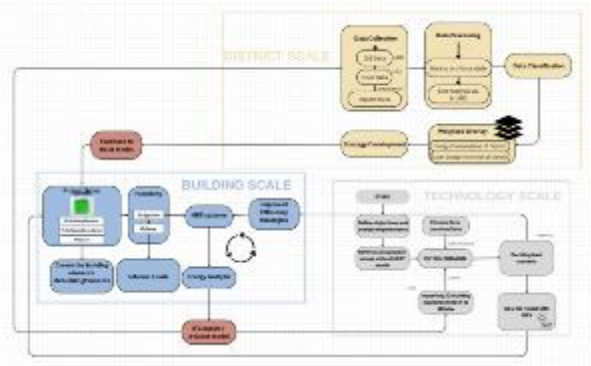

Figure 4 illustrates the whole picture of our three-scale integration target. District, building, and technology scale integration with seamless data flow and feedback loops are made possible by IFC standards. District-level energy strategy is informed by information on solar potential and energy use obtained by district-level analysis of data from GIS, Revit, and eQUEST. Building geometry and energy systems are defined at the building scale using IFC-based models, which link building design to district insights. Efficiency increases steadily as energy analysis and MEP improvements are reincorporated into the district model.PV*SOL Premium integrates temperature and geographic data into its simulation of renewable energy systems, such as BIPV. Scenario testing informs both the building design and the district energy strategy. This integration makes it feasible to implement a comprehensive approach that maximizes energy efficiency across the board in urban development, with one scale affecting and strengthening the others.

CONCLUSION

The integrated approach ensures a comprehensive thorough understanding of energy consumption patterns, renewable energy potential, and building performance. Interoperability among GIS, BIM, and energy modeling tools enhances the incorporation of environmental impacts on building-level energy usage. Furthermore, the evaluation of specific renewable energy system modeling and simulations serves as a basis for identifying areas for improvement. These models interact, facilitating discussions among their input and output data, as detailed within the developed model presented in this paper.

REFERENCES

[1] Alpagut, B., Romo, A.L., Hernandez, P., Tabanoğlu, O. (2021). A GIS-Based Multicriteria Assessment for Identification of Positive Energy Districts Boundary in Cities.
[2] Attia, S. (2018). BIM and Energy Simulation: A Synopsis of the Integration Challenges. Energy and Buildings, 158, 329-339.
[3] Eastman, C., Teicholz, P., Sacks, R., & Liston, K. (2011). *BIM Handbook: A Guide to Building Information Modeling for Owners, Managers, Designers, Engineers, and Contractors*. John Wiley & Sons.
[4] Jeong, Y. S., Eastman, C. M., Sacks, R., & Kaner, I. (2009). Benchmark Tests for BIM Data Exchanges of Precast Concrete. Automation in Construction, 18(4), 469-484.
[5] Volk, R., Stengel, J., & Schultmann, F. (2014). Building Information Modeling (BIM) for Existing Buildings: Literature Review and Future Needs. Automation in Construction, 38, 109-127.
[6] A. Acquaviva, L. Blaso, D. Dalmasso, M.D. Giudice, G. Fracastoro, V.L. Verso, E. Macii, A. Osello, A. Pace, E. Patti, A. Pellegrino, P. Piumatti (2012). From Historical Buildings to Smart Buildings via Middleware and Interoperability
[7] A. Gupta, A. Cemesov, C.J. Hopfe, Y. Rezgui, T. Sweet(2013).A conceptual framework to support solar PV simulation using an open-BIM data exchange standard**.**

ISBN: 978-618-5765-04-0
ISSN 3057-4269

Optimal Application of a Concentrating Solar System in an Existing Dairy

Marcello Braglia
Department of Civil and Industrial Engineering
University of Pisa
Pisa, Italy
marcello.braglia@unipi.it

Francesco Di Paco
Department of Civil and Industrial Engineering
University of Pisa
Pisa, Italy
francesco.dipaco@phd.unipi.it

Marco Frosolini
Department of Civil and Industrial Engineering
University of Pisa
Pisa, Italy
marco.frosolini@unipi.it

Roberto Gabbrielli
Department of Civil and Industrial Engineering
University of Pisa
Pisa, Italy
roberto.gabbrielli@unipi.it

Leonardo Marrazzini
Department of Civil and Industrial Engineering
University of Pisa
Pisa, Italy
leonardo.marrazzini@unipi.it

***Abstract*— This work explores the technical feasibility of installing an innovative thermal concentrating solar system (TCSS) for high-pressure steam production in a dairy facility in the north part of Tuscany (Italy). The production process for soft cheeses requires the injection of saturated steam at about 190°C into washtubs containing semi-finished materials which are consequently heated together with the required ingredients for the specific recipe. Currently, this steam is generated by natural gas-fired tube boilers by 110 kW of nominal thermal power, resulting in significant steam usage and necessitating large amount of make-up fresh treated water at atmospheric conditions.**

We propose the installation of a TCSS based on linear Fresnel concentrating systems technology to supply a portion of the necessary steam, thereby reducing fossil fuel consumption and enhancing the environmental performance of the process. The fresh water at atmospheric temperature flows directly through the horizontal absorber tube and it becomes saturated steam at the end of the solar field.

To optimize the use of the solar power source, we considered and refined the adoption of a storage system based on a pressurized vessel containing a mixture of water and steam. This is particularly relevant given that dairy production is confined to six hours each morning per 5 days per week. The unique thermal load profile presents challenges for integrating an intermittent solar power source, which peaks during midday hours. Special attention has been given to the operational behaviour of the integrated system, defining suitable control strategies facilitated by the installation of valves and sensors.

A detailed analysis of the integration between the new solar system and the existing plant has been carried out. The analysis involves the investigation of several sizes of the solar system and the storage tank ensuring the required service levels for the thermal end-user.

Following the technical analysis, the system has demonstrated significant potential for improving the overall energy efficiency and reducing the carbon footprint of the production process.

Keywords—thermal concentrating solar system, dairy production, energy efficiency, thermal storage

INTRODUCTION

The global demand for energy and electricity is rising rapidly, driven by population growth, industrial expansion, and accelerating urbanization. As conventional energy sources, such as fossil fuels, become increasingly scarce and contribute significantly to greenhouse gas (GHG) emissions, the world faces critical challenges in securing a clean and sustainable energy supply. It is projected that global primary energy demand could increase by 1.5 to 3 times by 2050, reflecting the growth of energy needs across several regions [1]. In 2023, approximately 60% of the global energy supply is derived from fossil fuels, including coal, petroleum, and natural gas [2]. These non-renewable resources are not only depleting but also account for the majority of GHG emissions, exacerbating the climate change crisis. In this perspective, increasing the usage of renewable resources for energy production is pivotal for emission reduction. According to the International Panel on Climate Change (IPCC), the exploitation of solar energy could mitigate between four and five gigatons of CO_2-eq (Figure 1). More specifically, the use of concentrating solar power (CSP) systems would save about 200-300 kg CO_2-eq per square meter of concentrator surface [1].

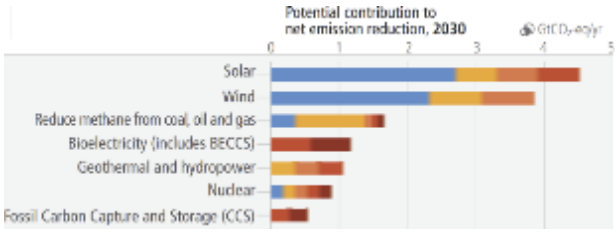

Figure 1: Mitigation options in the near term [3]

The application of solar thermal energy in industrial processes holds significant potential for achieving multiple advantages. Integrating solar heat not only reduces the reliance on costly fossil fuels but also enhances the environmental profile of production processes, which is increasingly valued by consumers seeking low-impact and sustainable products [4], [5]. Utilizing solar energy for small-scale heat demand presents a straightforward and cost-effective alternative to combined heat and power solutions, particularly for small and medium-sized enterprises. The lower capital investment required makes solar integration more accessible and practical for these industries.

ISBN: 978-618-5765-04-0
ISSN 3057-4269

The scientific and technical literature has seen a growing number of studies exploring the most efficient and economically viable methods for integrating solar thermal energy into industrial processes. Various authors have provided comprehensive overviews of the potential and effectiveness of solar energy in industrial applications [6], [7], [8]. Energy consumption analysis reveals that approximately 13% of industrial thermal applications require low-temperature heat (up to 100°C), 27% require medium-temperature heat (up to 200°C), with the remaining demand in high-temperature processes such as those in the steel, glass, and ceramics industries.

Solar thermal applications in industry are diverse, including processes such as hot water and steam generation, drying, preheating, concentration, pasteurization, sterilization, washing, chemical reactions, and industrial space heating [9]. Some examples of solar thermal use at low and medium temperatures include:

- Diary: Pasteurization, sterilization, drying, and boiler feed water.
- Tinned Food: Sterilization, pasteurization, cooking, and bleaching.
- Textile: Bleaching, dyeing, drying, degreasing, and pressing.
- Paper: Cooking, drying, and bleaching.
- Meat Processing: Washing, sterilization, and cooking.
- Beverages: Washing, sterilization, and cooking.

Numerous technical assessments have demonstrated the feasibility of solar energy integration in specific industrial processes, underscoring its technical and economic benefits [10], [11], [12], [13], [14]. Most studies focus on the integration of low-temperature solar thermal systems, typically using conventional flat-plate or evacuated tube collectors for hot water production. However, for processes requiring high-pressure steam, as in many industrial applications, thermal concentrating solar systems (TCCS) such as linear Fresnel collectors (LFC) are necessary [15], [16]. LFC technology offers advantages in terms of land use efficiency, lower capital costs, and simpler maintenance compared to other TCCS options like parabolic troughs and dishes.

This paper presents an innovative application of concentrated solar LFC technology in a dairy facility for steam production, aimed at enhancing both the economic and environmental performance of a process with substantial heat demand. Previous studies have explored solar integration in dairy processes using standard plate thermal collectors for hot water production [17], [18]. In contrast, our study focuses on steam production using a parallel circuit with a concentrated solar field.

Following a brief overview of the dairy process under consideration, we describe the solar LFC system and its integration with the conventional fossil-fuel fired boiler. The technical design of the proposed system is analysed in detail, and we conclude with recommendations for future research and practical implementation.

DESCRIPTION OF THE PRODUCTION PROCESS

In the dairy located in the northern part of Tuscany, Italy, soft cheese production involves the injection of saturated steam at approximately 190 °C into washtubs filled with semi-finished materials. These materials are heated along with the necessary ingredients for specific recipes. The water used in this process is pumped from suitable wells and undergoes rigorous treatment to meet the stringent standards of the food industry. This treatment includes filtration with sand and activated carbon filters, chlorination, and softening.

The heat demand in the dairy is met by two natural gas-fired boilers, each with a nominal thermal power of 110 kW (Figure 2). When both boilers operate at 50-60% of their nominal capacity, they produce 140 kg/h of saturated steam. This steam is used to heat the process water to 60 °C and to produce the final products. The domes of the boilers function as steam storage, with steam bleeding controlled by the product temperature inside the washtubs.

The factory's other energy needs include electricity for driving the process equipment and thermal energy for heating the factory buildings. The production process operates year-round without maintenance stoppages. The daily heat demand remains constant from 5 a.m. to 11 a.m., Monday through Friday.

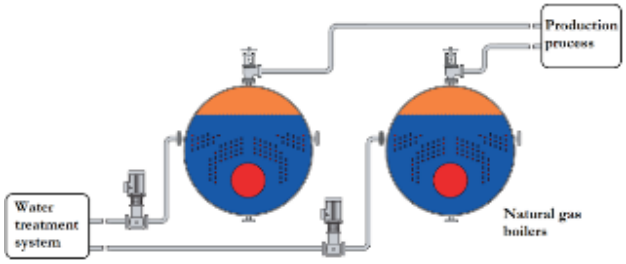

Figure 2:Current thermal plant layout

THE LINEAR FRESNEL CONCENTRATING SOLAR SYSTEM

Linear Fresnel concentrating solar systems are modular assemblies typically aligned in a south-north direction. Each module consists of several horizontal reflective surfaces arranged east to west, tracking the sun's apparent movement across the sky. These reflectors focus solar direct normal irradiance (DNI) onto an absorber—a pressurized horizontal tube positioned a few meters above the ground. The thermal fluid, usually water or steam, is heated from the liquid phase at ambient conditions to high-pressure saturated steam as it passes through the absorber tube. These solar systems can be installed either on the ground, such as on a lawn, or on the roofs of industrial buildings. In the described application, the system is installed above the process building, with a 14° deviation from the north-south direction.

By using hourly solar DNI data, it is possible to evaluate the monthly average values of the thermal energy collected by the thermal fluid per unit of collector surface for each hour of the day at the selected installation site (Figure 3). Note that the peak values generally occur from 10 a.m. to 4 p.m., a time window that significantly differs from the dairy's operation hours. The total monthly values of the energy collected by the thermal fluid per unit of collector surface are summarized in Figure 4. The total annual thermal energy collected by the thermal fluid amounts to approximately 790 kWh/m².

ISBN: 978-618-5765-04-0
ISSN 3057-4269

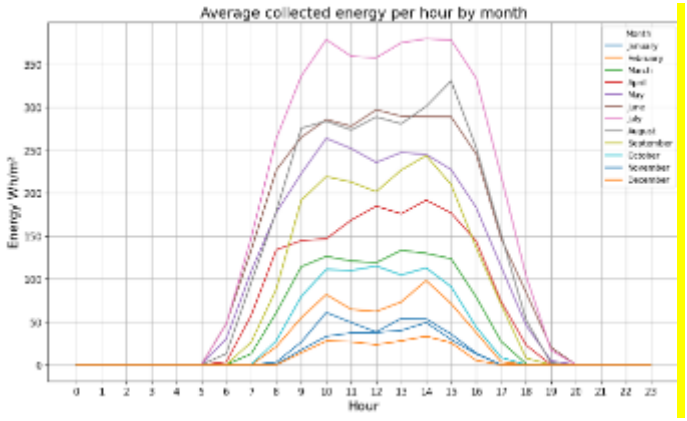

Figure 3: Monthly average values of the specific thermal energy collected for each hour of the day

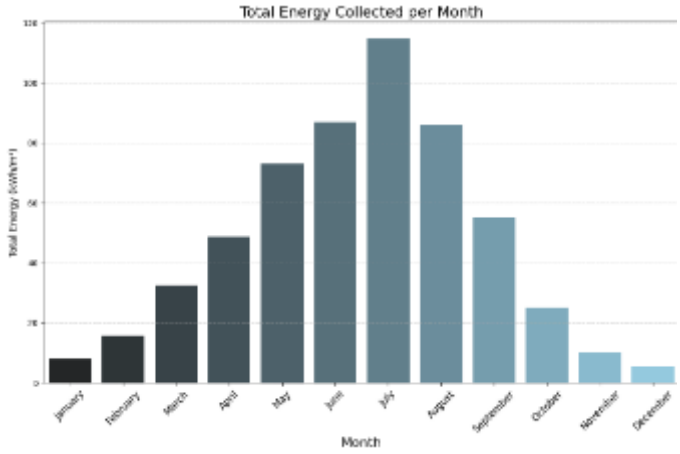

Figure 4: Monthly average values of the specific collected thermal energy

INTEGRATION OF THE SOLAR CONCENTRATED THERMAL SYSTEM WITH THE ORIGINAL THERMAL PLANT

Technical features

The integrated solar field-fossil boiler system (Figure 5) consists of a thermal concentrating solar system (TCSS) configured in parallel with the conventional fossil-fuel boilers. The solar system, fed by treated fresh water, generates saturated steam under the same thermodynamic conditions as the steam produced by the natural gas-fired boilers. The entire steam flow is directed into a flash storage tank, where it is stored in a two-phase state. This steam is then supplied to the heat end-users within the dairy production process, effectively positioning the solar field as a secondary boiler operating in parallel with the existing ones.

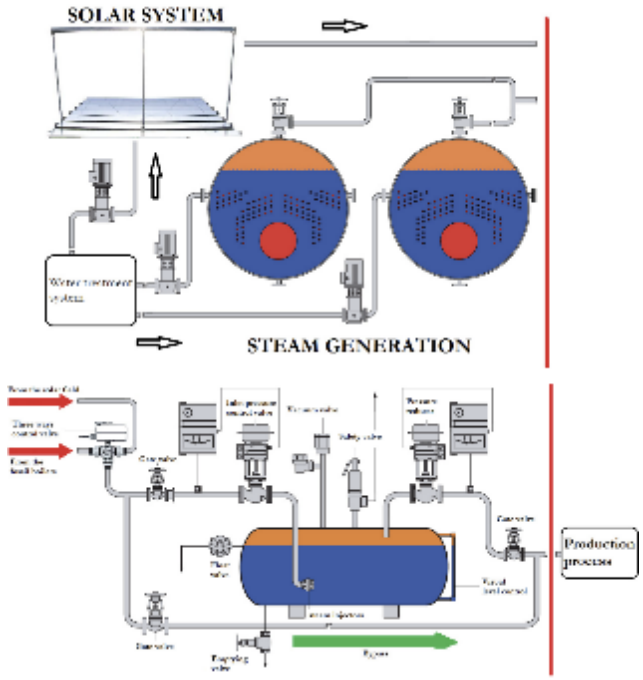

Figure 5: Integrated solar thermal system

This parallel configuration ensures that the feedwater conditions for the fossil boilers remain unchanged and unaffected by the solar system's presence. The inclusion of the storage tank offers several operational advantages: (i) it enhances solar energy utilization by aligning the production of thermal energy with demand, despite the solar field's peak productivity occurring outside of typical production hours. Additionally, during weekends when the production process is idle, the storage tank allows for the accumulation of solar energy on Sunday for use on Monday morning. (ii) It improves production process reliability by reducing downtime caused by boiler failures, even when solar thermal production is temporarily unavailable due to insufficient direct normal irradiance (DNI). (iii) The storage tank enables the boilers to operate at their nominal load, filling the tank when solar contribution is insufficient, thereby smoothing out the demand fluctuations that are otherwise only moderated by the small domes within the boilers.

A flash storage tank was selected due to its smaller volume compared to dry tanks, where only dry steam is stored. In a flash tank, water is stored at the bottom, with steam above it in thermodynamic equilibrium. As steam enters the tank, a portion condenses while the rest accumulates at the top, increasing the pressure, temperature, and specific enthalpy of the mixture (i.e., the stored thermal energy), thereby raising the water level. Conversely, when steam is extracted, the pressure and temperature drop, causing some water to flash into steam, lowering the water level. Reliable operation of the storage and extraction processes requires an appropriate ratio between water and steam mass inside the tank, typically around 9:1, and a large contact surface between the two phases, which is why these cylindrical vessels are typically horizontal with a length much greater than their diameter.

Operation modes

Given the presence of two types of boilers operating in parallel, it is essential to precisely define the operating modes of the integrated system. To optimize both economic and environmental outcomes, the solar field is given operational priority. The conventional boilers are then used only to

ISBN: 978-618-5765-04-0
ISSN 3057-4269

supplement the steam that the solar field cannot provide. This is managed through the installation of a three-way control valve. The valve directs solar-generated steam to the storage tank when its pressure exceeds a specified minimum set point. If the solar steam pressure falls below this threshold, the valve connects the fossil-fuel boilers to the storage tank, ensuring that the storage pressure remains within the operational range.

When production is halted, the valve prevents the fossil fuel boilers from starting, allowing only solar steam to feed the steam storage tank. This approach prevents unnecessary natural gas consumption by avoiding boiler activation due to pressure drops in the storage tank caused by ambient heat losses.

TECHNICAL ANALYSIS OF THE INTEGRATED SYSTEM

At a generic instant, the steam mass of the storage tank is given by the following balance equation:

$$\frac{dM(t)}{dt} = \dot{m}_{in_s}(t) + \dot{m}_{in_b}(t) - \dot{m}_{out}(t) \qquad (1)$$

Where $M(t)$ is the instantaneous mass of stored steam, $\dot{m}_{in_s}(t)$ is the inlet steam mass flow produced by the solar system, $\dot{m}_{in_b}(t)$ is the inlet steam mass flow produced by the gas-fired boilers, and $\dot{m}_{out}(t)$ is the outlet steam mass flow that is required by the end-users.

When $M(t)$ is equal to the maximum capacity of the storage tank and $\dot{m}_{in_s}(t) - \dot{m}_{out}(t) > 0$, $\dot{m}_{in_b}(t)$ is null and it is necessary to reduce the solar steam production. This can be achieved by modifying the right focus of the tracking system of the reflector surfaces. On the other hand, when $M(t)$ is equal to zero (i.e. pressure at the minimum value) and $\dot{m}_{in_s}(t) - \dot{m}_{out}(t) < 0$, it is necessary to use the gas-fired boilers and thus $\dot{m}_{in_b}(t) > 0$. It is relevant to highlight that $\dot{m}_{in_s}(t)$ depends on the instantaneous value of DNI and on the hour of the day. Therefore, it cannot be scheduled to vary the steam mass inside the storage tank.

To evaluate the actual amount of thermal energy that can be stored and utilized by the end user, we developed a simulation model with an hourly time step. The simulation was conducted across various sizes of both the solar field and the steam storage tank.

Figure 6 illustrates the mass of solar steam consumed by the end user. As shown, solar steam consumption increases with the size of both the solar field and the storage capacity. However, for a given solar field size, steam consumption plateaus once the storage tank reaches a certain capacity. This indicates that beyond a specific tank size, further increases do not contribute to higher solar steam consumption, suggesting an optimal tank size for each solar field configuration.

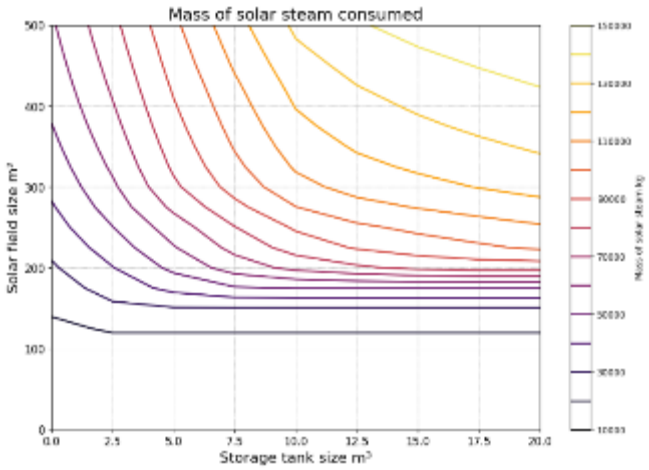

Figure 6: mass of solar steam consumed as the size of the storage tank and the solar field vary

Figure 7 shows the ratio between solar steam consumed and solar steam produced. As observed, this ratio increases with the size of the storage tank. Notably, when no storage tank is present (blue curve), the ratio remains nearly constant before slightly declining. Additionally, the ratio peaks between 200 and 250 m² of solar field area, indicating that for maximum solar heat utilization, the solar field should be sized within this optimal range.

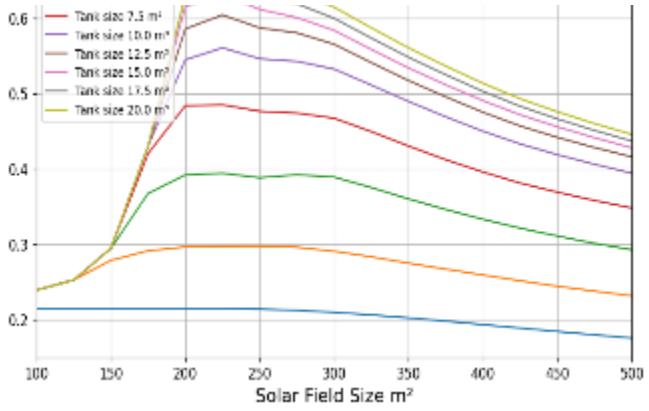

Figure 7: Ratio between solar steam consumed and solar steam produced

Figure 8 illustrates the ratio between solar steam consumed and total steam produced, representing the percentage of gas-fired steam saved by the solar system. The trend closely mirrors that of the previous figure. Notably, the peak occurs at a solar field size of approximately 300 m², indicating that to maximize natural gas savings, the solar field should be sized accordingly.

ISBN: 978-618-5765-04-0
ISSN 3057-4269

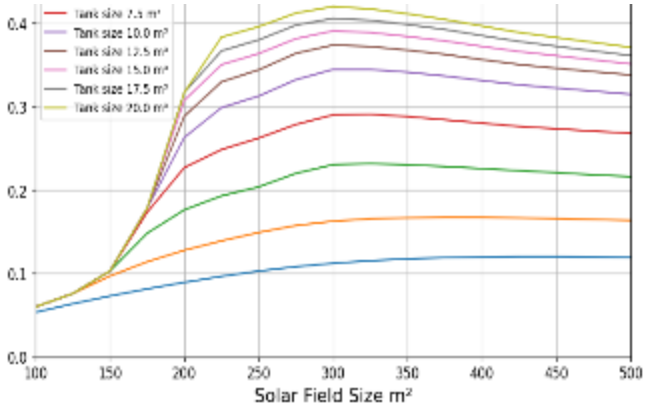

Figure 8: Ratio between solar steam consumed and total steam produced

Figure 9 illustrates the ratio between solar steam that must be discharged and the total solar steam produced, highlighting two critical aspects. First, it emphasizes the importance of the storage tank. The blue curve, representing the scenario without a tank, shows a ratio that remains nearly constant with a slight upward trend as the solar field size increases. In this case, approximately 80% of the solar steam goes unused due to the mismatch between production and demand, making the system highly unprofitable. Second, when a storage tank is introduced, there is a range of solar field sizes where no steam is wasted, allowing the system to fully utilize the generated solar energy without any losses. In this perspective, the bigger the tank and the less steam mass must be discharged.

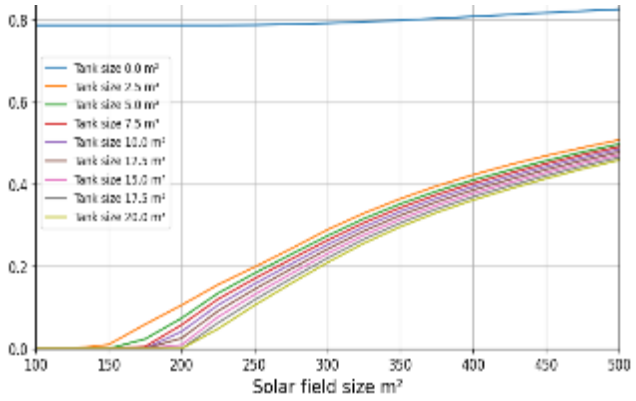

Figure 9: Ratio between solar steam to be discharged and solar steam produced

CONCLUSIONS AND FUTURE DEVELOPMENTS

This paper presents an innovative approach to improving the energy efficiency and reducing the environmental impact of a cheese production process. The proposed modification integrates a solar system into the existing setup, which relies on two gas-fired boilers. The new configuration introduces a Fresnel linear concentrating solar system (CSS) in parallel with the existing boilers, allowing both systems to produce the required steam under the same thermodynamic conditions while remaining separate. To better align steam demand with solar production, a flash steam storage tank is incorporated. This addition enables steam storage and allows the fossil boilers to operate at higher thermal loads, thereby improving thermal efficiency and reducing transient periods.

To evaluate the technical feasibility of the integration, an hourly time-step simulation model was developed. The simulation results demonstrate that natural gas consumption can be significantly reduced through the effective use of solar heat. Furthermore, the analysis underscores the importance of the storage tank, which increases the amount of energy that can be captured and utilized. Indeed, without the storage tank, a large portion of the solar-generated steam would be wasted.

An intriguing extension of the current analysis would be to include an economic assessment to evaluate the financial feasibility of the new system under varying gas prices. Additionally, given the urgent challenge of climate change, a detailed evaluation of the carbon footprint could be integrated to quantify the reduction in emissions achieved by the system. This would provide a comprehensive understanding of both the economic and environmental benefits of the integration.

ACKNOWLEDGMENT

This study was carried out within the NEST - Network 4 Energy Sustainable Transition (D.D. 1243 02/08/2022, PE00000021) and received funding under the National Recovery and Resilience Plan (NRRP), Mission 4 Component 2 Investment 1.3, funded from the European Union - NextGenerationEU. This manuscript reflects only the authors' views and opinions, neither the European Union nor the European Commission can be considered responsible for them.

REFERENCES

[1] A. Shahsavari and M. Akbari, 'Potential of solar energy in developing countries for reducing energy-related emissions', *Renewable and Sustainable Energy Reviews*, vol. 90, pp. 275–291, Jul. 2018, doi: 10.1016/j.rser.2018.03.065.

[2] EMBER, 'Global Electricity Review 2024', 2024.

[3] K. Calvin *et al.*, 'IPCC, 2023: Climate Change 2023: Synthesis Report. Contribution of Working Groups I, II and III to the Sixth Assessment Report of the Intergovernmental Panel on Climate Change [Core Writing Team, H. Lee and J. Romero (eds.)]. IPCC, Geneva, Switzerland.', Intergovernmental Panel on Climate Change (IPCC), Jul. 2023. doi: 10.59327/IPCC/AR6-9789291691647.

[4] S.-P. Chuang and C.-L. Yang, 'Key success factors when implementing a green-manufacturing system', *Production Planning & Control*, vol. 25, no. 11, pp. 923–937, Aug. 2014, doi: 10.1080/09537287.2013.780314.

[5] D. A. Dornfeld, 'Moving towards green and sustainable manufacturing', *Int. J. of Precis. Eng. and Manuf.-Green Tech.*, vol. 1, no. 1, pp. 63–66, Jan. 2014, doi: 10.1007/s40684-014-0010-7.

[6] M. T. Islam, N. Huda, A. B. Abdullah, and R. Saidur, 'A comprehensive review of state-of-the-art concentrating solar power (CSP) technologies: Current status and research trends', *Renewable and Sustainable Energy Reviews*, vol. 91, pp. 987–1018, Aug. 2018, doi: 10.1016/j.rser.2018.04.097.

[7] C. Lauterbach, B. Schmitt, U. Jordan, and K. Vajen, 'The potential of solar heat for industrial processes in Germany', *Renewable and Sustainable Energy Reviews*, vol. 16, no. 7, pp. 5121–5130, Sep. 2012, doi: 10.1016/j.rser.2012.04.032.

[8] G. Pirasteh, R. Saidur, S. M. A. Rahman, and N. A. Rahim, 'A review on development of solar drying applications', *Renewable and Sustainable Energy Reviews*, vol. 31, pp. 133–148, Mar. 2014, doi: 10.1016/j.rser.2013.11.052.

[9] S. Mekhilef, R. Saidur, and A. Safari, 'A review on solar energy use in industries', *Renewable and Sustainable Energy Reviews*, vol. 15, no. 4, pp. 1777–1790, May 2011, doi: 10.1016/j.rser.2010.12.018.

[10] A. Loris, S. Hosouli, G. Lennermo, M. Kulkarni, Y. Poursanidis, and J. Gomes, 'Evaluation of the Use of Concentrated Solar Photovoltaic Thermal Collectors (CPVT) in a Dairy and Swine Farm in Europe', in *Proceedings of the ISES Solar World Congress 2021*, Virtual: International Solar Energy Society, 2021, pp. 1–12. doi: 10.18086/swc.2021.29.05.

[11] D. Cocco, V. Tola, and M. Petrollese, 'Application of Concentrating Solar Technologies in the Dairy Sector for the Combined Production of Heat and Power', *Energy Procedia*, vol. 101, pp. 1159–1166, Nov. 2016, doi: 10.1016/j.egypro.2016.11.157.

[12] M. Biencinto, L. González, L. Valenzuela, and A. Fernández, 'Design and Simulation of a Solar Field Coupled to a Cork Boiling Plant', *Energy Procedia*, vol. 48, pp. 1134–1143, Jan. 2014, doi: 10.1016/j.egypro.2014.02.128.

[13] M. Cotrado, A. Dalibard, R. Söll, and D. Pietruschka, 'Design, Control and First Monitoring Data of a Large Scale Solar Plant at the Meat Factory Berger, Austria', *Energy Procedia*, vol. 48, pp. 1144–1151, Jan. 2014, doi: 10.1016/j.egypro.2014.02.129.

[14] A. Frein, M. Calderoni, and M. Motta, 'Solar Thermal Plant Integration into an Industrial Process', *Energy Procedia*, vol. 48, pp. 1152–1163, Jan. 2014, doi: 10.1016/j.egypro.2014.02.130.

[15] O. Iglauer and C. Zahler, 'A New Solar Combined Heat and Power System for Sustainable Automobile Manufacturing', *Energy Procedia*, vol. 48, pp. 1181–1187, Jan. 2014, doi: 10.1016/j.egypro.2014.02.133.

[16] R. Gabbrielli, P. Castrataro, F. Del Medico, M. Di Palo, and B. Lenzo, 'Levelized Cost of Heat for Linear Fresnel Concentrated Solar Systems', *Energy Procedia*, vol. 49, pp. 1340–1349, Jan. 2014, doi: 10.1016/j.egypro.2014.03.143.

[17] J. A. Quijera and J. Labidi, 'Pinch and exergy based thermosolar integration in a dairy process', *Applied Thermal Engineering*, vol. 50, no. 1, pp. 464–474, Jan. 2013, doi: 10.1016/j.applthermaleng.2012.06.044.

[18] J. A. Quijera, M. G. Alriols, and J. Labidi, 'Integration of a solar thermal system in a dairy process', *Renewable Energy*, vol. 36, no. 6, pp. 1843–1853, Jun. 2011, doi: 10.1016/j.renene.2010.11.029.

ISBN: 978-618-5765-04-0
ISSN 3057-4269

Evaluation of Hydrogen Production with Fuzzy Cognitive Mapping Approach

Gülçin Büyüközkan
Industrial Engineering Department
Galatasaray University
Ortaköy, İstanbul, Türkiye
gulcin.buyukozkan@gmail.com
ORCID: 0000-0002-2112-3574

Pelinsu Uygur
Industrial Engineering Department
Galatasaray University
Ortaköy, İstanbul, Türkiye
psuygur@gmail.com

***Abstract*— Hydrogen stands out as an energy resource primarily because of its sustainability and cleanliness, making it a vital component of the worldwide shift towards sustainable energy. Because of its high energy density and low environmental effect, it is a highly practical replacement for fossil fuels. Hydrogen energy is not an entirely novel concept; it has been employed for many years, but its significance has grown tremendously in the ongoing quest for sustainable energy sources. This study aims to assess hydrogen production as a renewable energy source by conducting an in-depth investigation of the technological, environmental, and economic facets of hydrogen generation. This work simulates noteworthy production of hydrogen processes and cause-effect relationships using the Fuzzy Cognitive Mapping (FCM) method. When it comes to making insightful forecasts for decision support systems, FCMs possess expertise in modeling the evolution of a system over time. Using the FCM technique, two models were put together for this paper: one was based on previously published research and literature, while the other was the result of careful consideration and refinement by two experts. The aim of the research is to recognize the crucial elements impacting the production of hydrogen, examine how these elements interact throughout the process, and envision potential outcomes under various scenarios. Each scenario had been selected with diligence to ensure that it precisely embodied significant and plausible future circumstances that may have an influence on the production of hydrogen. Software via MATLAB was used to perform scenario studies to scale the relationships between each factor. The findings of the investigation demonstrated the importance of feasibility and scalability in the production of hydrogen energy. The outcomes of the present study will hold significance for scholars and industry participants, in addition to driving worldwide goals regarding sustainable development and clean energy.**

Keywords— Hydrogen Production, Fuzzy Cognitive Map, Sustainable Energy, Energy Transition, Scenario Analysis

INTRODUCTION

In the 21st century, global energy consumption has increased as a result of rising living standards, fast growth in populations, and technological improvements [1]. Fossil fuels are utilized primarily to meet this demand, which has raised concerns with pollution, resource depletion, and greenhouse gas emissions [2]. The global energy sector continues to shift toward renewable energy to overcome these problems. Collaboration amongst communities, businesses, and governments is necessary to make this transformation happen. In order to limit the increase in global temperature to less than 2°C, the 2015 Paris Agreement calls for a reduction in CO_2 emissions to a maximum of ten gigatons by the year 2050 [3]. A growing number of individuals are looking to hydrogen energy as a way to mitigate climate change and replace fossil fuels [4]. However, only 4% of the hydrogen produced is produced by the electrolysis of water, with the majority of the hydrogen being generated from fossil fuels such as coal, heavy oils, and natural gas [5]. Hydrogen is more costly than conventional sources of energy due to the high expense of production. Yet, due to the extensive use of these resources in the production of energy, the supply of conventional fossil fuels is limited and is being depleted [6]. As a result, future research on producing hydrogen from renewable resources will be very important [7].

Hydrogen, which is abundant, highly efficient, and produces water vapor when burned, is becoming increasingly important in reducing greenhouse gas emissions as the popularity of smart cities and the integration of renewable energy sources grows [8]. In order to fully realize the potential of hydrogen, it is necessary to evaluate investment prospects and projections for the future. Depending to the manner in which it is produced, hydrogen is divided into a number of different groups: green hydrogen from renewable sources, blue hydrogen with carbon capture, and gray hydrogen from fossil fuels [9]. The most environmentally sustainable approach is provided by green hydrogen, which is generated by electrolysis utilizing renewable energy; photocatalytic processes and thermolysis are additional contributing techniques [10]. Thanks to its high energy density and minimal transportation and storage losses, hydrogen is an ideal option for smart energy systems and future energy storage requirements [11]. As Acar and Dincer [1] point out, hydrogen makes it possible to integrate renewable energy sources into the present system while still delivering clean, dependable energy for a variety of uses, including industrial, transportation, and home heating. As a result, the energy ecology becomes more efficient and emissions decline. In conclusion, hydrogen energy has a lot of promise for the global energy shift. Hydrogen has the potential to provide 30 million jobs, fulfill 18% of the world's energy needs, and cut CO2 emissions by 6 gigatonnes per year by the year 2050 [12]. The IEA's Future of Hydrogen report also provides important information on the role of hydrogen in the transport and heating sectors. Vehicles such as cars, trucks, and buses may operate on hydrogen, especially in areas in which it is difficult to lower emissions through alternatives. Additionally, it performs well for long-distance and heavy transportation, where electrification might not be as beneficial. In heating, hydrogen is a viable

ISBN: 978-618-5765-04-0
ISSN 3057-4269

way for reducing emissions in residential and commercial buildings because it can be blended with natural gas and used in existing infrastructure for heating [13]. This potential of hydrogen energy in many different areas can play a critical role in shaping a sustainable future in which hydrogen emerges as the cornerstone of the global transition towards a clean and renewable energy economy. With ongoing research, development, and advancements in hydrogen technologies, studies could position hydrogen as a cost-effective alternative to traditional energy sources.

The structure of this study is organized as follows: the second section provides a detailed explanation of the methodology employed. The third section focuses on the development and analysis of the model and scenarios. The final section presents the findings of the study, identifies areas for potential improvement, and offers insights into future perspectives.

METHOD:FUZZY COGNITIVE MAPPING

A cognitive map represents the thought process surrounding a problem, emerging from the mapping procedure. These maps consist of a network of nodes connected by arrows, a specific form of directed graph, where the arrow direction indicates perceived causality [14]. Prominent for examining and illustrating the connections between different concepts within a system, cognitive mapping improves our knowledge of how different elements interact and influence each other by providing an organized approach to representing complex interdependencies [15]. By incorporating fuzzy logic, which allows for the representation of uncertainty and varying degrees of impact among factors within a system, FCM enhances this paradigm. As a result, FCM is particularly effective for simulating dynamic systems characterized by complexity, ambiguity, and non-linearity. FCM is perfect for assessing systems where the variables are vague or subject to change since it allows researchers to cope with imprecise data and identify delicate correlations [16]. Presented Figure 1 shows an example of FCM and its corresponding weighted adjacency matrix, which forms a central element of this work.

Figure 1: Graphical Representation of the FCM and its Weighted Matrix Form

This study employs FCM to analyze the complex and interrelated factors influencing hydrogen production globally. FCM is widely regarded as an effective tool for modeling systems characterized by uncertainty and multiple interacting variables [17]. By incorporating fuzzy logic, FCM enables the representation of nuanced causal relationships, which is essential for studying real-world systems where the strength of influence between variables can vary significantly [18]. The FCM model in this research includes critical factors such as renewable energy capacity, technological advancements, economic incentives, and regulatory frameworks. These factors are interconnected through a set of weighted relationships that indicate either positive or negative influences. A positive weight suggests that an increase in one factor will lead to an increase in another, while a negative weight implies an inverse relationship [16]. FCMs use nodes for key concepts and directed edges for causal relationships. Unlike traditional cognitive maps, FCMs assign weights between [-1, 1] to these edges, reflecting both the direction and strength of influences [19]. The strength of these relationships allowing for a detailed understanding of how these factors interact within the hydrogen production ecosystem.

MODEL DEVELOPMENT AND ANALYSIS

Three sections comprise the model's development and analysis: the first addresses the study's content and the model's explanation; the second section focuses on creating scenarios and provides a brief synopsis of each scenario; and the third section presents the results of the scenarios.

Model Development

This study's methodology combines a survey of the literature with the insights of experts to determine and evaluate the major variables affecting hydrogen generation. The content of the study, which was started with literature review and expert opinion, is shown in Figure 2.

Figure 2: Content of the Study

In the beginning, a thorough literature analysis was carried out, utilizing a variety of reports, case studies, and scientific papers to ascertain the state of knowledge and new developments in the energy industry. The foundation for identifying factors related to hydrogen production was established by this review. To refine and validate the factors identified in the literature review, insights were gathered from two experts. One expert has extensive experience in various departments of the energy sector and currently serves as the general manager of a prominent energy company. The second expert, affiliated with the Energy Institute at a leading university in Turkey, holds a PhD in hydrogen energy. The insights of the experts ensured that the model included both practical and scholarly viewpoints by validating and refining the elements found in the literature. The identified factors were then used to develop a relationship matrix, which quantified the interactions and influence between different variables. The model underwent an iterative procedure to further refine the relationships inside the system by adjusting factor values depending on preliminary results. Subsequently, a detailed model analysis was performed to derive insights into how various factors interact within the hydrogen production system. A number of scenarios were

ISBN: 978-618-5765-04-0
ISSN 3057-4269

created based on the model to investigate possible future circumstances, such as changes in technological, environmental, and economic aspects. Subsequently, these scenarios were analyzed to determine how changes in key factors could impact hydrogen production, providing valuable predictions for future advancements in the industry. A scaling was implemented to measure the interactions between key factors. A nine-point scale shown in Table 1 was used for a detailed and nuanced analysis of the relationships within the matrix. This approach allowed the study to capture the varying degrees of influence each factor has on the others, facilitating a more comprehensive understanding of the dynamics involved in hydrogen production.

Table 1: Nine Point Scale

Linguistic Terms	*Values*	*Linguistic Terms*	*Values*	*Linguistic Terms*	*Values*
Negatively Very Strong (NVS)	-1	Negatively Week (NW)	-0,25	Positively Medium (PM)	0,5
Negatively Strong (NS)	-0,75	Zero(Z)	0	Positively Strong (PS)	0,75
Negatively Medium (NM)	-0,5	Positively Weak (PW)	0,25	Positively Very Strong (PVS)	1

In Table 2, the relationship matrix generated through the literature review is presented, whereas Table 3 illustrates the relationship matrix constructed based on expert opinions. Subsequently, MATLAB was employed to visualize these matrices, enabling a more detailed and comprehensive analysis. MATLAB, a powerful software platform widely used in scientific and technical fields, was chosen for its advanced numerical analysis and modeling capabilities. The use of MATLAB enhanced the efficiency of handling the relationship matrix, which was central to this study's analysis.

Table 2: Relationship Matrix Based on Literature Review

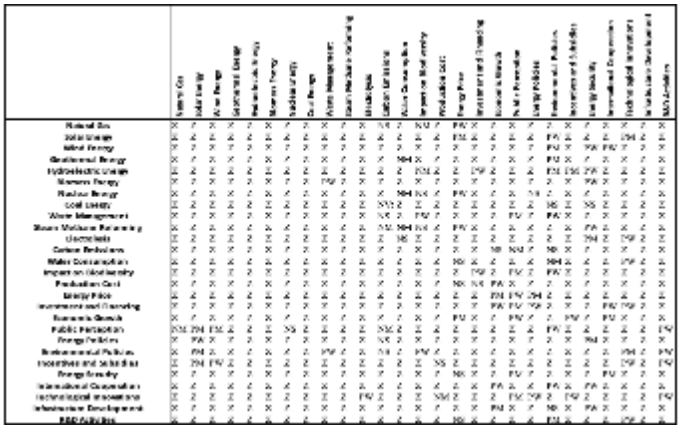

The visualization of the matrix derived from the literature review is presented in Figure 3, while the visualization of the matrix based on expert opinions is shown in Figure 4. Graphical representations of the relationships between the factors were generated within MATLAB, providing a clear visualization of the underlying patterns and dynamics.

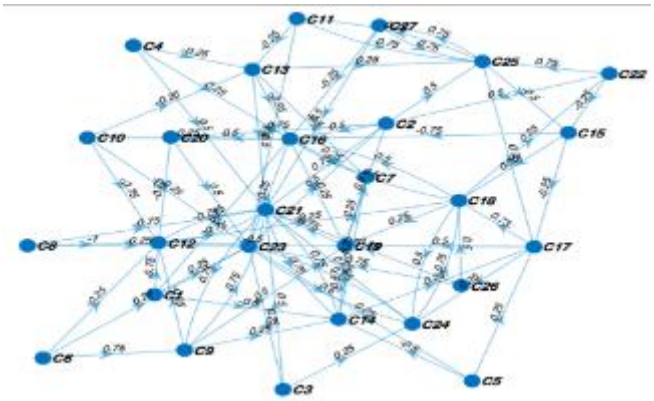

Figure 3: Visualization of Matrix Based on Literature Review

These visual tools were critical for interpreting the complex interdependencies among the factors and offered valuable insights into how different factors influence hydrogen production. Furthermore, MATLAB's capacity for managing huge datasets made it possible to investigate possible interactions between variables in greater detail, revealing nuanced relationships that would not have been seen using more conventional techniques.

Table 3: Relationship Matrix Based on Expert Opinions

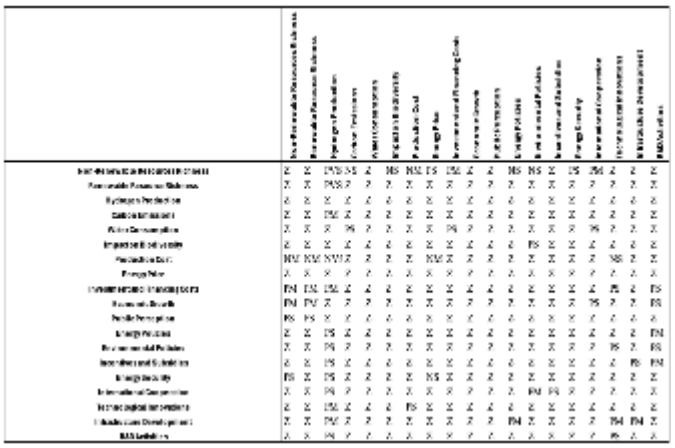

In addition to aiding in the identification of important drivers, the visualization assisted scenario analysis by offering a solid framework for assessing various potential scenarios.

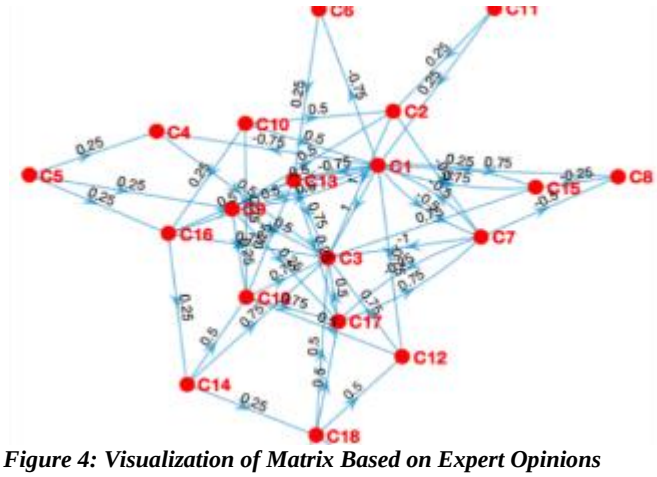

Figure 4: Visualization of Matrix Based on Expert Opinions

ISBN: 978-618-5765-04-0
ISSN 3057-4269

The initial iterations of the MATLAB model produced outputs that highlighted the most influential factors identified in the literature is shown in Figure 5. These included:

Public Perception: Public perception has a major role in the adoption of green hydrogen. Even though renewable energy is widely supported, local issues like the landscape impact may make it difficult for people to accept it [20]. Effective public education and awareness campaigns are crucial for dispelling falsehoods. Community participation initiatives that promote inclusiveness and openness have also been effective in fostering support for renewable energy projects [21].

Technological innovations: To improve the financial feasibility and efficacy of green hydrogen, advancements in technology are required. Innovations contain high-temperature electrolysis and photoelectrochemical cells have increased manufacturing efficiency [20]. Wider usage is encouraged by the application of nanomaterials, which have enhanced catalysts, reduced prices, and sustained energy grids via integration with renewable energy sources [22].

Environmental Policies: Strong environmental regulations must be put in place for green hydrogen to thrive. Initiatives like the EU's Green Deal demonstrate how important hydrogen is to attaining carbon neutrality by 2050 [23]. International collaboration and financial incentives like subsidies are crucial to overcoming investment and regulatory challenges and promoting the sector's growth [22].

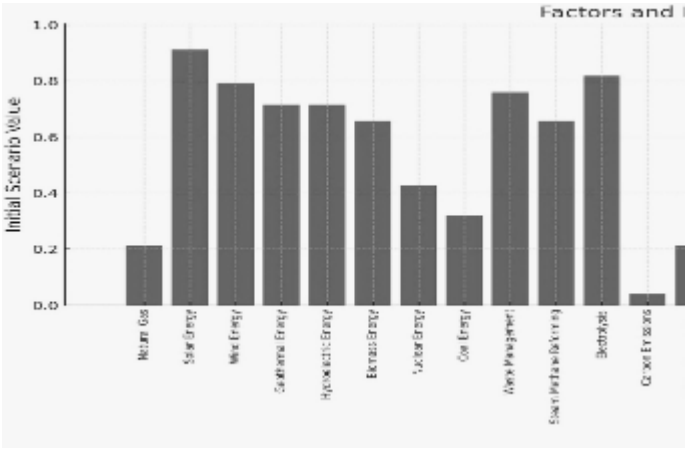

Figure 5: Initial Outputs From Literature Review Model

The initial iterations of the MATLAB model produced based on expert opinions is shown in Figure 6. As in the model analysis based on literature review, technological developments were among the factors with the highest value in the model based on expert opinions. The two factors with the highest value, other than technological developments, are hydrogen production and research and development (R&D) activities.

Hydrogen production: A variety of technologies are commonly utilized in the production of hydrogen. On an industrial scale, methods like coal gasification, pyrolysis of natural gas, and steam reforming are already in use. Although other methods have been extensively investigated, they nevertheless remain too costly to implement on a large scale at present [24]. In the ongoing effort to reduce carbon emissions on a worldwide scale, green hydrogen, generated through renewable energy sources, has become a pivotal force [25]. Its sustainable production processes position it as a key contributor to the decarbonization efforts across various sectors [26]. Technological developments in solar water splitting, biomass gasification, and electrolysis have been major forces behind the advancement of green hydrogen technologies. Proton exchange membrane (PEM) and alkaline electrolyzers are two instances of electrolysis techniques that have undergone substantial advances in cost-effectiveness, scalability, and efficiency, making them more viable for widespread application [27]. Large-scale hydrogen generation is now more feasible due to these advancements' notable improvements in performance and efficiency.

R&D Activities: The advancement of hydrogen producing technology depends on R&D activities. Material innovations such laser-structured nickel electrodes have greatly increased the efficiency of producing hydrogen. To commercially deploy these technologies economically, PEM and SOEC systems must be enhanced through improved catalysts and materials [28]. Alternative techniques like photoelectrolysis and biophotolysis, which produce hydrogen using biological processes and solar energy, are being developed, but further research is needed before they can be implemented on an extensive basis [23]. Governments are supporting hydrogen R&D through various initiatives. For instance, the US Bipartisan Infrastructure Law and Canada's Clean Fuels Fund both contribute significantly to lowering the price of producing green hydrogen [13]. The European Clean Hydrogen Alliance is promoting collaboration between industry and research institutions to drive innovation and meet climate targets. These efforts illustrate how important research and development is to transforming hydrogen into a sustainable and affordable energy source.

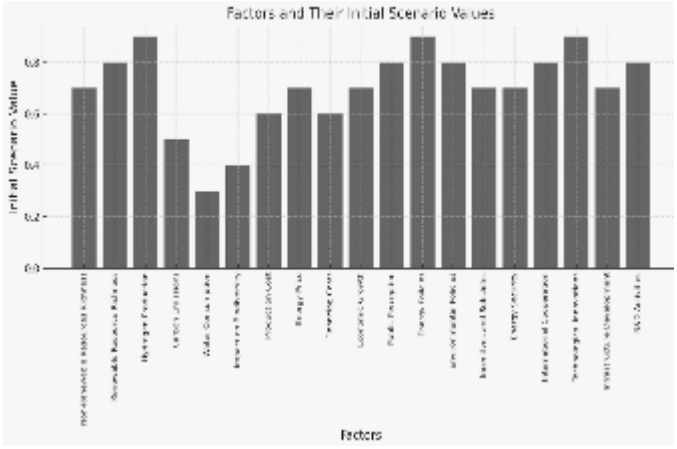

Figure 6: Initial Outputs From Expert Opinions Model

Scenario Analysis

After the first outputs are obtained, in order to investigate possible future trajectories for the production of hydrogen, several kinds of scenarios were created, each meant to reflect

ISBN: 978-618-5765-04-0
ISSN 3057-4269

considerable and plausible changes in the world's energy environment. The scenarios included:

- Isolation of Major Influences: Examining the impact of isolating key factors that influence hydrogen production.
- Increase in Investments and Subsidies: Evaluating the potential for increased government funding and financial investments to accelerate the production of hydrogen.
- Economic Recession: Examining the potential effects of a downturn on investments associated with producing hydrogen.
- Strict Environmental Regulations: Assessing how strict environmental policies affect the development and application of hydrogen.
- Global Energy Crisis: Considering how the development of hydrogen technologies may be impacted by a global energy crisis.

Each scenario involves giving alternative values to the major elements discovered earlier in the study, allowing for a more in-depth exploration of how alterations in these values may affect the system's overall dynamics. Significant insights into the adaptability and robustness of producing hydrogen in response to changing global conditions have been obtained from this scenario investigation.

Scenario Results

Significant findings were obtained as a result of the scenario analysis applied to both models. Three the following sections can be used to examine these results.

Detailed vs. Aggregated Insights: A more thorough examination of the dynamics of the system was made possible by the detailed matrix, which offered a refined and broad understanding of the particular factors affecting hydrogen production. On the other hand, the consensus matrix provided a higher-level, more comprehensive viewpoint that enabled a more comprehensive comprehension of hydrogen production. The relationship matrix allowed it possible to classify renewable and non-renewable energy sources and remove less important factors, providing a more coherent examination of how the energy conditions influence the production of hydrogen.

Analysis of Scenarios Consistency: Both models demonstrated consistency in their outcomes over a range of scenarios, despite differences in the degree of detail between them. This constancy indicates that whether a comprehensive or aggregated method is used, the general patterns within the hydrogen production system stay consistent. This result emphasizes how well the system adapts to adjustments in significant factors.

System Resilience: In both models, the hydrogen production system showed a high level of resilience, especially in maintaining stability in spite of challenging situations such economic downturns or the demise of important drivers. This resilience demonstrates the system's ability to adapt to external factors without seriously impairing the production of hydrogen.

CONCLUSIONS AND PERSPECTIVE

The implementation of the FCM approach in this study has provided significant insights into the intricate relationships between technical, economic, and environmental factors influencing hydrogen production. The FCM simulations underscore the critical importance of feasibility and scalability as essential outcomes across all assessed scenarios. The findings emphasize that the establishment of robust regulatory frameworks, continuous technological advancements, and the effective integration of renewable energy sources are crucial prerequisites for ensuring the long-term viability and growth potential of hydrogen generation. These elements collectively serve as foundational pillars for advancing hydrogen production in a sustainable and scalable manner.

The results additionally emphasize the need for robust financial incentives and environmental regulations to get over early obstacles, advance technology, and ensure the long-term viability of hydrogen as a clean energy source. Utilizing the FCM methodology, the study was able to simulate several scenarios and provide strategic insights into how various circumstances may impact the ability to scale and effect of hydrogen in the future. It has been demonstrated that hydrogen is essential for managing environmental issues, especially because of its ability to lower greenhouse gas emissions and enhance air quality. From a financial standpoint, hydrogen stimulates economic growth and job creation while also diversifying the energy mix to improve energy security. Technological developments in hydrogen generation strategies, such as fuel cells and electrolysis, were found to be crucial to promoting innovation and guaranteeing the sector's expansion. The study also emphasizes how crucial it is to maintain R&D spending and international cooperation in order to boost competitiveness on a worldwide scale. Ensuring long-term sustainability and energy resilience requires coordinating hydrogen production with international environmental goals.

Overall, this research underscores hydrogen’s transformative potential and the strategic need for technological, economic, and environmental synergies to unlock its full impact on the global energy landscape. To address the limitations of this study, future research could benefit from refining the model in greater detail and incorporating a group decision-making approach based on input from a larger pool of experts. In the future scope of the study, implementing these adjustments would allow for a more comprehensive comparison of the results.

ACKNOWLEDGMENT

The authors express their deep gratitude to the specialists whose invaluable insights significantly enhanced the quality of this manuscript. This research was financially supported by the Galatasaray University Research Fund (FOA-2023-1181).

REFERENCES

[1] C. Acar and I. Dincer, "Hydrogen-based energy systems: Present and future copes and challanges," *International Journal of Hydrogen*, vol. 43, pp. 4878-4895, 2018.

[2] M. Rezai, K. R. Khalilpor and M. Jahangiri, "Multi-criteria location identification for wind/solar based hydrogen genaratin: The case of

capital cities of a developing country.," vol. 45, no. 58, pp. 33151-33168, 2020.

[3] UNFCC, "The Paris Agreement," UNFCC, Paris, 2019.

[4] J. E. Garzón Baquero and D. Bellon Monsalve, "For fossil fuel energy to hydrogen energy: Transformation of fossil fuel energy economies into hydrogen economies through social entrepreneurship," *International Journal of Hydrogen*, vol. 54, pp. 574-585, 2024.

[5] M. Balat and E. Kırtay, "Major technical barriers to a hydrogen economy," *Energy Source A*, vol. 32, pp. 863-876, 2010.

[6] J. Turner, G. Sverdrup, M. K. Mann, P. Maness, B. Kroposki, M. Ghirardi, R. Evans and D. Blake, "Renewable hydrogen production," *International Journal of Energy Research*, vol. 32, pp. 379-407, 2008.

[7] A. Bhattacharya, A. Bhattacharya and A. Datta, "Modeling of hydrogen production process from biomass using oxygen blown gasification," *International Journal of Hydrogen Energy*, vol. 37, no. 24, pp. 18782-18790, 2012.

[8] J. Ren and S. Toniolo, "Life cycle sustainability decision-support framework for ranking of hydrogen production pathways under uncertainties: An interval multi-criteria decision making method. Journal of Cleaner Production,," *Journal of Cleaner Production*, vol. 170, pp. 512-526, 2018.

[9] M. E. Emetere, M. I. Oniha, D. A. Akinyosoye, G. N. Elughi and S. A. Afolalu, "Progress and challenges of green hydrogen gas production: Leveraging on the successes of biogas," *International Journal of Hydrogen Energy*, vol. 79, pp. 1071-1085, 2024.

[10] R. Li, "Latest progress in hydrogen production from solar water splitting via photocatalysis, photoelectrochemical, and photovoltaic-photoelectrochemical solutions," *Chinese Journal of Catalysis*, vol. 38, no. 1, pp. 5-12, 2017.

[11] F. S. Alamri, M. H. Saeed and M. Saeed, "A hybrid entropy-based economic evaluation of hydrogen generation techniques using Multi-Criteria Decision Making," *International Journal of Hydrogen Energy*, vol. 49, pp. 711-723, 2024.

[12] T. Uyar and D. Beskci, "Integration of hydrogen energy systems into renewable energy systems for better design of 100% renewable energy communities," *International Journal of Hydrogen Energy*, vol. 42, no. 4, pp. 2453-2456, 2017.

[13] I. E. Agency(IEA), "The future of hydrogen - seizing today's opportunities - report prepared for G20," IEA, Japan, 2019.

[14] F. Harary, R. Norman and D. Cartwright, "Structural models: An introduction to the theory of directed graphs," Wiley, 1965.

[15] C. Eden, "Analyzing cognitive maps to help structure issues or problems," *European Journal of Operational Resarch*, vol. 159, no. 3, pp. 673-686, 2004.

[16] G. Napoles, E. I. Papageorgiou, A. Jetter and D. Bochtis, "A new approach using mixed graphical models for automatic design of fuzzy cognitive maps for ordinal data," *IEEE Transactions on Fuzzy Systems*, vol. 25, no. 2, pp. 339-352, 2017.

[17] B. Kosko, "Fuzzy cognitive maps," *International Journal of Man-Machine Studies*, vol. 24, no. 1, pp. 65-75, 1986.

[18] P. Groumpos, "Fuzzy cognitive maps: Basic theories and their application to complex systems," in *Fuzzy cognitive maps: Advances in theory, methodologies, tools and applications*, Springer, 2010, pp. 1-22.

[19] H. Amirkhani, "Modeling uncertain dynamic systems using Fuzzy Cognitive Maps," in *IEEE International Conference on Fuzzy Systems(FUZZ-IEEE)*, 2018.

[20] A. Mdallal, M. Mahmoud, E. T. Sayed, M. Abdelkareem, A. Alami and A. Olabi, "Green hydrogen production: Advances and challenges," in *Reference Module in Materials Science and Materials Engineering*, Elsevier, 2024.

[21] V. Bertsch, M. Hall, C. Weinhardt and W. Fichtner, "Public acceptance and preferences related to renewable energy and grid expansion policy: Empirical insights for Germany," *Energy*, vol. 114, pp. 465-477, 2016.

[22] G. Yilmaz, A. K. Sadvakasova, B. D. Kossalbayev, M. O. Bauenova, S. K. Zharmukhamedov, G. K. Ziyayeva, D. E. Zaletova, H. F. Alharby and S. I. Allakhverdiev, "Hydrogen energy development in Turkey: Challenges and opportunities," *International Journal of Hydrogen Energy*, vol. 52, pp. 1304-1311, 2024.

[23] T. Capurso, M. Stefanizzi, M. Torresi and S. M. Camporeale, "Perspective of the role of hydrogen in the 21st century energy transition," *Energy Conversion and Management*, vol. 251, p. 114898, 2022.

[24] P. Afanasev, A. Askarova, T. Alekhina, E. Popov, S. Markovic, A. Mukhametdinova, A. Cheremisin and E. Mukhina, "An overview of hydrogen production methods: Focus on hydrocarbon feedstock," *International Journal of Hydrogen Energy*, vol. 78, pp. 805-828, 2024.

[25] S. R. Naqvi, B. Kazmi, S. A. A. Taqvi, W. Chen and D. Juchelková, "Techno-economic analysis for advanced methods of green hydrogen production," *Current Opinion in Green and Sustainable Chemistry* , vol. 48, p. 100939, 2024.

[26] A. Villarreal Vives, R. Wang, S. Roy and A. Smallbone, "Techno-economic analysis of large-scale green hydrogen production and storage," *Applied Energy*, vol. 346, p. 121333, 2023.

[27] S. Sollai, A. Porcu, V. Tola, F. Ferrara and A. Pettinau, "Renewable methanol production from green hydrogen and captured CO2: A techno-economic assestment," *Journal of CO2 Utilization*, vol. 68, p. 102345, 2023.

[28] R. Bhandari, C. Trudewind and P. Zapp, "Life cycle assessment of hydrogen production via electrolysis-A review," *Journal of Cleaner Production*, vol. 85, pp. 151-163, 2014.

ISBN: 978-618-5765-04-0
ISSN 3057-4269

Renewable Energy Resources Selection for Türkiye with Interval Valued Intuitionistic Fuzzy MULTIMOORA Approach

Gülçin Büyüközkan
Industrial Engineering Department
Galatasaray University
Ortaköy, İstanbul, Türkiye
gbuyukozkan@gsu.edu.tr
ORCID: 0000-0002-2112-3574

Orhan Feyzioğlu
Industrial Engineering Department
Galatasaray University
Ortaköy, İstanbul, Türkiye
ofeyzioglu@gsu.edu.tr
ORCID: 0000-0002-8919-191X

Fethullah Göçer
Industrial Engineering Department
Kahramanmaraş Sütçü İmam University
Kahramanmaraş, Türkiye
fgocer@ksu.edu.tr
ORCID: 0000-0001-9381-4166

***Abstract*— The global demand for electricity continues to rise due to factors such as population growth, industrialization, and urbanization. Persistent challenges, including rising energy costs, increased awareness of climate change, and the depletion of fossil fuel reserves, further complicate the global energy landscape. In particular, Türkiye faces growing energy demands, with the potential for significant shortages in the coming decades. Addressing these concerns requires coordinated efforts from the government, public, private, and institutional investors to ensure sustainable development. Achieving affordable, clean, and reliable energy is essential for Türkiye's future, making the development of sustainable energy sources, particularly renewable alternatives, crucial to reducing dependence on fossil fuels and mitigating environmental impacts. This study seeks to identify key decision-making criteria relevant to selecting renewable energy resources (RER) from an investor's perspective, proposing an integrated framework to evaluate and choose the best options for Turkiye. The decision-making process for RER investments is inherently complex, involving both quantitative and qualitative factors. As a multi-criteria problem, it is characterized by conflicting and uncertain parameters. The Interval Valued Intuitionistic Fuzzy (IVIF) set is an effective method for managing these uncertainties by incorporating both membership and non-membership degrees within an interval. This study introduces a multi-criteria decision-making approach using an extended MULTIMOORA (Multi-objective Optimization by Ratio Analysis plus the Full Multiplicative Form) technique, which integrates decision-makers' limited knowledge and addresses various pressures in the evaluation process. This approach ranks alternatives and manages imprecise data to determine the most suitable RER options. An application of the proposed method is provided, with its effectiveness validated through sensitivity and comparative analyses.**

Keywords*— *Renewable Energy Resources, Decision Making, Interval Valued Intuitionistic Fuzzy, MULTIMOORA Technique

INTRODUCTION

The ever-increasing global population, coupled with rapid industrialization and urban expansion, has led to a substantial rise in electricity demand. This surge in energy needs presents different challenges, including escalating energy prices, increased awareness of global climate change, and the ongoing depletion of fossil fuel resources. As energy consumption continues to climb, these issues are expected to persist and even intensify [1].

Türkiye faces critical energy challenges, as growing demands, if unmet, could lead to shortages that threaten both energy security and economic stability.[2]. Therefore, it is imperative for various stakeholders, including the government, public sector, private enterprises, and institutional investors, to collaborate on developing sustainable energy solutions.

In this context, the pursuit of sustainable energy resources is of paramount importance. Renewable energy resources (RER), characterized by their cleanliness and potential for long-term sustainability, offer a promising alternative to traditional fossil fuels. The strategic selection of suitable RERs is crucial for ensuring that Türkiye meets its future energy needs while minimizing environmental impact [3]. However, the process of selecting the most appropriate RER is complex and multifaceted process. It involves considering a range of criteria that encompass both quantitative and qualitative factors. The decision-making process is further complicated by the inherent uncertainties and conflicting parameters associated with RER investments [2], [3].

To address these challenges, this study proposes an integrated decision-making framework that utilizes a multi-criteria analysis approach. Moreover, the integration of Interval Valued Intuitionistic Fuzzy (IVIF) set is employed to handle uncertainties by incorporating both membership and non-membership degrees within an interval [4], [5]. The MULTIMOORA (Multi-objective Optimization by Ratio Analysis plus the Full Multiplicative Form) technique [6], [7] is extended to evaluate and rank potential RER options based on limited decision-makers' knowledge and the pressures of the evaluation process. Through this framework, the study aims to identify and prioritize the most suitable RER alternatives for Türkiye, thereby contributing to the country's energy security and sustainable development goals.

The study begins by identifying the key criteria and sub-criteria necessary for selecting RER in Türkiye. These criteria are then evaluated using the IVIF set to account for uncertainties and imprecise data. Next, the extended MULTIMOORA technique is applied to rank the RER alternatives based on the evaluated criteria. Following this, the results are validated through sensitivity and comparative analyses to ensure the robustness and reliability of the rankings. Finally, the study concludes by identifying the most suitable RER options for Türkiye and discussing the implications of these findings for energy policy and investment.

PROBLEM DEFINITION

Energy demand is escalating globally due to rapid industrialization and population growth. Addressing this

ISBN: 978-618-5765-04-0
ISSN 3057-4269

increasing demand presents significant challenges, particularly for countries like Türkiye, where energy security and sustainable development are critical concerns [1]. The conventional reliance on fossil fuels is no longer viable due to their finite nature and the adverse environmental impacts associated with their use. As a result, there is a pressing need to shift towards RER that can provide clean, sustainable, and reliable energy [2]. RER are defined as domestic sources with the potential to provide energy services while emitting little to no air pollutants and greenhouse gases [8]. Examples of RER include biomass, hydropower, geothermal, solar, and wind energy, all of which are inexhaustible and offer significant environmental and economic advantages over conventional energy sources. Each type of RER has distinct benefits that make it particularly suitable for specific applications in certain regions [9]. However, during the application process, decision-makers may face challenges in the energy planning process, especially when selecting the most appropriate renewable energy alternative among various options.

The selection of appropriate RERs for investment is a complex, multi-faceted problem that involves evaluating a variety of criteria. These criteria include not only the technical and economic feasibility of the energy resources but also their environmental impact and social acceptability. Additionally, the decision-making process is complicated by the presence of uncertainties and conflicting objectives. For instance, an energy resource that is economically viable may not be the most environmentally friendly option, and vice versa.

Given these complexities, traditional decision-making approaches may fall short in effectively evaluating and selecting the most suitable RERs. To overcome these limitations, advanced multi-criteria decision-making (MCDM) methods are required. These methods must be capable of handling both the quantitative and qualitative aspects of the decision-making process, as well as the uncertainties inherent in the evaluation of RERs.

In evaluating RER, the main criteria considered include technical (C1), economic (C2), political (C3), social (C4), and environmental aspects (C5) [10]. Under the technical aspects [11], Efficiency (C11) is a key sub-criterion, assessing how much useful energy can be derived from a given energy resource. Feasibility (C12), another technical sub-criterion, involves assessing the likelihood of successful policy implementation and evaluating the security of its execution. Safety (C13) focuses on the system's ability to protect the surrounding environment and ensure the safety of individuals. Lastly, Risk (C14) measures the potential for implementation issues by examining the frequency and severity of failures in tested scenarios.

Economic aspects are crucial in RER decision-making, encompassing several sub-criteria [2]. Investment cost (C21) is a primary economic factor, covering the expenses associated with purchasing mechanical equipment and technological installations, and is widely used to evaluate energy systems. Operation and maintenance cost (C22) is another economic sub-criterion, encompassing the costs related to system maintenance, equipment, labor, and energy-related products and services. Return on investment (C23) evaluates the financial viability of the proposed renewable energy alternative, considering whether the project is worth the investment.

Political aspects [12] also play a significant role, with sub-criteria like Foreign dependency (C31), which assesses how the national energy policy aligns with the renewable energy alternative and examines the country's dependence on international regulations. Compatibility with political and legislative situation (C32) measures the alignment between government policies and the proposed energy policy, considering factors such as government incentives, institutional actors' stances, and public information policies. Compatibility with national energy policy (C33) looks at how well the renewable energy resources align with the country's overall energy strategy.

Social aspects are evaluated through criteria such as social benefits, social acceptability, and job creation [13]. Social benefits (C41) include the advantages provided by renewable energy sources, such as enhancing social life and generating income, which can prevent rural depopulation and improve public welfare. Social acceptability (C42) reflects the local population's overall opinions and acceptance of renewable energy sources. Job creation (C43) relates to the direct and indirect employment opportunities generated by renewable energy projects, as well as the potential for new professional fields to emerge.

Lastly, environmental aspects focus on factors like greenhouse gas emissions, land use requirements, ecosystem impact, and waste disposal [3]. Greenhouse emissions (C51) include gases like CO2 and NOx, which contribute to air pollution, acid rain, and climate change. Land use requirement (C52) refers to the space needed for energy systems to operate efficiently, emphasizing the importance of securing appropriate land to avoid economic losses. Finally, Impact on ecosystem (C53) examines the potential risks to ecosystems, such as the disruption to wildlife caused by wind turbines.

In this study, we address this problem by proposing an integrated decision-making framework that combines the IVIF set with an extended version of the MULTIMOORA technique [5], [14]. The IVIF set is particularly useful for dealing with the uncertainties associated with the decision-making process, as it allows for the incorporation of both membership and non-membership degrees within an interval [4]. The extended MULTIMOORA technique, on the other hand, provides a comprehensive approach to evaluating and ranking RER options based on multiple criteria.

By applying this integrated framework, we aim to identify the most suitable RER alternatives for Türkiye, taking into account the various challenges and uncertainties associated with the decision-making process. The proposed methodology not only addresses the complexities of RER selection but also offers a practical tool for policymakers and investors to make informed decisions that contribute to Türkiye's energy security and sustainable development goals.

METHODOLOGY

In this study, we propose a comprehensive methodology to address the complexities involved in selecting the most suitable RER for Türkiye. The methodology is designed to handle the inherent uncertainties and conflicting criteria associated with MCDM in the context of energy investments. Our approach integrates the IVIF set with an extended version of the MULTIMOORA technique.

IVIF Set

The IVIF set is employed to manage the uncertainty and vagueness inherent in the decision-making process. Traditional fuzzy sets consider only the degree of membership of an element to a fuzzy set [15]. However, the IVIF set extends this by incorporating both membership and non-

ISBN: 978-618-5765-04-0
ISSN 3057-4269

membership degrees within an interval, thus providing a more flexible and comprehensive framework for handling uncertainty [16]. This approach is particularly useful in situations where decision-makers have limited information or where the criteria are subject to subjective judgment.

MULTIMOORA Technique

The MULTIMOORA method is a robust MCDM technique that combines three distinct methods: Ratio System, Reference Point Approach, and the Full Multiplicative Form [7]. This combination allows for a comprehensive evaluation of alternatives based on multiple criteria [7], [17]. The extended MULTIMOORA technique used in this study is adapted to incorporate the IVIF set, enabling it to effectively manage the imprecise data and uncertainties associated with RER selection.

Integrated Decision-Making Framework

The proposed methodology begins by identifying the relevant criteria and sub-criteria for RER selection. These criteria are then evaluated using the IVIF set to account for the uncertainties in the decision-making process. Following this, the extended MULTIMOORA technique is applied to rank the RER alternatives. The integration of these methods ensures that the decision-making process is both rigorous and adaptable to the complexities of RER investment.

Let X be a fixed set. An IVIF set in relation to an element x in $\tilde{A}$ is defined as an ordered pair consisting of an interval-valued membership degree and an interval-valued non-membership degree. The IVIF set, denoted as$\tilde{A}$, has membership values $\tilde{\mu}_{\tilde{A}}(x) \subset [0,1]$ and non-membership values $\tilde{\nu}_{\tilde{A}}(x) \subset [0,1]$, where x ∈ X, subject to the condition that $\tilde{\mu}_{\tilde{A}}(x)$ + sup $\tilde{\nu}_{\tilde{A}}(x) \leq 1$. For ease of notation, the lower and upper bounds of the IVIF set are referred to as $\tilde{A} = \left[\mu_{\tilde{A}}^{L}, \mu_{\tilde{A}}^{U}\right], \left[\nu_{\tilde{A}}^{L}, \nu_{\tilde{A}}^{U}\right]$ or $\tilde{B} = \left[\mu_{\tilde{B}}^{L}, \mu_{\tilde{B}}^{U}\right], \left[\nu_{\tilde{B}}^{L}, \nu_{\tilde{B}}^{U}\right]$.

IVIF MULTIMOORA Methodology

The steps for applying the IVIF MULTIMOORA methodology are outlined as follows:

Step 1: Collect Judgments from Decision Makers (DMs)

Based on their expertise and prior knowledge, DMs are required to provide their judgments for each factor in the decision matrix using linguistic terms. This involves expressing their opinions on alternative A_i across criterion C_j from the perspective of each DM.

Step 2: Convert Linguistic Variables into IVIF Numbers

Since linguistic variables are not directly usable in mathematical operations, the next step is to standardize the DMs' evaluations by transforming these variables into IVIF numbers. The decision matrix is then built using these IVIF numbers, representing the alternatives and criteria as well as the weights assigned by DMs to each criterion.

Step 3: Determine the Weights of DMs

Assuming there are *k* DMs, the weights assigned to each DM, $\lambda^k (1 < k < K)$, are calculated using a predetermined equation (Eq. 1) [18]. The importance of the DMs is assessed using a linguistic scale, as shown in Table II.

$$\lambda^k = \frac{\sqrt{\frac{1}{2}\left[\left(1-\pi_{\tilde{A}}^{L\,k}\right)^2 + \left(1-\pi_{\tilde{A}}^{U\,k}\right)^2\right]}}{\sum_{l=1}^{K}\sqrt{\frac{1}{2}\left[\left(1-\pi_{\tilde{A}}^{L\,l}\right)^2 + \left(1-\pi_{\tilde{A}}^{U\,l}\right)^2\right]}} \qquad (1)$$

Step 4: Calculate Criteria Weights

To evaluate the m alternatives $A_1, A_2, \ldots, A_m$, based on n criteria$C_1, C_2, \ldots, C_n$, the weight vectors $w_1, w_2, \ldots, w_n$are determined. These weights must satisfy the condition $w_j \geq 0$, $j = 0, j = 1, 2, \ldots, n$ and $\sum_{j=1}^{n} w_j = 1$, representing the relative importance of each criterion. Entropy weights of criteria are determined using Eq. (2).

$$\breve{w}_j = 1 - \frac{\sum_{j=1}^{n} \frac{w_j(\mu_{\tilde{A}ij}^{L} + \mu_{\tilde{A}ij}^{U})}{2}}{\sqrt{\sum_{j=1}^{n} \frac{w_j(\mu_{\tilde{A}ij}^{L\,2} + \mu_{\tilde{A}ij}^{U\,2} + \nu_{\tilde{A}ij}^{L\,2} + \nu_{\tilde{A}ij}^{U\,2})}{2}}}, w_j = \frac{1-\breve{w}_j}{n-\sum_{i=1}^{n}\breve{w}_j} \qquad (2)$$

Step 5: Construct the Aggregated Matrix

IVIF numbers are aggregated into group TIFNs (Triangular Intuitionistic Fuzzy Numbers). The Interval Valued Intuitionistic Fuzzy Weighted Averaging (IIFWA) operator [19] is used for this aggregation (Eq. 3). The aggregated decision matrix is formed for each alternative, incorporating the opinions of all DMs. Let $R(k) = \left(r^{(k)}{}_{ij}\right)_{mxn}$represent the decision matrix of the kth DM for alternatives, which is then merged into a group decision matrix using the DMs' weights {λ1, λ2, . . . λn} calculated earlier.

$$IIFWA = \left(\left[1-\prod_{j=1}^{n}\left(1-\mu_{\tilde{A}}^{L}\right)^{\lambda^k}, 1-\prod_{j=1}^{n}\left(1-\mu_{\tilde{A}}^{U}\right)^{\lambda^k}\right], \left[\prod_{j=1}^{n}\left(v_{\tilde{A}}^{L}\right)^{\lambda^k}, \prod_{j=1}^{n}\left(v_{\tilde{A}}^{U}\right)^{\lambda^k}\right]\right) \qquad (3)$$

Table 1: Lınguıstıc Variables For Ratıng Alternatıves.

Linguistic Terms		[μ^L,	μ^U],	[ν^L,	ν^U],	[π^L,	π^U]
Extremely Good	EG	1.00	1.00	0.00	0.00	0.00	0.00
Very Very Good	VVG	0.85	0.90	0.01	0.05	0.05	0.14
Very Good	VG	0.75	0.80	0.10	0.15	0.05	0.15
Good	G	0.65	0.70	0.20	0.25	0.05	0.15
Medium Good	MG	0.55	0.60	0.30	0.35	0.05	0.15
Medium	M	0.45	0.50	0.40	0.45	0.05	0.15
Medium Bad	MB	0.35	0.40	0.50	0.55	0.05	0.15
Bad	B	0.25	0.30	0.60	0.65	0.05	0.15
Very Bad	VB	0.15	0.20	0.70	0.75	0.05	0.15
Very Very Bad	VVB	0.01	0.05	0.85	0.90	0.05	0.14
Extremely Bad	EB	0.00	0.00	1.00	1.00	0.00	0.00

Table 2: Importance Weigts As Lınguıstıc Varıables.

Linguistic Terms		[μ^L,	μ^U],	[ν^L,	ν^U],	[π^L,	π^U]
Extremely Important	EI	0.95	1.00	0.00	0.00	0.00	0.05
Very Important	VI	0.80	0.85	0.05	0.10	0.05	0.15
Important	I	0.60	0.65	0.10	0.15	0.20	0.30
Medium	M	0.30	0.35	0.25	0.30	0.35	0.45
Unimportant	U	0.20	0.25	0.30	0.35	0.40	0.50
Very Unimportant	VU	0.00	0.05	0.45	0.50	0.45	0.55

Step 6: Normalize the Decision Matrix

The initial values of the criteria are normalized using Eqs. (4) and (5). The normalized decision matrix is denoted as $\tilde{R} = \left[\tilde{r}_{ij}\right]_{mxn}$ where, $\tilde{r}_{ij}$=$\left[a_{ij}^{L}, a_{ij}^{U}\right], \left[b_{ij}^{L}, b_{ij}^{U}\right]$

$$a_{ij}^{L} = \frac{\mu_{ij}^{L}}{\left(\sum_{l=1}^{m}\left(\left(\mu_{ij}^{L}\right)^2 + \left(\mu_{ij}^{U}\right)^2\right)\right)^{\frac{1}{2}}}, a_{ij}^{U} = \frac{\mu_{ij}^{U}}{\left(\sum_{l=1}^{m}\left(\left(\mu_{ij}^{L}\right)^2 + \left(\mu_{ij}^{U}\right)^2\right)\right)^{\frac{1}{2}}} \qquad (4)$$

$$b_{ij}^{L} = \frac{v_{ij}^{L}}{\left(\sum_{l=1}^{m}\left(\left(v_{ij}^{L}\right)^2 + \left(v_{ij}^{U}\right)^2\right)\right)^{\frac{1}{2}}}, b_{ij}^{U} = \frac{v_{ij}^{U}}{\left(\sum_{l=1}^{m}\left(\left(v_{ij}^{L}\right)^2 + \left(v_{ij}^{U}\right)^2\right)\right)^{\frac{1}{2}}} \qquad (5)$$

Step 7: Establish the Weighted-Normalized Decision Matrix

Using the criteria weights calculated in Step 4, the weighted-normalized decision matrix is constructed. This is done using the IVIF scalar multiplication operator, denoted as

ISBN: 978-618-5765-04-0
ISSN 3057-4269

$\dot{\tilde{R}} = \dot{\tilde{r}}_{ij}$ representing the weighted performance rating of the i^{th} alternative with respect to the j^{th} criterion.

$$\dot{\tilde{R}} = \tilde{r}_{ij} * w_j \quad (6)$$

Step 8: Calculate the Score of Alternatives for the Ratio System

The criteria are divided into two groups: benefit criteria ("more is better") (bc) and cost criteria ("less is better") (cc). The score for each alternative, $\tilde{y}_i, i = 1, 2, \ldots, m$, is computed using Eq. (7), where benefit criteria are ranked as $C_1, C_2, \ldots, C_g$, and cost criteria are ranked as $C_{g+1}, C_{g+2}, \ldots, C_n$.

$$\tilde{y}_i = \sum_{j=1}^{g} \dot{\tilde{r}}_{ij} - \sum_{j=g+1}^{n} \dot{\tilde{r}}_{ij} \quad (7)$$

Step 9: Calculate the Score of Alternatives for the Reference Point Approach

For each alternative, $\tilde{P}_i$ represents an IVIF number, and r_j corresponds to the best criteria values. IVIF mathematical operations are applied to calculate the Min-Max metric based on the Tchebycheff formula (Eq. 8).

$$\tilde{P}_i = \min_{(i)} \left\{ \max_j \left| r_j - \dot{\tilde{r}}_{ij} \right| \right\} \quad (8)$$

Step 10: Compute the Overall Utility Function Using the Full Multiplicative Form

This step involves applying a utility function that combines maximization and minimization. The overall utility of each alternative is expressed as a dimensionless number, calculated using Eq. (9) with the IVIF division operator. For each alternative $\tilde{A}_i = \prod_{j=1}^{g} \dot{\tilde{r}}_{ij}$, the IVIF product is maximized for the criteria g = 1, …, and n, and minimized for the criteria $\tilde{B}_i = \prod_{j=g+1}^{n} \dot{\tilde{r}}_{ij}$.

$$\tilde{U}_i = \tilde{A}_i / \tilde{B}_i \quad (9)$$

Step 11. Rank the Alternatives

Finally, the alternatives are ranked based on the Ratio System, Reference Point Approach, and Full Multiplicative Form. To do this, the defuzzification process (Eq. 10) [20] is applied to obtain the defuzzified values Yi, Pi, and Ui corresponding to $\tilde{y}_i$, $\tilde{P}_i$, $\tilde{U}_i$. A dominance theory approach [17] is then used to consolidate the three rankings into a final ranking.

$$\frac{\mu_{\tilde{A}}^{L} + \mu_{\tilde{A}}^{U} + \left(1 - \nu_{\tilde{A}}^{L}\right) + \left(1 - \nu_{\tilde{A}}^{U}\right) + \mu_{\tilde{A}}^{L} * \mu_{\tilde{A}}^{U} - \sqrt{\left(1 - \nu_{\tilde{A}}^{L}\right) + \left(1 - \nu_{\tilde{A}}^{U}\right)}}{4} \quad (10)$$

Application and Validation

A case study is conducted to demonstrate the practical application of the proposed methodology by evaluating and ranking renewable energy alternatives for Türkiye. The results are validated through sensitivity and comparative analyses, ensuring the robustness of the methodology and alignment of the selected options with Türkiye's energy security and sustainable development objectives.

This integrated decision-making framework offers a powerful tool for policymakers and investors to navigate the complexities of RER selection. By combining the strengths of the IVIF set and the MULTIMOORA technique, the methodology provides a balanced approach to managing uncertainty and evaluating multiple criteria, ultimately guiding the selection of the most suitable RER for Türkiye. The model is developed by investors focused on researching, developing, constructing, and operating power generation plants utilizing RER. There are three DMs, each with equal importance, who assess the criteria from the investors' perspectives. The hierarchical structure for selecting the most appropriate renewable energy source is illustrated in Figure 1.

Results and Discussion

The proposed integrated methodology was applied to a case study in Türkiye to identify and rank the most suitable RER. This section presents the findings of the study and discusses the implications of the results. Equal importance is given to all DMs. The varying rankings in the literature can be attributed to factors such as the choice of experts, decision criteria, and the use of different MCDM methods. Each MCDM technique has its own strengths and weaknesses, performing differently depending on the decision-making context. Therefore, there isn't a universally "best" method, but rather one that is more appropriate for a given situation. The prioritization of solar energy, followed by wind energy, in Türkiye can be interpreted in several ways. One reason could be that these two energy sources are more viable across multiple dimensions, including favorable legislation, easier licensing from local authorities, and fewer environmental challenges associated with their deployment. The rise of solar and wind energy in Türkiye is also linked to the establishment of a more supportive institutional framework, recent developments in national regulatory processes, improvements in technical infrastructure, and increasing interest from investors.

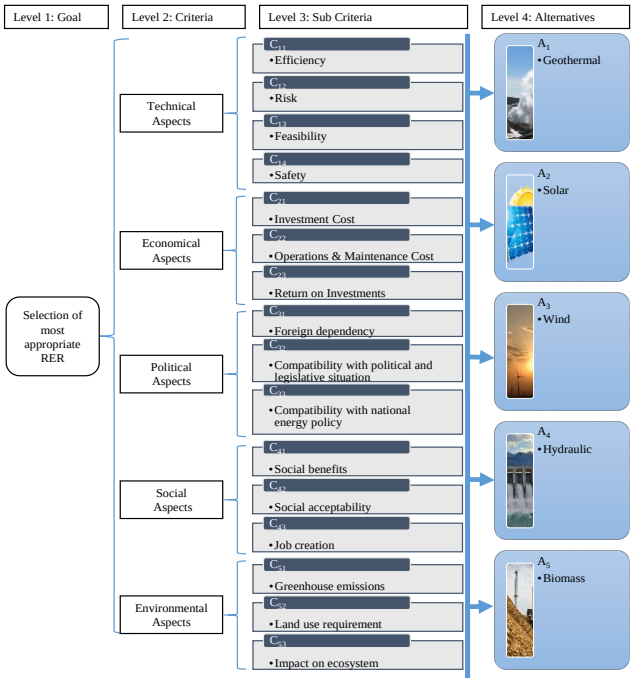

Figure 1: The hierarchical structure for selecting renewable energy source

Criteria Weighting and Evaluation

The initial step in the analysis involved identifying and assigning weights to the relevant criteria and sub-criteria for RER selection. The criteria were chosen based on their significance in the context of Türkiye's energy needs and sustainable development goals. Utilizing the IVIF set, DMs were able to express their preferences with a degree of uncertainty, reflecting the complexities inherent in RER evaluation.

ISBN: 978-618-5765-04-0
ISSN 3057-4269

The criteria included factors such as economic feasibility, environmental impact, social acceptability, and technical reliability. Each criterion was evaluated using the IVIF set, allowing for a nuanced assessment that accounted for both the membership and non-membership degrees within an interval. This approach provided a more flexible and accurate representation of the decision-makers' preferences compared to traditional fuzzy methods.

Application of the MULTIMOORA Technique

Following the evaluation of the criteria, the extended MULTIMOORA technique was employed to rank the RER alternatives. This technique, which integrates the Ratio System, Reference Point Approach, and Full Multiplicative Form, allowed for a comprehensive evaluation of the alternatives based on the weighted criteria. The use of the IVIF set in conjunction with MULTIMOORA facilitated the handling of imprecise data and uncertainties, ensuring that the rankings were robust and reflective of the complex decision-making environment. Table 3 through Table 9 gives the numerical results of the applied methodology.

Table 3: Ratings of Alternatives by DMs

	A_1			A_3			A_5			C_j		
DM	DM_1	DM_2	DM_3	DM_1	DM_2	DM_3	DM_1	DM_2	DM_3	DM_1	DM_2	DM_3
C_{11}	MG	B	MG	MG	MB	B	G	VG	MB	EG	B	G
C_{12}	B	B	MB	VVB	VG	VG	VVG	VG	VG	M	VB	MB
C_{13}	MG	VB	VG	VVG	G	VG	VVB	MG	G	MG	VVG	VVG
C_{14}	MB	M	VVG	G	G	G	G	VG	G	VG	G	VB
C_{21}	MG	G	G	VVB	B	MB	MB	VVG	B	MG	VG	M
C_{22}	VVB	VG	G	MB	VB	VVG	B	G	VB	G	VB	VB
C_{23}	MB	VVG	VB	G	G	G	VVG	VVG	G	M	VVG	VVG
C_{31}	B	G	B	VVG	MB	MB	MG	VG	MB	VG	M	VG
C_{32}	VG	B	MG	VVB	MB	B	VVB	VG	MB	B	MB	MB
C_{33}	EB	B	MB	G	VG	VG	G	VG	VG	VB	G	VVG
C_{41}	MB	VB	VG	MG	G	VG	MB	MG	G	VVB	VVG	VG
C_{42}	VB	M	VVG	G	G	G	VVG	VG	G	VB	VG	VG
C_{43}	EB	G	G	G	B	MB	G	VVG	B	MG	VB	G
C_{51}	MG	VG	G	MG	VB	VVG	MB	G	VB	M	MG	MG
C_{52}	VB	VVG	VB	VVB	G	G	VVG	VVG	G	MG	M	EG
C_{53}	VB	G	MB	G	VVG	G	VVB	VVG	VVG	VVG	MB	MG

Table 4: Respective Criteria Weights

C_j	C_{11}	C_{12}	C_{13}	C_{14}	C_{21}	C_{22}	C_{23}	C_{31}
w_j	0.071	0.038	0.071	0.065	0.066	0.044	0.071	0.069
Rank	1	15	3	11	10	14	4	8
C_j	C_{32}	C_{33}	C_{41}	C_{42}	C_{43}	C_{51}	C_{52}	C_{53}
w_j	0.037	0.069	0.069	0.067	0.057	0.059	0.071	0.069
Rank	16	6	5	9	13	12	1	7

Table 5: Benefit/Cost Ratio

	A_1				A_3				A_5			
	$[\mu^L,$	$\mu^U],$	$[\nu^L,$	$\nu^U]$	$[\mu^L,$	$\mu^U],$	$[\nu^L,$	$\nu^U]$	$[\mu^L,$	$\mu^U],$	$[\nu^L,$	$\nu^U]$
bc	0.09	0.11	0.35	0.37	0.08	0.10	0.35	0.37	0.08	0.12	0.34	0.36
cc	0.07	0.08	0.47	0.49	0.06	0.08	0.45	0.47	0.05	0.07	0.48	0.50

Table 6: Ratio System Variables

$\tilde{Y}_i$	$[\mu^L,$	$\mu^U],$	$[\nu^L,$	$\nu^U]$
A_1	0.024	0.032	0.737	0.751
A_2	0.007	0.010	0.803	0.808
A_3	0.024	0.022	0.782	0.785
A_4	0.020	0.024	0.765	0.772
A_5	0.029	0.050	0.711	0.728

Table 7: Reference Point Variables

$\tilde{P}_i$	$[\mu^L,$	$\mu^U],$	$[\nu^L,$	$\nu^U]$
A_1	0.032	0.033	0.938	0.941
A_2	0.024	0.023	0.923	0.929
A_3	0.029	0.032	0.925	0.933
A_4	0.029	0.031	0.933	0.939
A_5	0.023	0.021	0.932	0.939

Table 8: Full Multiplicative Form Variables

$\tilde{U}_i$	$[\mu^L,$	$\mu^U],$	$[\nu^L,$	$\nu^U]$
A_1	5.58E-05	1.82E-04	9.81E-01	9.83E-01
A_2	4.05E-05	5.50E-05	9.88E-01	9.89E-01
A_3	3.52E-04	1.73E-04	9.82E-01	9.83E-01
A_4	2.86E-04	2.34E-04	9.83E-01	9.84E-01
A_5	1.56E-04	8.09E-04	9.71E-01	9.75E-01

Table 9: Respective Values and Final Ranking

	Y_i	Rank	P_i	Rank	U_i	Rank	Ranking
A_1	0.922	4	0.969	2	0.995	4	4
A_2	0.947	1	0.970	4	0.997	1	1
A_3	0.934	2	0.967	1	0.996	3	2
A_4	0.931	3	0.969	3	0.996	2	3
A_5	0.910	5	0.973	5	0.993	5	5

Ranking of Renewable Energy Resources

The application of the integrated methodology yielded a ranking of RER alternatives, providing valuable insights into the most suitable options for Türkiye. The results indicated that certain RERs, such as solar and wind energy, emerged as the most favorable options due to their high scores across multiple criteria. These resources were found to offer a balanced combination of economic viability, environmental sustainability, and social acceptance, making them strong candidates for future energy investments in Türkiye.

In contrast, other RERs, such as biomass and geothermal energy, received lower rankings due to their comparatively higher costs, potential environmental concerns, or lower levels of social acceptance (see Table 9). However, these resources still represent viable options for specific contexts or regions within Türkiye, particularly where local conditions are favorable.

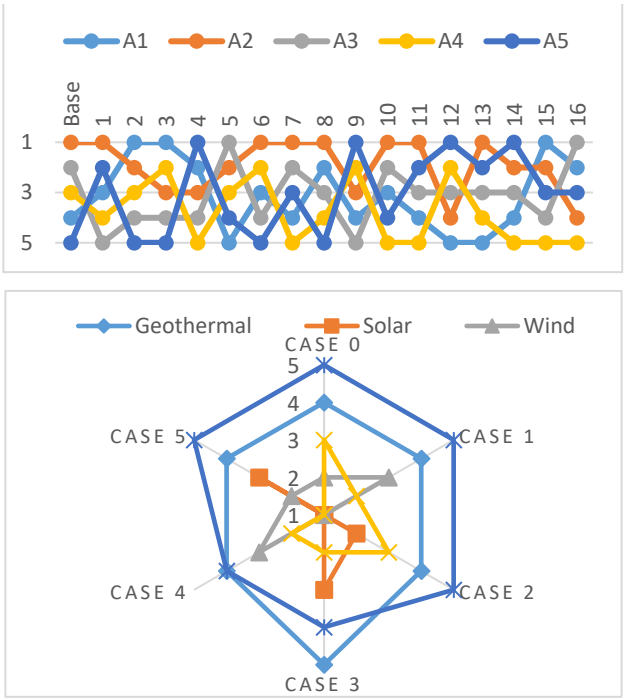

Figure 2: Sensitivity Performance of Criteria and Alternatives

Sensitivity and Comparative Analysis

To ensure the robustness of the results, sensitivity and comparative analyses were conducted. The sensitivity analysis involved varying the weights of the criteria to assess the stability of the rankings. The results demonstrated that the rankings were generally stable, with solar and wind energy consistently emerging as top choices across different weight scenarios. This stability underscores the reliability of the

ISBN: 978-618-5765-04-0
ISSN 3057-4269

proposed methodology in guiding RER selection (see Figure 2).

The comparative analysis involved comparing the results of the proposed methodology with those obtained from traditional decision-making approaches. The comparison revealed that the integrated methodology provided more nuanced and accurate rankings, particularly in managing the uncertainties associated with RER evaluation (see Figure 2). This highlights the advantages of using advanced MCDM techniques, such as the IVIF set and MULTIMOORA, in complex decision-making contexts.

CONCLUSION

In this study, we developed and applied an integrated decision-making framework designed to address the complexities of selecting RER for Türkiye. The framework effectively combines the IVIF set with an extended version of the MULTIMOORA technique to handle the uncertainties and conflicting criteria inherent in MCDM. The findings underscore the importance of a systematic and comprehensive approach to RER selection. By integrating the IVIF set, we were able to account for the uncertainties associated with the subjective judgments of decision-makers, providing a more accurate and flexible assessment of the criteria. The use of the extended MULTIMOORA technique further enhanced the robustness of the evaluation process, allowing for a thorough ranking of RER alternatives based on multiple, often conflicting, criteria. The results of the case study applied to Türkiye highlighted solar and wind energy as the most suitable options for future energy investments, given their strong performance across economic, environmental, and social criteria.

The consistency of these findings, even under varying criteria weights as in sensitivity analysis, confirms the reliability of the proposed methodology in guiding RER selection. Furthermore, the comparative analysis demonstrated that the integrated framework offers significant advantages over traditional decision-making approaches, particularly in managing imprecise data and uncertainties. Accordingly, this suggests the methodology could be broadly applied in other complex and uncertain decision-making contexts.

In conclusion, this study provides a valuable tool for policymakers and investors in Türkiye as they seek to meet the country's growing energy demands while advancing its sustainable development goals. The integrated decision-making framework not only facilitates the selection of the most appropriate RERs but also contributes to the broader objective of ensuring energy security and environmental sustainability. Future research could build on this work by applying the methodology to different geographic regions or sectors, thereby expanding its applicability and relevance. Additionally, further refinement of the criteria and incorporation of emerging energy technologies could enhance the framework's effectiveness in addressing the dynamic nature of the energy sector.

ACKNOWLEDGMENT

The authors express their deep gratitude to the specialists whose invaluable insights significantly enhanced the quality of this manuscript. This research was financially supported by the Galatasaray University Research Fund (FOA-2023-1181).

REFERENCES

[1] U. Calikoglu and M. Aydinalp Koksal, "Green electricity and Renewable Energy Guarantees of Origin demand analysis for Türkiye," *Energy Policy*, vol. 170, no. September, p. 113229, 2022.

[2] G. Büyüközkan, Y. Karabulut, and F. Göçer, "Spherical fuzzy sets based integrated DEMATEL, ANP, VIKOR approach and its application for renewable energy selection in Turkey," *Appl. Soft Comput.*, vol. 158, p. 111465, Jun. 2024.

[3] F. Göçer, "A Novel Extension of Fermatean Fuzzy Sets into Group Decision Making: A Study for Prioritization of Renewable Energy Technologies," *Arab. J. Sci. Eng.*, vol. 49, no. 3, pp. 4209–4228, Mar. 2024.

[4] G. Büyüközkan, F. Göçer, and O. Feyzioğlu, "Cloud computing technology selection based on interval-valued intuitionistic fuzzy MCDM methods," *Soft Comput.*, vol. 22, no. 15, pp. 5091–5114, Aug. 2018.

[5] O. Feyzioğlu, F. Göçer, and G. Büyüközkan, "Interval-valued intuitionistic fuzzy MULTIMOORA approach for new product development," in *Data Science and Knowledge Engineering for Sensing Decision Support*, 2018, pp. 1066–1073.

[6] W. K. M. Brauers and E. K. Zavadskas, "The MOORA method and its application to privatization in a transition economy," *Control Cybern.*, vol. 35, no. 2, pp. 445–469, 2006.

[7] W. K. M. Brauers and E. K. Zavadskas, "Project management by multimoora as an instrument for transition economies," *Technol. Econ. Dev. Econ.*, vol. 16, no. 1, pp. 5–24, 2010.

[8] I. Iskin, T. Daim, G. Kayakutlu, and M. Altuntas, "Exploring renewable energy pricing with analytic network process — Comparing a developed and a developing economy," *Energy Econ.*, vol. 34, no. 4, pp. 882–891, Jul. 2012.

[9] A. Karaaslan and M. Gezen, "The evaluation of renewable energy resources in Turkey by integer multi-objective selection problem with interval coefficient," *Renew. Energy*, vol. 182, pp. 842–854, Jan. 2022.

[10] G. Büyüközkan and S. Güleryüz, "An integrated DEMATEL-ANP approach for renewable energy resources selection in Turkey," *Int. J. Prod. Econ.*, vol. 182, pp. 435–448, Dec. 2016.

[11] G. Büyüközkan, Y. Karabulut, and E. Mukul, "A novel renewable energy selection model for United Nations' sustainable development goals," *Energy*, vol. 165, pp. 290–302, Dec. 2018.

[12] G. Büyüközkan and S. Güleryüz, "Evaluation of Renewable Energy Resources in Turkey using an integrated MCDM approach with linguistic interval fuzzy preference relations," *Energy*, vol. 123, pp. 149–163, Mar. 2017.

[13] G. Büyüközkan and S. Güleryüz, "A new GDM based AHP framework with linguistic interval fuzzy preference relations for renewable energy planning," *J. Intell. Fuzzy Syst.*, vol. 27, no. 6, pp. 3181–3195, 2014.

[14] G. Büyüközkan, F. Göçer, and O. Feyzioglu, "Cloud computing technology selection based on interval valued intuitionistic fuzzy group decision making using MULTIMOORA approach," in *2017 IEEE International Conference on Fuzzy Systems (FUZZ-IEEE)*, 2017, pp. 1–6.

[15] L. A. Zadeh, "Fuzzy sets," *Inf. Control*, vol. 8, no. 3, pp. 338–353, Jun. 1965.

[16] K. . Atanassov and G. Gargov, "Interval valued intuitionistic fuzzy sets," *Fuzzy Sets Syst.*, vol. 31, no. 3, pp. 343–349, Jul. 1989.

[17] W. K. M. Brauers and E. K. Zavadskas, "Multimoora Optimization Used to Decide on a Bank Loan to Buy Property," *Technol. Econ. Dev. Econ.*, vol. 17, no. 1, pp. 174–188, Mar. 2011.

[18] F. Zhang and S. Xu, "Multiple Attribute Group Decision Making Method Based on Utility Theory Under Interval-Valued Intuitionistic Fuzzy Environment," *Gr. Decis. Negot.*, vol. 25, no. 6, pp. 1261–1275, Nov. 2016.

[19] Z. Xu and X. Cai, "Intuitionistic Fuzzy Information Aggregation," in *Intuitionistic Fuzzy Information Aggregation*, Springer, Berlin, Heidelberg, 2012, pp. 1–102.

[20] B. Oztaysi, S. C. Onar, K. Goztepe, and C. Kahraman, "Evaluation of research proposals for grant funding using interval-valued intuitionistic fuzzy sets," *Soft Comput.*, vol. 21, no. 5, pp. 1203–1218, Mar. 2017.

AI-Driven Optimization of an Integrated Multi-Energy System for Sustainable Consumption and Production

Davoud Garmroudi
Energy Institute
Istanbul Technical University
Istanbul, Turkey
seyedgarmroodi19@itu.edu.tr

Gülgün Kayakutlu
Energy Institute
Istanbul Technical University
Istanbul, Turkey
kayakutlu@itu.edu.tr

Mehmet Özgür Kayalica
Energy Institute
Istanbul Technical University
Istanbul, Turkey
kayalica@itu.edu.tr

***Abstract*— This paper introduces an innovative AI-driven model designed to optimize an integrated multi-energy system that incorporates renewable energy sources (RESs) and demand response programs. The model aims to minimize operational costs and carbon footprint while maximizing the penetration of renewable energy, thereby enhancing system efficiency and sustainability. As Dr. Asaridis highlights the importance of reducing carbon emissions in energy systems through the application AI algorithms, this model, effectively coordinates the production, and consumption of energy, optimizing the use of various renewable sources and adaptive demand response mechanisms. This approach not only addresses the reduction of carbon emissions but also significantly improves the affordability and reliability of energy supply. The results from simulations illustrate substantial improvements in economic and environmental performance metrics, underlining the model's capability to support a sustainable energy transition. This work contributes to advancing sustainable consumption and production by promoting the integration of clean energy technologies, echoing the principles of SDG 12 and indirectly supporting the universal access to sustainable energy.**

Keywords—AI, optimization, consumption, energy

INTRODUCTION

Decarbonization has become one of the most important goals of global energy policy, driven by the urgency to mitigate climate change through sustainable practices. Meeting rising energy demand in a sustainable way requires a shift to clean, affordable energy sources. Renewable energy sources (RES) such as solar and wind energy are particularly promising and have the potential to position electricity as the dominant environmentally friendly and cost-effective fuel for future energy systems [1, 2]. However, the intermittent and unpredictable nature of renewable energy, which is largely influenced by weather conditions, poses a major challenge to maintaining stable grid operations. This variability requires the development of advanced energy management systems (EMS) that can balance generation and consumption in real time [3].

Microgrid (MG) technology provides a robust solution for harnessing distributed renewable energy (DRE) and ensures stable and efficient operation through the integration of an advanced EMS. In grid-connected mode, MGs have the added ability to swap energy with the wider distribution grid, optimizing energy flow and cost efficiency [4]. Beyond electricity, MGs are increasingly evolving into multi-energy microgrids (MEMGs), which are capable of managing and optimizing multiple forms of energy — such as electricity, heat and gas — in a single, interconnected system. In this context, MEMGs offer a promising solution as they integrate multiple energy sources and customers, providing flexibility, resilience and improved distribution efficiency. This global shift towards sustainable, modernized energy systems is also supported by international agreements that aim to minimize environmental impact. One such initiative is the sustainable development goals (SDGs) introduced by the United Nations. They emphasize the importance of efficient energy use and the development of smart cities to accelerate the transition to a low-carbon future [5].

These systems can operate under centralized control, managed by a single entity, or under decentralized control, where multiple players share responsibility for management. Both approaches can coexist in a unified management framework and improve flexibility and resilience in energy optimization. Energy management in MGs is usually considered as an optimization task to reduce costs, distinguishing between model-based, deterministic methods that use predefined models and model-free, learning-based methods that adaptively optimize performance [6]. In [7], a mixed-integer linear programming (MILP) model for unbalanced three-phase AC microgrids was proposed, which aims to minimize operating costs by optimally scheduling resources for the day in advance. Similarly, [8] employed a stochastic p-robust optimization method using the ϵ-constraint technique to account for uncertainties in MEMGs, excluding emissions related to the external grid and LNG transactions. In addition, [9] introduced a cumulative relative regret decision approach for optimal MEMG energy management under renewable energy-related uncertainties, focusing solely on thermal demand response programs (DRPs) without considering emissions.

Developing a model-based energy management strategy for microgrids (MGs) requires accurate modeling of each component, as the choice of models and parameters directly affects dispatch results. While these methods are effective when well defined, they are prone to inaccuracies in parameter selection and may require a complete redesign of the system if the topology, size, or capacity of the MG changes, making them labor intensive [10]. In contrast, learning-based approaches for energy management tasks such as renewable energy and load forecasting, frequency control, and genset optimization have gained prominence. These data-driven techniques eliminate the need for explicit models and instead use data to adaptively optimize the MG performance, where the problem is often formulated as a Markov Decision Process (MDP) [4]. For instance, in [11], reinforcement learning (RL) was combined with Monte- Carlo tree search (MCTS) for the dynamic dispatch of battery energy storage systems (BESS) in MGs to optimize the charge/discharge cycles to extend battery

ISBN: 978-618-5765-04-0
ISSN 3057-4269

lifetime. Similarly, an energy management system (EMS) in [12] used a finite MDP and a Q-learning algorithm to minimize operational costs in a campus MG, considering network and technical constraints through sequential decision making.

Motivation and contribution

Artificial intelligence (AI) is a transformative tool with significant potential to advance the United Nations Sustainable Development Goals (SDGs). In particular, AI can contribute to SDG 7 (Affordable and Clean Energy), SDG 11 (Sustainable Cities and Communities) and SDG 13 (Climate Action) by optimizing energy systems, improving the resilience of cities and strengthening climate action initiatives. AI can also support SDG 12.2 by promoting sustainable consumption and production patterns in the energy sector. AI-driven approaches can better balance energy production and consumption, use resources efficiently and minimize environmental impacts. The integration of AI into energy systems promotes efficient resource management, reduces carbon emissions and improves access to clean energy. However, while AI could support progress on 128 SDG targets, it also poses challenges that could hinder progress on 58 targets. This underscores the need for ethical and well-regulated AI applications to ensure alignment with sustainability goals [13, 14]. In the light of the introduction discussed above, the contributions can be outlined as follows:

- Developing a MADRL-based framework for MEMG energy management that dynamically learns optimal strategies for energy flow control.
- Integration of DRPs and EV parking lots (EVPL) in V2G mode to increase flexibility, reduce costs and minimize environmental impact.
- Incorporating uncertainties in renewable generation, load demand and energy prices to ensure robust performance across all scenarios.
- Alignment with the Sustainable Development Goals (SDGs) through the proposed energy management and the defined targets that support SDG 7 (affordable and clean energy), SDG 11 (sustainable cities and communities), SDG 13 (climate action) and SDG 12.2 (sustainable consumption and production patterns).

Organization

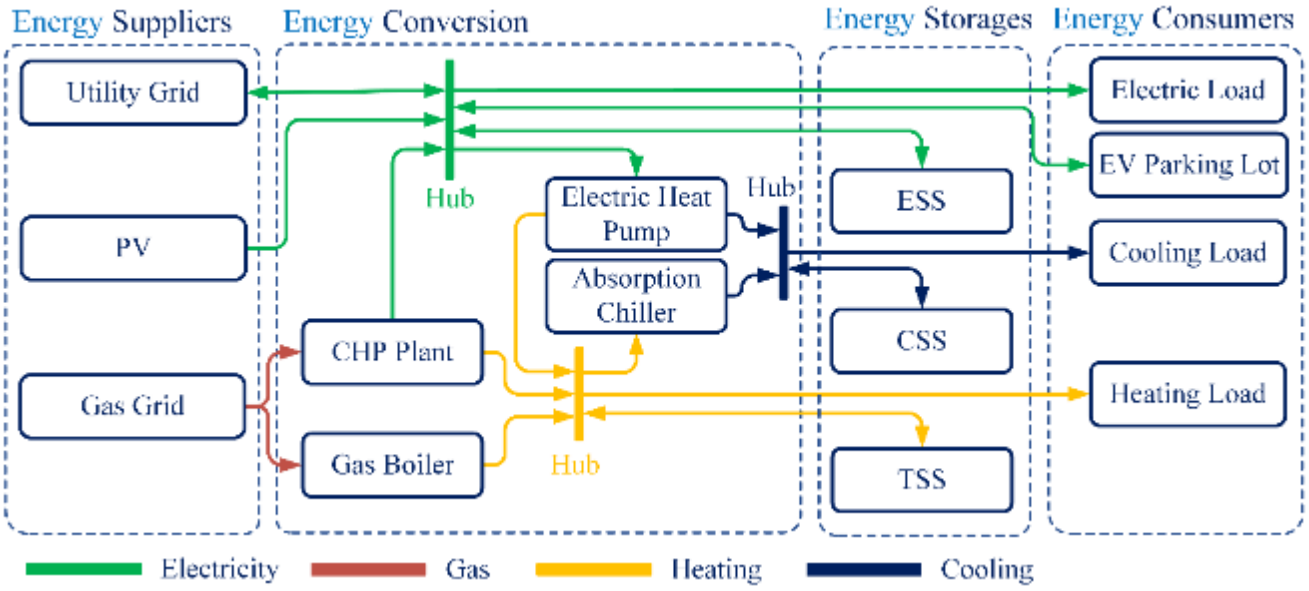

Figure* 1*: (Left) Structure of the MEMG; (Right) Structure of the DDPG algorithm.

The rest of the paper is organized as follows: Section II gives an overview of the components of the MEMG. The problem formulation and methodology is described in detail in Section III. Section IV presents and discusses the simulation result. Finally, Section V gives conclusion.

System Architecture and Components

With the increasing use of renewable energy sources (RES) and the growing diversity of energy consumption patterns, multi-energy microgrids (MEMGs) have emerged as an important solution for efficient energy management. As illustrated in ***Figure* 1** (left), a typical MEMG integrates various components to optimize energy flows. The energy suppliers include the upstream utility grid, the upstream gas grid and renewable energies such as photovoltaic systems. The system utilizes energy conversion units such as combined heat and power (CHP) plants, gas boilers (GB), electric heat pumps (EHP) and absorption chillers (AC) to meet the heating, cooling and electricity demand. In addition, storage units such as electrical (ESS), thermal (TSS) and cooling storage systems (CSS) enhance system reliability by storing excess energy. On the consumption side, MEMGs efficiently manage electrical loads, EV parking lots (EVPLs) through V2G operation, and heating and cooling loads to ensure seamless energy distribution and consumption.

Energy conversion units model

CHP model

The CHP unit efficiently generates electricity and heat from natural gas, thus reducing transmission losses and emissions. Due to its high efficiency, environmental friendliness and cost effectiveness, it is widely used in decentralized energy systems. The operating model of the CHP unit is defined in (1) and (2) [15].

$$P_t^{CHP,Gas} = a^{CHP}(P_t^{CHP})^2 + b^{CHP}P_t^{CHP} + c^{CHP}(H_t^{CHP})^2 + e^{CHP}P_t^{CHP}H_t^{CHP} + d^{CHP}H_t^{CHP} \quad (1)$$

$$\begin{cases} P_t^{CHP} = \eta_P^{CHP} G_t^{CHP} \\ H_t^{CHP} = \eta_H^{CHP} P_t^{CHP} \end{cases} \quad (2)$$

ISBN: 978-618-5765-04-0
ISSN 3057-4269

The gas consumption, modeled as a quadratic, non-linear function of the required power, is described in (1). The energy conversion level is presented in (2).

Gas boiler model

A gas boiler generates thermal energy by burning natural gas and provides reliable heat for various applications. The energy is converted as follows:

$$H_t^{GB} = \eta_t^{GB} G_t^{GB} \tag{3}$$

Electric heat pump model

In energy management systems, heat pumps are optimized together with CHP systems to efficiently cover heating and cooling requirements [15]. The energy conversion processes are as follows:

$$H_t^{\mathrm{EHP}} = P_t^{\mathrm{EHP}} \eta^{\mathrm{EHP,H}} \tag{4}$$

$$Q_t^{\mathrm{EHP}} = P_t^{\mathrm{EHP}} \eta^{\mathrm{EHP,C}} \tag{5}$$

Absorption chiller model

Absorption chillers in district cooling systems use the waste heat from the CHP unit for cooling, thereby increasing the efficiency of the system. The energy conversion process works as follows:

$$Q_t^{AC} = \eta^{AC} H_t^{AC}. \tag{6}$$

Multiple energy storage system model

The electrical, thermal, and cooling storage systems in MEMGs are represented by (7), (8), and (9) respectively. these equations indicate that the energy stored at time t depends on the residual energy from the prior hour and the current charging and discharging activities [16].

$$SoC_t^{ESS} = SoC_{t-1}^{ESS} + \left(\eta^{Ch,ESS} P_t^{Ch,ESS} - \frac{P_t^{Dch,ESS}}{\eta^{Dch,ESS}}\right)\Delta t \tag{7}$$

$$SoC_t^{ESS} = SoC_{t-1}^{TSS} + \left(\eta^{Ch,TSS} H_t^{Ch,TSS} - \frac{H_t^{Dch,TSS}}{\eta^{Dch,TSS}}\right)\Delta t \tag{8}$$

$$SoC_t^{CSS} = SoC_{t-1}^{CSS} + \left(\eta^{Ch,ESS} Q_t^{Ch,ESS} - \frac{Q_t^{Dch,CSS}}{\eta^{Dch,CSS}}\right)\Delta t \tag{9}$$

EV parking lot model

Electric vehicle parking lot (EVPL) operates in both vehicle-to-grid (V2G) and grid-to-vehicle (G2V) modes to achieve the MEMG operator's goal. Using the EVPL concept, EVs are connected to the grid and function as an ESS [16].

$$SoC_{v,t}^{EV} = SoC_{v,t-1}^{EV} + \left(\eta^{Ch,EV} P_{v,t}^{Ch,EV} - \frac{P_{v,t}^{Dch,EV}}{\eta^{Dch,EV}}\right)\Delta t \tag{10}$$

Integrated DRP model

This model incorporates an incentive-based demand response for managing electrical, thermal, and cooling demands [15].

$$\sum_{t=1}^{NT} \Re^{Dn} = \sum_{t=1}^{NT} \Re^{Up} \tag{11}$$

$$DT_t^{DR} = DT_t^{init} + \Re_t^{Up} - \Re_t^{Dn} \tag{12}$$

$$DT_t^{init}(1 - \gamma^{DT}) \le DT^{DR} \le DT_t^{init}(1 + \gamma^{DT}) \tag{13}$$

Where $\Re$ denotes the relocation of various demand types (DT). Equation (11) ensures that shifted power, heat, and cooling loads reallocated to other periods are balanced at each specific time. Equation (12) represents the adjusted demands post-DRP application, while (13) limits load flexibility for each hour.

Problem Formulation and Methadology

This section outlines the objective function, the constraints, and the solution methods used to solve the problem.

Mathematical model for optimal EMS

Objective function

The overall objective of the energy management is to minimize the total of the operating cost of the MEMG which includes the energy exchange cost with the grid, IDRPs cost, and the emission cost [15].

$$TC = min(F^{TOC} + F^{Em}) \tag{14}$$

where

$$F^{TOC} = \underbrace{\sum_{t=1}^{T}\left(C_{t,s}^{E,Grid,Buy} + C_{t,s}^{Gas,Grid,Buy}\right)}_{\text{Purchase from upper grid}} + \underbrace{\sum_{t=1}^{T}\left(C_{t,s}^{E,IDRP} + C_{t,s}^{H,IDRP} + C_{t,s}^{Q,IDRP}\right)}_{\text{IDRPs}} \tag{15}$$

The emission cost serves as a penalty for purchasing electricity from the grid and for the emissions of non-renewable energy units that use purchased gas.

$$F^{Em} = \sum_{t=1}^{T=24}\left(C_{t,s}^{Em,E,Grid} + C_{t,s}^{Em,CHP} + C_{t,s}^{Em,GB}\right) \tag{16}$$

Model constraints

The equality and inequality constraints are defined in this subsection.

Equality constraints/energy balance constraints:

To ensure reliable and efficient operation, electrical, thermal, cooling energy and natural gas must be balanced simultaneously [15].

$$P_t^{Buy,Grid} + P_t^{PV} + P_t^{CHP} + P_t^{Dch,ESS} + \sum_{v=1}^{N_{EV}} P_{v,t}^{Dch,EV} = P_t + P_t^{EHP} + P_t^{Ch,ESS} + \sum_{v=1}^{N_{EV}} P_{v,t}^{Ch,EV} + P_t^{Sell,Grid} \tag{17}$$

$$H_t^{CHP} + H_t^{GB} + H_t^{EHP} + P_t^{Dch,TSS} = H_t + H_t^{AC} + P_t^{Ch,TSS} \tag{18}$$

$$Q_t^{AC} + Q_t^{EHP} + P_t^{Dch,CSS} = Q_t + P_t^{Ch,CSS} \tag{19}$$

$$. \; G_t^{Buy,Grid} = G_t^{CHP} + G_t^{Boiler} \tag{20}$$

Capacity and operating constraints:

The energy conversion units must operate within set limits to ensure the security and stability of the system.

$$Cap^{Min,\,CHP} \le P_t^{CHP} + H_t^{CHP} \le Cap^{Max,\,CHP} \tag{21}$$

ISBN: 978-618-5765-04-0
ISSN 3057-4269

$$H^{Min,\,GB} \le H_t^{GB} \le H^{Max,\,GB} \quad (22)$$

$$H^{Min,\,EHP} \le H_t^{EHP} \le H^{Max,\,EHP} \quad (23)$$

$$Q^{Min,\,EHP} \le Q_t^{EHP} \le Q^{Max,\,EHP} \quad (24)$$

$$Q^{Min,\,AC} \le Q_t^{AC} \le Q^{Max,\,AC} \quad (25)$$

Charging and discharging rate of ESS, TSS, and CSS units are limited as follows:

$$P_{ch}^{Min,ESS/TSS/CSS} \le P_t^{Ch,ESS/TSS/CSS} \le P_{ch}^{Max,ESS/TSS/CSS} \quad (26)$$

$$P_{Dch}^{Min,ESS/TSS/CSS} \le P_t^{Dc,ESS/TSS/CSS} \le P_{Dch}^{Max,ESS/TSS/CSS} \quad (27)$$

To maintain storage system health and extend lifespan, the state of charge must stay within specified permissible limits.

$$SoC_{min}^{ESS/TSS/CSS} \le SoC_t^{ESS/TSS/CSS} \le SoC_{max}^{ESS/TSS/CSS} \quad (28)$$

MEMG are allowed to realize the transaction with the upper grid, which are constrained

$$0 \le P_t^{Buy/Sell,Grid} \le P_t^{Max,Buy/Sell,Grid} \quad (29)$$

$$0 \le G_t^{Buy,Grid} \le G_t^{Max,Buy,Grid} \quad (30)$$

For the PV generation capacity we have:

$$P_t^{PV} \le P_t^{Max,PV} \quad (31)$$

MADRL formulataion for EMS

Reinforcement learning (RL) enables agents to learn and adapt through continuous interaction with the environment. By taking actions, observing the results, and receiving rewards or penalties, the agent gradually refines its behavior to maximize the cumulative reward. This interaction process is demonstrated in ***Figure*** 1. This process, modeled as a Markov decision process (MDP), allows the agent to optimize its decision-making.

System states:

The system state comprises information received by the agent from the MEMG, and represents current conditions and operating parameters. The state vector is defined as follows:

$$S_{s,t} = \left(\lambda_{s,t}, L_{s,t}, P_{s,t}\right)$$
$$\begin{cases} \lambda_{s,t} = \begin{pmatrix} \lambda_{s,t}^{E,Grid,Buy}, \lambda_{s,t}^{Gas,Grid,Buy}, \lambda_{s,t}^{Em}, \\ \lambda_{s,t}^{E,Grid,Sell}, \lambda_{s,t}^{E,IDRP}, \lambda_{s,t}^{H,IDRP}, \lambda_{st}^{Q,IDRP} \end{pmatrix} \\ L_{s,t} = \left(P_{s,t}^{EL}, P_{s,t}^{HL}, P_{s,t}^{QL}\right) \\ P_{s,t} = \left(P_{s,t}^{PV}, SoC_{s,t}^{BESS}, SoC_{s,t}^{HSS}, SoC_{s,t}^{QSS}, P_{s,t}^{EV}\right) \end{cases} \quad (32)$$

Actions:

The system actions refer to the operational decisions made by the MEMG controller to allocate the energy resources and adjust the power flows efficiently. These actions are described below:

$$a_{s,t} = \begin{pmatrix} P_{t,s}^{E,Grid}, P_{t,s}^{Gas,Grid}, P_{t,s}^{CHP}, P_{t,s}^{BESS}, P_{t,s}^{PV}, \\ P_{t,s}^{EV}, P_{t,s}^{EL,IDRP}, P_{t,s}^{HL,IDRP}, P_{t,s}^{QL,IDRP}, \\ H_{t,s}^{HSS}, Q_{t,s}^{CSS}, H_{t,s}^{CHP}, H_{t,s}^{GB}, H_{t,s}^{EH}, Q_{t,s}^{EHP} \end{pmatrix} \quad (33)$$

Reward functions and related penalties:

The reward function r represents the immediate gain that the MEMG controller receives at time t for performing the action a based on the current system state s. This relationship can be defined mathematically as follows:

$$r_{s,t} = -\left(C_{s,t}^{total} + C_{s,t}^{penalty}\right) \quad (34)$$

Where The penalty function is formulated as the cost associated with unmet load (for each type of load) as follows:

$$C_{s,t}^{penalty} = \lambda^e \cdot \Delta P_{s,t} + \lambda^h \cdot \Delta H_{s,t} + \lambda^q \cdot \Delta Q_{s,t}$$
$$\begin{cases} \Delta P_{s,t} = \left|P_{s,t}^{EL} - P_{st}^{Supplied}\right| \\ \Delta H_{s,t} = \left|P_{s,t}^{HL} - H_{st}^{Supplied}\right| \\ \Delta Q_{s,t} = \left|P_{s,t}^{QL} - Q_{st}^{Supplied}\right| \end{cases} \quad (35)$$

DDPG-Based Energy Management

DDPG utilizes an actor-critic structure, making it ideal for continuous action spaces for decisions on energy distribution, storage management and grid interaction.

Critic Network and Q-Function

In DDPG, the critic network is responsible for estimating the action-value function (Q-function), which represents the expected cumulative reward for taking action a_t in state s_t. The loss function for the critic network is defined as:

$$L(\theta^Q) = \frac{1}{B}\sum_i \left(y_i - Q(s_i, a_i|\theta^Q)\right)^2 \quad (36)$$

where B is the mini-batch size, y_i is the target Q-value, and θ^Q are the critic network parameters. The target Q-value y_t is computed using the following Bellman equation:

$$y_t = r_t(s_t, a_t) + \gamma Q\left(s_{t+1}, \mu\left(s_{t+1}\middle|\theta^{\mu'}\right)\middle|\theta^{Q'}\right) \quad (37)$$

Where $r_t(s_t, a_t)$ is reward obtained after taking action a_t in state s_t, γis discount factor, $\mu\left(s_{t+1}\middle|\theta^{\mu'}\right)$ is the action selected by the target actor network for the next state s_{t+1}, $Q\left(s_{t+1}, \mu(s_{t+1})\middle|\theta^{Q'}\right)$ is Q-value predicted by the target critic for the next state-action pair.

Actor Network and Policy Gradient

The actor network in DDPG is responsible for learning the optimal policy $\pi(s_t|\theta^\mu)$, which maps states to continuous actions. The goal of the actor is to maximize the expected cumulative reward. The actor's parameters θ^μ are updated using the policy gradient, defined as:

$$\nabla_{\theta^\mu} J = E_{s_t\sim\rho^\pi}\left[\nabla_a Q(s_t, a_t|\theta^Q)|_{a=\mu(s_t)} \nabla_{\theta^\mu}\mu(s_t|\theta^\mu)\right] \quad (38)$$

Where $\nabla_{\theta^\mu} J$ is the gradient of the expected return with respect to the actor's parameters θ^μ. $\nabla_a Q(s_t, a_t|\theta^Q)$ is the gradient of the Q-value with respect to the action a.$\nabla_{\theta^\mu}\mu(s_t|\theta^\mu)$ the gradient of the actor's output (action) with respect to its parameters θ^μ.

State and action value function

The state value function $V^\pi(s_t)$defines the maximum expected reward from a given state $s_t$when following the policy π. And action value function evaluates the quality of a state-action pair (s_t, a_t) under the current policy. These functions are expressed as follows:

$$V^\pi(s_t) = \max_{a_t\in A(s_t)} Q^\pi(s_t, a_t) \quad (39)$$

$$Q^\pi(s_t, a_t) = E_{s_{t+1\!\!1}\sim P}[r_t + \gamma V^\pi(s_{t+1})|s_t, a_t] \quad (40)$$

The actor network selects actions by maximizing the expected Q-values estimated by the critic network.

$$\theta' \leftarrow \tau\theta + (1-\tau)\theta' \quad (41)$$

To improve the stability of the training, DDPG utilizes an experience replay buffer in which past interactions between

ISBN: 978-618-5765-04-0
ISSN 3057-4269

the agent and the environment are stored. These stored interactions (s_t, a_t, r_t, s_{t+1}) are randomly sampled to train both the actor and critic networks. This process helps break correlations between consecutive samples, leading to a more stable training.

Structure of the deep neural network

In the proposed energy management system, a Deep Neural Network (DNN) is used to determine the optimal policy for dispatching energy in a MEMG. The DNN architecture is designed to handle the complexity of continuous actions and high-dimensional input states such as solar radiation, electricity prices, electric vehicle loads and thermal demand. The input state variables are fed into the neural network and the output is a continuous action vector that determines the energy dispatch and storage decisions.

For stable training, the network normalizes the input data, uses ReLU activation in the hidden layers to avoid gradient issues, and applies tanh in the last layer to limit output actions. The DNN includes three hidden layers, each with 64 neurons, which promote fast convergence and prevent overfitting, while an inverse transformation block ensures output within the action range. The hyperparameters are listed in ***Table 1***.

Table 1: Hyperparameters of the DDPG algorithm

Hyperparameter	**Value**
Learning rate actor (lr^a)	$1e^{-6}$
Learning rate critic (lr^c)	$1e^{-4}$
Discount factor (γ)	0.96
Soft update parameter (τ)	$1e^{-2}$
Replay buffer size	50000
Batch size (B)	64
Traning episodes	5000
Exploratin noise	Ornstein-Uhlenbeck process

Scenario Generation

Given the uncertainties inherent in the system, including variable solar radiation, electricity prices and energy demand, future scenarios must be generated. Monte Carlo simulations are employed to create a wide range of possible conditions. To handle computational complexity, the number of scenarios is reduced using the K-nearest neighbor (KNN) method, while maintaining diversity. This refined set of scenarios is then used to train the DDPG agent to ensure that it is exposed to different system states.

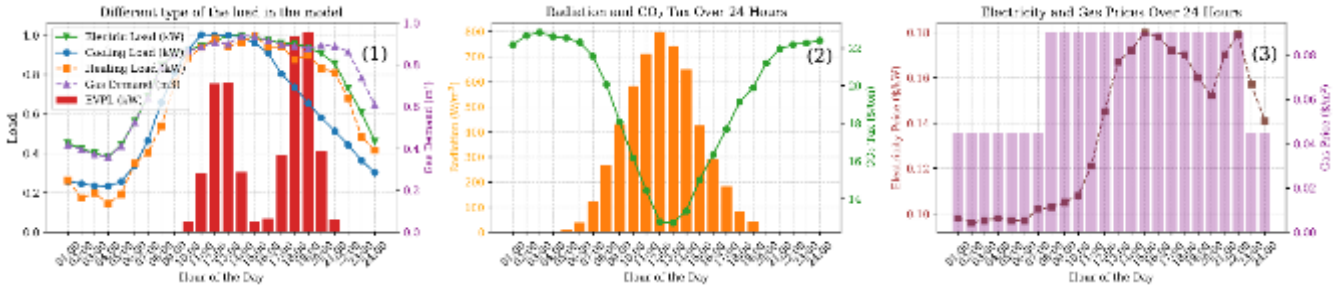

Figure 2: Input data used in the simulation.

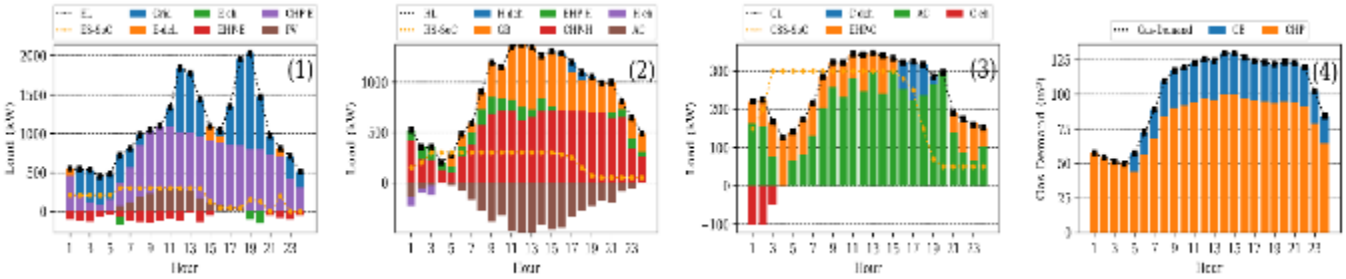

Figure 3: Dispatch Results

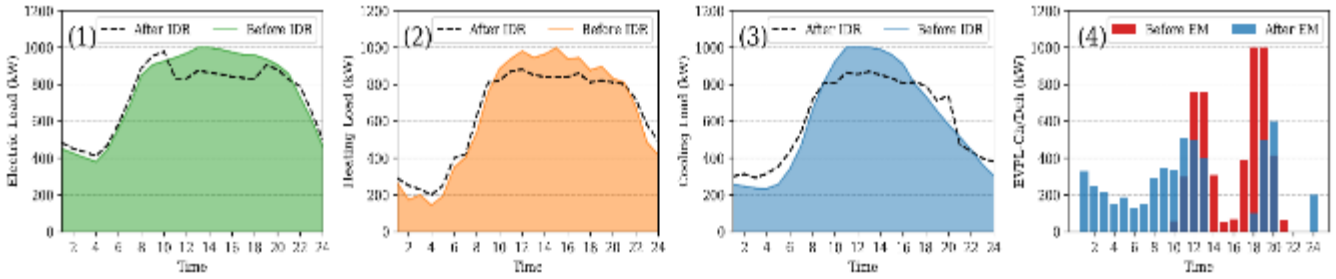

Figure 4: Result of applying DR program for different load type

Table 2: Information of the MEMG components

Unit	**CHP**	**GB**	**AC**	**EHP**	**PV**	**ESS**	**TSS**	**CSS**
Cap(kW)	800	700	700	300	300	300	300	300

Simulation Results and Discussion

Three scenarios are examined in this study: The first ignores emissions, demand response, and parking restrictions (base case); the second adds emissions constraints; and the third includes all programs. The definition of these scenarios enables a comprehensive assessment of the ability of the AI-based model to achieve different system objectives. The simulation data from [16] are shown in ***Figure 2*** and. They show the load types of the system, solar radiation with carbon tax variations, and electricity and gas prices. The capacity of the system components can be found in ***Table 2***.

In the first scenario, the focus is solely on minimizing costs and enhancing economic efficiency. Ignoring environmental

ISBN: 978-618-5765-04-0
ISSN 3057-4269

factors, all units are operated purely for cost reduction, resulting in the lowest total costs of all scenarios with the value about $4653.8 and 102.43 tons/day emission. In the second scenario, due to additional emission constraints, the units must be dispatched in such a way that they meet the environmental targets. Consequently, the total costs are higher compared to the other scenarios, despite the model's efforts to maximize the use of renewable energy. The total cost and emission are about $5231.2 and 98.23 tons/day. Due to space, the simulation results are only shown for the most comprehensive scenario. ***Figure 3***-1 to 4 illustrate the results of energy generation and conversion, while ***Figure 4***-1 to 4show the effects of demand response programs on different loads. In addition, ***Figure 4***-4 shows the operational planning for electric vehicle parking.

It can be observed that the PV unit operates at maximum capacity during periods of high availability of renewable resources. The battery charges during periods of low electricity prices (hours 6, 19 and 20) and discharges during peak load and high price hours, a pattern also observed in other storage systems. they discharge when units such as EHP and AC are not heavily utilized (***Figure 3***-1). As an electricity consumer, the EHP operates primarily when renewable generation is high and is only minimally active during high price hours. The GB unit normally operates at full capacity to meet heat demand when the carbon tax is low. The simulation results demonstrate the effectiveness of the proposed energy management framework in optimizing system performance. By aligning unit operations with system goals, the approach enables cost reduction and emissions control. For instance, the electric vehicle parking lot, though not interacting with the grid, adjusts its consumption patterns based on price signals, contributing to lower overall system costs. Demand response programs also successfully shift peak loads to off-peak hours, reducing system stress and enhancing economic performance. Incorporating all the listed technologies achieves a total system cost of $4,866.7, marking a 6.97% decrease in operational costs compared to Scenario 2, along with a 2.1% reduction in emissions compared to Scenario 1. These results affirm the framework's potential to meet both economic and environmental targets effectively.

CONCLUSION

This study proposes a MADRL-based energy management framework for MEMG systems that integrates physical and environmental constraints to achieve the Sustainable Development Goals (SDGs). The framework optimizes energy distribution through dynamic coordination of units to balance production and consumption and improve both cost efficiency and emission reduction. The simulation results highlight the adaptability of the system, which is supported by well-defined states, actions and reward functions, ensuring robust performance in different scenarios. In addition, flexible resources such as electric vehicle parking, multi-energy storage and demand response programs contribute to a more robust planning model that balances demand and supply fluctuations. By accounting for energy price uncertainties with a robust optimization approach, the framework provides a versatile solution that advances modern energy systems towards sustainable, cost-efficient and reliable operation.

NOMENCLATURE

P, H, Q	Electric, Heat, cooling power
η	Efficiency coefficient
λ	Price coefficient
Ch/Dch	Charge /discharge
γ	Participation factor
C	Cost of operation of each unit

REFERENCES

[1] P. Boza and T. Evgeniou, "Artificial intelligence to support the integration of variable renewable energy sources to the power system," *Applied Energy*, vol. 290, p. 116754, 2021.

[2] S. SeyedGarmroudi, G. Kayakutlu, M. O. Kayalica and Ü. Çolak, "Improved Pelican optimization algorithm for solving load dispatch problems," *Energy*, vol. 289, p. 129811, 2024.

[3] T. Zhang and B. Sobhani, "Optimal economic programming of an energy hub in the power system while taking into account the uncertainty of renewable resources, risk-taking and electric vehicles using a developed routing method," *Energy*, vol. 271, p. 126938, 2023.

[4] C. Guo, X. Wang, Y. Zheng and F. Zhang, "Real-time optimal energy management of microgrid with uncertainties based on deep reinforcement learning," *Energy*, Vols. 283, Part C, p. 121873, 2022.

[5] A. Pigola, P. R. da Costa, L. C. Carvalho, S. L. F. da, K. C. Terezinha and E. A. Maccari, "Artificial Intelligence-Driven Digital Technologies to the Implementation of the Sustainable Development Goals: A Perspective from Brazil and Portugal," *Sustainability*, vol. 13, no. 24, 2021.

[6] L. Ding, Z. Chuanzhi, Z. Peng, L. Wanting, W. Xin, L. Yuqi and X. Shuqing, "Deep reinforcement learning for real-time economic energy management of microgrid system considering uncertainties," *Frontiers in Energy Research*, vol. 11, 2023.

[7] J. A. A. Silva, J. C. López, N. B. Arias, M. J. Rider and L. C. d. Silva, "An optimal stochastic energy management system for resilient microgrids," *Applied Energy*, vol. 300, p. 117435, 2021.

[8] V. Khaligh, A. Ghezelbash, M. Mazidi, J. Liu and J.-H. Ryu, "P-robust energy management of a multi-energy microgrid enabled with energy conversions under various uncertainties," *Energy*, vol. 271, p. 127084, 2023.

[9] T. Chen, Y. Cao, X. Qing, J. Zhang, Y. Sun and G. A. Amaratunga, "Multi-energy microgrid robust energy management with a novel decision-making strategy," *Energy*, Vols. 239, Part A, p. 121840, 2022.

[10] Y. Ji, J. Wang, J. Xu, X. Fang and H. Zhang, "Real-Time Energy Management of a Microgrid Using Deep Reinforcement Learning," *Energies*, vol. 12, 2019.

[11] Y. Shang, W. Wu, Z. M. Jianbo Guo, Z. L. Wanxing Sheng and C. Fu, "Stochastic dispatch of energy storage in microgrids: An augmented reinforcement learning approach," *Applied Energy*, vol. 261, pp. 114423,, 2020.

[12] Y. Yoldas, S. Goren and A. Onen, "Journal of Modern Power Systems and Clean Energy," *Optimal Control of Microgrids with Multi-stage Mixed-integer Nonlinear Programming Guided Q-learning Algorithm*, vol. 8, pp. 1151-1159, 2020.

[13] R. Vinuesa, H. a. L. I. Azizpour, M. Balaam, V. Dignum, S. Domisch, A. Felländer, S. D. Langhans, M. Tegmark and F. Fuso Nerini, "Stochastic dispatch of energy storage in microgrids: An augmented reinforcement learning approach," *Applied Energy*, vol. 261, p. 114423, 2020.

[14] Z. Fan, Z. Yan and S. Wen, "Deep Learning and Artificial Intelligence in Sustainability: A Review of SDGs, Renewable Energy, and Environmental Health," *Sustainability*, vol. 15, 2023.

[15] M. A. Mirzaei, K. Zare, B. Mohammadi-Ivatloo, M. Marzband and A. Anvari-Moghaddam, "Techno-economic, environmental and risk analysis of coordinated electricity distribution and district heating networks with flexible energy resources," *IET Renewable Power Generation*, vol. 17, no. 12, pp. 2935-2949, 2023.

[16] Y. Meng, S. A. Mansouri, A. R. Jordehi and M. Tostado-Véliz, "Eco-environmental scheduling of multi-energy communities in local electricity and natural gas markets considering carbon taxes: A decentralized bi-level strategy,," *Journal of Cleaner Production*, vol. 440, p. 140902, 2024.

ISBN: 978-618-5765-04-0
ISSN 3057-4269

Improving the Power Distribution Grid Resilience through the Integration of Distributed Energy Resources: Case Studies in Greece

Aikaterini Gkika
Department of Geology & Geoenvironment
National & Kapodistrian University of Athens
Athens, Greece
aikgkika@gmail.com

Fotios Gakis
Network Users Department
Hellenic Electricity Distribution Network Operator (HEDNO S.A.)
Athens, Greece
f.gakis@deddie.gr

Efstratios Zacharis
General Management
Hellenic Electricity Distribution Network Operator (HEDNO S.A.)
Athens, Greece
e.zacharis@deddie.gr

Ilias Manolis
Department of Environment
University of the Aegean
Athens, Greece
iliasmanolis@hotmail.com

***Abstract*—With the energy transition well underway, grid operators are increasingly facing the challenges of maintaining reliability but also ensuring the resilience of the energy system, i.e., its ability to adapt to changing conditions, as well as withstand and recover from disruptive events. Resilience becomes, hence, an emerging concept of top priority for power distribution utilities, encompassing the components of robustness, redundancy, resourcefulness, response, and recovery. In this context, the contribution of distributed energy resources to the power system resilience is crucial to be examined, since such resources can add flexibility capacity already from the planning stage. This paper aims to highlight the relation of grid resilience with renewable-integrated power grids and storage schemes by capturing lessons learned from case studies in Greece, such as residential (rooftop) applications and large-scale pilot projects. A holistic climate change adaptation approach aimed at grids to be resilient by design can mitigate climate-related disruptions, especially in highly vulnerable countries like Greece.**

Keywords—Climate Change, Distributed Energy Resources, Electricity Distribution Networks, Extreme Weather Events, Renewable Energy Sources, Resilience

INTRODUCTION

The energy transition represents a real change of paradigm at the distribution level, and Distribution System Operators (DSOs) are expected to become the backbone of the electricity system that will become the dominant energy carrier over the coming decades. In parallel, it is clear that the threat landscape at the global level is currently very complicated and DSOs are faced with concurrent challenges, such as:

- The need for transformation and fundamental changes both in assets and system operation towards the net zero emissions commitment (more grid investments, network reinforcement stemming from rapidly expanding distributed generation, increased network planning and forecasting of innovative technologies, flexibility management, etc.);
- The expansion of the scope of their responsibilities and the increasing expectation to take on a broader leadership role in the resilience of the communities they serve, including critical facilities, cyber-attacks, and societal outcomes;
- The impacts of climate change (i.e., changing trends, increasing variability, greater extremes, and large inter-annual variations in climate parameters in some regions) across the entire energy supply chain;
- The requirement to maintain at steep costs the aging network assets or proceed with essential renovations;
- The operational and regulatory implications of the above challenges, as well as the increased liability losses to third parties which in some cases come at a cost that utilities are unable to bear.

Nonetheless, climate change is considered one of the highest risks in severity that DSOs will face in the upcoming years. According to the Global Risks Report 2023 of the World Economic Forum, climate mitigation and adaptation efforts are set up for a risky trade-off [1]. Climate risks are the core focus of global risk perceptions over the next decade – and are the risks for which we are seen to be the least prepared. The discrepancy between what is politically practicable and what is scientifically required to reach the net zero target has been made clear by the lack of significant, coordinated progress on climate action targets.

The acceleration of the frequency and intensity of extreme climate incidents represents a multitude of risks for energy systems. Extreme temperatures, precipitation, and winds cause numerous breakdowns of the electricity networks. Indeed, in the EU, according to the monthly statistics of ENTSO-E, around 33% of the power interruptions between 2016 and 2020 were caused due to extreme weather [2]. In consequence, DSOs face large amounts of deterioration or even destruction of their infrastructure. They also need to mobilize emergency teams to fix the electricity grid and keep the lights on.

In this context, the concept of power system resilience emerges as an imperative need and is increasingly established

ISBN: 978-618-5765-04-0
ISSN 3057-4269

as a policy priority, especially for critical entities. However, resilience is not a very new concern in Europe and it has been included as a term in major regulations (i.e., Regulation (EC) No 714/2009 of the European Parliament and the Council, Regulation (EU) No 347/2013 of the European Parliament and of the Council). Resilience is even more important for today's power companies, though, due to the growing concern over the disastrous effects of climate change on grid infrastructure.

The definition of resilience has generated an intricate and continuous discussion due to its multifaceted nature, encompassing several aspects such as the correlation between resilience and reliability [3], event-specific vs agnostic, and qualitative versus quantitative indices [4]. According to the Intergovernmental Panel on Climate Change (IPCC), a system's resilience is defined as its ability to anticipate, absorb, and recover from the effects of harmful events efficiently and within a reasonable timeframe. The US Federal Energy Regulatory Commission defines grid resilience as the "ability to withstand and reduce the magnitude and/or duration of disruptive events, which includes the capability to anticipate, absorb, adapt to, and/or rapidly recover from such an event". While power distribution networks have traditionally been regarded as reliable (mainly concerning energy supply) against the most common threats, recent extreme weather events from around the world have highlighted the growing importance for distribution grids to achieve high levels of resilience as well, to mitigate the effects of low-probability, high-risk events and recover quickly. As shown in the graph below, resilience is divided into operational and infrastructure resilience. Following a system degradation, the key is to absorb the shock, bounce back to normal operation with minimal downtime or business disruptions, and adapt operation.

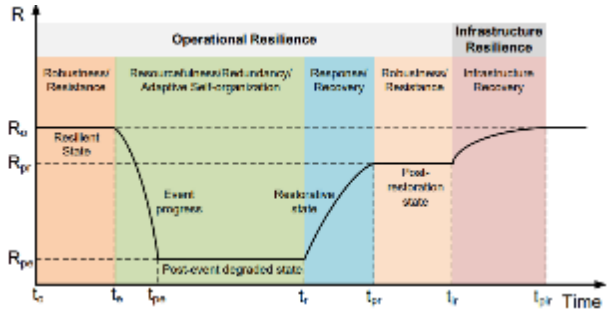

Figure 1: Operational vs Infrastructure Resilience [5]

THE ROADMAP TOWARDS RESILIENCE

Initiatives for Building Power Grid Resilience

Extreme weather events present risks to grid integrity. For instance, flooding can inundate key infrastructure, such as substations or transformers, blacking out large areas; high winds can down overhead power lines; extreme heat can cause electricity demand to exceed system capacity, and also cause lines to sag into trees. Hence, withstanding and quickly recovering from such incidents must be a critical function of modern power distribution grids. An effective resilience enhancement strategy is based on the following pillars:

- **Hardening the grid.** Hardening means strengthening the network by applying a variety of solutions such as raising seawalls around key assets, restoring natural coastal protections, undergrounding overhead power lines, relocating key assets, replacing wooden poles with concrete ones, improving line materials, such as high-temperature, low-sag conductors, and expanding tree-trimming programs. However, although these measures can be simple in concept, they must be resilient for the long term, considering future changes in sea level, temperatures, storm intensity, etc.
- **Smartening the grid**. In recent years, utilities have begun to deploy smart grid technologies, from advanced metering at the customer level to enable automatic outage detection and service restoration, to sensors and controls to enable rapid detection, isolation, and restoration of service at the circuit and substation levels. After an event, the data collected through these technologies can be used to find opportunities for further resilience improvements.
- **Distributing generation**. Extreme weather can force power outages by driving power demand past the limits of available generation resources. Damage to the distribution system also limits restoration efforts, even if generation capacity is available. One practice applied in other countries is to increase distributed generation (DG) resources; by increasing the number of generation sources, diversifying their fuel types, and locating them in a more distributed fashion around the service area, DG can both limit the risk of outages and allow faster restoration of service. Long-term access to reliable energy through distributed RES reduces vulnerability of local communities to climate change and increases their capacity for self-resilience and adaptation, without needing significant upfront infrastructure investment [6]. Nonetheless, DG poses challenges to utilities to fully integrate such resources into planning and operational practices.
- **Optimizing business operations**. Enhanced business operations support organizational resilience, which is the capacity of an organization to anticipate, prepare for, respond to, and learn from disruptions, crises, and opportunities. It is not just about surviving a shock or bouncing back, but also about evolving and growing stronger from the experience. Towards this direction, power utilities should establish robust business operations frameworks to guide the design, execution, and improvement of business processes, systems, and resources. These frameworks provide a clear and consistent way of defining roles, responsibilities, standards, and expectations to reduce ambiguity, confusion, and errors. They also enable organizations to adapt to uncertainty and changing conditions, by supporting them to anticipate risks, threats, and vulnerabilities. Indicative actions include emergency exercises, crisis management workshops, disaster and crisis management planning, etc.

The above actions should be supported by R&D initiatives and pilot projects.

The Integration of Distributed Generation Resources

As the frequency and magnitude of extreme weather incidents become more difficult to forecast because of climate change, large generators and power grids become easier to fail and harder to restore [7]. On the other hand, enabling a wide portfolio of DG such as solar plus batteries and microgrids can make the overall energy system more versatile and efficient and less prone to power outages or supply problems [8, 9], thus demonstrating proven resilience benefits associated with the ongoing evolution of grid technologies [10, 11]. When centralized systems are disabled by a disaster, DG can enable some parts of the grid to operate and serve critical loads. In this case, production loss can be only partial during long-

ISBN: 978-618-5765-04-0
ISSN 3057-4269

duration outages on the broader electricity grid (thus leading to limited voltage disruptions at the local level in comparison with the disruption that would have been caused by the loss of a large production unit). Moreover, the shift to serving loads with decentralized and more DG has driven the need for network renovation and modernization using telemetering [12]. The traditional supervisory control and data acquisition (SCADA)-based control and monitoring of power systems is reliant on sensors, monitored by intelligent electronic devices (IEDs), which can facilitate restoration efforts.

Furthermore, storage technologies (i.e., batteries) coupled with renewable energy sources (RES) can provide power support to local autonomous grids or weak grids inside islanding areas during long-duration outages on the broader electricity grid, maximize the contribution of RES, whilst they can provide ancillary services for the DSOs, such as voltage and frequency regulation and reactive power support.

Microgrids (MGs) have also gained a lot of attention in the power system market while constituting a strategy to increase energy resilience and enhance the ability to serve an installation's electrical loads during a contingency situation. MGs are small-scale energy systems including DG located close to the local load demand, energy storage and control units which could work in a grid-connected or off-grid mode, ensuring the power supply for a defined region [13]. Hence, they tend to become both the source of energy generation and consumption simultaneously. Microgrid solutions can integrate with the grid to be part of its operational and resource mix, and can also "island" and operate autonomously, if needed, to keep running during grid outages, thus providing a reliable power source to critical infrastructure facilities, like hospitals, emergency centers, military installations, etc.

Due to their ability to operate in a controlled, coordinated way, when connected to the main power grid and in islanded mode during disturbances, resilience is enhanced as follows (see Figure below) [14]:

- **Resilience at the distribution level**. MGs connected to the distribution system (MG2-MG4) can function as power sources to supply the local demand of the distribution system if a failure isolates the distribution system. Furthermore, to reduce load shedding, the distribution system may be divided into self-sufficient MGs by leveraging the numerous connected DERs.
- **Resilience at the MG level.** If an individual MG (MG4) is isolated due to a failure in the distribution system, it can effectively operate in islanded mode by appropriately allocating its resources to meet its minimum critical load.

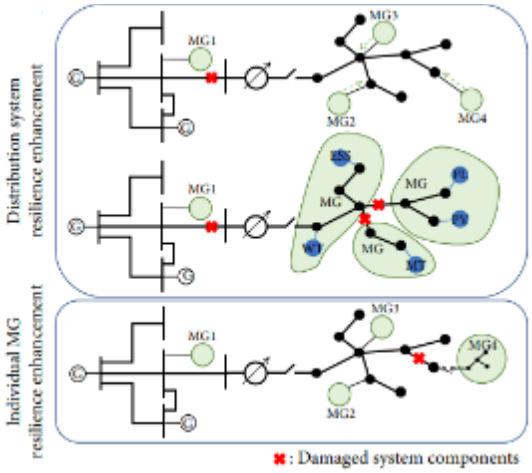

Figure 2: The Role of Microgrids for System Resilience [14]

In the future, an energy community could constitute a MG to ensure the power supply of the community's consumers.

Challenges for the Transition to Islanded Mode

The planning and operation of electricity distribution grids are undergoing significant changes due to RES integration. Uncertainty analysis should be considered for both generator scheduling and for evaluating physical vulnerabilities, i.e., natural disasters. Furthermore, the multiplication of smart electronic devices to enable DERs has contributed to the grid's increased digitalization, which raises cybersecurity concerns and necessitates monitoring [12].

Hence, although the MG concept and its benefits buck the trend of reliance on centralized systems, their operation management is essential to mitigate the unbalanced power supply and increase its quality in the case of disconnection from the grid [13]. To fully utilize dynamic entities such as MGs, more intelligent control and improved monitoring are needed. MGs need to be able to operate both autonomously and intelligently when connected to the grid. There are also many technical challenges for the effective transition into the islanded mode of operation [15]:

- **Earth fault protection requirements.** The earthing requirements should be revised to ensure sufficient protection both in grid-connected and islanded modes of operation.
- **Quality of supply to customers.** The operation of portions of the network in islanded mode may create some difficulties in the operation of distribution network automation systems and affect the continuity of supply. Faults on networks cause interruptions, increasing the related indexes, i.e., System Average Interruption Duration Index (SAIDI) and System Average Interruption Frequency Index (SAIFI). During the operative cycles of the circuit breaker operating in automation and where the automation relies on voltage sensing, there could be a significant degradation of automation's effectiveness.
- **Synchronizing & reclosing issues**. Synchronization needs a way of comparing the voltages between the island and the system with the appropriate measuring and control equipment to ensure the voltage differences, in phase and magnitude, are within safe limits before reclosing the switch. Thus, switching points need to be appropriately equipped to perform synchronization. Almost none of this equipment currently exists in DSOs' substations because there has

ISBN: 978-618-5765-04-0
ISSN 3057-4269

been no need.

- **Regulatory and market issues.** During normal operation, customers receive power at frequencies and voltages within precisely defined ranges. However, when an unintended island has formed, the supply-dispatch-frequency management responsibili-ty is currently not determined through regulations:
    - No single party is structurally in control of frequency or voltage.
    - DSOs do not have contracts to dispatch generation connected to their networks.
    - In many EU countries, there is no clear regulatory or legal framework for the liability of DSOs for islanded operation outside of normal voltage and frequency limits, nor for the risks posed by unearthed and/or unprotected operation.

CASE STUDIES IN GREECE

Being highly vulnerable to the effects of climate change, and in alignment with the ambitious European goals for climate neutrality by 2050, the Hellenic Electricity Distribution Network Operator (HEDNO S.A.) has taken several actions for the promotion of renewables in Greece. More specifically, HEDNO closed the year 2022 with a total power of 6.5 GW, i.e., an increase of 64% between the period 2019-2022. The total power is estimated to have exceeded 8.7GW at the end of 2023, while, according to HEDNO's planning, the total power is estimated to reach around 10GW in 2024. The interconnection of islands is also a point to consider since it can enhance the stability and resilience of systems that have been weak up to now.

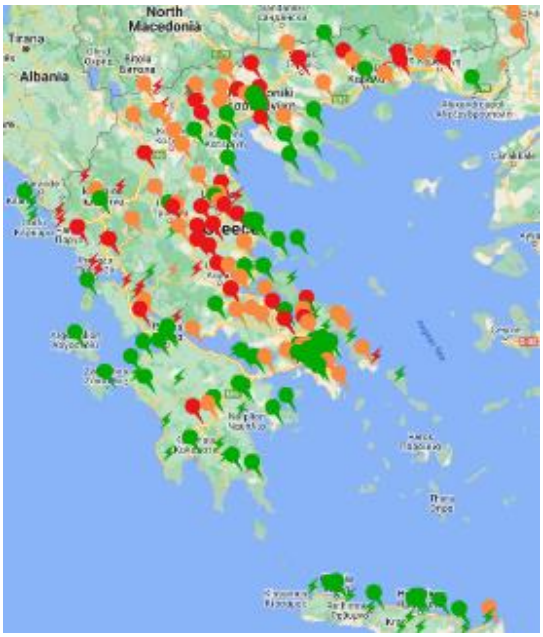

Figure 3: The Renewables Landscape in Greece – Power Absorption Capabilities

The above Figure illustrates the renewables landscape in Greece, based on data provided by HEDNO at the end of 2023. The map shows the saturated regions (red), regions with limited capacity (orange), and regions with available hosting capacity (green). The red regions have reached high levels of RES penetration, meaning that RES could be utilized to improve resilience.

Residential (Rooftop) Applications

In Greece, a subsidy program is established for residential applications up to 10kW (PVs and batteries). According to the program, the excess energy from a PV plant installed at the premises of a consumer is injected into the grid and can be used at a later time to offset consumption during times when onsite generation is absent or not sufficient. The Battery Energy Storage System (BESS) is operated to increase the PV self-consumption so that the energy absorbed by the grid is reduced. As presented in Figure 4, the PV energy is stored at noon hours to be used at afternoon hours. Since regulated charges are mainly volumetric-based (i.e., imposed in the amount of energy absorbed), the prosumer can achieve an extra reduction to his/her bill.

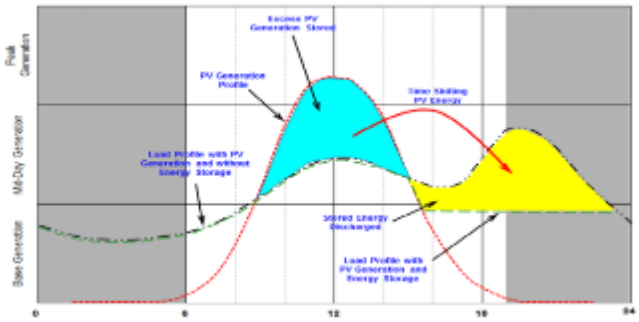

Figure 4: The Role of Microgrids for System Resilience

The operating modes of a BESS are described in detail in the following Table. The safety control of the installation is required for both operating modes.

Table 1: Operation of a Battery Energy Storage System (BESS)

Mode of Operation	Description
Normal Operating Conditions	• If PV production is higher than the load, then the battery is charged AND when the battery is full, power is injected from the PV into the main grid • If PV production is lower than the Load, then the battery is discharged AND when the battery is empty, power is absorbed by the main grid
In case of emergency	• The battery undertakes the role of the main grid AND self-production must cover at least the critical loads • In this case, the following must be noted: o The inverters should be appropriately specified to be able to operate in islanded mode. o The DSO determines the requirements so that there is no power injection into the grid. o The switching device from the connected to islanded mode should have a "Loss of Mains" protection.

Indicative configurations of residential applications with PVs and storage are presented in the following Figures 5-7.

- **Configuration 1: Power Supply from BESS.** After grid failure, the PV inverter is disconnected from the grid due to its "Loss of Mains" protection. The BESS converter remains connected and supplies the loads inside the installation.
- **Configuration 2: Power Supply from BESS & PV.** The whole installation is disconnected from the grid and the hybrid converter remains connected to supply the loads.
- **Configuration 3: Power Supply of Critical Loads from BESS & PV.** The hybrid converter possesses one output for normal operation that is disconnected during grid failure and a second "emergency" output used to supply critical loads, which are separated from the installation in case of grid failure.

ISBN: 978-618-5765-04-0
ISSN 3057-4269

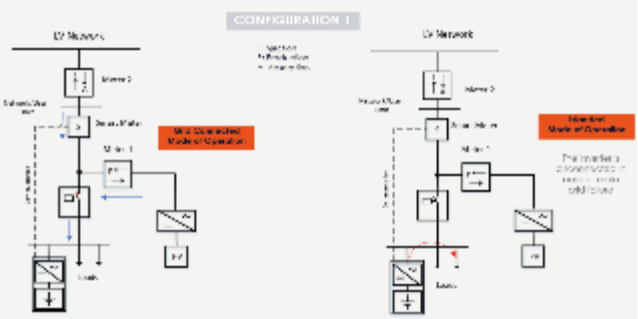

Figure 5: Configuration 1 of Residential Application – Power Supply from BESS

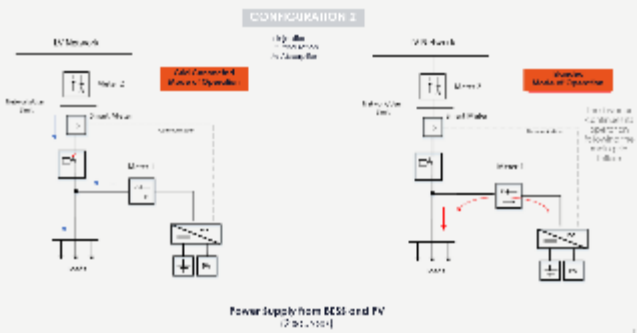

Figure 6: Configuration 2 of Residential Application – Power Supply from BESS and PV

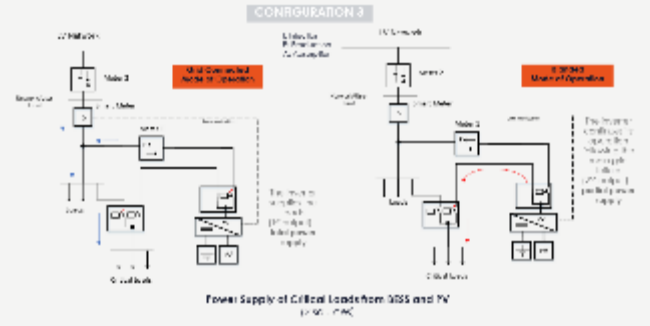

Figure 7: Configuration 3 of Residential Application – Power Supply of Critical Loads from BESS and PV

Large-scale Pilot Projects

The Tilos Hybrid Microgrid

To ameliorate energy supply security and energy autonomy of the Aegean islands, an integrated solution was deployed in the Greek Tilos island in the framework of the Tilos-Horizon 2020 program. Standing at a distance of 240 n. miles from the Greek mainland, Tilos belongs to a very special group of remote, small-scale European islands. The solution was based on the exploitation of the existing RES potential in conjunction with the application of an appropriate energy storage scheme, and complementary smart-grid elements [16].

Given the successful implementation of the Tilos project the first-ever batter-based, wind, and PV hybrid power station in Greece has been developed. At the same time, an integrated MG has also been developed on the island and several innovative elements have been introduced, altogether transforming Tilos into an exemplary island case in terms of local-scale clean energy production and management. This comprised a breakthrough, not only for Tilos but also for the Greek market as a whole, disrupting the norms of the past and presenting a new energy paradigm and solution for the electrification of island regions. The integrated Tilos energy solution suggests an energy MG that is normally found to interact with the host electricity system of Kos and Kalymnos, or, in rare cases, operated in isolation (such as in cases of emergency or MG testing).

Figure 8: Description of Tilos Island MG and Geographical Location of Main Assets [17]

Concerning the power generation sector, the main assets that are currently in operation on Tilos include [16]:

- Tilos hybrid power station, comprising an 800 kW medium-scale wind turbine, a 160 kWp PV station, and an 800 kW / 2.88 MWh integrated BESS.
- The backup diesel genset of 1.45 MW
- Distributed, small-scale PV installations supporting early prosumer schemes including two monitored PV installations (capacity of 3.36 kWp at local residence and 4.93 kWp at the Tilos info-kiosk / EV charging station respectively) and four non-monitored PV installations (capacity of ~ 10kWp in total).

The Tilos island MG is a great success story introducing several important innovative characteristics in the European market, like the combined operation of a wind turbine and a PV installation, the application of new technology BESS, the installation of a DSM network/platform and the development of a large number of reliable forecasting algorithms.

The Lighthouse Project in Chania Airport

The Lighthouse Project in Chania Airport is particularly pioneering in a traditional source of pollutants to drastically reduce the plant's environmental footprint. It includes the conversion of Chania Military Airport (115 Combat Wing) into a "green" military unit, covering all needs for electricity, heating, and cooling of the facilities 100% from RES. As part of the project, the facility is equipped with state-of-the-art intelligent energy management systems, without reducing its operational capabilities in any way. The total Capital Expenditures for the entire system were equal to 3,5 M€, while the annual benefit of the Unit's complete exemption from the cost of supplying electricity and meeting heating needs will exceed 400,000 €.

It is worth mentioning that Chania Airport was one of the world's first facilities to receive Net Zero Energy Airport & Net Zero Carbon Emissions Airport Certifications. The Table below provides a short description of the project services and equipment, as well as the certifications gained.

ISBN: 978-618-5765-04-0
ISSN 3057-4269

Table 2: The Lighthouse Project in Chania Airport in a Nutshell

Category	Description
Services	• Interventions in the AC systems and lighting of buildings and facilities to save energy and create thermal comfort for Combat Wing staff • Training of the appropriate technical staff of the Air Force for the needs of business operation, monitoring, and maintenance of the entire system. • System design and annual production considered the future heavy use of electric vehicles and their charging inside the Combat Wing
Equipment	• PV installation of 1.7 MWp (net metering scheme), to completely exempt the Unit from the cost of supplying electricity which currently exceeds € 400,000 / year. The power of the PV was calculated based on the annual needs increased by 20% due to the addition of the electrification load and future needs. The power factor has been regulated to be equal to 1 – the compensation of reactive power has been accomplished through innovative equipment • An energy storage system with very large capacity Lithium-ion cells using liquid-cooled batteries - to ensure an uninterrupted power supply for the airport, even during grid outages, for days or even weeks based on weather conditions. A seamless connection/reconnection of the batteries has been achieved for an uninterruptible power supply of loads in case of a power outage (synchronization check for voltage, frequency, and phase). Tests have been completed and have confirmed the continuity of supply upon power disruptions or interruptions. • Smart energy management and control system of the energy produced and consumed at the plant's facilities, to enhance resiliency and substantially improve energy efficiency. • Electric car charging infrastructure to electrify transport with RES and exempt it from the use of fossil fuels • Supply of electric bicycles for professional use
Certifications (expected to be concluded in the upcoming period)	• Certification as a Net Zero Carbon Emissions facility based on the Carbon Accreditation program of the Airport Council International (ACI) • Certification as Net Zero Energy Airport according to the National Laboratory of the US Department of Energy for Military Installation specifications

The installation includes the following equipment:

- Trina Solar PV Panels
- Inverter PV and converter BESS: Power Electronics (central)
- BESS: Leclanche, CATL LFP cells, liquid-cooled, with a lifespan of 6,000 cycles for charge/discharge from 2,5% to 100% (2.6 MWh)
- Steel base structure with magnelis coating

The MG is connected to the MV grid through a circuit breaker with the appropriate protection schemes imposed by the DSO, and a synchronism check to ensure that when the MG is connected to the grid, the voltage vectors do not differ. During grid failure, this circuit breaker 'opens', while the rest three downstream circuit breakers, protecting the loads, the PV, and the BESS, remain 'closed' to permit the energy flow from BESS and/or PV to the loads. Only in case green energy is not sufficient, the backup generator starts to operate.

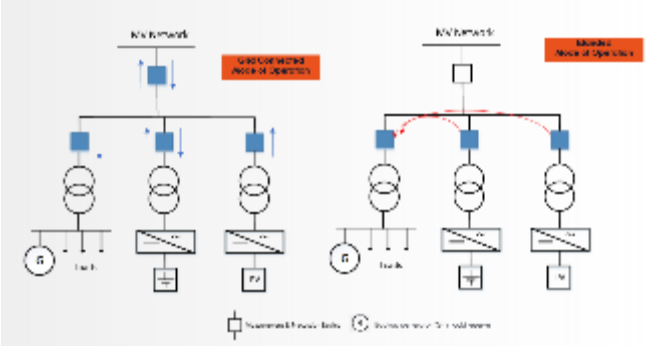

Figure 9: The Lighthouse Project in Chania Airport - Grid-connected and Islanded Modes of Operation

Indicative photos of the project are presented in Figure 9.

Figure 10: The Lighthouse Project in Chania Airport: PV panels and BESS

CONCLUSION

The energy transition poses new challenges for the DSOs. Significant grid development will be required in the longer term; it is estimated that annual investments in distribution grids should increase from 50% to 70% over the period 2020-2030. Moreover, to be able to connect RES and new loads, grids will need to be significantly expanded and reinforced. In addition, they will need to be modernized, since they are still relatively "blind". To properly manage the future system, much more observability and controllability will be required. In this context, DSOs should also focus on enhancing system's adaptive capacity to withstand potentially disruptive events through infrastructure hardening (hard resilience / focus on resistance) and on improving system's coping capacity so that, if disrupted, it can rapidly recover operations, minimizing downtime and maintaining an adequate functionality (soft resilience / focus on absorption). Potential future research could integrate forecasting load demand and renewable generation models to remove the uncertainty of using historical data.

REFERENCES

[1] World Economic Forum (WEF), "The Global Risks Report 2023", 18th Edition, Insight Report, 11 January 2023.

[2] European Commission (2018), "Study on the quality of electricity market data of transmission system operators, electricity supply

ISBN: 978-618-5765-04-0
ISSN 3057-4269

disruptions, and their impact on the European electricity markets", Final Report, March 2018

[3] B. Vaagensmith, T. Mcjunkin, K. Vedros, J. Reeves, J. Wayment, L. Boire, C. Rieger, J. Case, "An Integrated Approach to Improving Power Grid Reliability: Merging of Probabilistic Risk Assessment with Resilience Metrics", In *Proceedings of the 2018 Resilience Week*, Denver, CO, USA, pp. 139–146, 2018.

[4] S. Hosseini, K. Barker, & J. E. Ramirez-Marquez, "A Review of Definitions and Measures of System Resilience", *Reliability Engineering and System Safety*, 145, 47–61, 2016.

[5] M. Panteli & P. Mancarella, P., "The Grid: Stronger, Bigger, Smarter?: Presenting a Conceptual Framework of Power System Resilience". IEEE Power and Energy Magazine. Vol. 13. No 3, pp. 58-66, May-June 2015.

[6] IRENA, "Bracing for Climate Impact: Renewables as a climate change adaptation strategy", International Renewable Energy Agency, Abu Dhabi, 2021.

[7] I. Oleinikova, A. Iliceto, & E. Hillberg, "Flexibility for resilience : how can flexibility support power grids resilience?", European Commission, Directorate-General for Energy, 2022.

[8] O. Erdinc, N. G. Paterakis, & J. P. S. Catalão, "Overview of insular power systems under increasing penetration of renewable energy sources: Opportunities and challenges", *Renewable and Sustainable Energy Reviews*, vol. 52, pp. 333–346, 2015.

[9] P. Bertheau & P. Blechinger, "Resilient solar energy island supply to support SDG7 on the Philippines: Techno-economic optimized electrification strategy for small islands", *Utilities Policy*, vol. 54, pp. 55–77, 2018.

[10] M. Dyson & B. Li, "Reimaging Grid Resilience", A Framework For Addressing Catastrophic Threats to the US Electricity Grid in an Era of Transformational Change, Rocky Mountain Institute, 2020.

[11] A. Kartalidis, K. Atsonios, & N. Nikolopoulos, "Enhancing the self-resilience of high-renewable energy sources, interconnected islanding areas through innovative energy production, storage, and management technologies: Grid simulations and energy assessment", *International Journal of Energy Research*, 2021.

[12] P. Cicilio, D. Glennon, A. Mate, A. Barnes, V. Chalishazar, E. Cotilla-Sanchez, B. Vaagensmith, J. Gentle, C. Rieger, R. Wies et al., "Resilience in an Evolving Electrical Grid", *Energies* 2021, 14, 694, 2021.

[13] N. Shirzadi, H. Rasoulian, F. Nasiri, & U. Eicker, "Resilience Enhancement of an Urban Microgrid during Off-Grid Mode Operation Using Critical Load Indicators", *Energies*, 15, 7669, 2022.

[14] E-I. E. Stasinos, D. N. Trakas, & N. D. Hatziargyriou, "Microgrids for power system resilience enhancement", *iEnergy*, vol. 1, issue 2, 2022.

[15] EU DSO, "Entity position paper on un-intended islands in the context of ENTSO-E proposals on Rate of Change of Frequency (RoCoF) and Grid Forming Capability (GFC)", February 2023.

[16] J. K. Kaldellis, "Supporting the Clean Electrification for Remote Islands: The Case of the Greek Tilos Island", *Energies* 2021, 14, 1336. https://doi.org/10.3390/en14051336, 2021

[17] K. Kaousias, T. Xygkis, G. Papoutsis, E. Stavropoulou, T. Patsaka, C. Kourelis et al., "The European Research Project TILOS", CIGRE C6-204_2018, 2018

ISBN: 978-618-5765-04-0
ISSN 3057-4269

Wastewater Recycling in Dairy Industry using Membrane Processes

David Horňák
Institute of Processes Engineering, Faculty of Mechanical Engineering
Brno University of Technology
Brno, Czech Republic
david.hornak1@vut.cz

Michal Touš
Institute of Processes Engineering, Faculty of Mechanical Engineering
Brno University of Technology
Brno, Czech Republic
michal.tous@vut.cz

***Abstract*— The dairy industry generates a significant amount of wastewater, presenting a potential opportunity for recycling that could mitigate environmental impact and provide economic benefits for dairies. Membrane processes are suitable technologies for wastewater recycling. Numerous studies have been conducted on this topic. However, they are usually dealing with application on a specific separate stream of wastewater such as flushing water or vapour condensate. In this contribution, we focus on the recycling of the mixture of all effluents from a dairy plant, which is typically highly polluted and more common in the practice. The main goal of this paper is to experimentally assess the efficiency of reverse osmosis in treating real dairy wastewater. The experimental apparatus consists of pre-treatment filtration, ultrafiltration and two-stage reverse osmosis. The COD removal efficiency exceeded 99.8%, and the final COD concentration was approximately 80 mg/L. These results demonstrate that the reverse osmosis is a suitable method for the recycling of this type of wastewater. However, heavy fouling occurred during pre-treatment and ultrafiltration, which limits its practical application. Future research will build on these findings and will focus on the fouling problem and long-term operation.**

Keywords—sustainability, reverse osmosis, water reuse, fouling

INTRODUCTION

Water scarcity and pollution are growing issues in many countries. Industry consumes large amounts of drinking water, much of which is discharged as wastewater. Recycling this wastewater can significantly reduce industrial water consumption and provide opportunities to recover valuable by-products for reuse or sale. The food industry is a major consumer of water, with the dairy sector alone accounting for up to 30%. Wastewater is generated during dairy production, with levels ranging from 0.3 to 10 L_{ww}/L_{milk} [1]. The majority of this wastewater is generated from the cleaning of equipment and tools, as well as from various process operations such as pasteurisation, high temperature treatment, or cooling [2]. Increased recycling of dairy wastewater could reduce water consumption, contributing to the sustainability and environmental friendliness of the industry. Additionally, wastewater recycling offers economic benefits for dairies, as recycled water can be used for various thermal processes such as boilers, heat exchangers, and cooling towers, as well as cleaning operations, such as tanks, floors, and tools [3], [4]. The recovery of secondary raw materials from wastewater, such as milk proteins, lactose, or caseins, has potential applications in pharmaceutical and biotechnological products, as well as in certain dairy products [3], [5]

Membrane technologies, including ultrafiltration (UF), microfiltration (MF), reverse osmosis (RO), membrane distillation (MD), or forward osmosis (FO), are becoming increasingly popular in the field of industrial wastewater recycling due to their advantages over traditional methods. The main benefits of membrane processes are their high efficiency in removing pollutants, scalability, small built-up area, no use of chemicals, and ability to separate secondary raw materials [6], [7]. However, these processes also have some drawbacks, such as membrane fouling and the cost of membrane replacement. Furthermore, some technologies, such as reverse osmosis, may require higher energy consumption.

The recycling of dairy wastewater using these technologies is not yet widely implemented in industrial practice, despite the increasing attention it receives in the literature. Several studies have investigated the experimental treatment of dairy wastewater using membrane processes. Vourch et al. [8] investigated the treatment of flushing dairy wastewater from skim milk and whey processing by reverse osmosis. TOC (total organic carbon) removal efficiency was greater than 99% for all wastewater samples. Additionally, after the second treatment with reverse osmosis TOC was reduced below the French drinking water standard limit (TOC < 2 mg/L). The treatment of dairy wastewater by microfiltration, nanofiltration and reverse osmosis was studied by Bortoluzzi et al. [9]. The most efficient configuration was MF + RO with reductions of 100% turbidity, 100% colour, 94% TKN (total Kjeldahl nitrogen) and 84% TOC. Brião et al. [3] compared nanofiltration and reverse osmosis as treatment methods for simulated and real dairy wastewater. The RO showed better performance in terms of rejection efficiency as well as fouling propensity. Although the COD (chemical oxygen demand) reduction was high (88 mg/L after the first stage and 42 mg/L after the second stage), it was still higher than drinking water quality requirements. A comprehensive review of membrane processes used for water reuse in the food processing industry including the dairy industry has been conducted by Garnier et al. [2]. In general, it can be stated that reverse osmosis is capable of efficiently treating of dairy wastewater. However, most of the mentioned articles dealt with specific separate streams of dairy wastewater such as rinse water, vapour condensate or water from flash coolers. In practice, dairy wastewater is usually a mixture of all plant effluents, including grey water or toilet water. This type of wastewater is usually highly polluted and may be more difficult to treat with membrane processes. The main goal of this paper is to evaluate the efficiency of reverse osmosis on a mixture of all effluents from a dairy factory and its potential for wastewater recycling. Additionally, we identify the major limitations for

This research was conducted with the financial support of the Ministry of Education, Youth and Sports under the OP VVV grant number CZ.02.1.01/0.0/0.0/16_026/0008413 "Strategic Partnership for Environmental Technologies and Energy Production" and the internal BUT project FSI-S-23-8173 "Process Integration for Sustainability".

ISBN: 978-618-5765-04-0
ISSN: 3057-4269

the application of reverse osmosis in industrial scale. Firstly, the experimental apparatus, operating conditions and treated wastewater are described. The results of the experiment are the disclosed and discussed in more detail. Also, the shortcomings of the experiment are presented and corrective measures are proposed. Finally, the future research is presented.

MATERIALS AND METHODS

Feed Wastewater

The dairy wastewater was provided by a Czech dairy company. The wastewater was a mixture of the most effluents from the plant, including grey water and toilet water (Figure 1). A total of 100 L of wastewater was collected. The experiments were conducted on the same day as the collection in order to avoid changing the properties of the wastewater due to biological processes.

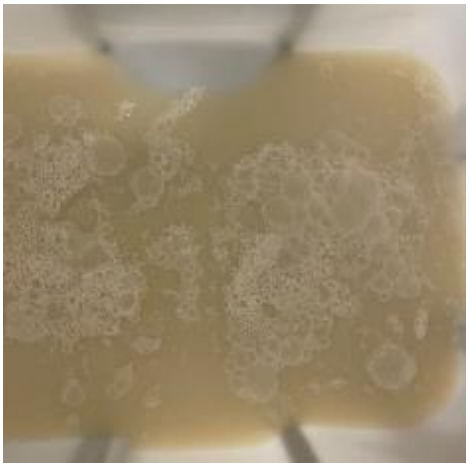

Figure 1: Feed dairy wastewater

Membranes and Apparatus

The experimental apparatus consists of three stages: pre-treatment, ultrafiltration, and reverse osmosis. The pre-treatment includes AQUA RLA nylon filter cartridge with 80 µm pore size, Pentair polypropylene filter cartridges with 25 µm and 5 µm pore size and Pentair carbon block filter cartridge with 10 µm on pore size. A hollow fibre membrane IONICORE UF 11 with 10 nm pore size was used for ultrafiltration. Reverse osmosis consists of two modules with spiral wound polyamide thin film composite membrane (RE2521-BE) from CSM company. The membrane characteristics are summarised in Table 1.

Table 1: Membranes characteristics

Treatment stage		**Parameters**						
		Manufacturer	***Material***	***Max pressure [bar]***	***Max temperature [°C]***	***Pore size [µm]***	***Rejection***	***Effective membrane area [m²]***
Pre-tretatment	***P80***	AQUA	Nylon	8	50	80	–	0.047
	P25	Pentair	Polypropylene	8	63	25	–	0.047
	P10	Pentair	Pressed activated carbon	8	82	10	–	0.047
	P5	Pentair	Polypropylene	8	63	5	–	0.047
UF		IONICORE	Polysulfone	8.5	40	0.01	–	0.025
RO		CSM	Polyamide	41.4	45	–	99.7	1.1

Additionally, the experimental apparatus consists of three storage vessels and three pumps. A simplified scheme of the apparatus is shown in the Figure 2. Storage vessels (V1–V3) were used to store the wastewater between the individual stages. Also, different pumps were used for each stage due to different requirements for wastewater flow characteristic. Pump-1 was a diaphragm pump VerderAir VA 15 PP, pump-2 was a diaphragm pump E-CHEN EC-204-600A, and pump-3 was a rotary pressure pump MWG. Pre-treatment filters (P80–P5) and ultrafiltration (UF) was used in dead-end mode, therefore only one stream came out from these modules. Two streams, permeate and retentate, came from reverse osmosis modules (RO1 and RO2). These modules were connected in series so that the retentate from the first module flows into the second module.

ISBN: 978-618-5765-04-0
ISSN 3057-4269

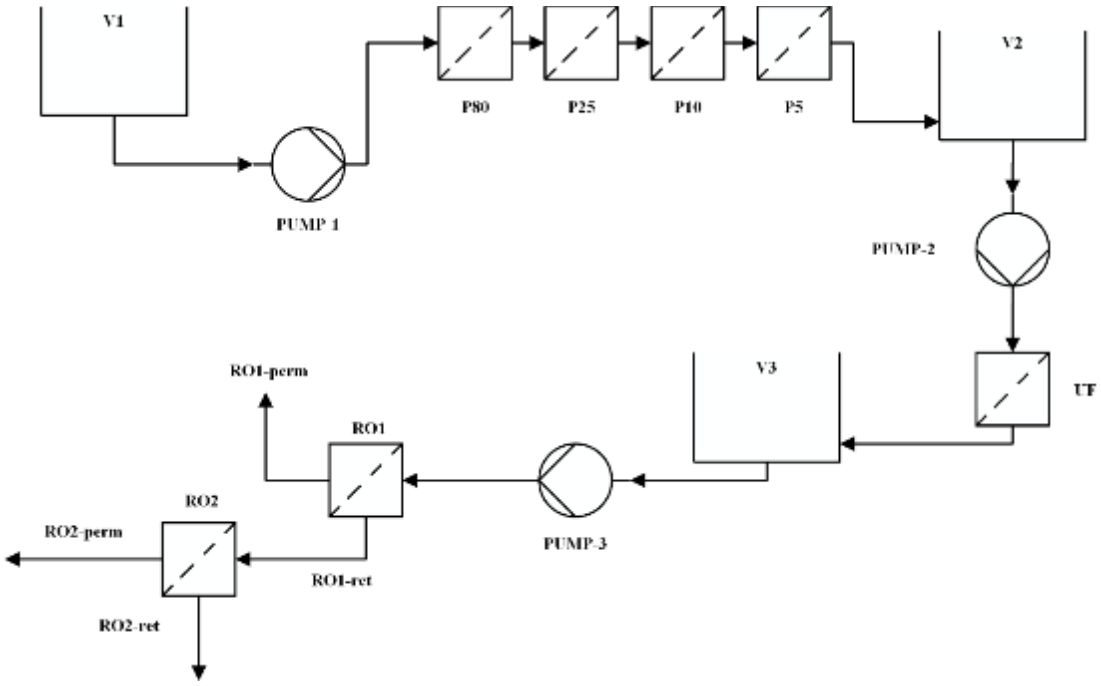

Figure 2: Scheme of experimental apparatus

The experimental apparatus also contains instrumentation for measuring pressure, temperature, and volume flow. All the sensors were supplied by the IFM company. Pressure was measured on all stages by PN 2594 pressure sensors. each stage had a SM 8020 magnetic-inductive flow meter. Temperatures were measured using a TCC 831 sensor.

Treatment process

The experiment was carried out at the Brno University of Technology, NETME Centre in the Laboratory of energy intensive processes. The total volume of treated dairy wastewater was 50 L. Feed dairy wastewater was put into vessel V1 and pumped to the pre-treatment stage. When all the wastewater was treated by the pre-treatment stage, then it went to the ultrafiltration. After ultrafiltration, all the wastewater continued to the reverse osmosis stage. Between the stages the wastewater was stored in vessels V2 and V3. In all stages the wastewater had the same temperature of 23 °C. The operating pressures and flow rates are summarised in Table 2. These conditions are not described for the pre-treatment stage because they did not stabilise during the experiment. This will be discussed in more detail in the results and discussion section. The duration of the experiment was 55 minutes.

Table 2: Operating conditions

Treatment stage	Operating parameters	
	Trans membrane pressure [barg]	***Volume flow rate [L/min]***
UF	9.5	0.13
RO1	10.0	2.63
RO2	9.9	2.44

The efficiency of the membrane processes was determined in terms of species removal efficiency (E_R, %) based on the concentrations of determined species in the permeate (C_P, mg/L) and in the feed (C_F, mg/L).

$$E_R = \left(1 - \frac{C_P}{C_F}\right) \cdot 100 \quad (1)$$

The performance of reverse osmosis was also evaluated in terms of water recovery (R, %) given by the ratio of permeate volume (V_P, m^3) and feed volume (V_F, m^3).

$$R = \frac{V_P}{V_F} \cdot 100 \quad (2)$$

Additionally, the COD rejection of the membrane was evaluated according to the following equitation (3):

$$RJ = \left(1 - \frac{C_P}{C_R}\right) \cdot 100 \quad (3)$$

where C_P and C_R are the permeate and the retentate COD concentrations.

Analysis

The characteristics of the raw wastewater, permeates from pre-treatment, ultrafiltration and reverse osmosis, and retentates from reverse osmosis were evaluated in terms of six parameters (pH, electrical conductivity, dry matter, total dissolved solids-TDS, total suspended solids-TSS, COD). The analyses followed the methodologies described in international standard ISO 15705:2002, European standard EN 872:2005, European standard EN 15934:2012 and Czech standard ČSN 75 7346 for COD, TSS, dry matter and TDS, respectively. Conductivity was measured by conductivity probe from Vernier (accuracy ± 4% of full scale reading) and pH was measured by pH sensor from Vernier (accuracy ± 0.2).

RESULTS AND DISCUSSION

The main objective of the experiment was to determine whether membrane processes, in particular reverse osmosis, are capable of reducing the concentration of pollutants in highly polluted dairy wastewater to a level low enough for water reuse. The results are summarised in Table 3. The most important parameter is COD, which gives us information

ISBN: 978-618-5765-04-0
ISSN 3057-4269

about organic pollution. This type of pollution is the most abundant in dairy wastewater. The overall COD removal efficiency was 99.8 %. The other removal efficiencies of TDS, TSS and electrical conductivity were 99.6%, 100%, and 88.6%, respectively. The water recovery for the RO stage was 17.1%. The COD rejection of the RO membranes was 97.6% and 98.0 % for RO1 and RO2, respectively.

Table 3: Wastewater characteristics after the treatment stages

Treatment stage	Wastewater parameters					
	COD [mg/L]	*El. Conductivity [µS/cm]*	*Dry matter [%]*	*TDS [mg/L]*	*TSS [mg/L]*	*pH [–]*
Feed	44,469	3,600	1.11	6,019	5,317	3.6
Pre-treatment	16,451	3,100	0.90	3,181	4,883	3.8
UF	10,090	3,120	0.73	–	–	3.7
RO1-perm	86	450	0.014	142	–	4.5
RO1-ret	18,857	3,240	0.88	3,457	4,973	3.8
RO2-perm	78	410	0.002	21	–	3.9
RO2-ret	20,870	3,510	1.00	3,560	5,427	3.8

The results show that RO is capable of significantly reducing organic pollution. The final COD levels in the RO permeate were below 125 mg/l, which is the discharge limit for municipal wastewater treatment plants, which is also used as a minimum requirement for recycled water quality for agricultural irrigation, and this value can be used as the minimum benchmark for recycled water quality in industry. Additionally, there were no suspended solids in the permeate. From this point of view, the experiment can be considered successful. However, in the Czech Republic there are no general requirements for the quality of recycled water. The assessment of the appropriate recycled water quality is up to the relevant authorities. Therefore, the minimum requirements can differ according to the final use of recycled water. This is also a problem throughout the European Union, as discussed in more detail in reference [10].

However, there were some complications during the experimental procedure. A significant decrease in volume flow rate and a simultaneous increase in operating pressure were observed during pre-treatment. This was caused by heavy fouling of the filters. Moreover, the dead-end configuration of these filters may have enhanced and intensified the fouling. The same phenomenon was observed on the ultrafiltration membrane, where the volume flow rate decreased at a very low level (0.13 L/min). Additionally, the operating pressure increased above the recommended limit. Therefore, the ultrafiltration was aborted when approximately 4 litres had been filtered. The rest of the dairy wastewater was then directly fed to the reverse osmosis without passing through ultrafiltration. The heavy fouling was probably enhanced by the type of hollow fibre module and the dead-end configuration of the ultrafiltration. This is because hollow fibre modules have a poor resistance to fouling. No signs of fouling were observed during the RO process. However, the process only lasted 15 minutes, which is not sufficient for a proper assessment of the fouling.

This experiment showed that reverse osmosis is an efficient treatment method even for highly polluted dairy wastewater. However, fouling occurred as a major limitation during the experiment, especially during pre-treatment and ultrafiltration. This problem could be mitigated by using a different type of pre-treatment, e.g. coagulation/flocculation, or by using a different type of membrane, e.g. cross-flow microfiltration, tubular or spiral wound membranes. Solving the fouling problem is the key aspect for industrial scale application. Also, a greater degree of wastewater stream separation could lead to the fouling minimisation and greater application of membranes in the dairy industry. This is because separate wastewater streams could be easier for treatment than one stream with all effluents due to the lower complexity of pollution. In addition, wider industrial deployment could be supported by validation of applicability on a wider range of dairy wastewater, investigation of long-term membrane operation in terms of fouling, optimisation of operating parameters and appropriate maintenance, or integration with other technologies to approach zero liquid discharge (ZLD). Therefore, future work will concentrate on the assessment of efficient dairy wastewater pre-treatment prior to reverse osmosis. Additionally, long-term experiments will be conducted to evaluate reverse osmosis fouling.

CONCLUSION

An experimental assessment of the reverse osmosis efficiency for highly polluted dairy wastewater treatment has been presented. The overall COD removal efficiency was 99.8% with an absolute value of around 80 mg/L. This value is below the discharge limit for municipal wastewater treatment plants, which can serve as a minimum benchmark for wastewater recycling. Additionally, the TDS, TSS and electrical conductivity were significantly reduced by 99.6%, 100%, and 88.6%, respectively. These results show that RO is suitable for dairy wastewater recycling. However, heavy fouling occurred during pre-treatment and ultrafiltration, which limits the potential industrial scale application. This fouling was probably enhanced by an inappropriate choice of membrane type. Therefore, corrective measures have been proposed to reduce the fouling. These measures include the use of a different type of membranes (cross-flow, tubular or spiral wound) or the use of a different or additional pre-treatment step, e.g. coagulation/flocculation. Future research will focus on a dairy wastewater pre-treatment in terms of fouling mitigation as well as long-term experiments with reverse osmosis to assess fouling.

ISBN: 978-618-5765-04-0
ISSN 3057-4269

ABBREVIATIONS

COD	Chemical oxygen demand
FO	Forward osmosis
MD	Membrane distillation
MF	Microfiltration
RO	Reverse osmosis
TDS	Total dissolved solids
TKN	Total Kjeldahl nitrogen
TOC	Total organic carbon
TSS	Total suspended solids
UF	Ultrafiltration
ZLD	Zero liquid discharge

REFERENCES

[1] Joint Research Centre (European Commission), "Best Available Techniques (BAT) reference document for the food, drink and milk industries," 2019. [Online]. Available: https://data.europa.eu/doi/10.2760/243911. [Accessed 1 6 2023].

[2] C. Garnier, W. Guiga, M.-L. Lameloise and C. Fargues, "Water reuse in the food processing industries: A review on pressure-driven membrane processes as reconditioning treatments," *Journal of Food Engineering*, 1 5 2023.

[3] V. B. Brião, A. C. Vieira Salla, T. Miorando, M. Hemkemeier and D. P. Cadore Favaretto, "Water recovery from dairy rinse water by reverse osmosis: Giving value to water and milk solids," Resources, Conservation and Recycling, pp. 313-323, 1 1 2019.

[4] D. F. Galvão and N. Koca, "Membrane Technology and Water Reuse in a Dairy Industry," in Technological Approaches for Novel Applications in Dairy Processing, IntechOpen, 2018.

[5] K. Nath, H. K. Dave and T. M. Patel, "Revisiting the recent applications of nanofiltration in food processing industries: Progress and prognosis," Trends in Food Science & Technology, pp. 12-24, 1 3 2018.

[6] V. Shrivastava, M. M. Marjub, E. R. Rene and A. M. F. Soto, "Wastewater in the food industry: Treatment technologies and reuse potential," Chemosphere, 1 4 2022.

[7] N. Pervez, M. R. Mishu, G. K. Stylios, S. W. Hasan, Y. Zhao, Y. Cai, T. Zarra, V. Belgiorno and V. Naddeo, "Sustainable Treatment of Food Industry Wastewater Using Membrane Technology: A Short Review," Water, 5 12 2021.

[8] M. Vourch, B. Balannec, B. Chaufer and G. Dorange, "Treatment of dairy industry wastewater by reverse osmosis for water reuse," Desalination, pp. 190-202, 25 1 2008.

[9] A. C. Bortoluzzi, J. A. Faitão, M. Di Luccio, R. M. Dallago, J. Steffens, G. L. Zabot and M. V. Tres, "Dairy wastewater treatment using integrated membrane systems," Journal of Environmental Chemical Engineering, pp. 4819-4827, 1 10 2017.

[10] M. Procházková, M. Touš, D. Horňák, V. Miklas, M. Vondra and V. Máša, "Industrial wastewater in the context of European Union water reuse legislation and goals," Journal of Cleaner Production, 10 11 2023.

ISBN: 978-618-5765-04-0
ISSN 3057-4269

Waste-to-Energy Technology Selection and Capacity Planning in a Multi-Facility Waste Management System

Ahmed Saif
Department of Industrial Engineering
Dalhousie University
Halifax, NS, Canada
ahmed.saif@dal.ca

Hatem Masri
College of Administrative Sciences
Applied Science University
East Al-Ekir, Bahrain
hatem.masri@asu.edu.bh

***Abstract*— Waste-to-energy (WtE) technologies provide a viable solution for dealing with the large quantities of municipal solid waste (MSW) generated in modern societies. However, they must be optimally integrated with waste management and energy distribution networks to maximize their economic and environmental benefits. We propose a strategic optimization model for locating waste processing facilities, allocating waste-generating communities to them, determining the types and capacities of equipment in each, and directing the flow of energy products (electricity, heat and hydrogen) from them to demand nodes, aiming to achieve two objectives: minimizing total cost and minimizing greenhouse gas emissions. The cost, emission, and conversion functions of three WtE technology alternatives (TAs) are meticulously derived so they can be incorporated into the mathematical model. The proposed approach is applied to a realistic case study in Canada. Results show that the type and location of WtE technologies depend on the objective sought, the cost structure of TAs, and the price of energy products.**

Keywords— Waste-to-Energy, Location-Allocation, Technology Selection, Capacity Planning, Environment

INTRODUCTION

Effective management of municipal solid waste (MSW) represents a major challenge for policymakers nowadays. On the one hand, around one-third of the approximately 2 billion tons of MSW generated globally each year are not being adequately managed from an environmental standpoint [1]. On the other hand, collecting, transporting, sorting and disposing of these vast quantities of MSW consume a lot of energy and generate substantial amounts of greenhouse gas (GHG) emissions [2]. Recent advances in Waste-to-Energy (WtE) technologies like incineration, anaerobic digestion (AD), pyrolysis, and gasification offer a promising solution to the MSW problem faced by communities worldwide. This is why some agencies like the *United States Environmental Protection Agency* have listed MSW as a renewable energy source usable to attain sustainable development goals [3].

Nevertheless, successful integration of WtE solutions within existing energy systems requires a thorough assessment of both the technologies themselves and the networks used to carry their inputs (i.e., waste) and outputs (i.e., energy). Indeed, large, centralized WtE processing facilities enjoy a cost advantage over small ones due to economies-of-scale and improved technical efficiency. However, they are also associated with higher costs and GHG emissions for shipping MSW from communities and energy products to demand points. Furthermore, the technical, economic and environmental feasibility of each WtE technology depends on the quantity and composition of the MSW it utilizes. Hence, it is necessary to jointly consider the WtE technology selection, location and capacity planning, and the configuration of waste collection and energy distribution networks when assessing the viability of utilizing WtE solutions in energy systems.

Despite the growing researchers' interest in optimizing waste collection (see, e.g., [4]) and WtE plant location and technology selection (see, e.g., [5], [6]), little attention has been paid to addressing the two problems simultaneously. Among the few studies that consider this combination is the two-stage stochastic optimization model proposed in [7], which optimizes the location of WtE plants and the shipment of MSW to then under waste composition uncertainty. However, the issues of technology selection and capacity planning were overlooked in this work. Conversely, in works that focused on the latter issues, e.g., [6], the spatial aspects of waste management, i.e., collection and transportation of MSW, were ignored.

This paper aims to fill the afore-described gap by proposing a high-level, strategic optimization model for designing an integrated MSW-to-energy (MSWtE) system that can process the MSW generated in a given geographical region. Unlike previous studies that had a narrow focus on certain aspects of the system, we jointly address the interconnected decisions of locating waste processing facilities and determining the types and capacities of WtE technologies in them, the assignment of MSW-generating communities to facilities, and the flow of energy products (electricity, heat and hydrogen) to demand points. The proposed bi-objective model aims to maximize the total revenue from selling energy products, net of MSW and energy products' shipping costs and facilities' capital and operational costs, and minimizing the total GHG emissions from the entire process. Three technology alternatives (TAs) are considered for installation in WtE processing facilities: 1) incineration with a steam power generator, 2) AD with combined heat and power (CHP) units, and 3) plasma arc gasification (PAG) with hydrogen separation. Given that equipment cost functions are concave, the formulation results in a nonconvex optimization problem that can be handled using modern global optimization solvers. The proposed approach is applied to a realistic case study in Canada to design an MSWtE system that can supply electricity, heat, and hydrogen while reducing landfilling, and the results are analyzed.

The remainder of this paper is organized as follows. The next section provides a brief description of the problem and its mathematical formulation. The cost, emission, and conversion functions of the different TAs are meticulously derived in

ISBN: 978-618-5765-04-0
ISSN 3057-4269

Section III such that they can be incorporated into the mathematical model. Sections IV describes the case study and the results obtained based on it, whereas a conclusion is presented in Section V.

PROBLEM DESCRIPTION AND FORMULATION

Problem Description

The decision-maker in the problem under consideration is an entity responsible for collecting and managing MSW in a given geographical area (e.g., city, province, country). This area is subdivided into zones/communities, indexed by $i \in I$. Currently, MSW is collected from these zones and sent to landfills. However, to reduce the negative environmental impacts associated with landfilling and generate some revenue, the decision-maker is contemplating utilizing some combinations of WtE and energy conversion technologies. These combinations, referred to hereinafter as *technology alternatives*, are indexed by $t \in T$. Each TA takes MSW as an input and generates one or more energy products, e.g., electricity, heat or hydrogen, indexed by $p \in P$. For example, a TA can consist of an incinerator that burns waste to generate heat combined with a steam power generator that converts heat to electricity, which is then sold to potential customers. The list of TAs and their outputs is provided in the next subsection. TA equipment is to be installed in processing facilities (or, simply, facilities) that can be located in a subset of predetermined potential locations indexed by $j \in J$. Moreover, demand points (i.e., sinks) are indexed by $k \in K$, and each energy product can be shipped/transmitted from the facilities to one or more of these sinks. Examples of sinks include downstream processing facilities, residential communities, and industrial complexes. Therefore, the MSWtE system can be represented as the digraph $G(\mathcal{N}, \mathcal{A})$, where $\mathcal{N} := I \cup J \cup K$ encompasses the nodes of this graph and $\mathcal{A}$ is the set of arcs connecting these nodes.

The problem aims to determine the optimal MSWtE system configuration, which entails the locations of processing facilities, the types and capacities of TA equipment to be installed in each facility, the flow of MSW from zones to facilities, and the flow of the energy products from them to demand nodes. Two objectives are sought: maximizing monetary profit and minimizing GHG emissions. The profit to be maximized is the difference between the products' sales revenue and the total cost of the system, which includes the waste collection cost, the TAs' capital and operating costs, and the costs associated with delivering products to sinks and the residual waste (if any) to landfills. Since waste management is considered a "cost center" by municipalities, the optimal profit can be negative, i.e., the system cost can be greater than the revenue generated. On the other hand, GHG emissions include those emitted in transporting MSW to facilities, processing the MSW, and delivering end products to sinks.

Modeling Assumptions

The following assumptions are used to formulate the problem:

i. The quantity and composition of the MSW collected from each zone are known and fixed throughout the planning horizon. This is a reasonable assumption given that the model deals with the steady-state, long-term operation of the system and does not consider seasonal fluctuations. This assumption enables us to formulate the problem as a single-period, infinite-horizon optimization model.

ii. MSW originating from each zone is assigned to a single processing facility. This assumption aligns with the current practices in waste management and simplifies the calculation of waste collection costs and emissions.

iii. The cost and GHG emissions for collecting the MSW from a given zone and sending it to a given facility can be computed externally, e.g., by solving a vehicle routing problem, and used as input in the model. In other words, the issue of optimal routing is beyond the scope of this model.

iv. An installed piece of equipment will be operated continuously and steadily at its rated capacity. Thus, the rated capacities of WtE equipment are calculated based on the quantities of MSW to be processed by them.

Notations

To formulate the problem, we introduce the binary decision variables x_{ij} and y_{jt} to denote, respectively, whether the MSW originating from zone i is processed in facility j (i.e., the facility opened in location j, if any), and whether TA t is used in it, in addition to the continuous variable q_{jt} to denote the installed capacity of TA t in facility j. The installed capacity of all equipment is measured in terms of the MSW mass they can process per unit time (ton/year). We also introduce the continuous flow variable z_{jkp}, which represents the quantity of product p shipped/transmitted from facility j to sink k. Each TA has cost and emission functions, $c_t(q_{jt})$ and $e_t(q_{jt})$, respectively. Moreover, TA t delivers an amount of product p according to the conversion function $f_{tp}(q_{jt})$. This function returns the product amount produced by a TA per unit mass of MSW processed. The annual quantity of MSW generated in zone i is w_i, whereas the cost and GHG emissions resulting from collecting this quantity and sending it to facility j are a_{ij} and b_{ij}, respectively. A unit of product p can be sold in demand/sink node k for s_{kp}, and it costs d_{jkp} to ship/transmit a unit of product p from facility j to sink k, whereas the GHG emissions associated with this shipment is h_{jkp}. Furthermore, if TA t is used in a facility, there are upper and lower limits ($\underline{q}_t$ and $\overline{q}_t$) on its installed capacity. The set of feasible arcs for shipping product p is denoted by $\mathcal{A}_p$.

Mathematical Formulation

Based on the aforementioned problem description, modeling assumptions and notations, the problem can be formulated as follows:

$$\begin{aligned}\text{maximize } TP = &\sum_{j\in J}\sum_{k\in K}\sum_{p\in P}\big(s_{kp} \\ &- d_{jkp}\big)z_{jkp} \\ &- \sum_{j\in J}\sum_{t\in T} c_t(q_{jt}) \\ &- \sum_{i\in I}\sum_{j\in J} a_{ij}x_{ij}\,;\end{aligned} \tag{1}$$

$$\begin{aligned}&\text{minimize } TE \\ &= \sum_{j\in J}\sum_{t\in T} e_t(q_{jt}) + \sum_{i\in I}\sum_{j\in J} b_{ij}x_{ij} \\ &+ \sum_{j\in J}\sum_{k\in K}\sum_{p\in P} h_{jkp}z_{jkp}\,;\end{aligned} \tag{2}$$

Subject to:

ISBN: 978-618-5765-04-0
ISSN 3057-4269

$$\sum_{j\in J} x_{ij} = 1, \quad \forall i \in I; \tag{3}$$

$$\sum_{i\in I} w_i x_{ij} = \sum_{t\in T} q_{jt}, \quad \forall j \in J; \tag{4}$$

$$\sum_{t\in T} f_{tp}(q_{jt}) = \sum_{k\in K} z_{jkp}, \quad \forall j \in J, \forall p \in P; \tag{5}$$

$$\underline{q}_t y_{jt} \le q_{jt} \le \overline{q}_t y_{jt}, \quad \forall j \in J, \forall t \in T; \tag{6}$$

$$z_{jkp} = 0, \quad \forall (j,k) \notin \mathcal{A}_p; \tag{7}$$

$$x_{ij}, y_{jt} \in \{0,1\}, \quad \forall i \in I, \forall j \in J, \forall t \in T; \tag{8}$$

$$z_{jkp} \ge 0, \quad \forall j \in J, \forall k \in K, \forall p \in P. \tag{9}$$

The three terms of the profit maximization objective function (1) represent the revenue from selling products (net of shipping cost), the TA costs and the MSW collection and shipping costs, respectively. The GHG emissions minimization objective function (2) consists of the emissions generated by the TAs, and the emissions related to the shipping of MSW and energy products. The first constraint (3) stipulates that each waste-collection zone is assigned to a single processing facility. Constraint (4) ensures that the installed capacity of equipment is sufficient to process all MSW allocated to the processing facility, whereas constraint (5) ensures the quantity shipped equals the quantity generated for each facility and product type. The limits on installed capacity are enforced by constraint (6). Constraint (7) prevents any shipment of products when it is not technically feasible, e.g., when the distance prevents it or there is no demand for the product, while (8) and (9) are variable domain constraints. The class of this multi-objective optimization model depends on the functions $c_t(q_{jt})$, $e_t(q_{jt})$ and $f_{tp}(q_{jt})$. The next section discusses their functional form.

SYSTEM CHARACTERISTICS

Technology Alternatives

The following TAs are considered for installation in processing facilities:

[TA1]: Incineration with a steam power generator: the heat generated by incinerating MSW is used to boil water into steam that turns a turbine to generate electricity.

[TA2]: Anaerobic digestion with combined heat and power units: a series of biological processes in the absence of oxygen convert organic waste to biogas, which is then used in a CHP unit to generate heat and electricity.

[TA3]: Plasma arc gasification with hydrogen separation: PAG is an extension of conventional gasification, wherein plasma torches are used to substantially raise the temperature of MSW in an oxygen-starved environment to generate synthetic gas (syngas). The syngas is then purified, before being sent to a hydrogen recovery system that consists of a water gas shift (WGS) unit to convert the carbon monoxide to hydrogen and a Pressure Swing Adsorption (PSA) unit for the separation and purification of hydrogen [8]**.**

Cost, Emission and Conversion Functions of TAs

The total cost of each piece of equipment includes both capital (acquisition, commission, installation) costs and operation and maintenance (O&M) costs, whereas only the direct (operational) GHG emissions are considered. Table 1 depicts the cost, emission, and conversion functions of the different TAs. A detailed description of how these functions are derived is outlined next.

Table 1: Cost, emission and conversion functions for the TAs

TA	$c_t(q_{it})$ ($/year)	$e_t(q_{it})$ (kg-CO_2e/year)	$f_{tp}(q_{jt})$
1	$1{,}691.9q_{j1}^{0.7753} + 256.4q_{j1}^{0.8594}$	$1{,}191.3q_{j1}$	$893.6q_{1j}$ kWh-e
2	$140.4q_{j2} + 141.9q_{j2}^{0.667}$	$1{,}085.0q_{j2}$	$449.8q_{j2}$ kWh-e $642.6q_{j2}$kWh-h
3	$179.7q_{j3} + 81.8q_{j3}^{0.8111}$	$1{,}506.3q_{j3}$	$78.5q_{j3}$ kg-H_2

Technology Alternative # 1

The cost function of the first TA, ($t = 1$), which consists of an incinerator, a boiler, and a steam power generator, is based on [9]. The investment cost in \$M for the plant is estimated at $2.3507Cap_{INC}^{0.7753}$, where Cap_{INC} is the plant capacity in 1000 metric tons per year. We first change the units in this equation to \$'s and tons of MSW/year and adjust for inflation (3% per year for 9 years), then amortize the capital cost while assuming a useful life of 15 years, a discount rate of 8%, and no salvage value, i.e., using a capital recovery factor (CRF) of 0.11683. Thus, the capital cost function becomes $1691.9q_{j1}^{0.7753}$\$/year. The annual O&M cost according to [9] is $0.0744Cap_{INC}^{0.8594}$, which is similarly adjusted to $256.4q_{j1}^{0.8594}$ \$/year after changing the units and accounting for inflation.

The CO_2 emissions depend on the carbon content of the MSW, its moisture content, and the oxidization factor, according to the IPCC GLs mass balance method explained in [10]. Table 2.2.1 shows the breakdown of different organic materials in the MSW and the corresponding mass ratios of carbon, hydrogen and oxygen, as estimated in [6] for a landfill in NS. Based on 38.0% carbon content, 14.5% moisture content (since the remaining components have virtually no moisture) and an oxidization factor of 1 (the default value), each ton of MSW generates 1191.3 kg of CO_2.

The electricity generated is $\eta_{inc} LHV_{MSW} q_{j1}$, where $\eta_{inc}$is the efficiency of the incineration power plant, estimated in [9] using the T-S diagram at 17.25%. On the other hand, LHV_{MSW}, the lower heating value of MSW, is calculated in [11] as:

$$LHV_{MSW} = 0.0041868(1 + 0.15[O])\left(7{,}837.667[C] + 33{,}888.889[H] - \frac{[O]}{8}\right),$$

where $[O]$, $[H]$ and $[C]$ are the oxygen, hydrogen, and carbon contents in the MSW, respectively. Based on this formula, the LHV of MSW equals 18.65 GJ/ton. This value is close to those estimated in [12] using different methods. Thus, the incineration plant generates 893.64 kWh of electricity per ton of MSW.

Table 2: MSW Composition

Waste Type	Fraction (%)	Carbon (%)	Hydrogen (%)	Oxygen (%)	Moisture (%)
Food	28.1	51	5	39	65.2
Paper	12.3	45	5	45	6.9
Plastic	20.2	56	6	26	0.3
Textile	11.6	59	6	19	7.8
Gross	**72.2**	**38.0**	**3.9**	**24.0**	**20.1**

ISBN: 978-618-5765-04-0
ISSN 3057-4269

Technology Alternative # 2

The second TA ($t = 2$) includes an Anaerobic digester and a CHP unit. The capital cost for a new AD facility in Canada that produces biogas is estimated in [13] to be \$630/ton of annual processing capacity, whereas the operating cost is estimated to be \$80/ton of feedstock. A wide range of cost estimates has been provided in [14], depending on the feedstock type, end product, specific AD technology, and facility capacity and location. However, the above estimates seem reasonable and will be used herein. First, we adjust these values for inflation (3% per year for 14 years). Upon amortizing the capital cost using a CRF of 0.11683 (similar to the first alternative), the total annual cost per ton of feedstock amounts to \$232.34/ton. It should be noted, however, that only the organic (food) part of the MSW can be used for AD. Hence, for a ton of MSW, only 281 kg are processed through AD, whereas the remainder ends up in a landfill for a tipping fee of \$100/ton, a typical rate in North America.

The biogas yield from organic waste ranges between 0.3 and 0.5 m^3/kg volatile solids (VS) [15]. The VS fraction in MSW depends on its composition, but can be reasonably taken as the fraction of food waste, i.e., 28.1%. This value is close to the 20%, by weight, VS fraction suggested in [16]. Hence, each ton of MSW generates about 112.4 m^3 (5016 moles) of biogas (assuming a mid-point yield of 0.4 m3/kg), or equivalently 129.41 kg of biogas (assuming 35% CO_2 65% CH_4 composition). Although the solid residues resulting as byproducts of AD might have some industrial and agricultural usages, we disregard them here and focus on the energy products. Based on the aforementioned composition of the generated biogas, its LHV is 65% of that of methane (55MJ/kg), amounting to 35.75 MJ/kg, or equivalently 4,626.5 MJ per ton of MSW.

To compute the capacity of the CHP unit, the input energy per year, $4{,}626{,}500q_{j2}$ kJ is divided by ($365 \times 24 \times 60 \times 60$) to obtain around $0.14671q_{j2}$ kW power input. We assume a constant electrical efficiency of 0.35 and a constant heat efficiency of 0.5 for the CHP unit. These values are quite typical in the literature (see, e.g., [17]). Thus, the CHP unit shall have a rated (electrical) capacity of $0.051347q_{j2}$kW and delivers $0.073355q_{j2}$kW of heat. In terms of energy delivery per year, these power rates correspond to $449.8q_{j2}$kWh of electricity and $642.57q_{j2}$ kWh of heat, which define the conversion function. The investment cost function of a sparkplug ignition (SI) biogas-fueled CHP unit is estimated to be $4{,}639Cap_{CHP}^{-0.333}$ Euros/kW, where Cap_{CHP} is the rated capacity in kW, in 2005 [17]. Accounting for inflation and the currency exchange rate (\$1.08181/Euro), the investment cost is estimated to be $8{,}800\left(0.051347q_{j2}\right)^{0.667} = \$1{,}214.5q_{j2}^{0.667}$. Again, amortizing the capital cost over the same useful life yields an annual cost of $141.9q_{j2}^{0.667}$. On the other hand, the O&M cost is estimated in [18] to be 4 Euros/MWh in 2007, which is equivalent to \$3.22/ton of MSW after accounting for inflation and exchange rate, and considering that each ton of MSW generates $4{,}626{,}500 \times 35\%/3600 = 449.8$ kWh-e. Hence, the cost function becomes: $(0.281 \times 232.33 + 0.719 \times 100 + 3.22)q_{j2} + 141.9q_{j2}^{0.667} = 140.4q_{j2} + 141.9q_{j2}^{0.667}$.

The GHG emissions for this technology alternative have three main sources. First, some biogas escapes during the AD process, estimated in [19] as 6.3% of the total production. Based on the aforementioned biogas composition, each ton of MSW generates 42.29 kg of CO_2 and 84.12 kg of CH_4. The 100-year global warming potential (GWP) of methane is 27.9 [20]. Thus, the CO_2-equivalent emissions from this source are 150.52 kg/ton. The second source of GHG emissions is the combustion of biogas in the CHP unit to generate electricity and heat. In particular, one mole of methane generates one mole of carbon dioxide according to $CH_4 + 2O_2 \rightarrow CO_2 + 2H_2O$, or equivalently, every 16 grams of CH_4 generates 44 grams of CO_2. Thus, the 84.12 kg/ton of methane generate 231.32 kg/ton of CO_2, to be added to the remaining CO_2 in biogas to get 273.61 kg/ton from the second source. The third source corresponds to landfilling the remaining (non-organic) part of the MSW. landfills are notorious for generating large amounts of GHGs, especially methane and carbon dioxide. Besides the organic waste used in the AD process, the other primary degradable waste type is paper, which has a carbon content of 55.35kg/ton of MSW. According to [21], the dissimilation factor of biogenic carbon as landfill gas is estimated at 0.5, besides another 0.04 as leachate, totaling 0.54, which is the fraction of carbon that leaves the landfill as gas within 100 years. It is estimated that 55% of this carbon becomes CH_4 and 45% becomes CO_2 [21]. Thus, each ton of MSW processed using TA2 generates 21.92 kg of CH_4 and 49.32kg of CO_2, or equivalently, 660.89 kg-CO_2e. Adding this quantity to the emissions from the first two sources, the emission function is $1{,}085q_{j2}$ kg-CO_2e/year.

Technology Alternative # 3

The third TA ($t = 3$) includes a PAG unit that uses heat to generate syngas from MSW and a PSA unit that recovers hydrogen from syngas. The syngas generated using PAG is typically composed (by volume) of 42.9% CO, 34.8% H_2 and 16.6% CO_2, with the remaining volume consisting of Nitrogen and traces of CH_4 [22]. These fractions correspond to approximately 57.8% CO, 3.3% H_2, and 35.1% CO_2 by weight, with a carbon percentage of 34.34% in the syngas. The quantity and composition of the syngas depend on the equivalence ratio, reactor temperature, waste composition and physical properties, and composition and inlet temperature of the gasifying medium [23]. However, for simplicity, we assume that these operating parameters are predetermined and fixed. Assuming a carbon conversion efficiency (CCE) of 95%, out of each ton of MSW, 361.5 kg of carbon is converted to syngas, implying that approximately 1,051 kg of syngas is generated per ton on MSW (i.e., 606.7 kg CO, 35.2 kg H_2 and 368.9 kg CO_2). The calorific value of the generated syngas quantity per ton of MSW is 10.391 GJ, which represents 55.72% of the LHV for MSW (in GJ/ton). This value is within the 50-80% typical cold gas efficiency values for gasification as reported in [23]. The carbon monoxide is then converted to hydrogen in the hydrogen recovery system according to $CO + H_2O \rightarrow CO_2 + H_2$, i.e., each 28 kg of CO generates 44 kg of CO_2 and 2 kg of H_2, assuming perfect conversion. Thus, the total quantities of H_2 and CO_2 generated per ton of MSW are 78.5 kg and 1,322.3 kg, respectively.

PAG is a relatively new technology with only a few pilot and small-scale projects completed. It is, therefore, quite difficult to extract the technology cost function from the few data points available. We rely on the 6 projects reported in [8] and perform power regression for the relationship between capital cost and capacity (in tons of MSW per year) to obtain the relation $\$491.11q_{j3}^{0.8111}$. By accounting for inflation (3% per year over 12 years) and amortizing the capital cost using the CRF of 0.11683, we get the investment cost function for the plasma reactor as $81.8q_{j3}^{0.8111}$ \$/year. As for the O&M costs, we use the estimate of \$126.5/ton made in [24]. As for the hydrogen recovery process, [6] estimated the cost to be

ISBN: 978-618-5765-04-0
ISSN 3057-4269

$26,712/MWh of energy output from the PSA. Given that hydrogen has a calorific value of 39.4 kWh/kg, the cost is $0.677/kg-$H_2$, or equivalently $53.2/ton of MSW.

Besides the CAPEX and OPEX, the PAG technology uses significant quantities of electricity to generate heat. [23] estimated that PAG consumes between 1,200 and 2,500 MJ (333.3 and 694.4 kWh) of electricity per ton of MSW, whereas [25] estimated that for a large-scale (3,600 MW) plasma gasification power plant, the electricity consumption is 115 kWh per ton of MSW for the reactor only. Assuming the almost-midrange electricity consumption of 1,800 MJ/ton (i.e., 500 kWh/ton), and assuming a cost of 8 cents per kWh, the electricity cost is $40/ton of MSW. The GHG emissions associated with electricity consumption depend on the power generation mix. Assuming GHG emissions of 368 kg-CO_2/MWh (the 2023 US average), each ton of MSW generates 184 kg of CO_2 from electricity consumption.

Shipping Costs and Emissions

We first consider the costs and GHG emissions corresponding to the collection of MSW from zones and shipping them to processing facilities. Given that these facilities are usually located far away from residential communities to protect people from their negative health and environmental effects [7], it is reasonable to separate the processes of collecting and shipping the MSW. The waste collection process is performed at each community independently, and its economic and environmental costs are not dependent on the facility to which the waste is shipped. Hence, these costs can be computed offline, e.g., by solving a routing problem, irrespective of the allocation of zones to facilities. On the other hand, the shipping costs depend on the quantities shipped and the distance traveled. Since the MSW amounts collected from any community are vast relative to the capacity of a single waste truck, we can assume that shipping costs and emissions are linearly proportional to the MSW quantity. Likewise, the shipping economic and environmental costs are linearly proportional to the distance between the community and the facility. Given that the capacity of a typical garbage truck is 18 tons, that it consumes an average of 0.5 liters of diesel per km [26], and that the price of diesel is around $1.2/liter, the fuel cost is $0.033/km/ton. We then add overheads (e.g., driver, maintenance) of 50% to reach an MSW shipping cost of $0.05/km/ton. A diesel engine generates around 2.7 kg-CO_2/liter, thus the emissions from MSW shipping is 0.075kg-CO_2/km/ton. Note that these values must be multiplied by 2 to account for the round trip.

Hydrogen is transported in tube trailers having a capacity of 1,042 kg. Using the same parameters for the truck as above, the hydrogen shipping cost is around $1.73/km/ton and the corresponding CO_2 emission is 2.59 kg-CO_2/km/ton (both ways). The transmission costs of electricity (heat) include both the capital cost of the transmission line (pipe) and the transmission losses. Both of these costs are assumed proportional to the distance. In contrast, the carbon emissions are calculated based on the transmission losses only. Hydrogen is assumed to be sold for $3/kg, which is a quite typical price of "grey" hydrogen in 2024, whereas electricity is sold to the utility at $0.175/kWh, the feed-in tariff in NS for electricity generated using CHP from biomass. Estimating the selling price of heat is a challenging task since it depends on the application. However, considering that most of it will be used in district heating to substitute heat generated by 90%-efficiency furnaces that use propane (heating value = 7 kW/liter, bulk price = $0.8/liter), it is reasonable to assume a selling price of $0.125/kWh-h.

CASE STUDY

The proposed approach is implemented to design a MSWtE system in the Province of Nova Scotia (NS) , Canada. The residential MSW (i.e., garbage) quantities for each of NS's 29 municipalities between April 2022 and March 2023 (the latest available data) is extracted from [27], totaling around 120 thousand tons. As for potential locations for the processing facilities, we use the locations of the existing seven MSW disposal sites in NS [28]. The shortest driving distance between each municipal office/town hall and potential facility location is found using *Google Maps* and used to calculate MSW shipping costs and emissions. Since all facilities are currently connected to the electricity grid, the cost associated with delivering the generated electricity is set to zero. On the other hand, heat is sent to the closest community within 30 km of the facility for district heating. A penalty of 2% per km of the heat selling price is assumed to account for losses and infrastructure cost (e.g., pipes). GHG emissions for electricity and heat transmission are assumed negligible. As for hydrogen, it is shipped to the closer of the ports of Halifax or Point Tupper, the two ports that can be used to export hydrogen in NS. To avoid unrealistic solutions, if a TA is used at any location, its installed capacity cannot be less than 5,000 ton/year of MSW.

Table 3: Optimal solutions and values

Scenario	**Max Profit**	**Min Emission**	**Bi-Objective**
Facility	**TA Installed Capacity (ton MSW)**		
1	-	TA2: 9,916	-
2	-	TA2: 5,092	TA2: 8,244
3	TA3: 23,004	TA2: 22,276	TA2: 23,004
4	TA3: 97,150	TA2: 52,562	TA2: 29,016 TA3: 59,890
5	-	TA2: 7,849	
6	-	TA2: 7,309	
7	-	TA2: 15,152	
TP (millio $)	3.84	-2.22	0.99
TE (kiloton CO_2e)	183.23	131.48	157.35

The problem is solved using Gurobi. Table 3 depicts the results for three scenarios, namely single-objective profit maximization and emission minimization cases, and a bi-objective case that optimizes both objectives. The well-known ε-constraint method is used in the bi-objective scenario, by which profit maximization is considered the primary objective, whereas the quantity of GHG emissions is capped to its mid-point value (i.e., 157.353 kiloton CO_2e) between the optimal values of the two single-objective models. The table shows the installed capacity of each TA in each facility, in addition to the total profit and the total GHG emissions.

For the profit maximization case, only two processing facilities (in Guysborough and Halifax) are opened, and TA3 (PAG with hydrogen separation) is used in both. This result reflects both the impact of economies-of-scale, which favors large, centralized facilities, and the high revenue from hydrogen sales compared to electricity and heat. Both facilities are very close to the hydrogen exportation ports to minimize the relatively high hydrogen shipping costs. It is interesting to note that this solution generates a positive profit

ISBN: 978-618-5765-04-0
ISSN 3057-4269

of around \$32 and about 1.525 ton-CO_2e per ton of MSW. In contrast, the emission minimization objective led to a decentralized MSWtE system with all 7 potential facilities opened and each municipality is assigned to the closest facility to minimize shipping-related GHG emissions, while respecting the minimum allowable capacity constraint. Since the emission functions for all TAs are linear in processing capacity, there is no value in consolidation. Furthermore, TA2 (AD with CHP) is used in all facilities since it has the lowest per unit amount of GHG emissions. The emissions generated per ton of MSW has decreased to 1.095 ton-CO_2e, but at a monetary loss of \$18.5/ton of MSW. In the bi-objective case, which tries to balance economic and environmental considerations, three facilities are opened in Cumberland, Guysborough and Halifax. The first two facilities use TA2 exclusively, whereas the third one combines TA2 and TA3 to generate electricity, heat and hydrogen. This scenario results in a modest profit of \$8.27 and GHG emissions of 1.31 ton-CO_2e per ton of MSW. Interestingly, TA1 (incineration) is not used under any scenario due to the high cost and emissions of the steam power plant, which becomes economically viable only with a large processing capacity ($q_{j1} > 300{,}000$ ton/year).

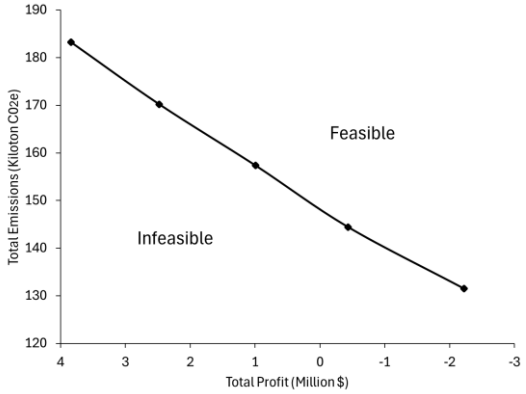

Figure 1: Pareto Frontier

Fig. 1 presents the Pareto Frontier of the feasible solutions, which represents the best trade-offs between the economic and environmental objectives. Decision-makers can select the solution that matches their priorities and limitations.

CONCLUSION

Clearly, the optimal MSWtE system design depends on the objective sought and the available TAs. Economies-of-scale plays an important role in determining the level of centralization and the TA to be installed. Furthermore, the selling price of energy products significantly affect the profitability of the system, with the high-priced hydrogen being the most lucrative. Inevitably, there is a trade-off between maximizing profitability and minimizing the environmental impact. This research can be extended by considering additional WtE technologies such as gasification and pyrolysis, the possibility of generating high-value downstream products from syngas such as liquid fuels and chemicals, and the incorporation of waste truck routing.

REFERENCES

[1] The World Bank, "Trends in Solid Waste Management," [Online]. Available: https://datatopics.worldbank.org/what-a-waste/trends_in_solid_waste_management.html. [Accessed 10 05 2024].

[2] R. Eisted, A. Larsen and T. Christensen, "Collection, transfer and transport of waste: accounting of greenhouse gases and global warming contribution," *Waste Management & Research: The Journal for a Sustainable Circular Economy*, vol. 27, no. 8, pp. 738-745, 2009.

[3] EIA, The U.S. Energy Information Administration, [Online]. Available: www.eia.gov. [Accessed 10 05 2024].

[4] A. Santos Neto and C. S. R. Simões, "Optimization of municipal solid waste collection system: systematic review with bibliometric literature analysis," *Journal of Material Cycles and Waste Management* , vol. 26, pp. 1906-1917, 2024.

[5] M. Silva, P. AL and C. Piekarski, "Location as a key factor for waste to energy plants," *Journal of Cleaner Production*, vol. 379, no. 2, p. 134386, 2022.

[6] M. Mostafavi Sani, H. Afshari and A. Saif, " robust framework for waste-to-energy technology selection: A case study in Nova Scotia, Canada," *Energy Conversion and Management*, vol. 284, p. 116965, 2023.

[7] J. Pluskal, R. ˇSompl´ak, D. N.´. V. Hrabec and L. Magnus, "Optimal location and operation of waste-to-energy plants when future waste composition is uncertain," *Operational Research*, vol. 22, no. 5, pp. 5765-5790, 2022.

[8] Y. Byun, M. Cho, S. Hwang and J. Chung, "Thermal plasma gasification of municipal solid waste (MSW)," in *Gasification for Practical Applications*, Rijeka, Croatia, IntechOpen, 2012.

[9] F. Tehrani and E. Haghi, "Techno-economic assessment of municipal solid waste incineration plant-case study of Tehran, Iran," in *The First Sustainable Development conference of Engineering Systems in Energy, water and Environment.*, Tehran, Iran, 2015.

[10] H. Lee, H. T. Yi, Y. Seo and E. Cho, "Estimation of CO2 emissions from waste incinerators: Comparison of three methods," *Waste Management*, vol. 73, p. 247–255, 2018.

[11] A. Abuadala, I. Dincer and G. Naterer, "Exergy analysis of hydrogen production from biomass gasification," *International Journal of Hydrogen Energy*, vol. 35, no. 10, p. 981–4990, 2010.

[12] R. Ibikunle, I. Titiladunayo, B. Akinnuli, S. Dahunsi and T. Olayanju, "Estimation of power generation from municipal solid wastes: A case study of Ilorin metropolis, Nigeria," *Energy Reports*, vol. 5, p. 126–135, 2019.

[13] L. Arsova, *Anaerobic digestion of food waste: Current status, problems and an alternative product*, New York, NY: Columbia University, 2010.

[14] J. Vasco-Correa, S. Khanal, A. Manandhar and A. Shah, "Anaerobic digestion for bioenergy production: Global status, environmental and techno-economic implications, and government policies," *Bioresource Technology*, vol. 247, p. 1015–1026, 2018.

[15] Y. Li, S. Park and J. Zhu, "Solid-state anaerobic digestion for methane production from organic waste," *Renewable and Sustainable Energy Reviews*, vol. 15, no. 1, pp. 821-826, 2011.

[16] A. Selvam, P. Ilamathi, M. Udayakumar, K. Murugesan, J. Banu, Y. Khanna and J. Wong, "Food waste properties," in *Current Developments in Biotechnology and Bioengineering*, Elsevier, 2021, pp. 11-41.

[17] M. Lantz, "The economic performance of combined heat and power from biogas produced from manure in sweden – a comparison of different CHP technologies," *Applied Energy*, vol. 98, pp. 502-511, 2012.

[18] B. Eder, Biogas-Praxis: Grundlagen, Planung, Anlagenbau, Beispiele, Wirtschaftlichkeit, Rastede, Germany: ökobuch, 2006.

[19] J. Murphy and E. McKeogh, "echnical, economic and environmental analysis of energy production from municipal solid waste," *Renewable Energy*, vol. 29, no. 7, p. 1043–1057, 2004.

[20] K. Mar, C. Unger, L. Walderdorff and T. Butler, "Beyond CO2 equivalence: The impacts of methane on climate, ecosystems, and health," *Environmental Science & Policy*, vol. 134, pp. 127-136, 2022.

[21] S. Manfredi, D. Tonini, T. Christensen and H. Scharff, "Landfilling of waste: accounting of greenhouse gases and global warming contributions," *Waste management & research*, vol. 27, no. 8, pp. 825-836, 2009.

[22] A. Chanthakett, M. Arif, M. Khan and A. Oo, "Performance assessment of gasification reactors for sustainable management of municipal solid waste," *Journal of Environmental Management*, vol. 291, p. 112661, 2021.

[23] U. Arena, "rocess and technological aspects of municipal solid waste gasification. A review," *Waste Management*, vol. 32, no. 4, pp. 625-639, 2012.

[24] A. Ramos, J. Berzosa, J. Esp´ı, F. Clarens and A. Rouboa, "Life cycle costing for plasma gasification of municipal solid waste: A socio-economic approach," *Energy Conversion and Management*, vol. 209, p. 112508, 2020.

[25] C. Ducharme, *Technical and economic analysis of Plasma-assisted Waste-to-Energy processes*, New York: Columbia University, 2010.

[26] T. Nguyen and B. Wilson, "Fuel consumption estimation for kerbside municipal solid waste (MSW) collection activities," *Waste Management & Research*, vol. 28, no. 4, pp. 289-297, 2010.

[27] NS Department of Environment and Climate Change, "Municipal Solid Waste Disposal Totals," [Online]. Available: https://data.novascotia.ca/Environment-and-Energy/Municipal-Solid-Waste-Disposal-Totals/mp68-kdz7/about_data. [Accessed 10 06 2024].

[28] NS Department of Environment and Climate Change, "Municipal Solid Waste Disposal Sites," [Online]. Available: https://novascotia.ca/nse/waste/solidwastedisposal.asp. [Accessed 10 06 2024].

ISBN: 978-618-5765-04-0
ISSN 3057-4269

Development of an Innovative All-Electric Propulsion Scheme for Inland Marine Transportation

Nick Rigogiannis
Dept. of Electrical & Computer Eng.
Democritus University of Thrace
Xanthi, Greece
nrigogia@ee.duth.gr

Faidra Kotarela
Dept. of Electrical & Computer Eng.
Democritus University of Thrace
Xanthi, Greece
fkotarel@ee.duth.gr

Stamatia Kaliampetsou
Indigital S.A.
Athens, Greece
mkaliampe@gmail.com

Anastasios Kyritsis
Department of Environment
Ionian University
Zakynthos, Country
kyritsis@ionio.gr

Ioannis Gonos
School of Electrical & Computer Eng.
National Technical University of Ahens
Athens, Greece
igonos@cs.ntua.gr

Nick Papanikolaou
Dept. of Electrical & Computer Eng.
Democritus University of Thrace
Xanthi, Greece
npapanik@ee.duth.gr

***Abstract*—This paper focuses on the development of an innovative system for all-electric sea vessels, used in inland marine transportation, with a specific emphasis on minimizing the environmental footprint of maritime tourism activities. The design of a marine transport-leisure vessel for domestic inland routes is presented, along with the key design considerations, requirements and limitations of the particular application. The main parameters of this study include vessel capacity, range, maximum speed, propulsion power and total weight. Moreover, emphasis is placed on the selection of the most appropriate energy storage system, taking into account the battery technology and the proper sizing. Additionally, the potential for swapping vessel battery pack (replacing the discharged battery pack with a fully charged one and recharging it outside of the vessel) is considered and discussed. Finally, a significant part of this study is devoted to the electric motors' selection to find the most suitable solution, in terms of performance and weight.**

Keywords—all-electric propulsion, all-electric ship, batteries, battery sizing, electric motor, energy storage, marine transportation

INTRODUCTION

Nowadays, the majority of new vessels are electrically propelled. This means that internal combustion engines are used as prime movers for electrical generators rather than vessels' direct movement. Vessels' primary and auxiliary loads are supplied by the electrical generators either directly or via advanced power electronic converters. This configuration reduces both fuel consumption and operating costs and improves their reliability and flexibility. On the other hand, it relies on fossil fuels, producing thus significant amounts of air pollutants, such as sulfur oxides (SOx), nitrogen oxides (NOx), soot (carbon particles), fine dust, carbon monoxide (CO) and carbon dioxide (CO2). Those air pollutants present adverse effects both on the environment, by worsening the climate change issue, and on human health [1].

It is worth indicating that a single large ship emits a CO2 amount equivalent to the daily use of 70,000 cars, an amount of NOx equivalent to the daily use 2 million cars, and fine dust and carcinogenic particles equivalent to the daily use of approximately 2.5 million cars. Due to the aforementioned harmful emissions, ships are among the most serious sources of pollution in ports [2], [3]. What is more, the overwhelming majority of global goods (i.e., approximately 80% in 2022) is carried by sea [4]. Indeed, the global economy and international trade are based heavily on cargo ships, such as bulk carriers, container ships and tankers.

As a result of the above, in 2018, the International Maritime Organization decided to drastically reduce air pollutant emissions. Hence, from 2020, only fuels containing less than 0.5% sulfur are allowed to be used in maritime transport, whilst for inland sea routes the exclusive use of marine diesel is mandatory, which is less harmful than heavy oil, because less dangerous pollutants are emitted during its combustion. However, marine diesel is significantly more expensive, resulting in increased maritime transport costs. Nevertheless, regardless of the environmental and financial costs, it is an indisputable fact that fossil fuels are not inexhaustible.

Considering the above facts, it is deduced that there is still much ground to cover for the decarbonization of marine transportation. The primary means to achieve the decarbonization of marine transportation are the hybrid [5], [6] and all-electric ship concepts [6]-[10]. In both concepts, the development of a reliable vessel requires a thorough investigation to determine vessel purpose (ferry, leisure boat, sea taxi, cruise ship, bulk carrier, container ship, tankers etc.), vessel operating conditions (e.g. maximum range, speed, weight), the selection of energy storage system (size and technology) and motors (power, torque, efficiency, etc,) as well as the operational principals of the energy management system (battery, motor and loads monitoring and protection).

The study presented in this paper is carried out within the framework of the DELEMAR project [11]. The objective of this research project is the development of an innovative electrification scheme, applicable to vessels used for inland marine transportation (e.g., small leisure boats, sea-taxis etc.), aiming to minimize the environmental footprint of this form of maritime tourism.

This work was supported in part by the European Regional Development Fund of the European Union and in part by Greek National Funds through the Operational Program "ATTICA" 2014 – 2020, under the call "Research and Innovation Collaboration in the Region of Attica" (Project code: ATTP4-0359279 / MIS 5184666).

ISBN: 978-618-5765-04-0
ISSN 3057-4269

Electrification of Marine Transportation and Infrastructure

In this light, the electrification of port infrastructure and marine transportation means, as well as their smart energy management strategies, are technological areas of particular research and investment interest for ports and maritime transport. The above are some of the most important conclusions recorded in the proceedings of the "3rd Conference on Ports, Maritime Transport & Insularity", regarding future challenges and opportunities on maritime transport and ports of the future [12]. Furthermore, it is noted that relevant IDTechEx analyses predict that global sales of all-electric and hybrid ships will grow significantly, reaching $20 billion by 2027 [13].

However, in contrast to land transportation, where massive efforts have been made for hybridization or complete electrification of vehicles through the combined use of electric motors (as auxiliary or main propulsion engines) and electrochemical energy storage systems (EESS), this is not the case in maritime transportation. The volume, weight and cost of energy storage systems, as well as the need for high energy self-sufficiency – maritime means of transport cover long distances without being able to connect to charging points – are the main techno-economic factors that blocks the full transportation electrification in the open ocean. Therefore, the main efforts to electrify maritime transport are currently focused on inland sea transportation.

In general terms, ships with hybrid propulsion configurations presuppose the integration of small EESS or fuel-cell systems for mainly supplying auxiliary electrical loads. The EESS are either charged by introducing small renewable energy systems (e.g., photovoltaics) or energy recovery systems [5], [6], [14]. In all-electric ship concepts, the electrical power required for shipboard loads should be supplied by EESS and/or fuel cell systems. In other words, EESS replaces the internal combustion engines that work as prime movers for electrical generators. Enhancements in the design of electric power systems, semiconductor devices, power electronic converters, propulsion technologies, and drives are the key enabling technologies for both hybrid and all-electric ship concepts [6]-[10].

The technological maturity of both hybrid propulsion of ships and pure electrification schemes in inland marine transport has already been demonstrated, at research and applied level. Typical examples with particularly encouraging environmental and techno-economic results can be found in inland maritime transportation in the northern European countries [15]-[17].

Inland Marine Transportation

Although EESS (i.e., batteries) are the most expensive subsystem of an electric vessel, the cost of recharging them is considerably lower than using marine diesel. Furthermore, given the global trend towards increasing electricity generation from Renewable Energy Sources (RES), it is presumed that electrified waterborne transport is environmentally friendly (as the energy required for recharging comes from green technologies). Moreover, the smart scheduling of battery charging is a promising solution to mitigate the disturbances caused by the intermittent nature of non-dispatchable RES plants on electricity networks [18].

In parallel, it is worth highlighting the competitive advantage of inland marine transportation electrification (e.g., ferries, sea taxis, leisure boats). These vessels require smaller storage systems due to their frequent berthing. The challenges of fast battery charging and EESS capacity minimization for small vessels can be addressed by adopting intelligent practices such as (a) the innovative battery swapping concept (i.e., replacement of discharged batteries with charged ones at the port infrastructure per a predefined number of berths [19]) and (b) the partial (limited time) recharging of the vessel EESS at each berth [20].

The battery swapping concept constitutes an upcoming technology in electromobility, that provides significant benefits for both electric vessels and the electricity grid. At first, the navigation distance is longer, considering that the ships are capable of swapping their depleted batteries and continue their voyage [20]. Furthermore, the waiting time is reduced, considering that the total needed time at the battery swapping station quay is reduced compared to the charging mode [21]. Indeed, taking into account that the batteries' replacement with fully charged ones is performed by the aid of robotic systems or cranes, the overall procedure could take a few minutes, based on the number of batteries to be swapped.

Another benefit is that the batteries can be charged during off-peak hours or during high RES generation, which alleviates the issue of overloading, caused due to the increasing penetration of electric ships or EVs, in order to avoid grid-related problems, such as power quality degradation [21]. Last, conducting scheduled charging, the fully charged batteries stored at the battery swapping station could supply the stored energy to cover other loads of the battery swapping station, to eliminate the dependence from the utility grid; the latter feature provides high flexibility on both the charging power and the charging time [22], whereas in conjunction with RES operation, it leads to significant benefits in the electricity grid stability, as the batteries can be charged according to the renewables' generation [22]. However, despite the aforementioned benefits, there are several challenges to overcome, such as the competitive battery swapping fee over the charging fee, in order the battery swapping solution be more attractive to ship owners and the accomplishment of the appropriate short-time battery swapping procedure within the time intervals of the navigation stops.

A generic example of the battery swapping concept for electric vessels is presented in Fig 1. When the vessel arrives at the quay, the batteries installed in the vessel are moved with the aid of a robotic railway to an appropriate position at the bottom of the lower deck. Afterwards, a robotic crane replaces the discharged batteries with fully charged ones. The discharged batteries are placed at special infrastructure where they can be charged mainly (but not exclusively) from photovoltaics or other RES plants and stored for the next swapping procedure.

ISBN: 978-618-5765-04-0
ISSN 3057-4269

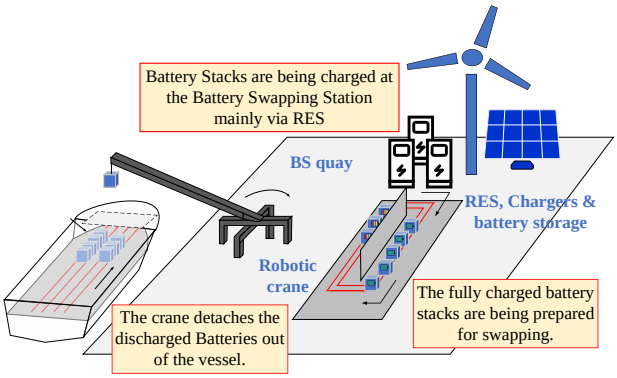

Figure 1: Port infrastructures for battery swapping of vessels.

In this context, Greek inland marine transport is expected to be an appealing field of application for the electrification concept, as it is characterized by a dense network of short sea routes (along island clusters, ferry links, etc.) and an extensive network of leisure transportations (tourist travels to sea resorts).

VESSEL SPECIFICATIONS

As it was mentioned above, within the general concept to minimize the environmental footprint of marine tourism (e.g., cruise, diving, leisure sea-travel etc.), this work studies the design and development of an innovative electrification scheme for vessels performing inland marine routes. In particular, the optimal shipbuilding and electromechanical design of an all-electric vessel is aimed, capable of serving the needs of domestic inland marine transportation and tourism industry. Taking into account the features of the vessels currently serving those needs, the specifications and requirements of the studied all-electric vessel are defined, as follows:

- A capacity of 12 adults, in order to be used either as a sea-taxi, or for the needs of specific forms of marine tourism (e.g., leisure boat).
- Minimum range of 20 nautical miles, to cover the majority of sea routes between island clusters in Greece, as well as between key ports on the mainland and neighboring island destinations.
- Maximum speed of 25 knots, to be competitive with similar conventional vessels.
- Maximum output power (electric) of the propulsion system of 350 kW (for the speed of 25 knots), derived from measurements on conventional vessels.
- The overall electric vessel weight should be to that of conventional vessels; therefore, the electrification system to be developed (including batteries, electric motors and drives, power converters, etc.) should be kept at approximately 3 tons.
- The electrification scheme should include an additional (spare) electric motor capable of moving the vessel (with reduced speed) to the nearest port in case of main propulsion system failure.
- A small photovoltaic (PV) system should be placed at the vessel top to partially supply the vessel's electrical loads or charge the EESS during high sunshine hours.
- The battery placement points should be selected with special care, in order not to affect the boat stability and to facilitate their replacement, in case of battery swapping.
- The battery management system (BMS) should prevent the deep discharge of the EESS (e.g., acceptable Depth-of-Discharge (DOD) values lower than 85% in normal operating conditions) and monitor the voltage and temperature values of each cell or each battery subsystem (to maintain the life expectancy of the EESS). Additionally, to avoid impermissible operating situations, monitoring of both the propulsion system and the vessel's main loads is required.

The compliance with the above specifications will be achieved by the appropriate study, design, development and experimental validation of the optimal available individual subsystems of the overall electrification system.

Energy Storage Systems

As regards the EESS, undoubtedly, the dominant trend nowadays is lithium-ion technology, which features significant advantages compared to other technologies [23], [24]. Specifically, lithium batteries present high energy and power densities, allow high current values during their charging and discharging, and thus can achieve short charging times (under the supervision of a Battery Management System, BMS). Additionally, lithium batteries exhibit extended thermal immunity (permissible operating temperature range from -10oC to 60oC), long life, high depth of discharge (theoretically almost up to 100%), constant voltage during discharge (at least for 75% of the capacity of the battery), high degree of efficiency in a full charge-discharge cycle (ranging between 95-98%), do not produce dangerous gases during charging (hydrogen and oxygen), do not contain caustic electrolytes, and do not require frequent full charge cycles to maintain their life expectancy. Last but not least, their costs are continuously decreasing due to technological advancements. Therefore, lithium batteries seem to be the optimal choice for the development of all-electric sea vessels.

In addition, the development of a suitable fast charging strategy is being studied, which will take advantage of the frequent docking of the vessel, whereas a smart system for monitoring of the batteries' condition (health monitoring) is being developed. This system protects batteries from overcharging or undercharging and indicates, in case that replacement is needed. The weight and size of the batteries, along with the possibility of replacing for a full charge, outside the vessel (i.e., battery swapping concept), are key factors in the design of the vessel's hull.

Propulsion and Auxilliary Subsystems

Regarding the electric propulsion system, the most appropriate options for the main motors, based on recent scientific literature and applied experience are brushless and reluctance motors [25]. The selection of motors is based on their performance, the robustness of the propulsion system and the operational specifications of the battery energy storage system. In parallel, electric motors require electric drives, i.e., power converters, for effective operation. Among others, those converters protect both batteries and motors from abnormal operating conditions, such as overloading, short circuits, etc. Finally, the auxiliary subsystems constitute a significant part of the electrical system. They are responsible for power conditioning and distribution to the vessel loads, along with protection.

ISBN: 978-618-5765-04-0
ISSN 3057-4269

Proposed Design

The 3D model of the proposed sea-taxi vessel, designed in the context of DELEMAR project is presented in Fig. 2. In particular, the configuration of both the upper part of the vessel and the interior of the hull are depicted, where the battery energy storage system, the motors and the electrical drives are placed. Specifically, in the interior of the hull, the spots for the positioning of the eight (8) battery stacks that compose the EESS are marked, as well as the spots for the positioning of the four (4) electric motor drives. Based on the above-described specifications and constraints, the propulsion of the vessel is chosen to be based on a system of three 165 hp (123 kW, 144 VDC, 5,000 rpm) brushless AC motors, weighing 68 kg, with an efficiency of 88%. Therefore, the overall propulsion system power is 369 kW and its total weight is 204 kg. Finally, the vessel will be equipped with a redundant motor (of the same electrical characteristics), to increase its reliability.

In parallel, Fig. 3 depicts the characteristic curves of torque, power, voltage and current as a function of the motor rpm. It is apparent that, in order to achieve maximum power, the electric motor must be supplied with current of 854 A; a value that requires the proper sizing of the electrochemical storage system, as well as the design of a robust condition monitoring system for the battery bank.

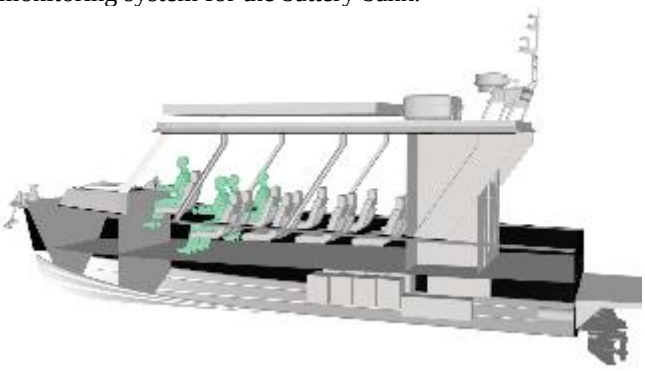

Figure 2: The 3D model of the designed sea-taxi vessel.

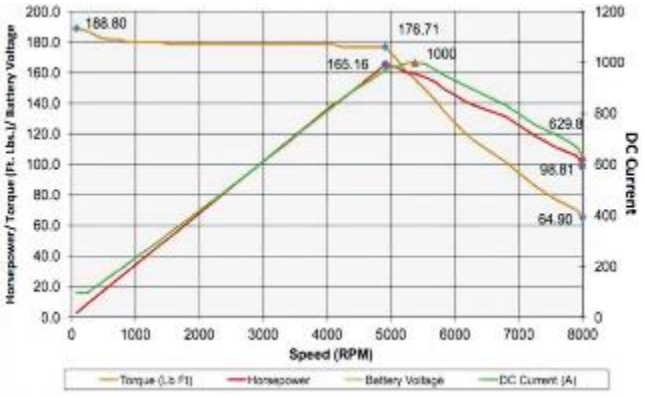

Figure 3: Characteristic curves of torque, power, voltage and current as a function of the motor rpm, for the selected brushless AC motors.

Moreover, Table 1 presents the main characteristics of the lithium-ion cells, selected for the development of the electrochemical energy storage system.

Table 1: Main parameters of the selected lithium-ion cell for the development of the battery energy storage system.

Parameter description	Value [Unit]
Typical capacity	38,000 [mAh]
Typical voltage	3.8 [V]
Full charge voltage	4.35 [V]
Cut-off voltage	3.0 [V]
Continuous discharge	38 [A]
Pulse discharge	190 [A]
Standard charging	6 [A]
Fast charging	15 [A]
Internal resistance	≤ 1.2 [mΩ]
Charging temperature	0 – 45 [˚C]
Discharging temperature	-10 – 60 [˚C]
Thickness	≤ 10.3 [mm]
Width	≤ 120.5 [mm]
Length	≤ 240.5 [mm]
Weight	≤ 595 [g]
Volumetric energy density	≤ 528.24 [Wh/L]
Gravimetric energy density	≤ 240.34 [Wh/kg]

Fig. 4 depicts the configuration of the EESS that supplies power to the three main motors. Specifically, eight (8) battery stacks are connected in parallel. Each battery stack is made up of four (4) mega-modules connected in parallel, with each mega-module composed of two modules also connected in parallel. The modules are composed of two sub-modules connected in series, and each sub-module is composed of 19 cells (at least) connected in series. The capacity of each battery stack is approximately 45 kWh, and the total capacity of EESS is 360 kWh. In total, there are 2,508 cells, weighing approximately 1.5 tons.

Finally, it is noted that the vessel will be equipped with a PV array, featuring nominal power of approximately 6 kWp, aiming at the auxiliary generation of roughly 30-40 kWh on a daily basis, during summer period.

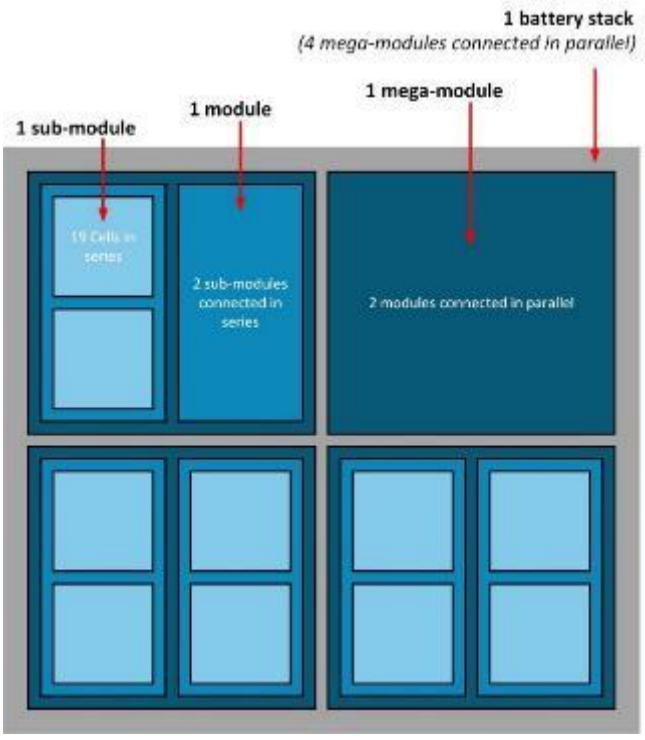

Figure 4: Battery stack configuration.

CONCLUSIONS

In this paper, the design principles of the electrical system of a marine transport-leisure vessel for domestic inland routes

ISBN: 978-618-5765-04-0
ISSN 3057-4269

were presented. Key considerations included vessel capacity, range, maximum speed, propulsion power, and total weight. Special attention was given to the selection of the energy storage system and the electric motors for the propulsion of the vessel. Additionally, the potential for swapping vessel battery packs was discussed.

REFERENCES

[1] M. Kampa, E. Castanas, “Human health effects of air pollution,” *Environmental Pollution*, vol. 151, no. 2, pp. 362-367, Jan. 2008, doi: 10.1016/j.envpol.2007.06.012.

[2] D. Pillot, B. Guiot, P. Le Cottier, P. Perret, P. Tassel, “Exhaust emissions from in-service inland waterways vessels,” *TAP 2016, 21st International Transport and Air Pollution Conference*, May 2016, LYON, France. pp. 205-225. ffhal-01488528v2.

[3] N. Olmer, B. Comer, B. Roy, X. Mao and D. Rutherford, "Greenhouse gas emissions from global shipping 2013–2015" in Washington, DC, USA, pp. 1-38, Oct. 2017.

[4] Review of Maritime Transport. *United Nations Conference on Trade and Development*, 2022. [Online]. Available: https://unctad.org/meeting/launch-review-maritime-transport-2022

[5] J. J. Valera-García and I. Atutxa-Lekue, "On the Optimal Design of Hybrid-Electric Power Systems for Offshore Vessels," *IEEE Transactions on Transportation Electrification*, vol. 5, no. 1, pp. 324-334, March 2019, doi: 10.1109/TTE.2018.2883870.

[6] G. Sulligoi, A. Vicenzutti and R. Menis, "All-Electric Ship Design: From Electrical Propulsion to Integrated Electrical and Electronic Power Systems," *IEEE Transactions on Transportation Electrification*, vol. 2, no. 4, pp. 507-521, Dec. 2016, doi: 10.1109/TTE.2016.2598078.

[7] S. Guo and L. Dai, "Voyage Optimization for Swappable Battery-Powered Inland Containerships: Considering Heterogenous Flow Velocity and Multi-Battery Swapping," *2023 IEEE/IAS Industrial and Commercial Power System Asia (I&CPS Asia)*, Chongqing, China, 2023, pp. 01-07, doi: 10.1109/ICPSAsia58343.2023.10294788.

[8] T. Zhao, J. Qiu, S. Wen and M. Zhu, "Efficient Onboard Energy Storage System Sizing for All-Electric Ship Microgrids Via Optimized Navigation Routing Under Onshore Uncertainties," *IEEE Transactions on Industry Applications*, vol. 58, no. 2, pp. 1664-1674, March-April 2022, doi: 10.1109/TIA.2022.3145775.

[9] C. Shang, D. Srinivasan and T. Reindl, "Economic and Environmental Generation and Voyage Scheduling of All-Electric Ships," *IEEE Transactions on Power Systems*, vol. 31, no. 5, pp. 4087-4096, Sept. 2016, doi: 10.1109/TPWRS.2015.2498972.

[10] M. Rafiei, J. Boudjadar and M. -H. Khooban, "Energy Management of a Zero-Emission Ferry Boat With a Fuel-Cell-Based Hybrid Energy System: Feasibility Assessment," *IEEE Transactions on Industrial Electronics*, vol. 68, no. 2, pp. 1739-1748, Feb. 2021, doi: 10.1109/TIE.2020.2992005.

[11] https://delemar.indigital.gr/

[12] https://smartports.gr/en/

[13] Electric Boats and Ships 2017-2027 – Technologies, Markets, Forecasts, Key Players and Opportunities. IDTechEx Technical Report, 2017. [Online]. Available: https://www.idtechex.com/en/research-report/electric-boats-and-ships-2017-2027/509

[14] N. Rigogiannis et al., "Power Quality Measurements in Shipboard Microgrids: A Case Study," *2023 International Conference on Electrical Drives and Power Electronics (EDPE)*, The High Tatras, Slovakia, 2023, pp. 1-8, doi: 10.1109/EDPE58625.2023.10274026.

[15] https://zeroemissionservices.nl/en/zero-emission-services-commences-operation/

[16] https://e360.yale.edu/features/europe-takes-first-steps-in-electrifying-worlds-shipping-fleets

[17] https://eu.boell.org/en/2021/07/07/all-aboard-e-ferry-ellen-and-future-electric-shipping

[18] A. Kyritsis, D. Voglitsis, N. Papanikolaou, S. Tselepis, C. Christodoulou, I. Gonos, S.A. Kalogirou,Evolution of PV systems in Greece and review of applicable solutions for higher penetration levels, *Renewable Energy*, Vol. 109, 2017, pp. 487-499, ISSN 0960-1481, https://doi.org/10.1016/j.renene.2017.03.066.

[19] Y. Zhang *et al*., "Bilevel Optimal Infrastructure Planning Method for the Inland Battery Swapping Stations and Battery-Powered Ships," in *Tsinghua Science and Technology*, vol. 29, no. 5, pp. 1323-1340, October 2024, doi: 10.26599/TST.2023.9010138.

[20] M. Gu, S. Wen, M. Zhu, C. Chen and Y. Huang, "Voyage Optimization for All-Electric Vessels Integrated with Swappable Containerized Battery," *2021 11th International Conference on Power and Energy Systems (ICPES)*, Shanghai, China, 2021, pp. 586-591, doi: 10.1109/ICPES53652.2021.9683806.

[21] Shubham Jain, Zaurez Ahmad, Mohammad Saad Alam, Yasser Rafat, "Battery Swapping technology," *5th IEEE International Conference on Recent Advances and Innovations in Engineering- ICRAIE 2020*, pp. 1-4, 2020.

[22] EU Commission, "Effect of electromobility on the power system and the integration of RES," 2018.

[23] Abbas, Q.; Mirzaeian, M.; Hunt, M.R.C.; Hall, P.; Raza, R. Current State and Future Prospects for Electrochemical Energy Storage and Conversion Systems. *Energies* 2020, 13, 5847. https://doi.org/10.3390/en13215847.

[24] P. F. Ribeiro, B. K. Johnson, M. L. Crow, A. Arsoy, and Y. Liu, “Energy storage systems for advanced power applications,” *Proc. IEEE*, vol. 89, no. 12, pp. 1744–1756, Dec. 2001.

[25] J. L. Kirtley, A. Banerjee and S. Englebretson, "Motors for Ship Propulsion," *Proceedings of the IEEE*, vol. 103, no. 12, pp. 2320-2332, Dec. 2015, doi: 10.1109/JPROC.2015.2487044.

ISBN: 978-618-5765-04-0
ISSN 3057-4269

Complementarity Analysis of Wind and Wave Power in the Eastern Mediterranean Sea

Burak Aydoğan
Department of Civil Engineering
Gebze Technical University
Kocaeli, Türkiye
baydogan@gtu.edu.tr

Tahsin Görmüş
Department of Civil Engineering
Gebze Technical University
Kocaeli, Türkiye
tgormus@gtu.edu.tr

Berna Ayat
Department of Civil Engineering
Yildiz Technical University
İstanbul, Türkiye
bayat@yildiz.edu.tr

***Abstract*— In this study we aimed at quantifying the complementarity of wind and wave power for specified nearshore locations in the Eastern Mediterranean Sea. Complementarity of two energy sources is an important indicator of their ability as a hybrid working couple. ERA5 hourly dataset from the European Centre for Medium-Range Weather Forecasts (ECMWF) between the years 1959 and 2021 is used as the data source with the variables of 100 m altitude wind speed components and significant wave heights and periods of the surface waves. Three analysis locations are selected to investigate wind and wave power computed from the raw variables. Selected analysis locations included Northern Aegean Sea (P1), Southern Aegean Sea (P2), and the Levantine Basin (P3). Yearly and seasonal averages of wind and wave power are investigated. Statistical properties of time-series are investigated with average and 95% values, and bivariate histograms considering different magnitude classes for the two sources. Among the selected locations, P2 has the highest potential of wind power with 416.3 W/m^2 mean value and 1268.6 W/m^2 95% value. The highest wave power potential is also obtained in P2 with nearly 5 kW/m average and 17.6 kW/m 95% value. These findings highlighted the differences between the regions in the Eastern Mediterranean in terms of wind and wave power and their complementarity levels.**

Keywords*— *complementarity, offshore energy, wind and wave hybrids

INTRODUCTION

Offshore renewable energy is an important component of blue economy. Decarbonization of the power sector can benefit from enormous potential in the world oceans which can be harnessed through offshore wind turbines, wave energy converters, and/or floating solar photovoltaics (PV) and other emerging ocean energy technologies.

Offshore wind is expected to increase from 34 GW in 2020 to reach 380 GW by 2030 and more than 2,000 GW by 2050 (1). The attainability of the wind power depends on the location and the temporal variations of the wind resource at site. In that manner the seasonal, inter-annual and intra-annual variability and the versatility and persistence of the resource become important (2).

The wind power potential in the Mediterranean Sea is widely studied on a local scale by different researchers and reported to be maximum of 900 W/m^2 in the Alboran Sea, 100 W/m^2 in the Gulf of Lion, and 800 W/m^2 in the Aegean Sea (3). Wave power potential in the Mediterranean Sea is also studied at different temporal scales by different researchers (4-7), locally or regionally. Both wind and wave energy devices have some limitations. Due to the variability in the climate and the device limitations complementarity of the two sources becomes an important aspect. Different indexes are proposed in the literature to evaluate the hybrid exploatibility of the wind and wave power including the statistical properties such as skewness, kurtosis, correlation coefficient, and co-location feasibility index (8).

In the Mediterranean Sea, complementarity of wind and wave powers is studied by (9) based on exploitability index and reported a limited potential for the hybrid exploitability. Colocation feasibility index based on the statistical characteristics of the wind and wave are used in Canary Islands (10). The complementarity of the wind and wave is reported to be low Aegean Sea and high in the Eastern Aegean Sea.

Due to the limited studies on the matter, we aim at quantifying the complementarity of wind and wave power for specified nearshore locations in the Eastern Mediterranean Sea, in this study.

STUDY AREA, DATA, AND METHODOLOGY

Study area

Three locations are chosen for the study where Point 1 (25°E; 39.5°N), Point 2 (25°E; 39.5°N), and Point 3 (25°E; 39.5°N) is representing the Northern Aegean Sea, Southern Aegean Sea, and the Levantine Sea, respectively. Selected locations are shown in Figure 1. Aegean Sea is one of the most active regions within the Mediterranean Basin in means of wind and wave power up to 373 W/m^2 at 100 m height (11) and 5 kW/m (6) in average, respectively.

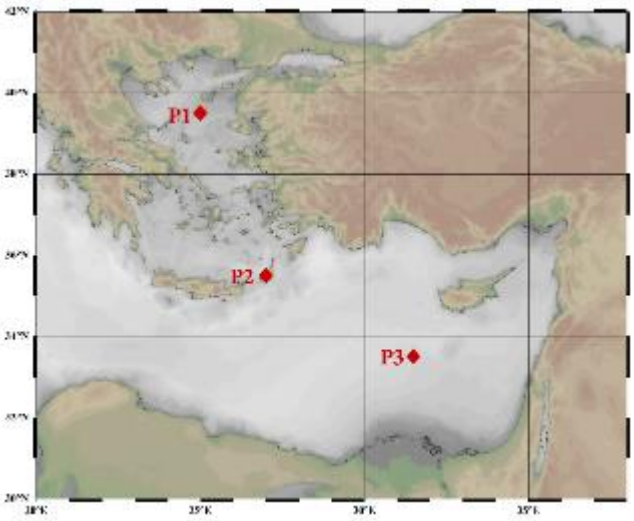

Figure 1: Study area, Aegean and the Eastern Mediterranean Sea

ISBN: 978-618-5765-04-0
ISSN 3057-4269

Annual and seasonal averages of wind and wave power at selected locations are shown in Table 1.

Table 1: Annual and seasonal averages of wind and wave power at selected locations

Season	(kW/m)	P1	P2	P3
Annual	P_{wind}	637.33	708.48	280.64
	P_{wave}	4.25	4.94	4.84
Winter	P_{wind}	925.56	770.87	424.07
	P_{wave}	8.32	7.34	9.25
Spring	P_{wind}	557.23	582.65	308.56
	P_{wave}	3.28	4.08	4.37
Summer	P_{wind}	425.84	920.09	215.78
	P_{wave}	1.32	4.22	2.69
Fall	P_{wind}	646.25	559.9	175.75
	P_{wave}	4.18	4.14	3.12

Table 1 shows that wind power potential is always much higher than the wave power potential all three locations. Based on the yearly averages, P2 at the southern Aegean Sea has the highest offshore renewable energy potential than the other two. Winter season has the highest offshore wind and wave power potential, and it is followed by fall, spring, and summer seasons.

Data

In the analysis we used 100 m wind speed, combined wind waves and swell wave height, and mean wave period data from ERA5 reanalysis dataset (12). Considered time period covers the years between 1959 and 2021. ERA5 dataset is chosen for being widely validated (6, 13-16) and reliable reanalysis dataset among others. Temporal resolution of the wind and wave data is 1 hour.

Methodology

We used equation (1) to estimate the offshore wave power.

$$P_{wave} = 0.5 H_s^2 T_e \quad (1)$$

Where H_s is the significant wave height, T_e is the wave energy period, and P_{wave} is the potential energy density per wave front (kW/m). For the computation of the wind power (P_{wind}), equation (2) is used.

$$P_{wind} = 0.5 \rho_{air} U^3 \quad (2)$$

Where ρ_{air} is air density and U is the wind speed. In this study, Siemens SWT-3.6–120 type Offshore wind turbine is considered. The turbine is selected as the most suitable one for the studied area in (11). Cut-in wind speed is $U_{cut\text{-}in}$=3.5 m/s, cut-off wind speed is $U_{cut\text{-}off}$=25 m/s, and the rated wind speed is U_{rated}=12 m/s for the turbine. The rotor diameter of the selected wind turbine is 120 m. Capacity factors (CF) of the wind turbine is evaluated based on these properties and via the normalization which is made to the average power values with the rated power values obtained by using the rated wind speed of the wind turbine. Obtained normalized CF values indicate what percent of the device's potential power can be harvested at different locations by means of both wind and wave power. To present the wave climate at the selected locations the interrelation among the wave parameters is defined by using the equation (3) based on the nonlinear least squares.

$$T_e = a \times (H_s)^b \quad (3)$$

Coefficients a and b are obtained at all three locations based on the wave height and wave period time series and allow the estimation of one parameter based on the other when one of the parameters is lacking.

In this study, prevailing wind and wave directions are also investigated since these are important for the working conditions of wave energy converters (17). Dominant wind and wave directions are estimated by means of occurrence percentages from 16 direction bins (North-N, North-NorthEast-NNE, Northeast-NE, East-NorthEast-ENE, East-E, East-SouthEast-ESE, SouthEast-SE, South-SouthEast-SSE, South-S, South-SouthWest-SSW, SouthWest-SW, West-SouthWest-WSW, West-W, West-NorthWest-WNW, NorthWest-NW, North-NorthWest-NNW). Hence the prevailing direction is decided as the highest percentage.

Complementarity of wind and wave power at the selected locations is studied in means of complementarity hours which is estimated as the percentages in total time when one of the sources is in production whereas the other is not.

In the estimation of CFs and the complementarity of two power sources evaluated separately for the previously selected wind turbine combined by 8 different WECs. The properties of studied WEC devices are given in Table 2. Power matrices for the considered WECs are taken from (18).

Table 2: The main features of the selected WECs (Modified from (18) and (19)).

No	WEC Device	Device Properties		
		Classification/Energy Mode	***Structure***	***Rated Power (kW)***
1	Pelamis	Attenuator/Heave and sway	Four-body floating	750
2	OE_buoy	Oscillating water column/ Surge	Single body floating	2880
3	AquaBuoy	Point absorber/Heave	Two-body floating	250
4	AWS	Point absorber/Heave	Two-body submerged	2470
5	SeaPower	Attenuator/Pitch	Two-body platform	3587
6	Wavebob	Point absorber/Heave	Two-body floating	1000
7	Pontoon	Multiple point absorber/Heave	Multibody floating	3619
8	Langlee	Oscillating wave surge converter/Surge	Semi-submergible	1665

RESULTS AND DISCUSSION

Capacity factors

Annual and seasonal averages of CFs for the selected wind turbine and other 8 WECs are shown in Table 3.

Selected wind turbine is much more productive than all the WECs on both yearly and seasonal scales at all the locations. On a yearly average basis CF values for the wind turbine varies between 23 to 50 % for the selected locations. Seasonal variability of the CFs indicates that the CFs in winter season higher than that of the yearly averages for all devices up to 2.25 times whereas they are almost 5 times smaller than the yearly averages during spring and summer season, and almost the same with the yearly averages during the fall season. Results shows that the highest CF values are provided by

ISBN: 978-618-5765-04-0
ISSN 3057-4269

Pelamis among the WEC devices for all seasons and almost at all locations. Pelamis is followed by Aquabuoy and Pontoon type WECS. All three mentioned WECs are showed almost same CFs on a yearly basis. In the winter season all WECs provided CF values almost two times greater than the yearly average values. The lowest CFs are obtained from AWS type WEC for all seasonal scales and at all three considered locations. For the wind turbine CF values only 20% greater than that of the yearly averages in the winter season based on a spatial average evaluation. Among the considered locations highest CF values are obtained at P2 both yearly and seasonal basis. The highest CF values are obtained in summer season at P2 whereas the highest CF values are obtained in winter season at the other two locations for the wind turbine.

Table 3: Yearly and seasonal averages of capacity factors for the selected wind turbine and 8 WECs.

	Device	P1	P2	P3
Annual	Wind turbine	0.3937	0.4996	0.2279
	Pelamis	0.0578	0.0706	0.0705
	OE_buoy	0.0094	0.0093	0.0131
	AquaBuoy	0.0455	0.0552	0.0537
	AWS	0.0095	0.0093	0.0149
	SeaPower	0.0170	0.0215	0.0237
	Wavebob	0.0329	0.0392	0.0433
	Pontoon	0.0570	0.0554	0.0599
	Langlee	0.0433	0.0522	0.0471
Winter	Wind turbine	0.4760	0.4825	0.3090
	Pelamis	0.1178	0.1116	0.1326
	OE_buoy	0.0180	0.0147	0.0272
	AquaBuoy	0.0898	0.0829	0.1087
	AWS	0.0215	0.0171	0.0328
	SeaPower	0.0347	0.0349	0.0461
	Wavebob	0.0610	0.0577	0.0772
	Pontoon	0.0710	0.0655	0.0802
	Langlee	0.0735	0.0719	0.0723
Spring	Pwind_turbine	0.3548	0.4143	0.2511
	Pelamis	0.0436	0.0576	0.0645
	OE_buoy	0.0074	0.0081	0.0117
	AquaBuoy	0.0347	0.0441	0.0491
	AWS	0.0068	0.0078	0.0130
	SeaPower	0.0129	0.0178	0.0213
	Wavebob	0.0264	0.0333	0.0397
	Pontoon	0.0539	0.0541	0.0589
	Langlee	0.0360	0.0448	0.0445
Summer	Wind turbine	0.3400	0.6790	0.2000
	Pelamis	0.0130	0.0560	0.0401
	OE_buoy	0.0037	0.0068	0.0055
	AquaBuoy	0.0129	0.0491	0.0256
	AWS	0.0016	0.0052	0.0054
	SeaPower	0.0039	0.0160	0.0125
	Wavebob	0.0124	0.0327	0.0264
	Pontoon	0.0488	0.0489	0.0479
	Langlee	0.0199	0.0466	0.0357
Fall	Wind turbine	0.4057	0.4215	0.1522
	Pelamis	0.0580	0.0578	0.0457
	OE_buoy	0.0085	0.0078	0.0082
	AquaBuoy	0.0457	0.0452	0.0323
	AWS	0.0085	0.0072	0.0088
	SeaPower	0.0170	0.0176	0.0152
	Wavebob	0.0325	0.0334	0.0302
	Pontoon	0.0545	0.0535	0.0530
	Langlee	0.0444	0.0456	0.0363

Wave climate

Analysis of the relation between significant wave height and the mean wave period is important since this relation is an indicator of the axial locations wave power extraction. This relationship determines the design conditions and performances of the WECs. 2D histogram plots of H_s vs. T_m together with the power level curves of 1, 5, 10, and 20 kW/m are shown in Figure 2 for all three locations. Fitting coefficients calculated from the H_s and T_m time series based on the equation (3) are also given on the graphs.

Figure 2 shows that coefficient a of the equation (3) varies between 4.32 and 5.16 whereas the b values vary between 0.349 and 0.374 at all three locations. Histogram graphs indicate that the waves with heights smaller than 2 m. and the wave periods smaller than 6 s have the highest occurrences at the considered locations. Wave climate analysis shows that the wave climate characteristics are similar at all three locations with the highest H_s= 8.8 m and the highest T_m= 11.66 s at P3.

Analysis of wind directions at the selected locations indicated that the dominant wind direction is NE in the northern Aegean Sea (P1), WNW in the southern Aegean Sea (P2), and W in the Levantine Basin (P3) with the occurrence percentages of 24, 34, and 28, respectively.

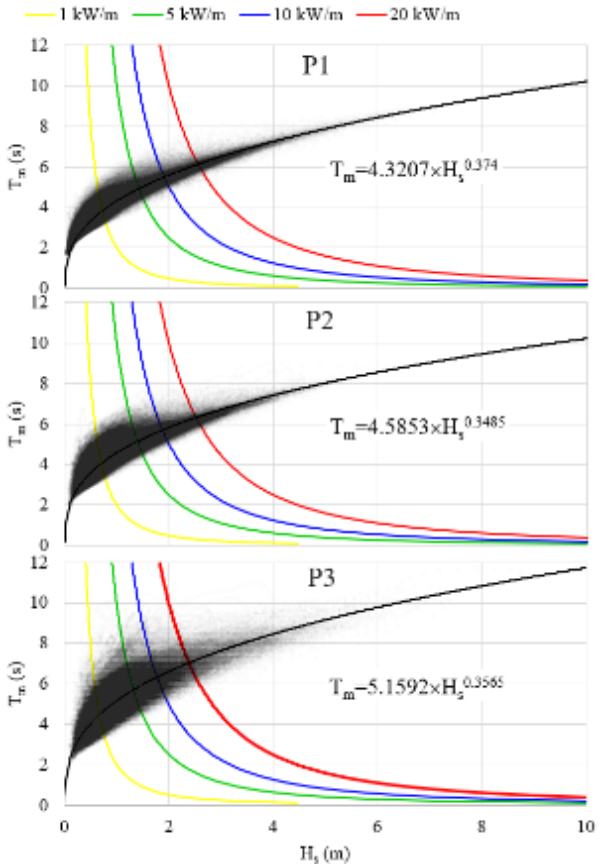

Figure 2: Wave height (H_s) vs wave period (T_m) relations at all three locations. 2D histogram plot with a fit to the function $T_m = a \times H_s b$ and wave power level curves

Analysis of wave directions at the selected locations indicated that the dominant wave direction is NE in the northern Aegean Sea (P1), WNW in the southern Aegean Sea (P2), and W in the Levantine Basin (P3) with the occurrence percentages of 31, 30, and 49, respectively.

Results indicated that dominant wind and wave directions are correlates at all three considered locations, but the wave directions tend to be more consistent in means of percentages of occurrences. The concordance between the dominant wind

ISBN: 978-618-5765-04-0
ISSN 3057-4269

and wave directions highlights that the wind waves are significant in the region rather than the swell waves.

Complementarity

To have a better insight on how effective harvesting the wind and wave power in a hybrid manner, we studied the complementarity of the two sources for all considered WEC devices, separately. Results are shown in Table 4 for wind complementing wave case.

Table 4: Complementarity of the wind and wave power in a hybrid setup for 8 WECs at the three locations.

Case	Device	P1	P2	P3
P_{wind} (W/m^2)	Pelamis	270.5	346.9	152.0
	OE_buoy	348.3	466.5	183.6
	AquaBuoy	349.3	459.9	171.9
	AWS	274.1	346.9	180.4
	SeaPower	324.3	422.5	174.5
	Wavebob	135.1	125.0	77.8
	Pontoon	266.7	325.7	101.6
	Langlee	135.1	125.0	77.8
P_{wind} (%)	Pelamis	77.9	63.4	60.7
	OE_buoy	89.1	83.5	69.5
	AquaBuoy	89.5	85.0	78.5
	AWS	78.3	63.4	63.9
	SeaPower	83.7	68.2	52.5
	Wavebob	54.2	31.0	39.4
	Pontoon	63.3	39.5	40.4
	Langlee	54.2	31.0	39.4

Similarly, the percentage of time when one of the wind or wave power sources is inactive is computed for all devices. Results are shown in Table 5.

Table 5: Percentage of total time fro the wave complementing wind condition for all 8 WEC devices at the three locations.

Time	Device	P1	P2	P3
P_{wave} (kW)	Pelamis	1.39	3.13	10.23
	OE_buoy	1.44	0.86	4.23
	AquaBuoy	0.14	0.21	1.30
	AWS	1.46	1.52	6.34
	SeaPower	1.39	5.37	15.08
	Wavebob	1.66	2.95	7.44
	Pontoon	10.43	29.57	47.52
	Langlee	2.66	7.12	15.93
P_{wave}(%)	Siemens SWT-3.6–120 Offshore wind turbine	30.4	22.3	26.5

Although the analysis of the wind and wave climate at the selected locations indicated a strong concordance between the two power sources, complementarity analysis shows that they still can complement to each other in case of nonoperating wind turbine or WEC. Table 4 and 5 supports the previous findings of CF values for different WECs that OE buoy and Aquabuoy type WECs takes the highest wind power complementarity at all three locations whereas the lowest complementarity from wind power is obtained by Wavebob and Langlee. This situation represents the "wind complementing wave" scenario. Wind complementing wind situation occurs over 80% of the time for QE buoy and Aquabuoy at locations P1 and P2. According to Table 4 and 5 "wave complementing wind scenario" occurs much less than the former one. "wave complementing wind scenario" occurs only 30.4, 22.3, and 26.5% of the time at the P1, P2, and P3, respectively.

CONCLUSION

Offshore wind and wave hybrid power potential of three locations representing the Northern Aegean Sea, Southern Aegean Sea, and the Levantine Sea are studied in means of complementarity. Wind power potential is always much higher than the wave power potential at all three locations. Based on the yearly averages, southern Aegean Sea has the highest offshore renewable energy potential than the other two basins. Winter season has the highest offshore wind and wave power potential, and it is followed by fall, spring, and summer seasons. Selected wind turbine is much more productive than eight considered WEC devices on both yearly and seasonal scales at all three basins. On a yearly average basis CF values for the wind turbine varies between 23 to 50 % for the selected locations. the highest CF values are provided by Pelamis among the WEC devices for all seasons and almost at all locations. Pelamis is followed by Aquabuoy and Pontoon type WECS. Analysis of wind and wave directions at the selected locations showed concordance between the two directions. The dominant wind and wave direction is NE in the northern Aegean Sea (P1), WNW in the southern Aegean Sea (P2), and W in the Levantine Basin (P3) with the occurrence percentages of 24, 34, and 28 for wind and 31, 30, and 49 for wave, respectively. The concordance between the dominant wind and wave directions highlights that the wind waves are significant in the region rather than the swell waves. Evaluation of the complementarity of wind and wave powers indicated that "wave complementing wind scenario" occurs much less than the "wind complementing wave scenario".

ACKNOWLEDGMENT

This research is a part of a project supported by The Scientific and Technological Research Council of Turkey (TÜBİTAK) under grant number 122M279. Tahsin Görmüş is supported by TÜBİTAK 2211 PhD scholarship programme.

REFERENCES

[1] https://www.irena.org/ (Accessed on 25.08.2024)

[2] S Bhattacharya, S Pennock, B Robertson, S Hanif, MJE Alam, D Bhatnagar, et al. "Timing value of marine renewable energy resources for potential grid applications", *Applied Energy, vol.* 299, pp.117281, 2021. https://doi.org/10.1016/j.apenergy.2021.117281.

[3] I Koletsis, V Kotroni, K Lagouvardos, T Soukissian "Assessment of offshore wind speed and power potential over the Mediterranean and the Black Seas under future climate changes", *Renew Sustain Energy Rev*; vol. 60, pp. 234–45, 2016. https://doi.org/ 10.1016/j.rser.2016.01.080.

[4] G Iglesias, R Carballo, "Wave energy potential in the Estaca de Bares Area (Spain) ", *Renewable Energy,* vol. 35, pp.1574-1584, 2010.

[5] Iglesias G, Carballo R. Offshore and inshore wave energy assessment: Asturias
(N Spain). Energy 2010;35:1964e72.

[6] B. Ayat, "Wave power atlas of Eastern Mediterranean and Aegean Seas, *Energy*, vol. 54, pp. 251-262, 2013.

[7] A Özdamar, KT Gursel, G Orer, Y Pekbey, "Investigation of the potential of wind-waves as a renewable energy resource: by the example of Çeşme-Turkey", *Renewable and Sustainable Energy Reviews*, vol. 8, pp. 581-92, 2004.

[8] RP Patel, G Nagababu, SS Kachhwaha, SVVA Kumar, M Seemanth, "Combined wind and wave resource assessment and energy extraction along the Indian coastV. *Renewable Energy*, vol. 195, pp. 931–945, 2022. https://doi.org/10.1016/j.renene.2022.06.082.

[9] A Ulazia, J Saenz, A Saenz-Aguirre, G Ibarra-Berastegui, S Carreno-Madinabeitia, "Paradigmatic case of long-term colocated wind–wave energy index trend in Canary Islands", *Energy Conversion and Management*, vol. 283, pp. 116890, 2023. https://doi.org/10.1016/j. enconman.2023.116890.

[10] K Kardakaris, I Boufidi, T Soukissian, "Offshore wind and wave energy complementarity in the greek seas based on ERA5 data", *Atmosphere*, vol. 12(10), pp. 1–172021. https://doi.org/10.3390/atmos 12101360.

[11] T Görmüş¸ B, Aydoğan, B Ayat, "Offshore wind power potential analysis for different wind turbines in the mediterranean region, 1959–2020", *Energ Conversion and Management*, vol. 274, pp. 116470, 2022. https://doi.org/10.1016/j.enconman.2022.116470.

[12] H Hersbach, B Bell, P Berrisford, G Biavati, A Horanyi, J Munoz Sabater, et al. "ERA5 hourly data on single levels from 1979 to present. Copernicus climate change service (C3S) "\ Climate Data Store 2023. https://doi.org/10.24381/cds.adbb2d47.

[13] SA Gil Ruiz, JEC Barriga, JA Martínez, "Wind power assessment in the Caribbean region of Colombia, using ten-minute wind observations and ERA5 data", *Renewable Energy*, vol. 172, pp. 158–176, 2021. https://doi.org/10.1016/j.renene.2021.03.033.

[14] T Görmüş¸ B, Ayat, B Aydoğan, "Statistical models for extreme waves: Comparison of distributions and Monte Carlo simulation of uncertainty", *Ocean Engineering*, vol. 248, pp. 110820, 2022.

[15] B Aydoğan, "Offshore wind power atlas of the Black Sea Region", *Journal of Renewable and Sustainable Energy*, vol. 9, pp. 013305, 2017.. https://doi.org/10.1063/1.4976968.

[16] J Wang, J Liu, Y Wang, Z Liao, P Sun, "Spatiotemporal variations and extreme value analysis of significant wave height in the South China Sea based on 71-year long ERA5 wave reanalysis", Applied Ocean Research, vol. 113, pp.102750, 2021. https://doi.org/ 10.1016/j.apor.2021.102750.

[17] O Choupin, M Henriksen, R Tomlinson, "Interrelationship between variables for wave direction-dependent WEC/site-configuration pairs using the CapEx method", *Energy*, vol. 248, pp. 123552,2022. https://doi.org/10.1016/j.energy.2022.123552.

[18] S Bozzi, G Besio, G Passoni, "Wave power technologies for the Mediterranean offshore: Scaling and performance analysis", *Coastal Engineering*, vol. 136, pp. 130–146, 2018. https://doi.org/10.1016/J.COASTALENG.2018.03.001.

[19] T Görmüş¸ B, Ayat, B Aydoğan, "Analysis of hybrid exploitation of wind and wave power in the Mediterranean and the Black Sea", *Energ Conversion and Management*, vol. 299, pp. 117820, 2024.

ISBN: 978-618-5765-04-0
ISSN 3057-4269

Group Cross-Efficiency Evaluation Based on Prospect Theory and Decision Consensus

Xing Shao
Guizhou University of Traditional Chinese Medicine
596218594@qq.com.

Meiqiang Wang
Guizhou University
wangmq@mail.ustc.edu.cn.

***Abstract*- In data envelopment analysis (DEA), cross-efficiency evaluation is used to assess the performance of decision-making units (DMUs). Most existing group cross-efficiency evaluation approaches assume that decision-makers (DMs) are completely rational and thus do not establish a mechanism to reach consensus among them. In this study, we combine decision consensus, prospect theory, and group cross-efficiency, propose a complete group cross-efficiency evaluation framework, and establish a new group cross-efficiency evaluation based on prospect theory and decision consensus. To the best of our knowledge, the present work provides the first real group cross-efficiency evaluation model, and it comprises three key elements. (1) A consensus degree and conflict degree measurement model based on prospect theory under the framework of group cross-efficiency evaluation is proposed. (2) Moreover, we propose a weight updating and DM preference modification model based on contribution degree, along with a corresponding iterative algorithm to help DMs reach consensus. (3) We further propose new definitions of intra-group cross-efficiency and inter-group cross-efficiency, which realize realistic peer evaluation of decision making groups. The weighted average aggregation method is used to obtain the final DMU efficiency values. Finally, an example of supplier evaluation is provided to verify the effectiveness and practicability of the proposed model in terms of DMU efficiency evaluation and ranking.**

Keywords-- data envelopment analysis; group cross-efficiency evaluation; prospect theory; decision consensus

INTRODUCTION

In real decision-making processes, some problems impact multiple stakeholders, and thus a considerable number of stakeholders should participate in the decision-making process. Meanwhile, as the decision-making environment becomes increasingly complex, it becomes more difficult to obtain reliable decision-making results by relying on a single decision-maker (DM). Therefore, group decision-making is crucial in practice. Currently, most cross-efficiency evaluations involve only one DM, and their performance is evaluated based on evaluation indices of $DMUs$. Only a few studies pertaining to group cross-efficiency have been conducted.

Generally, group decision-making problems are solved using a consensus process and a selection process [5]. The consensus process aims to maximize the agreement among DMs, whereas the selection process obtains the best alternative(s) or ranking of alternatives. Consensus is typically defined as the full and unanimous agreement of DMs regarding all alternatives. However, unanimity may be difficult to obtain owing to differences in the knowledge structure, personal preference, and social background of DMs, and a complete agreement is not always necessary in practice. Therefore, [7] proposed the concept of a "soft" consensus degree. Based on a "soft" consensus degree, various consensus-reaching processes ($CRPs$) have been proposed. However, relevant studies regarding multiple-attribute decision-making for $CRPs$ under group DEA cross-efficiency (GCE) evaluation have not been reported in the literature.

Based on the abovementioned studies, in existing group cross-efficiency and $CRPs$, it is assumed that DMs are completely rational and generally adhere to the expected utility theory framework. However, substantial experimental evidence suggests that human behavior may significantly deviate from or contradict these classical principles under uncertain conditions [4]. Considering the limitations of the expected-utility theory, [8] proposed a prospect theory that captured the non-rational psychological aspects of DMs facing uncertainties. To adapt to complicated decision-making environments the establishment of a complete group cross-efficiency evaluation framework is necessary to support the acceptance of decision-making by all DMs. Hence, we introduce prospect theory and decision consensus degree in group cross-efficiency evaluation, consider the bounded rational behavior of DMs and decision consensus, and propose a novel group cross-efficiency evaluation method and associated framework based on prospect theory and decision consensus.

The remainder of this study is organized as follows. Section 2 presents a brief introduction to conventional cross-efficiency evaluation, prospect theory, and consensus-reaching processes. In Section 3, group cross-efficiency evaluation is analyzed based on prospect theory and decision-making consensus. Section 4 provides an example of a supplier evaluation to demonstrate the application of the proposed group cross-efficiency evaluation model and presents a comparative analysis to verify its effectiveness. Finally, Section 5 presents some concluding remarks.

GROUP CROSS-EFFICIENCY BASED ON PROSPECT THEORY AND DECISION CONSENSUS

In this section, we propose group cross-efficiency based on prospect theory and decision consensus, considering the bounded rational behavior and decision consensus degree of DMs in cross-efficiency evaluation. The decision framework, as shown in Figure 1.

Let n $DMUs$ be evaluated. The ith input and pth output of $DMU_j(j = 1, \dots, n)$ are denoted as $x_{ij}(i = 1, \dots, m)$ and $y_{pj}(p = 1, \dots, s)$, respectively. Let $tDMs$ participate in the decision-making process. The qth DM is denoted as $e_q(q = 1, \dots, t)$. The weight of DMs is denoted as $\lambda_q(q = 1, \dots, t)$ and satisfies $\sum_{q=1}^{t} \lambda_q = 1$. $r_i^{in(q)}, r_p^{out(q)}$ denote the input and

ISBN: 978-618-5765-04-0
ISSN 3057-4269

output interval reference points of DMs e_q.$L_{ij}^{in(q)}, G_{ij}^{in(q)}, L_{pj}^{out(q)}, G_{pj}^{out(q)}$ represents the perceived loss and gain of DMs e_q to the inputs and outputs of DMU_j, respectively. The input and output decision consensus degree of DMU_j is denoted as CP_j^{in}, CP_j^{out}, and the total decision consensus degree is denoted as CP. θ_q, D_qrepresents the decision conflict degree and degree of contribution of DMs e_q, while θ represents the total degree of decision conflict, and δ represents the conflict degree threshold.

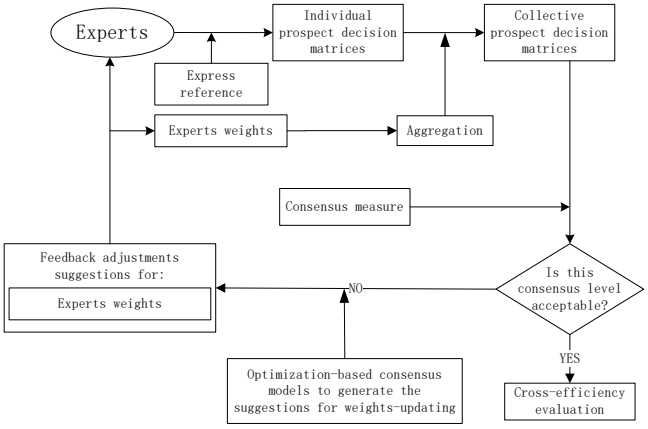

Figure 1. Decision-making framework for group cross-efficiency evaluation

Establish prospect value decision matrix

In the actual decision-making process, it is difficult for DMs to express their preferences in terms of a precise value because of the lack of complete knowledge and information regarding the decision-making problem. Based on the idea of [10] regarding interval reference $DMUs$, interval reference points are defined as follows.

Definition 1 For DMs, the interval reference points of the inputs and outputs of $DMUs$ are defined as follows.

$$r_i^{in(q)} = \left[a_i^q x_i^{\min}, b_i^q x_i^{\max}\right] \quad 1 \le a_i^q \le \frac{x_i^{\max}}{x_i^{\min}}, \frac{x_i^{\min}}{x_i^{\max}} \le b_i^q \le 1, \frac{b_i^q}{a_i^q} \ge \frac{x_i^{\min}}{x_i^{\max}}$$

$$r_p^{out(q)} = \left[c_p^q y_p^{\min}, d_p^q y_p^{\max}\right] \quad 1 \le c_p^q \le \frac{y_p^{\max}}{y_p^{\min}}, \frac{y_p^{\min}}{y_p^{\max}} \le d_p^q \le 1, \frac{d_p^q}{c_p^q} \ge \frac{y_p^{\min}}{y_p^{\max}} \cdot$$

$$i = 1,\ldots,m \quad p = 1,\ldots,s \qquad (1)$$

In model (3), $x_i^{\min_j\{x_{ij}\}}$ and $x_i^{\max_j\{x_{ij}\}}$ represents the minimum and maximum inputs in the decision matrix, respectively. $y_p^{\min_j\{y_{pj}\}}$, $y_p^{\max_j\{y_{pj}\}}$ represents the maximum and minimum outputs in the decision matrix. $a_i^q, b_i^q, c_p^q, d_p^q$ is a set of parameters, which are given by DMs e_q within the value range of the parameters according to their own professional judgment and psychological behavior characteristics under risk or uncertainty when determining the reference points of inputs and outputs.

Definition 2 For the aspiration level a_i, let y_1 and y_2 be two arbitrary values in the interval number $[a_i^L, a_i^U]$ and let $\delta(y_1, y_2)$ denote the perceived difference between y_1 and y_2; therefore, $\delta(y_1, y_2) = 0$, i.e., y_1 and y_2 are equivalent [1].

In practical decision-making problems, the aspiration level is generally regarded as a reference point for DMs [8]. The gain and loss of the outputs of DMU can be calculated as follows.

$$G_{pj}^{out(q)} = \begin{cases} y_{pj} - r_p^{U(q)} & y_{pj} > r_p^{U(q)} \\ 0 & y_{pj} < r_p^{L(q)} \\ 0 & r_p^{L(q)} \le y_{pj} \le r_p^{U(q)} \end{cases}$$

$$L_{pj}^{out(q)} = \begin{cases} 0 & y_{pj} > r_p^{U(q)} \\ y_{pj} - r_p^{L(q)} & y_{pj} < r_p^{L(q)} \\ 0 & r_p^{L(q)} \le y_{pj} \le r_p^{U(q)} \end{cases}$$

$$p = 1,\ldots,s \; j = 1,\ldots,n \; q = 1,\ldots,t \qquad (2)$$

For the DMUinput x_{ij}, if $x_{ij} > r_i^{U(q)}$, the deviation can be regarded as the $DM's$ loss. By contrast, if $x_{ij} < r_i^{U(q)}$, the deviation can be regarded as the $DM's$ gain. Hence, the gain and loss of the inputs of $DMUs$ can be calculated as follows.

$$G_{ij}^{in(q)} = \begin{cases} 0 & x_{ij} > r_i^{U(q)} \\ r_i^{L(q)} - x_{ij} & x_{ij} < r_i^{L(q)} \\ 0 & r_i^{L(q)} \le x_{ij} \le r_i^{U(q)} \end{cases}$$

$$L_{ij}^{in(q)} = \begin{cases} r_i^{U(q)} - x_{ij} & x_{ij} > r_i^{U(q)} \\ 0 & x_{ij} < r_i^{L(q)} \\ 0 & r_i^{L(q)} \le x_{ij} \le r_i^{U(q)} \end{cases}$$

$$i = 1,\ldots,m \; j = 1,\ldots,n \; q = 1,\ldots,t. \qquad (3)$$

Using the prospect value function, the decision-making matrices $A^{in(q)} = \left(a_{ij}^{in(q)}\right)_{m\times n}$ and $A^{out(q)} = \left(a_{pj}^{out(q)}\right)_{s\times n}$ of the input and output prospect values of DM e_q for DMU_j are established. To facilitate the subsequent calculation, the

ISBN: 978-618-5765-04-0
ISSN 3057-4269

prospect-value-decision-making matrix must be normalized. Generally, the prospect value decision-making matrix can be categorized into cost and benefit types. Using the following formula, the prospect-valued decision-making matrix can be transformed into normalized decision-making matrices $V^{in(q)} = \left(v_{ij}^{in(q)}\right)_{m\times n}$ and $V^{out(q)} = \left(v_{pj}^{out(q)}\right)_{s\times n}$.

$$v_{ij}^{in(q)} = \frac{\max_i\left(a_{ij}^{in(q)}\right) - a_{ij}^{in(q)}}{\max_i\left(a_{ij}^{in(q)}\right) - \min_i\left(a_{ij}^{in(q)}\right)} \; i = 1,2,\dots,m \;\; j = 1,2,\dots,n \; q = 1,2,\dots,t$$

$$v_{pj}^{out(q)} = \frac{a_{pj}^{out(q)} - \min_p\left(a_{pj}^{out(q)}\right)}{\max_p\left(a_{pj}^{out(q)}\right) - \min_p\left(a_{pj}^{out(q)}\right)} \; p = 1,2,\dots,s \;\; j = 1,2,\dots,n \; q = 1,2,\dots,t. \quad (4)$$

Consensus measure and CRP

Because DMs have different opinions, it is impossible for all DMs to reach complete agreement on the evaluation results. Therefore, a consensus measure is required when the preferences of DMs are aggregated into group preferences. When the consensus degree fails to reach the preset threshold, a feedback mechanism must be established to enable DMs to reach consensus. This process is known as reaching a consensus. Generally, consensus approaches in the literature can be categorized into two groups. The first group considers a mathematical aggregated consensus. This type of consensus is achieved by changing the weights of DMs [9]. In the other type, DMs are encouraged to modify their preferences to reach a closer agreement in terms of preferences [6]. Preference modification and weight-updating methods have been proven effective for CRP [13, 12]. In this section, a consensus degree measurement model is introduced as a consensus-reaching model based on weight updating and preference modification under the framework of cross-efficiency evaluation.

In the consensus degree measurement process, we assume that the $DM's$ initial weight λ_q is constant, i.e., $\lambda_q = 1/t$.

Definition 3 Let $V^{in(q)} = \left(v_{ij}^{in(q)}\right)_{m\times n}$ be individual input prospect value decision matrices, $V^{out(q)} = \left(v_{pj}^{out(q)}\right)_{s\times n}$ be individual output prospect value decision matrices, $V^{in(c)} = \left(v_{ij}^{in(c)}\right)_{m\times n}$ be the collective input prospect value decision matrix, and $V^{out(c)} = \left(v_{pj}^{out(c)}\right)_{s\times n}$ be the collective output prospect value decision matrix. Then, $V^{in(c)}$ and $V^{out(c)}$ are expressed as follows.

$$v_{ij}^{in(c)} = \sum_{q=1}^{t}\lambda_q v_{ij}^{in(q)} \quad i = 1,\dots,m \;\; j = 1,\dots,n \;\; q = 1,\dots,t$$

$$v_{pj}^{out(c)} = \sum_{q=1}^{t}\lambda_q v_{pj}^{out(c)} \quad p = 1,\dots,s \; j = 1,\dots,n \; q = 1,\dots,t. \quad (5)$$

Definition 4 Let $V^{in(q)} = \left(v_{ij}^{in(q)}\right)_{m\times n}$ $V^{out(q)} = \left(v_{pj}^{out(q)}\right)_{s\times n}$ be the prospect-value decision matrix of DM e_q to DMU_j. $V^{in(c)} = (v_{ij}^{c})_{m\times n}$ and $V^{out(c)} = (v_{pj}^{out(c)})_{s\times n}$ be the collective prospect value decision matrix of DMU_j. Then, the input decision consensus CP_j^{in}, output decision consensus CP_j^{out}, and overall decision consensus CP_j are expressed as

$$CP_j^{in} = 1 - \sum_{q=1}^{t}\lambda_q\sum_{i=1}^{m} w_i\left|v_{ij}^{in(q)} - v_{ij}^{in(c)}\right|,$$

$$CP_j^{out} = 1 - \sum_{q=1}^{t}\lambda_q\sum_{p=1}^{s}\mu_p\left|v_{pj}^{out(q)} - v_{pj}^{out(c)}\right|,$$

$$CP_j = 1 - \sum_{q=1}^{t}\lambda_q\left(\sum_{i=1}^{m} w_i\left|v_{ij}^{in(q)} - v_{ij}^{in(c)}\right| + \mu_p\left|v_{pj}^{out(q)} - v_{pj}^{out(c)}\right|\right). \quad (6)$$

Similarly, the total consensus degree of all $DMUs$ is expressed as

$$CP = \frac{1}{n}\sum_{j=1}^{n} CP_j. \quad (7)$$

If the consensus degree $CP = 1$, all DMs reach a complete agreement on the evaluation results of all $DMUs$. The higher the CP value, the higher the degree of consensus of the DMs regarding the evaluation result, and vice versa.

Definition 5 Let $V^{in(q)} = \left(v_{ij}^{in(q)}\right)_{m\times n}$ $V^{out(q)} = \left(v_{pj}^{out(q)}\right)_{s\times n}$ be the prospect-value decision matrix of DM e_q to DMU_j. $V^{in(c)} = (v_{ij}^{c})_{m\times n}$ and $V^{out(c)} = (v_{pj}^{out(c)})_{s\times n}$ be the collective prospect value decision matrix of DMU_j. Then, the conflict degree between the individual decision matrices and the group decision matrix of DMs e_q is expressed as

$$\theta_q = \frac{1}{n}\sum_{j=1}^{n}\left(\sum_{i=1}^{m} w_i\left|v_{ij}^{in(q)} - v_{ij}^{in(c)}\right| + \mu_p\left|v_{pj}^{out(q)} - v_{pj}^{out(c)}\right|\right). \quad (8)$$

Similarly, the total conflict degree θ for all DMs is expressed as

$$\theta = \sum_{q=1}^{t}\lambda_q\theta_q. \quad (9)$$

Let δ be a pre-specified threshold for an acceptable level of group conflict. If $\theta < \delta$, then the level of conflict between DMs is acceptable.

In CRP, the DMs must adhere to consensus rules. Traditionally, CRP is based on identification and direction rules [2]. We propose a DMs weight-updating model.

ISBN: 978-618-5765-04-0
ISSN 3057-4269

$$CP_{j\bar{q}} = 1 - \sum_{d=1}^{t} \beta_d \left(\sum_{i=1}^{m} w_i \left| v_{ij}^{in(d)} - v_{ij}^{in(c)} \right| + \sum_{p=1}^{s} \mu_p \left| v_{pj}^{out(d)} - v_{pj}^{out(c)} \right| \right)$$
$$d = 1,2,\dots,t \quad d \neq q$$
$$\beta_d = \frac{\lambda_d}{\sum_{b=1}^{t} \lambda_b} \quad b = 1,2,\dots,t \quad b \neq q$$
$$D_{jq} = CP_j - CP_{j\bar{q}} \quad j = 1,2,\dots,n$$
$$D_q = \sum_{j=1}^{n} D_{jq}, \quad (10)$$

where $CP_{j\bar{q}}$ is the group consensus level of DMU_j, without $DM\ e_q$. D_{jq} denotes the decision contribution degree of $DM\ e_q$ to DMU_j, and D_q denotes the aggregation decision contribution degree of $DM\ e_q$. The larger the value of D_q, the higher the contribution of $DM\ e_q$ to the group decision-making. If the conflict level exceeds the threshold δ, i.e. $\theta > \delta$, the weights of the DMs must be updated to reach a new group decision consensus. The weights are updated as follows.

$$\gamma_q = \lambda_q (1 + D_q)^{\sigma}, \tilde{\lambda}_q = \frac{\gamma_q}{\sum_{q=1}^{t} \gamma_q}, q = 1,2\dots,t. \quad (11)$$

The parameter σ represents the effects of the DMs' contribution on the weights.

Based on the definitions and weight-updating model in the previous section, we propose an iterative consensus-reaching algorithm to resolve conflict in group decision-making.

Step 1. Initialize the DMweight $\lambda_q = \frac{1}{t}$.

Step 2. Let $l = 0$, $V_0^{in(q)} = \left(v_{ij,0}^{in(q)}\right)_{m \times n} = V^{in(q)}$, and $V_0^{out(q)} = \left(v_{pj,0}^{out(q)}\right)_{s \times n} = V^{out(q)}$. Here, l is the number of iterations.

Step 3. Apply Eq. (14) to aggregate the normalized individual decision-making matrices $V_l^{in(q)}, V_l^{out(q)}$ into group decision matrices $V_l^{in(c)}, V_l^{out(c)}$. Eq. (17) and (18) are used to calculate the conflict degree $\theta_{q,l}$ between individual $DMs\ e_q$ and group decision-making, as well as the total conflict degree θ_l. If $\theta_l \leq \delta$ or $l = l^{max}$, proceed to Step 6. Otherwise, proceed to the next step.

Step 4. Apply Eqs. (19) and (20) to measure the contribution of D_q and update the weight $\tilde{\lambda}_q^l$of $DMs\ e_q$.

Step 5. Identify the position of $DMU_j$with maximum absolute deviations $o_{i_\tau j_\tau,l}^{in(q)}$ and $o_{p_\psi j_\psi,l}^{out(q)}$ for each DMe_q, where $o_{i_\tau j_\tau,l}^{in(q)} = \max_{i,j} \left(\left| v_{ij,l}^{in(q)} - v_{ij,l}^{in(c)} \right| \right)$ and $o_{p_\psi j_\psi,l}^{out(q)} = \max_{p,j} \left(\left| v_{pj,l}^{out(q)} - v_{pj,l}^{out(c)} \right| \right)$, and adjust the corresponding values as follows.

$$v_{ij,l}^{in(q)} = \begin{cases} v_{ij,l}^{(c)} \ if\ i = i_\tau, j = j_\tau \\ v_{ij,l}^{in(q)} \ otherwise \end{cases}$$
$$o_{pj,l}^{out(q)} = \begin{cases} v_{pj,l}^{(c)} \ if\ p = p_\psi, j = j_\psi \\ v_{pj,l}^{out(q)} \ otherwise \end{cases}$$
$$i = 1,\dots,m; j = 1,\dots,n; p = 1,\dots,s; q = 1,\dots,t. \quad (12)$$

Let $l = l + 1$ and return to Step 3.

Step 6. Let the $DM\ e_q$ weight $\lambda_q = \lambda_q^l$, total conflict degree $\theta = \theta_l$, and individual decision-making matrices $V^{in(q)} = V_l^{in(q)}$ and $V^{out(q)} = V_l^{out(q)}$.

Step 7 End.

Group cross-efficiency evaluation

Group cross-efficiency evaluation model

In group decision-making, the peer evaluation DMU should be reflected not only within the group, but also among the groups. Based on this idea, the following group DEA cross-efficiency evaluation model was established, and the intragroup cross-efficiency, intragroup cross-efficiency, and final cross-efficiency aggregation were defined.

For $DMs\ e_q$, the self-evaluation efficiency $E_{kk}^{(qq)}$ of DMU_k can be obtained as follows.

$$Max\ E_{kk}^{(qq)} = \sum_{p=1}^{s} \mu_{pk}^{(q)} v_{pk}^{out(q)}$$
$$s.t. \sum_{i=1}^{m} w_{ik}^{(q)} v_{ik}^{out(q)} = 1$$
$$\sum_{p=1}^{s} \mu_{pk}^{(q)} v_{pj}^{out(q)} - \sum_{i=1}^{m} w_{ik}^{(q)} v_{ij}^{in(q)} \leq 0$$
$$\sum_{p=1}^{s} \mu_{pk}^{(q)} v_{pj}^{out(d)} - \sum_{i=1}^{m} w_{ik}^{(q)} v_{ij}^{in(d)} \leq 0 \ q \neq d$$
$$w_{ik}^{(q)}, \mu_{pk}^{(q)} \geq 0$$
$$i = 1,\dots,m \ j = 1,\dots,n \ q = 1,\dots,t \ \ k = 1,\dots,n \ d = 1,\dots,t. \quad (13)$$

Let $(\mu_{pk}^{(q)*}, w_{ik}^{(q)*})$ be the optimal solution of Eq. (22); therefore,

$$E_{kk}^{(qq)} = \sum_{p=1}^{s} u_{pk}^{(q)*} v_{pk}^{out(q)}$$

ISBN: 978-618-5765-04-0
ISSN 3057-4269

$$E_{jk}^{(qq)} = \frac{\sum_{p=1}^{s} \mu_{pk}^{(q)*} v_{pj}^{out(q)}}{\sum_{i=1}^{m} w_{ik}^{(q)*} v_{ij}^{in(q)}}$$
$$q = 1,\dots,t; j,k = 1,\dots,n; i = 1,\dots,m; p = 1,\dots,s. (14)$$

In group decision-making, peer evaluation DMs should be considered. Therefore, we introduce cross-efficiency between groups and define the cross-efficiency $E_{jk}^{(qd)}$ between e_q and $e_d$as follows.

$$E_{jk}^{(qd)} = \frac{\sum_{p=1}^{s} \mu_{pk}^{(d)} v_{pj}^{out(q)}}{\sum_{i=1}^{m} w_{ik}^{(d)} v_{ij}^{in(q)}} \; j,k = 1,\dots,n; q,d = 1,\dots,t; q \neq d. \quad (15)$$

For each DMU_j, the cross-efficiency evaluation matrix is composed of intragroup cross-efficiency $E_{jk}^{(qq)}$ and intergroup cross-efficiency $E_{jk}^{(qd)}$, as follows.

$$E_{jk}^{(qq)} = \begin{pmatrix} E_{11}^{(qq)} & \dots & E_{1n}^{(qq)} \\ \vdots & \ddots & \vdots \\ E_{n1}^{(qq)} & \dots & E_{nn}^{(qq)} \end{pmatrix} \; q = 1,\dots,t \; j,k = 1,\dots,n,$$

$$E_{jk}^{(qd)} = \begin{pmatrix} E_{11}^{(qd)} & \dots & E_{1n}^{(qd)} \\ \vdots & \ddots & \vdots \\ E_{n1}^{(qd)} & \dots & E_{nn}^{(qd)} \end{pmatrix} \; q,d = 1,\dots,t \; q \neq d \; j,k = 1,\dots,n.$$

In this study, cross-efficiency aggregation is categorized into two levels, including intragroup and intergroup cross-efficiency aggregations. For DMU_j, the intragroup and intergroup cross-efficiencies are respectively defined as follows.

$$E_j^{(qq)} = \frac{1}{n}\sum_{k=1}^{n} E_{jk}^{(qq)} \; j,k = 1,\dots,n; q = 1,\dots,t,$$
$$E_j^{(qd)} = \frac{1}{n}\sum_{k=1}^{n} E_{jk}^{(qd)} \; j,k = 1,\dots,n; q,d = 1,\dots,t; q \neq d. \quad (16)$$

For DMs e_q, the cross-efficiency comprises intragroup cross-efficiency $E_j^{(qq)}$ and $t-1$ intergroup cross-efficiency $E_j^{(qd)}$. Subsequently, the aggregation cross-efficiency of DMU_j is defined as

$$E_j^{(q)} = \frac{1}{t}\left(E_j^{(qq)} + \sum_{d=1,d\neq q}^{t} E_j^{(qd)}\right) q,d = 1,\dots,t; q \neq d; j = 1,\dots,n. \quad (17)$$

Similarly, for DMU_j, the final efficiency is defined as

$$E_j = \sum_{q=1}^{t} \lambda_q E_j^{(q)} \quad j = 1,\dots,n; q = 1,\dots,t, (18)$$

where λ_q denotes the DM's weight when consensus is reached.

Neutral secondary goal model

Note that the optimal weights obtained from model (22) are usually not unique. .Based on the idea of [3], we propose the following neutral secondary goal model to select a set of appropriate weights from multiple weight sets.

$$\begin{aligned} Max & \sum_{p=1}^{s} \mu_{pk}^{(q)} \left(\sum_{j=1,j\neq k}^{n} v_{pj}^{out(q)} \right) \\ s.t. & \sum_{i=1}^{m} w_{ik}^{(q)} \left(\sum_{j=1,j\neq k}^{n} v_{ij}^{in(q)} \right) = 1, \\ & \sum_{p=1}^{s} \mu_{pk}^{(q)} v_{pk}^{out(q)} - E_{kk}^{(qq)*} \cdot \sum_{i=1}^{m} w_{ik}^{(q)} v_{ik}^{in(q)} = 0, \\ & \sum_{p=1}^{s} \mu_{pk}^{(q)} v_{pj}^{out(q)} - \sum_{i=1}^{m} w_{ik}^{(q)} v_{ij}^{in(q)} \leq 0, \\ & \sum_{p=1}^{s} \mu_{pk}^{(q)} v_{pj}^{out(d)} - \sum_{i=1}^{m} w_{ik}^{(q)} v_{ij}^{in(d)} \leq 0 \; d = 1,2,\dots t; d \neq q, \\ & w_{ik}^{(q)}, \mu_{pk}^{(q)} \geq 0, \\ & i = 1,\dots,m; j = 1,\dots,n; d,q = 1,\dots,t \;\; k = 1,\dots,n. \end{aligned} \quad (19)$$

In model (28), for DM e_q,the secondary goal is to choose the weights that maximize the cross-efficiency of all other units while maintaining the self-evaluation efficiency of the target DMU_k unchanged, instead of maximizing or minimizing the cross-efficiency of other DMs. Therefore, this is a neutral secondary goal model.

NUMERICAL EXAMPLE

To illustrate the effectiveness and rationality of the proposed group cross-efficiency evaluation method based on prospect theory and decision-making consensus, we provide a classical supplier evaluation example. In this example, a single moderator and five DMs participated in the evaluation, and 14 major international passenger airlines were evaluated in terms of three inputs and two outputs, as defined below.

x_1: aircraft capacity in kilometers,

x_2: operating cost,

x_3: non-flight assets, such as reservation systems, facilities, and current assets,

y_1: passenger kilometers,

y_2: non-passenger revenue.

ISBN: 978-618-5765-04-0
ISSN 3057-4269

Results and analysis of numerical example

As shown in Table 1, the group cross-efficiency evaluation method proposed herein provides better discrimination and can rank all $DMUs$. Moreover, the proposed method considers the $DM's$ bounded rational behavior and decision consensus, and fully considers the subjective preference and psychological behavior characteristics of DMs under risk. In the cross-efficiency evaluation, peer evaluations within the group and among groups are considered. In particular, in cross-efficiency aggregation, the weight of the DMs is obtained when consensus is reached. The evaluation results can reflect the differences in the evaluation of $DMUs$ by DMs, and the evaluation results are obtained based on the consensus reached by the DMs, i.e., the result of group decision-making. Therefore, the entire evaluation process can reflect the subjective preferences and bounded rationality under risk of the DMs; additionally, the process enables DMs to reach consensus regarding the evaluation results, and the evaluation results are more reasonable and easier for all the DMs to accept.

Table 1 DMUs aggregation cross-efficiency

$E_j^{(q)}$	e_q					E_j
	1	2	3	4	5	
1	0.193	0.246	0.365	0.166	0.290	0.235
2	0.008	0.013	0.036	0.011	0.009	0.012
3	0.069	0.104	0.058	0.098	0.073	0.079
4	0.282	0.274	0.141	0.226	0.300	0.264
5	0.155	0.340	0.480	0.135	0.147	0.199
6	0.020	0.021	0.046	0.016	0.021	0.022
7	0.568	0.644	0.371	0.278	0.497	0.488
8	0.228	0.219	0.216	0.234	0.222	0.226
9	0.335	0.497	0.204	0.334	0.423	0.369
10	0.422	0.665	0.531	0.542	0.808	0.589
11	0.612	0.520	0.464	0.411	0.614	0.551
12	0.452	0.568	0.340	0.242	0.712	0.488
13	0.100	0.178	0.244	0.069	0.107	0.118
14	0.112	0.155	0.072	0.136	0.128	0.123

Comparative analysis

Table 2 shows the evaluation results of the group cross-efficiency evaluation model proposed herein (CPGCE) and the classical cross-efficiency models for 14 passenger airlines. As shown in Table 2, the efficiency values of the group cross-efficiency evaluation model proposed herein were lower than those of the other classical cross-efficiency evaluation models.

Table 2 Efficiency comparison between proposed method and classical cross-efficiency evaluation methods

DMU	**CPGCE**	**IDMU**	**ADMU**	**[A-, A+]**	**Benevolent**	**Aggressive**	**Neutral**
1	0.235	0.645	0.632	0.610	0.754	0.599	0.661
2	0.012	0.187	0.171	0.187	0.189	0.165	0.209
3	0.079	0.640	0.657	0.610	0.768	0.623	0.629
4	0.264	0.698	0.711	0.673	0.822	0.673	0.709
5	0.199	0.767	0.838	0.779	0.891	0.798	0.796
6	0.022	0.637	0.674	0.609	0.755	0.639	0.592
7	0.488	0.728	0.682	0.686	0.821	0.648	0.754
8	0.226	0.648	0.614	0.615	0.724	0.586	0.681
9	0.369	0.692	0.659	0.669	0.759	0.631	0.747
10	0.589	0.702	0.708	0.707	0.780	0.681	0.799
11	0.551	0.800	0.814	0.816	0.919	0.774	0.908
12	0.489	0.778	0.766	0.756	0.885	0.731	0.837
13	0.118	0.804	0.783	0.763	0.919	0.750	0.820
14	0.123	0.732	0.772	0.708	0.866	0.732	0.709

In Figure 2, a–c represents the ranking comparison for 14 passenger airlines between the group cross-efficiency evaluation model in this study and the prospect cross-efficiency evaluation proposed by [10]. Here, d–f represents the ranking comparison for 14 passenger airlines between the group cross-efficiency evaluation model proposed herein and each of the benevolent and aggressive cross-efficiency evaluation models proposed by [3] and the neutral cross-efficiency evaluation model proposed by [11]. As shown in Figure 2, the proposed method and the other classical cross-efficiency evaluation methods showed similar trends in terms of the rankings of the 14 passenger airlines. In addition, the rankings for most passenger airlines did not change significantly. DMU_{13} had the largest difference in ranking, mainly due to the selection of reference points. In this study, the reference points were provided by five DMsaccording to their professional judgment and different psychological and behavioral characteristics under risk. The evaluation result is the result of group decision-making process, which is more realistic. However, [10] selected virtual points as reference points, such as A or B, which involved certain limitations and sometimes obtained incorrect evaluation results. Meanwhile, in the cross-efficiency evaluation proposed by [10] and [3], peer evaluation is data-driven and not real peer evaluation. The CPGCE model proposed in this paper established the definition of intragroup and intergroup cross-efficiency, and

ISBN: 978-618-5765-04-0
ISSN 3057-4269

five DMsparticipated in the decision-making, which truly realized peer evaluation. The method proposed herein can reflect the actual performance and characteristics of $DMUs$ and is an effective and practical group cross-efficiency evaluation method.

CONCLUSION

In this study, the concept of prospect theory and decision consensus degree have been introduced into group cross-efficiency evaluation, and a novel group cross-efficiency evaluation based on prospect theory and decision consensus has been established. Subsequently, a complete decision framework for group cross-efficiency evaluation based on prospect theory was proposed. The bounded rational behavior of DMs was considered in the consensus degree measurement, CRP, and group cross-efficiency evaluation. A group decision-making model under the framework of cross-efficiency has been established for the first time, which realizes the unity of DMs' subjective judgment with objective data in group decision-making, and truly reflects peer evaluation in cross-efficiency evaluation. To calculate the prospect value, a novel definition of the parameterized interval reference point has been established, along with gain and loss algorithms based on the aspiration level and interval reference point.

In consensus measurement and consensus reaching, a consensus degree measurement model, that is, a conflict degree measurement model based on prospect theory under the cross-efficiency evaluation framework, was established, a weight-updating model based on the contribution degree was established, and an iterative algorithm of consensus reaching was proposed. In group cross-efficiency evaluation, we considered both intragroup and intergroup peer evaluations, proposed a new definition of intergroup cross-efficiency, and established a novel cross-efficiency evaluation model based on prospect theory and decision consensus. By establishing a neutral secondary goal model, the non-uniqueness of cross-efficiency is addressed. Finally, an example considering a supplier evaluation has been provided to verify the effectiveness and practicability of the model in terms of ranking and efficiency evaluation of $DMUs$.

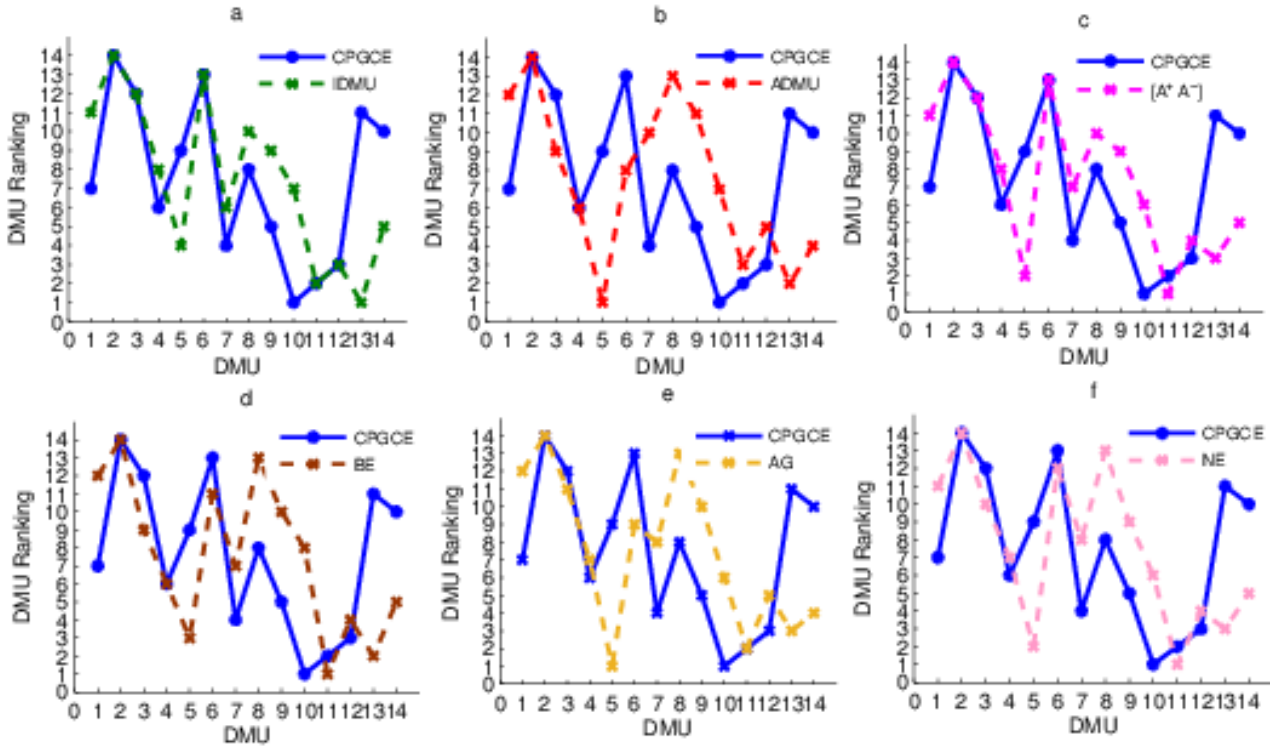

Figure 2 Ranking comparison between proposed method and classical cross-efficiency evaluation

The group cross-efficiency evaluation model proposed herein can be applied extensively in multiple fields, such as supplier evaluation and selection, energy efficiency evaluation, and portfolio selection. Although the model proposed in this study is innovative and versatile, it also involves some limitations. In future studies, we intend to determine the attribute weights of $DMUs$ objectively.

REFERENCES

[1] Bordley, R. F. & Kirkwood, C. W. (2004). Multiattribute Preference Analysis with Performance Targets. *Operations Research*, *52*(6), 823–835.

[2] Cabrerizo, F. J., Moreno, J. M., Pérez, I. J. & Herrera-Viedma, E. (2010). Analyzing consensus approaches in fuzzy group decision making: Advantages and drawbacks. *Soft Computing*, *14*(5), 451–463. https://doi.org/10.1007/s00500-009-0453-x

[3] Doyle, J. & Green, R. (1994). Efficiency and cross-efficiency in DEA:Derivations,Meanings and Use. *Journal of the Operational Research Society*, *45*(5), 567–578. https://doi.org/10.1057/jors.1990.166

[4] He, X. D. & Zhou, X. Y. (2011). Portfolio choice under cumulative prospect theory: An analytical treatment. *Management Science*, *57*(2), 315–331. https://doi.org/10.1287/mnsc.1100.1269

ISBN: 978-618-5765-04-0
ISSN 3057-4269

[5] Herrera-Viedma, E., Herrera, F. & Chiclana, F. (2002). A consensus model for multiperson decision making with different preference structures. *IEEE Transactions on Systems, Man, and Cybernetics Part A:Systems and Humans.*, *32*(3), 394–402. https://doi.org/10.1109/TSMCA.2002.802821

[6] Hsu, H. M. & Chen, C. T. (1996). Aggregation of fuzzy opinions under group decision making. *Fuzzy Sets and Systems*, *79*(3), 279–285. https://doi.org/10.1016/0165-0114(95)00185-9

[7] Kacprzyk, J. & Fedrizzi, M. (1988). A "soft" measure of consensus in the setting of partial (fuzzy) preferences. *European Journal of Operational Research*, *34*(3), 316–325. https://doi.org/10.1016/0377-2217(88)90152-X

[8] Kahneman, D. & Tversky, A. (1979). Prospect Theory:An analysis of decision under risk. *Econometrica*, *47*(2), 263–291.

[9] Lee, H. S. (2002). Optimal consensus of fuzzy opinions under group decision making environment. *Fuzzy Sets and Systems*, *132*(3), 303–315. https://doi.org/10.1016/S0165-0114(02)00056-8

[10] Shi, H. L., Chen, S. Q., Chen, L. & Wang, Y. M. (2021). A neutral cross-efficiency evaluation method based on interval reference points in consideration of bounded rational behavior. *European Journal of Operational Research*, *290*(3), 1098–1110. https://doi.org/10.1016/j.ejor.2020.08.055

[11] Wang, Y. M. & Chin, K. S. (2010). A neutral DEA model for cross-efficiency evaluation and its extension. *Expert Systems with Applications*, *37*(5), 3666–3675. https://doi.org/10.1016/j.eswa.2009.10.024

[12] Xu, Y., Li, K. W. & Wang, H. (2013). Distance-based consensus models for fuzzy and multiplicative preference relations. *Information Sciences*, *253*, 56–73. https://doi.org/10.1016/j.ins.2013.08.029

[13] Xu, Y., Zhang, W. & Wang, H. (2015). A conflict-eliminating approach for emergency group decision of unconventional incidents. *Knowledge-Based Systems*, *83*(1), 92–104. https://doi.org/10.1016/j.knosys.2015.03.013

ISBN: 978-618-5765-04-0
ISSN 3057-4269